DRAFT
EIC PDR
October 3, 2025

Electron Ion Collider
Preliminary Design Report

Contributors:

E-C. Aschenauer[1], R. Ent[2], S. Joosten[3], M. Żurek[3], ADD NAMES AND INSTITUTIONS

[1]Brookhaven National Laboratory, USA
[2]Thomas Jefferson National Accelerator Facility, USA
[3]Argonne National Laboratory, USA

Contents

0 Style Guide **2**

0.1 Chapter Abstract . . . 2
0.2 Wordsmithing . . . 3
0.2.1 Passive voice . . . 3
0.2.2 Verb tenses . . . 3
0.2.3 Apostrophes . . . 3
0.2.4 Capitalization and names . . . 3
0.2.4.1 Pieces of EIC . . . 3
0.2.4.2 Internal phrases . . . 3
0.2.4.3 Discipline-specific approaches or "guiding principles" or buzz phrases . . . 4
0.2.4.4 Formal group names . . . 4
0.2.4.5 Headings . . . 4
0.2.5 Captions . . . 4
0.2.6 Spelling . . . 4
0.2.6.1 Exceptions to U.S. spelling . . . 4
0.2.6.2 Capitalization . . . 4
0.2.7 Commas . . . 5
0.2.7.1 Commas in numbers . . . 5
0.2.8 Plurals and possessives . . . 5
0.2.9 Abbreviations . . . 5
0.2.9.1 Textual treatment of Figures and Tables . . . 5
0.2.9.2 Radio frequency . . . 5
0.2.9.3 etc., et cetera . . . 6
0.2.10 Hyphenation of multi-word adjectival phrases . . . 6
0.2.11 Double letters . . . 10
0.2.12 Mathematical symbols, subscripts and superscripts . . . 10
0.2.13 Quotation marks . . . 10
0.2.14 Citations, references and the bibliography . . . 10
0.2.15 Miscellaneous . . . 11
0.2.15.1 "Calculations show that . . . " . . . 11
0.2.15.2 "Should", "must", and reference to future studies . . . 11
0.2.15.3 "Enable" . . . 11
0.2.15.4 Reporting technical results without a clear statement of their import 11
0.2.15.5 Excessive and inconsistent use of lists . . . 11
0.2.15.6 Cross-references . . . 12
0.2.15.7 Isotopes . . . 12
0.2.15.8 *** asterisks in comments . . . 12
0.3 Dimensions and units . . . 12
0.4 Numbering – chapters, sections, and subsections . . . 13

0.4.1 This is the heading of a subsection . . . 13
0.4.1.1 A subsubsection heading like this has no period at the end . . . 13
This paragraph heading ends with a period. . . . 13
0.4.2 More formatting rules and standards . . . 14
0.4.2.1 Clearpages and Pagebreaks . . . 14
0.5 Equations, Tables, Figures, and plots . . . 14
0.5.1 Equations . . . 14
0.5.2 Tables . . . 14
0.5.3 Converting between LaTeX and Excel table formats . . . 14
0.5.4 Figures . . . 17
0.5.5 Plots . . . 17
0.6 Italics and bold face type . . . 17
0.7 Issues that this Style Guide does not yet address . . . 18

Executive Summary **20**

1 Introduction **21**

2 Detector Requirement **22**

3 Experimental Systems **23**
3.1 Experimental Equipment Requirements Summary . . . 23
3.2 General Detector Considerations and Operations Challenges . . . 24
3.2.1 General Design Considerations . . . 24
3.2.2 Backgrounds and Rates . . . 24
3.2.3 Radiation Level . . . 25
3.2.3.1 Doses and fluences from e+p minimum-bias events . . . 25
3.2.3.2 Doses and fluences from hadron beam+gas events . . . 27
3.2.3.3 Doses and fluences from electron beam+gas events . . . 29
3.3 The ePIC Detector . . . 30
3.3.1 Introduction . . . 30
The Context . . . 30
The Detector . . . 32
Technological Synergistic Aspects of the Detector Design . . . 37
3.3.2 Magnet . . . 38
Introduction . . . 38
Requirements . . . 39
Geometry and Materials of the Yoke . . . 40
Description of the magnet . . . 42
Magnet Design . . . 47
Conductor Design . . . 52
Mechanical Design . . . 53
Transient Analysis and Quench Protection . . . 55
Quench Analysis . . . 57
Cryogenic Design . . . 63
Instrumentation and Controls . . . 68
Summary . . . 70
3.3.3 Tracking . . . 70
3.3.3.1 The silicon trackers . . . 73
Requirements . . . 73
Justification . . . 76

Implementation . . . 81
3.3.3.2 The MPGD trackers . . . 95
Requirements . . . 95
Justification . . . 98
Performance . . . 102
Implementation: . . . 103
Additional Material: . . . 108
3.3.4 Particle Identification . . . 111
3.3.4.1 The time-of-flight layers . . . 115
Requirements and Justifications . . . 115
Implementation . . . 124
Additional Material . . . 135
3.3.4.2 The proximity focusing RICH . . . 136
Requirements . . . 136
Justification . . . 137
Implementation . . . 143
3.3.4.3 The high performance DIRC . . . 152
Requirements . . . 152
Justification . . . 152
Performance . . . 155
Performance Systematic Studies . . . 156
Simulation tools and validation . . . 156
Reconstruction methods . . . 157
Implementation . . . 158
Additional Material . . . 164
3.3.4.4 The dual radiator RICH . . . 165
Requirements . . . 165
Justification . . . 165
Performance . . . 170
Implementation . . . 172
3.3.5 Electromagnetic Calorimetry . . . 183
3.3.5.1 The backward endcap electromagnetic calorimeter . . . 184
Requirements . . . 184
Justification . . . 184
Implementation . . . 190
Additional Material: prototype and beam tests . . . 196
3.3.5.2 The barrel electromagnetic calorimeter . . . 198
Requirements . . . 198
Justification . . . 198
Implementation . . . 208
Additional Material . . . 215
3.3.5.3 The forward endcap electromagnetic calorimeter . . . 221
Introduction . . . 221
3.3.6 Hadronic Calorimetry . . . 233
3.3.6.1 The backward endcap hadronic calorimeter . . . 233
Requirements . . . 233
Justification . . . 234
Implementation . . . 240
Additional Material . . . 248
3.3.6.2 The barrel hadronic calorimeter . . . 251
Requirements . . . 251

Justification . . . 252
Performance . . . 256
Implementation . . . 260
3.3.6.3 The forward endcap hadronic calorimeter . . . 270
Requirements . . . 270
Justification . . . 270
Implementation . . . 275
Additional Material . . . 283
3.3.7 Far-forward detectors . . . 285
3.3.7.1 The detectors in the B0 bending magnet . . . 285
Requirements . . . 285
Justification . . . 286
Implementation . . . 288
3.3.7.2 The roman pots and the off-momentum detectors . . . 291
Requirements . . . 291
Justification . . . 293
Implementation . . . 295
Additional Material . . . 300
3.3.7.3 The Zero Degree Calorimeter . . . 300
Requirements . . . 300
Justification . . . 303
Implementation . . . 304
Additional Material . . . 313
3.3.8 Far backward detectors . . . 313
3.3.8.1 The luminosity system . . . 315
Introduction . . . 315
Requirements . . . 318
Systematic Uncertainties - . . . 319
Justification . . . 319
Implementation . . . 323
Additional Material . . . 325
3.3.8.2 The low Q^2 taggers . . . 325
Requirements . . . 325
Justification . . . 329
Performance . . . 332
Implementation . . . 332
Additional Material . . . 335
3.3.9 Polarimeters . . . 336
3.3.9.1 The electron polarimeters . . . 336
Requirements . . . 336
Justification . . . 336
Implementation . . . 337
Implementation . . . 345
3.3.9.2 Hadron polarimetry systems . . . 348
Overview and Requirements . . . 348
Proton beam polarimetry . . . 350
HJET absolute polarimeter . . . 350
pC fast polarimeters . . . 352
Helium-3 polarimetry . . . 357
Future light ion extensions . . . 358
System integration . . . 358

Critical technical developments . . . 360
Schedule and milestones . . . 361
Quality assessment and workforce . . . 362
Environmental and safety considerations . . . 362
3.3.10 Readout Electronics and Data Acquisition . . . 362
3.3.10.1 Requirements . . . 362
3.3.10.1.1 Requirements from Physics . . . 363
3.3.10.1.2 Requirements from Radiation Hardness . . . 363
3.3.10.1.3 Requirements from Data Rates . . . 363
3.3.10.2 Device Concept and Technological choice: Streaming Readout . . . 366
3.3.10.3 Subsystem Description (components) . . . 368
3.3.10.3.1 ASICS and digitization PCBs . . . 368
3.3.10.3.2 FEB . . . 375
3.3.10.3.3 RDO . . . 376
3.3.10.3.4 DAM - Data Aggregation and Manipulation Hardware 378
3.3.10.3.5 GTU - Global Timing Unit . . . 378
3.3.10.3.6 Protocols . . . 381
3.3.10.3.7 DAQ/Online Computing - Echelon 0 . . . 383
3.3.10.3.8 Slow Controls . . . 385
3.3.10.4 Implementation . . . 386
3.3.10.5 Calibration, alignment and monitoring: . . . 386
3.3.10.6 Status and remaining design effort: . . . 387
3.3.10.7 Environmental, Safety and Health (ES&H) aspects and Quality Assessment (QA planning: . . . 387
3.3.10.8 Construction and assembly planning: . . . 387
3.3.10.9 Collaborators and their role, resources and workforce . . . 388
3.3.11 Software and Computing . . . 388
Computing Use Cases . . . 389
Computing Resources . . . 391
Distributed Computing . . . 398
Project Organization and Collaboration . . . 400
Long Term Software and Computing Plan . . . 401
3.4 Detector Integration . . . 403
Facilities: . . . 403
Platforms: . . . 405
Movement, Alignment and Adjustment: . . . 406
Load Path and Support Structures: . . . 407
Services: . . . 408
3.4.1 Installation and Maintenance . . . 409
Choreography: . . . 409
Installation Sequence: . . . 411
3.5 Detector Commissioning and Pre-Operations . . . 423

4 Detector Performance for the EIC physics program 425
4.1 ePIC and the Science case of the EIC . . . 425
4.1.1 Connecting the Physics Processes to the NAS Science Pillars . . . 425
4.2 Global Performance Considerations . . . 425
4.2.1 Electron Identification . . . 425
4.2.2 Muon Identification . . . 426
4.2.3 Photon Identification . . . 427
4.2.4 Hadron Identification . . . 427

4.2.5 Jet Reconstruction and Calibration . . . 427
4.2.5.1 Jet Energy Scale and Resolution . . . 427
4.3 Incorporation of Beam Backgrounds in the Studies . . . 428
4.4 Physics Processes and Detector Performance . . . 428
4.4.1 Inclusive Processes . . . 429
4.4.1.1 Methods and Reconstruction of Inclusive kinematics . . . 429
4.4.1.2 Detector Impact on key Inclusive physics measurements . . . 431
4.4.1.3 Influence of beam Background on Inclusive measurements . . . 431
4.4.2 Semi Inclusive Processes . . . 432
4.4.2.1 Methods and Reconstruction of SIDIS kinematics . . . 432
4.4.2.2 Detector Impact on key SIDIS physics measurements . . . 432
4.4.2.3 Influence of beam Background on SIDIS measurements . . . 432
4.4.3 Exclusive and Diffractive Processes . . . 433
4.4.3.1 Methods and Reconstruction of Diffractive kinematics . . . 433
4.4.3.2 Detector Impact on key Exclusive and Diffractive physics measurements . . . 433
4.4.3.3 Influence of beam Background on Exclusive measurements . . . 433
4.4.4 Hard Probes . . . 434
4.4.4.1 Heavy Flavor Reconstruction . . . 434
4.4.4.2 Displaced vertex resolution and tracking . . . 434
4.4.4.3 Detector Impact on Key Heavy Flavor Physics Measurements . . . 434
4.4.4.4 Influence of beam on Background on Heavy Flavor measurements 434
4.4.4.5 Jets as a Hard Probe . . . 434
4.4.4.6 Detector Impact on Key Jet Physics Measurements . . . 434
4.4.4.7 Influence of beam on Background on Jet measurements . . . 434

5 Detector-Accelerator interfaces 435

References R-1

List of Figures

1 Example of a non-graphical figure. 17

3.1 Table presenting the Experimental Equipment Requirements Summary in the YR. At present, the table is not updated and it is here as a mere space holder. 23
3.2 Vacuum level at IP6 for three different integrated electron beam currents assumed for the bake-out. 25
3.3 This figure shows the total energy deposited in 2cm x 2cm x 1cm bins spanning the full size of the ePIC central detector from minimum-bias e+p events generated in PYTHIA6 for 10 GeV electrons colliding with 275 GeV protons. This energy combination represents the highest potential luminosity for the EIC. The results are shown as energy deposits per fb^{-1}. 26
3.4 Total ionizing dose per fb^{-1} for the central region of ePIC detector from minimum-bias e+p events. 27
3.5 1 MeV neutron equivalent fluences for the central ePIC detector from minimum-bias e+p events. Peak regions of MEQ fluence are seen near the beam pipe, and within the hadronic calorimeters, where the inclusion of dense absorber materials (e.g. iron) provides ample scattering centers to produce hadronic showers which can include high numbers of low-energy neutrons to provide peak MEQ fluences. . 28
3.6 Fluxes of protons (left) and neutrons (right) with kinetic energy $>$ 20 MeV from minimum-bias e+p events. These fluxes are important to understand areas where detector electronics could often experience SEUs, and require intervention (e.g. re-setting). 28
3.7 This figure shows the total energy deposited in 2cm x 2cm x 1cm bins spanning the full size of the ePIC central detector from hadron beam+gas events with 275 GeV protons. The results are shown as energy deposits per fb^{-1}. 29
3.8 Total ionizing dose from hadron beam+gas events per fb^{-1} for the central region of ePIC detector. 30
3.9 1 MeV neutron equivalent fluences for the central ePIC detector from hadron beam+gas events. Peak regions of MEQ fluence are seen near the beam pipe, and especially near the radial interior of the calorimeters, similar to what is seen in the minimum-bias events. 31
3.10 Fluxes of protons (left) and neutrons (right) with kinetic energy $>$ 20 MeV from hadron beam+gas events. 31
3.11 This figure shows the total energy deposited in 2cm x 2cm x 1cm bins spanning the full size of the ePIC central detector from electron beam+gas events with 10 GeV electrons. The results are shown as energy deposits per fb^{-1}. 32
3.12 Total ionizing dose from electron beam+gas events per fb^{-1} for the central region of ePIC detector. 33
3.13 A schematic showing how hadrons and the scattered electron for different x - Q^2 are distributed over the detector rapidity coverage. THIS FIGURES IS A PLACE HOLDER: IT IS FROM YR AND REQUIRES REVISION. 34

3.14 A schematic showing the ePIC central detector subsystems. THIS FIGURES IS A PLACE HOLDER . . . 35
3.15 Cumulative material budget in radiation lengths (top row) and interaction lengths (bottom row) for the whole CD (left column) and zooming at the CD tracking region (right column). THIS FIGURES IS A PLACE HOLDER BECAUSE IT HAS TO BE COMPLETED WITH SUBSYSTEM CONTOURS AND REQUIRES GRAPHICAL IMPROVEMENTS. . . . 35
3.16 A schematic showing the ePIC far detector subsystems. THIS FIGURES IS A PLACE HOLDER . . . 37
3.17 MARCO Magnet inside the iron yoke. . . . 39
3.18 IR Layout showing all the other magnets . . . 41
3.19 BH curve of 1020 steel . . . 42
3.20 MARCO cold mass layout inside the cryostat. . . . 42
3.21 Schematic cross section of coil pack and conductor . . . 43
3.22 Electric schematic of MARCO Solenoid . . . 44
3.23 Conductor entrance and exit schematic for each module . . . 44
3.24 Design of the Splices exits from the mandrel . . . 45
3.25 Schematic cross-section of the splice to be place inside the groove . . . 45
3.26 Schematics of the geometry at the interface between each coil . . . 45
3.27 Schematics of the tie-rods geometry . . . 46
3.28 Magnet assembly inside the cryostat . . . 46
3.29 Schematics of the cryostat with the magnet inside . . . 46
3.30 The 2D finite element model . . . 47
3.31 Magnetic field on the coil and yoke from 3D OPERA model for the 2.0 T field . . . 48
3.32 Field uniformity in the required area . . . 49
3.33 Projectivity in the required area . . . 49
3.34 5G line around the ePIC yoke. Thanks to the high level of symmetry, the field is the same in both Y and X direction . . . 49
3.35 5G line around the ePIC yoke. Thanks to the high level of symmetry, the field is the same in both Y and X direction . . . 50
3.36 Cross-section of the RICC conductor . . . 53
3.37 Jc curve @4.7 K, load line and load line margin . . . 54
3.38 2D axisymmetric mechanical model including the coils and the mechanical structure 55
3.39 3D model geometry . . . 56
3.40 Scheme of the electric circuit of the MARCO magnet . . . 58
3.41 Current flowing in the magnet and in the mandrel during a fast discharge . . . 58
3.42 Logic structure of the COMSOL quench model . . . 59
3.43 Model used in COMSOL . . . 60
3.44 Current decay in the coils and in the mandrel . . . 60
3.45 Number of quenched turns as a function of time in the three different modules . . . 61
3.46 Resistive coil voltage as a function of time for the three modules . . . 61
3.47 Power dissipated in the primary and secondary circuit . . . 62
3.48 Hotspot temperature in the three modules of the magnet . . . 62
3.49 Temperature distribution on the coils and mandrel after 65s from quench . . . 63
3.50 Cryogenics flowchart of the MARCO solenoid . . . 64
3.51 Schematics of the thermosiphon system . . . 65
3.52 Primary and spare tubes of the thermosiphon heat exchanger . . . 66
3.53 Primary and spare piping on top of the mandrel . . . 67
3.54 Helium phase separator and cryogenic chimney overview. . . . 67

3.55 Relative momentum resolution versus total momentum for charged pions (points) together with physics requirements (curves) in different pseudorapidity ranges as indicated. The results are based on full GEANT simulations of the central tracking system (SVT+MPGD+AC-LGAD) using the ePIC software stack and ACTS-based track finding and reconstruction using suitably tuned ACTS parameter settings. The error bars indicate the size of the statistical uncertainties in the simulation. 72
3.56 Distance of closest approach in the radial direction between reconstructed charged pion trajectories and the event origin versus transverse pion momentum (points) together with physics requirements (curves) in different pseudorapidity ranges as indicated. The results are based on full GEANT simulations of the central tracking system (SVT+MPGD+AC-LGAD) using the ePIC software stack and ACTS-based track finding and reconstruction. The error bars indicate the size of the statistical uncertainties in the simulation. 72
3.57 Tracking efficiency versus pseudorapidity η for charged pions with initial momenta of 1 GeV to 20 GeV. 73
3.58 The number of generated charged particles vs. the generated pseudorapidity of those particles (filled black). The number of reconstructed tracks vs. the reconstructed pseudorapidity of those tracks (red crosses). The y axis shows the number of particles (tracks) per pseudorapidity bin per event. The events were generated with a Q^2 minimum of 1 GeV^2; the scattered electron peak can be seen at negative pseudorapidity. The particles (tracks) shown all have a generated (reconstructed) transverse momentum greater than 500 MeV/c. 74
3.59 With 1000 time slices, 2μs each, of mixed DIS and background event samples, The blue bars show the number of good DIS particles – leaving at least 4 hits in the tracking system and originating from within 1 mm (100 mm) from the nominal interaction point in the transverse (longitudinal) direction versus η for different momentum regions. The orange bars show good DIS particles that are successfully reconstructed. The efficiency for each momentum region is calculated as the ratio of the sum. 75
3.60 Similar to Figure 3.59, the purity examined all valid tracks with at least 4 hits (blue), and checks how many of them are associated with a good DIS charged particle (orange). 76
3.61 Maps of simulated 1 MeV neutron equivalent fluence (left) and total ionizing dose (right) over the ePIC tracking envelope. This is a conservative estimate assuming 10 years of running at top luminosity with 100% efficient accelerator and detector. The black lines indicate the approximate location of the ePIC SVT detector layers. . 77
3.62 Schematic layout of the ePIC SVT showing the central region consisting of the inner and outer barrel made of three and two cylindrical layers, respectively, together with the endcap regions made of five annuli each. The figure also shows the surrounding Micro Pattern Gas Detector (MPGD) layers and the envelope of the Time of Flight PID detector. 77
3.63 Sketch of the MOSAIX sensor on a 300 mm wafer showing the size of the RSU, LEC, REC and of the full sensor for the three different widths. All positions are in mm. . 79
3.64 Left: A close-up of a beam telescope constructed using six single-RSU sensors from the ITS3 Engineering Run 1, with a seventh sensor, the Device Under Test (DUT), placed in the middle. Right: Comparison of results from beamtests at FNAL and from simulations for the cluster extent as a function of the beam incident angle onto the DUT. 81
3.65 Schematic overview of data and slow control lines to groups of up to four EIC-LAS in the OB and disks. 82

3.66 SVT global support structure, consisting of a surrounding carbon composite support tube and a projective arrangement of spokes that form cones connecting the IB, OB, and innermost disks. Also shown are several outer disks and the beampipe. . . 85
3.67 Left: CAD representation of the IB global support (top) and IB half-barrel CAD view with sensors and cable routing (bottom). Right: Exploded CAD view of IB. The sensors are shown in light green and cables in dark green. The orange element is the kapton shield. Air conveyors are shown in blue. 86
3.68 Left: OB staves for L3 and L4. Two staves per layer are shown. Right: Exploded view of an OB stave. 86
3.69 CAD model of the preliminary (half-) disk design. Modules are shown in alternatingly inward (dark gray) and outward (white) facing orientations. Common bus FPCs are shown in orange. RDOs (green) are arranged on the outside of the disk ring, inside of the interface to the SVT global support structure. 87
3.70 Co-cured support structure of first L4 quarter length stave prototype (without silicon sensors). The co-cure comprises carbon fibre skins, K9 cross ribs, central carbon fibre I beam spar and Kapton side closeouts (compare to fig. 3.68). 89
3.71 Left: Test pieces created with carbon composite corrugated disk core made in the LBNL composite shop. Heaters with two different heating zones that can mimic the sensor power density are placed on a carbon composite facesheet and then glued to the corrugation. Right: Temperature along the corrugation at various distances from the air inlet. The blue curve shows the measured temperatures of the single corrugation test piece on the top left. The orange dashed line is the FEA calculation for the same air temperature and velocity. 90
3.72 An example of a low technology readiness level prototype for the FPC of the OB L4. Prototype made by RPE LTU. The figure shows the main FPC with four bridge FPCs. 91
3.73 ePIC Tracking Subsystems 96
3.74 Nhits 96
3.75 Radiation dose 97
3.76 [CyMBaL CAD model](a) CyMBaL CAD model showing the assembly of the 32 modules. (b)CAD model of a CyMBaL module. The light blue represents examples of readout strips measuring the $r \cdot \varphi$ coordinate (called Z-strips as they run along the z axis). The light yellow represents examples of readout strips measuring the z coordinate (called C-strips as they are arcs of a cylinder). The light red lines represent examples of trail lines to bring the C-strip signals to the FEBs. For the explanation of the services see the text. 99
3.77 (a) μRWELL-BOT in ePIC central detector; (b) Arrangement of 24 μRWELL-BOT modules in dodecagon shape. 99
3.78 Hadron and lepton beam pipes and μRWELL-ECT disks layout. 101
3.79 Integration of the MPGD-ECT disks in the ePIC detector. 104
3.80 Design details of MPGD-ECT disks 105
3.81 MPGD General Timeline 106
3.82 Lorentz angle for different gas mixtures 108
3.83 μRWELL-BOT φ-module design view 109
3.84 Thin-gap GEM-μRWELL hybrid vs. std μRWELL detector 110
3.85 The histogram shows the relative yield of charged hadrons from Pythia simulations for 18×275 GeV ep collisions as a function of momenta and pseudorapidity, η. The contours indicate the 3σ separation region of the different ePIC PID subsystems for π/K (a), K/p (b), and e/π (c), respectively. 113
3.86 EPIC magnetic field map with the PID detector envelopes overlaid. Shown is the 1.7 T setup. 114

3.87 (a) Estimates of the 1-MeV neutron equivalent fluence in cm^{-2}/fb^{-1} and (b) the sum of electromagnetic and charged-hadron doses in $rads/fb^{-1}$ integrated in 1 fb^{-1} equivalent Pythia events for 10×275 GeV ep collisions. The values shown are averaged over the azimuthal angle. . . . 115
3.88 Geometries of BTOF with strip sensors and FTOF with pixel sensors. . . . 116
3.89 BTOF $1/\beta$ as a function of momentum (p) in the simulation performance with PYTHIA DIS events (left). Upper limits on the 3σ particle separation from BTOF and FTOF as a function of pseudorapidity (right). . . . 117
3.90 Fluence accumulated for 6 months at 100% time, corresponding to one year of data taking, the fluence has to be multiplied by the assumed 10 years of lifetime of the ePIC detector. Red squares highlight the barrel, endcap, and B0 tracker detectors. Simulation from Fluka. . . . 118
3.91 A schematic design of service hybrids for FTOF, which serves 3 modules or 12 sensors/ASICs. . . . 122
3.92 A schematic design of the module for FTOF, which consists of 2×2 AC-LGAD sensors and ASICs. . . . 123
3.93 Schematic of the AC-LGAD subsystem readout chain. Each component is undergoing design, (pre-)prototyping, testing under various environments, and customization to meet the specific requirements of individual subsystems. . . . 123
3.94 schematic drawings of the cooling pipes in one BTOF stave (left) and half of the whole FTOF (right). Each BTOF stave has one input line and a return line, while the FTOF has a total of 4 input lines and 4 return lines. . . . 124
3.95 BTOF supporting mechanical structure with engagement rings situated and supported by the EPIC global support tube structure (GST). The width of each of the three engagement rings is 5 mm. . . . 126
3.96 Left: Picture and beam test results for HPK strip sensor, 1 cm long, 500 μm pitch, and 50 μm metal electrode width. Right: Picture and beam test results for HPK pixel sensor, 4x4, 500 μm pitch, and 150 μm metal electrode width. Sensors were read out by an FNAL 16ch board, plots from Ref. [1]. . . . 128
3.97 Left: Degradation of the gain layer for AC-LGADs of several wafers (with different n+, oxide, and active thickness) from HPK latest sensor production, showing no change in gain layer doping up to 10^{13} Neq, which is an order of magnitude over the ePIC TOF radiation requirement. Sensors were irradiated at the TRIGA reactor (Lubjiana) with 1 MeV neutrons. Right: Normalized comparison of response profile of two nearby strips for two HPK 0.5 cm length, 500 μm pitch, 50 μm strip width: one before irradiation and one after 1×10^{14} Neq. Even if the total signal is degraded, the charge-sharing profile will remain unchanged. Bottom: Current over voltage measurement for irradiated HPK sensors. . . . 129
3.98 Left: FCFD Jitter measurements with 3.5 pF input capacitance and charge injection. Right: EICROC Discriminator jitter versus the injected charge, determined from data on an oscilloscope. Plots from the eRD112 and eRD109 2024 reports. . . . 130
3.99 Picture of ppRDO connected with CMS ETL module board v0 for testing. . . . 130
3.100 Assembled BTOF stave prototype at Purdue. . . . 131
3.101 Assembly process of BTOF stave. The drawing is not to scale. . . . 132
3.102 Assembly process of FTOF modules. RB3 type is shown as an example. The drawing is not to scale. . . . 133
3.103 Collaboration institutions and their potential responsibilities. . . . 134
3.104 simulation of $1/\beta$ as a function of particle momentum for BTOF and FTOF performance. . . . 136
3.105 The proposed pfRICH detector. See the text for more details. (Figure documentation) 139

3.106 HRPPD photosensor CAD model with a passive interface board. Compression interposers between anode base plate and this PCB are not shown. (Figure documentation) . . . 139
3.107 Left: EIC HRPPD QE as a function of wavelength. Center: QE map in the full active area at a wavelength of 365 nm. Right: Single photon timing resolution measured using Elmo 780 femtosecond laser with a wavelength of 390 nm. (Figure documentation) . . . 140
3.108 (Left) The reconstructed Cherenkov angle for electrons, pions, kaons, and protons as a function of momentum. (Middle) N_σ separation between the electron and pion hypotheses as a function of momentum. (Right) Same as the middle panel, for pion and kaon hypotheses. (Figure documentation) . . . 142
3.109 (left) Yield ratio of π^-/e_{scat} before (open black squares) and after (black full squares) pfRICH veto on π^- in PYTHIA 6 e+p collisions at 18×275 GeV for $-3.0 < \eta < -2.5$. (right) Kaon candidates identified using the pfRICH (full markers) in MC DIS e+p collisions at 18 × 275 GeV in PYTHIA 8. The open markers show contributions from correctly identified kaons and other hadrons misidentified as kaons. (Figure documentation) . . . 142
3.110 Left: Aerogel transmittance as a function of wavelength for factory, BNL, and Temple University measurements. Right: Mirror sample reflectivities as measured at BNL as a function of wavelength. (Figure documentation) . . . 144
3.111 Left: optical setup of an existing HRPPD QA station at BNL. Right: optical table of the future full size mirror QA station at BNL. See text for more details. (Figure documentation) . . . 148
3.112 ePIC hpDIRC geometry in the Geant4 standalone simulation. . . . 153
3.113 a) Schematic of the side view of one hpDIRC section and an exploded view of the 3-layer lens. b) Photo of prototypes of the 3-layer spherical lenses. c) Photec AuraTek MAPMT253 MCP-PMT. . . . 154
3.114 The expected performance of the hpDIRC as a function of the particle polar angle in terms of photon yield (a) for pions and π/K separation power (b). These results are based on a standalone Geant4 simulation of 6 GeV/c particles. Repository: `https://github.com/rdom/eicdirc/tree/master/macro/tdr_hpdirc` . . . 155
3.115 Photographs of the PANDA Barrel DIRC prototype (a), including a close-up of the readout section (b) taken during the CERN test beam. Performance plots illustrating the comparison between simulated and experimental data for photon yield (c) and single photon Cherenkov angle resolution (SPR) (d). . . . 157
3.116 Technical drawings of the ePIC hpDIRC detector, showing the XY cross-section of the bar box (a) and the YZ cross-section of the connection between the bar box and the readout box (b). . . . 158
3.117 ePIC hpDIRC schedule chart alignment with EIC Project schedule . . . 161
3.118 Photos of available setups developed during the hpDIRC R&D program that will be used for future QA of 3-layer lenses with laser setup at ODU (a), bars and other optics at Jefferson Lab (b) and readout chain including sensors and electronics and other hpDIRC components in hpDIRC prototype at CRT at SBU (c). . . . 162
3.119 (Left) dRICH detector model with highlighted the major components. (Center) Model of the dRICH photodetector unit (PDU) module with its major components highlighted. (Right) dRICH detector box model with 208 PDUs forming a curved active surface. . . . 166

3.120 (Left) Dark current measurements on sample SiPM sensors for the studies of repeated irradiation-annealing . (Right) Projected increase of the DCR of SiPM as a function of the integrated luminosity (delivered fluence) for the PDU closer to the beam pipe (worst case scenario). The "no annealing" and the "annealing limit" curves show the limits of possible operations. The dashed line indicate the desired maximum DCR threshold. 167
3.121 (Left) Transverse map of the expected 1-MeV equivalent neutron fluence per 1 fb^{-1} of integrated luminosity in e+p interactions at the maximum EIC center-of-mass energy at the location of the dRICH photodetector ($210 < z < 260$ cm). The average, maximum and minimum values within the region of the dRICH photodetector ($100 < R < 180$ cm, indicated by the dashed lines) are reported. (right) Block diagram of the dRICH gas system. 170
3.122 (Left) Contributions to the single-photon angular resolution for aerogel. (Right) Contributions to the single-photon angular resolution for radiator gas. 171
3.123 (Left) Reconstructed mass vs momentum for pions, kaons and protons. (Right) Reconstructed mass vs momentum for pions and electrons. Distinct values derived from aerogel and gas are shown, to highlight the complementary coverage and effective interplay of the two radiators. The study is performed at the large rapidity endpoint $3.2 < \eta < 3.5$. 172
3.124 (Left) dRICH mechanical model. (Center) Service routing around the dRICH. (Right) Installation and exctraction tool. 173
3.125 (Left) Test stand for SIPM characterization. (Center) Performance comparison between different SiPM models. (Right) Prototype version of the SiPM carrier board (top) and FEB (bottom). 174
3.126 (Left) Fraction of residual irradiation damage measured on multiple SiPM candidate samples after "forward-bias annealing" cycles at increasing temperature and integrated annealing time. The measurements are shown for individual sensors (gray points) and as averages (coloured points, uncertainty of the average and RMS are indicated on the plot). (Right) Temperature increase of the SiPM sensor with respect to the temperature of the SiPM carrier board as a function of the "forward-bias annealing" power at different temperature values of the circulating thermostat system. 175
3.127 (Left) C_2F_6 measured transmittance in the near UV-region. (Center) Aerogel tile real-size demonstrator. (Right) Mirror demonstrator with an optimized dRICH core structure. 176
3.128 (Left) Baseline prototype with reference multi-anode PMT sensors at the SPS-H8 beam line of CERN. (Center) First ePIC-drive SiPM detector box under test at the PS-T10 beam line of CERN. (Right) Real-scale prototype model mimicking the basic dRICH construction unit (sector). 177
3.129 (Left) Cherenkov angular resolution obtained for C_2F_6 as a function of the recorded number of photons. The SPE values is consistent with expectations. (Center) SPE angular resolution measured on aerogel as a function of the refractive index. The expected resolution is obtained for an index greater than n=1.025. (Right) Comparison in photon yield of sensor with different SPAD size. All the measurements has been obtained with the dRICH prototype. 178
3.130 (Left) Prototype PDU and assembled detector plane. (Center) Cumulated ring imaging for a mixed hadron beam at 10 GeV/c. (Right) Dual-radiator interplay at 10 GeV/c: After the gas information is used to tag pions (clear histogram), an effective separation between kaon an proton is provided by the aerogel (shaded histogram). 178
3.131 dRICH construction timeline 181

3.132 CAD drawing of the backward ECal attached to the Global Support Tube (GST) by means of rails. The outer structure shows the external cooling using Friction Stir Welding (FST) technology. The shape of the inner support structure is optimized to maximize the pseudo-rapidity coverage around the beam pipes. 187
3.133 Conceptual design of the ePIC electron endcap electromagnetic calorimeter support. 188
3.134 Left: waveform (top) and integrated signal (bottom) showing single photo-electron signals in Hamamatsu 15 um pixel SiPMs. Signals are produced with a low-intensity LED. Right: Linearity measurement, showing 2% linearity up to 3500 photo-electrons. 188
3.135 PCB holding the 16 SiPMs of a PWO-II crystal. An SMC LED is mounted on each PCB (the white component centered at the bottom of the board in this figure). . . . 189
3.136 EEEMCal performance estimated from single particle simulations using the full ePIC detector geometry. Left: energy resolution as a function of the incident particle energy. Right: pion rejection factor as a function of energy and different values of electron efficiency. (Performance plots were produced by the backwards_ecal benchmark) 190
3.137 Left: Layout of the EEEMCal subsystem showing the external and internal cooling plates (yellow), a front copper plate, and some insulating barrier (blue) between the crystals and the heat source (FEBs, inside cooled boxes). Right: Simulated temperature distribution of crystals in stationary mode with plates at 19° C and room temperature of 26° C. A uniform heat source of 1 kW is assumed behind the crystals. 192
3.138 Steady-state simulation at 2 different room temperatures. Data show the temperature difference across the detector for different configurations of the cooling system. The nominal configuration (dark green) shows the best performance and yields a maximum temperature variation of 0.4° C in the central crystals. 192
3.139 Left: Transient-state simulation showing the temperature variation of crystals as a function of time for a room temperature variation from 26° C to 23° in 6 hours. The thermal inertia of crystals is sufficiently high that the temperature variation of all of them is below 0.1° C. Right: typical temperature variations in IP6 as measured by the STAR experiment. Temperature is constant within $\pm$1.5° C within a few hours. 193
3.140 Temperature variation of PWO crystals measured in the NPS calorimeter, consisting of 1080 PWO crystals and 500 W FEBs. The cooling concept used for this detector is similar to the one planned for the ePIC backward ECal, and shows that the required crystal temperature stability is achieved. 193
3.141 EEEMCal installation fixtures that allow for installing the detector safely into the ePIC detector barrel. 194
3.142 Backward ECAL 5$\times$5 crystal prototype and full readout 400-channel electronic chain based on the HGCROC chip. 196
3.143 Waveforms for a 5-GeV electron in the 16 SiPM of a PWO crystal 197
3.144 Structure of Barrel Imaging Calorimeter and its sectors. 199
3.145 Components of Barrel Imaging Calorimeter imaging AstroPix layers. 200
3.146 Sketch of the mechanical envelopes for the BIC ESB. 200
3.147 Simulated energy resolution and sampling fraction for photons in different rapidity ranges of BIC. 204
3.148 Simulated angular resolutions for photons at BIC. 205
3.149 Simulated performance on particle identification from BIC 206
3.150 Simulated performance on MIP response in BIC 207
3.151 Example performance of AstroPix_v3 chip 209
3.152 Barrel Imaging Calorimeter high-level schedule for design and production phases. 216
3.153 Simulated energy response of photons and electrons in Pb/ScFi and energy response tail in different rapidity range of BIC. 217

3.154 Simulated energy resolution and sampling fraction for electrons in different rapidity ranges of BIC. . . . 218
3.155 Low-energy photon response in BIC at $\eta = +1$. . . . 218
3.156 Measured energy responses in Baby BCAL to positrons and pions 219
3.157 Barrel Imaging Calorimeter org chart. . . . 220
3.158 The front face of the ePIC hadron end-cap. . . . 223
3.159 Matrix of scintillating fibers prepared to build production FEMC blocks and SEM image of tungsten powder. . . . 224
3.160 Front and back views of LG plates with installed SiPMs. . . . 226
3.161 Structural and installation tests at BNL. . . . 227
3.162 Response of calorimeter vs position in hodoscope (left panel). Energy resolution for different impact angles (right panel). . . . 228
3.163 Signal (single photon) efficiency and background (merged di-photons) contamination for different cut value of the NN output for 60 GeV (left panel). Probability of misidentifying π^0 as a single photon vs energy (right panel) 229
3.164 FEMC front end electronics. . . . 230
3.165 Neutron detection efficiency vs. E and thresholds 235
3.166 Position resolution R_{xy} and cluster efficiency vs. E for different tile sizes 236
3.167 Ratio of e/π response vs. E 236
3.168 **Top:** Primary, generated particle E distributions in nHCal acceptance $-4.0 < \eta < -1.0$. **Bottom:** Primary, generated particle p distributions in nHCal acceptance $-4.0 < \eta < -1.0$. Repository: `https://github.com/OSUNuclearPhysics/ePIC_preTDR_nHCal_DIS_MCPart` 237
3.169 **Top:** Primary, generated particle E distributions in $-2.0 < \eta < -1.0$ range. **Bottom:** Primary, generated particle p distributions in $-2.0 < \eta < -1.0$ range. Repository: `https://github.com/OSUNuclearPhysics/ePIC_preTDR_nHCal_DIS_MCPart` . . . 238
3.170 **Top:** Primary, generated particle E distributions in $-3.0 < \eta < -2.0$ range. **Bottom:** Primary, generated particle p distributions in $-3.0 < \eta < -2.0$ range. Repository: `https://github.com/OSUNuclearPhysics/ePIC_preTDR_nHCal_DIS_MCPart` . . . 239
3.171 **Top:** Primary, generated particle E distributions in $-4.0 < \eta < -3.0$ range. **Bottom:** Primary, generated particle p distributions in $-4.0 < \eta < -3.0$ range. Repository: `https://github.com/OSUNuclearPhysics/ePIC_preTDR_nHCal_DIS_MCPart` . . . 240
3.172 Acceptance of photoproduced $J/\psi \to \mu^+\mu^-$ in $e+p$ collisions at $18+275$ GeV. **Top left:** Acceptance vs. μ_1 and μ_2 hitting different HCals. **Top Right:** Acceptance vs. $-t$ for different number of μ in nHCal. **Bottom Left:** Acceptance vs. Bjorken x_{bj} for different number of μ in nHCal. **Top Right:** Acceptance vs. Pomeron x_P for different number of μ in nHCal. Repository: `https://github.com/OSUNuclearPhysics/ePIC_preTDR_nHCal_VM_Sartre_kine` 241
3.173 Acceptance of photoproduced $J/\psi \to \mu^+\mu^-$ in $e+p$ collisions at $20+100$ GeV. **Top left:** Acceptance vs. μ_1 and μ_2 hitting different HCals. **Top Right:** Acceptance vs. $-t$ for different number of μ in nHCal. **Bottom Left:** Acceptance vs. Bjorken x_{bj} for different number of μ in nHCal. **Top Right:** Acceptance vs. Pomeron x_P for different number of μ in nHCal. Repository: `https://github.com/OSUNuclearPhysics/ePIC_preTDR_nHCal_VM_Sartre_kine` 242
3.174 Acceptance of photoproduced $\Phi \to K^+K^-$ in $e+p$ collisions at $18+275$ GeV. **Top left:** Acceptance vs. K_1 and K_2 hitting different HCals. **Top Right:** Acceptance vs. $-t$ for different number of K in nHCal. **Bottom Left:** Acceptance vs. Bjorken x_{bj} for different number of K in nHCal. **Top Right:** Acceptance vs. Pomeron x_P for different number of K in nHCal. Repository: `https://github.com/OSUNuclearPhysics/ePIC_preTDR_nHCal_VM_Sartre_kine` 243

3.175 Acceptance of photoproduced $\Phi \to K^+K^-$ in $e+p$ collisions at $20+100$ GeV. **Top left:** Acceptance vs. μ_1 and μ_2 hitting different HCals. **Top Right:** Acceptance vs. $-t$ for different number of K in nHCal. **Bottom Left:** Acceptance vs. Bjorken x_{bj} for different number of K in nHCal. **Top Right:** Acceptance vs. Pomeron x_P for different number of K in nHCal. Repository: `https://github.com/OSUNuclearPhysics/ePIC_preTDR_nHCal_VM_Sartre_kine` . . . 244
3.176 Energy resolution of jets vs. jet energy E compared for inclusive jets(squares) and jets with neutral veto(triangles). Track only jets(blue) are also compared to track and nHCal cluster jets(red). Repository: `https://github.com/OSUNuclearPhysics/ePIC_preTDR_nHCal_neutralJetRes` . . . 245
3.177 **Left:** Acceptance vs. x for 2, 1 and no diffractively produced jets with thrust axis in nHCal acceptance. **Right:** Acceptance vs. inelasticity y for 2, 1 and no diffractively produced jets with thrust axis in nHCal acceptance. Repository: `https://github.com/OSUNuclearPhysics/ePIC_preTDR_nHCal_Diff2Jet_Pythia` . . . 246
3.178 **Left:** Fraction of MC particle pairs per cm as a function of distance between straight line projections of particle pairs onto nHCal surface. **Right:** Fraction of MC particle pairs per cm as a function of distance between straight line projections of neutron paired with X(any particle) onto nHCal surface. Repository: `https://github.com/OSUNuclearPhysics/ePIC_preTDR_nHCal_Diff2Jet_Reco` . . . 246
3.179 **Left:** Fraction of MC truth cluster pairs per cm as a function of distance between clusters created by neutron paired with X(any particle). **Right:** Fraction of reconstructed cluster pairs per cm as a function of distance between clusters created by neutron paired with X(any particle). Repository: `https://github.com/OSUNuclearPhysics/ePIC_preTDR_nHCal_Diff2Jet_Reco` . . . 247
3.180 Position of the reconstructed clusters in x, y for 2-particle position resolution study. Repository: `https://github.com/OSUNuclearPhysics/ePIC_preTDR_nHCal_PosRes` . . . 247
3.181 Ratio of reconstructed, charged hadron corrected cluster energy to the sum of neutron MC energy deposits for different values of the distance between neutron and pion impact points on the nHCal surface. Repository: `https://github.com/OSUNuclearPhysics/ePIC_preTDR_nHCal_PosRes` . . . 248
3.182 Ratio of reconstructed, charged hadron corrected cluster energy to the sum of neutron MC energy deposits vs. neutron MC energy deposits in scintillator tiles only. Comparison for different values of the distance between neutron and pion impact points on the nHCal surface. Repository: `https://github.com/OSUNuclearPhysics/ePIC_preTDR_nHCal_PosRes` . . . 249
3.183 Work organization structure of nHCal project within ePIC. . . . 250
3.184 The charged (black lines), neutral EM (blue lines), and neutral hadron (red lines) fractions of jets at the truth level in $\eta \in (-3.5, 1.0)$ (upper left panel), $|\eta| < 1$ (upper right panel), and $\eta \in (1.0, 3.5)$ (lower left panel). Received from John Lajoie in private communication. . . . 251
3.185 Results of ePIC simulations in the BHCal region: the 1-MeV neutron equivalent (MEQ) fluence from all processes (DIS plus beam gas events) over 15 years of running (150fb^{-1}). . . . 252
3.186 Transverse cutaway view of an sPHENIX Outer HCal module, showing the tilted tapered absorber plates. Light collection and cabling is on the outer radius at the top of the drawing. . . . 253
3.187 Scintillator tiles in a layer of the Outer HCal. . . . 254
3.188 Leakage current in HCal measured once per fill as a function of total number of ZDC coincidence hits . . . 257

3.189 Energy deposited on BHCal tiles (left panels) and reconstructed tile energies (right panels) by single μ^- (top row) and μ^+ (bottom row) as a function of tile pseudorapidity. Muons were simulated using the 2024.11.1 simulation geometry with energies between 2 and 20 GeV. Repository: https://github.com/ruse-traveler/EpicBHCalPTDRStudies 258
3.190 Energy deposited on BHCal tiles (left panels) and reconstructed tile energies (right panels) by all particles in 10×100 (top row) and 18×275 (bottom row) NC DIS events as a function of particle pseudorapidity. Distributions were simulated using the 2024.11.1 simulation geometry with $Q^2 > 1000$ GeV^2. Repository: https://github.com/ruse-traveler/EpicBHCalPTDRStudies 259
3.191 Reconstructed energy of leading BHCal cluster for 1 (green) - 20 GeV (purple) single π^- (left) and π^+ (right) in BHCal-only simulations. Pions were simulated using the 2024.10.1 simulation geometry. Solid lines are Guassian fits. Repository: https://github.com/ruse-traveler/EpicBHCalPTDRStudies 260
3.192 Uncalibrated (top row) vs. LD-calibrated energy (middle row) and MLP-calibrated (bottom row) of lead BHCal clusters for 2 (orange), 5 (pink), 10 (blue), and 20 GeV (purple) π^- (left column) and π^+ (right column). Distributions were simulated using the 2024.10.1 simulation geometry. Repository: https://github.com/ruse-traveler/EpicBHCalPTDRStudies 263
3.193 Linearity (top row) and energy resolution (bottom row) of calibrated single π^- (left column) and π^+ (right column). Red lines indicate LD-calibrated energies, purple lines indicate MLP-calibrated energies, black lines indicate the linearity, resolution of summing BHCal clusters without calibration. Distributions were simulated using the 2024.10.1 simulation geometry. Repository: https://github.com/ruse-traveler/EpicBHCalPTDRStudies 264
3.194 Uncalibrated (to left) vs. LD-calibrated energy (top right) and MLP-calibrated (bottom) of lead BHCal clusters for 2 (orange), 5 (pink), 10 (blue), and 20 GeV (purple) neutrons. Distributions were simulated using the 2024.10.1 simulation geometry. Repository: https://github.com/ruse-traveler/EpicBHCalPTDRStudies 265
3.195 Linearity (left) and energy resolution (right) of calibrated single neutrons. Red lines indicate LD-calibrated energies, purple lines indicate MLP-calibrated energies, black lines indicate the linearity, resolution of summing BHCal clusters without calibration. Distributions were simulated using the 2024.10.1 simulation geometry. Repository: https://github.com/ruse-traveler/EpicBHCalPTDRStudies 266
3.196 ratio of uncalibrated lead BHCal cluster to the sum of all BHCal clusters for 2 (grey) - 10 GeV (blue) single neutrons. Distributions were simulated using the 2023.06.1 simulation geometry. Repository: https://github.com/ruse-traveler/EpicBHCalPTDRStudies 267
3.197 **JES/R for full (tracks + ECal + HCal):** The JES $-1 = \langle \Delta p/p \rangle$ (open markers) and JER (closed markers) plotted as a function of p_{jet} in the lab frame for jets in $\eta \in (-3.5, 1.0)$ (red points), $|\eta| < 1$ (black points), and $\eta \in (1.0, 3.5)$ (blue points). In the barrel region, jets are constructed from reconstructed tracks and ECal clusters *without* a nearby track. Neutral hadrons are included in the jets by smearing the particle energy by the measured energy resolution of the sPHENIX OHCal. Jets are reconstructed via the Centauro algorithm (R = 0.8) and transformed back into the lab frame. Jets are required to have at least 2 particles, and exclusively charged or neutral jets are rejected. From ECCE responses to the EIC DPAP Panel; received from John Lajoie in private communication. 268

3.198 JB variables at truth ("vertex", black) and reconstructed level for particle $|\eta| < 3.5$ (blue) and $|\eta| < 4$ (red) in 18×275 CC DIS events. Detector simulation and reconstruction was carried out using a fast simulation using Delphes. Figure 8.21 from the EIC Yellow Report. 268
3.199 **Truth vs. reconstructed $E_{\mathrm{T}}^{\mathrm{miss}}$:** the truth (x-axis) vs. reconstructed (y-axis) $E_{\mathrm{T}}^{\mathrm{miss}}$ for 10×275 CC DIS events. Detector simulation and reconstruction was carried out using a fast simulation using Delphes. Figure 4 from arXiv:2006.12520. 269
3.200 Renderings of the forward calorimeter assembly (top left), tile assembly of 8 scintillator tiles of the LFHCal with the SiPMs sitting in a dimple on each tile, detailed stacking example (middle right) and 8-tower module design (bottom). 272
3.201 Renderings of the absorber structure for the insert modules surrounding the beam pipe (top) and their individual layer composition (bottom). 273
3.202 Left: Visualization of 8M-scintillator assembly with its individual components. Right: Samples of the individual components used for the 2024 test beam campaign. 273
3.203 Combined energy resolution of the forward calorimeter system as a function of pseudo rapidity η for single pions, evaluated within the primary LFHCal acceptance. These results are obtained using the graph-neural network approach described in Ref. [2]. 275
3.204 Combined position resolution of the forward calorimeter system as a function of pseudo rapidity η for single pions, evaluated within the primary LFHCal acceptance. These results are obtained using the graph-neural network approach described in Ref. [2]. 276
3.205 Visualization of the individual components of an 8M module. 276
3.206 Visualization of the full LFHCal in its cradle (top) and details of its moving mechanism (bottom). 278
3.207 General timeline of the LFHCal design, construction and assembly. 281
3.208 Organizatorial chart of the LFHCal & insert consortium, indicated by the numbers are the associated WBS structures. 284
3.209 All four far-forward subsystems in the outgoing hadron beam direction. The green cylinders are accelerator dipole and quadrupole magnets. 285
3.210 Left: A cutaway view of the detectors in the B0 magnet. The beampipes are shown in blue and gray, the four tracking detectors are dark brown and the calorimeter is gray (the figure orientation is such that IP is to the left of the magnet). Right: The transverse profile of the calorimeter in the B0 magnet. Both figures are from the DD4HEP implementation of the detectors. 286
3.211 A simulation of the expected number of pixel hits for a 6x6 mm^2 SiPM coupled to a $PbWO_4$ crystal as function of the energy of a photon impinging on the crystal. An ideal SiPM response is shown as well as the response of a 10 μm pitch SiPM with 18% photo-detection efficiency and a 15 μm pitch SiPM with 32% photo-detection efficiency (matching the specs of S14160-6010PS and S14160-6015PS). The realistic SiPM responses are shown with and without occupancy effects. 287
3.212 Left: The B0 tracker's acceptance of protons (E=110 GeV), as a function of θ_x and θ_y. Right: The top panesl shows the reconstructed vs generated proton p_T. Each slice of this distribution is fit to a Gaussian function and from this fit a resolution (middle panel) and bias (bottom panel) are extracted. 288
3.213 Proton acceptance as a function of η spanning the central tracker, B0 tracker, and Roman Pots. 289

3.214 The B0 EM calorimeter's acceptance of photons shown for soft (less than 5 GeV) and hard (greater than 60 GeV) photons. Acceptance is defined as more than 100 MeV deposited in the calorimeter. The position of the calorimeter crystals is indicated as a grid. The un-instrumented regions which nevertheless high nominal acceptance, correspond to upstream interactions whose shower products are visible in the B0 calorimeter. 289
3.215 The energy reconstructed and associated resolution for the B0 EM calorimeter of photons with $\theta < 13$ mrad in the soft (left) and hard (right) energy reconstruction regimes. The top panels show the reconstructed photon energy vs the generated energy. Each slice of this distribution is fit to a Gaussian function and from this fit a resolution (middle panels) and energy scale shift (bottom panels) are extracted. . . 290
3.216 Depiction of the envelopes from protons with $x_L \sim 1.0$ (left) and with $x_L \sim 0.5$ (right). The RP and and OMD systems are placed to obtain an almost-continuous acceptance of protons across a broad range of proton rigidities. 292
3.217 Summary of transverse momentum resolutions for the Roman pots and off-momentum detectors using stand-alone detector simulations. Contributions are separated by those induced by intrinsic detector choices (e.g. pixel sizes) and those from beam effects (e.g. angular divergence), which have an outsized impact on momentum measurements at very-forward rapidity. 295
3.218 Transverse momentum resolution for Roman pots using the full ePIC simulation framework. This plot is from the ePIC framework, where Fig. 3.217 shows performance from standalone simulations which include beam effects and optimized matrix reconstruction, shows both the nominal performance with the current reconstruction algorithm (in blue), and (in red) the expected improvement from the machine learning model which has been developed and tested in standalone simulations. This ML algorithm (based on deep neural networks) is currently being implemented in ePIC. A presentation on this work and the resulting performance of the model was presented at the Deep-Inelastic Scattering conference in 2023 [3]. Work is underway to integrate this model into the ePIC framework for RP and OMD reconstruction. 296
3.219 Strawman concept for the layout of the RP and OMD sensor staves. Work is ongoing to get the necessary electronics engineering support to design the final PCB. The connector on the end of the PCB is presently assumed to be a TE connectivity Erni 354096-E 32 pin serial connector. Work is still needed to understand how to apply thermal cooling to the staves without using compressed gases or liquids (not allowed in the primary machine vacuum). Presently, cooling plates/heat sinks which are thermally coupled to outside the vacuum and cooled with an LN2 chiller are assumed, but only preliminary thermal analysis has been carried out. 297
3.220 Strawman concept a readout board concept to communicate with and readout RP and OMD sensor staves. Work needs to be done to solve the issue of power distribution, and to ensure the EICROC ASIC can indeed be readout by the lpGBT. 297
3.221 Current layout of a single RP layer using a 1x3 stave configuration, with the staves following the concept shown in Fig. 3.219. This configuration leads to a full detector layer with dimensions $\sim$ 26cm x 10cm, with some work to be done to finalize the exact amount of overlap between individual staves to provide uniform acceptance in the transverse plane. 298
3.222 Depiction of the location of the RP sensor packages for the three different "main" EIC hadron beam energies, all in the optics configuration with the maximal low-p_T acceptance. Optimization of the stave layout and movement stages is still underway to ensure best fiducial acceptance. 298
3.223 SiPM-on-tile ZDC. 305

3.224 SiPM-on-tile ZDC modular design is composed of quadrants. 306
3.225 ZDC mechanical 306
3.226 Left: ZDC neutron-shower position resolution for neutrons as a function of the generated energy. Results are shown with an unstaggered layout (blue) and staggered layout with the positions reconstructed with the baseline (orange), HEXPLIT (green), and GNN (red) reconstruction algorithms. Right: Energy resolution (top row) and scale (bottom row) obtained with the strawman (open symbols) and GNN (filled symbols) for simulated single neutrons. The resolutions are compared to those of the CALICE beamtest [?] (orange squares) with (filled) and without (open) software compensation, as well as the CALICE GNN reconstruction (orange diamond) [4]. 307
3.227 Energy resolution (top row) and scale (bottom row) obtained with the strawman (left) and GNN (right), at various ranges in θ. The positions on the face of the detector corresponding to each color are visualized in the inset. 307
3.228 Examples of 4 reconstructed 3D shower shapes in the ZDC for events with 1 neutron ($N_n = 1$), 2 neutrons ($N_n = 2$), 4 neutrons ($N_n = 4$), and 9 neutrons ($N_n = 9$). The color code represents hit energy in terms of E_{MIP}. The marker size is displayed proportionally to hit energy for display purposes. 308
3.229 Energy measured for each integer number of neutrons with energy equal to 100 GeV, reconstructed with GNN (orange) and strawman (blue). The events are weighted by a factor of e^{-N_n}. The black, vertical lines are drawn at the total true energies of events with different numbers of neutrons. Here we show events containing up to nine neutrons. This performance illustrates just instrumental effects, excluding nuclear effects like smearing caused by Fermi motion and fission. In the laboratory frame, these nuclear effects would contribute in quadrature about 5 GeV per 100 GeV neutron, according to BEAGLE [?], which happens to be similar to the widths of the strawman reconstruction shown here. 309
3.230 Topology of Λ^0 decay in neutral-channel decay. Not shown to scale. Figure reproduced from Ref. [5]. 309
3.231 Left: Decay position distribution, for different Λ^0 energies. Middle: acceptance as a function of energy and decay position. Right: Acceptance as a function of energy, integrated over decay position, for Λ^0s along the proton axis (black solid curve) and with varying amounts of transverse momentum (colored dashed curves). Figure reproduced from Ref. [5]. 310
3.232 Top row: event display for example events, with the hits color coded by energy deposited, in units of MIPs. Bottom row: the same events, with subcell hits from HEXPLIT algorithm color-coded by which cluster the subcell hits have been assigned to by the 3D topological clustering algorithm. The olive (cyan) line(s) represent the truth-level trajectories of the incident photons (neutron). Figure reproduced from Ref. [5]. 310
3.233 Distribution of the cluster shape parameters, at three different Λ^0 energies. The red lines show the cuts used to identify the photon clusters. 311
3.234 Left: truth decay position of Λ^0 (x axis), compared to the reconstructed values (y axis). A thin red dashed line is shown at $y = x$. Middle: the decay position resolution as a function of the Λ^0 energy. Right: distribution for the decay positions of reconstructed events for different Λ^0 energies. Figure reproduced from Ref. [5]. . . 311
3.235 Left: distribution for the reconstructed Λ^0 mass before (red) and after (blue) fitting the vertex position with the IDOLA algorithm. Middle: Same for the reconstructed Σ^0 mass. Right: the Λ^0 (Σ^0) mass resolution as a function of the Λ^0 (Σ^0) energy. Figure reproduced from Ref. [5]. 312

3.236 Energy resolution as a function of the Λ^0 energy. For comparison, the values obtained in Ref. [6] for single neutrons are shown in gray. Figure reproduced from Ref. [5]. . . . 312
3.237 Left: Polar angle resolution for Λ^0 (filled symbols) and neutrons (open symbols) with baseline reconstruction and GNN reconstruction. Right: The resolution for reconstructing the transverse momentum for Λ^0 (filled symbols) and neutrons (open symbols) using a GNN at 150 GeV (blue) and 250 GeV (orange). These values reflect the resolution without beam effects. The beam effects terms for σ_{beam}=150 μrad are shown as dashed curves. Figures reproduced from Ref. [5]. . . . 313
3.238 Assembly of a ZDC prototype representing approximately 10% of the full ZDC size. 314
3.239 The layout of the luminosity monitor in the ZEUS experiment [**?**]. . . . 315
3.240 Relative suppression due to the beam-size effects $(d\sigma_{corr}/dy)/(d\sigma_{BH}/dy)$ is shown as a function of $y = E_\gamma/E_e$ for three cases of collider parameters, HERA, EIC 1 & EIC 2. The corresponding beam energies and Gaussian lateral beam sizes at the interaction point are listed. Figure from Ref. [**?**]. . . . 317
3.241 Unpolarised Bethe-Heitler cross-Section (left panel) and the polarised component (right panel), calculated in Ref. [**?**] . . . 318
3.242 Luminosity system layout showing the Direct Photon Detector and Pair Spectrometer, as well as the sweeper and analyzing magnets. . . . 320
3.243 Pair Spectrometer calorimeters and their components: (1) The two Pair spectrometer calorimeters; (2) one layer, made out of three modules, with the fibers oriented perpendicular to the beam direction (the orientation of the fibers alternate from horizontal to vertical); (3) one module; (4) zoomed-in view of a set of 16 fibers which are read out by a SiPM. . . . 321
3.244 PSCal sampling fraction as a function of incident electron energy. Events incident on the top or bottom 2cm of the front face of the calorimeter have been excluded in this sample. This selection cut removes events where the full shower is not contained within the calorimeter. . . . 322
3.245 PSCal energy resolution as a function of generated electron energy. In this study, monoergetic electrons (at the discrete values shown) were generated at the front face of the calorimeter. . . . 322
3.246 Rate of single and coincidence events for the PS detectors. . . . 323
3.247 Multiple fibers threaded through a pair of brass meshes. . . . 324
3.248 (a) Tungsten powder and epoxy-only test module. (b) A section of another test module showing the interior. . . . 324
3.249 Left: Low-Q^2 taggers in relation to beamlines and central detector. Right: Tagger module with calorimeter and tracker from recent CAD model. . . . 326
3.250 Acceptance ranges of the Central Detector and Low-Q^2 Trackers as function of Q^2 and x. . . . 326
3.251 Low-Q^2 tagger coverage. . . . 327
3.252 Hit rates on tracker layers for Quasi Real (Top) and bremsstrahlung (bottom) electrons, incident on Tagger 1 (left) and Tagger 2 (right), This design is based on layers with three carrier boards, each containing twelve Timepix4 hybrid sensors. The dashed lines indicated the centre lines of the Timepix4 ASICS, where the vertical columns terminate. . . . 329
3.253 Maximum and integrated rates for Low-Q^2 trackers. . . . 330
3.254 Layout of SciFi calorimeter. . . . 331
3.255 Energy resolution for Cherenkov fiber calorimeter. . . . 332
3.256 Top - Reconstruction of the initial electron energy, θ and ϕ angles from fitted tracks. Bottom - Integrated reconstruction difference. . . . 333
3.257 Reconstruction of the initial electron as a function of Q^2. . . . 334

3.258 Acceptance as a function of Q^2 and $E_{e'}$. 334
3.259 Longitudinal (left) and transverse (right) analyzing powers assuming a 532 nm wavelength laser colliding with an electron beam at 5 GeV, 10 GeV, and 18 GeV. The transverse analyzing power is shown for the case $\phi = 0$, i.e., the backscattered photon angle is in the same plane as the (transverse) electron polarization direction. . . 337
3.260 Layout of the Compton Polarimeter in the ESR. The collision point between the laser and electron beam is about 74 m upstream of the ePIC detector IP. 338
3.261 Simulated synchrotron radiation in the ESR Compton Polarimeter photon detector at 18 GeV without (blue curve) and with (green curve) the "weak" dipoles introduced around the Compton IP. GeV 339
3.262 Schematic layout of the ESR Compton Polarimeter laser system. The gain-switched seed and fiber amplifier will be housed in a dedicated laser room outside the ring and transport to the Compton IP via fiber. A laser table under the beamline at the IP will include the frequency doubling crystal, beam focusing and polarization optics. 341
3.263 Simulated asymmetry from a diamond strip detector for Compton scattering from a transversely polarized electron beam at 18 GeV. The red points show the asymmetry vs. the generated x position, while the blue use the reconstructed value. 342
3.264 Asymmetry vs. scattered electron position at the Compton diamond strip electron detector position for the three ESR beam energies (5, 10, 15, GeV). Only the part of the scattered electron spectrum 1.8 cm or farther from the beam is shown (1.8 cm from the beam corresponds to 0.0 on the plot). 343
3.265 (left) Photograph of FLAT32 ASIC developed for Hall A at Jefferson Lab mounted on a test PCB. (right) Analog pulses and LVDS output from an initial prototype of the FLAT32 ASIC. The LVDS pulse width is less than 10 ns. 343
3.266 Layout of the Rapid Cycling Synchrotron. The RCS Compton Polarimeter laser will be located about halfway through the first straight section after the electron injector with the photon detector after the arc bend, about 20 m downstream of the Compton IP. 346
3.267 Simulation of photon detector system for the RCS Compton Polarimeter. (left) The photon calorimeter (black box) is shown along with a 5 cm tall diamond strip detector (green) with 1 RL tungsten radiator (blue). (right) Simulation of energy-asymmetry for each strip of the diamond strip detector. 10 laser pulses were simulated with an average of 10,000 backscattered photons per pulse. 347
3.268 Coulomb-nuclear interference (CNI) analyzing power A_N versus $-t$ for pp, pC, ^{3}HeC, and ^{3}He ^{3}He. (Figure taken from [7].) 349
3.269 Schematic layout of the HJET polarimeter, taken from Ref. [8], showing the atomic beam source, the scattering chamber, and the Breit–Rabi polarimeter. 351
3.270 One of the pC polarimeter vacuum chambers presently used in RHIC with in-beam target ladders installed inside the beam pipe. There are two target holders that are moved horizontally (shown) and two more (not shown) that are moved vertically, such that the chamber can hold 4×6 carbon-ribbon targets in total. 353
3.271 Present pC polarimeter: detector system and targets. Panels show (a) the azimuthal detector placement, (b) a Si-strip detector package, (c) a carbon ribbon target, and (d) the multi-position ladder. 354
3.272 Thermal modeling results for carbon ribbon targets showing temperature profiles during beam passage. Despite higher beam energy and total current at EIC, the larger beam size distributes the heat load sufficiently to maintain peak temperatures below the carbon sublimation threshold. (The modeling calculations use a framework developed by Peter Thieberger [9].) 355

3.273 Wakefield analysis for pC polarimeter target systems. Electromagnetic simulations demonstrate superior performance of dielectric target holders compared to metallic alternatives, validating the design choice for EIC operation. . . . 357
3.274 Effect of target holder positioning on wakefield characteristics. The three target geometries (a-c) demonstrate different displacement positions, with corresponding wake potential calculations (d) showing reduced electromagnetic interference when holders are shifted downward toward the chamber wall. . . . 358
3.275 Hadron polarimetry instrumentation concentrated at Interaction Point 4 (IP4) of the EIC high-energy storage ring (HSR). From left to right along the beam direction (yellow arrow): CNI polarimeter; ^{3}He jet target; hydrogen-jet (HJET) polarimeter; two warm D0 dipoles; longitudinal superconducting pickup; four horizontal and four vertical superconducting kickers; HJET tagger drift/tagging system of length 7.5 m; vacuum/ion-pump section; and quadrupole Q4. Co-locating these devices in a single straight section provides shared infrastructure, common alignment, and efficient absolute/relative beam polarimetry, and minimizes spin rotations between polarimeters. . . . 360
3.276 ePIC DAQ component counts . . . 364
3.277 ePIC DAQ component count summary . . . 365
3.278 Maximum data volume per RDO with noise estimates by detector. (Data Rate evaluation: `https://github.com/jml985/epicJTools`) . . . 365
3.279 Schematic of the ePIC Streaming DAQ . . . 367
3.280 ePIC Electronics and ASICs summary . . . 368
3.281 Scope of the electronics and ASICs developments . . . 368
3.282 Discrete block diagram . . . 369
3.283 Discrete Adapter (left) and digitizer FEB PCBs . . . 369
3.284 Discrete key specifications . . . 370
3.285 CALOROC block diagram . . . 370
3.286 CALOROC Key Specifications . . . 370
3.287 EICROC block diagram . . . 371
3.288 EICROC timing performance . . . 372
3.289 EICROC Key Specifications . . . 372
3.290 FCFD block diagram of the frontend . . . 373
3.291 FCFD timing performance . . . 373
3.292 FCFD Key Specifications . . . 373
3.293 ALCOR Si Die (left) and block diagram . . . 374
3.294 ALCOR Key Specifications . . . 374
3.295 TOF pre-prototype RDO . . . 377
3.296 3D model of dRICH RDO . . . 377
3.297 The FLX-155 board identified for use as a DAM board . . . 379
3.298 Schematic layout based for the GTU . . . 380
3.299 Physical concept for the fiber distribution for the GTU . . . 380
3.300 Operation of firmware trigger under assumption that the trigger decision for the dRICH depends upon data from fHCAL . . . 382
3.301 Proposed ePIC slow controls network topology . . . 386
3.302 DAQ/Computing schedule . . . 387
3.303 Electronics and DAQ Resources . . . 388
3.304 Butterfly Computing Model *see text for details).* . . . 392
3.305 Storage resource estimates aggregated over Echelon 1 and Echelon 2 sites, for a nominal Phase 1 datataking year. . . . 395
3.306 Processing resource estimates aggregated over Echelon 1 and Echelon 2 sites, for a nominal Phase 1 datataking year. . . . 396

3.307 Organizational chart of the Software and Computing Effort in ePIC. The Streaming Computing Working Group is joint with Electronics and DAQ Working Group in the Technical Effort to ensure that DAQ and Computing are developed together. . . 401
3.308 Isometric section view of 1006. . . . 403
3.309 Drawing of 1006 assembly hall. . . . 404
3.310 Drawing of 1006 wide angle hall. . . . 405
3.311 Three central platforms. . . . 406
3.312 Top down section view showing 8mrad rotation. . . . 407
3.313 Side Section View. . . . 409
3.314 Top section view showing services. . . . 410
3.315 Isometric side view showing services. . . . 411
3.316 Endcap choreography. . . . 412
3.317 Barrel installation sequence. . . . 412
3.318 Endcap installation sequence. . . . 413
3.319 fHCal mounting. . . . 414
3.320 Endcap installation sequence. . . . 415
3.321 HCal lower half. . . . 416
3.322 HCal lower half plus mag. . . . 417
3.323 HCal plus platform. . . . 418
3.324 HCal plus platform. . . . 419
3.325 HCal plus platform. . . . 420
3.326 DIRC, oMPGD, ToF Cymbal install. . . . 420
3.327 PST assembly. . . . 421
3.328 pfRICH and EEMCal installation. . . . 422
3.329 dRICH installation. . . . 422

4.1 Figure of merit for muon identification as a function of momentum in the ePIC central barrel. . . . 426
4.2 Jet energy scale (Left) and jet energy resolution (Right) as a function of particle-level jet energy for backward (blue squares), mid (red triangles), and forward (green diamonds) rapidities. . . . 427
4.3 Neutral-Current Deep Inelastic Scattering of an electron by a proton. . . . 429
4.4 Resolution of the inelasticity y, as a function of x_B and Q^2, when reconstructed using the electron method (blue), Σ method (green), or Double-angle method (orange). The color of each point indicates the best performing reconstruction method. . . . 431

List of Tables

1 Table illustrating “rules”. . . . 15
2 Short top-level parameters caption. . . . 15
3 A parameter table made available for export, using the /Tables subdirectory 15
4 A table with fixed third column width, enabling text filling. . . . 15
5 Two ways to squeeze tables. . . . 16
6 A third way to squeeze tables. . . . 16

3.1 The cross sections and rates for the signal process and the background processes . . 25
3.2 MARCO Magnet Requirements . . . 40
3.3 MARCO geometric Specifications . . . 43
3.4 MARCO Materials . . . 47
3.5 Design parameter for various fields . . . 48
3.6 Caption . . . 49
3.7 Impact of axial misalignment and tolerances . . . 51
3.8 Impact of radial misalignment- Cold Mass . . . 51
3.9 Impact of radial misalignment- Module 1 . . . 51
3.10 Impact of radial misalignment- Module 2 . . . 52
3.11 Impact of radial misalignment- Module 3 . . . 52
3.12 Impact of missing one layer . . . 52
3.13 Caption . . . 53
3.14 Caption . . . 54
3.15 Materials acceptance criteria . . . 55
3.16 Materials acceptance criteria . . . 57
3.17 Ramp up/down results . . . 57
3.18 List of cryogenic valves . . . 65
3.19 Thermosiphon load cases . . . 68
3.20 Heat load summary . . . 69
3.21 Heat Load budget . . . 69
3.22 Physics requirements on the relative momentum measurement, dp/p, at the event vertex, η, and on the determination of the radial distance of closest approach, DCA_r, of the particle trajectory to the event vertex. The requirements are given for different ranges in pseudorapidity as parametrizations in the total momentum, p, in GeV and transverse momentum, p_T, in GeV, respectively. . . . 71
3.23 Target radius, length and material budget of the SVT IB and OB layers. . . . 78
3.24 Position along the beam pipe, outer radius and material budget for the SVT layers in the EE and HE regions. Disks in the electron direction are labeled ED0 to ED4. Disks in the hadron direction are labeled HD0 to HD4. Disks ED0/1/2 and disks HD0/1 have the same inner opening. Each of the other five disks has a different inner opening. . . . 78

3.25 Summary of power and readout services for the different regions of the ePIC SVT (slow control and data links are differential pairs of wires). A services group is one MOSAIX segment in the IB, and up to four EIC-LAS sensors (i.e. four segments) in the OB and disks. . . . 82
3.26 SVT component temperature requirements (N/S is not specified). . . . 83
3.27 SVT cooling power requirements. . . . 84
3.28 Different sources of radiation dose . . . 97
3.29 Hit rate per unit area in the MPGD trackers for different beam gas . . . 97
3.30 Maximum rate per readout channel for different beam gas . . . 98
3.31 The ECT disks geometrical envelope and active areas dimensions. . . . 100
3.32 The ECT disks angular and pseudorapidity acceptance. . . . 101
3.33 Services requirements for the three MPGD tracking subsystems. . . . 103
3.34 Main equipment required in the production site and availability at sites. . . . 110
3.35 Main equipment required in the production site and availability at sites . . . 111
3.36 UVa Personnel Effort (%FTE) . . . 111
3.37 FIT Personnel Effort (%FTE) . . . 111
3.38 JLab Personnel Effort (%FTE) . . . 112
3.39 Required performance for physics and proposed configurations for the TOF detector system. The Barrel TOF consists of strip sensors with a pitch of 0.5 mm in the azimuthal direction and a length of 1 cm along the beam direction, while the Forward TOF consists of pixel sensors with a pitch of 0.5 mm. . . . 116
3.40 RAW and NEQ fluence per system for the lifetime of the ePIC experiment, assuming 10 years of data taking at 50% time. . . . 118
3.41 Baseline BTOF, FTOF and B0 AC-LGAD geometries. . . . 120
3.42 Readout chips BTOF, FTOF and B0 AC-LGAD geometries. . . . 121
3.43 Summary of BTOF and FTOF low voltage and high voltage power supply cables to distribution panels and then to the detector FEE (the exact numbers are being checked at the time of writing). . . . 125
3.44 The BTOF is designed with a barrel geometry surrounding the beam pipe and interaction point, while the FTOF is a disk geometry perpendicular to the beam direction on the hadron side (positive z). . . . 126
3.45 Expected pfRICH time of flight based particle identification performance. Highest momenta at which 3σ separation for a respective pair of mass hypotheses can be achieved is quoted, for aerogel and HRPPD window radiators separately. . . . 143
3.46 Institutions contributing to the pfRICH effort and their roles and resources. Starred entries indicate no institutional commitment. . . . 150
3.47 List of the voltage services to the dRICH electronics, indicating the number of primary power-supply channels and boards as well as the cross-section of the cables (AWG). The number of power-supply boards is defined assuming to use commercial 8-channel low-voltage boards. . . . 172
3.48 Planned quality assurance (QA) stations, organized in order to provide redundancy and support specific characterization studies. . . . 180
3.49 Overview of Institutes and roles in the dRICH activity. . . . 182
3.50 Table of crystal properties. . . . 185
3.51 PWO specifications. . . . 186
3.52 EEEMCAL WBS Structure . . . 191
3.53 Selected BIC Parameters. . . . 201
3.54 AstroPix and Pb/ScFi layer parameters. . . . 202
3.55 AstroPix chip parameters for BIC. . . . 202
3.56 SiPM specifications for BIC. . . . 203
3.57 Scintillating fiber specifications for BIC. . . . 203

3.58 Energy resolution parameters for photons in BIC for different η ranges. 204
3.59 Expected data rates for ScFi/Pb and Imaging layers of the BIC. 209
3.60 Some requirements on performance of FEMC and its parameters 222
3.61 Requirements and Technical specifications for FEMC scintillating fibers. 225
3.62 Requirements and Technical specifications for FEMC SiPMs. 227
3.63 Requirements for the FEB 229
3.64 Control and status registers on the FEB 231
3.65 Maximum expected background rates for backward HCal. The assumed threshold is 170 keV. 234
3.66 Properties of HCal scintillating tiles. 254
3.67 Properties of Kuraray Y-11 (200) wavelength shifting fibers. 255
3.68 Design parameters for the Barrel Hadronic Calorimeter w/o additional absorber, based on the sPHENIX Outer Hadronic Calorimeter. 256
3.69 Overview of the calorimeter design properties for the LFHCal. 271
3.70 Examples of reactions that yield high-energy neutral particles within the ZDC acceptance. In each case, the leading particle's energy and polar scattering angle are used to constrain the Mandelstam variables t or u. The azimuthal angle can also be exploited for spin-dependent modulation measurements and for studying Λ^0 polarization and deuteron structure. While these reactions are labeled as having an electron in the final state, it should be understood that they can correspond to either the electroproduction (large Q^2) or photoproduction ($Q^2 \approx 0$) regime. The references provided are representative of the literature discussing the corresponding channel, although they do not constitute an exhaustive list. 301
3.71 Bethe-Heitler ep bremsstrahlung cross section in mb (and the corresponding event rates in GHz, for the nominal EIC luminosities), for various beam energies in GeV and three selection criteria. Table from Ref. [**?**]. 318
3.72 Summary of systematic uncertainties at ZEUS DPD and PS detector. [**?**] 319
3.73 Beam polarization components at the ESR Compton laser IP for the EIC nominal electron beam energies. 338
3.74 Backscattered photon rates, analyzing powers and measurement times (per electron bunch) for the beam and laser parameters described in the text. The beam polarization is assumed to be 70%. 340
3.75 Deflection from nominal beam path for the Compton scattered electrons at the position of the diamond strip detector for electrons at the kinematic endpoint (Δx_{max}, where the asymmetry is largest) and at the zero-crossing of the asymmetry (Δx_0). . 342
3.76 Backscattered photon rates, analyzing powers and measurement times using the RCS Compton. We assume a 28 nC electron bunch colliding with 40 mJ laser pulse at 2 Hz. Measurement time is calculated for a beam polarization of 70% and a statistical uncertainty of $dP/P = 1\%$. 346
3.77 Comparison of carbon target coverage for pC polarimeters at RHIC and EIC. The coverage ratio indicates how many times longer the target is compared to the beam width ($4\sigma_{95}$). Values below 2 indicate marginal coverage with limited safety margin for beam positioning and alignment tolerances. EIC beam parameters from Ref. [10]. 355
3.78 Noise Estimates 366
3.79 Expected worse case data rate contributions for the ePIC detector. (`https://github.com/jml985/epicJTools`) 366
3.80 SALSA specifications. 375
3.81 Types of RDO 376
3.82 RDO downlink words 381

3.83 DAM/RDO Decoded Synchronous Command Structure. This structure is defined to allow continuous availability of the critical beam related bits and more rare commands. The data in the 40 bits worth of flexible command data encoding remains flexible but must contain enough control bits to select what structure it has. The ”type”, ”type specific” division is an potential holding this flexibility 381
3.84 DAQ Computing Resources 383
3.85 Slow Controls data volume and network traffic 386
3.86 Echelon 0 networking and storage requirements. 393
3.87 Echelon 1 networking requirements. Values shown are for a single E1 site. 394
3.88 Fractions of production workflows performed outside of Echelon 1 sites (i.e. at Echelon 2 and opportunistic sites) 394

multi-chapters

Chapter 0

Style Guide

The following is the Style guild as developed for the full design report. This is the guide the accelerator team is following and it will make merging the documents together much easier if everyone uses this guide.

0.1 Chapter Abstract

Summary: Each chapter begins with a stand-alone single "punch line" page that serves as a chapter abstract. Rather than simply duplicating the Table of Contents outline of the subject matter of the chapter, a well-constructed abstract will lay out the key ideas and conclusions that chapter editors wish to convey to readers. The Executive Summary will also describe these key ideas, in a modestly longer form (perhaps $\sim 250 - 1000$ words per chapter). This sample **non-EIC** chapter abstract emphasizes key ideas such as the separation of pre-existing and new subsystems, and the level of technical risk.

The Cryogenic System consists of the cryoplant that provides cooling for cryomodules; the test and instruments cryoplant that provides cooling for test stands and liquid helium for instruments; cryoplant that provides 16 K helium cooling for the target hydrogen moderators, and the distribution system that connects the linac cryoplant to cryomodules. The linac cryoplant and test/instrument cryoplant share common gas management and storage systems. The target cryoplant system is completely separate due to potential for tritium contamination.

The Vacuum System provides vacuum for the linac beam line, target system and instrument lines. It uses well established technology and procedures based on experience at similar facilities, including RHIC, Tevatron, and LHC. It has low technical risk.

Test Stands provide testing and validation of both RF equipment (klystrons and modulators) and cryomodules. Cryogenic connection to cryomodules in the test stands will prototype similar connections in the linac tunnel. The test stand program accommodates the unavoidable uncertainty in EIC construction schedule by allowing for RF equipment testing in a temporary location if necessary. Cryomodule testing will be carried out at the EIC site. All cryomodules will be tested at nominal temperatures and RF power levels before tunnel installation.

0.2 Wordsmithing

0.2.1 Passive voice

Authors should avoid the passive voice as much as possible – as in this sentence. This rule is sometimes made to be broken – as in this sentence :). The crucial point is that authors should not use passive voice to avoid identifying the specific individual or group of individuals within the EIC organization which is/are (or will be) responsible for fulfilling some specific function. It's not good enough to say, "Quality management will be implemented". The purpose of the Design Report is to explain for EIC itself, and for readers outside of EIC, who will implement quality management, and how they will do it. Excessive use of passive voice is not just bad writing. It communicates confusion or uncertainty about the path from aspiration to reality.

0.2.2 Verb tenses

The simplest way to make everything consistent is to apply a general rule:

> Use past tense for things that happened in the past, present tense for things that are happening now, and future tense for things that will happen in the future.

If the designs call for something to happen, they call for it in the present tense. But it will happen in the future tense. Avoid inconsistent usage across chapters, across authors, and even within the same paragraph by a single author.

0.2.3 Apostrophes

Decades are written as in the 1960s and 1970s, NOT as in the 1980's or 1990's.

0.2.4 Capitalization and names

0.2.4.1 Pieces of EIC

For example, linac, accelerator, target station, test stand. For the sake of consistency these terms will not be capitalized.

0.2.4.2 Internal phrases

Correct capitalization for specific "internal" EIC phrases and names will be accumulated here. For example:

> Pre-construction Phase NOT Pre-Construction phase
> Decommissioning Phase NOT De-commissioning phase
> Work Packages NOT Work-packages

0.2.4.3 Discipline-specific approaches or "guiding principles" or buzz phrases

Such as design integration, systems engineering, defense in depth. Recommend capitalizing none of them, but the important thing is to be consistent.

0.2.4.4 Formal group names

When authors identify the parts of the EIC organization who will be responsible for doing something, then capitalize the formal names of that groups from the org chart. Recommend avoiding informal terms such as "test stand personnel", where possible.

0.2.4.5 Headings

The titles of sections and subsections should have only the first letter capitalized.

0.2.5 Captions

Write Figure and Table captions in a self-contained way, to carry a complete self-contained description of the figure. Define symbology in all figures, either in the text or (preferably) in the caption. Captions always end with a period. Use the format:

```
\caption[Short caption for List of Tables or Figures.]{Long caption to carry a complete
self-contained description of the figure or table, in the chapter text.}
```

0.2.6 Spelling

The Design Report follows American spelling rules. For example, with "z" not "s", and "program" not "programme":

emphasize not emphasise
meter not metre

0.2.6.1 Exceptions to U.S. spelling

1. (None so far).

0.2.6.2 Capitalization

The words "Figure", "Table", "Chapter" and "Section" should always be capitalized in the text if they occur with a number. For example, Figure 3.8 occurs in Chapter 3 and Table 5.5 is in Section 5.1.3, but there are many other figures and tables in other section, subsections and chapters.

0.2.7 Commas

The incorrect placement of a comma can change the meaning of a sentence. For example, compare "Let's eat Mom" and "Let's eat, Mom". And compare "Scientists, who conduct important research, are well respected in the community" with "Scientists who conduct important research are well respected in the community".

Commas go where there is a natural pause in a long sentence, where additional information has been added to a sentence and where, if removed, the sentence would still make sense. They are used when listing items – between each item on the list. They are used where two shorter sentences are made into one (usually with the addition of "and"), but still consist of two separate parts. And they are used after "lead" words [however, therefore, consequently, in fact].

0.2.7.1 Commas in numbers

Write 2.4 million and not 2,4 million (as in some parts of Europe).

No commas in numbers below 10,000 – thus, write 1240 and 9999, but 12,400 and 99,999.

0.2.8 Plurals and possessives

For example, use

WPs not WP's (plural)
EIC's not EIC' (possessive)

0.2.9 Abbreviations

0.2.9.1 Textual treatment of Figures and Tables

The words "Figure" and "Table" should always be capitalized in the text. Include a reference or discussion of all Tables and Figures in the main text of the chapter. For example, "Figure 3.8 shows thus-and-such". The abbreviations Fig. and Tab. should not be used.

0.2.9.2 Radio frequency

The phrase "radio frequency" is always two words and is never hyphenated or capitalized, whether used as an adjective or as a noun. Thus, the two radio frequencies used in the radio frequency system are 352.21 MHz and 704.42 MHz. The upper case abbreviation "RF" is acceptable in many circumstances.

0.2.9.3 etc., et cetera

It is acceptable to use "e.g." within parentheses, but not outside. For example, Jack and Jill met many animals (e.g. Reynard the Fox) when going down the hill. It is also correct to say that Jack and Jill met many animals, for example Reynard the Fox, but no tortoise. Similar rules apply for "i.e.".

The periods (i.e. the full stops) should not be dropped, for example "ie" or "eg".

It is incorrect to use ok, o.k., or okay.

The following are acceptable:

e.g.
etc.
i.e.
RF (in many circumstances)

0.2.10 Hyphenation of multi-word adjectival phrases

In general, hyphenate an adjectival phrase where the second part is a past (-ed) or present (-ing) participle of a verb. Consider the following illustrative (nonsensical) paragraph:

> This chapter describes the *beam physics design* of the *neutron-generating* spallation target. Following a brief overview, the chapter presents a detailed description of the *beam physics* of EIC, which drive the accelerator design. The accelerator consists of several sections: the ion source, *normal-conducting* linac, *superconducting* linac and *beam transport* sections. The chapter also describes the *radio frequency* system.

Simplified advice available online includes: *"When two or more words are combined to form a modifier immediately preceding a noun, join the words by hyphens if doing so will significantly aid the reader in recognizing the compound adjective."* Not so simple are phrases like "high-power proton beam" where "proton beam" itself is a single idea. Some judgement is involved ....

For the sake of consistency, the editors have created and are expanding a spreadsheet of words and phrases specifying hyphenation policy for the Design Repoprt. Here are somewhat-arbitrary rules for whether or not to hyphenate some common multi-word phrases, *when they are used as an adjective, a noun, or as a verb*. Alphabetically:

1D, 2D, 3D, 4D
accelerator-driven
back up (verb)
back-flow (noun adj)
backscattering
backup (adj noun)
baseline (adj or noun)
beam dynamics
beam guide
beam instrumentation

beam physics
beampipe
beam port
beam time
beam transport
beamline
bispectral
bottom-up approach
broadband
by-product
clamshell clamshell-style
clean room
cold box
co-chair (noun)
contact-less
cool-down (noun or adj)
coordinate
cost-saving
cross reference (noun)
cross-reference (verb)
cross section
cryo-building
cryo-pump
cryo-system
cryomodule
cryoplant
debunched
decision making (noun)
decommissioning
de-excitation
deionised
down-mix
downtime
eigenmode (noun adj)
equipartitioning
failover
failsafe
feed box
feedthrough
follow up (verb)
follow-up (adj and noun)
hands-on (adj)
high level
high-β
high-current (adj)
high-power
high-resolution
hot cell
in situ (italicize)
innermost
inrush

interdependency
interlayer
intra-layer
intra-nuclear
Joule-Thomson valve
layout (noun)
life-cycle (noun)
line-of-sight
long-pulse
lookup
Lorentz detuning (noun)
Lorentz-detuning (adj)
low-resolution
magnetoresistance
medium-β
metadata
micropattern
microphonics
midpoint
middleware
multi-component
multi-layer
multi-pacting
multi-particle
multi-resistant
nanoparticle
nano-sized
nanostructure
neutron-generating
noninvasive (seen both ways in different dictionaries)
normal-conducting
on-board
ongoing
on-site (adj)
outermost
outgassing
overarching
phase space (noun)
phase-space (adj)
pinpoint
plug-in
post mortem (noun or adj)
pre-cools
premoderator
prequalification
radio frequency
radionuclide
radiotoxic
ramp up (verb)
ramp-up (noun)
read-back

ready-made
requalification
roadmap
safety-critical
short-pulse
short-term
shut off (noun verb)
shut-off (adj)
space charge (noun)
space-charge (adj)
staff-based
start-up
state-of-the-art
storm water
stripline
sub-atmospheric
subcomponent
sub-cool
sub-millimeter
sub-second
superconducting
switchyard
systemwide
thermo-mechanical
thermo-plastic
thermo-responsive
thermosyphon
time-frame
time scale
time-saving
time-stamp (noun and verb)
timeline
timesaving (adj and noun)
tool-set
top level
trade-off
tunable
tune up (verb)
tune-up (adj and noun)
twofold
uniaxial
uninterruptible
un-irradiated
up-mix
uptime
von Mises
waste water (noun)
waveguide
work flow (noun)
work-flow (adj)
workspace

world-leading
X-ray (upper case X)
zigzag (noun or adj)

0.2.11 Double letters

In UK spelling, both ”focussing” and ”focusing” are considered to be correct. In the Design Report we use single ”s” spelling in all cases.

Note the ’double “l” rule for UK English – label becomes labelled, travel becomes travelled, et cetera. Not so with U.S. English in the Design Report.

0.2.12 Mathematical symbols, subscripts and superscripts

Mathematical symbols are written in math-mode, even when they are embedded in text. For example, a longitudinal dimension L is often called a length. Descriptive subscripts and superscripts, as in L_{acc} or $L^{overhead}$, are not written in Roman font. They appear to be italics, no matter how long or short they are.

0.2.13 Quotation marks

LaTeX is fussy about some things, like quotation marks. Sooner or later an author, a chapter editor, or a general editor must pay attention. This the correct way to put “a certain piece of text” inside quotation marks. The following ”certain piece of text” is incorrect.

0.2.14 Citations, references and the bibliography

Please use inspire hep bibtex entries and notation whenever possible.

Don’t use a “pointer” (for example [4]) in place of naming a reference [11]. That is, use “Joe Blow [4] describes thus and such,” NOT, “[4] describes thus and such”. There should be a space in the text before the citation, so “Joe Blow[4]” is wrong. Multiple citations should be placed with the same square brackets. In the LaTeX vernacular, use `Joe Blow~\cite{Blow2011}` or `Joe Blow~\cite{Blow2011,Smith2012}`.

We are using `bibtex` to handle the references, which are gathered into one `bib` file per chapter, although all references appear in a single bibliography at the end of the Design Report.

During the editing process we are (currently by default) using the LaTeXpackage `showkeys`, which flags references (to Tables, Figures, sections and subsections) and citations (to references) above the text, or in the margin. This should aid in generating cross-references, for example, even though it is rather ugly. It will be turned off in the final stages of editing, before printing. (Comments and feedback, please!)

0.2.15 Miscellaneous

0.2.15.1 "Calculations show that . . . "

This usage, with no indication who carried out the calculations, provides no way for a reader to check the work, or to build upon it in the future. Citations of internal documents, or of individuals to contact to get more information would be helpful for readers, and would also convey a greater sense of credibility. For example, "Relativistic Heavy Ion Collider (2021), unpublished calculations by members of the XYZ working group. Contact Sven Larsson (sven.larsson@bnl.gov) for details."

0.2.15.2 "Should", "must", and reference to future studies

In general, authors should convey the conviction that EIC will do what it should do. In those cases where there is an ongoing internal debate, the Design Report should convey the sense that such debates will be resolved on the basis of a reasoned and careful assessment of the evidence. Only write about future studies in those limited cases where it is needed to show "that we know what we are doing".

0.2.15.3 "Enable"

Incorrect usage:

> "Neutrons pass easily through most materials, enabling the study of large or bulk samples and buried interfaces."

Correct usage:

> "In addition, as the BLM system will be a major tool for beam tune-up, it should also be designed in a way that enables it to pin-point the loss location as precisely as possible."

The point is that the direct object of enable is made capable of doing something – roughly a synonym for empower. You enable the direct object to do something (enable it to pin-point . . .). You could rewrite the first sentence to say, "enabling the study of large or bulk samples . . . to take place." Then it would be correct – although more unwieldy than just saying "making possible the study of . . . "

0.2.15.4 Reporting technical results without a clear statement of their import

In general, it is a mistake to assume that "the numbers speak for themselves". Using words to summarize the meaning of results helps readers to understand them; it also signals that the authors understand the implications of the results they report.

0.2.15.5 Excessive and inconsistent use of lists

Sometimes the use of lists is appropriate, but often there are too many in a draft. Authors should rework most lists into narrative form. For the remaining lists, authors should follow editorial guide-

lines to ensure consistent style across the entire Design Report.

After minimizing the number of lists, Design Report editors will convert most of the remaining lists to enumerated lists. The first letter of each item will be upper case, even when the items in the list are not formulated as complete sentences. Items will generally end with a semi-colon unless the phrases are very short, in which case a comma will be used. The last item in the list will be followed by a period. In those cases in which each item in a list consists of multiple sentences, items will be ended with a period.

0.2.15.6 Cross-references

Should be added throughout the whole Design Report, but only down to `\subsection` level, so that cross-references can be found and numbered in the Table of Contents. This implies that subsections should be reasonably balanced in length – not too many pages long.

0.2.15.7 Isotopes

Write ^{3}He, for example, not 3He or He-3.

0.2.15.8 *** asterisks in comments

Sometimes a comment is inserted in a sentence, perhaps indicating that something needs to happen later, such as add a value, a citation, or more text. In this case please include (at least) 3 asterisks in a row *** so that text searches (for example `grep *** *.f`) are made easier. ALSO CONSIDER WRITING IN UPPER CASE***.

0.3 Dimensions and units

Systeme Internationale (SI) units will be used wherever possible. For example, use MPa instead of bar. Some exceptions are inevitable, for example Kilpatrick units. Unusual units should be briefly explained, on their first introduction.

When in doubt, the `siunitx` package does the Right Thing, for example using:

- `\si{\units}` lower case si
- `\SI{numbers}{\units}` upper case SI

A longitudinal dimension – or length – L should be written in one of these ways:

- $L = 100$ m `$L = 100$~m`
- $L = 100$ µm `$L = 100$~\si{\micro\metre}`
- $L = 100$ km `$L = $ \SI{100}{km}`
- $L = 10^2$ km `$L = $ \SI{e2}{km}`

so that the dimension ("m" or "µm" or "km") is not in italics, and is separated from the numerical value by a non-breakable space – for example "~" in LaTeX vernacular. Do not write $L = 100$m, $100m$ or $100\ m$. Note that text and mathematical equals signs are different in length (= and $=$): always use the latter.

Powers of ten are written in one of these ways:

- 3.14×10^{39} `$3.14 \times 10^{39}$`
- 3.14×10^{39} `\SI{3.14e39}{}`

Complex dimensions may be written in one of these ways:

- $F = 42\,\mathrm{J\,cm^{-2}\,s^{-1}}$ `$F = 42$~J cm$^{-2}$ s$^{-1}$`
- $F = 42\,\mathrm{J\,cm^{-2}\,s^{-1}}$ `$F=$ \SI{42}{J.cm^{-2}.s^{-1}}`

Exceptionally, percentages are written without a space – 42% is correct but 42 % is not. In LaTeX vernacular a % sign is the beginning of a comment, so it is necessary to say \% . . . sentence is invisible in the pdf file.

Temperatures are written as 273 K or 100°C or 101°C, without a space between the number and the °C unit symbol.

Angles are preferably written $\theta = 7.5$ degrees, although 7.5° is acceptable.

0.4 Numbering – chapters, sections, and subsections

In the `\documentclass{report}` style, a "section" (such as this, with the numeric label 0.4) has two numbers associated with it.

0.4.1 This is the heading of a subsection

A "subsection" (like this, 0.4.1) is labelled by 3 numbers, namely "chapter_number.section_number.subsection_number". Sections and subsections begin with a bold face font.

0.4.1.1 A subsubsection heading like this has no period at the end

In bold font, it has no numerical label, and sits separately from the text that immediately follows, even if there is no white space between `\subsubsection{}` and the first word of the text. It does not appear in the Table of Contents.

This paragraph heading ends with a period. Subsequent text remains in the same paragraph. The editors will use their judgement to prevent the excessive use of paragraph headings and boldface text.

0.4.2 More formatting rules and standards

0.4.2.1 Clearpages and Pagebreaks

As a rule there is NO `\clearpage` or `\pagebreak` before a new section (or subsection), and hence no white space.

0.5 Equations, Tables, Figures, and plots

0.5.1 Equations

Start with a simple equation, like Equation 1:

$$H = \frac{\sqrt{3\left\langle x^4\right\rangle \left\langle x'^4\right\rangle + 9\left\langle x^2x'^2\right\rangle^2 - 12\left\langle xx'^3\right\rangle \left\langle x^3x'\right\rangle}}{2\left\langle x^2\right\rangle \left\langle x'^2\right\rangle - 2\left\langle xx'\right\rangle^2} \tag{1}$$

Avoid ending a sentence with an equation, in order to avoid deciding whether or not to put a period after the equation.

Here is a simple equation array:

$$\begin{aligned} M_{virg}(\sigma) &= M_{virg0} + k_{virg}.\sigma \\ M_{rel}(\sigma) &= M_{rel0} + k_{rel}.\sigma \end{aligned} \tag{2}$$

0.5.2 Tables

- Table 1 is a relatively complicated multi-column table, while Table 2 is a standard 3-column parameter table.
- Table 3 shows how to make a table exportable, for example to the Parameter Tables appendix.
- The source text for Table 4 shows how to enable text filling in columns.
- Table 5 shows 2 ways to squeeze tables, with the `\scalebox{}` and `\phantom{}` commands.
- Table 6 shows a third way, using `\tabcolsep{}`.

The vertical spacing of Table rows is set in "preamble.tex" by the line `\renewcommand{\arraystretch}{1.0}`.

0.5.3 Converting between LaTeX and Excel table formats

More than one free utility enables table conversion with a drag-and-drop interface. E.g.:

Excel to LaTeX try `https://tableconvert.com/excel-to-latex`

LaTeX to Excel try `https://tableconvert.com/latex-to-excel`

Facility	Location	Status	First oper.	Power [MW]	Instruments	Integrated flux [10^{14}cm^{-2}]	Peak flux [10^{15}cm^{-2}s^{-1}]
ESS	Lund	Pre-constr.	2019	5	22	–	40
J-PARC	Tokai	Re-furbish	2009			–	

Table 1: A standard Table looks like this, using "toprule", "midrule" and "bottomrule" separation lines.

Parameter	Unit	Value
Energy	GeV	2.5
Current	mA	50
Pulse length	ms	2.86
Pulse repetition frequency	Hz	14
Average power	MW	5
Peak power	MW	125

Table 2: Long version of caption for top-level parameters.

Parameter	Unit	Value
Energy	GeV	2.5

Table 3: A parameter table made available for export, for example to Appendix E "Parameter Tables", using input from a /Tables subdirectory file.

System	Subsystem	Test
Target	Shaft and drive	Run at up to 25 Hz.
	Target segments	Leak test at pressure.
	Target Safety System	Demonstrate trip signals generated for all defined cases.
Primary helium loop	Pump, heat exchanger, filter	Pressure and flow tests without target.
	Full loop with target	Full operational test without heat.

Table 4: A table with fixed third column width, enabling text filling.

Nuclide	Decay time [years]						
	0	6	40	100	1000	10^4	10^5
^{3}H	0.9	83.4	96.4	72	0	0	0
^{14}C	0	0	0	0	0.3	0.6	0
^{36}Cl	0	0	0	0	0	0	0.7
^{39}Ar	0	0	0	0.1	0.7	0	0
^{154}Dy	0	0	0	0	0	0.2	4.3
^{163}Ho	0	0	0	0.7	29.7	53.4	0

Table 5: Two ways to squeeze tables, with the "scalebox" and "phantom" commands.

Nuclide	**Decay time** [years]						
	0	6	40	100	1000	10^4	10^5
^{137}La	0	0	0	0	1.4	8.7	57.6
^{148}Gd	0	0.2	0.9	11.6	0.1	0	0
^{150}Gd	0	0	0	0	0	0.3	5.6
^{154}Dy	0	0	0	0	0	0.2	4.3
^{157}Tb	0	0.1	0.6	9.3	7.2	0	0
^{154}Dy	0	0	0	0	0	0.2	4.3
^{163}Ho	0	0	0	0.7	29.7	53.4	0

Table 6: A third way to squeeze tables, with the "tabcolsep".

0.5.4 Figures

Many figures, like Figure 1, are non-graphical images – perhaps a photograph, drawing or sketch.

Figure 1: This is an example of a non-graphical figure. We need to address the means by which we can give "all" graphs the same look and feel.

0.5.5 Plots

It is clear that for the ePIC detector sections we will mostly be using ROOT and Python, while the accelerator team most likely will be using a different package; so as soon as a figure style is agreed on, we will need to make style packages for ROOT and Python so all figures in the manuscript look stylistically the same.

As teams develop initial plots, please be sure to each the codes available so that they can be remade in a common style.

0.6 Italics and bold face type

In general, retsrain the use of *italics* and **bold face**.

Long quotations will be set in italics. Italics will also be used (sparingly) for traditional purposes of emphasis (e.g. "when she was good, she was *very* good.")

Occasionally, authors wish to draw attention to the subject matter being addressed in a block of text. Usually, this should be done by headings and subheadings. In those limited instances in which use of altered type face is appropriate within the body text, the editors will use bold face, rather than italics. One such situation is for short introductory phrases at the beginning of paragraph-long items in an enumerated list.

0.7 Issues that this Style Guide does not yet address

This Style Guide addresses "consistency of style" issues. Here is a numerical list of issues that could or should be significantly expanded:

1. the use of pronouns
2. specialized terminology
3. acronyms
4. the use of italics
5. the use of digits (e.g. 1) where written numbers are more appropriate
6. the overuse of capital letters (Boron vs. boron, User vs. user, etc.).
7. balancing the length of sections and subsections
8. global glossary
9. Lists
10. Plots (see placeholder 0.5.5)

Need to compile all sections to get references to work.

Executive Summary

Chapter 1

Introduction

Chapter 2

Detector Requirement

Chapter 3

Experimental Systems

3.1 Experimental Equipment Requirements Summary

The YR table (Fig. 3.1) is being reviewed and an updated table with accompanying text will be included in the draft Version1.

Table 10.6: This matrix summarizes the high level requirements for the detector performance. The interactive version of this matrix can be obtained through the Yellow Report Physics Working Group WIKI page (https://wiki.bnl.gov/eicug/index.php/Yellow_Report_Physics_Common).

η	Nomenclature			Tracking				Electrons and Photons			π/K/p		HCAL		Muons
Paste				Resolution	Allowed	minimum-pT	Si-Vertex	Resolution σ/E	PID	min E	p-Range	Separati	Resolution σ/E	Energy	
-6.9 to -5.8			low-Q2 tagger	σE/E < 1.5%; 10-6 < Q2 < 10-2 GeV2											
-5.0 to -4.5						300 MeV pions									
-4.5 to -4.0			Instrumentation to separate charged particles from photons			300 MeV pions		2%/√E(+1-3%)		50 MeV					
-4.0 to -3.5	↓ p/A	Auxiliary De								50 MeV			~50%/√E + 6%		
-3.5 to -3.0										50 MeV					
-3.0 to -2.5			Backward Detector	σpT/pT ~ 0.1%@0.5%			σ_xy ~ 30⊕pT μm +40 μm			50 MeV					
-2.5 to -2.0				σpT/pT 0.05%@0.5%			σ_xy ~ 30⊕pT μm +20 μm	2%/√E(+1-3%)		50 MeV	≤ 7 GeV/c		~45%/√E+6%		
-2.0 to -1.5								2%/√E(+1-3%)		50 MeV					muons useful for bkg. improve resolution
-1.5 to -1.0								2%/√E(+1-3%)		50 MeV					
-1.0 to -0.5			Barrel	σpT/pT ~0.05%⊕pT⊕0.5%	~5% or less X		dxyz ~ 20 μm, d0(z) ~d0(r0) ~ 20/pTGeV μm ⊕ 5 μm			50 MeV			~85%/√E+7%	~600 MeV	
-0.5 to 0.0		Central Detector								50 MeV	≤ 10 GeV/c	≥ 3 σ	~85%/√E+7%		
0.0 to 0.5										50 MeV			~85%/√E+7%		
0.5 to 1.0										50 MeV	≤ 15 GeV/c		~85%/√E+7%		
1.0 to 1.5			Forward Detectors	σpT/pT ~0.05%⊕pT⊕1.0%		<100MeV pions, 135MeV kaons	σ_xy ~ 30⊕pT μm +20 μm			50 MeV	≤ 30 GeV/c				
1.5 to 2.0										50 MeV	≤ 50 GeV/c				
2.0 to 2.5										50 MeV					
2.5 to 3.0				σpT/pT ~ 0.1%⊕pT⊕2.0%			σ_xy ~ 30⊕pT μm +40 μm	(10-12)%/√E(+1-3%)	3σ e/π	50 MeV	≤ 30 GeV/c		35%/√E		
3.0 to 3.5							σ_xy ~ 30⊕pT μm +60 μm			50 MeV	≤ 45 GeV/c				
3.5 to 4.0			Instrumentation to separate charged particles from photons	Tracking capabilities are desirable for forward tagging						50 MeV					
4.0 to 4.5	↑ e	Auxiliary Detectors								50 MeV			35%/√E (goal), <50%/√E (acceptable)*, 3mrad/√E (goal)		
4.5 to 5.0			Neutron Detection			300 MeV pions		4.5%/√E for photon energy > 20 GeV	<= 3 cm granularity	50 MeV					
>6.2			Proton Spectrometer	σintrinsic(E)/E < 1%; Acceptance: 0.2 < pt < 1.2 GeV/c											

Figure 3.1: Table presenting the Experimental Equipment Requirements Summary in the YR. At present, the table is not updated and it is here as a mere space holder.

3.2 General Detector Considerations and Operations Challenges

3.2.1 General Design Considerations

This section will discuss the detector challenges with cross-reference to the appropriate sections. The Sec.s to refer to are related to machine parameters (not in chapter 8), 8.1 "Experimental Equipment requirement Summary", 8.2.2 "Background and Rates" and 8.2.3 "Radiation Level". At present, all these sections are not available. Therefore, for Version0, a mere list of topics that will be covered is provided.

Discussion of challenges related to:

- Physics requirements (ref. to Sec. 8.1);
- Beams rates, polarization, luminosities (ref. to Sec.s in the machine chapters);
- Integration with the machine and hermeticity (ref. to Sec.s in the machine chapters, ref. to Sec. 8.1);
- Rates and multiplicity (ref. to Sec.c in the machine chapters, to Sec. 8.2.2);
- Radiation hardness (Ref. to Sec. 8.2.3).

3.2.2 Backgrounds and Rates

Different to hadron-hadron colliders the combination of the relatively low signal rate of the electron - hadron collisions and the requirement for stringent systematic control in deep inelastic scattering measurements calls for low beam backgrounds and detector noise. There are several backgrounds sources from the two beams:

- Hadron beam
  - Background from losses during injection: This background does not impact the data taking, but adds to the overall radiation dose in the detector.
  - Hadron beam scattering with the residual gas molecules in the beam pipe: The particles are produced like in a fixed target scattering in a forward cone in the hadron beam direction.
- Electron beam:
  - Beam-gas scattering through Coulomb and Bremsstrahlung (Bethe-Heitler) processes: Elastic and inelastic beam particle scatterings on residual gas molecules and the hadron beam
  - Touschek effect: Incoherent scattering of the particles in the same beam bunch.
  - Beam bunch replacement: The electron bunches get replaced at full energy with a frequency of 1 Hz to keep the average polarization at 0.7. This can lead to background due to the beam de-excitation, if the bunches are replaced.

All these backgrounds can be mitigated through the electron and hadron beam collimation system, but not if the scattering occurs directly at IR-6. For the scattering with the residual gas molecules the vacuum level in the extended interaction region is absolutely critical.

Figure 3.2 shows the vacuum level at IR-6 for different integrated electron current. The different integrated electron currents result in higher or lower vacuum levels as result of the vacuum bake-out, which is linearly dependent on the integrated electron current.

In the following we tabulate the cross sections and rates for the signal process and the background processes. Table **??** shows the cross sections for the total ep cross section and well as for the electron and hadron beam gas cross sections for a beam vacuum after 10000 Ahr., which can be achieved running at a luminosity of 10^{34} cm^{-2} s^{-1} for 6 month.

cross section	5 GeV x 41 GeV	5 GeV x 100 GeV	10 GeV x 100 GeV	10 GeV x 275
Total ep	28.5 μb	35 μb	41 μb	50 μb
hadron (p) beam gas	77.3 mb	76.8 mb	76.8 mb	78.5 mb
electron beam gas (Bethe-Heitler)	622 mb	622 mb	699 mb	699 mb

Table 3.1: The cross sections and rates for the signal process and the background processes

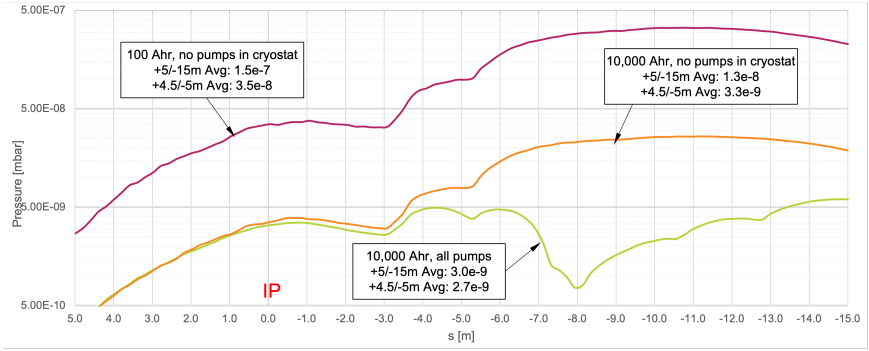

Figure 3.2: Vacuum level at IP6 for three different integrated electron beam currents assumed for the bake-out.

3.2.3 Radiation Level

Radiation levels for ePIC are detailed on the ePIC Wiki page for radiation doses [12], but relevant details will be discussed here.

3.2.3.1 Doses and fluences from e+p minimum-bias events

For all plots shown below, 1M minimum-bias PYTHIA6 e+p events (10 GeV electrons colliding with 275 GeV protons) were used, since that represents the largest potential luminosity (event rate) that the EIC will produce.

The radiation doses for ePIC are presently calculated using the Starsim framework for the STAR experiment, which uses a combination of GEANT3 [13] for particle transport and simulation of secondary particle production, and connects to both GCALOR and FLUKA for hadronic transport, especially important for calculation of fluences from non-ionizing energy loss (NIEL). NIEL fluences are cumulative in their impacts to silicon devices, and must be understood early in an experimental design.

Figure 3.3 shows the total energy deposit per fb^{-1} throughout the main ePIC detector. This is to verify the correct inclusion of the ePIC geometry into the Starsim framework, and enables rapid inspection of areas of ePIC where significant amounts of energy are deposited. It is clear that areas nearest to the outgoing hadron beam have the highest amounts of deposited energy from minimum-bias events.

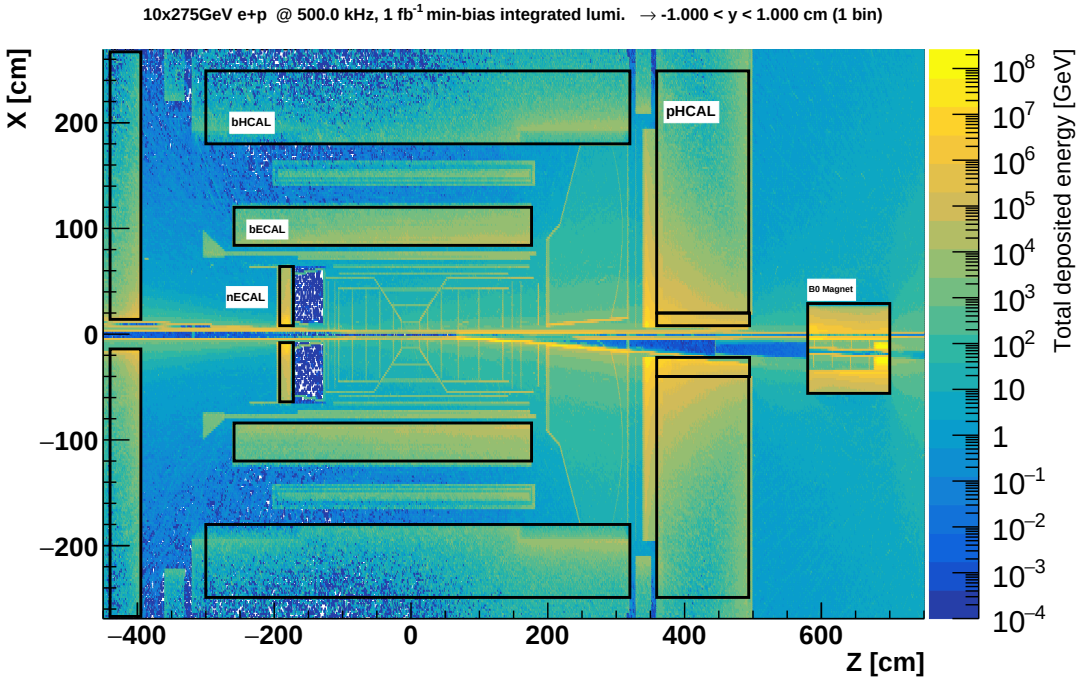

Figure 3.3: This figure shows the total energy deposited in 2cm x 2cm x 1cm bins spanning the full size of the ePIC central detector from minimum-bias e+p events generated in PYTHIA6 for 10 GeV electrons colliding with 275 GeV protons. This energy combination represents the highest potential luminosity for the EIC. The results are shown as energy deposits per fb^{-1}.

Figure 3.4 shows the total ionizing dose per fb^{-1}, and per 2cm x 2cm x 1cm bin (or voxel) throughout the main ePIC detector. The radiation dose has been calculated such that the dose per voxel is scaled by the GEANT step length and normalized to make the doses in a particular (x, y, z) location invariant to changing bin sizes. In general, the doses around the ePIC main detector from minimum-bias events are modest, and only peak at 1 kRad per fb^{-1} in the regions at the outgoing hadron beam pipe, and on the inner portion of the forward MPGD disks. There is also a significant peak of radiation dose ($\sim$ 1 kRad per fb^{-1}) in the PbWO4 calorimeter inside the B0 magnet.

For most of ePIC, total ionizing dose will not be the primary concern for radiation damage to detector components. In addition to total ionizing dose, 1 MeV neutron equivalent (MEQ) fluences are a concern for potential cumulative damage to silicon detectors, especially silicon photo multipliers, given that dark currents can notably increase with accumulation of neutron fluences, especially as they begin to exceed $10^{11} cm^{-2}$ 1 MEQ fluence. The 1 MEQ fluences are summarized for the central detector in Fig. 3.5.

The last important radiation type to consider is high energy proton and neutron ($E > 20$ MeV) fluxes which can lead to acute issues with detector electronics in the form of single event upsets

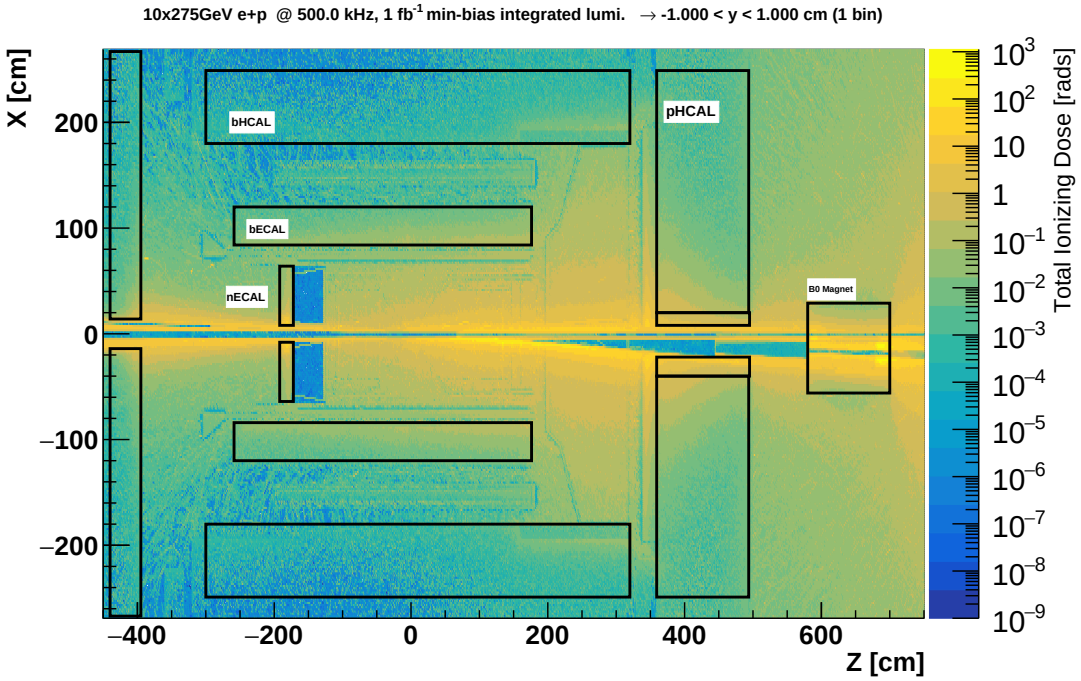

Figure 3.4: Total ionizing dose per fb^{-1} for the central region of ePIC detector from minimum-bias e+p events.

(SEU). These fluxes are shown for the ePIC central detector in Fig. 3.6.

In general, minimum-bias e+p events do not pose a major threat to most ePIC subsystems in terms of radiation damage, but there are areas of concern, especially for neutron fluences in the hadron-going calorimetry, and near the beam pipe.

3.2.3.2 Doses and fluences from hadron beam+gas events

For all plots shown below, 100k hadron beam+gas events with a 275 GeV proton beam energy (impinging on H2 molecules at rest) are used.

Figure 3.7 shows the total energy deposit per fb^{-1} throughout the main ePIC detector from hadron beam+gas events. The energy deposits from hadron beam+gas events look different from what we see in minimum-bias events because the hadron beam+gas are hadronic collisions, and also because the events are distributed along the entire beamline, up- and down-stream of the ePIC detector. This allows secondaries from many meters away from ePIC in the incoming hadron direction to impinge upon the ePIC detector, where minimum-bias collisions would not produce secondaries from those locations.

Figure 3.8 shows the total ionizing dose per fb^{-1}, and per 2cm x 2cm x 1cm bin (or voxel) throughout the main ePIC detector. In general, the ionizing doses around the ePIC main detector from hadron beam+gas events are even more modest than those from minimum-boas events, and only peak at $<$100 Rad per fb^{-1} in the regions nearest the beamline.

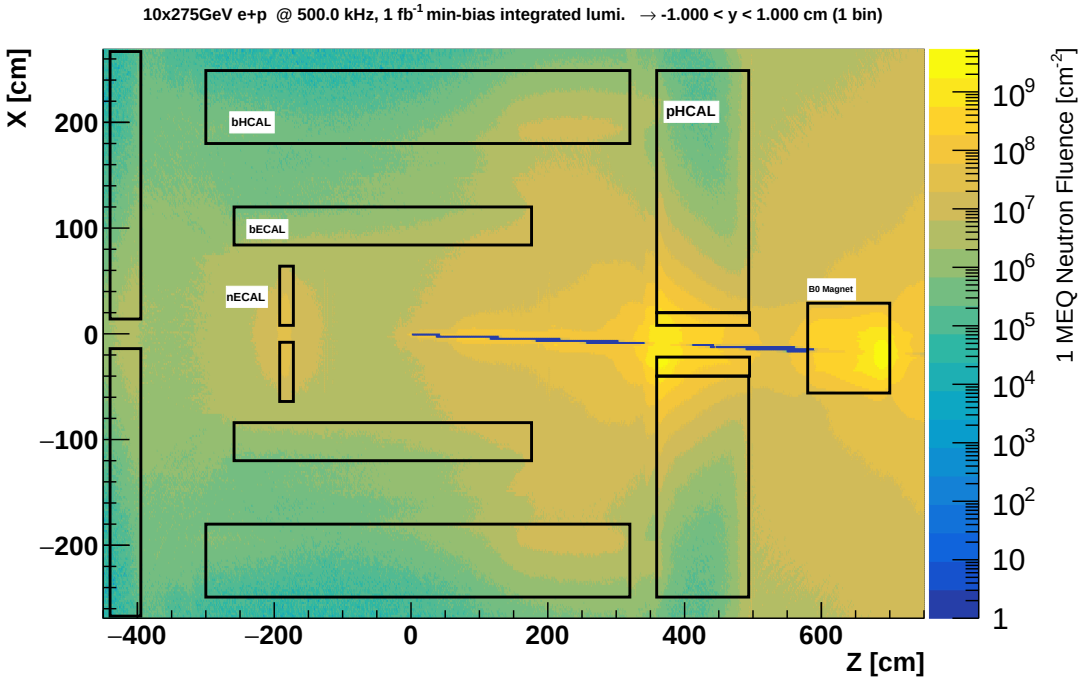

Figure 3.5: 1 MeV neutron equivalent fluences for the central ePIC detector from minimum-bias e+p events. Peak regions of MEQ fluence are seen near the beam pipe, and within the hadronic calorimeters, where the inclusion of dense absorber materials (e.g. iron) provides ample scattering centers to produce hadronic showers which can include high numbers of low-energy neutrons to provide peak MEQ fluences.

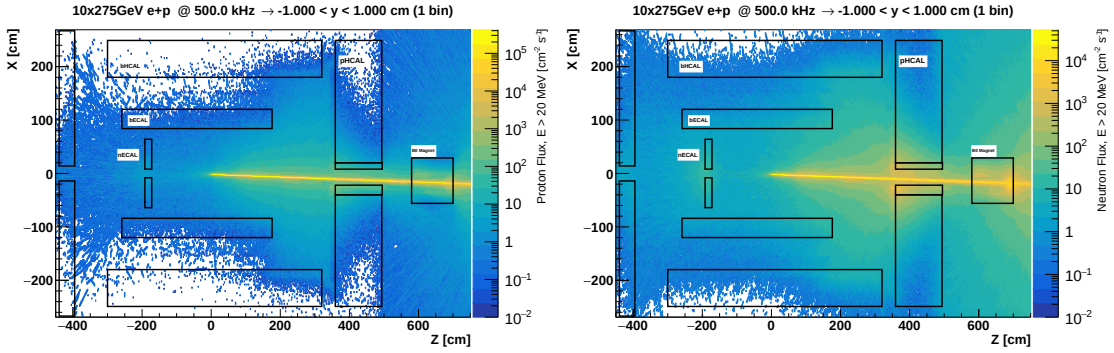

Figure 3.6: Fluxes of protons (left) and neutrons (right) with kinetic energy > 20 MeV from minimum-bias e+p events. These fluxes are important to understand areas where detector electronics could often experience SEUs, and require intervention (e.g. resetting).

For most of ePIC, total ionizing dose will not be the primary concern for radiation damage to detector components. In addition to total ionizing dose, 1 MeV neutron equivalent (MEQ) fluences are a concern for potential cumulative damage to silicon detectors, especially silicon photo multipliers, given that dark currents can notably increase with accumulation of neutron fluences, especially as they begin to exceed 10^{11}cm^{-2} 1 MEQ fluence. The 1 MEQ fluences are summarized for the central

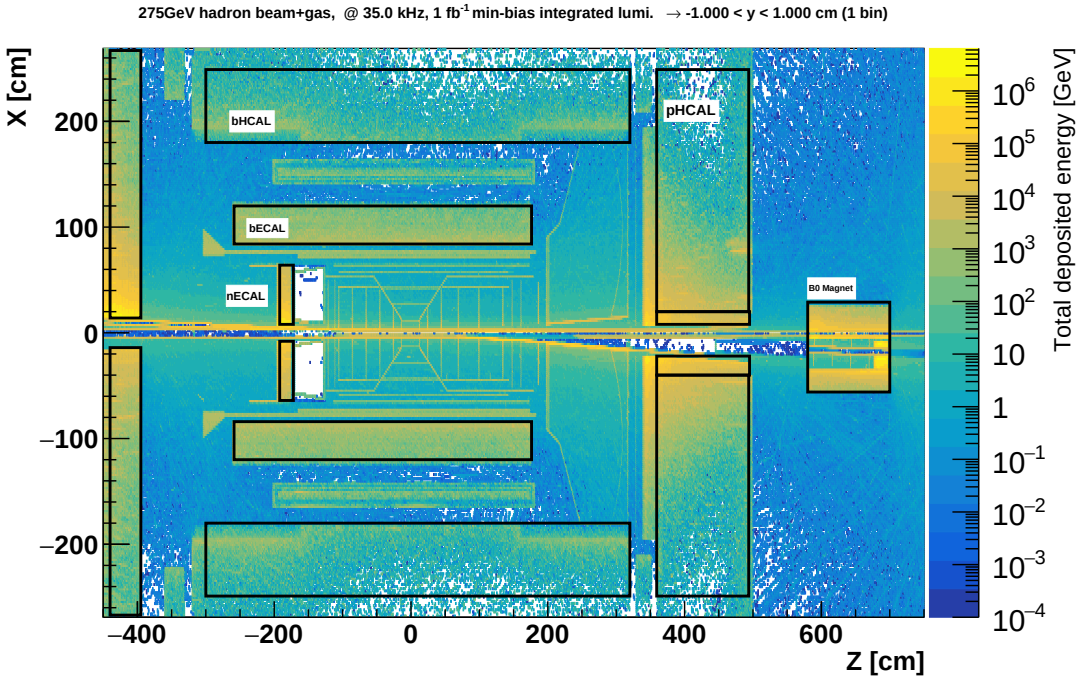

Figure 3.7: This figure shows the total energy deposited in 2cm x 2cm x 1cm bins spanning the full size of the ePIC central detector from hadron beam+gas events with 275 GeV protons. The results are shown as energy deposits per fb^{-1}.

detector in Fig. 3.9.

High energy proton and neutron ($E > 20$ MeV) fluxes are also considered, as before. These fluxes from hadron beam+gas events are shown for the ePIC central detector in Fig. 3.10.

3.2.3.3 Doses and fluences from electron beam+gas events

For all plots shown below, 300k electron beam+gas events with a 10 GeV electron beam energy (impinging on H2 molecules at rest) are used.

Figure 3.11 shows the total energy deposit per fb^{-1} throughout the main ePIC detector for electron beam+gas events. The energy is deposited asymmetrically in the ePIC detector due to the fact that beam+gas events produced upstream of ePIC (before the B0 magnet) can produce an off-energy electron which will then enter the B0 magnet and be bent off-axis into one side of the ePIC detector. This, combined with a very high rate for the electron beam+gas creates a narrow collimated beam of electrons with go through ePIC at angle, producing a high ionizing dose along the way.

Figure 3.12 shows the total ionizing dose per fb^{-1}, and per 2cm x 2cm x 1cm bin (or voxel) throughout the main ePIC detector from electron beam+gas events. As seen with the energy deposits, the ionizing doses are not deposited symmetrically in ePIC, and some hot spots are seen, ranging between 1 and 10 kRad per fb^{-1} in the tracking system, and in a small portion of the backward EMCAL.

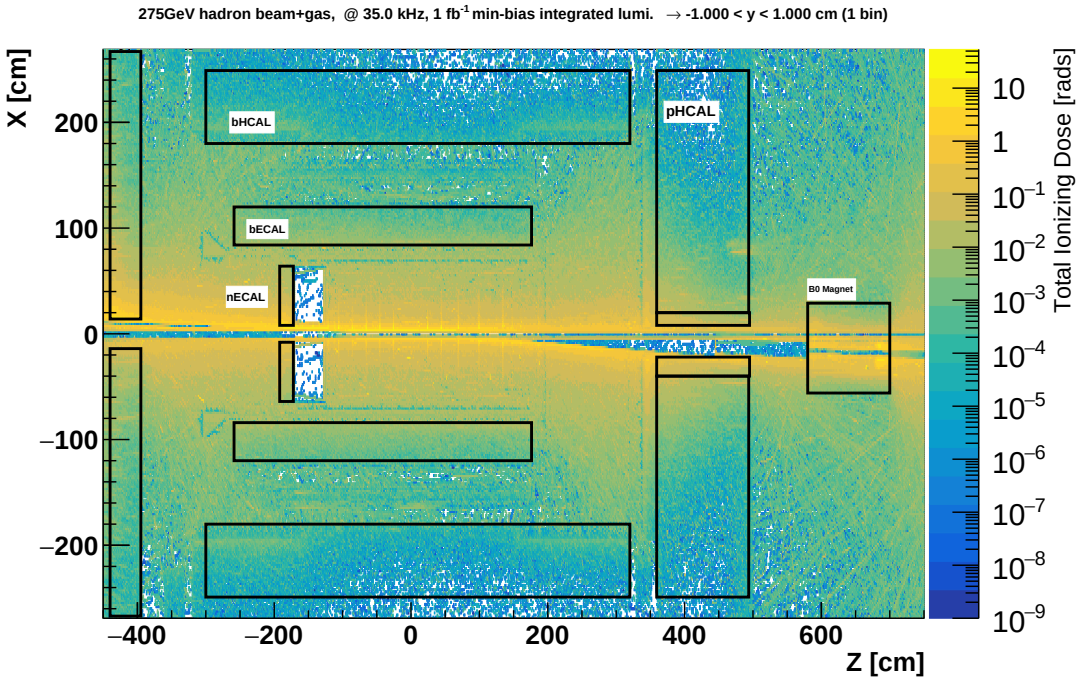

Figure 3.8: Total ionizing dose from hadron beam+gas events per fb^{-1} for the central region of ePIC detector.

Different from the other radiation sources, the total ionizing dose from the electron beam+gas events have the potential to provide a very significant amount of ionizing dose to a broader region of ePIC. In the hottest regions of the detector, doses from 1 to 10 kRad per fb^{-1} are possible.

These results are only a subset of what has been studied, and many more details are available on the Wiki page [12]. These radiation studies need to be repeated as the machine develops, and when the ePIC geometry changed. Even minor changes to the geometry of the detector can potentially have a large impact on the doses and fluences in sensitive areas of ePIC. Work is underway to import these calculations into the ePIC simulation framework to make it easier to track changes with the ePIC geometry.

3.3 The ePIC Detector

3.3.1 Introduction

The Context The development of the EIC science and the experimental equipment required to successfully implement the science as documented in the NSAC and NAS reports has been driven by an international EIC community, formalized in 2016 in the EIC User Group [14], at present (September 2024) formed by more than 1500 members from almost 300 institutions and 40 countries. Several conceptual general-purpose detectors had been elaborated. A next step effort was required by the EIC project approval with the signature of CD0 in December 2019. The User Group engaged in advancing the state of documented physics studies, which dictate the detector require-

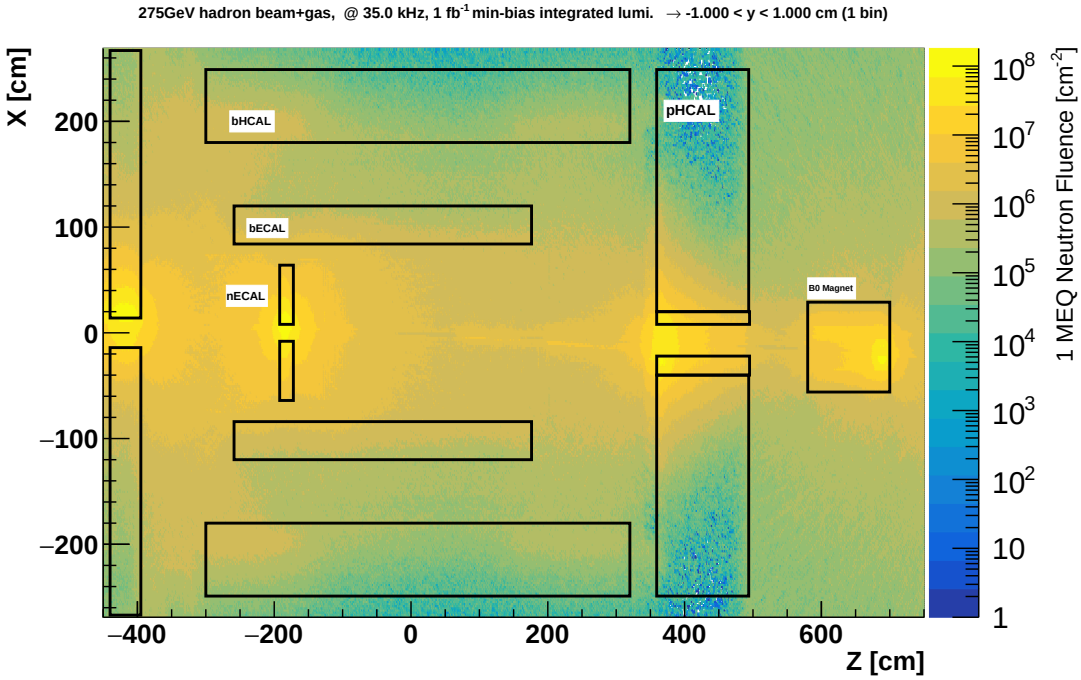

Figure 3.9: 1 MeV neutron equivalent fluences for the central ePIC detector from hadron beam+gas events. Peak regions of MEQ fluence are seen near the beam pipe, and especially near the radial interior of the calorimeters, similar to what is seen in the minimum-bias events.

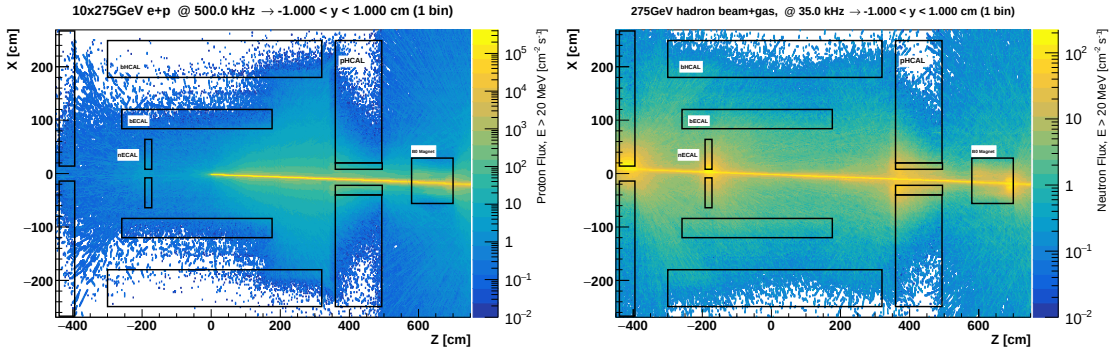

Figure 3.10: Fluxes of protons (left) and neutrons (right) with kinetic energy $>$ 20 MeV from hadron beam+gas events.

ments, and consolidate the general-purpose detector concept matching these requirements. This effort resulted in the EIC Yellow Report completed in early 2021 and then published in Nuclear Physics A [15]. This document guided the two proposals for a general-purpose detector elaborated in 2021, which resulted in further progress in the conceptual detector design. In 2022, a merging process of the communities presenting the two proposals and of the two conceptual approaches resulted in the formation of the ePIC Collaboration [16] (July 2022) and in baselining of the ePIC detector as EIC project detector. At present (September 2024), ePIC has more than 850 members

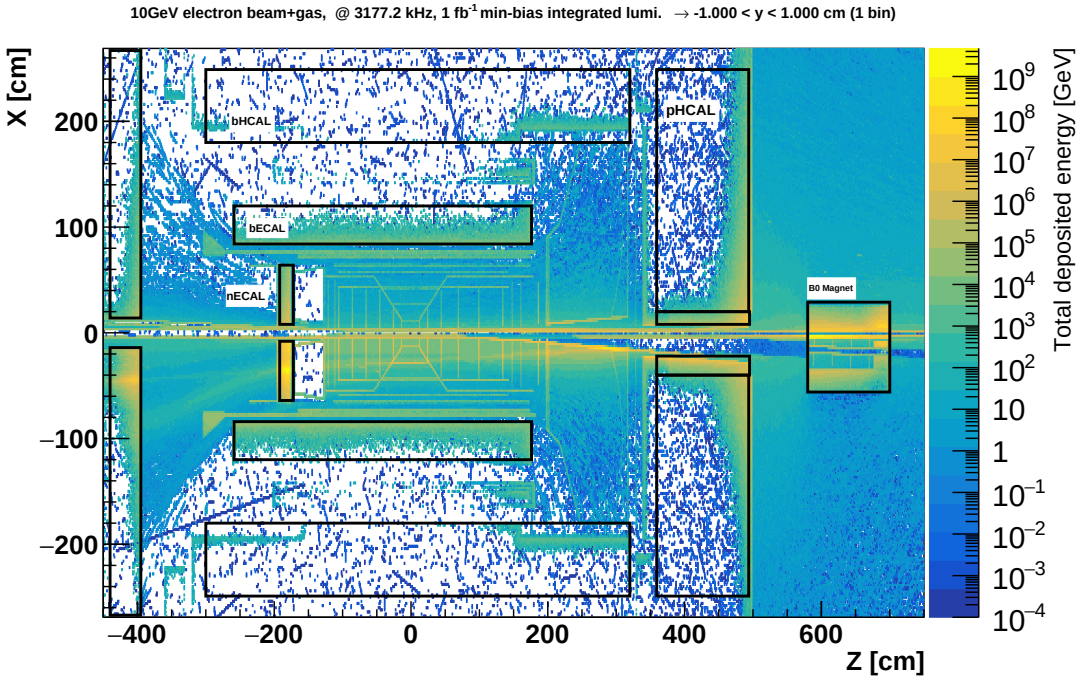

Figure 3.11: This figure shows the total energy deposited in 2cm x 2cm x 1cm bins spanning the full size of the ePIC central detector from electron beam+gas events with 10 GeV electrons. The results are shown as energy deposits per fb^{-1}.

from 177 Institutions and 25 countries, confirming the international vocation of the community pursuing the EIC science and detector.

The Detector THIS DETECTOR DESCRIPTION IS AN INTRODUCTION TO THE WHOLE SECTION 8.3. IT WILL BE REVISED WHEN THE SUBSYSTEM MATERIAL IS UPLOADED TO ENSURE A BETTER CONSISTENCY OF THE SECTION 8.3.

The detector challenges and the technologies matching these challenges are discussed in Sec. 8.2.1. The resulting design of the ePIC detector consists in a Central Detector (CD) surrounding the Interaction Point 6 (IP6) making optimal use of the space available at the Interaction Region (IR) complemented by equipment situated along the outgoing beam lines, the Far Detectors (FD), which complete the phase-space coverage.

Figure 3.13 illustrates the CD kinematic coverage; Fig. 3.14 presents a schematic overview of the CD structure. The overall CD length is imposed by the constrain of the IR design. The asymmetric beam energies reflect in an asymmetric design of the detector and, together with the requirements from physics, imposes the choice of the different detector technologies that have been adopted. The setup is designed around the solenoid providing the magnetic field for the momentum analysis. The adoption of a solenoid shapes the CD in a barrel region where the subsystem have pseudo-cylindrical layouts and two endcap regions, the forward one equipping the region around the outgoing ion beam and the backward endcap around the outgoing electron beam. The barrel subsystems cover, approximately, the pseudorapidity η region (-1.5, 1.5), while the endcaps equip the regions up to pseudorapidity $|3.5 - 4.0|$, the upper bound being dictated by the beampipe layout.

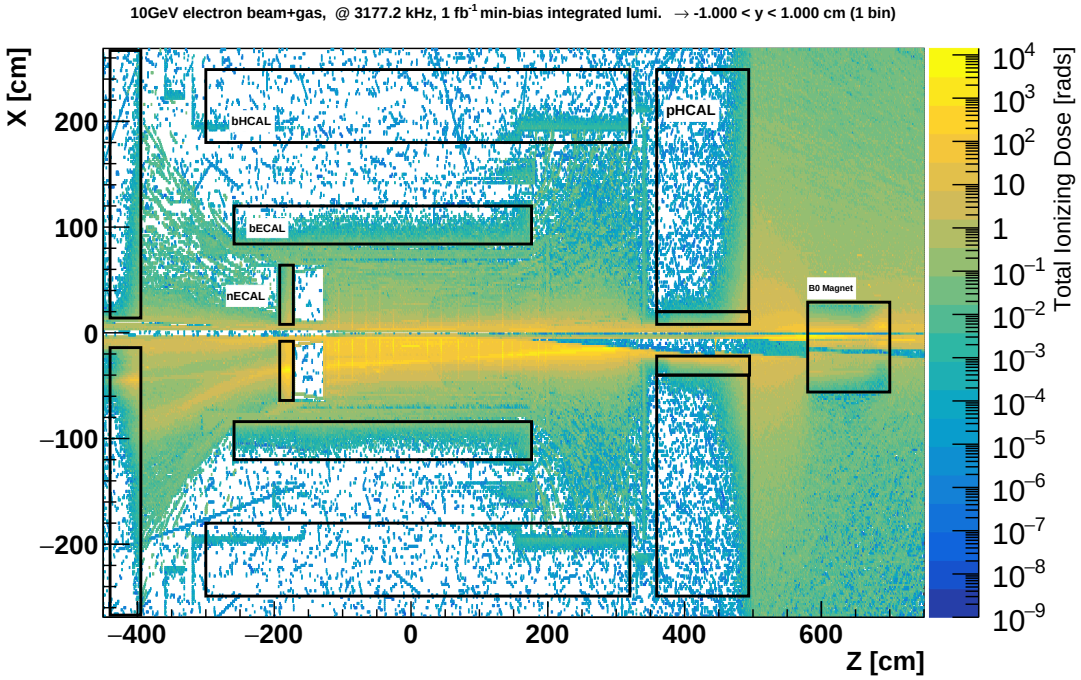

Figure 3.12: Total ionizing dose from electron beam+gas events per fb^{-1} for the central region of ePIC detector.

The separation in barrel and endcap region is not rigid with exceptions where the optimization of the detector design suggests it. For instance, the most inner layers of the tracking system have acceptance well beyond $\eta < |1.5|$, the barrel Cherenkov PID counter and the barrel electromagnetic calorimeter extends in the backward endcap.

The CD subsystems have a layered structure, from inside to outside: tracking subsystems, particle identification devices, electromagnetic calorimeters, solenoid coils in the barrel, and hadronic calorimeters.

The reference operation condition of the new **MARCO magnet** (Sec. 8.3.2), specifically designed for ePIC, is with 1.7 T field intensity and it can provide up to 2 T. It has good homogeneity in the central region and provides projective field lines in the forward endcap to match the requirements posed by the usage of a gaseous radiator in the forward RICH. The solenoid axis coincides with the electron beam line in the IR to limit the synchrotron radiation from the beam electrons. This results in helicoidal trajectories of the beam ions, due to the crossing angle of the two beams.

The **tracking system** (Sec. 8.3.3) is the most inner subsystem in order to ensure the minimum distortion of the trajectories by the material crossed by the particles. It consists of pseudo cylindrical layers completed by discs in the endcaps. The low material budget (Fig. 3.15) is guaranteed by the selected tracker technologies, with the thin ITS3 MAPS, even in support-less arrangement in the most inner layers, and MPGDs for the most external layers. The two tracker technologies support each other thanks to key complementary characteristics. MAPS sensors offer extremely fine space resolution, but poor timing information in the order of a few microsecond range. In-time hits can be selected combining MAPS information with the measurements in the MPGDs, which have time resolution of 10-20 ns. Further space and time information will be provided by the time-of-flight

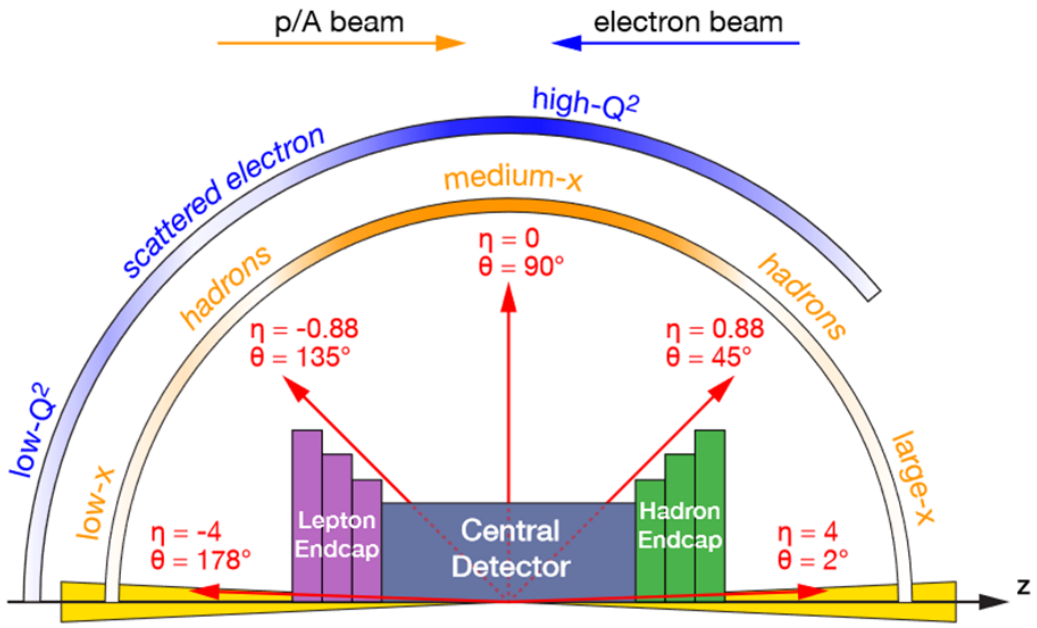

Figure 3.13: A schematic showing how hadrons and the scattered electron for different x - Q^2 are distributed over the detector rapidity coverage. THIS FIGURES IS A PLACE HOLDER: IT IS FROM YR AND REQUIRES REVISION.

layers in the barrel and the forward endcap and by the first layer of the barrel imaging electromagnetic calorimeter equipped with AstroPix MAPS sensors. The minimization of the material budget is one of the ingredients allowing fine resolution for momentum determination and vertex reconstruction. To this end, fine intrinsic resolution is requested for the trackers and it is provided by the ITS3 MAPS. The momentum resolution is affected by the available lever arm and the solenoidal configuration of the magnetic field, the latter having its largest impact on the very forward and backward trajectories.

The tracking information is also a key ingredient for the performance of the Cherenkov imaging devices; in particular, very fine resolution of the particle direction is needed for the barrel DIRC. The most external tracker layers in the barrel, positioned in front of the DIRC, further support this requirement.

The **particle identification subsystems** (Sec. 8.3.4) surround the tracking systems. Their mission is twofold: (i) supporting the electromagnetic calorimeters by complementing the pion/electron separation to ensure the high purity of the electron sample; (ii) identifying hadrons, as needed by a large fraction of the physics program. The coverage of the wide kinematic domain imposes the adoption of a variety of technologies with time-of-flight measurements complementing Cherenkov imaging devices. Time-of-flight dedicated layers by AC-LGADs are present in the barrel and in the forward endcap, the barrel layer being by strip sensor elements to reduce the material budget, while the forward endcap layer is by pixelized AC-LGADs. In the backward endcap, the fine time-resolution provided by the photosensors of the Cherenov counter, which are sitting in the endcap acceptance, provide timing information via the Cherenkov light generated in the sensor window. The Cherenkov imaging counter in the backward endcap is a proximity focusing RICH with aerogel radiator and extended proximity gap to increase the resolution and, correspondingly,

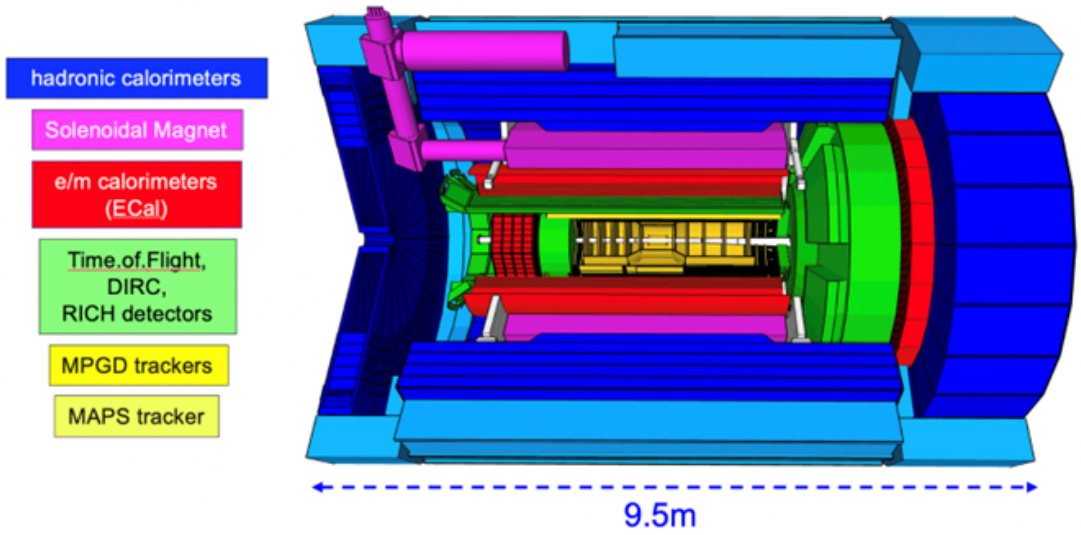

Figure 3.14: A schematic showing the ePIC central detector subsystems. THIS FIGURES IS A PLACE HOLDER

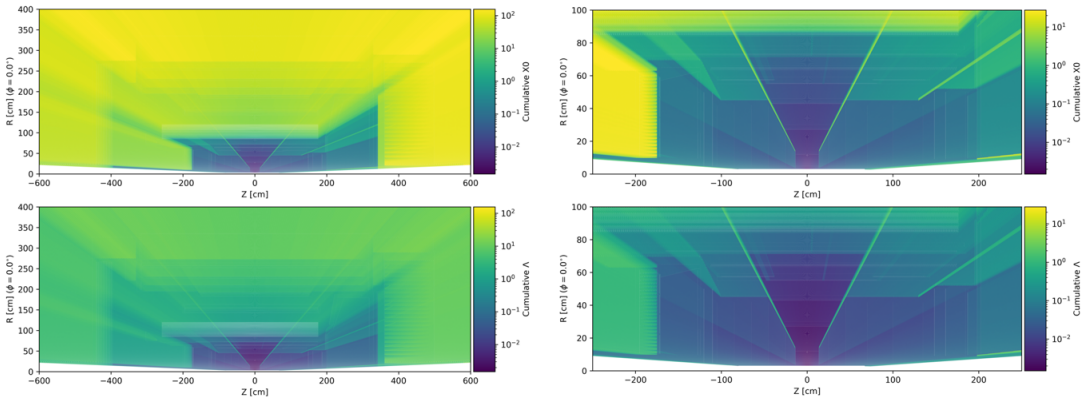

Figure 3.15: Cumulative material budget in radiation lengths (top row) and interaction lengths (bottom row) for the whole CD (left column) and zooming at the CD tracking region (right column). THIS FIGURES IS A PLACE HOLDER BECAUSE IT HAS TO BE COMPLETED WITH SUBSYSTEM CONTOURS AND REQUIRES GRAPHICAL IMPROVEMENTS.

enlarging the momentum range for particle identification. As already underlined, the use of fine-time resolution HRPPDs by MCP technology as photosensors also provides timing information. The whole detector components are positioned in the acceptance, in front of the electromagnetic calorimeter. This layout is compatible with the overall detector design; in fact, the bulky elements, namely the sensors with readout electronics and services are just in front of the calorimeter acting as a pre-shower element. In the barrel, a high performance DIRC is used, this choice being dictated by the reduced space. The DIRC fused silica bars, acting as radiator and as photon lightguides, make possible positioning the image expansion elements and the read-out electronics with its services in the backward region, outside the acceptance cone. The dual radiator RICH (Sec) in the forward endcap is equipped with two radiators, aerogel and gas, therefore acting as a couple of Cherenkov

imaging counters dedicated to particle identification in two different momentum ranges, while economizing in space and single photon sensors. It is a focusing RICH with spherical mirrors as focusing elements. The photosensors and related services are placed outside the acceptance thank to appropriate mirror orientation.

The electromagnetic calorimeters (Sec. 8.3.5) are external to the particle identification devices and, once more, the different technologies are imposed by the physics requirements, the kinematic ranges and the overall constrains. The budget of the material in front of the calorimeters is low and mainly concentrated near to the calorimeter front face. The backward endcap electromagnetic calorimeter is by fine granularity lead tungstate crystal offering very fine energy resolution. In the barrel, the electromagnetic calorimeter has a hybrid architecture combining imaging layers by AstroPix MAPS and sampling calorimetry by lead and scintillating fibers with sampling layer between the imaging layers and in the most external calorimeter portion. The layout is pseudo cylindrical with the read-out equipment at the cylinder edges minimizing the space requirement in the crowded barrel area. The electromagnetic calorimetry in the forward region is by sampling calorimetry with scintillating fibers inserted in matrices of tungsten powder embedded in epoxy. This calorimeter offer a near to 1 ratio of the signal amplitude response for electrons and hadrons and, therefore, it is design to operate in duet with the hadronic calorimeter place immediately behind.

All the **hadron calorimeters** (Sec. 8.3.6) are by iron as converter and scintillating active elements, even if with very different implementations. The forward endcap calorimeter is by SiPM-on-tile technology, with finer granularity in the central zone, near to the beam pipe, to cope with the higher rates. The barrel calorimeter, placed behind the solenoid coils, acts as a tail catcher. The backward endcap calorimeter ... (to be completed: layout in evolution).

All the calorimeter subsystem in the ePIC detector make use of SiPMs as photosensors, even if of different size and pixelization, with common approach for the readout chain.

The global layout of the FDs (Sec.s 8.3.7 and 8.3.8) is illustrated in a artistic view in Fig. 3.16.

The **forward FDs** include tracking and electromagnetic calorimetry inserted in the first dipole of the ion beam line B0, off-momentum detector trackers and roman-pot trackers and a zero-degree-calorimeter. The technology for the trackers is by AC-LGADs, which have good radiation hardness. The B0 electromagnetic calorimeter is by lead tungstate crystals. The zero-degree-calorimeter is formed by a long SiPM-on-tile module with fine granularity adequate for photon and neutron detection. A crystal layer can be inserted in front of it for those studies that require the detection of low energy photons.

The **luminosity system** is part of the backward FD. Based on the measurement of the photons from the Betha-Heitler process at IP, it consists of a high-rate calorimeter for direct photon detection and a couple of pair spectrometers to detect the electrons and positrons generated by the Betha-Heitler photons in the exit window. The high-rate calorimeter and the calorimeters in the pair spectrometers are by tungstate and scintillating fibers. Tracking in the pair spectrometer is by AC-LGADs. The **low-Q^2** taggers consist in tracking stations followed by an electromagnetic calorimeter. The selected technologies must cope with extremely high rate in this kinematic region. Therefore, tracking is by TimePix4 and calorimetry by tungstate and scintillating fibers.

Integral elements of the detector are the **electronic read-out chain**, the data acquisition system (Sec. 8.3.10) and the **software implementation and computing model** (Sec. 8.3.11). The overall underlining model that has guided the selection of the components and the design of the read-out/DAQ/software/computing architecture is the streaming readout concept. Streaming readout has been selected to simplify the readout scheme as no triggers are required and to increase the information selection flexibility, to improve the event building from the holistic detector informa-

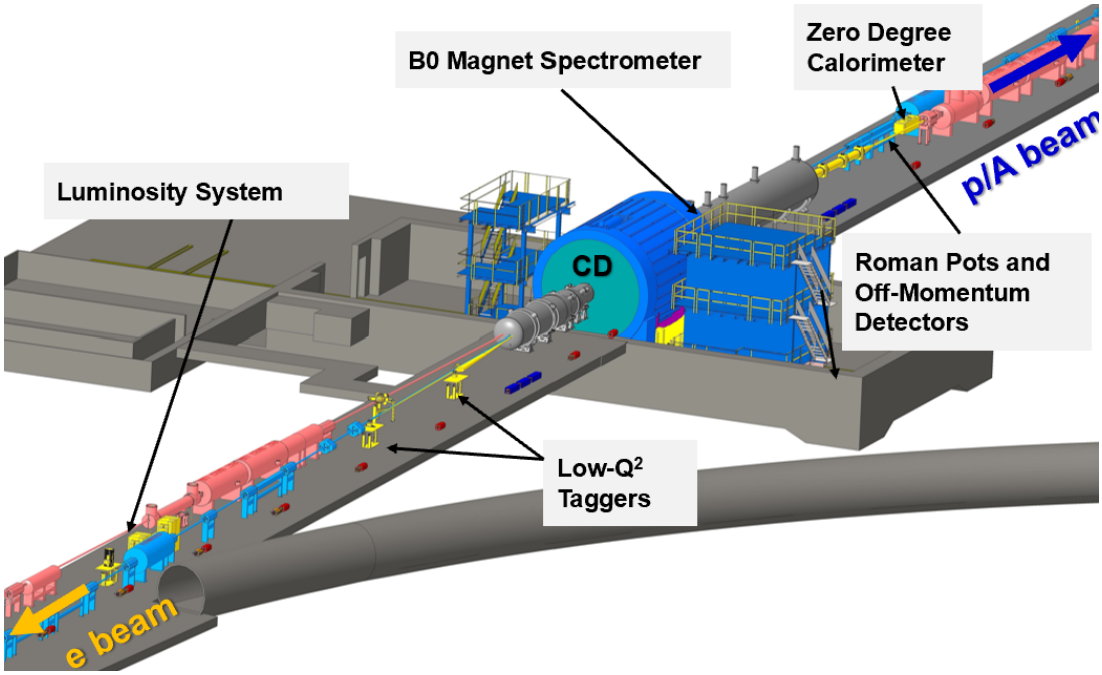

Figure 3.16: A schematic showing the ePIC far detector subsystems. THIS FIGURES IS A PLACE HOLDER

tion, to improve, via continuous dataflow, the knowledge of backgrounds and, therefore, enhances the control over systematics. In this approach, already at the front-end level, the ASICs, which are intimate related to the sensors and their performance, have been selected with architectures compatible with their usage in streaming readout mode.

Independent setups are designed to measure and monitor the **beam polarization** (Sec. 8.3.9). Rapid, precise beam polarization measurements will be crucial for meeting the goals of the EIC physics program as the uncertainty in the polarization propagates directly into the uncertainty for relevant observables as asymmetries. The basic requirements for beam polarimetry are non-destructive with minimal impact on the beam lifetime, uncertainty at the 1% level, the capacity of measuring the beam polarization for each bunch in the ring with rapid, quasi-online analysis in order to provide timely feedback for accelerator setting up. The electron beam polarimetry will be based on the well established Compton polarimeter techniques, where the polarized electrons scatter from 100% circularly polarized laser photons. This approach offers the advantage that both longitudinal and transversal polarizations are measured. Hadron polarimetry has been successfully performed on RHIC polarized proton beams for nearly two decades. Through continual development a relative systematic uncertainty ¡1.5% was achieved for the most recent RHIC polarized proton run. As the only hadron polarimeter system at a high energy collider it is the natural starting point for hadron polarimetry at the EIC. Hadron polarization will be measured via a transverse single spin left right asymmetry in the pp interaction on targets by plastic material (H-C composition), where the experimental challenge is the control of the background events.

Technological Synergistic Aspects of the Detector Design The synergistic aspects of the ePIC detector have been carefully maximized in view of the optimal usage of the workforce and the financial resources. This is illustrated by the following examples.

SiPM sensors, recently introduced in calorimetry applications, are adopted for all the electromagnetic and hadronic calorimeters in ePIC. They offer a cost-effective technology that can operate in magnetic field, can provide wide dynamic range when the sensor type is properly chosen to tune the response parameters, and present low noise level by applying appropriate thresholding. The use of a common technology makes possible to access the effect of the radiation by a single effort and the use of the same front-end ASIC CALOROC.

Also the calorimetry reconstruction software is synergistic for the overall set of subsystems.

In electromagnetic calorimetry, the sampling approach with tungsten and scintillating fiber is adopted for the forward endcap calorimeter and in FDs: calorimetry in B0, luminosity system and low-Q^2 taggers.

In hadron calorimetry, the SiPM-on-tile technology is used for the forward endcap calorimeter and its insert in the central area, as well as for the zero-degree calorimeter.

In particle identification by Cherenkov imaging counters, MCP-based photosensors are used for the backward endcap RICH and the barrel DIRC, that can be read by the same read-out ASIC HGCROC (information to be crosschecked). The backward endcap RICH and the forward endcap RICH use aerogel as radiator and the quality assessment station will be used for both batches. The reconstruction software in both RICHes has large communalities and it is based on the same ray-tracing algorithm.

AC-LGADs form the time-of-flight layers and are used for tracking in the forward FD in B0, off momentum detectors and roman pots, and selected for the pair spectrometers of the luminosity system.

In tracking by MAPS, the different sensors of the inner layers, the outer layers and the forward and backward disks are all evolutions of the ITS3 sensor, therefore all based on stitching the same readout chip element.

The same hybrid MPGD architecture with a preamplifying GEM layer followed by a μRWELL is used in the most outer tracker in the barrel and the most external discs in the endcaps. All MPGDs, namely the hybrid MPGDs and the cylindrical Micromegas in the barrel are coupled to the same front-end ASIC: SALSA.

A single integrated effort is at the basis of the tracking reconstruction with the use of the software package AC.

3.3.2 Magnet

Introduction A high-performance solenoid is required for the ePIC detector. The needed magnetic rigidity for secondary particles in the ePIC detector will be assured by a one-of-a-kind 2 T superconducting solenoid. The magnet design work is a collaborative work between JLab Magnet group, CEA, Saclay and BNL. MARCO (Magnet with Renewed Coils) presents some unusual design characteristics respect to other detector magnets: the most important is its conductor, a NbTi Rutherford cable in Copper Channel (RICC), especially optimized to stand the forces during the cool-down and energization while providing a high enthalpy stability and a fast quench propagation. The coils of the magnet are wound internally on a thin brass mandrel, which provides both a similar thermal retrain than the coil pack and, the needed rigidity without compromising the transparency of the magnet. The magnet will be cool-down by a thermosiphon, the cooling circuit is closed by a helium phase separator vessel placed outside the iron yoke and cryogenically connected to the main LHe circuit of the accelerator. The magnet is shifted of 10 cm towards the lepton

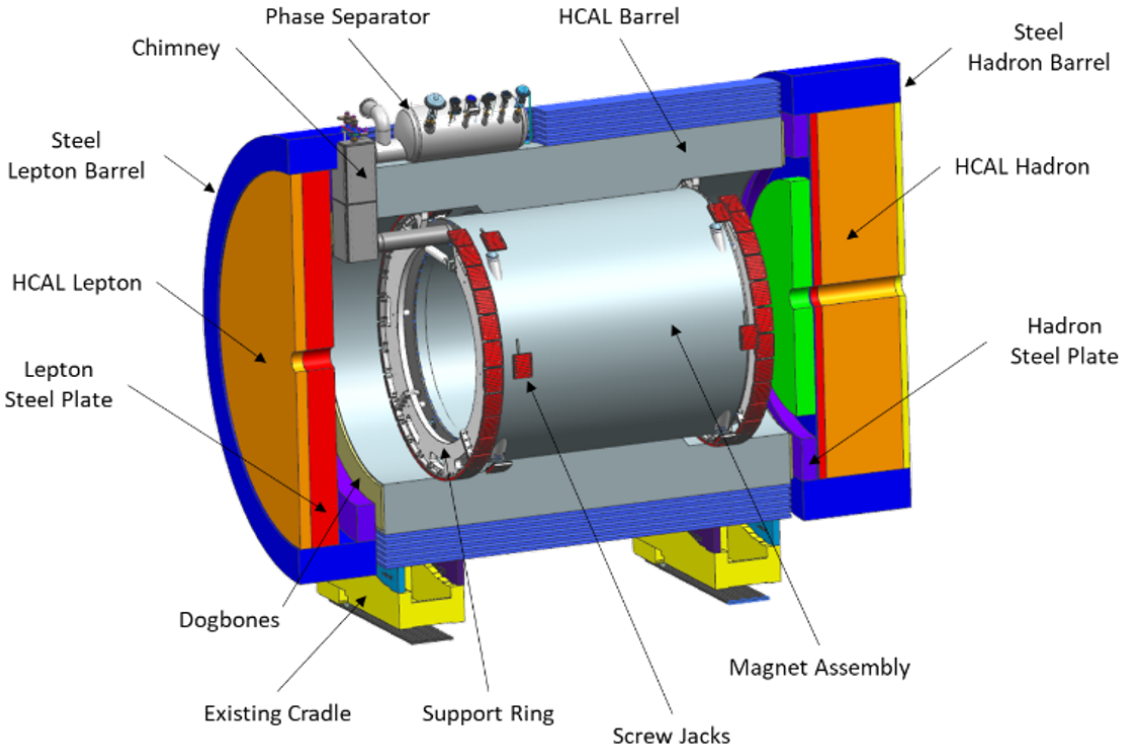

Figure 3.17: MARCO Magnet inside the iron yoke.

side respect to the interaction point to better accommodate the sub-detectors. Such asymmetry has been considered while designing the iron yoke around, in order to minimize the magnetic forces acting on the magnet. In the following sections, the design of the overall magnet will be presented. Figure 3.17 shows the magnet assembly overview in its iron yoke. The iron yoke is divided in three sections, respectively Lepton, Barrel and Hadron, made of several components, including some hadronic calorimeters. Their names indicate the sides from which the particles beams come.

Requirements The magnet is located in the interaction region of the EIC, therefore, some of the requirements are driven by the other magnets in the IR and nearby beam lines in the tunnel. Table 3.2 shows the MARCO magnet requirements.

Regarding the magnetic performances demanded, there are three zones of main interest:

The Flat Field area Described as cylinder of radius 80 cm for a total length of 200 cm, centered on the interaction point IP. The For this area, the requirement is to have a field uniformity defined as:

$$Field\ uniformity = 100\frac{dB}{Bcenter}$$

Where: TO BE COMPLETED

Parameter	Value	Unit
Nominal central field at IP	2.0	T
Operating field range	0.5 ÷ 2.0	T
Magnetic field polarity	Bipolar	
Coil length	3492	mm
Warm bore diameter	2840	mm
Cryostat length	¡ 3850	mm
Cryostat outer diameter	¡ 3540	mm
Yoke diameter	$\leq$ 6500	mm
Axial yoke length	$\leq$ 9500	mm
Field uniformity in Flat Field area	12.5	%
Integrated fringe field on RCS	¡ 0.007	Tm
Fringe field on IR magnets	¡ 10	G
Projectivity in RICH area	¡ 10	T/Amm²
Thickness/Nuclear interaction length	¡ 0.5	
Charging voltage	¡ 10	V
Fast discharge voltage (max)	±500	V
Quench hot spot temperature	¡ 150	K
Temperature margin	¿ 1.5	K
Current margin	30	%
Operating temperature	4.5	K

Table 3.2: MARCO Magnet Requirements

The RICH Area In order to maximize the RICH performances based on the gas radiator, it is critical to minimize the bending of the tracks in the volume of the gas radiator, for this one need to shape the field such that it is parallel to the different scattering angles of particles covered by the RICH. The RICH area extends from z=+180 cm to +280 cm with the shape of a truncated cone. The projectivity in this region should be less than 10 T/Amm² or less than 0.1 mrad @30GeV/c for a proton. The projectivity can be calculated as:

INSERT FORMULA

The IR magnets and RCS The detector solenoid has neighboring IR magnets, the B0ApF and Q1ApR are the closest to the solenoid magnet, these extends from z = 7.4 m to 8 m and z = -5.3 m to -7.1 m respectively. In order to not perturb the particle beams, the fringe field produced by the solenoid on these magnets needs to be less than 10 G. The Rapid Cycling Synchrotron (RCS) is radially 335.2 cm from the magnet central axis and stray field requirement there is ¡0.007 Tm. The IR layout is shown in Figure 3.18:

Geometry and Materials of the Yoke The magnetic flux generated by the superconducting coils is returned via three distinct sections of yoke: the Barrel Yoke, the Lepton Yoke and the Hadron Yoke (as shown in 3.17). Their geometry has been defined through an optimization process which includes both the experimental constraints and the requirements for the fringe field.

- **Barrel Yoke:** the Barrel Yoke consists of the HCal Barrel Calorimeter and the Steel Barrel

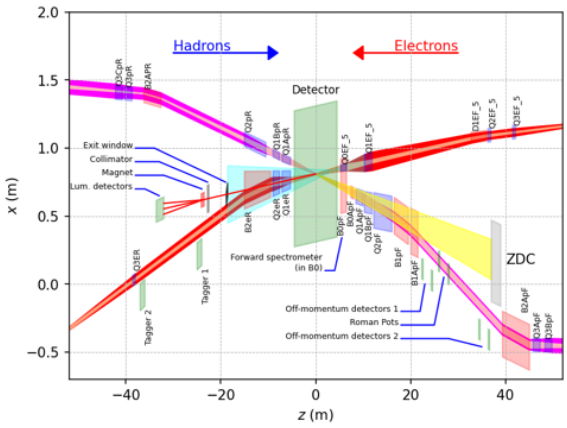

Figure 3.18: IR Layout showing all the other magnets

Yoke. The HCal Barrel Calorimeter is made with 32 assembled sectors composed by 10 rows of 8 mm scintillators tiles (24 tiles per row), tilted with an angle of 12°. In each sector, 26.1 mm x 42.4 mm x 6300 mm tapered 1020 steel plates are piled up and used to separate each scintillator tile. The total fraction of steel in the volume is 70%. Dogbones made by the same steel enclose the calorimeter. Their fraction of steel in the volume is 66%. The Steel Barrel Yoke is made by 6 concentric rings of steel 1020, 50 mm thick, 6300 mm long, surrounding the HCal Barrel Calorimeter. Each ring is separated from the other by 40 mm. A specific volume is dedicated to the installation of the He phase separator, from which all the cryogenics circuits inside the cold mass are supplied. The Steel Barrel Yoke main purpose is to reduce the stray field.

- **Hadron Yoke:** The Hadron Yoke consists of the HCal Hadron Calorimeter, the Steel Barrel Hadron Yoke and the HCal Hadron Oculus. Its name is given by the convention on the direction of the beams. In this case, the hadron beam is the one exiting the detector. The HCal Hadron Calorimeter is made by 70 pieces of 4 mm thick scintillator tiles, 10 pieces of 16 mm thick tungsten plates and 60 pieces of 16 mm thick steel 1020 plates. The average fraction of steel 1020 in the total volume is 75%. The Steel Barrel Hadron Yoke as well as the HCal Hadron Oculus are two structures in steel 1020 surrounding the calorimeter and returning the magnetic flux.

- **Lepton Yoke:** The Lepton Yoke is composed by the HCal Lepton Calorimeter, the Steel Barrel Lepton Yoke and the HCal Lepton Oculus. Its name is given by the convention on the direction of the beams. In this case, the electrons beam is the one exiting the detector. The HCal Lepton Calorimeter is made by 50 pieces of 4 mm thick scintillator tiles, 10 pieces of 16 mm thick tungsten plates and 60 pieces of 16 mm thick steel 1020 plates. The average fraction of steel 1020 in the total volume is 75%. The Steel Barrel Lepton Yoke as well as the HCal Lepton Oculus are two structures in steel 1020 surrounding the calorimeter and returning the magnetic flux.

For all the electro-magnetic simulations, the envelope of each component of the yoke has been considered, and for each volume a dilution percentage corresponding to the average fraction of steel present has been taken into account. The BH curve for 1020 steel is shown in Figure 3.19

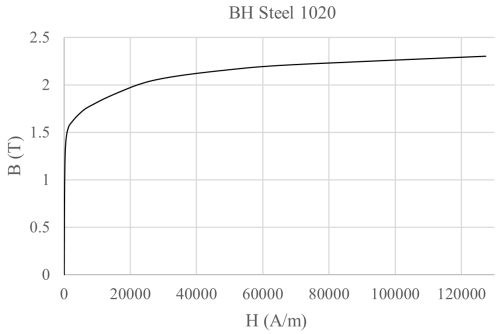

Figure 3.19: BH curve of 1020 steel

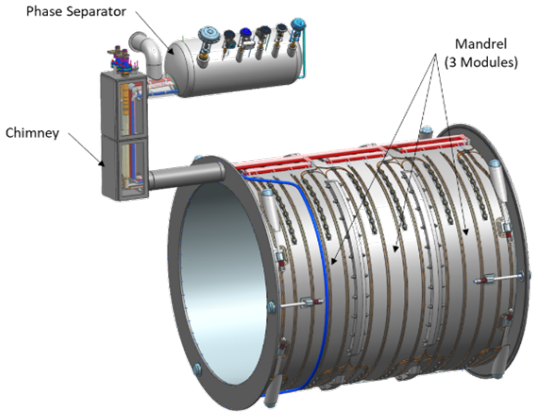

Figure 3.20: MARCO cold mass layout inside the cryostat.

Description of the magnet The solenoid is made of three modules with three identical superconducting coils winded internally on a mandrel in brass 70-30. The coils are indirectly cooled using a thermosiphon (as shown in Figure 3.20) . All the cryogenics circuits are connected to a LHe phase separator, connected itself to the main cryogenics circuit of the accelerator. The connection is made through a chimney, where the current leads are also placed.

For each module, 6 single layers of RICC conductor are wound internally to a mandrel, for a total number of turns per layer varying between 92 and 93, according to the conductor exits. The total number of turns per module is 556. Layers are named L1, L2, L3, L4, L5, L6 with L1 being the innermost and L6 the outermost. Each layer is separated by an inter-layer fiber glass insulation of 2 layers of 0.2 mm to achieve a good electrical insulation after winding and to prevent the conductor damages. The coil pack is separated from the mandrel by 1 mm of ground insulation, the same value as CMS solenoid, to prevent electrical short-circuits, to protect the conductor insulation during winding, and to facilitate the impregnation keeping a good thermal coupling for cool-down and quench-back. A schematic cross-section of the coil pack with the thickness of each item is shown in Figure 3.21. Figure 3.21 also shows the schematic cross-section of the RICC NbTi conductor chosen, with the dimensions of each element. On the inner side of the coil pack, the impregnation should provide an average thickness of G10 of 2 mm.

The geometric specifications and dimensions of MARCO solenoid are reported in Table 3.3. The electric scheme for the solenoid is shown in Figure 3.22. Each layer is made by winding one conduc-

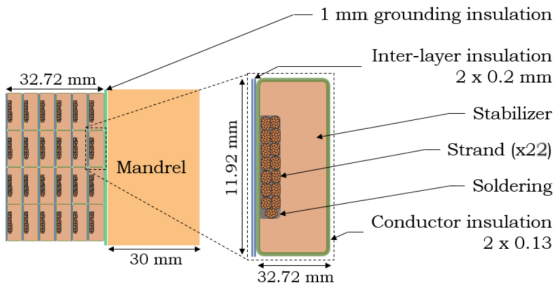

Figure 3.21: Schematic cross section of coil pack and conductor

Parameter	Value	Unit
Bore radius	1420	mm
Cryostat outer radius	1770	mm
Cryostat axial length	3850	mm
Mandrel Length (300K)	3620	mm
Mandrel Length (4K)	3608	mm
Number of Modules	3	
Z- (MOD1) / Z+ (MOD3) Modules Length (300K)	1228	mm
Central Module (MOD 2) Length (300K)	1164	mm
Coils Inner Radius (300K)	1509.5	mm
Coil Inner Radius (4K)	1502.5	mm
Coils Thickness	32.7	mm
Coils Outer Radius (300K)	1542.2	mm
Ground Insulation Thickness	1	mm
Mandrel Inner Radius	1543.2	mm
Mandrel Thickness	30	mm
Mandrel Outer Radius (300K) without Flanges	1573.2	mm
Number of Layers per Module	6	
Number of Turns per Module	556	

Table 3.3: MARCO geometric Specifications

tor unit length (1̃ km long), and all the layers are connected in series with conductor splices outside the mandrel. Conductor exits are positioned at approximately 120° on the mandrel as shown in Figure 3.23.

Such arrangement preserves the number of turns. The extremities (front/rear) of each coil pack have in total 5 turns over 6. The exits will be made with grooves cut in the mandrel. Each groove will be:

- Thick enough to double the conductor in order to increase the stability and to insulate it with G10 fillers and fiberglass insulation Figure E;
- Tangent to the outer diameter of each terminal with a 1 mm G10 plate between the splice and the mandrel;

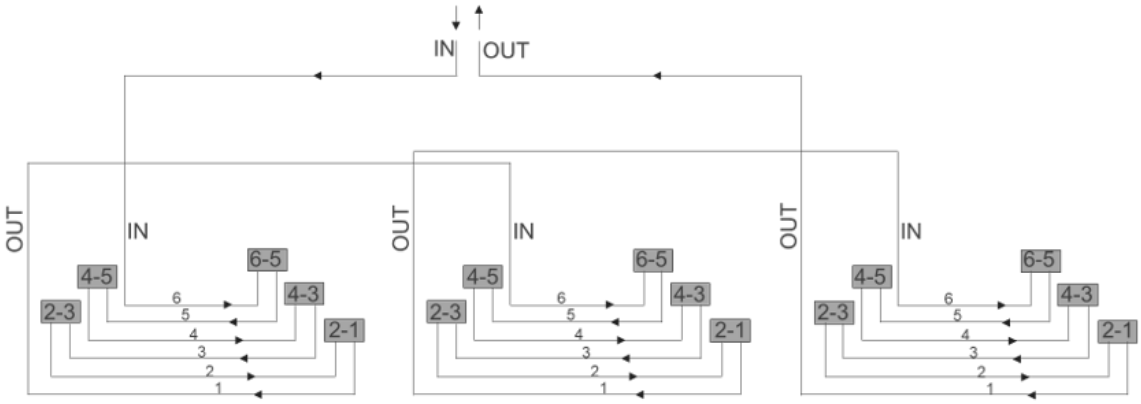

Figure 3.22: Electric schematic of MARCO Solenoid

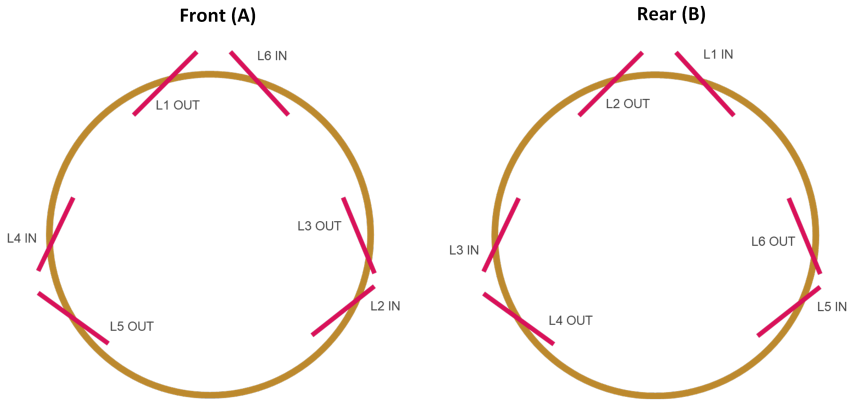

Figure 3.23: Conductor entrance and exit schematic for each module

- Separated with a distance larger than two times of the hard-way radius of the conductor (2 x 120 mm).

A schematic of the grooves' arrangement is shown in Figure 3.24 and Figure 3.25. Splices between doubled conductors are thermalized thanks to a series of copper plates connected to the mandrel itself cooled down by the thermosiphon.

In order to fulfill the requirements in Table 3.3, the mandrel is longer than the coil for each module. The extra length is equal to 24.84 mm (2x11.92 mm [2 turns] plus 1 mm for tolerances), which gives a separation of 55.5 mm between each coil. This gap will be filled with G10 wedges, which will be glue to the mandrel, plus a 3 mm insulation between each module to take care of the tolerances of manufacturing, positioning and tolerance stack up Figure 3.26.

Each module is impregnated independently and bolted together through flanges. Flanges are not continuous on the entire circumference of the mandrel in order to let the thermosiphon pipes, the conductor splices and wire sensors all the space required. On the two outer modules, 4 radial and 3 axial tie-rods in Ti_6Al_4V are present to sustain the mass of the magnet and the efforts during the cool-down and the energization. A schematic description of the tie-rods is shown in Figure 3.27. A general scheme of the magnet assembly inside the cryostat is shown in Figure 3.28. In the same

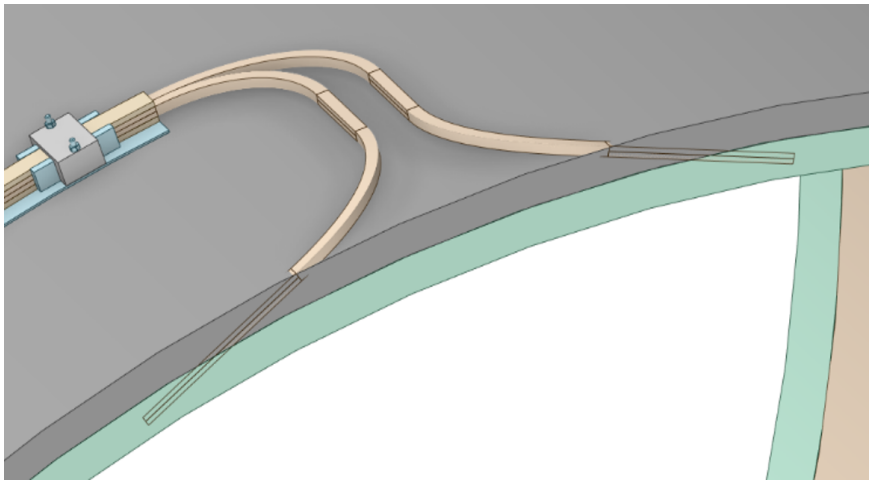

Figure 3.24: Design of the Splices exits from the mandrel

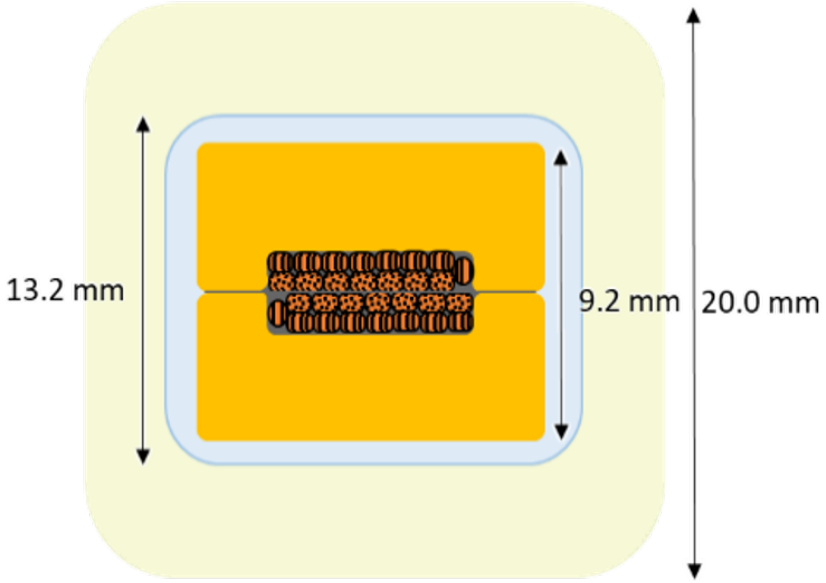

Figure 3.25: Schematic cross-section of the splice to be place inside the groove

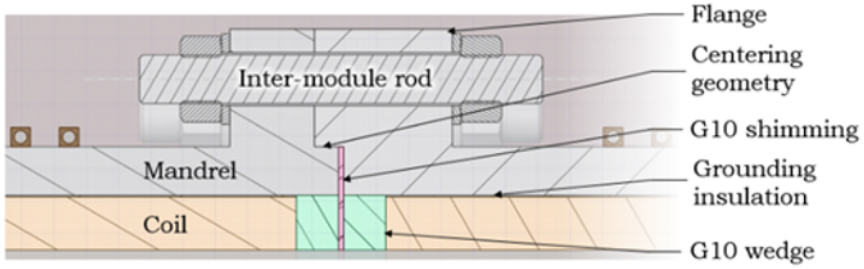

Figure 3.26: Schematics of the geometry at the interface between each coil

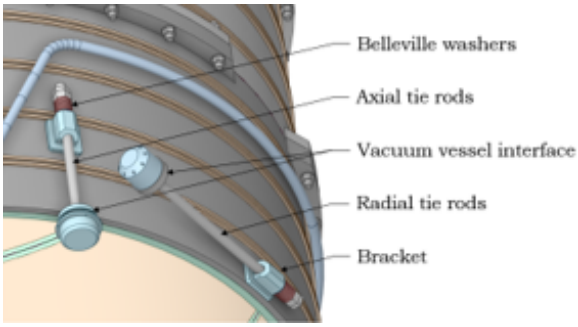

Figure 3.27: Schematics of the tie-rods geometry

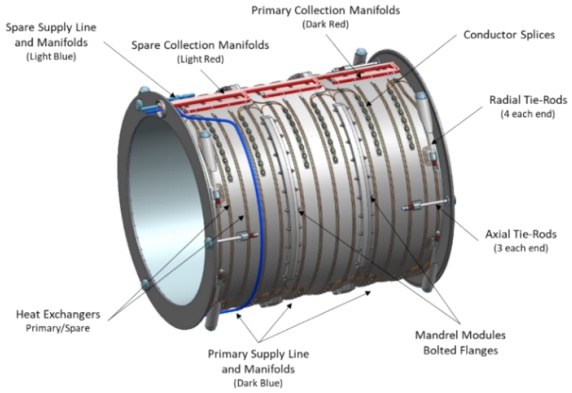

Figure 3.28: Magnet assembly inside the cryostat

figure, the two thermosiphon manifolds (the main and the spare) with the respective supply lines and heat exchangers are showed. The cold mass is placed inside a cylindrical vacuum vessel made in Al6061-T6 Figure 3.29, with a thickness on the inner and outer shell of respectively 14 mm and 25 mm. The two shells joint together through flanges 40 mm thick. Inside the cryostat, a thermal shield made in Al3003 with 3 4 internal panels and 3 4 outer panels is located. The thermal shield is cooled by 3 circuits in parallel, cooling the internal panels first. Between the vacuum vessel and the outer shield, there are 30 layers of MLI; while between the coil and the internal shield, there are 10 layers of MLI to guarantee the superinsulation.

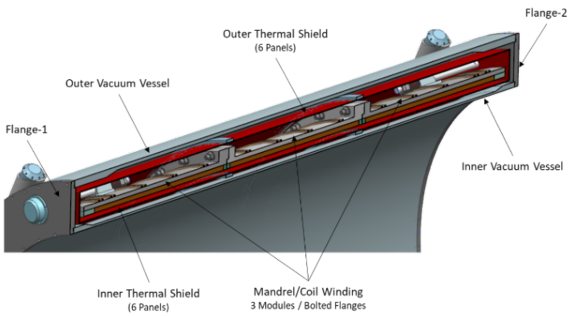

Figure 3.29: Schematics of the cryostat with the magnet inside

Component	Radial thickness (mm)	Material	Nuclear interaction l
Inner vacuum vessel	14	Al6061	107.2
Inner thermal shield	5	Al3003	107.2
Inner G10	2	G10	78.4
Coil	33.7	14 % Insulation 80 % Cu 6 % NbTi	Insulation: 78.4 Cu: 13
Mandrel	30	Brass 7030	137.7
Outer thermal shield	5	Al3003	107.2
Outer vacuum vessel	25	Al6061	107.2

Table 3.4: MARCO Materials

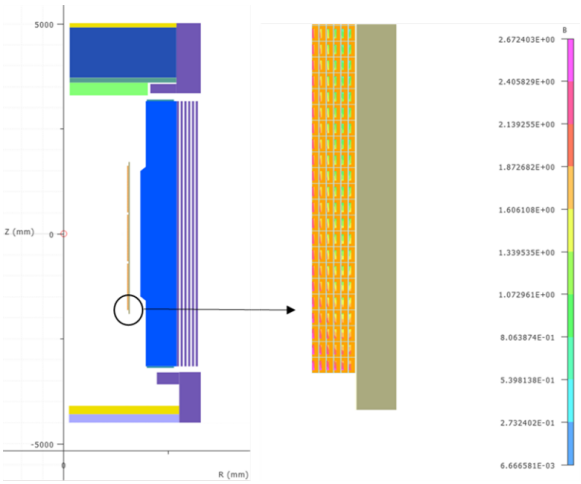

Figure 3.30: The 2D finite element model

The full list of the main materials is reported in Table 3.4, The Thickness/Nuclear interaction length weighted according to the material densities for MARCO is 0.495.

Magnet Design The magnetic design has been performed using OPERA, with 2D and 3D finite element models. Given the high level of symmetry in the magnet, both models give the same results in terms of magnetic field and magnetic performances. The 2D axisymmetric model is used to compute the magnetic field turn-by-turn and to determine the magnetic field peak on the cable Figure 3.30 (On the left, the geometry considered, on the right the results for the magnetic field peak on the cable, located at the extremity of module 1), while the 3D model (Figure 3.31) is to take into account the role of the mandrel during the ramp-up/ramp-down and the quench, as well as the effect of the cradles and the phase separator.

Three are the magnetic fields at the interaction point IP that are relevant for physics: 1.5T, 1.7T and 2.0T. The nominal magnet performances for each case are reported in Table 3.5:

It is important to notice that the primary inductance of the magnet L_{coils} is essentially constant. The iron yoke plays a negligible role on the performances of the magnet since it does not saturate Figure L. The same trend is observed on the secondary inductance $L_{mandrel}$. The total axial force acting on the magnet due to its interaction with the yoke is monotone respect to the current (it increases as the current increases) and it points always in the lepton direction (-z). The maximum value of the force

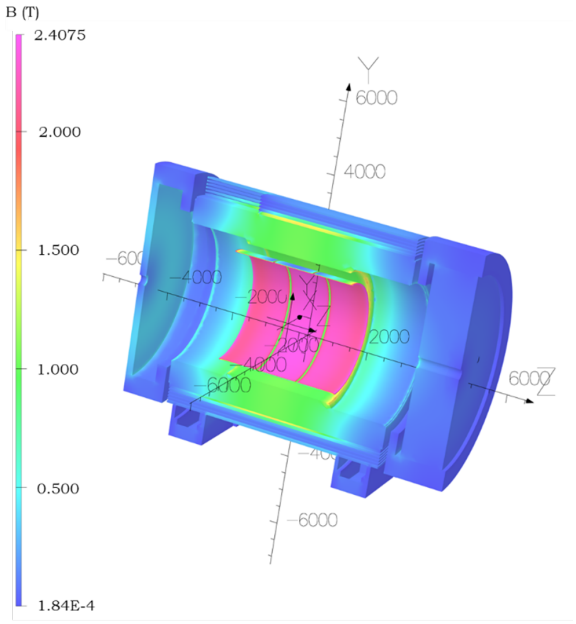

Figure 3.31: Magnetic field on the coil and yoke from 3D OPERA model for the 2.0 T field

Parameter	BIP = 1.5 T	BIP = 1.7 T	BIP = 2.0 T	Units
Current	2942	3335	3924	A
BIP	1.505	1.706	2.000	T
Bpeak	2.003	2.271	2.672	T
Energy	25.440	32.689	45.008	MJ
Lcoils	5.847	5.847	5.846	H
Lmandrel	2.347x10-6	2.347x10-6	2.347x10-6	H
Mcoils-mandrel	3.570x10-3	3.570x10-3	3.570x10-3	H
Fz	-23.8	-29.2	-32.2	kN

Table 3.5: Design parameter for various fields

is 32.2 kN, and it is negligible respect to the forces the magnet can stand during transportation. The magnet is well balanced respect to the yoke.

The difference on the magnetic field peak in 2D and 3D is because in 3D the contribution of the self-field of the cable cannot be taken into account.

The magnetic performances for the 2T central field are given in table 3.6. The simulated field uniformity and projectivity are shown in Figure 3.32 and 3.33 respectively.

The design meets the requirements for the field uniformity and the projectivity, however the fringe field is slightly high. Since the values for the fringe field are in the order of 1 mT, a series of local shields around the magnets and the RCS are investigated. The fringe field for 5 G and 15G are shown in Figure 3.34 and 3.35.

In order to assess the robustness of the design, different fault scenarios have been considered, these are

Parameter	Value	Requirements	Unit
Field uniformity	12.5 %	12.5 %	
Projectivity	3.28	¡ 10	T/Amm2
BRCS	0.035	¡0.007	Tm
BB0ApF	15.4	¡10	G
BQ1ApR	10.9	¡10	G

Table 3.6: Caption

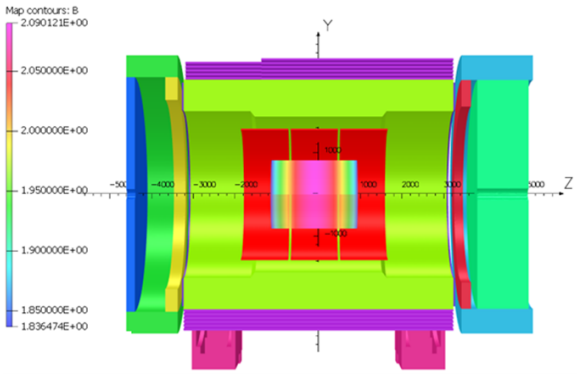

Figure 3.32: Field uniformity in the required area

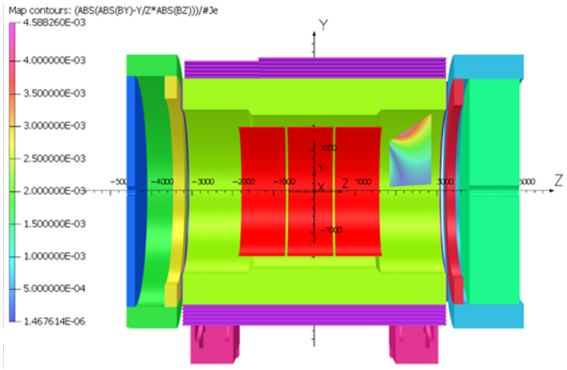

Figure 3.33: Projectivity in the required area

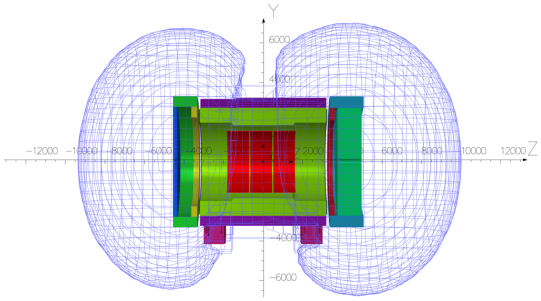

Figure 3.34: 5G line around the ePIC yoke. Thanks to the high level of symmetry, the field is the same in both Y and X direction

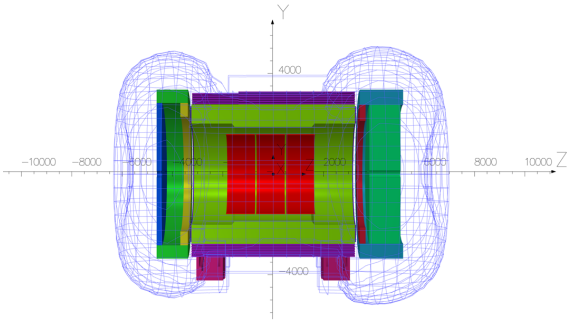

Figure 3.35: 5G line around the ePIC yoke. Thanks to the high level of symmetry, the field is the same in both Y and X direction

Table E summarizes the impact of axial misalignment and tolerance, Table F to table I summarizes the results of the radial misalignment, and table J summarizes the results of missing layer in any one module. It is important to notice that the total axial force F_z can change of direction respect to the nominal design, the tie-rods have been designed accordingly to stand these changes. The axial misalignment, the radial displacements of the modules or the cold mass have a negligible impact on the field quality and central field. The main concern is the forces acting on the magnet, they are of the order of the weight of the magnet itself and lower than the transportation loads. Therefore, a tolerance in the position of the coils of 5 mm is acceptable.

In order to assess the robustness of the design, different fault scenarios have been considered:

A) Tolerances

- Every module can be displaced along Z with a gaussian distribution $G(\mu, \sigma) = G(0.0, 5.0\ mm)$;
- Every module can have a different inner radius modeled with a gaussian distribution $G(\mu, \sigma) = G(1502.5\ mm, 5.0\ mm)$;
- Every module can have a different angle (as if the mandrel has a conical shape and not cylindrical) modeled with a gaussian distribution G(μ, σ) = G(0.0, 0.03 deg);
- The cold mass can be displaced along Z with a gaussian distribution G(μ, σ) = G(0.0, 10.0 mm);
- 1000 simulations are considered for this study.

B) Radial Misalignment

- Every module can be displaced along Y with a maximum displacement of 5.0 mm.
- The cold mass can be displaced along Y with a maximum displacement of 5.0 mm.

C) Impact of a missing layer

D) Impact of variation in permeability

E) Impact of misaligned yoke

- Every yoke element can be displaced along Z with a gaussian distribution G(μ, σ) = G(0.0, 5.0 mm) with respect to the nominal position.

Parameter	Value	Unit
Δ BIP	±10	mT
Δ Energy	±0.231	MJ
Δ Fz	+14.4/-50.4	kN
Δ Field uniformity	±1%	
Δ BRCS	1.9E-4	Tm
Δ BB0ApF	±0.2	G
Δ BQ1ApR	±0.15	G

Table 3.7: Impact of axial misalignment and tolerances

Parameter	MOD1	MOD2	MOD3	MAGNET	Unit
Δ y				± 5	mm
Δ Fy	±12.3	±14.5	± 15.3	± 42.2	kN
Δ Fz				-32.5	kN

Table 3.8: Impact of radial misalignment- Cold Mass

- Every yoke can have a different inner/outer radius modeled with a gaussian distribution G(μ, σ) = G(0.0, 5.0 mm) with respect to the nominal position.
- 1000 simulations are considered for this study.

Table 3.7 summarizes the impact of axial misalignment and tolerance, Table 3.8 to table 3.11 summarizes the results of the radial misalignment, and table 3.12 summarizes the results of missing layer in any one module. It is important to notice that the total axial force F_z can change of direction respect to the nominal design, the tie-rods have been designed accordingly to stand these changes. The axial misalignment, the radial displacements of the modules or the cold mass have a negligible impact on the field quality and central field. The main concern is the forces acting on the magnet, they are of the order of the weight of the magnet itself and lower than the transportation loads. Therefore, a tolerance in the position of the coils of 5 mm is acceptable.

In case that one layer is missing in MOD1 or MOD3, the operation of the magnet is compromised due to the high non-homogeneity of the magnetic field. Otherwise, the magnet can still respect the requirements if only MOD2 has one missing layer. The detail operating margins need to be calculated in the event of a missing layer and based on which the operating limits must be set accordingly for all materials. A variation of ± 10% of the BH curve in Figure 3.19 shows that the variation of the main parameters is negligible (less than 1 part per 10^4 for each).

The impact of axial misalignment, fabrication tolerances with respect to the nominal position, and dimensions of the yoke has been studied in the 2D model using Monte Carlo simulations. Only the fringe field was analyzed for this study. The impact of yoke misalignment is negligible with respect

Parameter	MOD1	MOD2	MOD3	MAGNET	Unit
Δ y	± 5				mm
Δ Fy	-0.5	±14.5	± 15.3	± 42.2	kN
Δ Fz	+0.7	-39.2		-32.5	kN

Table 3.9: Impact of radial misalignment- Module 1

Parameter	MOD1	MOD2	MOD3	MAGNET	Unit
Δ y		± 5			mm
Δ Fy	64.4	±14.5	± 15.3	± 42.2	kN
Δ Fz	-64.3	-39.7		-32.5	kN

Table 3.10: Impact of radial misalignment- Module 2

Parameter	MOD1	MOD2	MOD3	MAGNET	Unit
Δ y			± 5		mm
Δ Fy	27.8	±14.5	± 15.3	± 42.2	kN
Δ Fz	-27.6	-39.4		-32.5	kN

Table 3.11: Impact of radial misalignment- Module 3

to the fringe field. Even with misalignment / tolerances of 15 mm, the maximum variation of the fringe field is:

- $\Delta B_{B0ApF} = \pm 1.5$ G
- $\Delta B_{Q1ApR} = \pm 1.2$ G
- $\Delta B_{RCS} = \pm 3x10^{-5}$ Tm

Conductor Design The conductor chosen for MARCO is a NbTi "Rutherford In Copper Channel (RICC)". A schematic cross-section of the conductor is shown in figure 3.36. The insulation thickness is made in fiberglass and consists of 2 x 0.13 mm 50% overlap tape. The Rutherford cable is soldered into the copper channel. In the analysis performed in the mechanical design, the soldered has been considered as AgSn 3.5/96.5, however, for fabrication, the solder will be defined in accordance with the manufacturer. An alternative could be SbSn. The solder section is expected to be less than 2% respect to the overall section of the conductor.

The main specifications of the conductor are listed in table 3.13. Each layer will have its own conductor length.

The worst condition the conductor can experiment are in the first turn of the L1 layer, MOD1, where are located the magnetic field peak B_{peak} = 2.672 T and an expected temperature of 4.7K.

Parameter	MOD1	MOD2	MOD3	MAGNET	Unit
Δ BIP	1.923	1.838	1.906	2.000	mm
Δ Energy	40.610	39.679	40.590		kN
Δ Fz	-90.8	-39.4	+42.3	-23.3	kN
Δ Uniformity	19.3 %	8.5 %	19.3 %	12.5 %	
Δ BRCS	0.040	0.035	0.030	0.035	
Δ BB0ApF	13.7	14.6	14.6	15.3	
Δ BQ1ApR	10.5	10.5	9.7	10.9	

Table 3.12: Impact of missing one layer

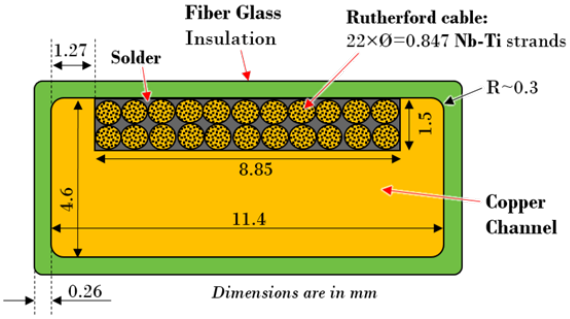

Figure 3.36: Cross-section of the RICC conductor

Parameter	Value	Unit
Strand diameter	0.847	mm
Cu/NbTi	1.3	
Ic @ 3T and 4.2K	¿ 630	A
Filament diameter	¡ 30	μm
Filament twist pitch	30	mm
NbTi strands	22	
Transposition pitch	50	mm
Width	6.8	mm
Thickness	1.26	mm
Copper channel section	39.1	mm^2
Insulated conductor section	61.1	mm^2
Nominal current	3924	A
RRR conductor	¿100	
σ0.2% @ 293 K	¿165	MPa
Unit length	1.05	km
Total length	18.9	km

Table 3.13: Caption

At the nominal current, according to the Bottura scaling law and a critical current degradation of 15% (cabling plus soldering), the expected current sharing temperature is T_{cs} = 7.15K, giving a temperature margin of 2.45K and a load-line margin of 46.1%. In terms of stability, the conductor has an enthalpy margin of 6.7 kJxm^{-3}, providing a quite large margin respect to other detector magnets. The conductor performances are reported in Table 3.14 and the load line plot for the reference case study B0=2T is shown in Figure 3.37, The working point (green rectangle) is shown, corresponding to a current sharing temperature of 7.15 K.

Mechanical Design The mechanical design has been performed using 2D and 3D finite element models, respectively in Cast3m and ANSYS. Material properties and coil pack homogenization. For both models, a certain level of homogenization of the material properties for the coil pack has been assumed. For the 2D model the cable has been homogenized, while for the 3D all the coil pack has been. The homogenization has been calculated using ANSYS Workbench 2023 R2 with the "Material Designer" module.

Parameter	BIP = 1.5 T	BIP = 1.7 T	BIP = 2.0 T	Units
Current In	2942	3335	3924	A
Top	4.7	4.7	4.7	K
Bpeak	2.003	2.271	2.672	T
T margin	3.06	2.82	2.45	K
LL margin	59.6%	54.2%	46.1%	
In/Ic	17.9%	22.1%	29.3%	

Table 3.14: Caption

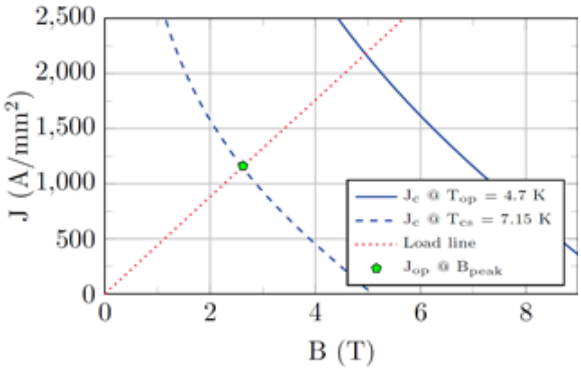

Figure 3.37: Jc curve @4.7 K, load line and load line margin

The 2D mechanical analysis was conducted in Cast3m using its magneto-static solver to calculate the Lorentz forces and its mechanical solver to analyze their impact on the magnet structure. The magnetic model includes the iron yoke, the mechanical one does not. A schematic of the mechanical model geometry is shown in Figure 3.38. A zoom of one of the two areas where the 3 modules are assembled is shown. The iron yoke is not shown in this model. Each turn is modeled, with its own cable, copper channel and insulation. As contact conditions, for each module, the coil, the ground insulation and the mechanical structure are bonded together to simulate the impregnation. The coil wedges are bonded to mechanical structure and have a sliding contact with possible separation with the coils and with the inter-module wedges.

The 3D mechanical analysis was conducted in ANSYS Workbench, importing the magnetic force density from the OPERA 3D model. Figure 3.39 (a) 3D model geometry and materials, b) zoom on the tie-rods and their warm interfaces and c) the tie-rods ball joints with their boundary conditions) shows the geometry of the model, the tie-rods warm interfaces and the ball joints definition with their boundary conditions.

The acceptance criteria for the design are given in Table 3.15. The main principle behind is to have an equivalent Von Mises stress and a shear stress in each component below the 2/3 of the corresponding elastic limits for each material. For what concerns the conductor, a minimum elastic limit of 165MPa is imposed to the manufacturer. This can be easily achieved through cold-work on the copper channel. For the shear limit on G10, a factor of 0.4 has been assumed as acceptance criteria in order to be more conservative.

Each component of the cold-mass fulfills the acceptance criteria. The results related to the Von Mises peak stress and shear peak stress between the 2D and 3D models are remarkably close especially for the coils. The effect of tie-rods is notable in 3D for the mandrel, which has a VM peak

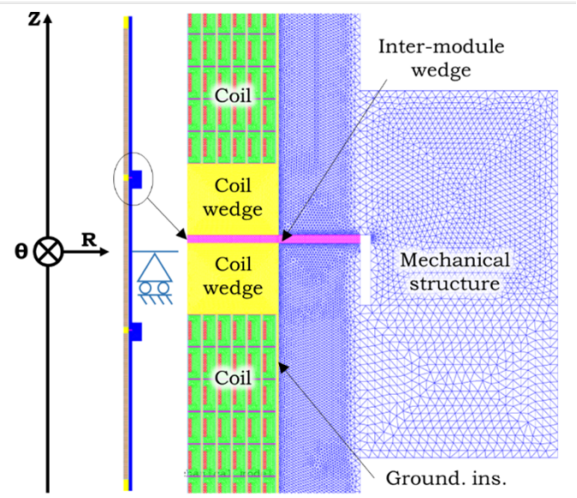

Figure 3.38: 2D axisymmetric mechanical model including the coils and the mechanical structure

295 K Material	Properties	Reference Value (MPa)	Acceptance criteria (MPa)
Coil	Yield strength	165	110
	Shear strength	15	10
G10	Yield strength	257	103
	Shear strength	42	17
Brass7030	Yield strength	413	275
	Shear strength	220	88
Ti6Al4V	Yield strength	1030	687
4.5 K			
Coil	Yield strength	200	133
	Shear strength	72	24
G10	Yield strength	496	198
	Shear strength	73	29
Brass7030	Yield strength	517	345
	Shear strength	264	106
Ti6Al4V	Yield strength	1693	1129

Table 3.15: Materials acceptance criteria

stress of 280 MPa (106 MPa for the 2D). The reason is the local stress induced by the tie-rods on their pads. Due to the lack of space caused by the Barrel Yoke, the tie-rods cannot be made to compensate totally the thermal shrinkage during the cool-down, inducing a higher stress than what could be forecast. However, thanks to the fact that the mandrel is in brass, this is not an issue. A summary of the results for cool-down and energization is shown in Table 3.16.

Transient Analysis and Quench Protection The transient analysis was performed for the magnet during different ramp-up and ramp-down scenarios. Since the mandrel is made from Brass

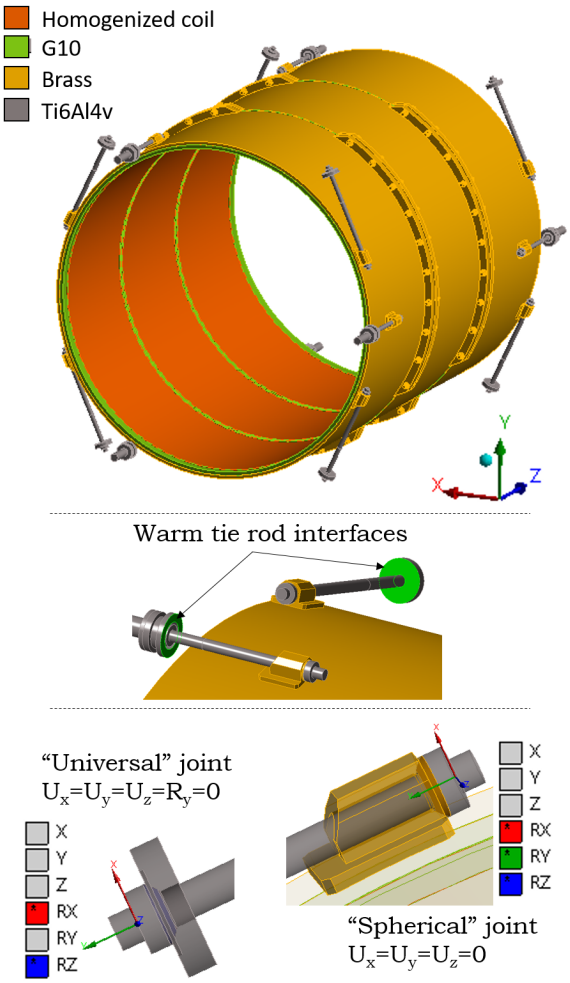

Figure 3.39: 3D model geometry

70/30, it plays a noticeable role during the transients of the magnet, in particular during ramp-up / ramp-down, fast discharge, and quench. Its magnetic behavior has been simulated using OPERA. The ramping rate (up and down) of the magnet is 1.0 A/s, which is a compromise found between ramping the magnet in approximately one hour and not overheating it at the same time due to the mandrel dissipated power. This case has been used to define the main magnetic specifications of the mandrel, the results are given in Table **??**.

The impact of the flanges is significant, showing that the current tends to pass through them between the adjacent modules.

Fast discharge is the worst case for induced eddy currents in the mandrel due to the dump resistor of the circuit, the dI/dt being the highest at the beginning of the discharge. As for the quench protection, for the fast discharge case the following circuit (Figure 3.40) has been considered:

The dump resistance R_d has been determined limiting the maximum voltage across the magnet to 1000 V. In case of fast discharge, the mandrel behaves as shown in figure 3.41. The current in the mandrel can increase up to 165 kA in 0.3 s; a vertical force of F_y = -22 kN acts on the mandrel, due

Material	Properties	Reference Value (MPa)	Acceptance criteria
COOL-DOWN			
Coil	Von Mises Peak Stress	55	70
	Shear Peak Stress RZ	14	11
G10	Von Mises Peak Stress	54	94
	Shear Peak Stress RZ	23	21
Brass7030	Von Mises Peak Stress	105	300
	Shear Peak Stress RZ		16
Ti6Al4V	Von Mises Peak Stress	NA	761
COOL DOWN + ENERGIZATION			
Coil	Von Mises Peak Stress	81	78
	Shear Peak Stress RZ	17	12
G10	Von Mises Peak Stress	84	77
	Shear Peak Stress RZ	23	18
Brass7030	Von Mises Peak Stress	106	280
	Shear Peak Stress RZ	NA	20
Ti6Al4V	Von Mises Peak Stress	NA	839

Table 3.16: Materials acceptance criteria

Parameter	Value	Unit
Ramping rate	1	A/s
Power dissipated at t = + ∞	3.642	W
Eddy current at t = + ∞	-1015.3	A
Resistance (P/I^2)	3.516	$\mu\Omega$
Mutual inductance	3.570	mH
Inductance of the mandrel	2.346	μH
Coupling coefficient btw mandrel and coils	0.964	

Table 3.17: Ramp up/down results

to the asymmetric distribution of the eddy currents around the flanges. Such force is well below the loads that the magnet can encounter during transportation, and it is well compensated by the tie-rods. The total time needed to fast discharge the magnet is 120 s.

Quench Analysis Both a single coil analytical quench analysis (more conservative) and a detailed FE quench analysis in COMSOL have been performed to design the quench protection. In this section only the detailed FE quench analysis is described. The quench analysis has been conducted using COMSOL, with a coupled 2D axisymmetric FE model and 1D model to consider the heat propagation—the first for the transverse propagation and the second for the azimuthal propagation. The logic structure of the model is shown in Figure3.42. Once the geometry, material properties and operational conditions are defined, the magnetic model is solved to determine the resistivity (ρ) of each element (with respect to the magnetic field and temperature) and thermal conductivity (k). Once the magnetic field, the temperatures and materials properties are defined over the domain, the model calculates the critical current density J_c and solves the coupled thermal and electric model associated to the geometry. The model considers the full geometry of the

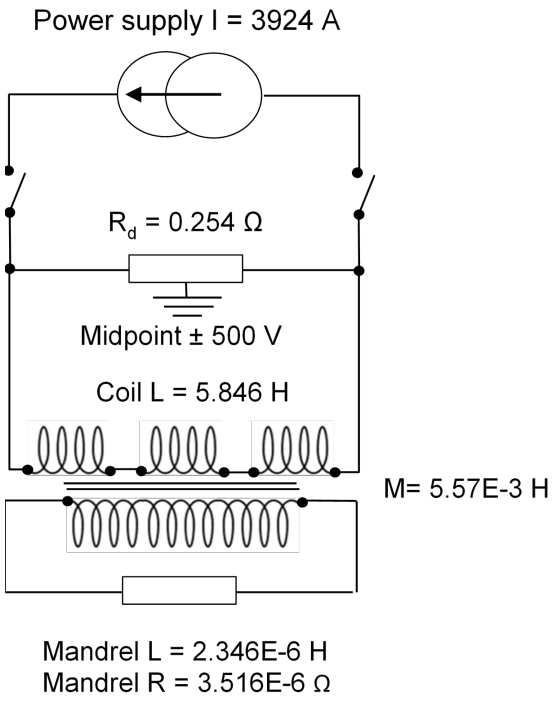

Figure 3.40: Scheme of the electric circuit of the MARCO magnet

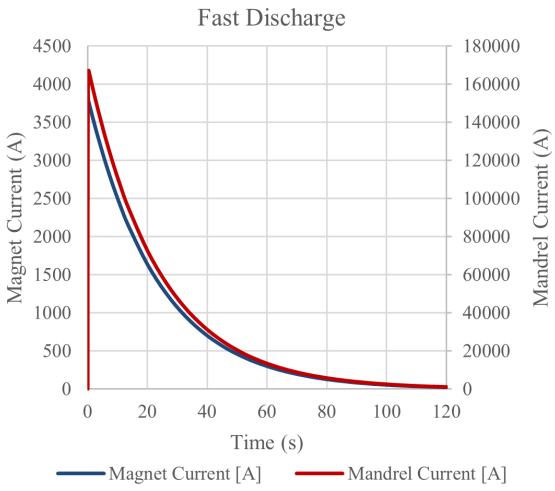

Figure 3.41: Current flowing in the magnet and in the mandrel during a fast discharge

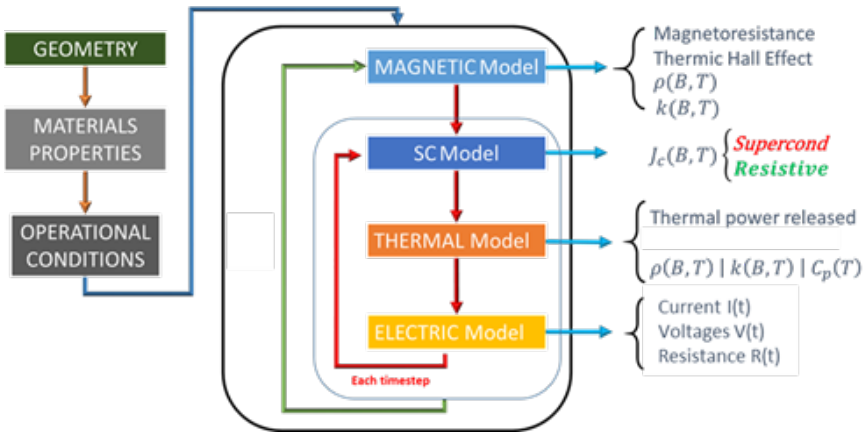

Figure 3.42: Logic structure of the COMSOL quench model

magnet, and it defines every turn with details of the conductor. The conductor is represented by a homogenized material (homogenized cable and copper stabilizer). The insulation is modelled separately to consider its own material properties. A representation of the geometry is shown in Figure 3.43.

The material properties are from Cryocomp. The thermal hall effect and magnetoresistivity in copper are considered. The quench starts at the bottom angle of MOD1, where the peak magnetic field is located. The case studied is the one at the nominal current (3924 A) and maximum nominal temperature (4.7 K). Once the quench starts and after that the resistive tension reaches 1 V, a validation time of 1 s is needed to validate the quench and open the breakers to activate the dump resistance. A dump resistance of 0.254 Ω is used to limit the maximum voltage to 1000 V. The magnetic model is solved by COMSOL with the same geometry and material properties used in the OPERA model. The superconducting model calculates at every turn to determine if the conductor is in the superconductive state, in the resistive state, or in the current sharing state. It uses the Bottura fit parameters used to design the MARCO conductor to calculate the critical current density in the cable. A simple model of current redistribution is considered: if the critical current $I_c \geq 0$ and I_c ¡ I(t), where I(t) is the current flowing through the cable, the ohmic power dissipated is smoothed by an inverse sigmoid.

The thermal model solves the heat transfer equations in 2D associated with every node of the model and the 1D propagation along the length of the conductor according to the computed azimuthal quench velocity. The ohmic power releases at every turn when quenched is considered starting at the node in the center of the conductor geometry. The electrical model calculates the resistivity and voltage associated with every turn and the eddy currents induced in the mandrel during the quench current decay.

In the nominal case scenario, the magnet is protected by the dump resistance R_d. Due to the high inductance, the current decay is very slow and it takes 65 s to reach less than 1% of the original current in the magnet. The time constant of the quench circuit is 20.31 s.

Figure 3.44 shows the current decay in the coils and the eddy current in the mandrel. Thanks to the good magnetic coupling between the coils and the mandrel, the mandrel is subjected to the high eddy current, which generates the quench-back in the coils as shown in Figure 3.45.

The resistive coils voltage profile during quench shows no issue; the maximum voltages inside the coils are around 1000 V, the acceptable criterion defined for the magnet as shown in Figure 3.46.

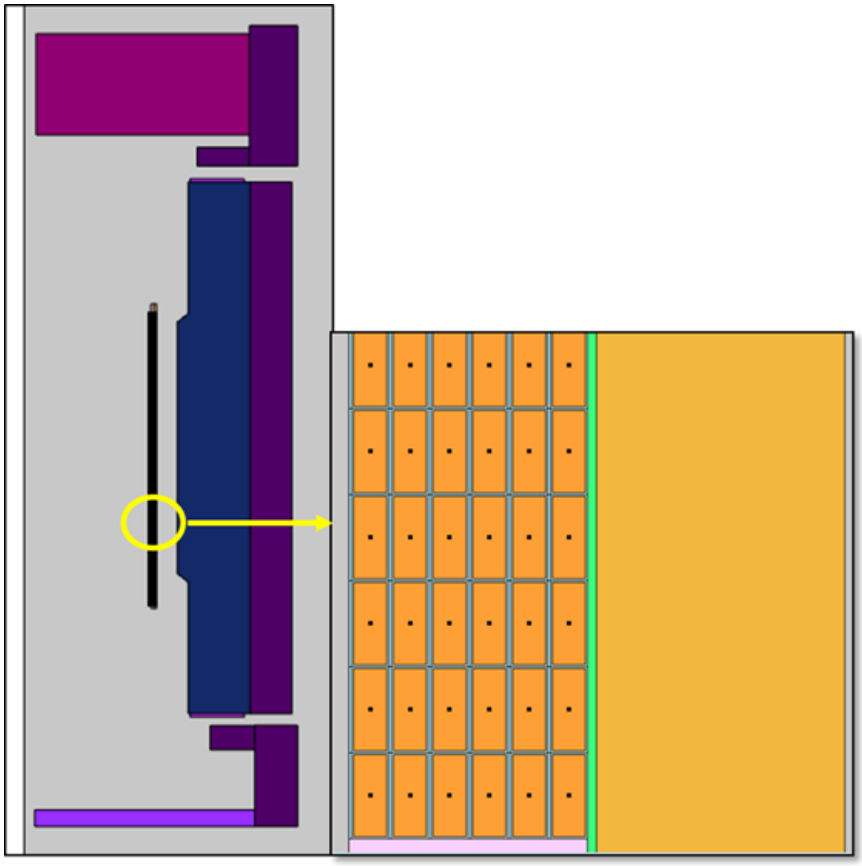

Figure 3.43: Model used in COMSOL

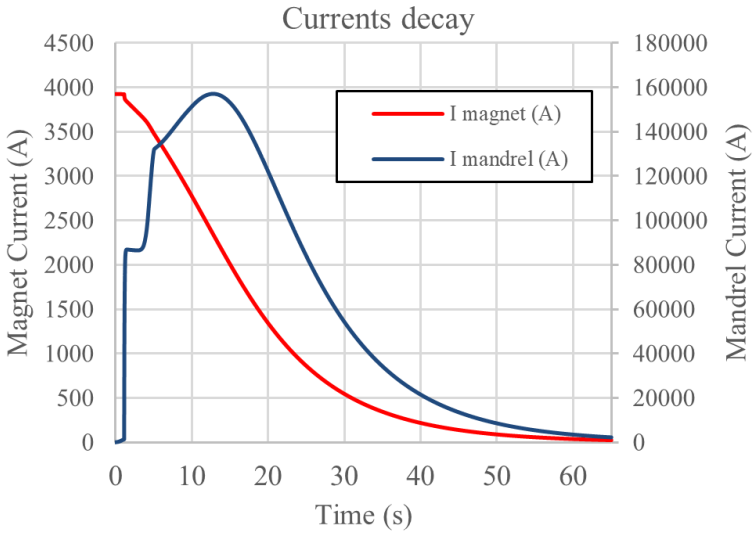

Figure 3.44: Current decay in the coils and in the mandrel

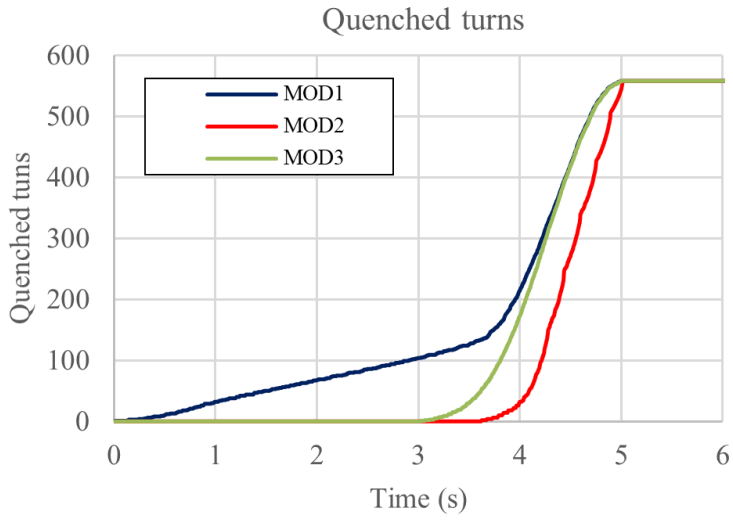

Figure 3.45: Number of quenched turns as a function of time in the three different modules

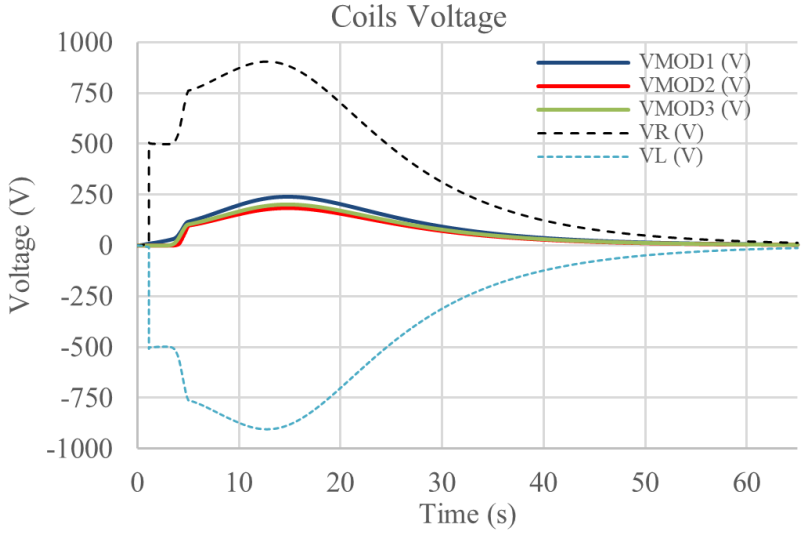

Figure 3.46: Resistive coil voltage as a function of time for the three modules

The total power dissipated in the circuit is shown in Figure 3.47. The dump resistance has a peak power of 3.8 MW; the coils, 1.5 MW; the mandrel, 86 kW. The maximum temperature (hotspot) reaches during quench is 96 K shown in Figure 3.48, showing no issue for the structural integrity of the magnet. The hotspot is located at the quench starting point as shown in Figure 3.49. Since the quench starts in MOD1 (blue line), the corresponding hotspot temperature is higher than the ones in the other two modules. The difference between MOD2 and MOD3 (both quench thanks to the quench-back by the mandrel) in maximum temperature is due to the different magneto-resistance the two modules have.

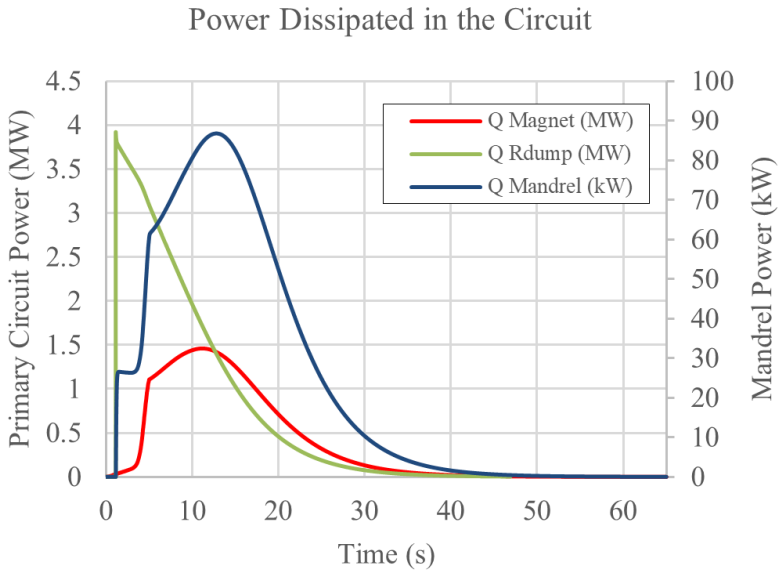

Figure 3.47: Power dissipated in the primary and secondary circuit

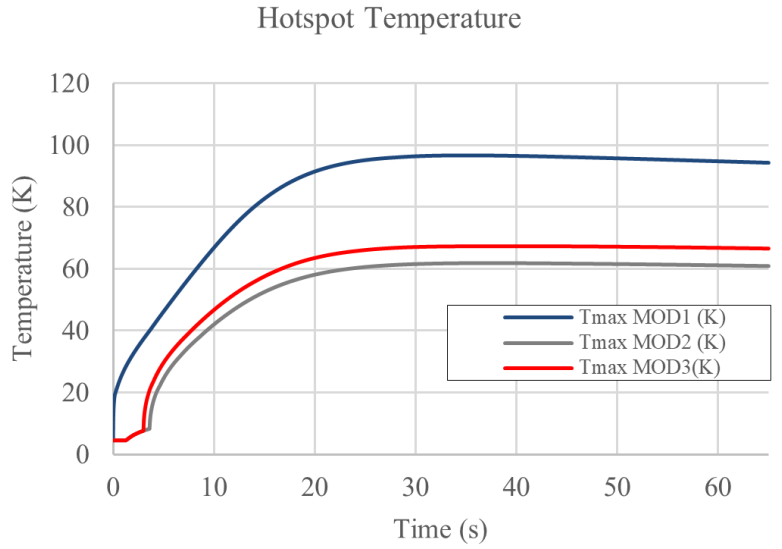

Figure 3.48: Hotspot temperature in the three modules of the magnet

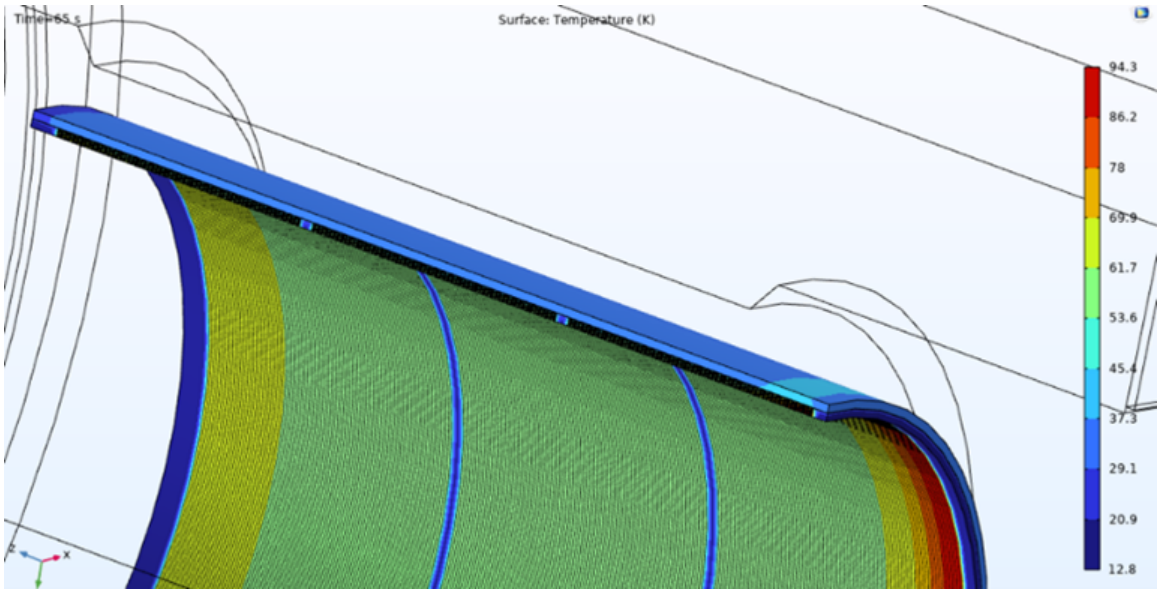

Figure 3.49: Temperature distribution on the coils and mandrel after 65s from quench

Cryogenic Design The MARCO magnet is a conduction-cooled magnet and it is indirectly cooled using the cooling tubes on the outside of the brass mandrel. The internal cryogenic system involves a cold mass, which consists of a mandrel and coils with two 28-tube exchangers of the thermosiphon soldered on the mandrel, a phase separator on top used also as a storage tank of liquid helium at 4.55 K, and one cryogenic chimney that holds the helium vapor cooled current leads and connect the phase separator to the cold mass. The solenoid is equipped with 5 cold valves with warm actuators and 3 warm valves (given in Table 3.18). It also has a thermal shield to insulate the parts at 4.5 K; the thermal shield is cooled by helium gas between 45 K and 65 K. The internal cryogenic system is connected to the BNL refrigeration supply through flexible lines. The cryogenics flow chart is shown in Figure 3.50.

The solenoid is cooled by a two-phase flow helium thermosiphon. Twenty-eight exchanger tubes (2x5 tubes for module 1, 2x4 tubes for module 2, 2x5 tubes for module 3) are soldered on the brass mandrel. Liquid helium is stored in the phase separator tank and flows through valve FV2 down in the downward branch to supply 6 distributors (bottom manifolds). This flow of helium is heated up in the exchanger tubes, collected by 6 collectors (top manifolds), and goes back to the tank through 3 return lines. Three heaters (10 W maximum each) are placed on the return lines in case that there is not sufficient heat load on the cold mass. Figure 3.51 shows the piping schematics of thermosiphon. The return lines go back in the phase separator tank at a higher level than the feeding line which is connected directly to the bottom of the tank, the difference of height is the riser. The risers make the return two phase flows pour out the return tubes above the liquid surface area in the phase separator tank. When the level of liquid is zero the tank is empty, when it is nominal it is equal to 0.3 m whereas the risers are 0.4 m high.

There are two thermosiphon piping systems. One is primary and one is spare. If the primary has a leak, it is possible to use the spare one by disconnecting the primary piping in the vacuum vessel of the phase separator tank and connecting the spare piping. The heat exchanger tubes are made of copper. They have an outer form of a square (14 mm x 14 mm) and an inner diameter of 8 mm. They are soft soldered onto the brass mandrel. At their extremities, stainless steel junction tubes (jumpers) are brazed inside the copper tubes, and these junctions is welded to the stainless-steel

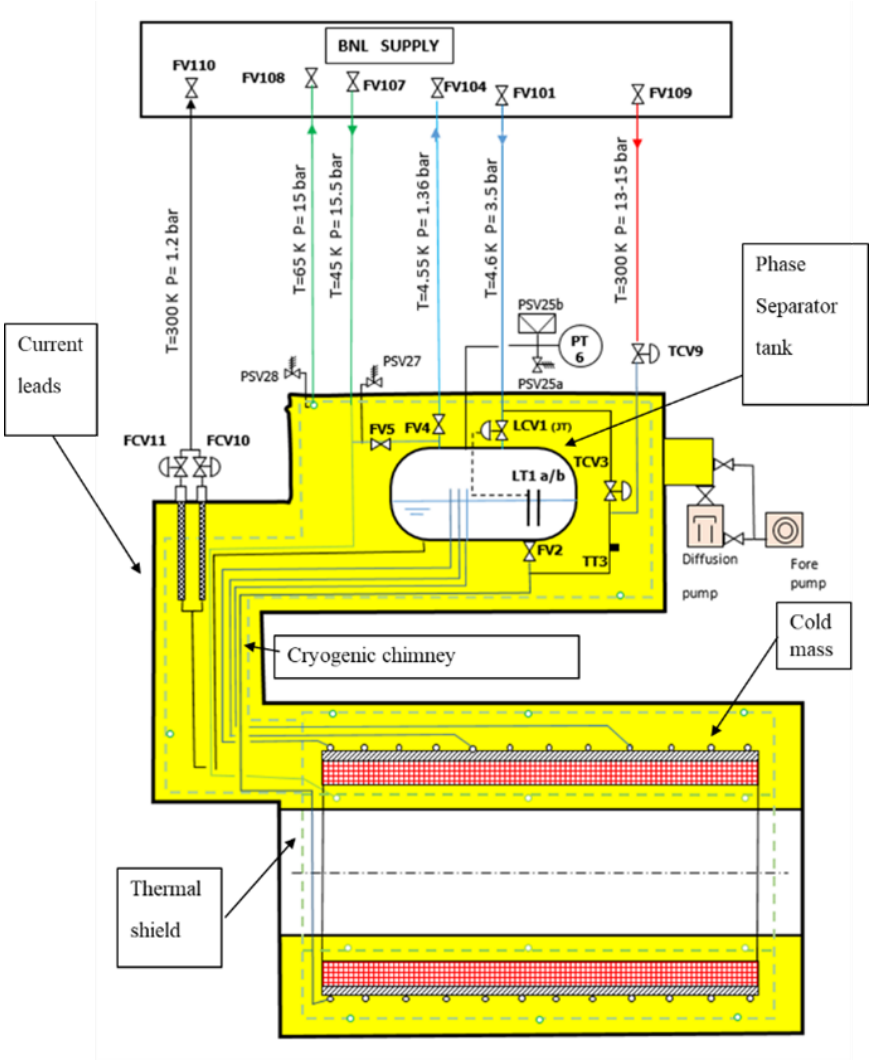

Figure 3.50: Cryogenics flowchart of the MARCO solenoid

manifolds. Figure 3.52 and 3.53 show in details how the thermosiphon is designed.

The outlet pressure of the return lines in the phase separator tank must be the same as the pressure inside the tank, defining thus the mass-flow rate and then the vapor quality. The case under consideration is the shut-down of the refrigerator when the liquid helium level is dropping in the phase separator tank. The limit is where the level is equal to zero and thus the tank is empty. This is the limiting case for the thermosiphon because the differential height between the downward branch and the return lines (upward branch) is maximum and equal to the riser (0.4 m). The riser is needed to ensure that the two-phase flow goes back to the phase separator tank above the liquid helium surface in any case. The diameters (Ø8 mm) of the exchanger tubes of the supply and return lines, and the diameter (Ø30 mm of manifolds) have been chosen to lower the frictional pressure drop. The main pressure drop is in the riser due to the gravity. In addition, the manifolds are almost isobaric as their pressure drop is less than 1 Pa. Several heat loads scenario has been considered for the thermosiphon, according to the possible heat loads (given in Table 3.19) present inside the

Name	Description
FV101	BNL supercritical helium shut-off valve
FV104	BNL vapor helium shut-off valve
FV107	BNL inlet helium for thermal shield shut-off valve
FV108	BNL outlet helium for thermal shield shut-off valve
FV109	BNL inlet warm helium for cool-down shut-off valve
FCV110	BNL outlet helium for current leads shut-off valve
PSV27	Inlet helium for thermal shield safety valve
PSV28	Outlet helium for thermal shield safety valve
PSV25a	Relief valve for the phase separator tank at 4.5 bar abs. (quench)
PSV25b	Burst disc for the phase separator tank at 6 bar abs. (vacuum loss)
PT6	Pressure measurement of the phase separator tank
FCV10	Flow control valve for current lead a
FCV11	Flow control valve for current lead b
TCV9	Warm temperature control valve for cool-down
TCV3	Cold temperature control valve for cool-down
TT3	Temperature of the mixed gas coming from TCV3 and TCV9 for the cool-down
FV2	Feeding shut-off valve of the thermosiphon
FV4	Vapor helium shut-off valve
FV5	Bypass shut-off valve for vapor helium into the shield in case of refrigerator shut-off
LCV1	Level control valve for the liquid helium in the tank (Joule Thomson valve)
LT1a/b	Liquid helium measurement in the tank with spare

Table 3.18: List of cryogenic valves

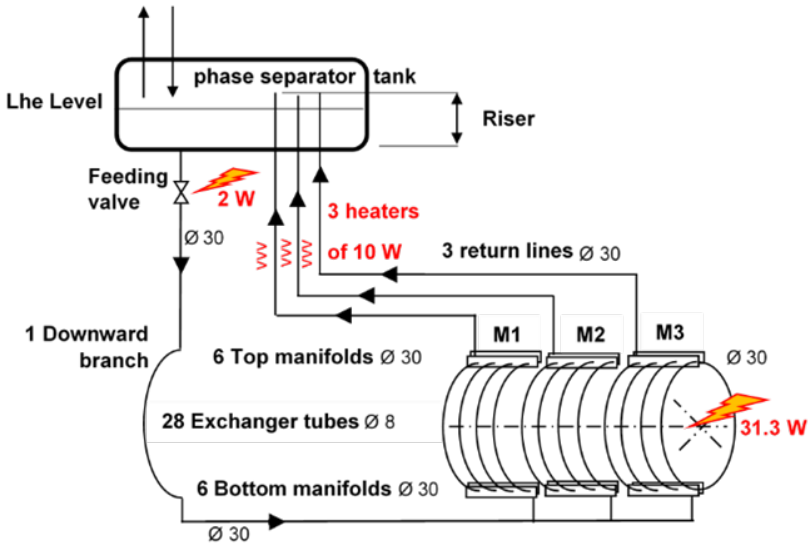

Figure 3.51: Schematics of the thermosiphon system

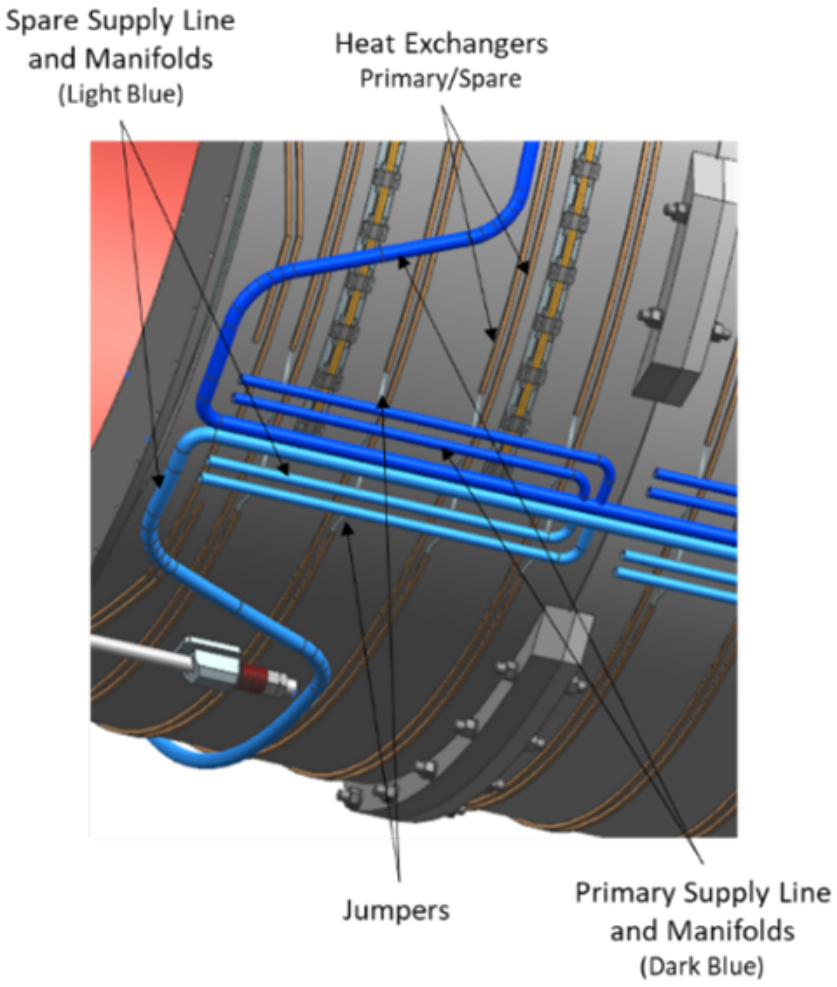

Figure 3.52: Primary and spare tubes of the thermosiphon heat exchanger

cryostat. For any of these cases, the vapor quality is below 10% and the speed of the He in the return line is always greater than 0.1 m/s, assuring the proper operation of the thermosiphon.

The thermal shield of the cold mass is made of 3 x 4 internal panels, 3 x 4 external panels, and end plates. It is made of Al 3003 with a thickness of 5 mm. The tube, which connects the BNL flexible supply line and the thermal shield piping, has an inner diameter of 10 mm and an outer square form of 14 mm x 14 mm. This tube passes through the phase separator vacuum vessel and the cryogenic chimney without cooling any surface; it goes directly to the inner part of the cold mass thermal shield and supplies, in parallel, the left circuit and the right circuit. The left and right external shields are then cooled afterwards. The end plates are indirectly cooled by connecting with them. The two half flows are joined together at the inlet of the cryogenic chimney and then cools the thermal shield in the cryogenic chimney. Like the thermosiphon system, there are two cooling circuits for the thermal shield. One is the primary and the other is the spare.

The helium phase separator is on top of the detector, embedded in the iron and connected to the magnet assembly through the cryogenic chimney shown in Figure 3.54. In addition to the cryo-

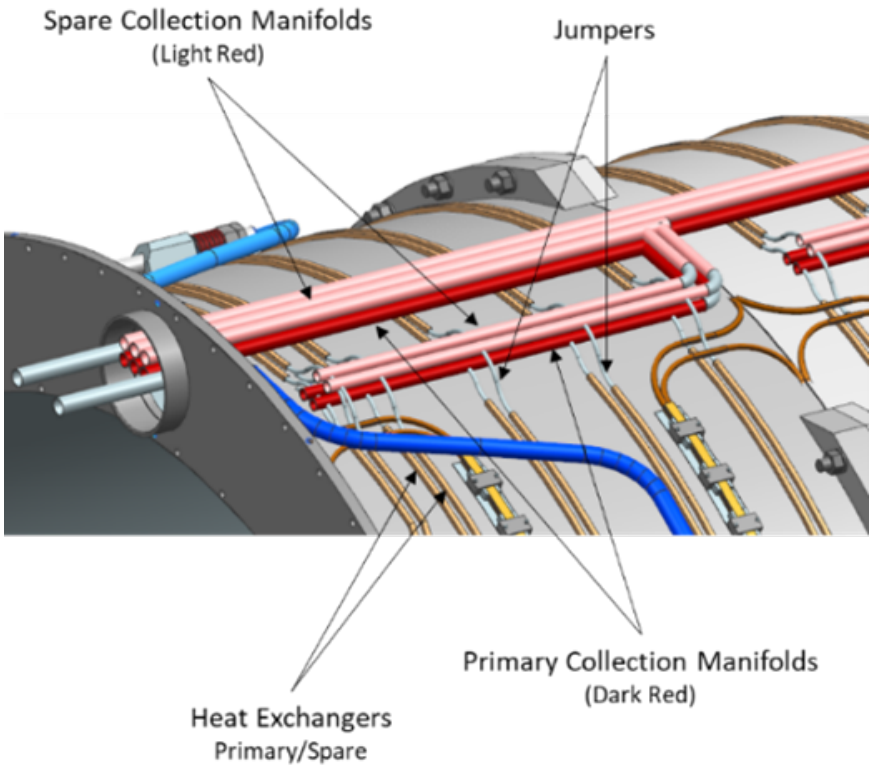

Figure 3.53: Primary and spare piping on top of the mandrel

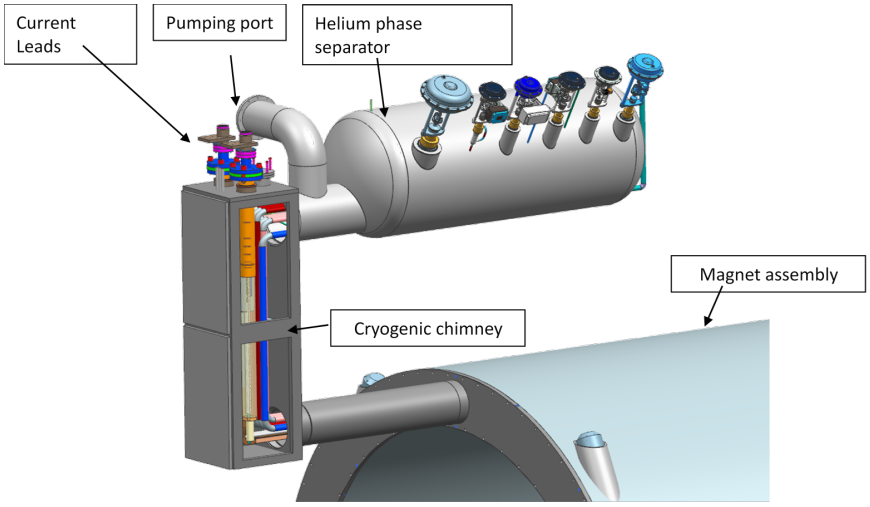

Figure 3.54: Helium phase separator and cryogenic chimney overview.

Cold mass heat load at zero current	25	W
Heaters (off)	0	W
Total mass flow rate	25.4	g/s
Vapor quality	6 %	
Flow speed in the return lines	0.13	m/s
Cold mass heat load during ramp-up/down	30	W
Heaters (off)	0	W
Total mass flow rate	29.1	g/s
Vapor quality	6.2	
Flow speed in the return lines	0.14	m/s
Cold mass low level heat load	10	W
Heaters (on)	20	W
Total mass flow rate	18.3	g/s
Vapor quality	9.8	
Flow speed in the return lines	0.10	m/s
Cold mass high level heat load	60	W
Heaters (off)	0	W
Total mass flow rate	45.6	g/s
Vapor quality	9.8	
Flow speed in the return lines	0.24	m/s

Table 3.19: Thermosiphon load cases

genic lines, the cryogenic chimney also houses the helium vapor cooled current leads. A vacuum pumping port is located between the cryogenic chimney and the phase separator vacuum vessel. The total volume of the inner helium vessel is 284 L; the liquid helium buffer used in normal operation is 110 L which is the volume of liquid needed to ramp down the current at 1 A/s in case of a refrigerator shut-down the liquid helium level in the tank is then 0.3 m. The set pressure of the burst disc is 6 bar. The protection against overpressure is studied according to European regulations, for the helium circuits including the phase separator (inner vessel): EN21013-3 and for the vacuum vessel (outer vessel): EN 13458-2.

The cryogenic heat loads are calculated for all the components of the cryogenic system and they are listed in Table 3.20 and the heat load budgets at 4.5 K and 65 K are given in Table 3.21.

The maximum heat load (when ramping up the current) at 4.5 K is 57 W. The total heat load budget on the thermal shield is 600 W.

Instrumentation and Controls In order to operate and monitor the MARCO solenoid an extensive instrumentation plan have been conceived. The instrumentation covers the electrical measurements, the cryogenics data measurements as well as the mechanical ones. The electrical measurements gather the voltage measurements and the current measurements. The cryogenics ones collect the temperature data, the pressure, the liquid helium level, the He mass flows and the vacuum level. Finally, the mechanical measurements concern especially the tie-rods whose stress is

Heat load source	Value	Unit
Tie-rods for the cold mass @4.5K	3.68	W
Tie-rods for the cold mass @65K	79.2	W
Tie-rods for the phase separator tank @4.5K	0.48	W
Tie-rods for the phase separator tank @65K	12.8	W
Cold valve LCV1 @ 4.5K	0.31	W
Cold valve FV2 @ 65K (@4.5K)	10 / (3)	W
Cold valve TCV3 @ 4.5K	0.36	W
Cold valve FV4 @ 65K (@4.5K)	5 / (1.4)	W
Cold valve FV5 @4.5K	0.31	W
Bellows for valve PSV25a / burn disc PSV25b @4.5K	0.19	W
Flexible lines @ 4.5K	2	W
Thermal shield supports @ 55K	32	W
Heat radiation (radiation flux = 0.3W/m2) @4.5K	23.1	W
Heat radiation (radiation flux = 5 W/m2) @65K	420	W
Conductor junctions (1.0nΩ each)	0.32	W
Hysteresis from NbTi filaments	0.8	W
Eddy current in strand copper (ramp-up/down)	0.2	W
Eddy current in the mandrel (ramp-up/down)	3.7	W
Helium vapor cooled current leads	12	W

Table 3.20: Heat load summary

4.5 K Element	Value	Unit
Cold mass at zero current	25	W
Cold mass at ramping up/down (1 A/s)	30	W
Phase separator tank	10.2	W
Current leads	12	W
Margin	5	W
45 K - 65 K (loads on thermal shields)		
Thermal radiation	420	W
Support conduction	32	W
Thermal intercept	107	W
Margin	61	W

Table 3.21: Heat Load budget

monitored during all the magnet life.

Voltage Taps: The electrical instrumentation scheme has been done based on the magnet protection analysis and choices. As the magnet will be protected by a Main Safety System (MSS) the voltage will be monitored for each coil segment with a redundancy. The quench detector will be made by making the difference between two segments of the coil having the same inductance, allowing to remove the inductive voltage and read only the resistive voltage. This will permit the MSS to detect the transition time and protect the magnet by opening the contactor to discharge the magnet on the dump resistor. With the redundancy, 50 voltage taps shall be positioned in the magnet giving 25

differences of potential to measure and send to the MSS and acquisition system. These measured values can be combined in 16 quench detectors with 12 for the coils, 2 for the current leads and 2 for the busbars (one per current lead and one per busbar). For the coils the voltage threshold has been set to 0.1 V to 1 V in the simulation with at least one second of validation time. For the busbars, the voltage threshold is smaller and have been set to 10 mV with a validation time of 10 ms. Finally, the voltage threshold of the current leads shall be smaller than the maximum operating voltage in the current leads. Two DCCTs shall be position to monitor and regulate the current. The first one between the power supply and the contactor shall be used for the power supply regulation while the second one be-tween the coil and the dump resistor will be used to monitor the current in case of quench or contactor opening.

Cryogenic Instrumentation: For the cryogenic instrumentation plan, different type of sensors will be used. The first ones are the temperature sensors whose are divided in two types, the PT100 for all the temperature above 50 K i.e., for the thermal screen and the CERNOX® sensors used for all the 4.5 K measurements. For the PT100, 10 will be placed on the thermal screen while 6 will be placed on the current leads. Concerning the CERNOX, 12 will be distributed all over the magnet and shell and 6 distributed between the bus-bars, the phase separator, the thermosiphon inlet and outlet. Completing the thermal sensors flow meters (2 for the current leads, 2 to 4 for the thermosiphons inlet and outlet and 2 for the 50 K shield inlet and outlet) will be used to monitor the cryogenic operation as well as 2 liquid helium level gauges, 2 manometers and 2 vacuum gages.

Mechanical sensors: To monitor the tie-rods preload during the magnet assembly in its cryostat, the transport, the mag-net cool down and energization, it is planned to use load cells placed at the end of each tie-rods. These load cells shall be dimensioned adequately pending the stress analyses made during the manufacturing design phase.

Summary MARCO will be a unique solenoid for detector magnets, it will use a Rutherford in Copper Channel Conductor (RICC) and a mandrel in brass 70/30, it will meet the stringent criterion on the transparency typical of every detector magnet.

3.3.3 Tracking

The tracking system occupies a volume at the center of the ePIC detector with a radius of $R = 75cm$ and a length of $-165\ cm < z < 200\ cm$ along the beam axis. It consists of a combination of the Silicon Vertex Tracker (SVT) based on thinned Monolithic Active Pixel Sensors (MAPS), at its core that are surrounded by outer Micro-Pattern Gas Detectors (MPGD) along with Time-of-Flight layers based on AC-LGAD technology in the barrel and forward acceptance regions which also provide hit points with good resolution. The system provides tracking for charged particles over a wide pseudo-rapidity of $-3.5 < \eta < 3.5$ and momenta larger than 0.5 GeV. The SVT consists of five barrel layers and two arrays of five disks on either side of the beam collision region. The SVT has low mass and high-granularity, thereby ensuring high spatial resolution. The outer MPGD and AC-LGAD layers provide additional space points with large lever arms, while also allowing for noise rejection, background rejection, and the association of a track with a specific bunch crossing based on the timing information. They are configured such that their hits can be used to form tracklets and their comparatively fast timing improves noise and background rejection. Detailed descriptions of these subsystems are provided in subsequent sections.

Table 3.22 summarizes the resolution requirements on the particle momentum measurement at the event vertex and the determination of the radial distance of closest approach of the particle trajectory to the event vertex for different ranges in pseudorapidity and with the dependencies

on momentum and transverse momentum, respectively. The momentum threshold is lower than 0.5 GeV for most of the tracking acceptance.

η **range**	dp/p [%]	$\mathbf{DCA}_r$ [μm]
$(-3.5, -2.5)$	$0.10 \times p \oplus 2.0$	$30/p_T \oplus 40$
$(-2.5, -1.0)$	$0.05 \times p \oplus 1.0$	$30/p_T \oplus 20$
$(-1.0, 1.0)$	$0.05 \times p \oplus 0.5$	$20/p_T \oplus 5$
$(\ 1.0, 2.5)$	$0.05 \times p \oplus 1.0$	$30/p_T \oplus 20$
$(\ 2.5, 3.5)$	$0.10 \times p \oplus 2.0$	$30/p_T \oplus 40$

Table 3.22: Physics requirements on the relative momentum measurement, dp/p, at the event vertex, η, and on the determination of the radial distance of closest approach, DCA_r, of the particle trajectory to the event vertex. The requirements are given for different ranges in pseudorapidity as parametrizations in the total momentum, p, in GeV and transverse momentum, p_T, in GeV, respectively.

To study the tracking performance, we have implemented the preliminary design – its geometry, material, and point resolutions – in the ePIC software stack (version 24.10.1). In the initial studies, we have generated single pions at the nominal collision vertex of (0,0,0) in the momentum range from 500 MeV to 20 GeV. These pions were then propagated through the detector volume in the GEANT4-based DD4hep simulation package. We then processed the recorded detector hits with the reconstruction framework called "EICrecon" for digitization, and track finding and fitting via the ACTS combinatorial Kalman Filter.

Figure 3.55 shows the simulated relative momentum resolution for single charged pions versus their total momentum for different pseudorapidity regions, together with the requirements. The simulations show that the momentum resolutions are substantially met over most of the SVT acceptance. The performance in the range of smallest pseudorapidity, $-3.5 < \eta < -2.5$, is limited by constraints on the SVT lever arm from ePIC's outer subsystems in this region and overall detector size. In this range, the momentum measurement of the scattered electron in coherent diffraction poses the most stringent resolution requirement and achieving the physics objectives will rely on the combination with calorimetric energy measurement. The requirements in the range of largest pseudorapidity, $2.5 < \eta < 3.5$ can be met for the ultimate solenoidal field strength of 2 T.

Figure 3.56 shows the simulated radial distance of closest approach, DCA_r, for the reconstructed trajectories of simulated charged pions to the event origin versus pion transverse momentum in different pseudorapidity regions, together with the requirements. The simulations show that the requirements on DCA_r are substantially met over the SVT acceptance.

Figure 3.57 shows the track reconstruction efficiency versus pseudorapidity for representative momenta. The track finding and reconstruction efficiencies are above 95% for $-3.5 < \eta < 3.5$ over a wide kinematic range. The detector acceptance drives the drop-off in efficiency near extreme η for all momenta, whereas current algorithmic limitations are responsible for the somewhat stronger drop-off for the lowest momenta.

In addition to single-track simulations, we have also performed multi-track simulations in the form of simulated Neutral Current (NC) DIS events and studied the tracking performance. These events were generated using Pythia8, and they incorporate a realistic beam spot distribution as well as beam angular and energy divergence effects at the event generation level. Their reconstruction

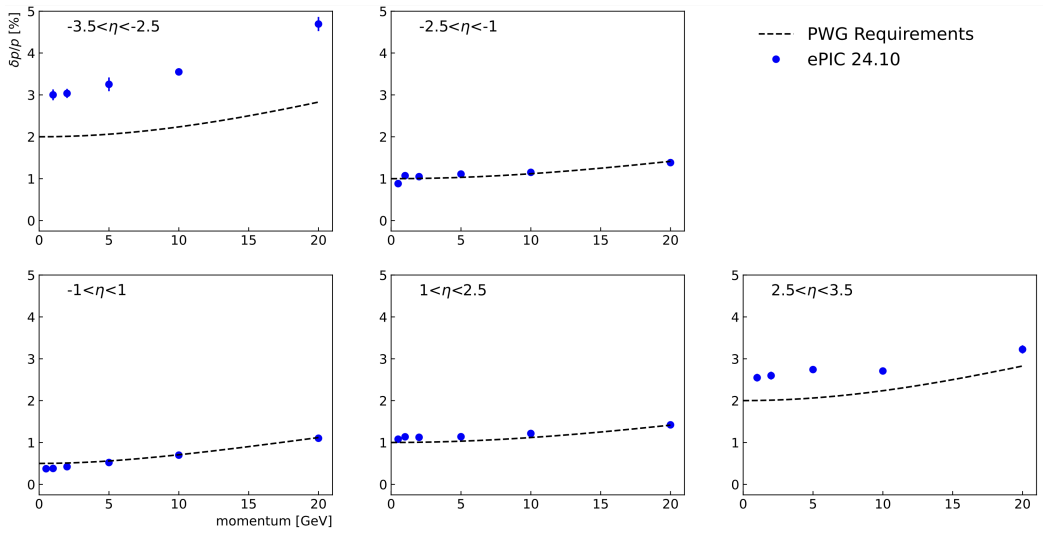

Figure 3.55: Relative momentum resolution versus total momentum for charged pions (points) together with physics requirements (curves) in different pseudorapidity ranges as indicated. The results are based on full GEANT simulations of the central tracking system (SVT+MPGD+AC-LGAD) using the ePIC software stack and ACTS-based track finding and reconstruction using suitably tuned ACTS parameter settings. The error bars indicate the size of the statistical uncertainties in the simulation.

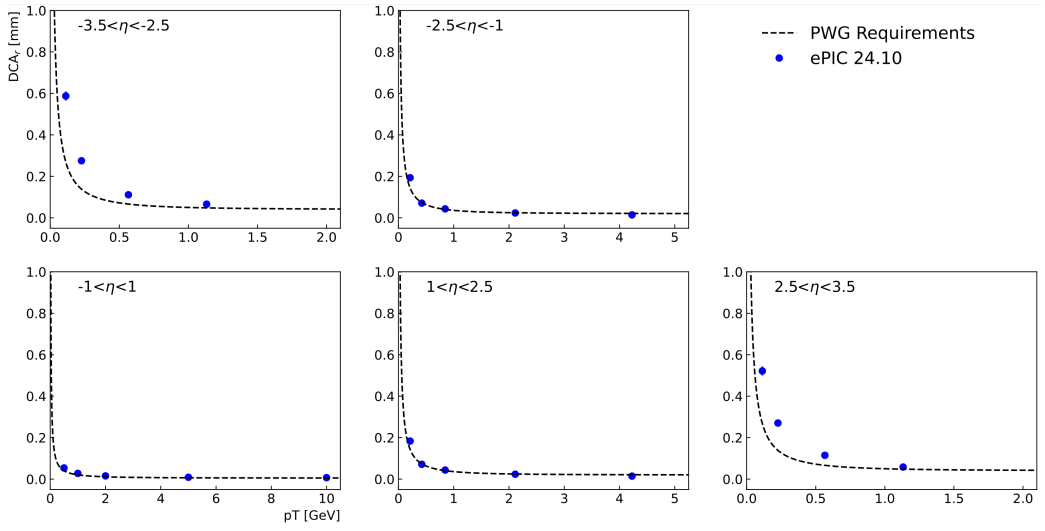

Figure 3.56: Distance of closest approach in the radial direction between reconstructed charged pion trajectories and the event origin versus transverse pion momentum (points) together with physics requirements (curves) in different pseudorapidity ranges as indicated. The results are based on full GEANT simulations of the central tracking system (SVT+MPGD+AC-LGAD) using the ePIC software stack and ACTS-based track finding and reconstruction. The error bars indicate the size of the statistical uncertainties in the simulation.

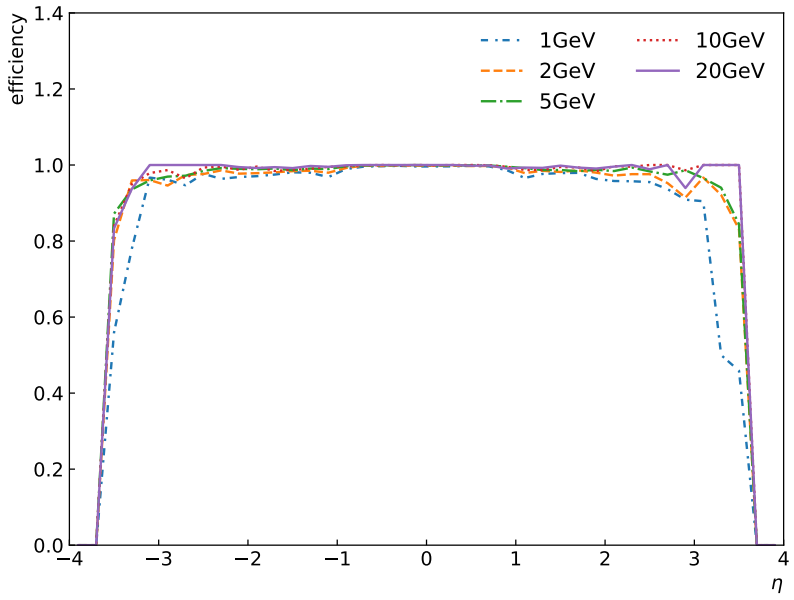

Figure 3.57: Tracking efficiency versus pseudorapidity η for charged pions with initial momenta of 1 GeV to 20 GeV.

used the same framework and settings as used for the single-track simulations.

Figure 3.58 shows the pseudorapidity distribution for both the generated charged particles and for the reconstructed tracks. The reconstructed track pseudorapidity distribution qualitatively agrees with the truth spectrum above the transverse momentum of 500 MeV/c shown. This result demonstrates the ability of the ePIC tracking detector system and track finding and fitting software to efficiently and accurately reconstruct tracks in DIS events where multiple tracks are present.

Figures 3.59 and 3.60 show the tracking efficiency and purity from simulations of DIS events mixed with beam backgrounds sampled at appropriate rates. Particles and trajectories are required to have at least four hits to reject ghost tracks. The observed efficiency is qualitatively consistent with that from single particle simulations as well as simulations that contained DIS events only. High efficiency is seen for momenta above 1 GeV/c and η between -3.5 and 3.5. The efficiency at lower momenta and higher $|\eta|$ is lower. The tracking purity, defined as the ratio of good DIS tracks to all valid tracks, is above 95% across momentum and η.

3.3.3.1 The silicon trackers

Requirements

Requirements from physics: The Silicon Vertex Tracker (SVT) needs to meet stringent performance requirements, set by the EIC science program, on acceptance and resolutions for charged-particle trajectories. At a high level, the SVT needs to precisely measure the trajectories of the

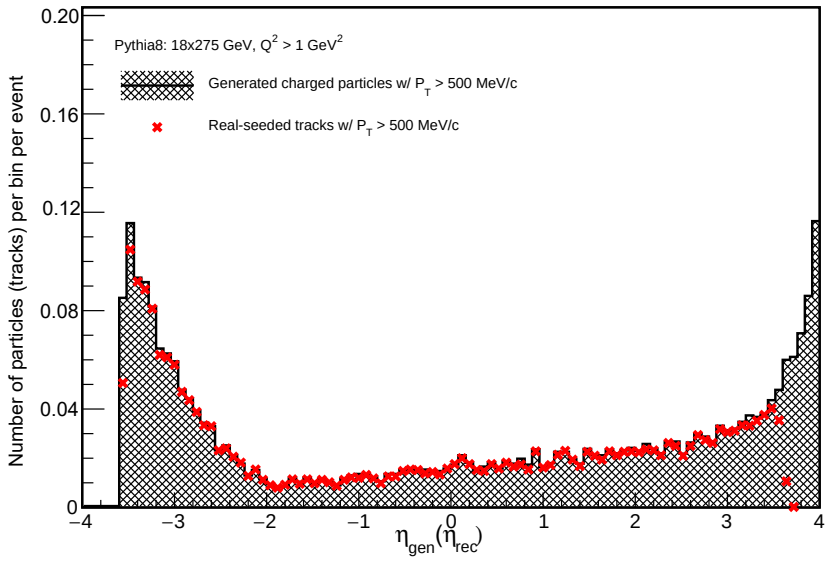

Figure 3.58: The number of generated charged particles vs. the generated pseudorapidity of those particles (filled black). The number of reconstructed tracks vs. the reconstructed pseudorapidity of those tracks (red crosses). The y axis shows the number of particles (tracks) per pseudorapidity bin per event. The events were generated with a Q^2 minimum of 1 GeV^2; the scattered electron peak can be seen at negative pseudorapidity. The particles (tracks) shown all have a generated (reconstructed) transverse momentum greater than 500 MeV/c.

scattered electron and charged hadrons produced in electron-ion beam collisions over a wide kinematic range. The scattered ion, if it remains intact, is outside of the SVT acceptance. The SVT also needs to measure charged decay-particles from hadrons containing heavy quarks and from vector mesons. It is to aid in particle-identification a) through determination of the displacement of the geometrical origin of the decay particles (secondary vertex) from the collision point (event vertex) via precision reconstruction of both vertices and b) by providing direction and position information on charged-particle trajectories through the outer gaseous tracking subsystems and into the outer particle-identification subsystems.

The SVT is the innermost subsystem of the ePIC central detector. Constraints from the overall detector size and the outer subsystems limit the active volume of the SVT to $-105 < z < 135$ cm and a radius of approximately 42 cm. In combination with the 1.7 T solenoidal field, this leads to a requirement on the point resolution of better than 10 μm as well as the need to minimize traversed material by limiting the number of detection surfaces and minimizing their radiation lengths.

Requirements from Radiation Hardness: We have evaluated the radiation levels in the SVT using the current knowledge of the beam configuration and beam backgrounds from beam gas interactions and synchrotron radiation. Figure 3.61 shows the current estimates for neutron equivalent fluence, and dose. The black lines indicate the approximate locations of the SVT detection surfaces. These radiation maps have been estimated for the beam configuration with the highest luminosity (10 GeV electron beam and 275 GeV proton beam at 10^{34} cm^{-2} s^{-1}), and include contributions from hadron and electron beam gas interactions. The results assume that the machine and

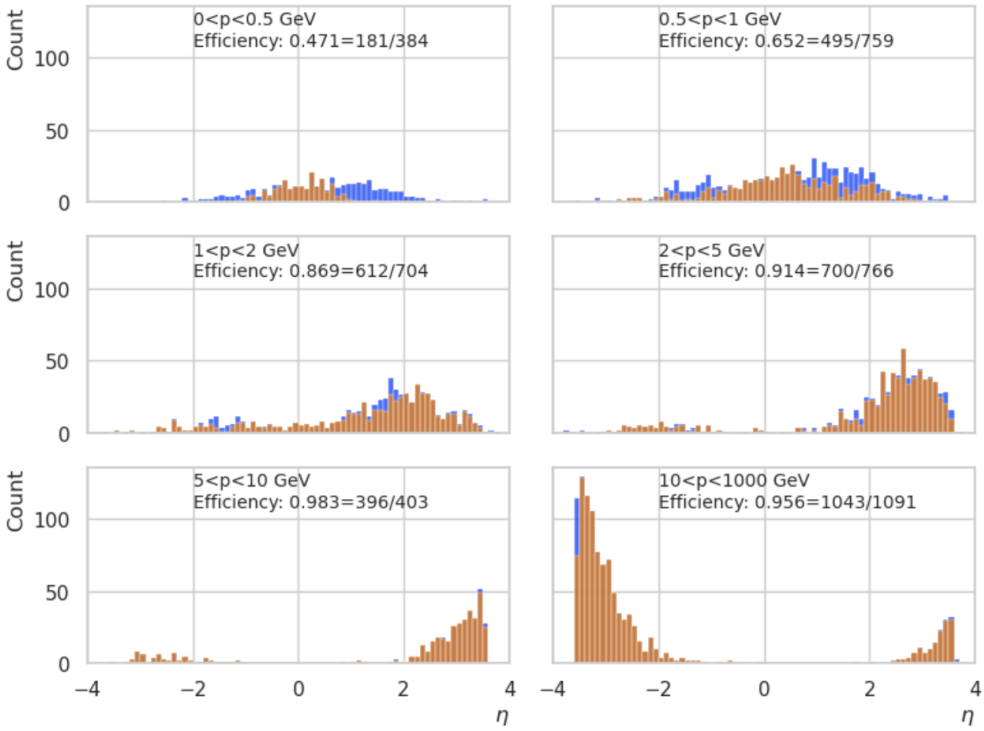

Figure 3.59: With 1000 time slices, 2μs each, of mixed DIS and background event samples, The blue bars show the number of good DIS particles – leaving at least 4 hits in the tracking system and originating from within 1 mm (100 mm) from the nominal interaction point in the transverse (longitudinal) direction versus η for different momentum regions. The orange bars show good DIS particles that are successfully reconstructed. The efficiency for each momentum region is calculated as the ratio of the sum.

detector run at 100% efficiency for 6 months per year over a period of 10 years. Even under these conservative assumptions, the radiation doses in the SVT will be low to moderate, and are expected to be acceptable. The majority of the SVT will see fluence levels well below 10^{11} n_{eq} cm^{-2}. The innermost central layers and layers in the hadron going direction will experience slightly higher fluence between 10^{11} and 10^{12} n_{eq} cm^{-2}, with some small regions reaching above 10^{12} n_{eq} cm^{-2}. The dose rate map indicates that areas close to the beam pipe will experience a total ionizing dose between ten and a few hundred krad, while the rest of the SVT remains below 10 krad.

Requirements from Data Rates: EIC physics rates are expected to be below 0.5 MHz. That is, only a small fraction of the EIC beam crossings produces a physics event and physics event pileup from within a single beam crossing is negligible. The dominant fraction of these events originate from a region, $|z| < 80 - 100$ mm, surrounding the nominal interaction point. We thus estimate that event pileup within the SVT is determined by its readout frame or integration window of 2 μs or a small multiple thereof. Within this window, SVT will also accumulate hits from noise and beam backgrounds. We estimate that the associated hit load and data volume will exceed that from physics events. Hit occupancies will be low in view of the high SVT granularity. We estimate a hit

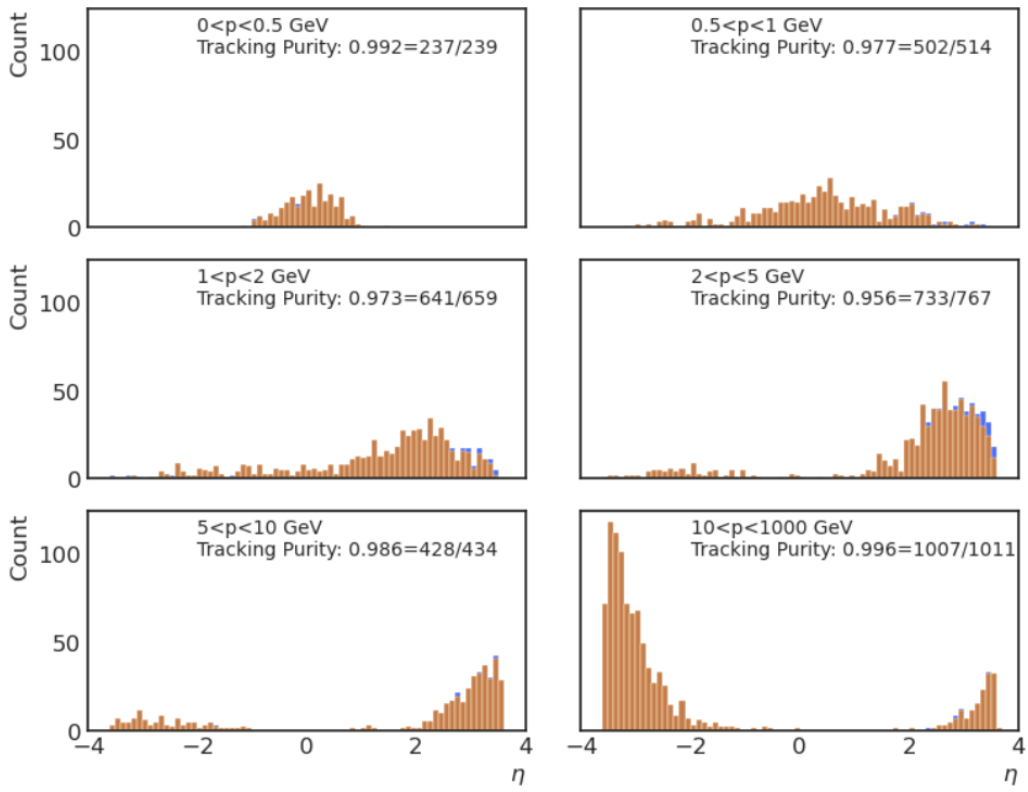

Figure 3.60: Similar to Figure 3.59, the purity examined all valid tracks with at least 4 hits (blue), and checks how many of them are associated with a good DIS charged particle (orange).

probability per pixel per readout frame of $\mathcal{O}(10^{-7})$ and a typical total data rate at the level of 15 Gb/s. The sensor and readout chain need to be efficient under these conditions.

Justification

Device concept and technological choice: To meet the stringent requirements on charged-particle tracking and vertexing, we have designed the SVT as a well-integrated, large acceptance, high granularity, and low-mass tracking and vertexing subsystem. The SVT has four regions covering a total active area of approximately 8.5 m^2. An Inner Barrel (IB) and Outer Barrel (OB), made of three and two active layers, respectively, cover the mid-central pseudorapidity range and have an active volume that extends radially to approximately 42 cm. Endcaps, each with five active annuli surrounding the beampipe, are placed on either side of the nominal interaction point at z-positions at z-positions between -105 and 135 cm and an outer radius equal to that of the OB. The Electron Endcap (EE) is positioned in the direction of the electron beam and has acceptance for a large fraction of the scattered electrons, while the Hadron Endcap (HE) provides acceptance for many of the hadrons produced in physics collisions. Figure 3.62 shows the SVT regions and geometrical layout.

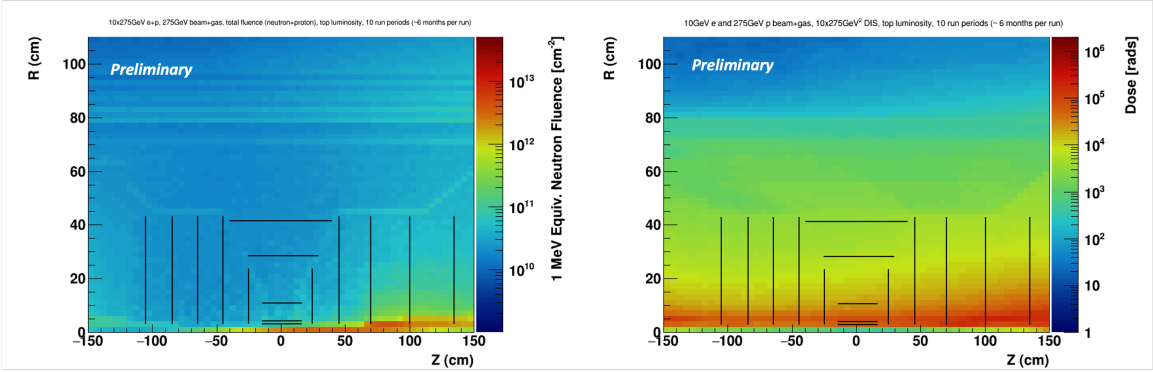

Figure 3.61: Maps of simulated 1 MeV neutron equivalent fluence (left) and total ionizing dose (right) over the ePIC tracking envelope. This is a conservative estimate assuming 10 years of running at top luminosity with 100% efficient accelerator and detector. The black lines indicate the approximate location of the ePIC SVT detector layers.

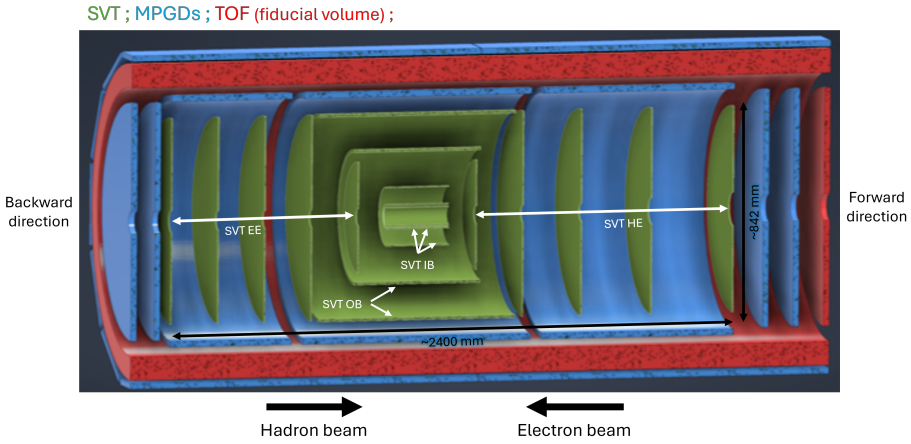

Figure 3.62: Schematic layout of the ePIC SVT showing the central region consisting of the inner and outer barrel made of three and two cylindrical layers, respectively, together with the endcap regions made of five annuli each. The figure also shows the surrounding Micro Pattern Gas Detector (MPGD) layers and the envelope of the Time of Flight PID detector.

We designed the SVT to cover the required pseudorapidity range and to reach spatial resolutions as low as ≤ 6 μm through a combination of high granularity (~ 20 μm pixel pitch), lightweight support structures, cooling, and electrical services enabled by a low power sensor design (≤ 40 mW cm^{-2}). Our development aims at achieving 0.05% X/X_0 in the IB, 0.25% X/X_0 in the innermost OB layer and in the disks, and 0.55% X/X_0 in the outermost OB layer. We selected a sensor technology based on the ALICE-ITS3 development [17] to meet our requirements. This is a new generation, large area Monolithic Active Pixel Sensor (MAPS) in a commercial 65 nm CMOS imaging process.

Subsystem description:

General device description: Tables 3.23 and 3.24 show the positioning and size of the SVT active layers, together with their material budget target. We designed the IB to provide precise

vertex reconstruction, while also contributing to momentum measurement. This is achieved with a combination of very thin layers at optimized radii. The IB will use the ALICE ITS3 wafer scale sensor [17] with a suitable adaptation of the ITS3 ultra-thin detector concept to the large EIC beam pipe diameter. The IB design has three layers of silicon sensors thinned below 50 μm and bent around the beam pipe, with minimal mechanical support, air cooling, and no electrical services in the active area, to reach the very low material budget target of $X/X_0 = 0.05\%$. The innermost layer is positioned as close as possible to the beam pipe, taking into account the constraints coming from the large beam pipe radius and the requirements from beam pipe bake-out, which will be performed with the IB installed. The position of the second layer is chosen to maximize vertex resolution. The outermost layer of the IB aims at maintaining the very low material budget at a radius of 120 mm and serves both vertexing and sagitta measurements. The OB, EE and HE will be equipped with the EIC Large Area Sensor (LAS), a modified version of the ITS3 sensor, optimized for high yield, low cost, and large area coverage. These sensors will be thinned to 50 μm and mounted on lightweight support structures, in the form of staves for the OB and disks for the endcaps, with integrated cooling and electrical interfaces for power, data and slow control. The OB layers and the endcap disks are positioned to provide high precision measurements over a large lever arm to improve momentum resolution and optimize acceptance at large pseudo-rapidity. The inner openings of the disks will accommodate beam pipe bake-out constraints as well as beam pipe divergence. These translate into six different inner opening geometries over ten disks.

Region	**Layer**	**radius** [mm]	**length** [mm]	X/X_0
IB	L0	36	270	0.05%
	L1	48	270	0.05%
	L2	120	270	0.05%
OB	L3	270	540	0.25%
	L4	420	840	0.55%

Table 3.23: Target radius, length and material budget of the SVT IB and OB layers.

Region	**Disk**	**z** [mm]	$\mathbf{r}_{out}$ [mm]	X/X_0	**Region**	**Disk**	**z** [mm]	$\mathbf{r}_{out}$ [mm]	X/X_0
EE	ED0	-250	240	0.25%	HE	HD0	250	240	0.25%
	ED1	-450	415	0.25%		HD1	450	415	0.25%
	ED2	-650	421	0.25%		HD1	700	421	0.25%
	ED3	-850	421	0.25%		HD3	1000	421	0.25%
	ED4	-1050	421	0.25%		HD4	1350	421	0.25%

Table 3.24: Position along the beam pipe, outer radius and material budget for the SVT layers in the EE and HE regions. Disks in the electron direction are labeled ED0 to ED4. Disks in the hadron direction are labeled HD0 to HD4. Disks ED0/1/2 and disks HD0/1 have the same inner opening. Each of the other five disks has a different inner opening.

Sensors: The SVT will be constructed with MAPS sensors that integrate sensing and front-

end electronics functionalities in one device. The ePIC SVT will use MAPS sensors developed in a 65 nm CMOS imaging process based-off the ALICE ITS3 development [17]. This technology enables a high granularity and low power consumption design, and offers stitching on 300 mm wafers for the development of large area sensors. These characteristics are key to delivering a high precision detector through high spatial resolution and minimized material budget.

The SVT IB will use the ALICE ITS3 sensor, called MOSAIX. A sketch of MOSAIX on a wafer is shown in figure 3.63. MOSAIX is composed of an active matrix of Repeated Sensor Units (RSUs). Twelve RSUs are stitched along the length of the sensor, giving a total length close to 27 cm. The sensor will be three, four, and five RSUs wide (about 6, 8, and 10 cm) for L0, L1 and L2 respectively. Each RSU is further divided into 12 tiles that can be switch off independently in case of faults to improve yield over such large area device. A row of 12 RSUs, together with the left and right endcap (LEC, REC) is called a segment. The LEC contains circuits for power, slow control and data. The REC hosts another set of power connections to ensure a uniform power distribution over the full sensor length. Data links for each segment can be configured with three links, plus one spare, at 10.24 Gb/s or six links, plus two spares, at 5.12 Gb/s. For each segment, seven electrical links provide clock, synchronization and control signals, referred to here as slow control signals. The clock runs at 160 MHz, while the control signals will run at 5 Mb/s. MOSAIX has different power domains for analogue and digital circuitry at 1.2 V, plus two more domains for specific blocks, one at 1.2 V and one at 1.8 V [17]. The sensor bias voltage will between -1.2 and -4.8 V.

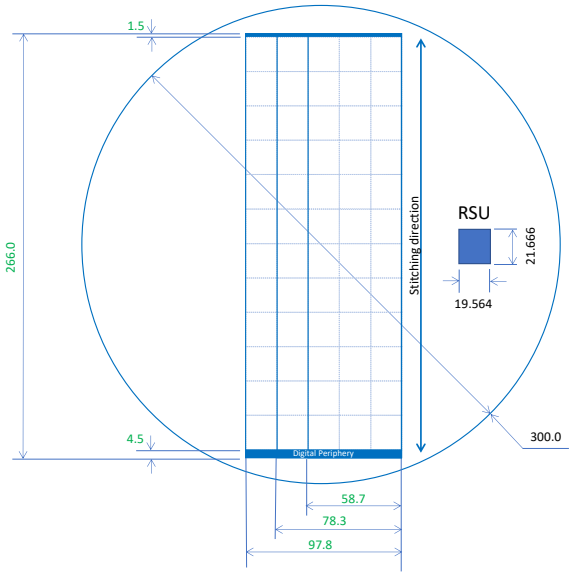

Figure 3.63: Sketch of the MOSAIX sensor on a 300 mm wafer showing the size of the RSU, LEC, REC and of the full sensor for the three different widths. All positions are in mm.

The SVT OB and disks cover an area of approximately 8 m^2. Considerations based on yield, cost, integration, and coverage require the use of a sensor with a smaller size than the wafer-scale sensor used in the IB. These regions will use the MOSAIX sensor with modifications to reduce the size. This sensor would still be large in traditional terms and is therefore referred to as the EIC Large Area Sensor (EIC-LAS). The EIC-LAS will be one RSU wide and either 5 or 6 RSUs long. Power will need to be fed into the EIC-LAS only from the LEC given the reduced length. In addition to reducing the size of the sensor, the EIC-LAS will see a reduction of the

number of data links to match the lower SVT data rate, reduce material and ease integration aspects. To further ease the integration of the EIC-LAS in the OB and disks, EIC-LAS sensors will be powered in series by a constant current and a dedicated communication protocol will be used to reduce the number of slow control links from the counting room to the sensor. These features will be provided by a supporting ASIC, referred to as the Ancillary ASIC (AncASIC).

FEE: One AncASIC will be used per EIC-LAS. This chip includes three main features. It integrates the shunt low-dropout (SLDO) regulator for serial powering. This regulator will generate the voltages needed by the EIC-LAS from the input current. This design is adapted from the original SLDO design for the upgrades of the ATLAS and CMS pixel detectors at the HL-LHC [18]. One AncASIC will integrate five SLDO regulators for the different power domains on the EIC-LAS. The AncASIC will also contain a Negative Voltage Generator (NVG) block. The NVG is a diode-based charge-pump circuit (Dickson-type charge pump voltage multiplier). It will generate the sensor's negative bias voltage from one of the regulated power supplies at 1.2 V generated by the SLDOs. The third block is the Slow Control (SC). Slow control signals from the counting room will be transmitted over I2C for multiple EIC-LAS sensors over one link. The SC block will decode them into the MOSAIX format (i.e. into seven links). The AncASIC will be produced in a 110 nm SOI process offering multiple Multi-Project Wafer (MPW) runs per year and the required transistor ratings for the SLDO and NVG.

Other components: All components of the SVT detector are designed with the goal of achieving the low material budget target, while providing a robust, high precision system. Traditionally, a significant fraction of the material in silicon detectors is contributed by the powering system. While the IB will be powered using a traditional voltage-based powering scheme, a current-based power distribution scheme (called serial powering) is adopted for the OB and disks to reduce the mass associated with the SVT power distribution. Groups of up to four EIC-LAS sensors are powered in series by a constant current, with the electronics low voltage generated close to the sensors by the SLDO regulators in the AncASIC. This scheme reduces cabling material and provides the only viable powering solution to fit within the available space for services in the ePIC detector. For the smaller IB system, a traditional voltage-based, direct powering scheme is foreseen. Data, slow control signals and power are routed over aluminum-based flexible printed circuits (FPC) between the SVT active elements (MOSAIX, EIC-LAS, AncASIC) and the readout (RDO) boards. Four different RDO boards are used in the SVT: the interface board, the control board, the fiber aggregator board, and the power board. The interface board receives data from the sensors for transmission to the counting room. The control board receives slow control signals from the counting room to be transmitted to the MOSAIX and EIC-LAS (through the AncASIC), and to the VTRX+ devices. Lightweight communication between these RDO boards and the counting room is achieved by use of optical fibers. A fiber aggregator board achieves a reduction of the optical fiber lines through multiplexing via FPGA to match the number of fibers to the available channels of the data acquisition board in the counting room. The data acquisition board is common to all ePIC sub-detectors, the FELIX board developed for CERN experiments [19]. The electro-optical interface components used on the interface and control boards are the lpGBT [20] and VTRx+ [21] devices developed by CERN. The power board provides interface for power distribution for sensors and AncASIC as well as devices on the RDO boards. Whilst the functionality of the RDO boards and FPC remains the same, different designs will be needed for IB, OB and disks to accommodate the different powering schemes, number of data links, and sensors grouping. The preferred cooling solution for the SVT detector is air cooling, baselined for the two innermost layers of the IB and under study elsewhere. The OB, EE and HE are designed to allow air flow through the low mass staves and disks, made of carbon

composite material, that support the sensors.

Performance As discussed in the preceding section, we have simulated track finding and reconstruction within the ePIC software framework to quantify momentum and vertexing resolutions in the nominal 1.7 T solenoidal field strength of the MARCO magnet. The sensor response in these simulations requires cross-validation with actual measurements.

We have performed beamtests at FNAL with a single-RSU sensor, called babyMOSS, from the ITS3 Engineering Run 1 (ER1) submission. In these tests, a particle telescope was constructed using six sensors, with a seventh sensor, the Device Under Test (DUT), placed in the middle. The angle of the DUT with respect to the incident beam was varied in the horizontal plane of the telescope. Figure 3.64 shows a close-up of the telescope and results for the cluster extent as a function of the incident beam angle onto the DUT from data and simulations. The results show that the cluster size increases with the particle incident angle, consistent with a geometrically driven expectation. The analysis of the point resolution as a function of the particle incident angle is in progress. Initial results are consistent with the expectation from the pixel pitch.

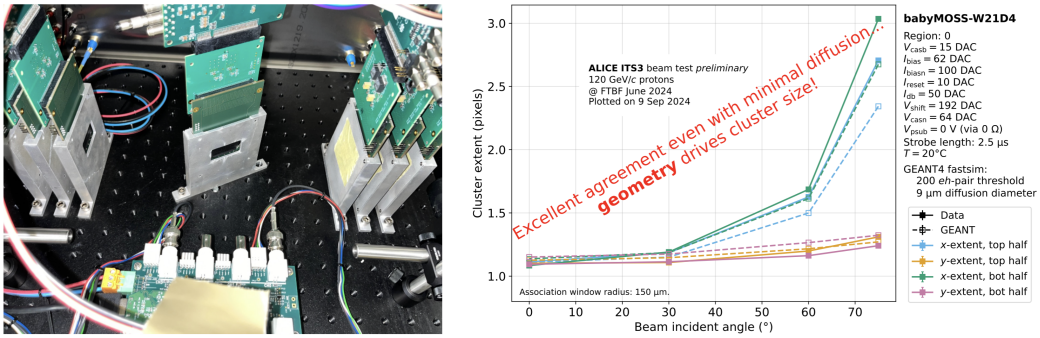

Figure 3.64: Left: A close-up of a beam telescope constructed using six single-RSU sensors from the ITS3 Engineering Run 1, with a seventh sensor, the Device Under Test (DUT), placed in the middle. Right: Comparison of results from beamtests at FNAL and from simulations for the cluster extent as a function of the beam incident angle onto the DUT.

Implementation

Services: Services to the SVT are of two types: electrical/fiber-optical services and cooling. Electrical/fiber-optical services to the SVT comprise power, data and slow control. Services are routed to/from the IB from the hadron-going direction. Services for OB are routed to/from the electron- and hadron-going directions. For the IB (MOSAIX sensor and direct powering), electrical services will be by MOSAIX segment. For the OB and disks (EIC-LAS and serial powering), they will be by group of up to four EIC-LAS. A summary of the data, slow control and power lines needed in the different regions of the SVT is given in Table 3.25.

The table illustrates the reduction in power lines using serial powering versus direct powering. In the IB, each MOSAIX segment will need ten lines (including the return line) to serve the four power domains of the electronics plus the sensor bias. For each segment, the full MOSAIX current will be transmitted. In the OB and endcaps two lines (including the return line) will be needed to deliver the same power to up to four EIC-LAS (i.e. four segments). The current flowing on these lines will

Region	Sensor	Electrical services group	per group # power lines	per group # slow control links	per group # data links
IB	MOSAIX	MOSAIX segment	10	7	8
OB	EIC-LAS	Up to 4 EIC-LAS	2	3	4
EE/HE	EIC-LAS	Up to 4 EIC-LAS	2	3	4

Table 3.25: Summary of power and readout services for the different regions of the ePIC SVT (slow control and data links are differential pairs of wires). A services group is one MOSAIX segment in the IB, and up to four EIC-LAS sensors (i.e. four segments) in the OB and disks.

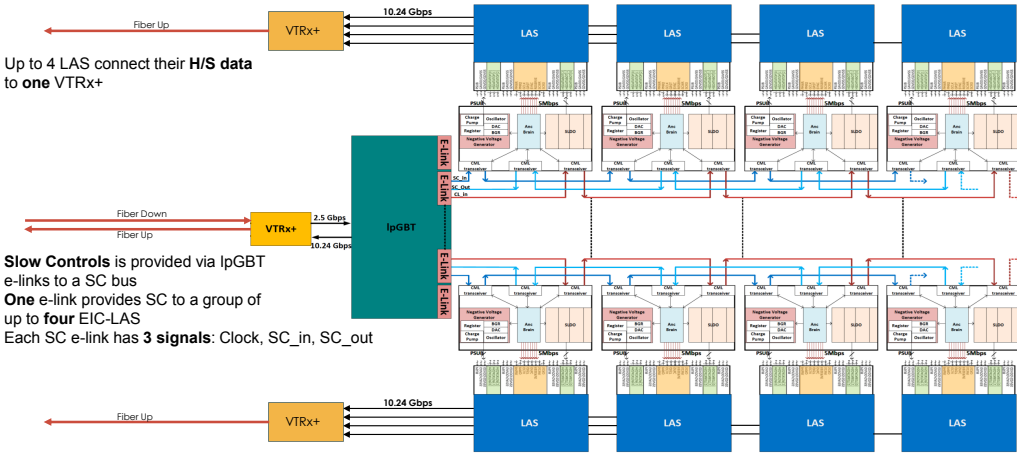

Figure 3.65: Schematic overview of data and slow control lines to groups of up to four EIC-LAS in the OB and disks.

be the current needed by one EIC-LAS only, reducing the current being transmitted to the detector by up to a factor four, and correspondingly reducing cables cross section and material budget.

Figure 3.65 shows the data and slow control distribution for a group of four EIC-LAS in the OB and disks. Each data line connects to one input of a VTRx+ on the interface board. Given the high speed of the data transmission, this board will be placed at the end of each stave and disk for signal integrity. The VTRx+ transmits the data of a group of up to four EIC-LAS over a bundle of optical fibers to the counting room (each VTRx+ has a pigtail ribbon with up to five active optical fibers). Slow control signals are transmitted over optical fibers to the control board, placed along the SVT support structure. Once converted into electrical signals, one lpGBT eLink provides the slow control signals to up to four AncASICs. Each lpGBT has 16 eLinks, meaning that each control board will serve multiple groups of up to four EIC-LAS. The slow control signals are transmitted between the control board and the AncASIC either in a daisy-chain architecture (as shown in the figure) or via multi-drop. The exact configuration is still being evaluated. The AncASIC converts the incoming I2C protocol to the MOSAIX protocol expected by the EIC-LAS. As the sensors in the OB and the disks are powered in series, each EIC-LAS is on a different ground potential. A dedicated communication scheme is thus needed. Data lines will be AC-coupled. For the slow control, a standard DC transmission is also being investigated with the ground difference between EIC-LAS sensors being accommodated.

Flexible printed circuits (FPCs) are required to electrically connect MOSAIX sensors, EIC-LAS sen-

sors and AncASIC chips to the interface and control boards. In the IB the FPC will connect to the LEC of the MOSAIX sensor. In the OB and disks, a main FPC will run along staves and disks, serving groups of up to four EIC-LAS sensors. It will connect to the AncASICs through bridge FPCs (see prototype in fig. 3.72). The maximum length of the main FPC is constrained to a maximum of 40 cm based on signal integrity and power drop considerations. Two and four main FPCs will be needed on L3 and L4, respectively, to cover the full length of the stave. The FPCs must have a low mass in order to maintain the low material budget of the SVT. It is therefore advantageous to select conductive tracks made of aluminum (X_0 = 8.9 cm) instead of traditional copper (X_0 = 1.4 cm). Dielectrics like polyimide (X_0 = 28.57 cm) are the default solution for the manufacturing technologies of aluminum-based FPCs deployed in scientific experiments. The selection of the dielectric material is dependent on its loss-tangent properties versus the frequency of the signals to be transmitted. Typically, the most stringent requirements for signal attenuation are set by the high-speed data transmission lines. In case of the ePIC SVT, it is envisaged that data links can transmit signals as fast as 10.24 Gb/s for a length of $\sim$50 cm. The baseline configuration for the FPCs assumes a stack-up made of two aluminium conductive layers (each $\sim$15 μm thick) separated by a polyimide dielectric substrate ($\sim$35 μm), and then additional polyimide cover layers ($\sim$35 μm combined thickness) to insulate the conductive tracks from external electrical shorts. This cross section ($\sim$100 μm in total) would equate to a combined material budget of $\sim$0.06% X_0. The combination of serial powering, slow control daisy-chained/multi-drop configuration and impedance matching at 100 Ω for clock, control lines and data, enables a reduction of the number of signals to be propagated. This is particularly important for staves and disks where the FPCs overlap the sensitive area of the MAPS. By combining these power and signal distribution techniques, it is estimated that the minimum width for the FPC can be as narrow as 6 mm. This is $\sim$1/3 of the width of the LAS ($\sim$19 mm).

The transmission of the signals to the counting room will see a further stage of processing. The data fiber-optic lines will be aggregated in the aggregator board, common to all SVT regions, which has multiple fiber inputs, an FPGA for extracting the payload from these fibers, and one fiber output towards the FELIX board, thus reducing the number of fiber inputs at the data acquisition boards. For the FPGA, we are considering both a radiation tolerant PolarFire FPGA and an SRAM based FPGA, with the choice to be made depending on the location of this board and radiation levels present. For the optical interface, we are considering both a FireFly optical transceiver and a standard SFP (Small Form Factor Plugable) transceiver. It is estimated that approximately 5000 data fiber links run from the sensors to the aggregator board. Assuming an aggregation factor of 10, there will be approximately 500 fibers towards the DAQ FELIX boards, which can be accommodated by 11 FELIX boards (assuming each FELIX board will have 48 fiber inputs).

Cooling adds to the service load, including the target radiation lengths in the SVT active areas. The preferred cooling solution for the SVT detector is air cooling (using dry air), baselined for the two innermost layers of the IB and under study elsewhere, with liquid cooling in strategic places as necessary. The chip temperature requirements are given in Table 3.26. FEA analysis is underway based on current power dissipation estimates.

Table 3.26: SVT component temperature requirements (N/S is not specified).

Requirement	LEC	RSU	REC	AncASIC
Maximum T [°C]	65	40	N/S	80
Maximum T variation [°C]	10	1 over 3 mm 10 over full length	N/S	10

For the inner layers of the IB, the baseline is air cooling with thermally conductive foam near the

LEC. Measurements from ALICE ITS3 show this is reasonable to cool the MOSAIX sensor [17]. Air will be forced between L0 and L1. To cool L2, the possibility for natural convection with liquid cooling near the LEC if necessary is under study. The air inlet and outlet are under design, with the bulk of the material to be placed on the hadron-going side of the detector.

In addition to cooling during operation, the IB will need to be kept cool during beam-pipe bake-out. The aim is for no additions to the operational cooling, i.e. no additional material (e.g. insulators) or changes (i.e. liquid instead of air). Ongoing ANSYS studies at Jlab and LBNL, discussed further down, have shown that there are options to keep the detector cool under these constraints. Tests of sensor prototypes by ePIC (flat sensor prototypes) and ITS3 (wafer-scale, curved mechanical prototypes) institutes, at temperatures up to 50 °C in a climate chamber have shown no electrical and no mechanical failures.

The baseline for both the OB staves and the EE and HE disks is air cooling. The expected heat loads on local supports in the SVT are listed in Table 3.27. In addition to these loads, readout boards like the sector/FPC interface and control boards will contribute about 1.4 kW to the SVT internal heat load, which will not be cooled by air-flow but by a dedicated liquid cooling system, which could be expanded to support the air-flow cooling where needed. The SVT power will be interlocked to turn off in the case of failure of its cooling system.

Table 3.27: SVT cooling power requirements.

Layer/disk	Nominal power [W]	Max power [W]
L0	30	37
L1	40	50
L2	101	124
L3	706	1037
L4	2199	3377
Disks	5051	7345
Total cooling power [kW]	8.12	11.97

Subsystem mechanics and integration: The SVT IB, OB, and disks are supported by their own support structure. The outermost components of this structure are carbon composite half-cylinders, which jointly form the experiment's so-called inner support tube. The inner support tube surrounds the entire SVT and spans its entire length. Cones inside the inner support tube connect the OB to the IB and to the innermost disks. These cones are supported from the inner support tube and are projective to the nominal collision point. They are currently designed to consist of spokes. The outermost disks connect to the inner support tube. This entire SVT support structure, shown schematically in fig. 3.66, is integrated in and supported off the experiment's global support tube. All SVT structures split on a horizontal plane containing the beam pipe. During integration the two halves of the SVT will be clam-shelled around the beam pipe before insertion of the SVT into ePIC. The up-down split allows for symmetric construction of the two halves.

The IB layers will be made of two symmetric half-cylinders, which will be the basic assembly elements of the detector. The two innermost layers (L0 and L1) will be based on four MOSAIX sensors (two for each half-layer), while the outermost layer (L2) will contain eight MOSAIX sensors (four for each half-layer). The MOSAIX sensors for L0, L1, L2 will be three, four and five segments wide, respectively. All the sensors equipping a given half-layer will be placed one next to the other to fully cover the half-layer surface and bent on a cylindrical shape at the corresponding radius (c.f.

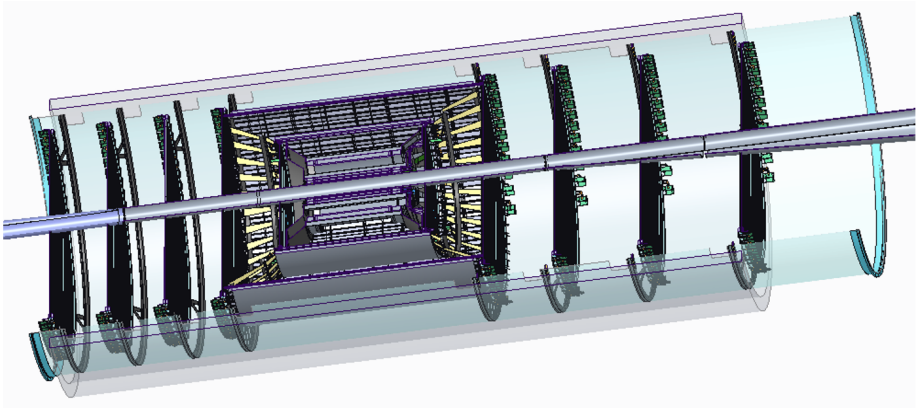

Figure 3.66: SVT global support structure, consisting of a surrounding carbon composite support tube and a projective arrangement of spokes that form cones connecting the IB, OB, and innermost disks. Also shown are several outer disks and the beampipe.

table 3.23).

Each IB half-layer will consist of the following components: the MOSAIX sensors, a local support structure mainly made in carbon foam shaped as a frame along the edges of the sensors, and two sets of FPCs wire-bonded to the sensor peripheries for powering and data/control transmission. The sensors will be cooled by air-flow delivered through appropriate ducts that will be part of the local support structure and matched to the global mechanics described below.

The IB global support will be the main structure supporting the MOSAIX sensors already assembled in half-barrels. The current design foresees a cylindrical frame structure for each layer, supported by two conical endcaps, one for L0-L1 and a second for L2, the last including a flange for connection to the L0-L1 half-cone and to the OB. structure will be made of carbon fiber composite with a thickness of approximately 0.5 mm. A half-cylindrical shell made of polyamide is placed outside and close to L2 for mechanical stability in the current design. Electrical services for the IB are brought in/out from the hadron-going side and are routed along the inner surface of the conical support. In the current design the routing of the power cables to the REC uses the longerons of the local mechanics as cable trays. The required rigidity and the geometry for the cable routing suggests carbon fiber composite as a preferred material choice for the longerons, while alternatives are being considered. Figure 3.67 shows CAD representations of the IB support.

For the OB, EE, and HE, we use a modular design approach to simplify the assembly process of these complex detector elements, reduce risks and increase the predictability of the production rate. EIC-LAS sensors and AncASICs will be assembled into modules, that will be pre-assembled and -tested and then mounted in the final staves or disks. The EIC-LAS sensors and AncASICs will be connected via flexible printed circuits and micro-electronics interconnection techniques to form electrical units. The disks will be supported by a mechanical frame to be interfaced with cooling systems and to meet handling requirements.

The design of a module for the outer barrel envisions two EIC-LAS with their respective two AncASIC (see figure 3.68), supported by a mechanical frame made of a thin film of polyimide that holds together all the module components. The design of a module for the disks envisages one LAS and one AncASIC and a mechanical frame made of a carbon fiber plate. We will test modules standalone after their assembly and before their assembly into staves or disks.

The outer barrel layers will be segmented in staves. The staves are composite structures using

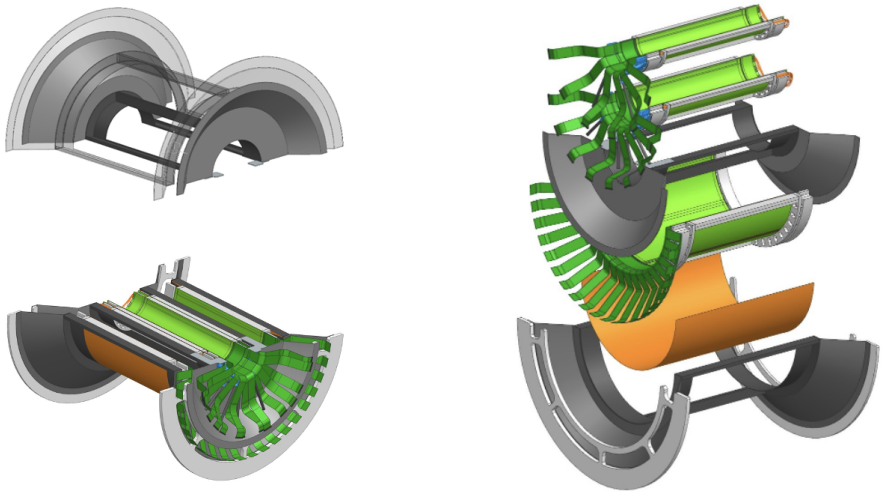

Figure 3.67: Left: CAD representation of the IB global support (top) and IB half-barrel CAD view with sensors and cable routing (bottom). Right: Exploded CAD view of IB. The sensors are shown in light green and cables in dark green. The orange element is the kapton shield. Air conveyors are shown in blue.

carbon fiber (CF) skins, a central CF I-beam spar and cross-ribs made of Lockheed Martin K9 foam. The side walls will be formed by the FPCs. The structure has openings where modules will be placed. During module mounting the modules are glued on top of these openings, forming a closed hollow structure with large second moment of area, and thus high stiffness. The closed structure provides a contained channel for the forced flow of air through the stave, that will remove the heat from the sensors and ancillary ASICs. In addition to their structural function, the cross-ribs made of highly thermally-conductive K9 foam are placed underneath high-power density components (the left endcap of the EIC-LAS and the AncASIC) to improve the transfer of the heat into the air coolant flow. Drawings of the stave design with all its components are shown in figure 3.68.

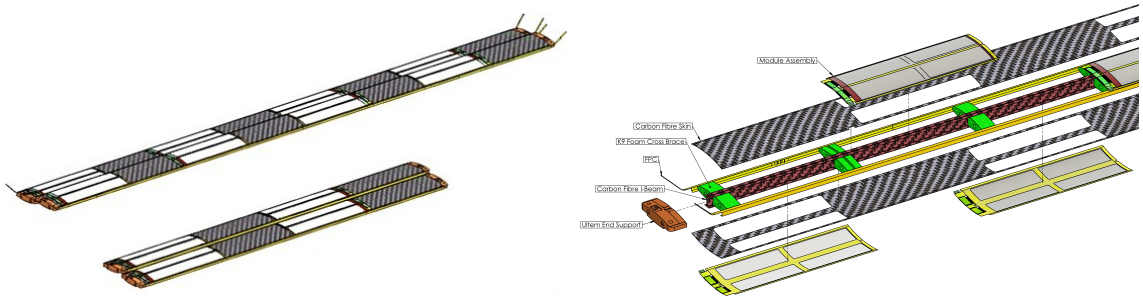

Figure 3.68: Left: OB staves for L3 and L4. Two staves per layer are shown. Right: Exploded view of an OB stave.

Each stave is one OB module (i.e. two EIC-LAS) wide, and has modules on both facings, staggered in z so that the active areas of the modules provide overlap for tracks from the vertex. L4 staves will hold 4 modules on each facing, or 8 modules in total, while L3 staves will have half that number. The dimensions of the staves are dictated by the layout of the SVT and we achieve the required coverage with LAS made up of 6 RSUs in L3 and 5 RSUs in L4, respectively. L3 will consist of two

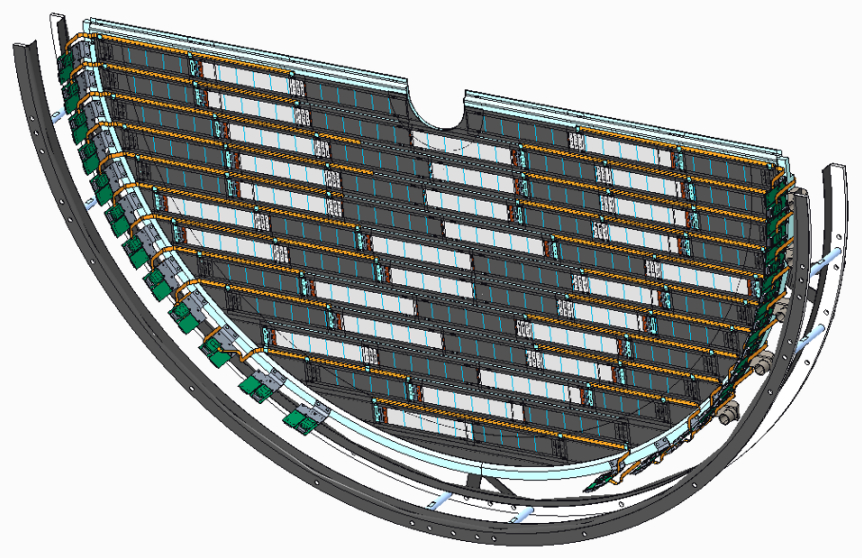

Figure 3.69: CAD model of the preliminary (half-) disk design. Modules are shown in alternatingly inward (dark gray) and outward (white) facing orientations. Common bus FPCs are shown in orange. RDOs (green) are arranged on the outside of the disk ring, inside of the interface to the SVT global support structure.

halves with 44 staves in total in a castellated layout to cover the full azimuth. L4 will consist of two halves and have 70 staves. Our initial FEA analysis of the modal frequencies finds $f_1 = 91.6$ Hz for an L4 stave.

The staves will connect mechanically at their ends to segmented half-cones that are part of the SVT support structure. This interface still needs to be detailed, but will constrain stave rotations at the support, while allowing for limited misalignment of the support cones and thermal expansion of components. The interface will also contain the couplings of the air channel inputs to the supply distribution. The cones interface at their outer radius with a support tube surrounding the entire SVT, including its services, and also connect to the the global support structure of the IB and the innermost disks.

The EE and HE disks utilize a two-sided design featuring a corrugated carbon composite core, as illustrated by the CAD model in Figure 3.69. The corrugation increases structural strength without significantly adding mass, while also creating channels that can facilitate airflow for disk cooling. Preliminary FEA analysis of the modal frequencies indicates that the first mode exceeds 100 Hz ($f_1 > 100$ Hz), demonstrating adequate mechanical stiffness in the current design iteration.

Modules – each comprising one EIC-LAS, a bridge FPC, and an AncASIC, supported by a carbon fiber flat sheet backing – will be tiled over the valleys of the corrugation on both sides of the disk. This arrangement creates overlap along the long axis of the sensor. Furthermore, the modules will be installed in an alternating inward- and outward-facing orientation along the corrugation, ensuring that the active area of one sensor covers the insensitive LEC region of its neighbor.

Each disk will have a ring at the outer radius that will sandwich the corrugated core to provide mechanical support, a mounting point for the RDOs, and an inlet for air cooling. Those rings will then connect mechanically to either the SVT support cone (ED0-1, HD0-1) or support cylinder (ED2-4, HD2-4). This design is currently being optimized in conjunction with the global mechanics.

Calibration, alignment and monitoring: Calibration procedures are needed to optimize the settings for the pixels in the MOSAIX and EIC-LAS sensors. We anticipate these to be similar to those used for the existing ITS2 sensor (i.e ALPIDE), and ITS3 sensor prototypes, consisting of data-taking scans involving charge injection into groups of pixels with varying settings. We have made initial estimates of the time required to perform such scans and anticipate that they can be done in a parallel fashion with the final readout system in approximately half an hour.

Alignment procedures are needed to achieve the required position reconstruction. We will survey the IB (half-) layers, the OB staves, and the EE and HE disks with precision coordinate measuring machines during their construction and will pursue a global survey during installation. For the determination of sense element positions used in the reconstruction of tracks from SVT data we will use track-based (software) alignment algorithms.

Regular online performance checks will include monitoring of sensor settings and other slow-control data, including temperatures, as well as analysis in near-realtime of residuals in alignment and other observables.

Status and remaining design effort:

R&D effort: The development of the MOSAIX sensor is well underway. Two submissions have already taken place in 2020 and 2022. The former, so called MLR1, included numerous test structures for technology exploration and to develop prototype circuit blocks for future sensors. The latter, ER1, contained exploratory designs to study stitching principles, methodology and yield. The submission of the MOSAIX sensors (ER2) aiming to satisfy ITS3 requirements took place in Summer 2025. ePIC designers are integrated in the MOSAIX design team and contributing to the development of logic libraries, and circuitry for data transmission over the full sensor length between RSUs. The final submission (ER3) will be the MOSAIX production version for the ITS3 detector and the ePIC SVT IB.

Work on the EIC-LAS has started in terms of defining the required modifications (reduction of size and data links). Design work will start once the design database is available upon signature of the necessary CERN-EIC agreement.

The AncASIC is in development with good progress on all functional blocks. The design of the first NVG prototype is completed both at schematics and layout level. The SLDO prototype schematic is ready and simulated, and work on the layout is ongoing. Parts of the slow control block relating to the communication with the lpGBT are begin designed, with the interface to the EIC-LAS to be defined once the MOSAIX slow control interface is completed. MPW runs are foreseen to prototype and verify each block, before submitting the full chip, ready for production in early 2027.

E&D status and outlook – IB: We have developed a preliminary design for the two innermost (L0 and L1) half-layers of the IB and its global support mechanics. Different solutions have been explored for bending and assembly of each half-layer: connecting two sensors in a single object and following a "half-layer" based procedure has been considered largely preferable mainly due to advantages from overlaps with the ITS3 building concept. Once the two half-layers have been individually built, they are assembled in a L0-L1 half-barrel. Blank silicon pieces with dimensions corresponding to the final MOSAIX sensors have been used to advance the design of the L0-L1 assembly and will serve to build the first half-barrel prototypes. In parallel, a preliminary design of the whole SVT IB mechanics, including an external shell to L2, has been also developed and a first mock-up is being built.

We will evolve the designs for the half-barrel assembly and for the global mechanics, towards properly engineered realistic ones. The next half-barrel assembly to be built will integrate

prototypes of most of the components of the final detector and allow for thermo-mechanical studies to finalize the cooling design. Test campaigns in a climate chamber and in a wind tunnel facility for ageing and cooling studies are planned. Building of a first L2 half-layer prototype, based on the guidance from the L0-L1 assembly experience, is also scheduled to happen in parallel.

For the SVT IB global mechanics, we will use carbon fiber composites as the main material for the support, given the low mass and excellent mechanical properties. In the coming months an engineered version is planned, with the goal of both verifying possible space conflicts within the global mechanics and matching with the SVT IB assembly procedures.

E&D status and outlook – OB: We are currently prototyping (fig. 3.70) the curved surface stave design for L4 to evaluate the performance of the design, as well as tooling and assembly procedures. In the first phase we are prototyping the stave design with the curved facings, as this is the more challenging to construct. Interfaces to the support cones will be designed in parallel with the design work on these structures.

These prototypes will be equipped with mechanical dummy sensors (40 μm unpatterned silicon) for mechanical studies, and thermo-mechanical dummy sensors (40 μm silicon encapsulated in 25 μm and 50 μm thick Kapton layers with a 5 μm thick Cu trace layer). In particular, we will verify/measure: Manufacturability (co-cure), mechanical integrity and good compaction of carbon fiber; Mechanical response spectrum up to 500 Hz and associated Q values; Deformations with air flow up to 20 m/s; Surface temperatures with thermo-mechanical dummy sensors powered up to 50 W per stave; Thermo-mechanical deformations with thermo-mechanical dummy sensors powered up to 50 W per stave. The results from these studies will guide us in finalizing the stave design. In the first phase we are pro-

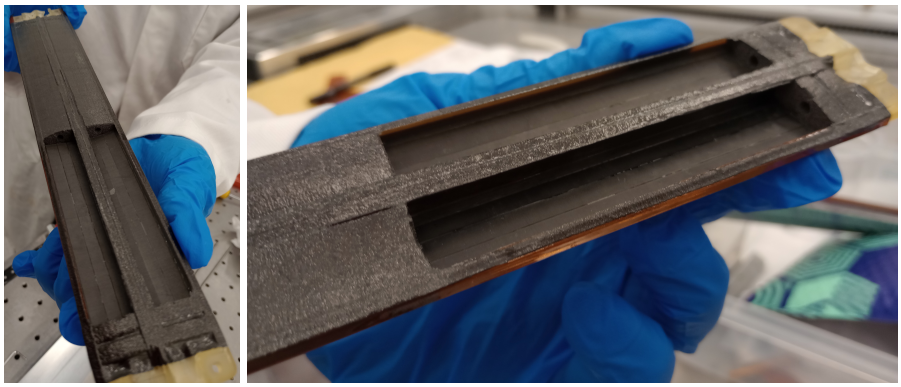

Figure 3.70: Co-cured support structure of first L4 quarter length stave prototype (without silicon sensors). The co-cure comprises carbon fibre skins, K9 cross ribs, central carbon fibre I beam spar and Kapton side closeouts (compare to fig. 3.68).

totyping the stave design with the curved facings, as this is the more challenging to construct. Interfaces to the support cones will be designed in parallel with the design work on these structures.

E&D status and outlook – Disks: Work continues on the design and layout of the disks. We are finalizing the carbon fiber layouts for both the corrugated core and the flat module sheets. The first prototype was made using a non-woven, randomly oriented mat of thin carbon fiber called carbon fiber veil for both the face sheets and corrugation and had a density of 500 gsm. However, the veil is not ideal for thermal performance and can be challenging to lay up on the corrugated tooling. New test pieces have been made with K13C2U unidirectional carbon

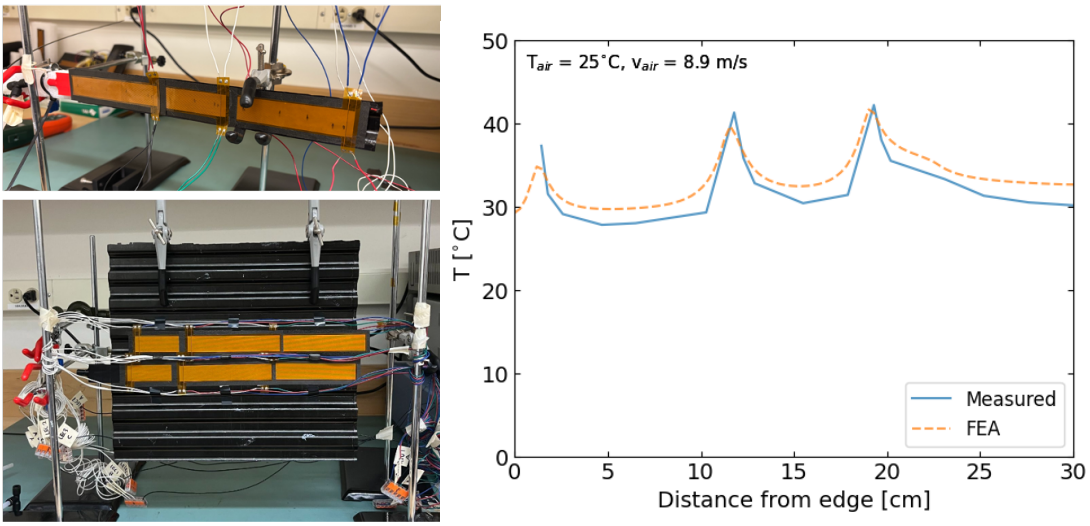

Figure 3.71: Left: Test pieces created with carbon composite corrugated disk core made in the LBNL composite shop. Heaters with two different heating zones that can mimic the sensor power density are placed on a carbon composite facesheet and then glued to the corrugation. Right: Temperature along the corrugation at various distances from the air inlet. The blue curve shows the measured temperatures of the single corrugation test piece on the top left. The orange dashed line is the FEA calculation for the same air temperature and velocity.

fiber pre-preg, which has a much improved thermal conductivity. Corrugated panels and flat sheets are made with three layers of the K13C2U pre-preg to ensure enough strength and counteract any twisting.

The K13C2U test pieces were evaluated for thermal performance using copper trace heaters. Two of these test pieces are shown on the left side of Figure 3.71, while the thermal test measurements and corresponding FEA results with the heaters are displayed on the right. The temperature peaks correspond to regions of the heater that simulate the LEC, which has the highest power density. The measured data show good agreement with the FEA calculations. The maximum temperature observed is slightly above the 40°C limit specified for the RSUs. However, since the tests were conducted with room temperature air flow, we anticipate that the maximum temperature will decrease approximately linearly with lower air temperatures.

We are currently working on engineering test articles focused on the development of assembly tooling, module handling, and thermal and mechanical performance. Vibration tests will be performed to understand mechanical stability. Mechanical dummy silicon (40 μm unpatterned silicon) is in hand to construct a quarter disk mechanical prototype. We expect thermo-mechanical dummies (as described above for the OB staves) at the end of 2025 to create a thermo-mechanical test article.

The bench tests will be paired with ANSYS structural and fluent simulations to understand the performance under air flow and the structural integrity of the disk. This will also need to be accompanied by bench tests and simulations that include the disk support ring and the outer ring.

E&D status and outlook – FPCs: The first iteration of FPC prototypes is underway targeting an initial design for OB L4. A definition stage captured the current design requirements for powering, data transmission and geometrical factors. This was followed by a design stage

and then by an order submission to RPE LTU (Ukraine). The first set of articles (Figure 3.72) are currently undergoing tests. In parallel, prototypes from Omni Circuit Board (Canada) are being evaluated and a third supplier, Q-Flex Inc. (USA), has been approached to procure low level prototypes. The aim is to evaluate the capabilities of three different suppliers to manufacture FPCs with aluminum conductors. Signal and power integrity of the FPCs will be tested and the performance over samples of different suppliers compared. A key requirement is signal attenuation for the high speed differential transmission lines (10 Gb/s). Wire bonding and single point Tape Automated Bonding (spTAB) are being evaluated as potential interconnection techniques in ongoing and future articles.

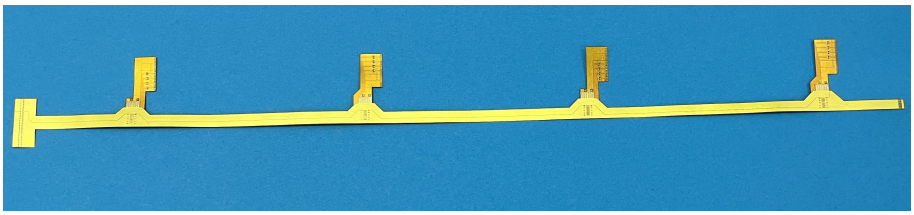

Figure 3.72: An example of a low technology readiness level prototype for the FPC of the OB L4. Prototype made by RPE LTU. The figure shows the main FPC with four bridge FPCs.

E&D status and outlook – Powering: The need to regulate voltages for the MOSAIX sensors as close to the IB (to minimize losses) dictates the need for a(t least one) powering board. Considerations for the design and development of these boards are ongoing; this includes deciding how many regulation stages give the best balance between power losses (fewer stages is likely to mean longer lengths of the most lossy cables, when delivering low voltage and high current), versus additional material in the detector volume (more stages equals more high material powering board, and the final voltage regulation is likely closer to the active area of the IB).

Conceptual powering schemes were developed and used to define specifications for the AncASIC and FPC designs for the OB and Disks. Requirements are being iterated based on limitations introduced by these designs so that they can be iteratively improved. Testing and confirmation of requirements will occur as prototypes become available; this includes:

- Verifying output voltages and current capacity of the individual SLDOs.
- Verifying output voltages of NVGs.
- Daisy-chaining AncASICs to verify serial powering chain performance.
- Quantifying performance of the FPCs in terms of current carrying capacity and voltage-drop along the conductor lengths.
- Combining the above elements to test full serial powering chain engineering articles (1 FPC feeding current to 4 AncASICs, each connected to a load mimicking EIC-LAS current consumption.).

E&D status and outlook – Powering: The need to regulate voltages for the MOSAIX sensors as close to the IB (to minimise losses) dictates the need for one or more types of powering board. Considerations for the design and development of these boards are ongoing; this includes deciding how many regulation stages give the best balance between power losses (fewer stages is likely to mean longer lengths of the most lossy cables, when delivering low voltage and high current), versus additional material in the detector volume (more stages equals more high material powering board, and the final voltage regulation is likely closer to the active area of the IB).

The design of the serial powering scheme is evolving alongside the AncASIC and FPC designs for the staves and disks, to define length of serial powering chain, the data and slow control transmission schemes.Testing and confirmation of requirements will occur as prototypes become available. This includes:

- Verifying output voltages and current capacity of the individual SLDO regulators.
- Verifying output voltages of the NVG.
- Daisy-chaining AncASICs to verify current flow in the powering chain.
- Quantifying performance of the FPCs in terms of current carrying capacity and voltage-drop along the conductor lengths.
- Combining the above elements to test full serial powering chain prototypes (one FPC feeding current to four AncASICs, each connected to a load mimicking the EIC-LAS current consumption).

E&D status and outlook – Readout: Work on readout electronics has mainly concentrated on testing evaluation boards of the various components being considered for SVT readout: lpGBT, VTRx+, radiation-tolerant FPGA PolarFire, optical FireFly. An initial prototype for the fiber aggregator board was discussed and is now under development using a commercial FPGA board (ZCU102) mated with the optical FireFly FMC card to provide up to 8 fiber inputs and multiple fiber outputs. The VLDB+ board from CERN (containing both lpGBT and VTRx+) was used to setup a full chain starting from a Skyworks clock generator board as a stand-in for the Global Timing Unit (GTU), a Xilinx ZCU102 board running lpGBT-FPGA firmware as a stand-in for the FELIX board, and the VLDB+ board as the RDO. A measurement of the jitter of the clock recovered by the lpGBT demonstrated adequate performance of this chain to provide a low-jitter clock to the sensors.

We are currently developing a test system for the serializer chiplet of the ER1 prototype submission in collaboration with ITS3 colleagues. This serializer is a prototype for the 10Gbps serializer to be deployed in the LEC the MOSAIX. The test system consists of an FMC card which contains the bonding pads for the serializer chiplet, as well as various drivers and connectors including the possibility to drive the high-speed signal onto a Flex-PCB to test the signal integrity over those traces. The FMC card itself will connect to a commercial Xilinx FPGA board for pattern generation and checking.

Another prototype development is the "MOSAIX Mock-up" board, consisting of an FMC daughter card which contains the various readout components (2 data VTRx+ and an lpGBT / VTRx+ combination for the slow control interfaces). It will interface to a ZCU102 board where firmware will simulate the responses to slow controls commands, while also allowing to simulate data packets to be sent over the up to 8 fiber optic lines of the 2 VTRx+ interfaces in order to develop both data acquisition protocols and slow controls interfaces of the readout electronics to the MOSAIX sensor without the need of an actual MOSAIX sensor.

E&D status and outlook – Cooling: Our prior work has shown that foam can be an important factor in the cooling and thermal performance of staves and disks. This is an integral part of the OB stave design and is being pursued as an option for under the LEC and AncASIC in the disk design. Both will be tested using thermal and thermo-mechanical dummies with upcoming prototypes.

The final air cooling system will be designed based on the overall air flow of the SVT. Current estimates put the total air volume around 1000 cfm total, which would require a pressurized system. The air will be pressurized before entering the ePIC detector volume and then regulated down to various pressures as required by the different parts of the SVT (e.g. the OB design requires air above 1 atm).

Simulations from LBNL and JLab have shown that during beam-pipe bake-out a 5 mm distance from the beam-pipe can keep the silicon below 30 °C with air flow below 10 m/s. However, air flow between the beam-pipe and L0 brings down the temperature of the beam-pipe and can affect the ability to reach the 100 °C required inside. Studies are ongoing to determine what hot gas temperature is needed to bring the beam-pipe to temperature and what effect that has on the silicon. We also plan to study if airflow only between L0 and L1 is sufficient to keep the detector below the current 30 °C requirement as this will help mitigate the effect of the air cooling on the beam-pipe itself. Simulations will be paired with thermo-elastic studies in a climate chamber that will study cycling, longevity, and assess the point of failure.

Other activity needed for the design completion: We are continuing our testing characterization of the products from the ITS3 sensor development sequence. We are currently preparing for the first tests on MOSAIX at CERN, in collaboration with ITS3, using a high-frequency wafer probe setup that we are jointly developing. Laboratory tests of thinned and diced wafers are also being planned, as well as beamtests and irradiation efforts.

The AncASIC will be manufactured in a different process than the MOSAIX and EIC-LAS sensors. We are about to receive products from two MPW submissions in this 110 nm process and are preparing its testing and validation. A third MPW submission is being readier for submission in the Fall of 2025. Test structures and the main functional modules of AncASIC, the SLDO, NVG and Slow Control, will undergo irradiation to verify their correct functioning in the expected radiation environment.

Status of maturity of the subsystem: The SVT underwent an incremental Preliminary Design Review (PDR1) in March, 2024. The maturity of the SVT is currently estimated to be at the 45% level overall, with considerable variation for different elements. The development of the EIC-LAS requires access to the MOSAIX design database, which is subject to a BNL-CERN agreement that has not been signed to date. The project identified the need for early procurement of the VTRx+ optical link module for data transmission and the lpGBT low power gigabit transceiver in the SVT readout and slow-control chain as part of potential CD-3B scope. The Final Design Review (FDR) for these elements was successfully passed in June 2024. The remaining effort, while substantial, is progressing and is anticipated to be more than 60% ready by the EIC CD-2 project phase at the end of 2025.

Environmental, Safety and Health (ES&H) aspects and Quality Assessment (QA planning: We will follow and adhere to all applicable ES&H standards during the development, construction, installation, and ultimately commissioning and operation of the SVT. Hazards include those associated with adhesives, carbon composites, flammables, wafer-probing and wire-bonding, use of radioactive sources, testbeams, and irradiation facilities, and electrical safety. Where possible, we will work across institutions to implement standardized controls and mitigation, as well as documented safety procedures.

System tests in the development phase of the SVT are integral to our quality assessment. Quality Control forms an integral part of the work breakdown structure (WBS) and schedule during construction and assembly.

Construction and assembly planning: The L0-L1 half-barrels will be manufactured in Italy by INFN: the current plan is to have a main assembly site in Bari and a second one in Padova currently being equipped. The L2 production half-layers will be built in the US. Both construction activities will rely on a first step fo QC of the sensors through wafer probing. They will also include a final

QC step of the corresponding complete assembly: this will include operation with air-cooling to verify thermal performance and testing of readout and control lines. After a successful pass of the QC step, L0-L1 half-barrels and L2 half-layer will be shipped to BNL. The global IB mechanics will be produced by INFN in Padova, undergo a QC step based on a metrological survey and finally be shipped to BNL. At BNL the L0-L1 half-barrels and L2 half-layers will be assembled to the global mechanics to form complete IB half-barrels. All the connections to services (powering, cooling and readout) will be put in place to allow a final QC step.

Modules and staves for the OB layers will be manufactured in the UK. Currently we plan to manufacture modules at two sites, Birmingham and Daresbury Lab. This production includes electrical bonding of the sensors and ancillary ASICs to the bridge FPC. Module construction concludes with a QC on the completed module before shipping to the stave loading sites. Stave production, which comprises manufacture of the stave composite structures, and gluing of modules onto the structures and electrical bonding of the bridge FPCs to the main FPCs, will be performed at Oxford and RAL. Again, the final step of the stave construction will be a QC of the completed stave. This will comprise operation with internal air cooling to verify thermal performance, operation of control lines and readout of modules. After successful pass of these QC steps, staves will be shipped individually to BNL. At BNL staves will be mounted on the support half-cones from the inside, starting with the outermost layer L4. This involves mechanical connection, connection of the air supply, and mounting of FPCs with their RDO boards on the support cones, and mounting of the RDOs on the outside of the support cones. After the mounting of the L4 staves they will be tested, and after that the same procedures will be repeated for the inner OB layer, L3.

Disks and their modules will be produced and assembled in the US. LBNL, Purdue, and LANL are expected to be disk assembly sites, with LBNL and Purdue also serving as module assembly sites. Assembly of modules includes gluing of sensors to carbon composite structures, as well as electrical connection (wire or tab bonding) to bridge FPCs and the AncASIC. Modules will undergo QC before being assembled onto disk structures. The corrugated carbon composite disk structures and module flat sheets will be produced at LBNL and shipped to LANL and Purdue. Disk support rings will be produced by an outside vendor, validated at LBNL, then shipped to disk assembly sites. Disks will be assembled in halves, first on one side and then the other. Disk assembly includes gluing modules and common bus FPCs onto the front and rear sides of the disks and making electrical connections. QC is planned for each corrugated row assembly and then again after completion of the front and rear sides of each disk. Disks will be shipped in halves to BNL, where they will be installed into the larger SVT assembly. Disks are the last piece to be installed, after the IB and OB. Installation will occur from the inner disks outward. ED0 and HD0 will be mounted to the SVT support cones. ED2–4 and HD2–4 will be mounted to the support cylinder. ED1 and HD1 could be mounted to either and will be iterated with global mechanics. Installation must include the connection of the services, connection of the air supply, and mounting of the RDOs. Each half disk will be tested after installation.

The IB, OB, and disks can thus be constructed concurrently. We plan to produce the outer global support structures at Purdue and/or LBNL. Readout will be led by ORNL with testing at multiple sites. The construction of the SVT can be completed in three to four years in a technically driven schedule.

Collaborators and their role, resources and workforce: The SVT currently has collaborators at 20 institutions with the main institutional roles and resources outlined above.

Risks and mitigation strategy: The SVT depends crucially on its sensors, the ITS3 sensor used in the IB and the ITS3-based EIC-LAS used in the OB, EE, and HE, since they form the only known way to meet the full performance requirements within ePIC. Their development is ongoing and thus presents a risk. The project and institutions involved in the SVT have identified one main branchpoint, related to the possibility that the EIC-LAS development is delayed and becomes incompatible with the overall EIC project schedule. If this branchpoint were triggered, the SVT OB will be replaced with two MPGD barrel layers derived from the outer MPGD tracker, specifically its innermost (micromegas) layer. The SVT EE and HE will in this case each be replaced with in total up to seven near-identical MPGD disks, specifically based on the existing uRWELL disks. The SVT IB remains based on the wafer-scale sensor of the ALICE-ITS3 upgrade in this case. The ALICE-ITS3 project is about to submit the second engineering run of its wafer-scale sensor and its timelines are compatible with those of the EIC project. In case of unforeseen future (sensor) delay, we will need to reprioritize ePIC efforts towards the ALICE-ITS3 sensor.

3.3.3.2 The MPGD trackers

Requirements

Requirements from physics: Micro-Pattern Gas Detector (MPGD) technologies have been chosen to complement the Si based tracking layers. MPGDs are relatively fast detectors able to provide precision space point measurements with good timing resolution, while also maintaining the overall conservative material budget that is required of the ePIC detector [22]. MPGDs will play a role in pattern recognition for central tracking system in the required pseudorapidity range of $-3.5 \leq \eta \leq 3.5$, and aid in PID reconstruction.

The EIC collider is expected to deliver collisions with bunches crossing every ∼10 ns [23], which will require the MPGD detectors to provide timing resolution of 10-20 ns to separate events from adjacent bunches. For ep collisions of 10 × 275 GeV, the DIS physics rate is expected to be around 500 kHz, while hadron and electron beam gas backgrounds rates are estimated to be 32.6 kHz and 3.17 MHz, respectively [24]. These rates are well within the rate capabilities of MPGDs. Combining the timing information from the MPGDs with information from the Si detectors will allow pattern recognition algorithms to discriminate between physics and background signals. In addition to providing hit information with good timing resolutions, the MPGDs will provide additional hit points needed for robust track reconstruction. Early simulations showed that the number of hit points used in the track reconstruction reduced from around 6 hits near $\eta = 0$, to only 3 hits at $|\eta| > 3$, due to tracks moving out of the acceptance of some of the Si layers. The ePIC endcap gaseous trackers, (µRWELL-ECT) were implemented to recover additional hits at larger η values. Figure 3.74 shows the average number of hits per event in the current ePIC tracking detector as a function of η for different momentum ranges. In this configuration the ePIC tracker measures at least 5 hits per event in the region ($|\eta| < 3.5$).
Finally, as detailed in the Yellow Report [22], the hpDIRC requires the track entering the PID volume to have good angular resolution (0.5 mrad at p = 6 GeV) in order to meet its performance requirements. This will be accomplished by providing the hpDIRC with precision hit points just before a particle enters its volume via the ePIC barrel outer tracker (µRWELL-BOT), and after it exits the hpDIRC volume via the first tracking layer of the barrel imaging calorimeter.

Requirements from Radiation Hardness: Detailed simulation on radiation dose in ePIC has been performed. Figure 3.75 shows the estimate of hadron and EM radiation doses in ePIC simula-

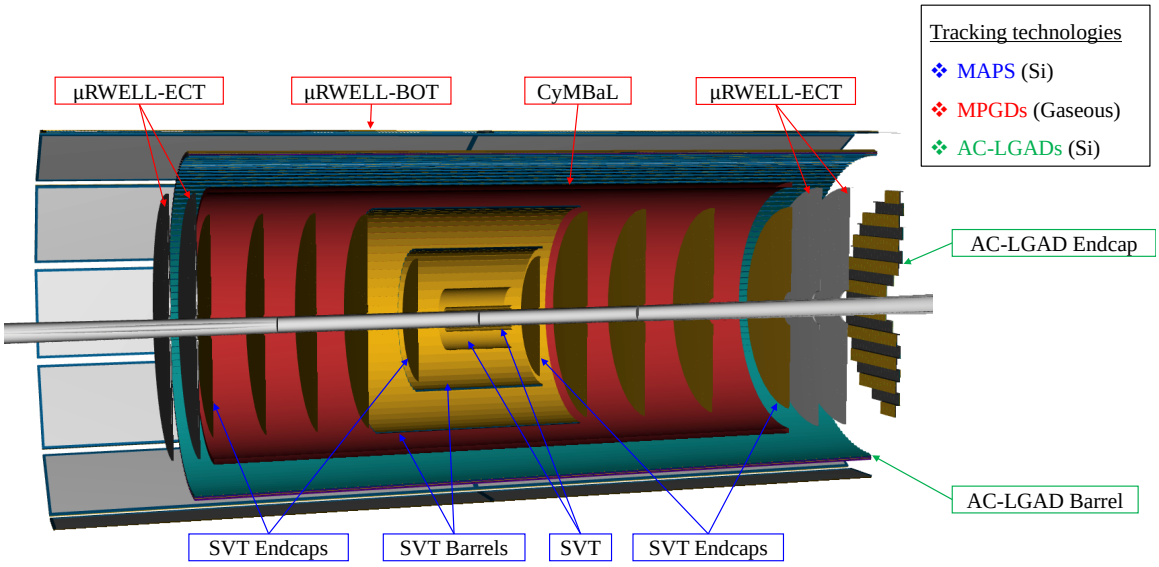

Figure 3.73: ePIC tracking subsystems.

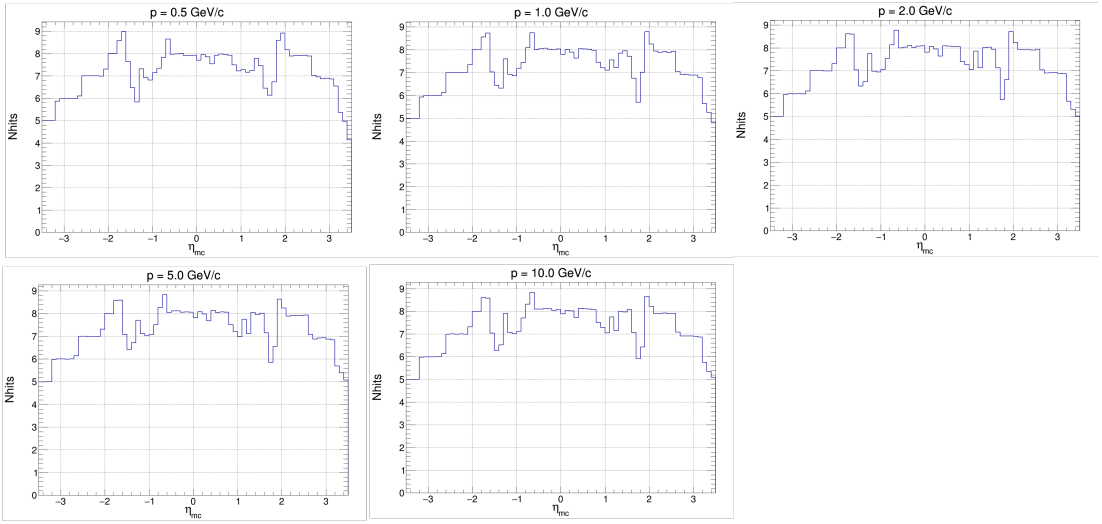

Figure 3.74: Total tracker hits vs. η for various momentum ranges (gitHub Repo).

tion along with location of MPGD layers [24]. Table 3.28 shows the maximum estimated radiation dose from various sources for MPGD trackers at various locations with 10 years of running at top machine luminosity and 100% detector and accelerator efficiency based on e+p PYTHIA simulation. The MPGD trackers in ePIC will experience low radiation dose and based on past experience with MPGD trackers in various experiments [26–28] there will be negligible aging issues. The electronics will be mounted close to the MPGD trackers, and will be based on SALSA readout ASICs. It will also require specific DC-DC converter components able to stand the ePIC radiation and magnetic field levels. Both components are described in section 8.3.10 of this document.

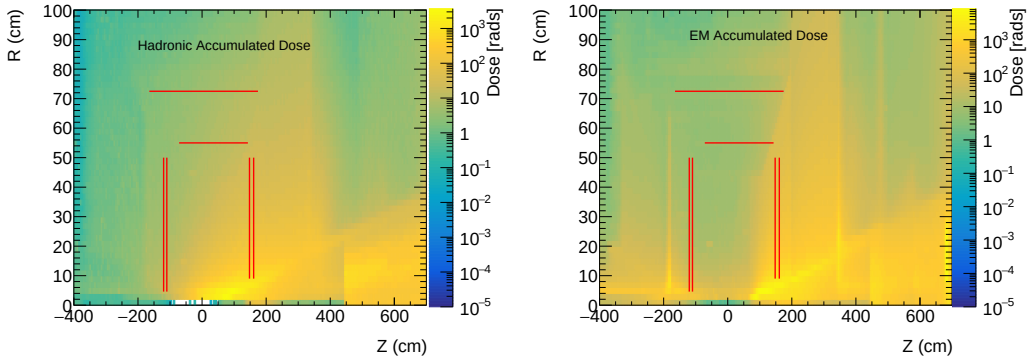

Figure 3.75: (*left*) EM radiation and (*right*) Hadron radiation dose estimate for minimum bias PYTHIA e+p events at 10x275 GeV at top machine luminosity for 6 months of running at 100% machine and detector efficiency [24]. The locations of MPGD trackers are shown by red lines [25]. (gitHub Repo).

MPGD tracker	EM Radiation dose [krad]	Hadron Radiation dose [krad]	1 MeV neutrons equivalent fluence [cm^{-2}]	1 MeV protons equivalent fluence [cm^{-2}]
CyMBaL	0.22	0.15	2.7×10^{10}	2.0×10^{10}
μRWELL-BOT	0.3	0.1	2.8×10^{10}	4.2×10^{9}
electron ECT	0.064	0.03	1.1×10^{10}	1.7×10^{9}
hadron ECT	0.87	0.23	3.0×10^{10}	8.5×10^{9}

Table 3.28: Maximum dose of radiation by different sources at MPGD tracker layers for e+p minimum-bias event at 500 kHz event rate for 10 years EIC running with 6 months run time per year and 100% efficiency [24].

Requirements from Data Rates: Table 3.29 shows hit rate per unit area for each MPGD subsystem in ePIC which is far lower than rate capability of MPGD detectors [29,30]. Table 3.30 shows the maximum hit rate experienced by a channel for various MPGD trackers in ePIC [24]. The rates are low enough for ASIC developed for MPGDs which can handle rate of 100 kHz/channel.

MPGD tracker	DIS e+p rate [Hz/cm^2]	Hadron beam gas rate [Hz/cm^2]	Electron beam gas rate [Hz/cm^2]
CyMBaL	26.37	14.33	5.5
μRWELL-BOT	9.82	5.33	1.7
electron ECT	144.68	78.63	437
hadron ECT	1326.36	720	201

Table 3.29: Hit rate per unit area of various MPGD trackers for e+p DIS events at 10×275 GeV with $1.54\times10^{34}cm^2s^{-1}$ luminosity scaled from e+p DIS events at 18×275 GeV and $1.54\times10^{33}cm^2s^{-1}$ luminosity, 10 GeV electron beam gas and 275 GeV hadron beam gas

MPGD tracker	DIS e+p events [Hz]	Hadron beam gas [Hz]	Electron beam gas [Hz]
CyMBaL	3.68	0.05	4.78
μRWELL-BOT	2.76	0.04	4.78
electron ECT	9.2	3.56	102
hadron ECT	101.2	4.39	39.88

Table 3.30: Maximum hit rate by a single channel of various MPGD trackers for e+p DIS events at 10×275 GeV with $1.54 \times 10^{34}\text{cm}^2\text{s}^{-1}$ luminosity scaled from e+p DIS events at 18×275 GeV and $1.54 \times 10^{33}\text{cm}^2\text{s}^{-1}$ luminosity, 10 GeV electron beam gas and 275 GeV hadron beam gas.

Justification The requirements cited above drives the necessity of using MPGD trackers at various locations of ePIC. MPGDs can be built over large area and their ability to handle high rates and good spatial resolution makes them excellent candidate for large trackers.

Device concept and technological choice: The MPGD trackers are based on two different technologies and are described below

CyMBaL: The role of the Cylindrical Micromegas Barrel Layer (CyMBaL) is to wrap around the SVT in its entire length to provide an additional hit point. Consequently, the main requirement is to have as little as possible acceptance gaps. In order to limit the impact on particle reconstruction in the outer detectors, CyMBaL has to be light in material budget, possibly less than $X/X_0 \sim 1\%$. CyMBaL (Figure 3.76a) is composed as a set of 32 Micromegas tiles arranged in a way to ensure full coverage in φ (8 modules) and in z (4 modules). The space envelope assigned to CyMBaL spans the range between 55 cm and 60 cm in radius and it is asymmetric in the longitudinal direction, covering the range -105 cm $< z <$ 143 cm. CyMBaL is designed in two symmetric halves that meet at $z = 19$ cm (due to the asymmetric keeping zone). In each half, the 16 modules are arranged in two cylinders, the inner one (in $|z|$) sitting at a radius of 55 cm and the outer one at 57.5 cm.
In order to limit the complexity of the detector production, the design is aiming at limiting the differences among the modules, possibly having only a single design for the module PCBs that will be assembled with different bending radii. The preliminary design of a CyMBaL module is shown in Figure 3.76b. A module is a cylindrical tile 48 cm wide (equivalent to about 50 degrees in the azimuthal direction) and 67 cm long, and the active region is about 46×59 cm^2. In the current design, the module dimensions allow for an overlap of 2.8 cm in the $r \cdot \phi$ direction and about 2 cm in z. The sensor is based on the bulk resistive Micromegas technology [31] with a 3 mm conversion gap.
The main purpose of the resistive layer (surface resistivity $1 - 10\text{M}\Omega/\square$) is to share the charge, induced by the amplification, to neighboring strips in order to improve the spatial resolution. The resistive layer will also prevent sparks in the amplification region, although the expected particle rates are low and spark limitation would not be a major concern. The signal will be readout by orthogonal strips to provide a two dimensional information of the position of the charged particle crossing the sensitive area. The strips running along the longitudinal direction (therefore called Z-strips) will provide the $r \cdot \varphi$ measurement of the hit and they will be directly routed to the connector area. The strips running along the azimuthal direction (C-strips, C for cylindrical) will provide the z information of the hit and they will need to be connected with vias to routing trails to bring the signals to the connectors. The pitch of the readout strips will be $\sim$ 1 mm and the

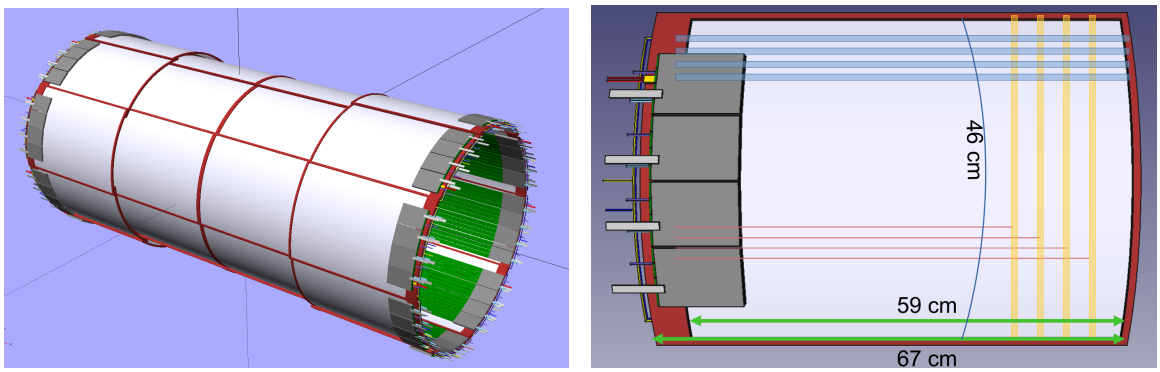

(a) (b)

Figure 3.76: [CyMBaL CAD model](a) CyMBaL CAD model showing the assembly of the 32 modules. (b)CAD model of a CyMBaL module. The light blue represents examples of readout strips measuring the $r \cdot \varphi$ coordinate (called Z-strips as they run along the z axis). The light yellow represents examples of readout strips measuring the z coordinate (called C-strips as they are arcs of a cylinder). The light red lines represent examples of trail lines to bring the C-strip signals to the FEBs. For the explanation of the services see the text.

resistive layer will allow the charges to be shared among neighboring strips for a better centroid reconstruction. The total number of strips per module will be 1024 and they will be readout by four FEBs, each one equipped with 4 × 64-channel SALSA chips. The module's frame will consists of carbon fiber hollow square beams and arcs of about 3 mm in size. Being hollow, these beams not only will provide the mechanical rigidity and support for the detector, but will be also used to distribute the gas inside the detector. As shown in Figure 3.76, the FEBs will be mounted at the two ends of CyMBaL to concentrate the material budget in just few areas. Low-mass micro-coaxial cables will be used to bring the signals from the modules to the FEBs: the inner modules will need cables of about 50 cm in length, while short (¡10cm) cables are sufficient for the outer modules. It is expected that the detector gain will be sufficiently high to overcome any noise induced by the additional capacitance of the cables.

µRWELL-BOT: ePIC MPGD Barrel Outer Tracker (µRWELL-BOT layer) is the outermost gaseous tracking layer installed in the barrel region of ePIC central tracker. The detector sits right

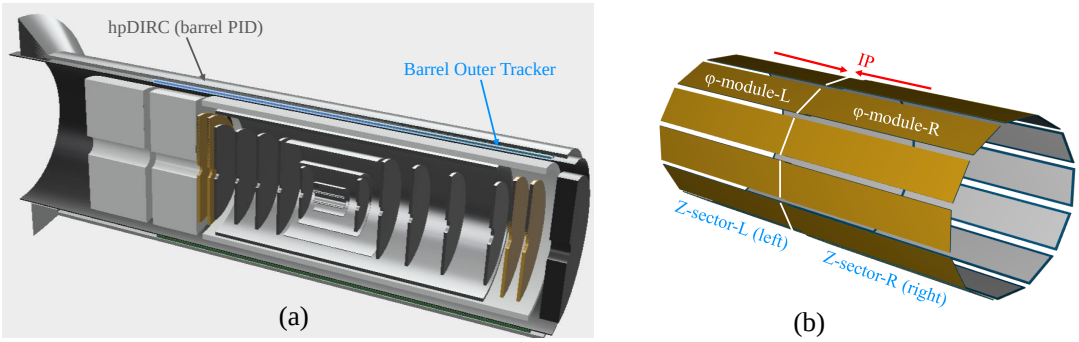

Figure 3.77: (a) µRWELL-BOT in ePIC central detector; (b) Arrangement of 24 µRWELL-BOT modules in dodecagon shape.

at a radius of 72.5 cm right in front of the high performance DIRC (hpDIRC) as shown in the layout at the top left of Figure 3.77. The tracker is split in two sectors (Z-sector) along the beam axis z. Each Z-sector is consists of 12 μRWELL-BOT rectangular modules (φ-modules) arranged in dodecagon shape to cover 2π acceptance in the azimuthal direction (φ) as shown in the top right of Figure 3.77. The μRWELL-BOT φ-modules are designed to match the hpDIRC acceptance in both z and φ as shown on the bottom right of Figure 3.77. Mechanical constraints associated to the detector support frames as well as the very limited space available for integration in the ePIC detector support frames result in an acceptance gap of ∼13% in φ and ∼1% in z. The material budget X/X_0 of the detector is ∼1.5% in the active area but will becomes significantly higher at the edges of the detector where the front end electronics cards, cables and services are be located. The design of the full size μRWELL-BOT module engineering test article shown in Figure 3.83 developed as part of the Project Engineering Design (PED) effort based on thin-gap GEM-μRWELL technology (see paragraph section 3.3.3.2 and Figure 3.84) is complete and the fabrication of the chamber is scheduled for the first half of 2025.

μRWELL-ECT: Monte Carlo simulations show that the endcap regions of the ePIC detector experience the highest backgrounds in the experiment and charged particle tracking requires several hit points in the $|\eta| > 2$ region for good pattern recognition. To optimize the ePIC baseline tracker design, two planar Micro-Pattern Gaseous Detectors (MPGD) disks, with a central hole for the beam pipe are located both in the hadronic and the leptonic sectors (see the right drawing of Figure 3.78). The ECT disks geometrical envelope is reported in Table 3.31. It takes into account the integration constraints within the ePIC detector and the beam pipes dimensions. As shown in the left drawing of Figure 3.78, the hadron and lepton beam pipes slightly diverge from the interaction point. Therefore the ECT inner radii are calculated taking into account the envelope radii and their center offset. For simplicity the inner radius if fixed by the largest of the two values calculated for the disk located at the larger z position at each endcap region. As a result the two lepton disks located closer to the interaction point, will have a smaller inner radius than the two hadron disks (4.65 cm vs 9 cm) as they are located closer to the interaction point, while the outer radii of 50 cm are equal for all the four disks and are fixed by the available volume inside the ePIC detector. The ECT disks envelope also includes the MPDG gas frames of 1.5 cm thickness, and a

MPGD Disk	Longitudinal location z (cm)	Outer Radius (cm)	Inner Radius (cm)	Outer Active Area Radius (cm)	Inner Active Area Radius (cm)
HD MPGD 2	161	50	9	45	10.5
HD MPGD 1	148	50	9	45	10.5
LD MPGD 1	-110	50	4.65	45	6
LD MPGD 2	-120	50	4.65	45	6

Table 3.31: The ECT disks geometrical envelope and active areas dimensions.

3.5 cm outer service ring, to locate services and electronics front-end boards. The resulting active area dimensions of the disks are also reported in Table 3.31 and the corresponding angular and pseudorapidity acceptances are reported in Table 3.32. The final active ranges in pseudorapidity are $2.0 < \eta < 3.3$ for the hadron sector and $-3.6 < \eta < -1.7$ for the lepton sector, constrained by the available space.

A GEM-μRWELL hybrid technology [32] with XY 2D readout, similar to the one described for the μRWELL-BOT and shown in Figure 3.84(b), has been chosen to match all the performance requirements.The main difference is related to the drift region gap, which is 3-6 mm wide to ensure an intrinsic efficiency higher than 97-98%. A 2D strip read-out COMPASS-like scheme, where the

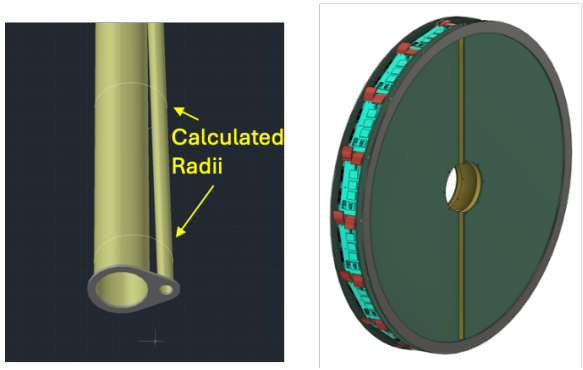

Figure 3.78: Left: Hadron and lepton beam pipes slightly diverge from the interaction point. The ECT inner radii are calculated taking into account the envelope radii and their center offset, the hadron beampipe forming a larger angle with the z axis. Right: layout of a couple of μRWELL-ECT disks.

MPGD Disk	$\lvert\theta\rvert$ min (deg)	$\lvert\theta\rvert$ max (deg)	$\lvert\eta\rvert$ min	$\lvert\eta\rvert$ max
HD MPGD 2	3.7	15.5	2.0	3.4
HD MPGD 1	4.0	16.9	1.9	3.3
LD MPGD 1	3.1	22.1	1.6	3.6
LD MPGD 2	2.8	20.4	1.7	3.7

Table 3.32: The ECT disks angular and pseudorapidity acceptance.

charge is collected by XY orthogonal strips located on two different printed circuit board (PCB) layers, has been chosen. The strip widths of the two coordinates must be optimized (in a ratio of about 1:3) to balance the signal amplitude in the two dimensions, since the upper layer strips screen the charge collected on the lower ones.

The XY Cartesian readout scheme was preferred over the Rφ geometry for two reasons: i) the high radial strip density at the center hole and ii) the possibility offered by the XY geometry to route all the strips to connectors located on the outer service ring. The cathode and the 2D readout PCB are supported by a 3 mm thick honeycomb structure to minimize the detector material budget, which amounts to $0.85\% X/X_0$ in the active region.

Front End Electronics (FEE): To meet the requirement of streaming readout new front-end chips for MPGD trackers in ePIC are being developed by Sao Paulo Universities and CEA Saclay IRFU. The SALSA chip, which associates an analog front-end adapted to MPGD detectors, an ADC per channel with a 50MS/s digitization rate on 12 bits, and a data processing unit, has the following characteristics:

- 64 channels with large input capacitance range (up to 1 nF), optimized for 50-200 pF.
- Large range of peaking times: 50-500 ns.
- Large gain ranges: 0-50 to 0-5000 fC.
- Large range of input rates, up to 100 kHz/ch.

- Reversible polarity.

Other components. The **gas mixing unit** will be a critical component of the MPGD trackers. The mixing unit preferably will use Mass Flow Controllers based on Proportional-Integral-Derivative (PID) control systems. Furthermore, the mixing unit should be able to mix either two or three different inert gases depending on the final composition of the operating gas. The preferred mixture for CyMBaL is Ar-isobutane (95:5) see Figure 3.82, however if concern is raised for flammability of this gas mixture then a three gas mixing unit will provide the possibility of adding a third gas (preferably CO_2) at the expense of isobutane. This will help in maintaining stability by operating the detector at lower voltage (due to the isobutane component), make the gas faster and non-flammable (due to the CO_2) component. Additionally **sensors** will be installed to monitor the temperature, pressure and humidity close to MPGD modules and if possible also to monitor temperature of incoming and outgoing gas to give an idea of heating of gas volume inside detector itself. The High Voltage Power Supplies (HVPS) are another important component for MPGD trackers to bias the detector. The preferred way of biasing each module of MPGD tracker is by using voltage divider. The HVPS will have low ripple (< 5 mVpp) to reduce noise from HVPS along with the capability of monitoring current drawn by the detector.

Performance The MPGD tracking detectors share 2D spatial resolutions performances better $\simeq$ 150 μm, timing resolutions of the order of $10 - 20$ ns, rate capability better than 10 kHz/cm^2, and detectors response not impacted by temperature instabilities, which may be compensated in the calibration procedures. The radiation hardness of the components material will sustain the doses reported in Table 3.28. The specific performances of each MPGD subsystem are reported in the following.

CyMBaL: The CyMBaL design aims at providing complete azimuth (φ) coverage. Along the longitudinal direction where the two halves of the system meet, only $\sim$3 cm will not be covered. CyMBaL modules are expected to provide a hit spatial resolution around 150 μm with a time resolution of $10 - 20$ ns. The modules are expected to operate with efficiencies above 95%. The magnetic field, being orthogonal to the drift field, will cause the primary electrons to drift away from the electric field lines, the so called Lorentz angle. This effect could degrade the $r \cdot \phi$ resolution. To limit the Lorentz angle, the module's drift fields will be set at about 3 kV/cm and adjusted among modules to account for possible longitudinal variation of the magnetic field.

μRWELL-BOT: The barrel outer tracker will provide hit space point resolution better than 150 μm on average in the eta range of $-1 \leq \eta \leq 1$ and 100 μm in the azimuthal direction and a timing resolution of $\sim$10 ns. The tracker has an acceptance gap of 13% along φ because of space constraints imposed by the limited space in the ePIC detector. The tracker will operate at a nominal efficiency of $\sim$95%. As shown in Figures 3.29 and 3.30, the particle rate per unit area and per readout channel is very low and will not pose any challenge in term of tracking performance, safety operation and long term stability of the μRWELL-BOT trackers for the lifetime of the ePIC detector.

μRWELL-ECT: The MPGD-ECT disks are designed to provide intrinsic spatial resolution for perpendicular tracks less than 150 μm. Technological solutions and data analysis procedures exist to guarantee similar performances also for inclined or curved tracks. The active area of the detector has a material budget less than 1% in units of radiation length (X_0) and will cover all azimuthal angels in the polar region specified in Table 3.32. A time resolution in the $10 - 20$ ns range is achievable using the gas mixtures described above. A single disk efficiency of $\simeq$ 96–97%

is required to provide 92–94% combined efficiency for two disks in the same region.

Implementation:

Services: The MPGD tracking detectors subsystem are divided in different modules, each one requiring: gas supply lines and outlet, front end boards (FEB) connected to 5-line optical fibers (VTRX+) for data transfer to the RDO, low voltage lines (four lines for each FEB: one pair for the 1.8 V and one for the 3.3 V.), high voltage cables, temperature and humidity sensors and cooling in and out lines. Studies on the type of cooling and possible implementation in a serialize distribution will be done in synergy with the other subsystem of ePIC.

The service requirements for each MPGD tracking subsystem is summarized in Table 3.33.

Subsystem	**CyMBaL**	**μRWELL-BOT**	**μRWELL-ECT**
Number of Modules	32 Micromegas tiles	24 GEM-μRWELL φ-modules	4 GEM-μRWELL disks
Gas supply lines per module	1 in / 1 out	1 in / 1 out	8 in / 8 out
Number of FEB per module	4	14	32
Low voltage lines per module	16	56	128
High voltage lines per module	2	1 (or 4)	16
Cooling lines per module	1 in / 1 out	1 in / 1 out	4 in / 4 out
VTRX+ lines per module	4	14	32

Table 3.33: Services requirements for the three MPGD tracking subsystems.

Subsystem mechanics and integration: CyMBaL integration and mechanics rely on the central tracker global support structures. CyMBaL modules will be connected to the support structure. For μRWELL-BOT, the support structure connecting the carbon fiber tube and EM-Cal will serve as μRWELL-BOT and HP-DIRC support structure whereas for μRWELL-ECT, the outer ring of each disk hosts all the services listed in Table 3.33. The FEB are mounted perpendicularly to the disks.

Because of the divergence of the beam pipes, the disks cannot longitudinally slide along them but need to be shaped in sectors to be mounted around the pipes. Moreover, as the width of the Cu-kapton foil base material for the MPGD detectors restricts one dimension to about 550 mm, an implementation of the endcap trackers would consist of two half-circular disks with "D-shaped" cut-outs for the beam pipe, eventually sub segmented in four quadrants. As sketched in Figure 3.79, the disks integration and mechanics rely on the central tracker global support structures, using the same layout of the Silicon trackers. The MPGD-ECT disk are the most outer elements in the endcap region and the last to be installed in the mounting scheme of the tracking system.

Calibration, alignment and monitoring: The three MPGD subsystems will generally follow similar calibration, alignment and monitoring procedures. There are two main calibration tasks that have been identified. The first is to determine the optimal HV settings for the MPGDs, which will be determined through efficiency scans. These scans will be performed prior to data taking campaigns and after changes in running conditions (e.g. changes in gas composition). The second

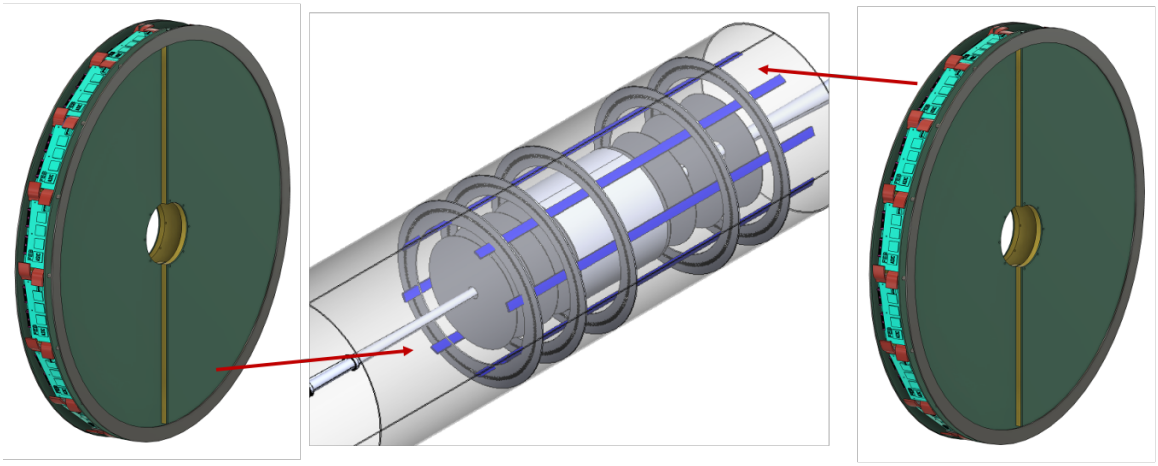

Figure 3.79: Integration of the MPGD-ECT disks in the ePIC detector.

calibration task is to determine pedestal values and the common noise to be subtracted from the ADC samples, which will be determined through dedicated calibration runs. To meet the overall ePIC tracking performance precise knowledge of the tracking detector positions will need to be known. The alignment of the MPGD modules will be surveyed and entered into a database before integration. This information will be used to establish a starting point for the software alignment, which will be based on track reconstruction with and without magnetic field applied and will involve all of the ePIC tracking detectors. To assure that the MPGD detectors are performing optimally there are several criteria that will be monitored, which include the gas composition, the environmental conditions near the MPGDs (e.g. temperature, humidity and pressure), currents drawn by the MPGD layers from the power supply and general detector performance. Changes in the environmental conditions can be addressed by adjusting the detector gain via a feedback loop. The currents drawn by each high voltage channel will be read out and logged with a frequency of about 1 Hz. Additionally, we will need to monitor and log the low voltage currents and FEB temperatures. Not only will this allow us to monitor for abnormal values, but also implement automatic safety measures should a particular value fall outside of an acceptable range. Finally, during data taking we will monitor basic detector performance parameters such as hit occupancy maps, 2D efficiency, signal amplitude and timing distributions will be constantly monitored.

Status and remaining design effort: R&D and PED

CyMBaL: The resistive Micromegas technology has been extensively used in nuclear and particle physics experiments. In particular, 1D-readout cylindrical Micromegas tiles are in use at JLab in the Barrel Micromegas Tracker (BMT) of the CLAS12 experiment since 2017 [33], in experimental conditions which are more challenging than those expected at the EIC. The main focus of the ongoing R&D is to upgrade the BMT technology to 2D readout. In order to limit the number or readout channels, the R&D also focus on exploiting the charge sharing through the resistive layer and using $\sim$1 mm pitch readout strips. Several combinations of strip readout patterns together with layers of different resistivity have been tested in a beam test in MAMI in 2023. Further studies are ongoing with the cosmic rays test bench in Saclay and an additional beam test at CERN is planned for 2025. The design of a CyMBaL module prototype has begun and its production and tests are expected to be completed in 2026.

µRWELL-BOT: The R&D phase for the development of the µRWELL-based trackers for EIC detector was completed in summer 2023 and transitioned into project engineering design (PED) effort. The goal for PED effort is to develop a full size thin-gap GEM-µRWELL engineering test article as a beta version of pre-production φ-module of µRWELL-BOT tracker in ePIC detector. The design effort including the CAD drawings of all mechanical parts that is frames and support structures as well as the sensitive devices such as the GEM foil, the µRWELL and the U-V strip readout PCB is in advanced stage and expected to be completed by the end of 2024. The fabrication of the full size engineering test article will take place during the first half of 2025. The second half of the year 2025 will be dedicated to a full characterization of the prototype on a cosmic test bench setup and in beam at the CERN NA H4 beam test area including test in its 1.5 T GOLIATH magnet to study the performance of the detector in a magnetic field strength similar to the one expected from the ePIC magnet. The PED effort to develop the µRWELL-BOT module including a detailed review of the design choices and options, the timeline and outlook for the completion of the engineering test article effort.

µRWELL-ECT: Disk design and modules segmentation is undergoing. The choice of the connectors will have in impact on the final strip pitch and the total number of read-out channels for each disk: usage of Hirose connectors (140 pins for 126 channels) would limit the maximum number of connectors and read-out channels if compared with obsolete Panasonic ones. Segmentation of the disks in four quadrants may avoid the use of a support structure for the GEM foil. A final decision on the final layout will be based on the results of prototype testing. Figure 3.80 shows some design details under investigation.

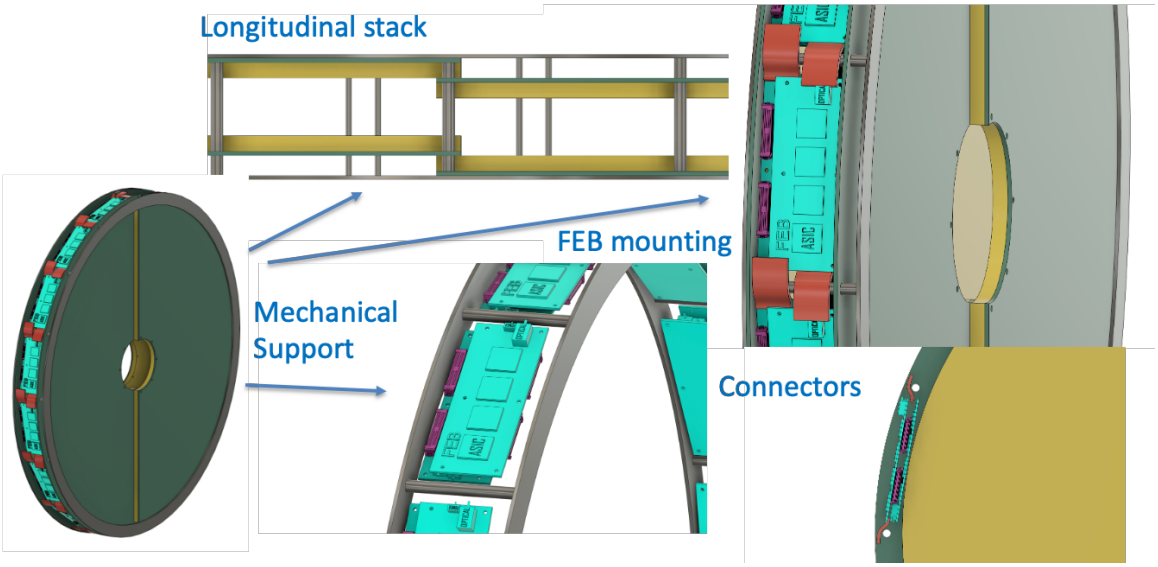

Figure 3.80: Design details of MPGD-ECT disks

Environmental, Safety and Health (ES&H) aspects and Quality Assessment: Considering MPGD consortium is composed of international collaboration so each production site for module assembly will follow guidelines of their local government to be in compliance with ES&H requirements. This include minimizing wastes during assembly procedure and disposal of harmful wastes in safe manner as directed by local government along with general electric and mechanical safety. During final integration of the detector subsystem at BNL , scientists and technicians will

follow DOE guidelines as directed by BNL ES&H department.
The Quality Assessment protocol will cover the entire production lane of MPGD detectors. The readout PCBs will be assessed for mechanical precision and electrical continuity. The resistive layers will be checked for uniformity. During each step of the assembling, electrical continuity and high voltage capability of the different electrodes will be tested. Once the assembly of the module is finished, the module is checked for gas leakage and HV stability before bringing it outside of the clean rooms. Each finished detector will be then tested with cosmic rays in dedicated test benches. In these tests, the main parameters that will be studied for each module are the noise levels and the number of dead channels, efficiency and effective gain uniformity over the detector active area . A database will be used to log all the information and results for each produced module.

Construction and assembly planning. Each of the MPGD detectors share a similar construction, assembly and QA timeline for having the detectors arrive at BNL in late 2029. This general timeline is shown in Figure 3.81.
The construction and assembly of the MPGD subsystems will take place at various places. CEA-Saclay will be the main production site for CyMBaL modules, while the readout PCBs will be produced by industry partners. At Saclay, all the remaining parts of the production process will be realized. The resistive layer will be added using serigraphy and the low-tension micromesh will be added using the bulk process [34], which will be performed in the Saclay MPGD Lab. The curving and mechanical integration of the final detector will be done in a dedicated clean room.
CERN will serve as the primary source for μRWELL and GEM foils, as well as the readout PCBs for the μRWELL-BOT and μRWELL-ECT detectors. Other components, such as the frames, will be produced by industry partners. The production sites of the μRWELL-BOT subsystem are Jefferson Lab, Florida Institute of Technology and University of Virginia whereas INFN and Temple University will be in charge of the μRWELL-ECT subsystem.

A set of technical documents will be developed for each MPGD sub-detector, ensuring that all modules are produced under consistent conditions, using appropriate infrastructure, and following standardized procedures for construction and quality control testing. Each production site will procure and inspect the components separately. It is crucial that all production sites are equipped with suitable clean room infrastructure for the construction and assembly of their respective μRWELL modules, as well as identical instrumentation for a standardized component inspection and module characterization. Each of the institutes will be responsible for the construction and characterization of their respective μRWELL modules (+ spares). The equipment needed for each subsystem will listed in in appendix before the next draft. Each institution will leverage its existing MPGD infrastructure (clean room and detector lab and existing equipment) to minimize instrumentation costs but will upgrade where needed to meet the more demanding requirement of μRWELL technology assembly.

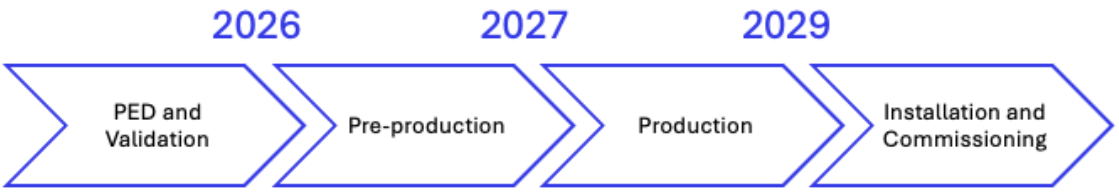

Figure 3.81: General overview ePIC MPGD tracker construction and assembly timeline.

Collaborators and their role, resources and workforce :

CyMBaL: Design, production and tests will be lead by CEA Saclay.The details of the workforce, role and resources for each subsystem will be added in appendix before the next draft.

μRWELL-BOT: Jefferson Lab, Florida Institute of Technology, and the University of Virginia will participate in the construction, assembly, and characterization of μRWELL-BOT φ-modules to ensure timely mass production. Each of the three institutes will be responsible for the construction and characterization of eight μRWELL-BOT φ-modules (+. The essential equipment needed for each institute are listed in Tab. 3.35. Wherever possible, existing equipment from the collaborating groups will be utilized to minimize instrumentation costs. They will collaborate to develop a set of technical documents, ensuring that all modules are produced under consistent conditions, using appropriate infrastructure, and following standardized procedures for construction and quality control testing. All components of a μRWELL-BOT φ-module will be designed by Jefferson Lab, however, each production site will procure and inspect the components separately. It is crucial that all three production sites are equipped with suitable clean room infrastructure for the construction and assembly of μRWELL-BOT φ-modules, as well as identical instrumentation for a standardized component inspection and module characterization. Each of the three institutes will be responsible for the construction and characterization of eight μRWELL-BOT φ-modules (+ spares). The essential equipment needed for each institute are listed in Table 3.35. Each institution will leverage on its existing MPGD infrastructure (clean room and detector lab and existing equipment) to minimize instrumentation costs but will upgrade wherever possible to meet the more demanding requirement of μRWELL technology assembly. The personnel effort, expressed as a percentage of research time over the duration of the project, at each institute is provided in Tables 3.36, 3.37, 3.38.

μRWELL-ECT: Temple University and INFN Roma Tor Vergata — will participate in the design, production, assembly, and characterization of μRWELL-ECT disks, with the engineering support from Jefferson Lab and the collaboration of INFN LNF MPGD group lead by Gianni Bencivenni, inventor of the μ-RWELL technology. INFN Roma Tor Vergata will focus on the two hadron disks while Temple University will be in charge of the lepton disks. Each of the two institutes will be responsible for the construction and characterization of 4-8 μRWELL-ECT modules, depending on final design. The essential equipment needed for each institute are listed in Table 3.34. Wherever possible, existing equipment from the collaborating groups will be utilized to minimize instrumentation costs.

Risks and mitigation strategy: Based on past experiences with MPGD technology following risks and mitigation strategies are identified.

- Delay in production of MPGD foils at CERN is the biggest risk. Considering this it has been decided to place procurement request well in advance to provide enough time to procure the MPGD foils. Additionally there is possibility of using additional person power and also prepare additional set up for assembling each module in each assembly sites so that at least 2 modules are assembled at the same time.
- Minor risk of higher humidity content within the MPGD modules is possible however it can be mitigated by flowing gas at higher rate.
- It is possible that the gain provided by any of the MPGD module after installation in experimental hall is lower than what has been estimated during QA. This can be mitigated either by increasing the content of primary ionized gas in gas mixture or increasing the high voltage on MPGD electrodes without affecting detector stability.

Additional Material:

Gas choice: MPGDs will preferably operate with a mixture of argon-isobutane 95:5. This choice is being driven by two factors. On the one hand, MPGDs will operate in a solenoidal magnetic field of up to 2 T, while the drift electric field will be in the radial direction. This induces a Lorentz force on the primary electrons moving them in the azimuthal direction. In order to limit the effective angle of the resulting drift velocity with respect the electric field, one should aim at using a gas mixture that has a low electron drift velocity. A comparison of the Lorentz angle versus the drift

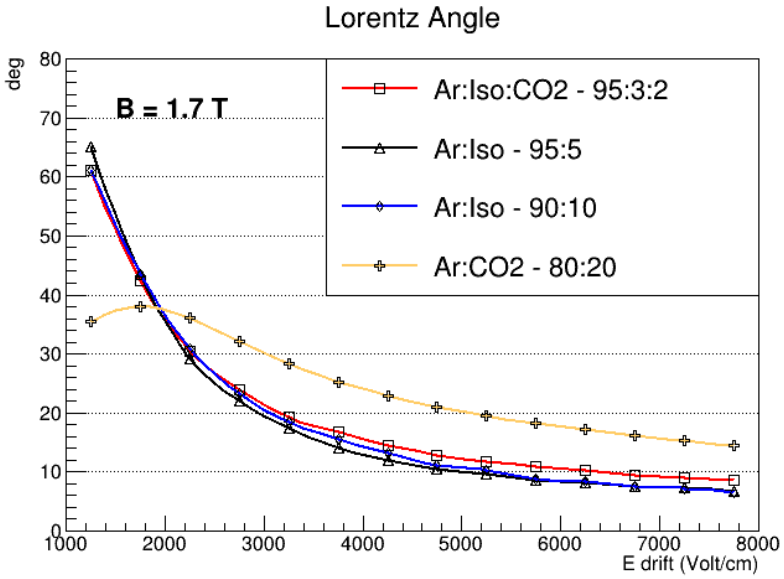

Figure 3.82: Comparison of the Lorentz angle as a function of the drift field for several gas mixtures. This study was done using Magboltz in Garfield++ [35].

filed among several argon based gas mixtures, commonly used in MPGD applications, is shown in Figure 3.82. One can see that in a 1.7 T magnetic field, an with drift voltages higher than 3 kV / cm, the Lorentz angle for Ar:Isobutane 95:5 mixture is lower than 20 degrees. On the other hand, the gas mixture must provide enough gain to ensure a good signal-over-noise ratio. Gases with a high fraction of argon ensure enough primary electrons and achieve high gains.

μRWELL-BOT φ-module design: is a large rectangular MPGD detector based on the thin-gap GEM-μRWELL hybrid detector concept described in detail in 3.84. The detector has an active area of 1700 mm $\times$ 330 mm and an overall dimension of 1815 mm $\times$ 360 mm and a thickness of 2 cm including the on-detector front end electronic boards (FEB cards) and cables and services. The thin-gap concept, defined by smaller drift gap of $\sim$1 mm in the drift region of the detector, combined with the double amplification with GEM and μRWELL structures and the proper choice of gas mixture guarantees a high performance the detector in all aspects satisfying the main requirement of the ePIC tracker such as a detector efficiency above 95%, a timing resolution better than 10 ns and space point resolution better than 150 μm on average in the pseudorapidity range of $-1 \leq \eta \leq 1$.

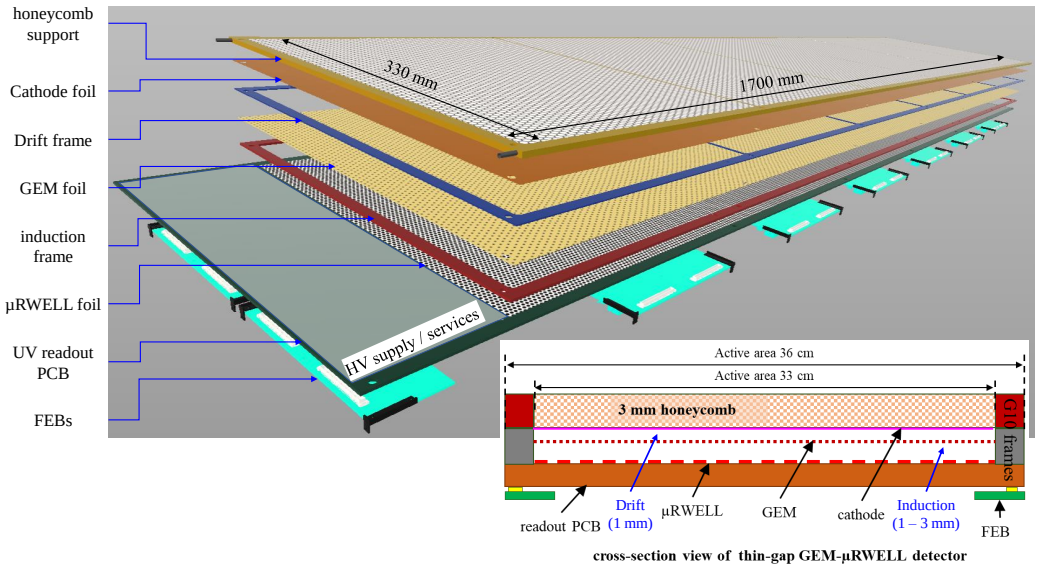

Figure 3.83: Exploded 3D view of the CAD design of the μRWELL-BOT φ-module with a breakdown of its essential sensitive items. *Bottom right:* Cross section view of the detector.

Thin-gap GEM-μRWELL hybrid detectors: Thin-gap GEM-μRWELL hybrid technology [36] was developed to satisfy the requirements of MPGD in term of space point and timing resolutions as well as detection efficiency above 95% and stable operation condition in the full angular acceptance of the ePIC detector. Three distinctive features are implemented in a thin-gap MPGD detector:

1. **Thin gap drift:** The basic idea of a thin-gap MPGD is to minimize the thickness of gas volume in the ionization region between the cathode and the first amplification stage of detector from the 3 mm typically used in a standard MPGD to ∼1 mm gap as shown on the two cartoons (a) and (b) of Figure 3.84). A smaller gas volume reduce the length of the ionization trail left by the particles traversing the detector at large angle. This, subsequently minimize the impact on the degradation of the spatial resolution.

2. **Hybrid amplification:** To recover from the smaller total charge produced in the ionization region due to the smaller gap, a higher gain from the amplification layer is needed. An optimal way to achieve large gain is to use a two-stage amplification with hybrid MPGD structures composed of a GEM foil used as pre-amplification and the μRWELL layer for the second amplification. A second advantage with the hybrid amplification is the flexibility to safely operate the detector at large gain.

3. **2D capacitive-sharing strip readout:** Capacitive-sharing readout structure is critical for thin-gap MPGDs to achieve required spatial resolution performance. Performance of μRWELL detector implementing capacitive-sharing 2D-strip readout is described in detail in [37]. For thin-gap μRWELL-GEM hybrid detector, without capacitive-sharing structure, smaller strip segmentation (with pitch $\leq$200 μm) would be required to achieve the the required spatial resolution. One can achieve same level of spatial resolution with larger pitch $\geq$1 mm) capacitive-sharing strip readout and therefore reducing the number of electronics channel by more than a factor 5. This represents a significant cost saving and reduction of the volume of cabling, services regarding the complexity of integration and maintenance for experiment.

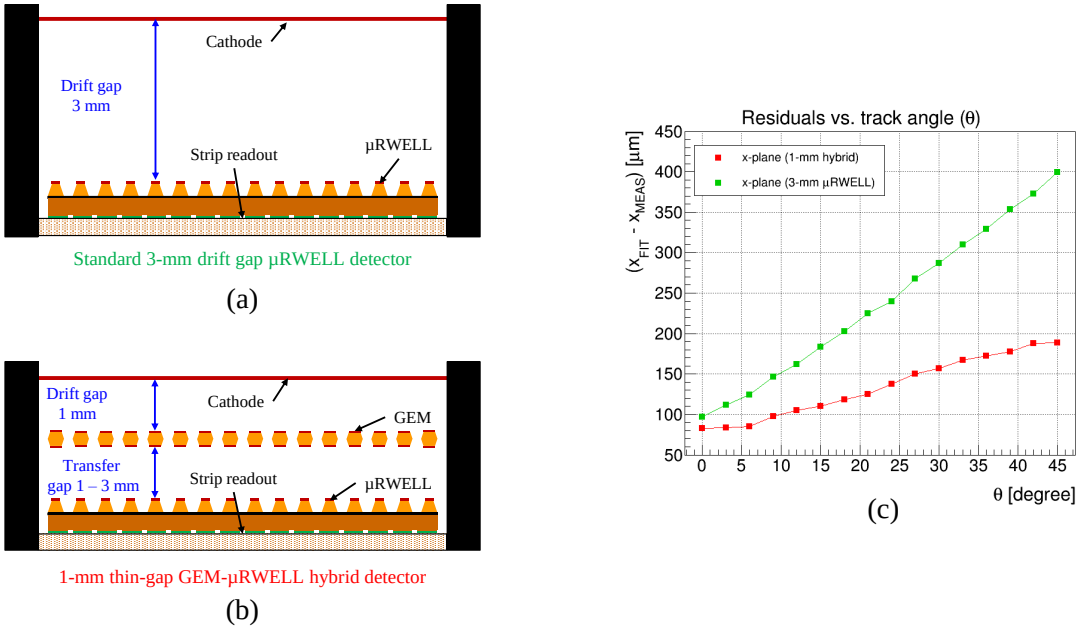

Figure 3.84: (a) Cross sectional view of a standard 3-mm gap μRWELL detector; (b) Cross sectional view of a 1-mm gap thin-gap GEM-μRWELL hybrid detector; (c) Spatial resolution as a function of the angle of impinging particle for standard gap μRWELL prototype (green) and for thin-gap GEM-μRWELL detector (red).

The plot (c) of Figure 3.84) shows some preliminary results from beam test studies of the improvement of the spatial resolution as a function of the angle of incoming particles with the thin-gap (red curve) μRWELL-GEM hybrid prototype compared to the standard gap μRWELL prototype. Detailed description of the beam test setup and additional performance results will be provided in Appendix in future version.

Table 3.34: Main equipment required in the production site and availability at sites.

Equipment	**Purpose**	**INFN Roma Tor Vergata**	**Temple University**
ISO7 cleanroom	Inspection & Assembly	y	y
Stretcher system	Construction process	y	n
Ultrasonic Cleaner	GEM frame prep	n	y
Fume hood	GEM frame prep	y	y
Microscope	GEM visual inspection	y	y
Giga-Ohm insulation meter	GEM electrical inspection	y	n
HV box	GEM electrical cleaning	y	n
Oven	Construction process	y	n
Electronic instrumentation	Module characterization	y	n
Gas supplies	Module characterization	y	n
Shipping containers	Transport b/w sites	y	n

Table 3.35: Main equipment required in the production site and availability at sites

Equipment	Purpose	JLab	UVA	FIT
ISO7 cleanroom	Inspection & Assembly	y (need upgrade)	y	y
Stretcher system	Construction process	n	y	n
Assembly system	Assembly process	n	n	n
Isonic Ultrasonic Cleaner	GEM frame prep	n	y	n
Fume hood	GEM frame prep	n	y	n
Microscope	GEM visual inspection	n	y	y
Giga-Ohm insulation meter	GEM electrical inspection	n	y	y
HV box	GEM electrical cleaning	n	n	n
Oven	Construction process	n	n	n
Electronic instrumentation	Module characterization	y (partial)	n	y
Gas supplies	Module characterization	y	n	y
Shipping containers	Transport b/w sites	n	n	n

Table 3.36: UVa Personnel Effort (%FTE)

Personel	Effort
Faculty	25%
Research Scientist	50%
Graduate Student	50%
Graduate Student	50%
Undergraduate Student	25%
Technician	50%

Table 3.37: FIT Personnel Effort (%FTE)

Personel	Effort
Faculty	20%
Graduate Student	50%
3 Undergraduates	10%
2 Technicians	100%

3.3.4 Particle Identification

In addition to tracking and calorimetry, Particle IDentification (PID) is a crucial component of the ePIC experiment's physics program. The identification of stable particles is achieved either by analyzing the way they interact, or by determining their mass measuring their velocity and momentum simultaneously. The difference in interaction is primarily used for identifying leptons, photons and

Table 3.38: JLab Personnel Effort (%FTE)

Personel	Effort
Staff scientist	50%
Staff scientist	50%
Post doc	50%
1 Technicians	100%

neutral hadrons, which leave very different signatures in the electromagnetic calorimeters. Charge hadrons cannot be distinguished by their interaction in the calorimeter, but their velocity can be measured using dedicated time-of-flight and Cherenkov detectors. All dedicated ePIC PID detectors discussed in this section measure the velocity, β, of the particle and thus allow to determine its mass. In short, they tie together $\vec{p}$, β, and m. In a second step this PID information can of course also be used in a refit of the particle's trajectory. The knowledge of the particle type and its mass does improve the multiple scattering evaluation and serve as a further constraints.

ePIC has stringent requirements on its PID capabilities as detailed in the Yellow Report [11]. The two-dimensional histogram in Fig. 3.85 illustrates the simulated yield of charged hadrons as a function of momentum and pseudorapidity, η, over the range $-5 < \eta < 5$ at the highest EIC energy of $\sqrt{s} = 141$ GeV. Studies of the key semi-inclusive and exclusive processes define the upper limit requirements for 3σ separation of $\pi/K/p$ for different pseudorapidity regions [11]:

- $p \leq 7$ GeV/c for $-3.5 < \eta < -1.0$
- $p \leq 6$ GeV/c for midrapidity $-1.0 < \eta < 1.0$
- $p \leq 50$ GeV/c for the forward region or $1.0 < \eta < 3.5$

Pure and efficient kaon identification is particularly relevant to semi-inclusive DIS studies, where quark flavor tagging provides critical insights into the transverse momentum distribution and potentially the orbital angular momentum of the strange sea quarks. Kaon identification is also needed to reconstruct charmed hadrons, which are sensitive probes of gluon distributions in protons and nuclei.

Achieving the PID goals of the ePIC experiment requires multiple detection technologies tailored to specific momentum and pseudorapidity ranges. Cherenkov radiation detection is the primary method at higher momenta but is limited in its low-momentum reach. After the Yellow Report, it was realized that improving low-momentum PID is critical for light vector meson and charm meson/baryon reconstruction. To address this, Time-of-Flight (ToF) detectors based on finely pixelated AC-LGAD sensors were added in the barrel (0.5×10 mm pixels) and forward region (0.5×0.5 mm pixels). In addition to PID they will additional hits for tracking. The η-dependence of the momentum spectrum along with space constraints necessitate different technologies in the forward, backward, and barrel regions. The solution chosen by ePIC involves:

- A dual radiator RICH (dRICH) in the forward region utilizing aerogel and gas radiators, a set of focusing mirrors, and instrumented by SiPMs.
- Additional low-momentum PID in the forward region is achieved by an AC-LGAD based ToF that also provides an additional layer of tracking points.
- A large radius high-performance DIRC (hpDIRC) in the barrel, which adds focusing to the original DIRC design.

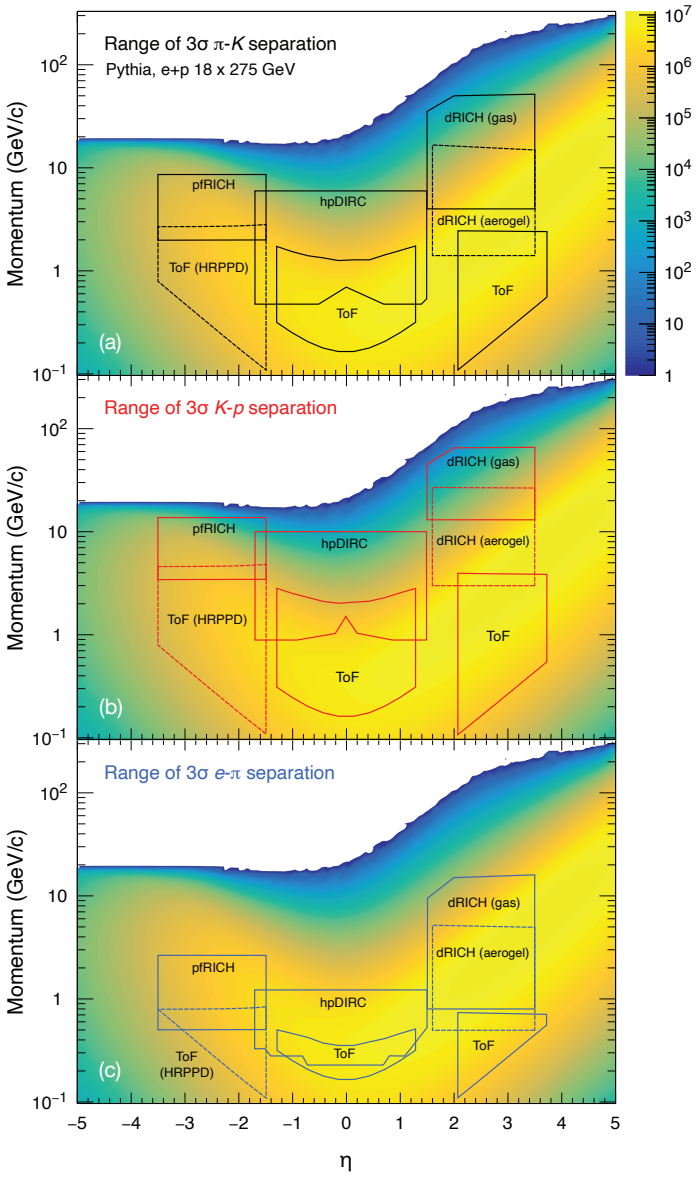

Figure 3.85: The histogram shows the relative yield of charged hadrons from Pythia simulations for 18 × 275 GeV ep collisions as a function of momenta and pseudorapidity, η. The contours indicate the 3σ separation region of the different ePIC PID subsystems for π/K (a), K/p (b), and e/π (c), respectively.

- The hpDIRC is complemented by an AC-LGAD ToF detector at smaller radius. The AC-LGAD layer provides PID information for low momentum particles that do not reach the hpDIRC or are too slow to leave Cherenkov signal in it.
- A proximity-focusing aerogel RICH (pfRICH) to cover the electron endcap region. This design features minimal material budget and provides additionally excellent ToF through its novel HRPPD photosensors.

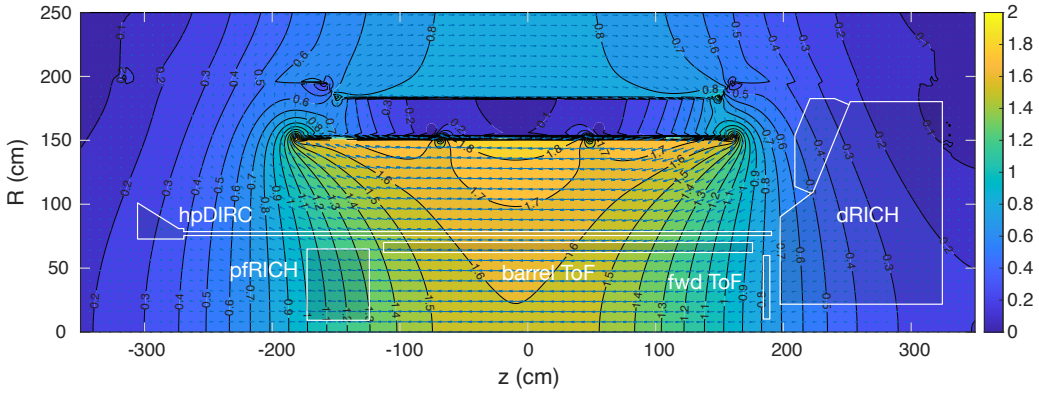

Figure 3.86: EPIC magnetic field map with the PID detector envelopes overlaid. Shown is the 1.7 T setup.

Figures 3.85 illustrates the achieved coverage in the η vs. p plane of the various PID subsystems. The contours indicate the 3σ range for e/π, π/K, and K/p-separation, respectively. This unprecedented wide coverage of PID in momentum and over a wide range of η makes ePIC a truly unique collider detector. As shown, the PID systems provide, in addition to hadron PID, a significant contribution to the e-identification and its purity (e/h). When combined with the EM calorimeters, these subsystems will provide excellent suppression of the low-momentum charged-pion backgrounds, which otherwise limit the ability of the EMCal to measure the scattered electron in kinematic reagion where it does not provide sufficient e/h separation.

ePIC's Cherenkov detectors, dRICH, pfRICH, and hpDIRC, must overcome various challenges related to their respective photosensors. One is the strong magnetic field that rules out the use of conventional photomultipliers. Figure 3.86 shows the realistic ePIC magnetic field for the 1.7 T setup with highlighted Cherenkov PID detectors envelopes. In the region of the hpDIRC detector plane, where the MCP-PMTs will be located, the magnetic field is at a level of 0.2-0.3 T. The field at position of the pfRICH HRPPD sensors is about 1.2 T and the field at the dRICH is 0.3-0.6 T.

Another significant challenge is the sensors' sensitivity to radiation, particularly in the forward region where the dRICH is located. Figure 3.87 depicts the radiation map for ePIC with the PID subsystem contours. Shown are the estimates of the 1-MeV neutron equivalent fluence and (b) the sum of electromagnetic and charged-hadron dose simulated with 10×275 GeV ep Pythia events. SiPMs, while ideal in terms of quantum efficiency and wavelength sensitivity, do suffer from increased dark currents due to radiation exposure. However, cooling during operation and thermal annealing have been demonstrated to mitigate this issue [**?**, 38]. Other photosensors used, show enough radiation hardness (HRPPD) or are situated in less radiation-intensive areas (MCP-PMT).

In the following subsection the different PID subsystems in ePIC are discussed in detail. Subsection 3.3.4.1 discusses the ToF systems, followed by 3.3.4.2 on the pfRICH, **??** describes the hpDIRC and we end with details on the dRICH system in 3.3.4.4.

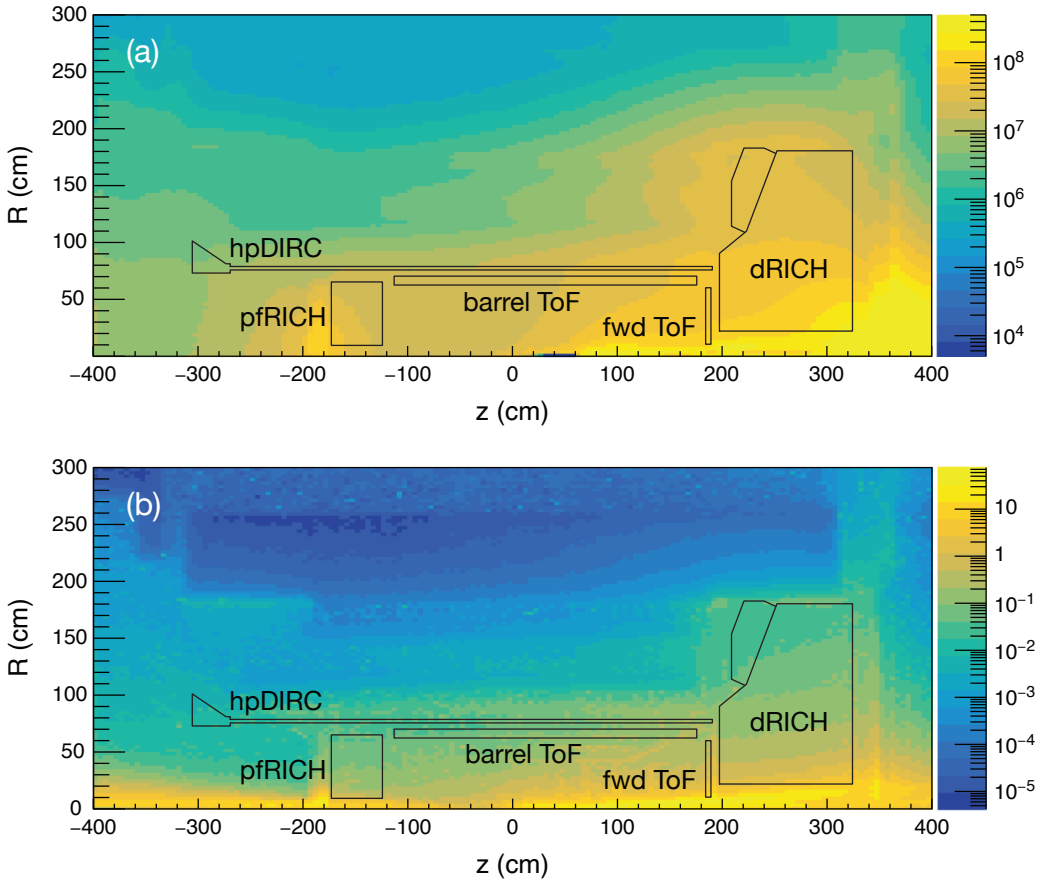

Figure 3.87: (a) Estimates of the 1-MeV neutron equivalent fluence in $\mathrm{cm}^{-2}/\mathrm{fb}^{-1}$ and (b) the sum of electromagnetic and charged-hadron doses in $\mathrm{rads}/\mathrm{fb}^{-1}$ integrated in 1 fb^{-1} equivalent Pythia events for 10×275 GeV ep collisions. The values shown are averaged over the azimuthal angle.

3.3.4.1 The time-of-flight layers

Requirements and Justifications

Requirements from physics: The ePIC detector is designed to provide charged particle identification for $e^{\pm}$, $\pi^{\pm}$, $K^{\pm}$ and $p(\bar{p})$ over a wide range of three-dimension momentum space (η and p_T). For specific physics justification, readers are referred to the physics sections; instead, specific PID requirements can be found in the overview of the particle identification preceding the present section. With a single-hit timing resolution of 35 ps from the Barrel TOF (BTOF) and 25 ps from the Forward TOF (FTOF), the AC-LGAD TOF detector system can provide particle identification for charged particles up to a few GeV. E.g., π-K separation at the 3σ level for $p_T < 1.2$ GeV/c for $-1.2 < \eta < 1.6$, and $p < 2.5$ GeV/c for $1.9 < \eta < 3.6$, respectively. By combining the PID information for low-momentum particles from the TOF detectors and high-momentum particles from the Cherenkov detectors, ePIC will have excellent PID capability over a wide momentum

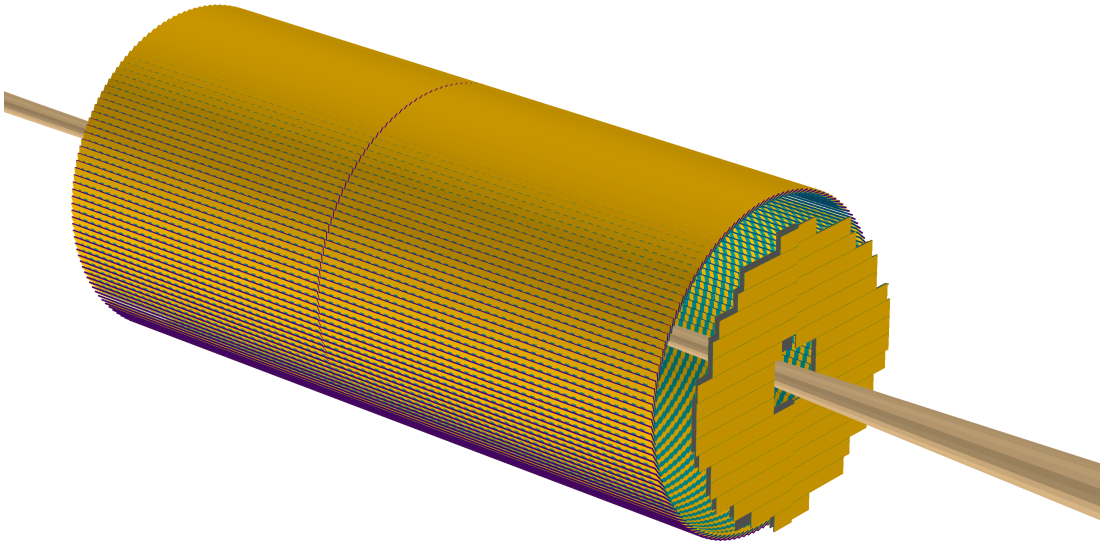

Figure 3.88: Geometries of BTOF with strip sensors and FTOF with pixel sensors.

range in a nearly 4π acceptance, which is crucial to achieving the goals of the EIC physics program. Besides precise timing resolution, AC-LGAD sensors can also provide precise spatial resolution, thus aiding track reconstruction and momentum determination. The timing and spatial resolution requirements and the material budget requirements are evaluated in the ePIC MC simulation framework to find the optimal configuration. The BTOF and FTOF layouts are shown in Fig. 3.88. Table 3.39 summarizes the current specifications of the timing and spatial resolutions, material budgets, spatial coverage, channel counts, and dimensions. Figure 3.89 shows the performance of the TOF detector in the form of $1/\beta$ as a function of particle momentum p for ep DIS events from PYTHIA+GEANT4 simulation. The TOF detector, combined with the other ePIC PID detectors, is crucial to demonstrate that ePIC's PID performance can meet the requirements.

Subsystem	Area (m^2)	dimension (mm^2)	channel count	timing σ_t (ps)	spatial σ_x (μm)	material budget (X/X_0)
Barrel TOF	12	0.5*10	2.4M	35	30 ($r \cdot \phi$)	3%
Forward TOF	1.1	0.5*0.5	3.2M	25	30 (x, y)	5%

Table 3.39: Required performance for physics and proposed configurations for the TOF detector system. The Barrel TOF consists of strip sensors with a pitch of 0.5 mm in the azimuthal direction and a length of 1 cm along the beam direction, while the Forward TOF consists of pixel sensors with a pitch of 0.5 mm.

Requirements from Radiation Hardness: The radiation fluence and dose at ePIC are significantly less than in the LHC experiments. The maximum fluence foreseen for the lifetime of the TOF detectors will be $< 5 \times 10^{12}$ n_{eq}/cm^2, as seen in Fig. 3.90 and Tab. 3.40. Here, the highest fluence between raw and 1 MeV n_{eq}/cm^2 fluence was considered, as the standard NIEL correction is not

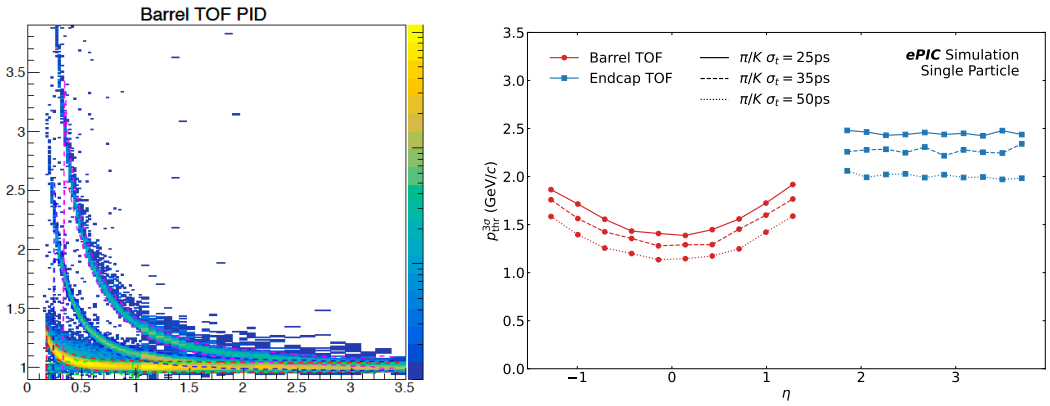

Figure 3.89: BTOF $1/\beta$ as a function of momentum (p) in the simulation performance with PYTHIA DIS events (left). Upper limits on the 3σ particle separation from BTOF and FTOF as a function of pseudorapidity (right).

applicable for some effects in AC-LGAD radiation damage.

Much work has been done to characterize and improve the radiation resistance ofAC-LGAD gain layers to meet the requirements at the LHC [39] (up to 2.5×10^{15} 1MeV n_{eq}/cm^2). Because of the sensitivity of the sensor performance to the value of the N+ sheet resistance (a feature absent from the conventional AC-LGADs used for the LHC), AC-LGADs may be significantly less radiation tolerant than their conventional cousins. Indeed, N-type doping is known to be particularly sensitive to hadronic irradiation, with N-bulk sensors inverting to P-bulk even before an exposure of 1×10^{14} is accumulated. Furthermore, LHC AC-LGAD detectors are designed to run at -30 ^{o}C to reduce the post-radiation leakage current, while in the ePIC, the sensors will be operated at room or slightly lower temperatures throughout the experiment's lifetime. The leakage current increase due to radiation damage has to be low enough to avoid thermal runaway in the system; that is, temperature increase triggers additional dark current in positive feedback. That is related to the cooling system extracting the heat of the sensor combined with the power dissipation from the readout chip. This is especially important for the far forward and endcap regions where the chips are bump-bonded on top of the sensors, and the thermal connection with the cooling system is sub-optimal.

Therefore, a radiation exposure run was performed before the ePIC AC-LGAD design was finalized. To probe the radiation effect from ionizing and non-ionizing particles, several sensors from HPK and BNL were irradiated at the FNAL ITA facility (400 MeV protons) and the TRIGA reactor in Ljubljana (MeV-scale neutrons). The radiation exposure was done in steps, allowing potential charge-collection pathologies, should they exist, to be mapped out to develop models and corrections. By studying the sensor performance before and after irradiation, the change in N+ resistivity can be characterized, and this particular risk can be addressed. Sensors irradiated with 1 MeV neutrons were received in the Summer of 2024 and subsequently tested. The results are encouraging, as seen in the following sections. Sensors irradiated at the FNAL ITA facility are still cooling down from the activation. They will likely be available for testing in early 2025.

Requirements from Data Rates: As the sensors and ASICs differ between the BTOF and FTOF, the rate requirements are presented separately for both sub-components. On top of that, the phase space coverage is different (mid-rapidity vs forward rapidity), which mandates different particle

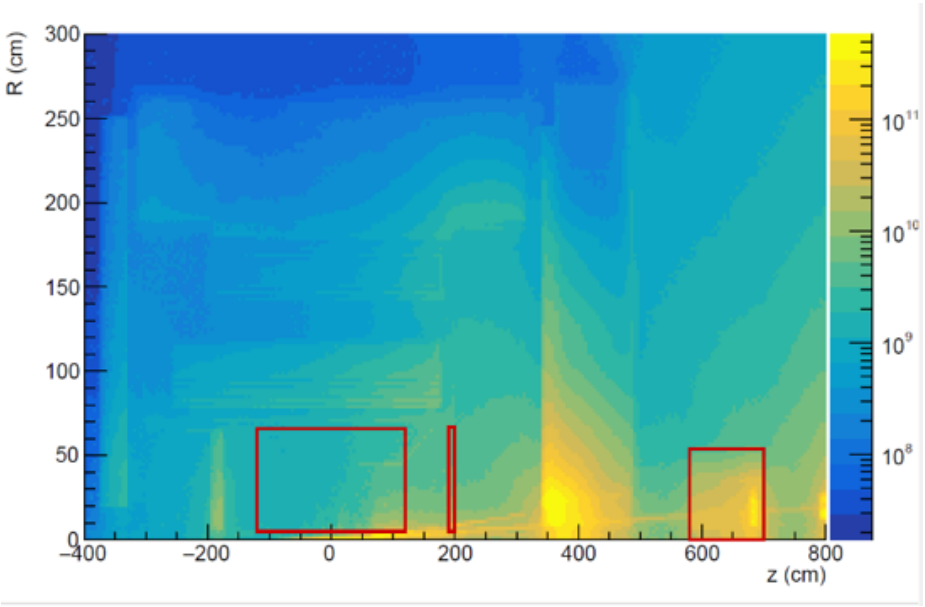

Figure 3.90: Fluence accumulated for 6 months at 100% time, corresponding to one year of data taking, the fluence has to be multiplied by the assumed 10 years of lifetime of the ePIC detector. Red squares highlight the barrel, endcap, and B0 tracker detectors. Simulation from Fluka.

RAW fluence			
System	Average	Min	Max
Barrel	5.4×10^{10}	3.4×10^{10}	5.9×10^{11}
End-cap	1.3×10^{11}	5.1×10^{10}	1.6×10^{12}
B0 trackers	3.9×10^{11}	3.3×10^{10}	1.8×10^{12}
NEQ fluence			
System	Average	Min	Max
Barrel	3.6×10^{10}	1.1×10^{10}	1.3×10^{12}
End-cap	1.2×10^{11}	3.2×10^{10}	8.4×10^{11}
B0 trackers	4.5×10^{11}	2.7×10^{10}	4.2×10^{12}

Table 3.40: RAW and NEQ fluence per system for the lifetime of the ePIC experiment, assuming 10 years of data taking at 50% time.

rates and background calculations.

BTOF: The BTOF simulations show an average of 5 charged particles per ep collision at the highest center of mass energy. At a 500 kHz collision rate, this amounts to a 2.5 MHz particle rate on the surface of the BTOF barrel. BTOF contains 2.4 million channels, which give an average hit frequency per channel of 1 Hz. Due to charge sharing of the AC-LGAD strips, a particle is expected to generate signals on a maximum of 3 strips/channels of the readout ASIC.

FTOF: The FTOF simulation shows an average of 2 charged particles per ep collision at the highest center of mass energy. At a 500 kHz collision rate, this amounts to a 1 MHz particle rate on the surface of the FTOF disk. Since FTOF is expected to contain 5.8 million channels, the average hit

frequency per channel is 0.2 Hz. Due to charge sharing of the AC-LGAD pixels, a particle hit is expected to generate signals on a maximum of 3×3 pixels/channels of the readout ASIC.

Electronics Noise: Noise measurements have consistently shown a rate of 30 Hz per channel. Such a noise rate is achieved with a 5σ cut and is deemed to be even somewhat pessimistic but is the number that is planned to be used during these calculations.

Data Rates: A typical CERN-developed ASIC's zero-suppressed data format will be assumed, which is: 32 bits header, Nx32 bits of channel data (ADC, TDC, ch Id), and 32 bits trailer. Such data formats are used in, e.g., HGCROC, which is a precursor to our expected ASICs.

For BTOF, the expected signal rate of bits per second per ASIC is 1 Hz (particle rate) $\times$ 5 $\times$ 32 (bits for 3 hits) $\times$ 64 (channels) = 10 kbps, while the noise rate is 30 Hz (noise) $\times$ 3 $\times$ 32 (bits for a single hit) $\times$ 64 (channels) = 185 kbps. Summing up these two contributions, the total data rate reaches 195 kbs per ASIC. Since an RDO reads out 128 ASICs per half stave, a rate per RDO (or fiber) of 24 Mbps is expected. For the entire BTOF, which contains 288 half staves, a total rate requirement of 7 Gbps is expected.

For FTOF, the expected signal rate of bits per second per ASIC is 0.2 Hz (particle rate) $\times$ 11 $\times$ 32 (bits for 9 hits) $\times$ 1024 (channels) = 72 kbps, while the noise rate is 30 Hz (noise rate) $\times$ 3 $\times$ 32 (bits for a single hit) $\times$ 1024 (channels) = 3000 kbps. The per-ASIC data rate arrives at 3.1 Mbps by summing up these two contributions. In the worst case of 28 ASICs per RDO (or fiber), it reaches 87 Mbs per fiber link to DAQ. In the total FTOF sub-detector of 212 RDOs, 18 Gbps is reached.

These rates are very small and well within the reach of the ASIC and interconnects, as well as the electronics and DAQ fiber interfaces. The data rates are dominated by the electronics noise, which can be controlled by raising or lowering the ASIC's various ADC or TDC thresholds, thus adjusting the system performance even ASIC-to-ASIC if required.

Subsystem description:

General device description: The BTOF consists of 144 tilted staves, each of which is made of two half staves with a total length of around 270 cm sitting at a radial position of around 65 cm. Strip sensors are mounted on low-mass Kapton flexible printed circuit boards (FPCs) and are wire-bonded with frontend ASICs. The FPCs are glued onto mechanical structures made from low-density carbon fiber (CF) materials, bringing power and input/output signals to the sensors and ASICs. The heat generated by the frontend ASICs is removed by an embedded aluminum cooling tube in the CF structure. The FTOF consists of detector modules made from pixel sensors bump-bonded with frontend ASICs. These detector modules are mounted from both sides onto a thermally conductive supporting disk with embedded liquid cooling lines located around 190 cm away from the center of the experiment. Since the irradiation flux at the EIC is much smaller than that at the LHC, it is assumed that the radiation damage will not be a concern; therefore, the sensors can be operated at room temperature.

Sensors: The sensors identified for the TOF timing layers are AC-coupled Low-Gain Avalanche Diode (AC-LGAD), a relatively new sensor technology that can provide both exceptional position resolution and timing resolution [1,40–42] while maintaining low channel density. In AC-LGADs, the signal produced by charged particles in the sensor active volume is amplified via an internal p+ gain layer near the sensor surface. The signal is induced on a continuous resistive n+ layer on top of the p+ gain layer, which is AC coupled to patterned metal readout electrodes, which are on the sensor surface and separated by a dielectric layer from the n+ layer. The internal signal amplification and thin active volume enable precise

timing measurement, while charge sharing among neighboring electrodes can provide precise position measurement. AC-LGADs will be used for TOF PID and tracking in the BTOF, FTOF, and far forward detectors.

The BTOF will employ strip sensors 1 cm long with a pitch of 500 μm and a metal electrode width of 50 μm (a larger pitch up to 1000 μm is also under investigation). The sensor thickness will likely be 50 μm to reduce the input capacitance to the preamplifiers, but 30 μm thick strip sensors are also under investigation. The full sensor size will be 3.2×2 cm^2 with 1 cm segments. The FTOF will use pixel AC-LGADs with a pitch of 500 μm and metal electrode size of 50 μm (a large pitch up to 1000 μm and electrode size of 150 μm are also under investigation). The thickness of the pixel sensors will likely be 20 μm to maximize the time resolution reach, as the input capacitance is not a concern for small pixels. Nevertheless, 30 μm thick pixel sensors are also under investigation. The full-size sensor will be 1.6×1.6 cm^2 with 0.5×0.5 mm^2 pixels. A summary of the geometry is in Tab. 3.41. Studies on smaller-scale devices are presented in [1, 40] and in the following sections. Different thicknesses and geometry were investigated in the scope of the eRD112 effort, and the best results obtained are shown in Sec 3.3.4.1. Full-size strip sensor prototypes have been produced for the first time in the most recent HPK fabrication and are received at the time of writing. Procurement of the full-size pixel sensor prototypes is still in progress. A complete evaluation of the full-size prototype sensors is expected by mid-2025.

System	Size	Type	Pitch	Ch/sensor	Thickness
Barrel	3.2x2 cm	Strips	500 μm x 1 cm	128	50 μm
End-cap	1.6x1.6 cm	Pixels	500 μm x 500 μm	1024	20 μm
B0 trackers	1.6x1.6 cm	Pixels	500 μm x 500 μm	1024	20 μm

Table 3.41: Baseline BTOF, FTOF and B0 AC-LGAD geometries.

Frontend Electronics (FEE): The FEE for AC-LGAD-based detectors is focused on the development of two different ASICs and service hybrids with performance and requirements aimed at the barrel (strips) and endcap (pixels), respectively. Different ASICs for the two subsystems are necessary since the geometry, integration method, and requirements differ between BTOF and FTOF. An ASIC featuring a Constant Fraction Discriminator (CFD) chip is being developed at Fermilab for the BTOF, focused on optimizing the analog frontend design to read out AC-LGAD strip sensors with large input capacitance. Two versions of the ASICs, FCFDv0, and FCFDv1, featuring single- and multi-channel preamplifier and CFD, respectively, have been fabricated and tested. The new versions, FCFDv1.1, with further improvement to the frontend design tailored to 1 cm AC-LGAD strip sensors, and FCFDv2, with digital readout, are under development with an expected delivery date in early 2025 and 2026, respectively.

The EICROC project by the French group is instead focused on designing an ASIC for reading finely-pixelated AC-LGAD sensors, optimized for the pixel-based AC-LGADs detectors at ePIC such as B0, OMD, Roman Pots, and FTOF. The first version, EICROC0, is a 4×4 channel ASIC with 0.5×0.5 mm^2 pixel size, featuring components like a trans-impedance preamplifier, 10-bit TDC for timing, 8-bit ADC for amplitude measurement, and an I2C slow control interface. It is designed for low capacitance and sensitivity to low charges (2 fC), operating with 1 mW per channel and targeting 30 ps timing and 30 μm spatial resolution. The prototype is currently under testing.The next version, EICROC1, expected in early 2025, will feature a 32×32 channel configuration to study power distribution; it will be followed by the final 32×32 channel version for full-scale implementation. This will be followed by EICROC2, the final 32×32 channel version, projected for full-scale implementation by the

end of 2026. EICROC2 will have a digital backend compatible with the ePIC DAQ system. Tab. 3.42 summarizes the current baseline ASICs for the different timing layers.

System	ASIC	Time Res.	Input C.	Hybridization
Barrel	FCFD	35 ps	10s pF	wire bonds
End-cap	EICROC	20 ps	100s fF	bump bonds
B0 trackers	EICROC	20 ps	100s fF	bump bonds

Table 3.42: Readout chips BTOF, FTOF and B0 AC-LGAD geometries.

The service hybrids (SH) consist of a readout board (RB) and a power board (PB). A schematic design of a service hybrid is shown in Fig. 3.91 for FTOF and serves 3 modules or 12 sensors/ASICs. The readout board aggregates data from multiple ASICs to an lpGBT (from CERN) transceiver chip via e-links. Then, it converts to optical signals via a VTRx+ chip (from CERN) to be transmitted to the backend data acquisition system. The lpGBT and VTRx+ are designed for HL-LHC and have proven to be sufficiently radiation-hard for the EIC environment. The VTRx+ has one uplink up to 10 Gbs (for receiving clock and control signals), and four downlinks (for data transmission), each up to 2.56 Gbs, and it can transmit data up to four lpGBTs. The readout board also hosts interface connectors for the module board (as described later) and the power board, as well as for input LV and HV cables. The power board provides low voltages for ASICs (1.2 V), lpGBT (1.2 V), and VTRx+ (2.5 V and 1.2 V) on the readout board from the DC-DC converters. The CERN bPOL48V module is chosen as the main converter, which takes an input of 15 V and converts it into 1.2 V and 2.5 V. As illustrated in Fig. 3.91, the RB is on top of the PB and sensor module. The PB directly contacts the cooling structure, facilitating efficient cooling of heat dissipating from the DC-DC converters. The SH has three different types with different lengths, serving 3 (12), 6 (24), and 7 (28) modules (sensor/ASICs). This will provide the most efficient coverage of a circular-shaped disk while minimizing the number of cables and fibers. The example shown in Fig. 3.91 is the shortest version (about 100 mm long) which serves 3 modules. The latest layout design for the FTOF disk is shown in Fig. 3.88 (right), where different colored boxes indicate different types of SHs. Prototyping of the SH is in an advanced stage. A pre-prototype readout board (ppRDO), based on an Xilinx FPGA chip and a commercial SFP+ optical transceiver, has been developed and is under testing. The first prototype RB and PB using the CERN chips will be under development soon and will be based on a similar existing CMS endcap timing layer (ETL) detector design.

Flexible Printed Circuit boards: A Flexible Printed Circuit (FPC) will read data and distribute power to the sensors and ASICs. A material budget of 3% X/X_0 is required in the acceptance region, meaning the FPC material should be as lightweight as possible. Additionally, the FPC must be up to 135 cm in length. To meet these stringent requirements, careful consideration of the FPC material is necessary, as signal loss is expected with such a long FPC, especially if using polyimide, a standard material in FPCs. The sPHENIX experiment encountered a similar challenge with their Inner Tracker (INTT, also a silicon sensor tracker). It successfully addressed the issue using Liquid Crystal Polymer (LCP) instead of polyimide as the dielectric material. This technology will be adopted for the TOF sub-detector as well.

BTOF stave design: Barrel staves are divided into two half-staves, with services and connections coming from the outer side. The half-staves are composed of several modules. The half-staves comprise a support structure with an integrated cooling pipe, flexible printed circuit (FPC), sensors, and ASICs. Sensors and ASICs will be mounted on both the top and bottom sides of the half-stave, making it double-sided, with enough overlap to achieve 100% coverage in the stave direction. The lateral overlap and tilting ensure 100% coverage in the

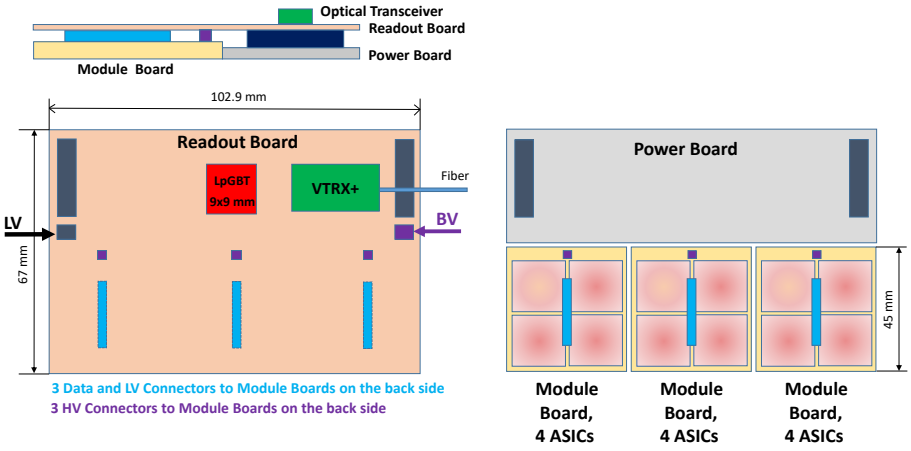

Figure 3.91: A schematic design of service hybrids for FTOF, which serves 3 modules or 12 sensors/ASICs.

direction parallel to the staves. There are 64 sensors and 64-128 ASICs on each side of the half-stave in total. The number of ASICs depends on the final design; each ASIC will serve either one sector for one sensor or one sector for two sensors.

FTOF module design: A schematic design of the module for FTOF is shown in Fig. 3.92. Each module consists of 2×2 AC-LGADs sensors and ASICs glued together. The unit is covered by a module PCB board (MB), which provides LV power (1.2 V) and transmits the data of ASICs via a board-to-board connector to the RB. In addition, the MB also has an HV connector for the RB to provide the HV to the AC-LGAD sensors. The ASIC readout will be wire-bonded to a metal pad near the edge of the module on the side facing the baseplate and cooling structure, as illustrated in Fig. 3.92 (right). The AC-LGAD sensors and ASICs will be connected via bump bonding. The dimensions shown are preliminary and will be adjusted as the prototyping progresses. In the current design, the AC-LGAD sensors are placed underneath the ASIC. The motivation is to have the sensor as close as possible to the cooling structure to ensure a lower and stable temperature, which has been proven essential for achieving optimal time resolution with a narrow range of temperature gradients. An alternative option would be to swap the ASIC and sensor layers, which has the advantage of more efficiently dissipating the heat primarily generated by the ASIC. A final choice will be made as the prototype progresses, especially after realistic thermal performance studies have been carried out.

Performance The AC-LGAD systems, including the BTOF, FTOF, and far-forward systems (Roman Pots, OMD, and B0 tracker), share a common readout chain that is currently under development. Performance evaluations are conducted in various laboratory environments as part of ongoing R&D efforts. A schematic of the full readout chain is shown in Fig. 3.93. The effort can be divided into two parts: 1) integrating the sensors with ASIC and 2) developing the readout and power boards.

The Fermilab team has been developing an ASIC targeting the AC-LGAD strip sensors for BTOF. Studies have shown that a Constant Fraction Discriminator (CFD) could provide a better timing resolution for small signal amplitudes from AC-LGAD than a leading-edge discriminator [43].

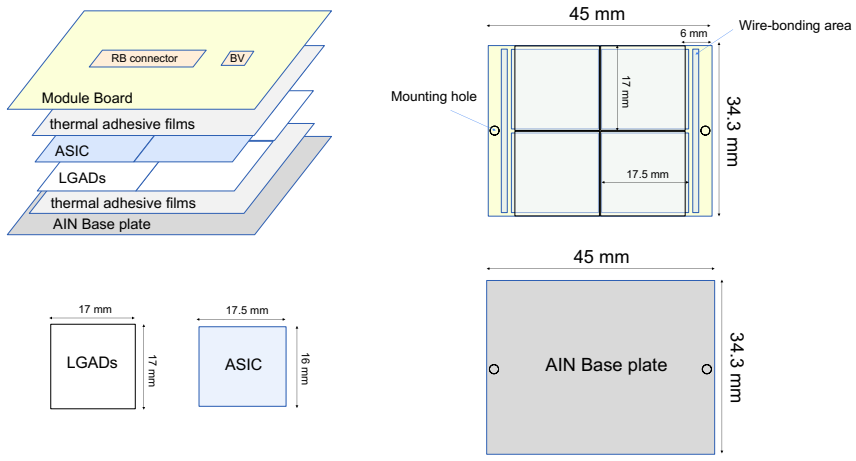

Figure 3.92: A schematic design of the module for FTOF, which consists of 2 × 2 AC-LGAD sensors and ASICs.

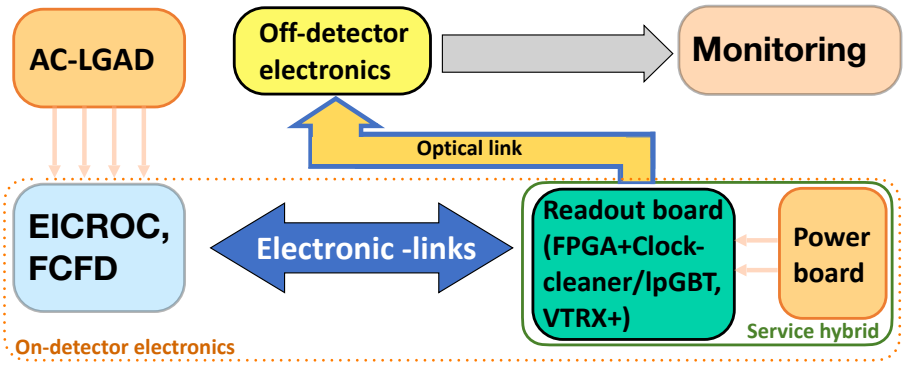

Figure 3.93: Schematic of the AC-LGAD subsystem readout chain. Each component is undergoing design, (pre-)prototyping, testing under various environments, and customization to meet the specific requirements of individual subsystems.

The first single-channel CFD-based ASIC (FCFDv0) wire-bonded to a DC-LGAD sensor achieved around 35 ps timing precision during test beams, where the dominant contribution is expected from the intrinsic resolution of the AC-LGAD sensor. A 6-channel prototype (FCFDv1) was developed for AC-LGAD sensors, demonstrating around 11 ps jitter in charge injection and around 50 ps time resolution with 0.5 cm AC-LGAD strip sensors during test beams. Ongoing efforts focus on optimizing the frontend design for 1 cm AC-LGAD strip sensors for the BTOF.

Assemblies of 4×4 AC-LGAD pixel sensors with 500 × 500 μm^2 pixelation and 30 μm thickness, and 4×4 EICROC0 ASICs, were completed by the BNL, IJCLab, OMEGA, and Hiroshima groups on test-boards developed by IJCLab/OMEGA. Testing included scans of the analog and digital components using charge injection and beta particles from a Sr-90 source, resulting in a measured jitter of 8-9 ps for charges above 20 fC. Both wire-bonded and flip-chip assemblies were developed for various characterizations. Additional tests using Transient Current Technique (TCT) laser scans were conducted to map out charge distribution, and various tests are still ongoing.

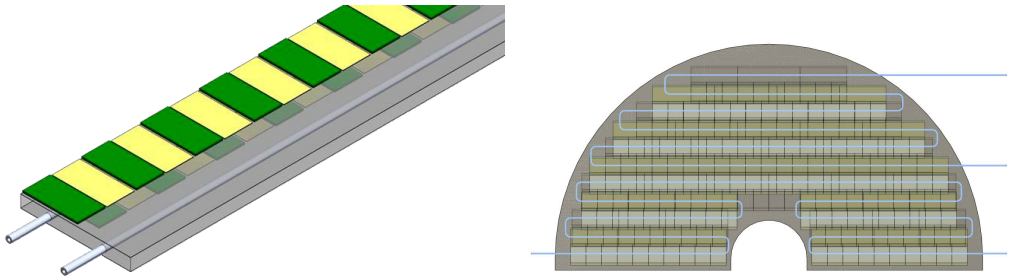

Figure 3.94: schematic drawings of the cooling pipes in one BTOF stave (left) and half of the whole FTOF (right). Each BTOF stave has one input line and a return line, while the FTOF has a total of 4 input lines and 4 return lines.

ORNL is developing flexible Kapton PCBs for TOF applications, where sensors and mock-up ASICs will be glued to the stave and wire-bonded at UCSC and then co-cured onto a composite structure at Purdue for evaluation. Flip-chip options will be available soon, aiming to support low-cost sensor-ASIC hybridization techniques.

In FY24, BNL, LBNL, and Rice developed a prototype board (ppRDO) for precise clock distribution and ASIC integration for AC-LGAD systems. Key milestones, including schematic designs, part orders, PCB layout, and initial testing, were completed ahead of schedule. Firmware development and performance tests on clock cleaning, jitter, and power distribution are ongoing. The collaboration aims to continue in FY25, focusing on developing a readout board (RBv1) and power board (PBv0) for AC-LGAD systems, supporting the TOF applications, and ensuring DAQ compatibility. The ppRDO includes three components: an FPGA, a clock cleaner, and an SFP+ module. Future versions will adopt an lpGBT to replace the FPGA, clock cleaner, and a VTRx+ to replace the SFP+ module, improving performance, radiation hardness, and integration.

Implementation

Services: Electric power is distributed to the detector components via the Power Board (PB), which is part of the Service Hybrid (SH). The SH also includes the functionality of the Readout Board (RDO). In the case of BTOF, one SH supports 64 sensors and 128 ASICs, with SHs placed on both sides of the stave. For FTOF, several types of SHs are used, covering 12, 24, or 28 sets of sensors and ASICs. The SH is distributed on the mechanical and support disk, together with sensor modules.

Low Voltage (LV) and High Voltage (HV) cables are connected to the PB, where multiple DC-DC converters step down or adjust the voltages as needed. HV is applied to groups of multiple sensors rather than distributed individually to each sensor. The size of each sensor group is determined by the design of the sensors and the electronics. Table 3.43 summarizes the services (cables and tubes) necessary for the TOF detectors.

A liquid cooling system is employed to control the temperature of the detector. For the BTOF stave, one or two cooling pipes are integrated into the stave sandwich structure, with liquid flowing in one direction along the length of the stave. In FTOF, a winding liquid pipe is integrated into the support sandwich structure. The flow rate and pipe diameter are determined by the amount of heat generated and the detector's performance requirements; thermal finite element analysis determines the design. The pressure must remain below the surrounding air pressure to ensure

subsystem	item	quantity	diameter (mm)	lengths (m)	description
BTOF	288 FEE LV s.hybrid dist.	24	20	15–25	Rack to Panel, 8AWG(24 AWG sense pairs)
BTOF	FEE LV	72	6.3	8	panel-to detector, Alpha-PN: 2424C SL005
BTOF	FEE HV	18	14	15–25	Rack to Dist. Panel
BTOF	FEE HV	144x2	1.5	8	panel to sensor
BTOF	cooling tubes	144x2	5	> 2.6	supply/return from panel to stave (Aluminum)
BTOF	cooling tubes	4x2			supply/return to panel
FTOF	132FEE/ sHybrids, service feeds	44	10.0	25	LV,rack-to-detector LV-dist,14AWG TC,w/24AWG-sense wires
FTOF	132FEE/ sHybrids, dist.	44	9	3	18 AWG TC, 6 cond.dist. panel-to s.hybrids
FTOF	FEE HV	212	2.42	10	panel to sensor
FTOF	cooling tubes	2x2	5		supply/return from panel to detector (Aluminum)
FTOF	cooling tubes	2			supply/return to panel

Table 3.43: Summary of BTOF and FTOF low voltage and high voltage power supply cables to distribution panels and then to the detector FEE (the exact numbers are being checked at the time of writing).

safe operation. Fig. 3.94 shows a single BTOF stave with cooling pipe (left) and half of the FTOF structure with cooling pipes (right). Possible cooling liquid choices are either water or the NOVEC 7200 engineered fluid [44].

Subsystem mechanics and integration: Both the BTOF and FTOF detector systems are supported by their own support structure, which is integrated and supported by the global support tube (GST). The BTOF is a barrel geometry time-of-flight detector system located at a radius of 63 cm from $z = -117.5$ cm to $z = +171.5$ cm along the beam direction as shown in Fig. 3.95. The BTOF detector subsystem has a dedicated 7.5 cm space in the radial direction, and similarly, the FTOF subsystem has a dedicated 7.4 cm space along the beam direction. Three engagement rings (each 5 mm width) are made from composite materials and support the BTOF detector - they are supported by the GST. A first concept was developed for a BTOF stave mounting mechanism employing the engagement rings by clips with staves at an 18° angle. Staves are individually removable to ease maintenance. The FTOF detector is designed in two half-disc structures, or dee's, that are kinematically mounted to the GST. Services (readout, power, cooling) of the BTOF are routed to both ends of the barrel, while those of the FTOF are routed to the outer radius, and all are sup-

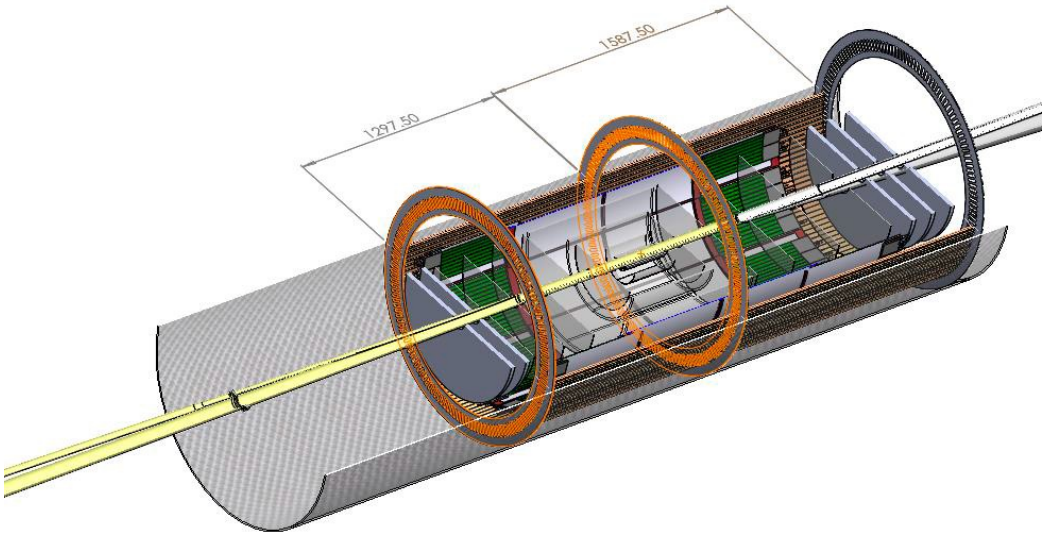

Figure 3.95: BTOF supporting mechanical structure with engagement rings situated and supported by the EPIC global support tube structure (GST). The width of each of the three engagement rings is 5 mm.

ported by the GST. Table 3.44 lists the positions of the BTOF and FTOF relative to the global ePIC geometry.

subsystem	z_{min} (cm)	z_{max} (cm)	inner radius (cm)	outer radius (cm)	stave angle
Barrel TOF	-117.5	171.5	62	69.5	18^o
Forward TOF	185	192.5	10.5	60	0

Table 3.44: The BTOF is designed with a barrel geometry surrounding the beam pipe and interaction point, while the FTOF is a disk geometry perpendicular to the beam direction on the hadron side (positive z).

Calibration, alignment and monitoring: **Calibration and alignment:** For spacial calibration and alignment, the TOF layer is essentially treated as a layer of the overall tracking system. Therefore, spacial alignment will be carried out as part of the entire tracker. This is typically based on the match between tracks reconstructed in other layers of the tracking, then extrapolated to the TOF and the hits in the TOF. By combining the information from many tracks, high precision can be achieved.

To exploit timing in the reconstruction of the charged tracks, the different TOF channels must be synchronized to a precision of a few picoseconds. The absolute time calibration (or phase shifts relative to the beam clock) is not a particular concern, as all the event reconstruction relies on the relative time between tracks within the same collision event. The time offsets of the TOF channels can be intercalibrated using all the tracks collected online through a fast reconstruction stream.

The distribution of the reconstructed time at the vertex of these tracks – assuming they are pions – should have an rms spread of approximately 50 ps, including the time spread of the luminous region and detector resolution. The mean time of this distribution over many tracks provides the reference calibration points. Non-pion particles will contribute to the tail of the distribution, which can be cleaned up using an iterative procedure. These calibrations can be made available for the prompt reconstruction of the events and updated frequently.

Monitoring: In the readout scheme of the TOF, a common clock is distributed to the individual channels belonging to the same service hybrid. The time stability of the clock distribution can be monitored with a precision of a few picoseconds every second.

Status and remaining design effort: eRD112 and eRD109

eRD112: Sensor R&D effort A brief summary of eRD112 activities is reported in this section, for a more detailed review of the sensor development effort consult the 2024 eRD112 report document. HPK sensors from the 2023 production have been tested at the Fermilab test beam facility; the results are summarized in Ref. [1]. HPK strip sensors from the latest full-size production were received in the fall of 2024 and are currently being characterized; HPK pixel sensors from the same production will be received by the end of the year. A summary of the best results is shown in Fig. 3.96. The same HPK production was tested in the laboratory with focused laser TCT and showed similar results as reported in Ref. [41]. The presented strip sensors (Fig. 3.96, left) show a constant time resolution of around 35 ps, which is within the requirements for the ePIC TOF (see Table. 3.39). The strip reconstructed position resolution is between 10-20 μm, which is also within the ePIC TOF requirement of 30 μm. The best result for pixel sensors (Fig. 3.96, right) shows a homogeneous time resolution of 20-25 ps, well within the ePIC TOF requirements. The position resolution is 20-70 μm across the device; the charge-sharing mechanism allows for precision reconstruction between metal electrodes, but the resolution is significantly worse for hits directly on the metal electrodes.

The position resolution requirement for the FTOF is 30 μm. Therefore, pixel technology needs to be refined to meet the requirements. The new HPK production (expected by the end of 2024) includes smaller electrode sizes and larger gaps between electrodes, which could provide good reconstruction across the sensor. However, it was observed that a larger gap decreases the total S/N between electrodes, which might degrade the overall performance of the sensors. Results from a BNL production provide a promising alternative to square metal pixels. The S/N is better across the sensor for a cross-shape electrode given the same central metal shape, allowing for better reconstruction using charge sharing. HPK did not include cross-shape geometry in the latest production, but it might be included in the next one. Another producer of cross-shaped AC-LGADs is Fondazione Bruno Kessler (FBK). The FBK prototypes were investigated with a laser TCT, and a similar behavior was observed for cross-shaped devices [42].

The sensors irradiated at the Triga Reactor with 1 MeV neutrons were received in Spring 2024 and characterized both for electrical proprieties (capacitance and current over-voltage) and with the laser TCT station. Gain degradation can be probed with measurements of capacitance over voltage by identifying the gain layer depletion point (V_{GL}). Figure 3.97 (left) shows the change in the gain layer for the irradiated HPK AC-LGADs from several wafers, with different n+, oxide, and active thickness, up to 1×10^{15} Neq. In the region of interest for ePIC ($< 10^{13}$ Neq), the gain layer is unchanged. The charge-sharing proprieties after irradiation were tested in the laboratory using a focused IR laser. As seen in Fig. 3.97 (right), the spatial response of the sensor is unchanged after irradiation up to 5×10^{14} Neq. The current increase in the irradiated HPK sensors is also negligible until $< 10^{13}$ Neq, as shown in Fig. 3.97 (bottom). The measurements were done at room temperature; therefore, no cooling will be necessary to reduce the dark current, which would

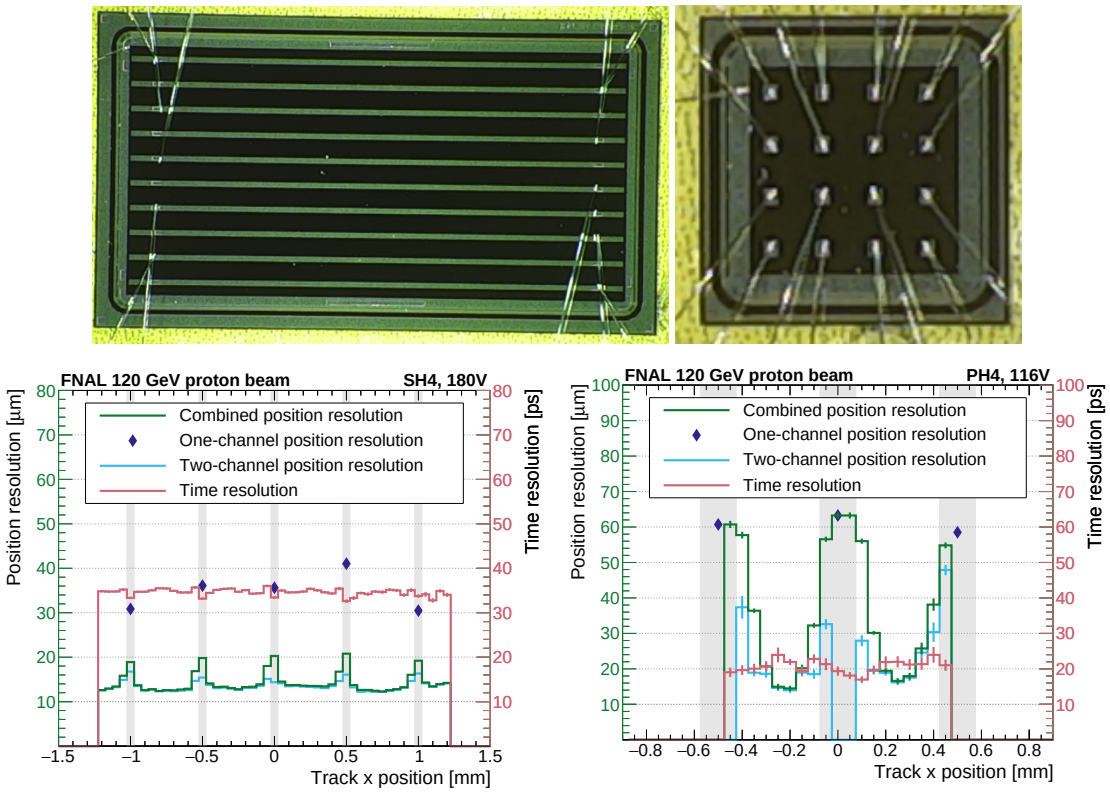

Figure 3.96: Left: Picture and beam test results for HPK strip sensor, 1 cm long, 500 μm pitch, and 50 μm metal electrode width. Right: Picture and beam test results for HPK pixel sensor, 4x4, 500 μm pitch, and 150 μm metal electrode width. Sensors were read out by an FNAL 16ch board, plots from Ref. [1].

increase the sensor power dissipation in the ePIC. In conclusion, no change in the behavior of the sensors is expected during the lifetime of the ePIC detector due to radiation damage.

eRD109: readout R&D effort A more detailed review of the electronics development effort can be found in the 2024 eRD109 report document. In the following section, a brief summary will be provided.

The Fermilab team has continued the development of the FCFD ASIC prototype and, in FY23, has designed the first multi-channel prototype with this approach, labeled FCFDv1. Numerous technical improvements were implemented based on the experience with FCFDv0, aimed at addressing the stability and performance of the system. The FCFDv1 ASIC was submitted for production in September 2023 and received in January 2024. A specialized readout board was designed to accommodate the FCFDv1 connected to a 0.5 cm HPK AC-LGAD strip sensor. Initial performance measurements were done using internal charge injections performed with an LGAD-like signal. With input capacitance ∼3.5 pF (mimicking AC-strip input capacitance), a jitter of around 11 ps was achieved, as shown in Fig. 3.98 (left). Test beam campaigns were performed in June 2024 to study the performance of the FCFDv1. The newly introduced amplitude readout was found to function well, and results show 100% efficiency when combining neighboring strips. The time resolution measured from the beam test was around 50 ps. A further design improvement is foreseen in FCFDv1.1 to accommodate a 1 cm AC-LGAD strip sensor and improve the timing resolution.

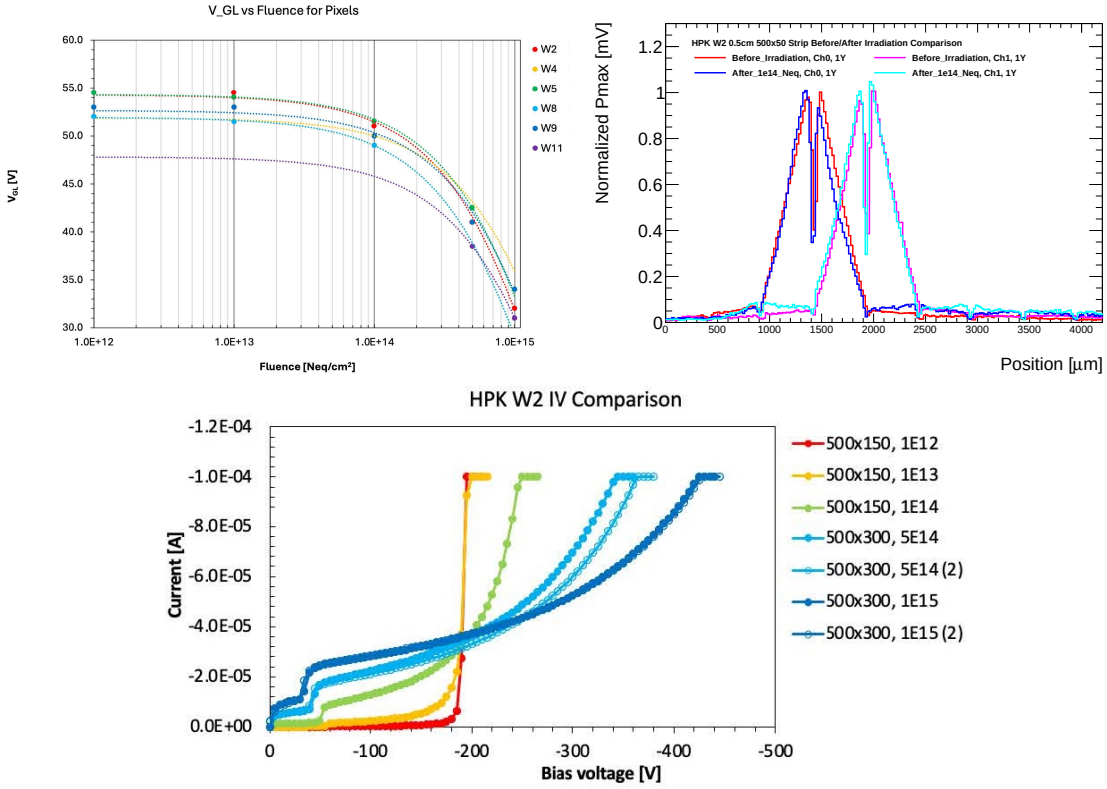

Figure 3.97: Left: Degradation of the gain layer for AC-LGADs of several wafers (with different n+, oxide, and active thickness) from HPK latest sensor production, showing no change in gain layer doping up to 10^{13} Neq, which is an order of magnitude over the ePIC TOF radiation requirement. Sensors were irradiated at the TRIGA reactor (Lubjiana) with 1 MeV neutrons. Right: Normalized comparison of response profile of two nearby strips for two HPK 0.5 cm length, 500 μm pitch, 50 μm strip width: one before irradiation and one after 1×10^{14} Neq. Even if the total signal is degraded, the charge-sharing profile will remain unchanged. Bottom: Current over voltage measurement for irradiated HPK sensors.

The development of the EICROC0 chip is proceeding as planned. In 2024, an updated PCB ("2024" PCB) was designed by the OMEGA group in France. This updated PCB features improved testability and grounding, as well as the removal of supplementary PLLs. The chip shows good homogeneity between channels and jitter below 35 ps for an injected charge of >4 fC, both for the preamplifier and for the discriminator output, as seen in Fig. 3.98 (left). A large correlated noise still remains with the updated "2024" PCBs (already observed in the "2023" PCB), which leads to large TDC jitters, over 50 ps, when by design, the TDC jitter is expected to be of the order of 10 ps. Nevertheless, the intrinsic performance of the preamplifier, the TDC, and the ADC, taken individually, agrees with the design and within the ePIC detector specifications.

The development of a pre-prototype readout board (RDO) with high-precision clock distribution has been completed. Figure 3.99 shows a picture of the ppRDO. It is connected with the CMS ETL module board v0, which consists of the full-sized ETROC2 chip for testing purposes. The ppRDO will be evolved into the prototype RB for the FTOF next, which consists of lpGBT and VTRx+ chips instead of FPGA and SFP+. Those efforts will be carried out under engineer designs as described later.

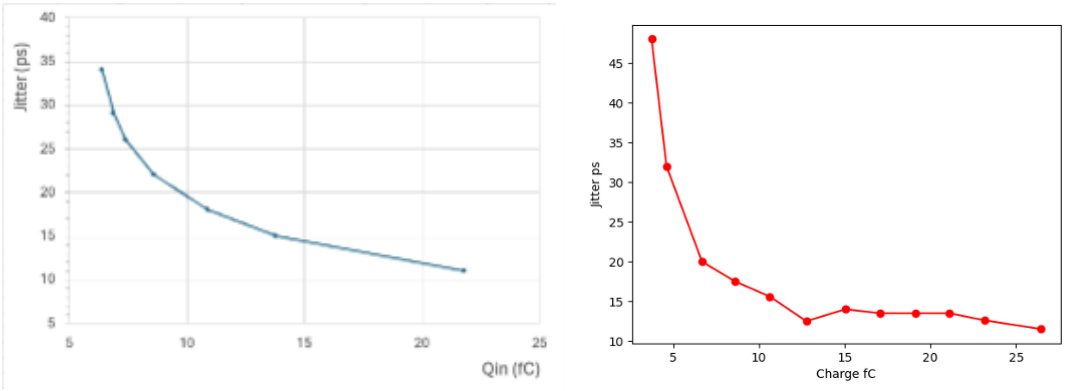

Figure 3.98: Left: FCFD Jitter measurements with 3.5 pF input capacitance and charge injection. Right: EICROC Discriminator jitter versus the injected charge, determined from data on an oscilloscope. Plots from the eRD112 and eRD109 2024 reports.

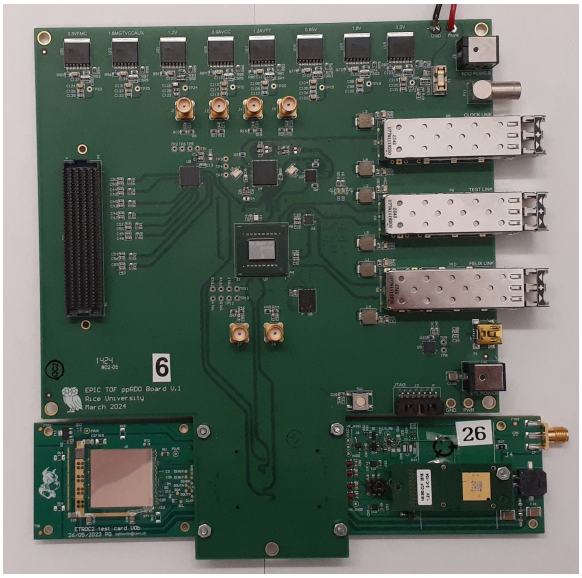

Figure 3.99: Picture of ppRDO connected with CMS ETL module board v0 for testing.

E&D status and outlook: E&D activities

Thermo-Mechanical demonstrator: The fabrication of a demonstrator stave following the double-sided design, as seen in Fig. 3.101, is ongoing. The demonstrator will be a thermal/mechanical demonstrator of the assembly procedure and chip/sensor power dissipation. A mock-up stave, see example in Fig. 3.100, will be co-cured with a readout flex with a cooling pipe in the center. A series of Si heaters and full-size HPK sensors from the latest production will be glued to the stave, then wire-bonded together and to the readout flex. The demonstrator will probe the power dissipation, the temperature gradient across the stave, and the mechanical assembly procedure. Demonstrator results are expected by Q1 2025.

Figure 3.100: Assembled BTOF stave prototype at Purdue.

Environmental, Safety and Health (ES&H) aspects and Quality Assessment (QA planning): We also carried out QA long-term and stress-test reliability studies of AC-LGADs as a stepping-stone towards studies on AC-LGADs. The tests were conducted in an ambient chamber at various environmental conditions. We kept the sensors under bias voltage over periods of weeks, at different temperatures, ranging from -60° to +80° C, and under different humidity conditions. Under these extreme conditions, we carried out I-V scans. At intervals of time between temperature cycles, we also collected signals from β particles from a Sr-90 source at room temperatures to study any deterioration in noise or charge collection. The results were presented at an IEEE conference. While we saw an impact of humidity and temperature on current and breakdown voltage, the sensors recovered their original performance in subsequent cycles. In addition, we also studied the impact of passivation on sensors to minimize charge build-up and early mortality. We confirmed that passivation is critical to minimize the impact of humidity on sensors and prevent early mortality. Such tests were critical after issues had been observed in silicon sensors used for tracking detectors in other experiments, such as those at the HL-LHC. As part of our QA strategy, we also sent BNL-made AC-LGADs to colleagues of UNM to have them irradiated at various fluences in a proton beam at ITA, in a gamma beam at SANDIA and with neutrons at the TRIGA reactor. The first results are shown in the previous sections.

For both sensors and readout chips, it is imperative to evaluate the yield of the test productions to adjust the final production orders. The QA plans to evaluate the yield of the sensor productions are as follows: each produced sensor will be tested in the laboratory in a probe station with simple current over voltage (IV) and capacitance over voltage (CV) tests. AC-LGADs have a single point of DC connection on the n+, so only 1 or 2 needles are necessary for the test; a probe card is not necessary for QA. The IV test will allow us to check the current level and the breakdown voltage for each produced device; the current level has to be $\ll 1\,\mu$A, not to introduce power dissipation issues. The breakdown voltage of all devices has to be within 10% spread to avoid issues in the HV distribution. The CV test will probe the gain layer depletion voltage and demonstrate that all devices have homogeneous gain. For LHC prototypes [39] as a reference, the gain homogeneity was within 1% spread. A selection of devices from the full production will be characterized by mounting them on analog frontend boards with laser TCT and at test beam facilities to ensure the homogeneity of the charge-sharing response.

To evaluate the yield of the chip (EICROC, FCFD) productions, a sample of chips from each batch will be tested and probed for homogeneity in all the channels using a calibration input. All channels have to be within 10% (spread) of homogeneity. A selection of chips will be coupled (wire bonded or bump bonded) with a matching working sensor and mounted on a prototype PCB to probe correct and homogeneous operation in a realistic configuration. Then, the boards will be tested with a laser TCT or at test beam facilities.

Once the state of sensors, readout chips, and flex is advanced, a fully loaded demonstrator stave is envisioned. The mounting procedure will already be tested during the assembly of the thermo-mechanical demonstrator. The full demonstrator will then be tested with radioactive sources in a laboratory or at test beams.

Construction and assembly planning: The BTOF detector has a cylindrical shape consisting of 144 tilted staves. These staves are assembled at designated sites within Class-7 or higher clean rooms before being transported to BNL for final construction. Each stave is approximately 270 cm long and is divided into two half-staves of 135 cm each. A half-stave includes a support structure with an integrated cooling pipe, a flexible printed circuit (FPC), sensors, and ASICs. The sensors and ASICs are mounted on both sides of the half-stave, with 64 sensors and 128 ASICs on each side. Wire bonding is used to connect the ASICs to the sensors and electronics. Only components that pass various quality inspections — such as visual checks, metrology, and electrical tests — proceed to the assembly stage. During the half-stave assembly, one FPC is glued onto the support structure; see Fig. 3.101(a). To ensure precise alignment, a specialized tool is used featuring pins and holes that guide the placement of the FPC and the correct application of glue. After assembly, the staves undergo both electrical and mechanical tests. Subsequently, sensors and ASICs are installed on the FPC surface using alignment tools similar to those used during the FPC mounting process, as shown in Fig. 3.101(b). These tools help position the components and apply adhesive. Electrical connections are verified, and in Fig. 3.101(c), the ASICs are bonded to the sensors using wire bonding, followed by wire encapsulation. Two support structures with wire-bonded sensors, ASIC, and FPC (front and back side), are attached to each other as in Fig. 3.101(d). The final round of testing is conducted after completing the installation on both sides (Fig. 3.101(e)). Fully tested staves are then shipped to BNL for integration into the global support structure of the ePIC detector, which contains 144 slots for precise alignment of the staves within the global coordinate system.

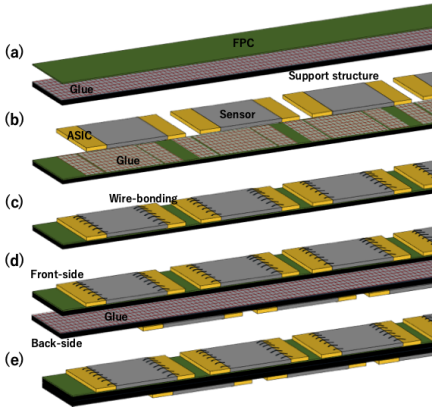

Figure 3.101: Assembly process of BTOF stave. The drawing is not to scale.

The FTOF is constructed in a double-sided disk shape by populating modules with dimensions indicated in Fig. 3.92. Each module includes 4 sensors, 4 ASICs, a module board, and an aluminum-nitride (AlN) base plate, which acts as a thermal conduit to the cooling system. The modules are connected to a service hybrid (SH) that consists of a power board (PB) and a readout board (RB). As mentioned earlier, three different configurations of SH are used, depending on the number of modules being supported: 3 modules (RB3), 6 modules (RB6), and 7 modules (RB7). There are about 780 modules in total to patch the disk shape. Sensor and ASIC are connected by bump-bonding. The module board is connected to the ASICs through wire bonding and has a connector to interface with the RDO. Assembly of the modules occurs in Class-7 (or higher) clean rooms, while the PB and RB can be assembled under standard conditions. The assembly of each module begins with the connection of one sensor to one ASIC using bump-bonding technology (Fig. 3.102(a)). Automated machines are used for sensor and ASIC placement, alignment, and bonding. After bonding, the electrical performance of the sensor-ASIC hybrids is tested. Following this, 4 sensor-ASIC hybrids are mounted on the module board, using a dedicated tool to ensure precise alignment (Fig. 3.102(b)). Thermal adhesive films are placed between the hybrids and the module board to

ensure efficient heat dissipation. Once mounted, the ASICs are wire-bonded to the module board, and the wires are encapsulated for protection. After the bonding process, the AlN base plate is attached to the opposite side of the hybrid (Fig. 3.102(b)), with thermal adhesive films again used between them to aid heat transfer. The thermal adhesive films are also put between them. The modules undergo thorough quality checks before moving on to SH assembly. The RBs and PBs are manufactured using standard circuit board techniques and come with dedicated connectors for integration. SHs are available in configurations supporting 3, 6, or 7 modules, with the RB and PB connected via dedicated interfaces (Fig. 3.102(c)). Once assembled (Fig. 3.102(d)), the modules and SHs are tested for connectivity and performance. After passing all tests, the modules and SHs are shipped to BNL, where they are attached to the disk-shaped support structure. Specialized tools ensure the accurate placement of the components. Modules and SHs are mounted on both sides of the support structure to eliminate acceptance gaps between sensors. A fixture maintains the required clearance between components when installing the modules and SHs on the opposite side. Finally, the fully assembled disk is installed into the ePIC detector.

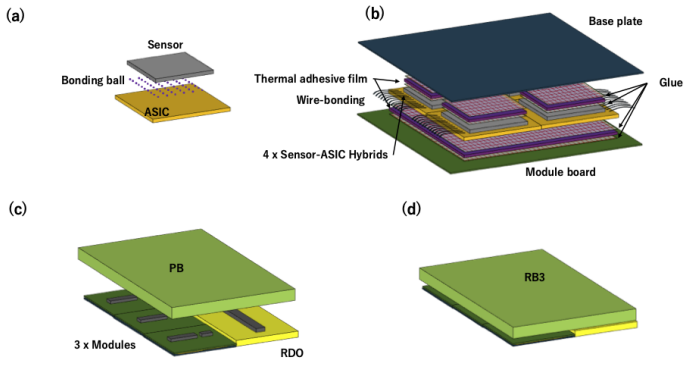

Figure 3.102: Assembly process of FTOF modules. RB3 type is shown as an example. The drawing is not to scale.

Collaborators and their role, resources, and workforce: Table 3.103 shows the participating institutes with their roles, the contact person, and potential commitments. This shows substantial participation by the international collaborators outside of the U.S.. We also anticipate substantial funding support from international collaborators for the BTOF detector.

Risks and mitigation strategy: Our R&D results (eRD112) show that the performance of the tested sensors would meet physics requirements for the TOF subsystems. Those studies were done with smaller chip dimensions. The production for the R&D study with a full-size sensor chip is underway. There is a potential risk that the performance of sensors with larger sizes would be worse. The mitigation is to reduce the sensor size.

The HPK sensors for R&D (eRD112) are of a small quantity. Mass production would be a risk in terms of chip yield and schedule delay. The mitigation is to explore other possible production sites (Taiwan/FBK).

FCFD ASIC design (eRD109) currently has analog signal readout only. The design and test of the digitization component is underway and is expected to have a first pass early next year. Additional resources may be needed to mitigate potential schedule delays and cost increases. In ad-

Institute	Contact Person	NOW (TDR->Project)
Brookhaven National Laboratory	Prithwish Tribedy tribady@bnl.gov	DAQ readout chain readout, sensor-ASIC integration, sensor with FF AC-LGAD; EICROC testing
Fermi National Accelerator	Artur Apresyan Artur.Apresyan@cern.ch	FCFD ASIC (no ePIC)
OMEGA	Dominique Marchand dominique.marchand@ijclab.in2p3.fr	EICROC
Los Alamos National Laboratory	Xuan Li xuanli@lanl.gov	
Rice University	Wei Li wl33@rice.edu	B/FTOF FEE?, Backend electronics (postdoc) , simulation and reconstruction
Oak Ridge National Laboratory	Oskar Hartbirch hartbricho@ornl.gov	sensor-ASIC integration, frontend electronics (waffle probing), module assembly
Ohio State University	Daniel Brandenburg Brandenburg.89@osu.edu	BTOF/FTOF: module assembly; backend electronics
Purdue University	Andreas Jung anjung@purdue.edu	Module assembly
Univ. of California, Santa Cruz	Simone Mazza simazza@ucsc.edu	Sensor, sensor-ASIC integration, module assembly (no in-kind)
University of Illinois at Chicago	Olga Evdokimov mailto:evdolga@uic.edu	
Hiroshima University	Kenta Shigaki shigaki@hiroshima-u.ac.jp	FTOF EICROC testing, sensor testing (30%), simulation
RIKEN	Yuji Goto. goto@bnl.gov	BTOF: module assembly
Shinshu University	Kentaro Kawaide kawade@shinshu-u.ac.jp	Sensor testing, simulations
University of Tokyo	Taku Gunji gunji@cns.s.u-tokyo.ac.jp	DAQ streaming readout
South China Normal University	Shuai Yang syang@scnu.edu.cn	
Univ of Sci. and Tech. of China	Yanwen Liu	
Indian Institute of Tech., Mandi	Prabhakar Palni prabhakar.palni@unigoa.ac.in	FTOF Module Assembly/QA, sensor testing
National Inst. of Sci. Edu. Res.	Ganesh Tambave ganesh.tambave@niser.ac.in	Module Assembly
National Central University		FF AC-LGAD (sensor QA)
National Cheng-Kung University	Yi Yang yiyang@ncku.edu.tw	Mechanics and cooling systems
National Taiwan University	Rong-Shyan Lu rslu@phys.ntu.edu.tw	FF AC-LGAD; module assembly
Univ. Técnica Federico Santa María		Simulations
LBNL	Zhenyu Ye yezhenyu2003@gmail.com	BTOF ASIC testing; SH
Kent State University	Zhangbu Xu zxu22@kent.edu	Simulation, readout test, machine shop (in-kind)
Nara	Takashi Hachiya hachiya@cc.nara-wu.ac.jp	BTOF module assembly/validation/FPCB

Figure 3.103: Collaboration institutions and their potential responsibilities.

dition to the baseline chips, EICROC and FCFD, third-party ASICs are also taken into consideration: FAST (INFN Torino), AS-ROC (Anadyne Inc. and UCSC), and HPSoC (Nalu and UCSC). The most advanced one is the High-Performance System-on-Chip (HPSoC) ASIC, designed by Nalu Scientific [45], in close collaboration with SCIPP, and fabricated in 65 nm CMOS by TSMC. HPSoC includes a fast analog frontend and, unique to all other current AC-LGAD readout ASICs, will capture the full signal waveform at a sampling rate of 10-20 GS/s. Together, these are expected to address the EIC goal of 25 ps timing resolution or better per measured space point. V2b of the chip has a working digital backend and is currently under review.

We have performed heat conductivity and cooling simulations, as well as tests on the cooling capacity (currently with PED funding). Those show promising outcomes for meeting the cooling needs. The potential risk is that the cooling capacity is insufficient to maintain a stable and relatively uniform temperature. A possible mitigation strategy is to use different materials for cooling pipes with better heat conductivity and higher flow rates.

Schedule The schedules for BTOF and FTOF projects have been incorporated into the overall EIC project schedule. A major inter-dependence of the schedule is the sensor and ASIC designs. In the preproduction phase, 10% will be made in six months, during which quality and procedures will be confirmed. Then, during the production phase, the remaining 90% will be produced in two years.

Additional Material

Low-voltage and High-Voltage power supplies Each service hybrid module will be powered by a radiation and magnetic field tolerant DC-DC regulation board as part of the hybrid module and mounted to the cooling plate. The minimum efficiency of the regulator board should be $\geq$ 70.0%. Input power to the DC-DC board is delivered from rack-mounted Wiener PL500 series power supplies to source 15 V DC $\pm$ 3.0%. The current demand from the rack-mounted PSU should not exceed 80.0% of the manufacturer's rating. Each channel of the PSU will have over-current fuse protection. The power-cable size is selected to operate at 125% of the total continuous maximum load. The estimated power consumption and LV cable feed size for each detector is designated as follows: Forward TOF system LV power: 6.0 kW (400 A). LV power feeds from the platform: Custom two-conductor 12 AWG tray-rated cabling with embedded low-voltage twisted-pair sense wires.

Barrel TOF system LV power: 15.0 kW (1,000 A). LV power feeds from the platform: Custom two-conductor 8 AWG or 10 AWG (depending on LV segmentation) tray-rated cabling with embedded low-voltage twisted-pair sense wires. Custom-enclosed LV power distribution PCBs will be installed at the detector side and outside the inner detector volume. A disconnect is required for each LV output port of the distribution box. Power distribution to the service hybrids will be configured not to exceed 10.0% channel segmentation from the rack-mount power control. Multi-channel ISEG ESH series power modules will provide up to negative 500 VDC bias at a current of 10 mA per channel. Multiconductor cables terminated with REDEL connectors or individual coax cables terminated with SHV connectors will feed an enclosed HV distribution box. The HV bias cabling to the detector hybrids will be carried over a multi-drop cable configuration to service the sensor hybrids in small groups.

Schedule Although there are still many uncertain elements at this stage, the latest schedule is shown in this section. The overall progress of development depends heavily on the advancement of the sensor. For instance, since the ASIC blueprint is based on the sensor's features, the ASIC design cannot be completed before the sensor development is finalized. This was the first principle we used to set up the schedule.

At least three sensor prototypes will be produced. The first prototype, the full-size sensor prototype, has already been manufactured by HPK. Based on the characteristics of this sensor, the FCFDv2 and EICROC2 ASICs will be developed. Based on our experience, we can also expect that the time required to fabricate the sensor and the ASIC will be 4 months from submitting the design to delivery. It could be up to 6 months for the ASICs. Additionally, prototypes of the Service Hybrid (SH), electronics (FPC for BTOF and module board for FTOF), and support structure will be created based on this sensor and ASIC.

Next, the design for the second full-size sensor prototype will incorporate improvements identified from the first prototype. The design will start 2 months after starting the first sensor validation. The design of the next ASICs (FCFDv3 and EICROC2_v1) will begin as soon as the sensor design is finalized. The SH, FPC, and stave support structure will also be developed in conjunction with this

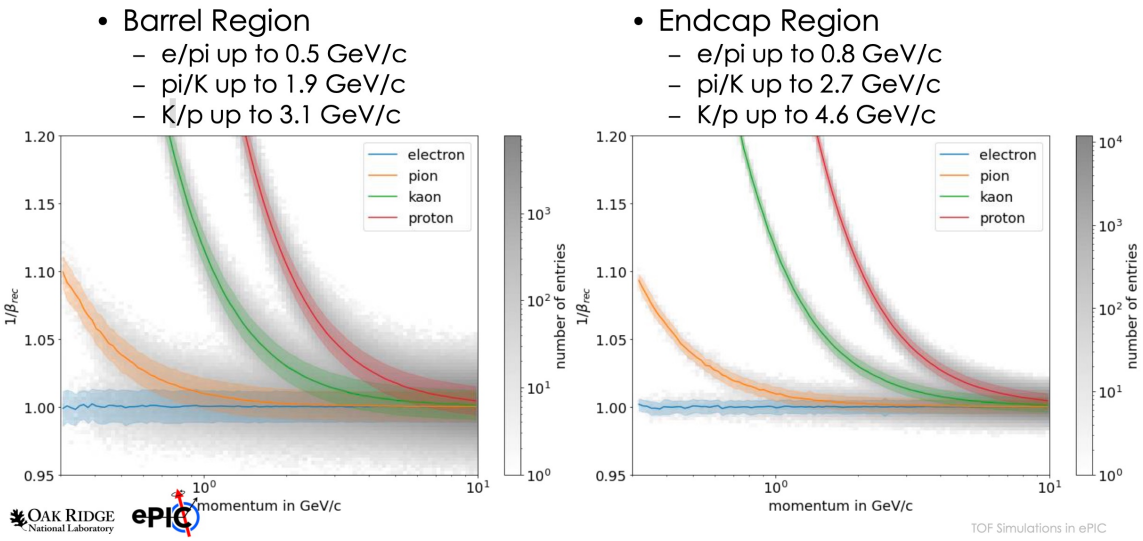

Figure 3.104: simulation of $1/\beta$ as a function of particle momentum for BTOF and FTOF performance.

sensor and ASIC. Some sensor characteristics can be estimated based on accumulated knowledge, which might allow certain designs to be completed simultaneously.

The second full-size sensor prototype will be the last, but we will make another prototype as a backup and make final adjustments for mass production. Depending on the budget, additional sensor and ASIC prototypes may be ordered.

During the development phase, assembly was carried out as soon as the other components became available. However, there will be a time lag between the arrival of components and the start of assembly in the preproduction and production phases. This is because additional time is required for quality assurance (QA) and quality control (QC) procedures before the components can be shipped to the dedicated assembly sites. As a result, the preproduction and production phases will begin two months later than other phases.

particle identification Figure 3.104 shows an example of a single-particle response simulation of $1/\beta$ as a function of particle momentum for BTOF and FTOF performance.

3.3.4.2 The proximity focusing RICH

Requirements

Requirements from physics: Particle identification capabilities in the electron going endcap region of the ePIC detector ($-3.5 \leq \eta \leq -1.5$) will be provided by a proximity focusing ring imaging Cherenkov detector (pfRICH). Driven primarily by the requirements from SIDIS measurements, the pfRICH will need to provide 3σ separation or better between pions, kaons, and protons for momenta $p < 7$ GeV/c. The pfRICH will also play a critical role in electron-hadron separation for momenta below roughly 3 GeV/c, where hadron densities are at their maximum and the

electron ID capabilities of the backward EM calorimeter will not be sufficient to achieve the overall required electron purity. In addition to electron and hadron identification, the excellent timing resolution of the pfRICH photosensors, High Rate Picosecond Photon Detectors (HRPPDs), will allow the pfRICH to provide a high quality t_0 reference for the barrel and forward endcap time-of-flight detectors.

Requirements from Radiation Hardness: The beam induced charged particle background impacts the pfRICH mainly via excess photons produced in the aerogel and fused silica windows of the HRPPD photo sensors. A fraction of the incoming photons are converted to photo-electrons (PE) by the photocathode according to its quantum efficiency. The amplification of PEs due to a secondary electron emission in the HRPPD MCPs desorpts ions off the micro-channel walls. These ions drift towards the photocathode, and can react with or even sputter the photocathode material which leads to degradation of its quantum efficiency. HRPPD gain can also be affected due to a degradation of the MCP secondary emission layer.

To estimate the flux of ion back flow during the expected life span of the detector, a simulation study was performed, combining the rates from DIS events and beam gas interactions. A mass-dependent minimum energy cutoff was applied so that only particles that would produce Cherenkov radiation in the aerogel plane or HRPPD window would be considered. Each particle producing Cherenkov photons in the aerogel (n = 1.04) was assumed to produce $\approx$ 10 photoelectrons, while $\approx$ 100 photoelectrons were assumed from the HRPPD window (n = 1.45) after factoring in the QE.

Convoluting an expected operating gain of 10^5 with a running period of 26 weeks/year and a luminosity of 10^{34} cm^{-2}s^{-1} yields a yearly estimate for accumulated charge of up to 0.011 C/cm^2 on the photocathodes of sensors closest to the beam line. For a running period of 10 years, this will result in 0.11 C/cm^2, or 1.1 C/cm^2 if one assume a higher gain of 10^6. Furthermore, the rates and running period are overestimated which gives a safety factor of around 2 from the most plausible scenario. Bench-top studies to evaluate the degradation of QE with the accumulated charge are underway.

Requirements from Particle Fluence: Estimations of the expected data rates for the pfRICH were made using the same DIS + beam gas simulations that were used for the radiation hardness studies. The hit rates from physics and background sources as well as a noise rate of roughly 2.5 MHz per HRPPD leads to a digitized data rate of 50 Gb/s for the entire detector. This is not divided evenly over all HRPPDs as those closest to the beamline see higher particle fluxes. The largest data rates per HRPPD are 1.5 Gb/s while the smallest are 0.2 Gb/s. These rates are not expected to pose a problem for the front-end electronics or data acquisition system.

Justification

Device concept and technological choice: The operation of a generic proximity focusing RICH detector is based on a very simple set of principles. A charged particle passing through a thin layer of radiator (often aerogel with an appropriate refractive index) with a velocity higher than the speed of light in that medium emits Cherenkov light (photons) at an angle which is solely determined by the particle mass, momentum, and refractive index of the radiator. The 3D momentum of the particle is typically provided by a tracking system. If the average refractive index of the radiator is also known, measurements of the Cherenkov light emission angle can determine the

particle mass, thus allowing identification of different particle species, e.g. distinguishing electrons, pions, kaons, and protons.

The ePIC pfRICH was designed as a conceptually simple detector, based on proven principles, providing a high degree of performance that is practically uniform over the whole available angular acceptance in η and ϕ. In order to reach the performance requirement of 3σ separation or better of $\pi/K/p$ for momenta up to 7 GeV/c, the pfRICH design was optimized in the following ways: (1) the proximity gap length was maximized as much as possible within the volume available in ePIC; (2) the radiator thickness was taken to be small enough to reduce the contribution to the single photon angular resolution to below $\sim$5 mrad, yet produce enough photons per track to robustly reconstruct the Cherenkov angle; (3) the HRPPD pixellation was chosen such that it contributes at most $\sim$2 mrad to the angular resolution; and (4) the acrylic filter cuts off all UV light produced in the aerogel below $\sim$ 300 nm, where the $dn/d\lambda$ dependency is strongest. In addition to satisfying the PID requirements in the backward direction, the small material budget of the pfRICH design minimizes the impact on the energy resolution of the endcap electromagnetic calorimeter which sits directly downstream.

Subsystem description

General device description: The layout of the proposed ePIC pfRICH detector is shown in Fig. 3.105. It consists of a 1.3 m diameter and $\sim$49 cm long cylindrical vessel with the outer and inner walls made from a lightweight honeycomb carbon fiber sandwich and front and rear plates made of a carbon fiber reinforced plastic (CFRP). The vessel sits 123.6 cm from the nominal interaction point. Forty-two 2.5 cm thick aerogel tiles of a trapezoidal shape are installed in individual opaque compartments in a container mounted on the upstream side of the vessel. A thin acrylic filter is installed immediately after the aerogel container. The vessel is continually flushed with dry purified nitrogen. Sixty-eight HRPPD photosensors are installed in individual slots in the rear CFRP mounting plate with their fused silica windows facing the aerogel. Inner and outer conical mirrors cover the cylindrical sides of the vessel in order to increase the η acceptance of the Cherenkov photons produced in the aerogel radiator. Readout boards equipped with FCFD ASICs are mounted on the rear ceramic anode plates of each of the HRPPDs.

Sensors: An improved version of the Micro-Channel Plate Photomultiplier Tubes (MCP-PMTs) manufactured by Incom Inc. [46], the so-called High Rate Picosecond Photon Detectors (HRPPDs), will be used as the photosensor solution, see Fig. 3.106.

The sensor dimensions will be 120 mm x 120 mm, with a 104 mm x 104 mm fully efficient active area in the center (75% geometric efficiency) and will have slightly tapered 5 mm thick UV-grade fused silica windows. A DC-coupled variety of these sensors will be used, with the inner side of the anode base plate patterned into 32 x 32 square pixels, corresponding to 1024 channels per sensor, and a pitch of 3.25 mm. The sensors will be equipped with a UV-enhanced high quantum efficiency (QE) bialkali photocathode, with peak values exceeding 30% at 365 nm (see left and center panels in Fig. 3.107) [47]. The HRPPDs will be fitted with a pair of 600 μm thick MCPs with a pore diameter of 10 μm, open area ratio in excess of 70%, and bias angle of 13 degrees in a conventional chevron configuration. These will be operated at an amplification voltage of up to $\sim$700 V to comfortably achieve an overall detector gain above 10^6 if needed. The anode base plates will be manufactured from multi-layer High Temperature Co-fired Ceramic (HTCC) by Kyocera (Japan). They will have a custom design, matching the uniform 32 x 32 pixellation on the inner (vacuum) side of the sensor, short shielded traces inside of the ceramic stack, and a pattern of square pads with a smaller pitch on the outer side, matching the readout PCB design.

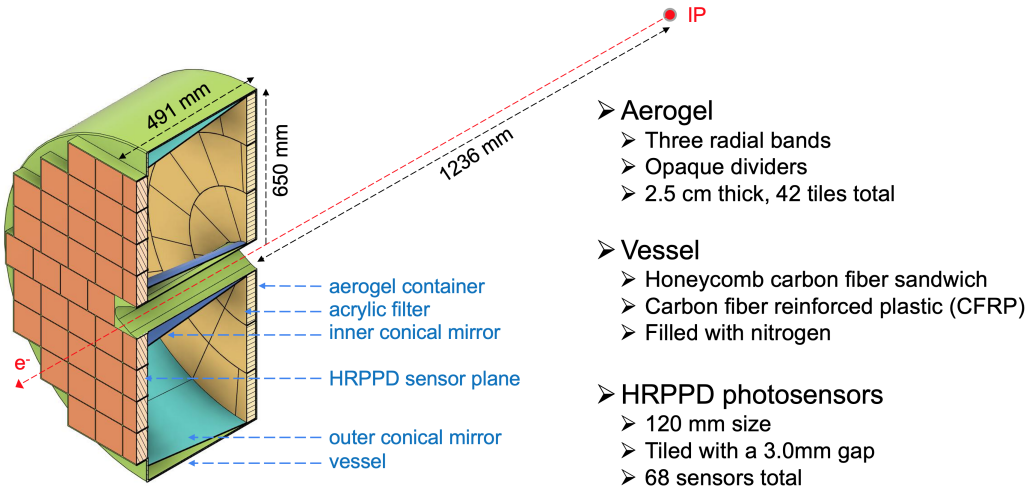

Figure 3.105: The proposed pfRICH detector. See the text for more details. (Figure documentation)

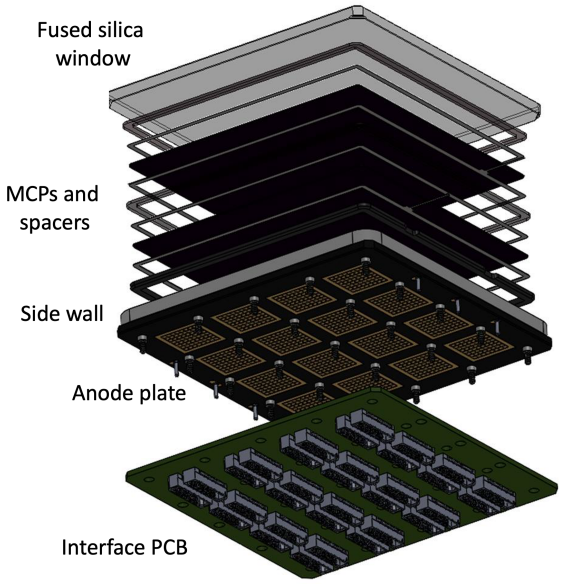

Figure 3.106: HRPPD photosensor CAD model with a passive interface board. Compression interposers between anode base plate and this PCB are not shown. (Figure documentation)

HRPPDs have a demonstrated single photon Transit Time Spread (TTS) of ∼20 ps or better (right panel of Fig. 3.107). They have low dark count rates (DCR), not exceeding few thousand Hz per square centimeter at a gain of 10^6 (see [48], slide 10). HRPPDs are expected to perform well in a 1.3 T magnetic field at the location of the pfRICH sensor plane in ePIC. Direct measurements will be performed in 2025, however the recent studies of LAPPDs with 10 micron pore MCPs indicate that HRPPD gain in a 1.3 T field should be recoverable to at least the level of 10^6 by increasing the MCP bias voltage [49].

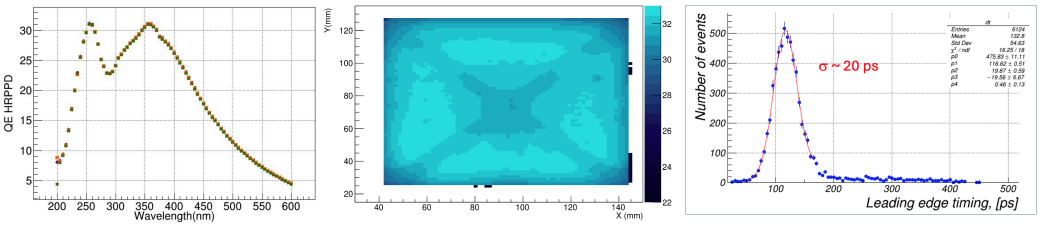

Figure 3.107: Left: EIC HRPPD QE as a function of wavelength. Center: QE map in the full active area at a wavelength of 365 nm. Right: Single photon timing resolution measured using Elmo 780 femtosecond laser with a wavelength of 390 nm. (Figure documentation)

FEE: Each sensor will be equipped with FCFD ASICs designed at Fermilab. EICROC ASICs will be built via a 130 nm technology process, with an expected power consumption of 1-3 mW/channel [50]. They will provide a Time of Arrival (TOA) and an ADC measurement with a dynamic range which should be sufficient for both single photon hits (both imaging and timing) and multi-photon hits (timing only) at a moderate HRPPD gain of a few times 10^5. The ASICs will be able to measure the TOA with a resolution around 30 ps per pixel assuming detector capacitance on the order of ∼10 pF, leading edge length of the HRPPD signal below 500 ps, and collected charge of a few dozens fC achieved by tuning the MCP gain [51]. These ballpark parameters seem to be easily within reach for pfRICH HRPPD sensors.

Each ASIC will be connected via a dedicated copper link to its respective readout unit (RDO), located on the outer circumference of the rear side of the pfRICH vessel. The RDOs will then be connected to a single Data Aggregation Module (DAM). The DAM board is envisioned to be a FrontEnd LInk eXchange (FELIX) board [52] installed in the DAQ. The RDO will be connected to the DAM via a high speed optical link capable of at least 5 Gb/s throughput. The RDOs will follow the same design used by the ePIC pixelated AC-LGAD detectors. These boards will utilize lpGBT for aggregation of ASIC data and VTRX+ to provide the fiber interfaces. The RDO should deliver timing signals synchronized to the beam crossings with jitter < 5ps.

Other components: In addition to the vessel structure and sensors described above, two other components will be critical to the pfRICH: the aerogel radiators and mirrors. The pfRICH will be equipped with aerogel tiles produced by Chiba Aerogel Factory Co., Ltd. [53] with a nominal refractive index, $n \sim 1.040$ and a thickness of 2.5 cm. The aerogel will be cut using a water jet technique into trapezoidal tiles providing a required radial and azimuthal segmentation with minimal dead area. This type of aerogel will replicate the performance of the material used in the Belle II experiment [54], and in particular, will be transparent in the near UV range, with an absorption length and Rayleigh scattering length in excess of 5 mm down to ∼275-300 nm. The aerogel tiles will be installed in segmented containers (slots) with ∼500 μm thick walls and held in place with a thin filament. The container walls will be opaque to suppress stray photons leaking out of the aerogel tile side facets, which are not expected to be of a high optical quality after water jetting.

The pfRICH will also utilize three types of mirrors to increase the active acceptance of the detector. The outer mirror cone consists of 12 segments approximately 40 cm in length which sit just inside the outer wall of the pfRICH vessel. These mirrors will recover Cherenkov photons from charged particles with large polar angles which pass through the aerogel but would exit the vessel before reaching the sensor plane. Similarly, a set of inner mirrors which wrap around the beam pipe and surrounding support structures will reflect photons emitted by small angle charged particles (close to $\eta \approx -3.5$) back onto the sensor plane. Finally,

small pyramidal mirrors will be placed on top of the HRPPD side walls to reflect (funnel) photons hitting this area back into the sensor acceptance. The mirrors themselves will have a reflectivity of approximately 90% for wavelengths between 300 and 600 nm and will be produced using an evaporator at Stony Brook University with a CFRP substrate material provided by Purdue University.

Performance

Monte-Carlo simulations: The performance of the pfRICH design was studied using a custom simulation and reconstruction software suite. The geometry of the detector, along with other relevant characteristics such as the ePIC magnetic field map, aerogel optical properties, mirror reflectivity, and HRPPD quantum efficiency were modeled in GEANT4 v10.05.p01 [13]. The reconstruction made use of the Inverse Ray Tracing (IRT) library, which is part of the ePIC software stack [55], and a ROOT [56] based data structure providing access to all photo-electron, track, and event level quantities.

Parameters relevant to the performance of the pfRICH were determined by simulating single particles thrown at a variety of energies and angles. On average, roughly 11 Cherenkov photons were detected from particles at the saturation momentum, which is in agreement with first principles estimates taking into account a realistic sensor quantum efficiency. The working acceptance of the detector, defined as the region in which the ratio of tracks producing at least one detected photon over the total number of tracks is greater than 80%, was found to cover $-3.5 < \eta < -1.5$. Single photo-electron (SPE) and track level resolutions in the working acceptance were also determined, with the SPE resolution being roughly 5 mrad and independent of momentum, while the track level resolution improved with the number of detected photons and reached a value of approximately 1.7 mrad.

The algorithm for event based reconstruction of the Cherenkov angles was validated using multi-particle simulations. The reconstructed Cherenkov angle (in units of mrad) as a function of particle momentum (in units of GeV/c) is shown in the left panel of Fig. 3.108 and compared to the theoretical expectations for a given mass hypothesis. It is seen that the reconstructed angles and theoretical expectations are in good agreement, confirming that the event based reconstruction is performing well. This plot also shows that the Cherenkov saturation angle is approximately 295 mrad. The N_σ separation count between the electron-pion and pion-kaon hypotheses as a function of momentum are shown in the middle and right panels of Fig. 3.108, respectively. It is seen that 3σ separation is possible up to roughly 2.5 GeV/c for electron-pion and 9 GeV/c for pion-kaon hypotheses. This performance was found to be relatively uniform across the whole acceptance of the detector.

One of the main purposes of the pfRICH detector is to identify low momentum scattered electrons in the backward direction. Specifically, it will help with separating the electrons from π^- mesons, which are expected to dominate in the pfRICH acceptance. Using PYTHIA-6 e+p collisions at 18×275 GeV, it was shown that the pfRICH will provide good π^--electron separation for $p < 2$ GeV/c and decreasing separation power for momenta up to ~ 5 GeV/c as seen in the left panel of Fig. 3.109.

Another important utilization of the pfRICH is hadron identification in the backward region in SIDIS studies. For that reason, the ability to separate π, K, and p hadrons was studied using simulation of e+p collisions at 18×275 GeV in PYTHIA 8. Specifically, the expected purity of leading K^- mesons was evaluated and was shown to be close to 100% up to hadron momenta of $p < 6\,\mathrm{GeV}/c$, as shown in the right panel of Fig. 3.109.

Timing performance: A primary use of the excellent HRPPD timing resolution is providing an independent t_0 reference to the barrel and forward endcap Time of Flight subsystems.

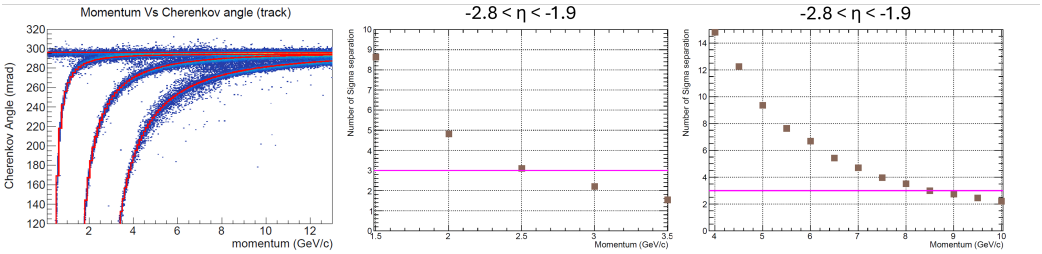

Figure 3.108: (Left) The reconstructed Cherenkov angle for electrons, pions, kaons, and protons as a function of momentum. (Middle) N_σ separation between the electron and pion hypotheses as a function of momentum. (Right) Same as the middle panel, for pion and kaon hypotheses. (Figure documentation)

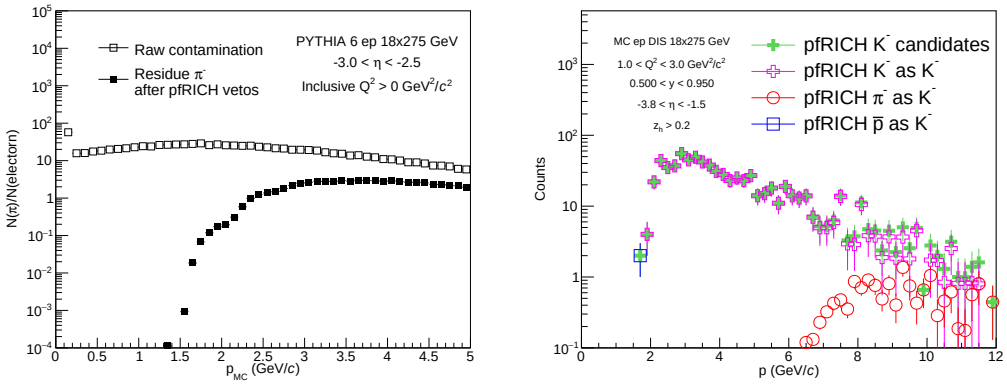

Figure 3.109: (left) Yield ratio of π^-/e_{scat} before (open black squares) and after (black full squares) pfRICH veto on π^- in PYTHIA 6 e+p collisions at 18×275 GeV for $-3.0 < \eta < -2.5$. (right) Kaon candidates identified using the pfRICH (full markers) in MC DIS e+p collisions at 18 × 275 GeV in PYTHIA 8. The open markers show contributions from correctly identified kaons and other hadrons misidentified as kaons. (Figure documentation)

However, one can make use of the t_0 ∼20 ps reference provided by the accelerator, and apply Time of Flight techniques to the pfRICH as a standalone subsystem. This functionality is built into the Inverse Ray Tracing reconstruction algorithm (IRT 2.0), for both ambiguity resolution between a variety of photon optical paths for a given pair of emission and detection point candidates, and in a combined particle identification procedure using imaging and timing information at once.

The pfRICH aerogel wall and HRPPD sensor plane will be located about 1250 mm and 1650 mm from the IP, respectively, which can serve as a conservative estimate of the flight paths. An energetic charged particle will produce ∼10 detected Cherenkov photons in aerogel, and - in cases when it crosses the HRPPD fused silica window - a photon flash resulting in at least a dozen neighboring pads hit. In either case one can conservatively assume that an overall timing measurement will be of a factor of at least 3 higher than the single photon resolution. Even assuming that the HRPPD single photon resolution under real life experimental conditions will be 25-30 ps rather than 15-20 ps as bench studies using a femtosecond laser indicate (see Fig. 3.107, right), one can come to a conclusion that a standalone pfRICH time of flight measurement will be dominated by the precision of the accelerator t_0 estimate

at the IP. If one takes 25 ps as an overall time of flight measurement resolution between the IP and aerogel and HRPPD windows, 3σ separation can be achieved between different particle hypothesis pairs as indicated in Table 3.45. In particular, one can clearly see that kaons and protons can be resolved at momenta far above kaon Cherenkov threshold in pfRICH aerogel. Therefore, a combined imaging and time of flight technique will provide a positive kaon identification in the whole momentum range, down to few hundred MeV/c.

	aerogel	HRPPD window
e/π separation	up to 0.75 GeV/c	up to 0.85 GeV/c
π/K separation	up to 2.50 GeV/c	up to 2.85 GeV/c
K/p separation	up to 4.20 GeV/c	up to 4.80 GeV/c

Table 3.45: Expected pfRICH time of flight based particle identification performance. Highest momenta at which 3σ separation for a respective pair of mass hypotheses can be achieved is quoted, for aerogel and HRPPD window radiators separately.

Hardware component evaluation: Hydrophobic silica aerogel manufactured by the Aerogel Factory [53] will be used for the radiator in the pfRICH detector. Three hydrophobic aerogel tiles, with nominal dimensions of 11 cm $\times$ 11 cm $\times$ 2.5 cm, density of 0.14 g/cm^3, and refractive index of 1.04, were ordered from the Aerogel Factory to verify and assess their refractive index and transparency. The refractive index was determined at Temple University by measuring the deflection of the refracted light exiting the corners of the aerogel (see QA section). The refractive index measured by Temple University (n_{TU}) and the Aerogel Factory (n_{AF}) were found to be in agreement, with a typical value of $(n_{TU} - n_{AF}) \,/\, (n_{AF} - 1) \sim 2\%$. The optical transparency was evaluated by measuring the transmittance as a function of wavelength. Transmittance curves for each tile were measured by the Aerogel Factory using a monochromator and spectrometer (Hitachi U-4100) [57], at BNL using a monochromator and spectrometer (Hitachi U-3210), and at Temple University using a LED and spectrometer setup which provides measurements at four discrete wavelengths (see left panel of Fig. 3.110). These three sets of measurements were found to be consistent with each other within the quoted errors. A sufficiently high transmittance of about 68.5% at 432 nm was found when averaging the results from three different measurements over the three produced aerogel tiles at Temple. The wavelength dependent transmittance measurements were used to extract additional information such as clarity, transmission length, and scattering length.

The mirrors will be produced by the pfRICH subsystem collaboration members, with substrates fabricated at Purdue University and coating performed at Stony Brook University. Optimization of the substrate and coating procedures is ongoing with a number of mirror samples being produced with different substrate manufacturing techniques, coating chamber settings, and coating material thickness. The reflectivity of the various mirror samples was evaluated at BNL using a dedicated test stand. The best performing mirror sample produced so far showed a measured average reflectivity of 0.89 for wavelengths between 300 and 600 nm (see right panel of Fig. 3.110).

Implementation

Services: Services relevant for the pfRICH include High Voltage (HV) and Low Voltage (LV) systems to operate the photosensors and power the front-end electronics, respectively, a cooling

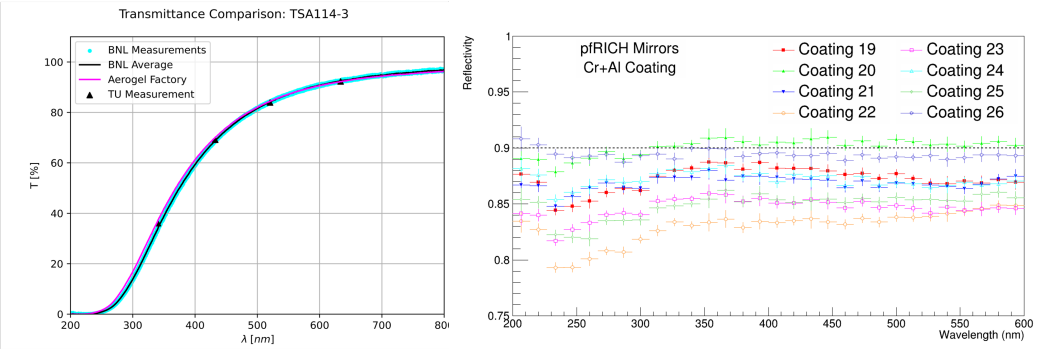

Figure 3.110: Left: Aerogel transmittance as a function of wavelength for factory, BNL, and Temple University measurements. Right: Mirror sample reflectivities as measured at BNL as a function of wavelength. (Figure documentation)

system to regulate the temperature of the electronics and sensors, and a gas system to maintain the proper environment inside the pfRICH vessel.

The HV and LV modules will be located on the electronics platform, about 15 meters away from the pfRICH detector, in a low Total Ionizing Dose (TID) environment. Therefore, standard off-the-shelf units can be used. The high-voltage system will consist of 340 individual stackable negative HV channels. Twenty three CAEN A1515BV 16-channel 1.4kV/1mA floating ground modules [58] will be used. The HV modules will be housed in a pair of CAEN SY4527 mainframes [59], equipped with additional 1200 W power module boosters. Each of the twenty three modules will be connected to an enclosed box distribution PCB installed on the rear side of the pfRICH vessel. The box is fed from individual 15 m long multi-conductor high voltage cables. For the HV interconnect, CERN-approved 52-pin Radiall cable connectors and receptacles will be used throughout the system. The distribution PCB will arrange five of the isolated channels of the A1515BV in a manner to provide five individual stacked voltage levels and a common ground referenced return to each HRPPD. The respective five bias levels and ground will be connected to the pads on the rear side of the HRPPDs via narrow profile Teledyne Reynolds shielded 26 AWG coaxial cables, conductive vias in the Front End Board (FEB) stackup with a matching pad pattern, and custom Samtec compression interposers.

Under the assumption that the FCFD ASIC will consume up to 3 mW/channel, this corresponds to 3 W power per photosensor FEB. Accounting for other electronics components present on such a FEB, and providing a 20% safety margin, we estimate the total power consumption to be less than 300 W for the whole system. This number is used as input for designing the cooling system discussed below. We will be using a single Wiener MPOD Mini LX crate with a MPOD-C controller and four MPV4008I1 4-channel LV modules [60]. One Low Voltage channel will serve four FEBs. 15 m long tray rated 10 AWG jacketed cables with 20AWG (sense wires) will run between the electronics platform and a LV distribution panel on the rear side of the pfRICH vessel. From there, 18 AWG multi-conductor cables will distribute power to the individual FEB cards.

The pfRICH cooling system will consist of several off-detector components and a few on-detector thermal interfaces and assemblies. The primary heat dissipating components will be the ASICs, which are anticipated to produce just over 1 W each (4 W per module), or about 300 W for the 68 total modules. In addition to the ASICs, the sensors are anticipated to dissipate just under 1.5 W each or 100 W total. Conservatively, the total power output will be roughly 400 W. Following the geometry, each row of sensors will have its own titanium cooling tubes in contact the ASICs. The tubes that contact the same row of sensors will be in series, and all rows will be in parallel with each

other. The tubes will be attached to aluminum plates with thermal epoxy, and a gap pad between the plate and ASIC will maximize thermal contact. Using a stock tube of 0.25" OD and 0.218" ID and maintaining a minimal temperature gradient in the water allows the mass flow rate to be calculated. From there the Reynolds number and pressure drop can be determined, confirming the viability of the system. Additionally, a finite element analysis (FEA) was performed to confirm the water temperature difference and determine the thermal gradient across the various components. With the described configuration, the sensors reach a maximum temperature of about 32 C in the analysis.

The three primary off-detector elements of the cooling system are a Polyscience chiller, Chilldyne circulator, and a distribution panel. The Polyscience chiller will allow the water to be slightly colder than room temperature, or about 15 C, which is the lowest recommended temperature without nearing the dewpoint in the interaction region. The unit is also capable of flowing about 10 liters per minute (lpm), dissipating about 800 W at that temperature and maintaining the temperature within +/-0.1 C. The Polyscience chiller would be paired with a Chilldyne negative pressure system capable of circulating water at about 8 lpm and $\sim$10 psi. It offers a significant advantage over a positive pressure solution, as if there is a leak in the system, it will draw air into the tube instead of letting water out and potentially damaging electrical components.

The gas system for the pfRICH detector is designed to circulate dry nitrogen at precise pressure and flow rates to remove moisture from within the pfRICH chamber. High-purity nitrogen (H_2O $<$ 3 ppm) will be supplied from cryogenic sources. To provide secondary protection, moisture traps such as silica gel dryers will be installed near the nitrogen source. The system will maintain both the required moisture levels and gas purity by ensuring that it is sufficiently gas tight and that the chamber is kept at a slight overpressure (4 mbar) above atmospheric pressure, preventing any infiltration of ambient air. A 0.5 μm filter will be added near the source to capture dust particles. A standby nitrogen source will be available to ensure continuous operation in the event of a primary source failure. To manage fluctuations in the source pressure, a digital pressure outlet controller will be used. Additionally, nitrogen flow will be regulated by a non-pressure-limiting digital mass flow controller. The nitrogen flow rate is expected to allow several complete volume exchanges per hour, with the precise rate to be finalized later.

Pressure inside the chamber will be controlled using a tank blanketing pressure regulator, which maintains a positive internal pressure relative to varying atmospheric conditions. An overpressure protection bubbler will serve as a safeguard against excessive pressure within the chamber. To ensure uniform nitrogen distribution and prevent localized air pockets, nitrogen will be introduced into the chamber at two locations near the top side of the pfRICH vessel, closer to the aerogel plane, and exhausted through two openings near the sensor plane at the bottom. All exhausted gases will be vented outside the experimental area. The entire gas system will undergo pressure testing at 1.5 times the operating pressure to ensure integrity. For monitoring and troubleshooting, pressure gauges and transmitters will be installed, with critical data such as chamber pressure and flow archived for reference.

Subsystem mechanics and integration: The shell that creates the volume of the detector will be made primarily of carbon fiber to optimize the radiation length in ePIC. Specifically, the sensor plane is intended to be made from a bulk carbon fiber layup at approximately 14.7 mm thick at its thickest point. The bulk carbon fiber will be molded and CNC-cut to allow for individual sensor frames and staves to be bonded in-place to create 68 sensor pockets along this plane of the detector. Each individual HRPPD sensor will be added into the sensor plane from the outside of the vessel and sealed in each of the sensor pockets with a face seal. The overall plane will be sealed to the cylinder at the outer and inner walls using a tightly spaced bolt-pattern and an o-ring groove on

the upstream end of the sensor plane to accommodate another face seal.

On the upstream end of the vessel, the aerogel plane will be made from a carbon fiber honeycomb layup around 1/4″ thick. The outer and inner circumferences of the aerogel plane will house a sealing ring made from bulk carbon fiber and an o-ring groove to create a face seal. Attached to this aerogel plane will be a web of carbon fiber that creates radial rows of pockets for the aerogel to be placed in. These tiles will be held into the pockets using a thin transparent line strung across the opening in order to contain them in place.

The cylindrical portion of the vessel includes identical end rings on the upstream and downstream end that house the threaded bolt holes and sealing surfaces for the sensor plane and aerogel plane face seals. These end rings are approximately 3/4″ (on the bolting surface) and 1″ in thickness (in the z-direction). They are made from bulk carbon fiber and contain threaded inserts that are placed by CNC-machining the insert locations and bonding and threading them into place. The rest of the cylinder is made from single sheets of carbon fiber on the inside and outside of the vessel, as well as a 3/4″ Nomex honeycomb layer in between.

The inner wall of the cylinder is created in a similar manner to the outer wall, namely a honeycomb construction with the end rings embedded into both ends for bolting and sealing to the aerogel and sensor planes. However, the shape of the inner wall is made such that there is 5 mm of clearance (radially) from the beam pipe flange that the pfRICH will need to pass by to be installed in ePIC. This makes the shape of this inner wall similar to an egg or an avocado.

Lastly, the conical mirrors are designed such that they are attached solely to the sensor plane. This is being done to ensure that the mirrors can be controlled in relation to the sensors and will be unaffected by manufacturing misalignments and tolerance stack-up issues throughout the rest of the vessel. As such, they will hang cantilevered perpendicular to the sensor plane for both the inner and outer mirrors. The outer mirrors will be concave and the inner mirrors will be convex. The construction will be a combination of a molded, bulk carbon fiber base with a bonded Lexan sheet on top of it (which will have been coated with a mirror film).

Once the pfRICH has been fully assembled and is ready to be placed in the overall ePIC detector, it will be moved around the assembly hall on a cart. The cart will integrate lifting eyelets for the installation of the pfRICH into ePIC, rails identical to its final location, and wheels to transport, store and work on the detector when it is out of the barrel. This tooling will allow us to lift the cart with the pfRICH secured in place with the crane in the detector hall, position it against the barrel, align the rails, and transfer the pfRICH into its final position by translating it along the z-axis.

Calibration, alignment and monitoring: A laser-based system will be used to monitor the pfRICH performance throughout its operational life. The purpose is to monitor, on a pixel-by-pixel basis, the single photon timing resolution, the single photon pulse hight amplitude (HRPPD gain), HRPPD QE, and the relative delays between channels on a few ps level. The system will also monitor the reflectivity of the conical and pyramidal mirrors. To measure the timing resolution, an array of six fibers is introduced inside the detector volume from the aerogel side which casts a broad profile of low-intensity light onto the sensor plane such that each HRPPD pixel accumulates some number of single photon hits after a given number of laser pulses. Similarly, a separate array of six fibers is arranged such that emitted photons reflect off of the outer mirror surface before impinging on the HRPPDs. In this case, the single photon counting rate is monitored for any degradation over time, which would indicate the deterioration of either the photocathode quantum efficiency or mirror reflectivity, or both.

The pfRICH monitoring system deploys a picosecond PiLas laser which produces a 405 nm laser

beam with a nominal $\sim$ 45 ps pulse width. The beam is coupled to a custom 1-to-14 optical fiber splitter by Thorlabs, that evenly distributes the light into arrays of fibers routed into the detector vessel. Two additional fibers are connected to silicon photodiodes to provide laser signal quality verification and an initial timestamp (t_0). A custom-sized 5 mm $\times$ 5 mm engineered diffuser is used to generate a uniform 50° square pattern to optimize the intensity profile emitted from each fiber. Additionally, a fiber delay line is added to each fiber branch to provide the ability to easily separate out in time photons originating from a given fiber. In all, there are three sets (segments) of fibers downstream of the splitter that deliver photons from the laser to the detector vessel: delay fibers, long extension fibers, and fibers mounted permanently inside the detector vessel. Finally, multiple fast photodiode sensors are used to sample the laser light before and after the splitter to monitor the light output intensity and the timing performance.

A relative alignment of the conical mirror segments inside of the vessel, and surface mapping will be performed on a fully assembled detector (up to the front wall removed) prior to the installation in ePIC, by using a 3D scanning system which is being built now for the purposes of first article mirrors QA assessment. The vessel as a whole will be aligned in ePIC after the installation, following a generic procedure developed by EIC engineers for all detector subsystems. Appropriate survey targets will be mounted on the rear and barrel sides of the vessel if required.

Status and remaining design effort: As shown in the previous text, the present pfRICH design fully meets the EIC Yellow Report requirements and subsequent amendments (see performance section):

- Pseudorapidity coverage from -3.5 to -1.5 in the electron-going endcap
- π/K separation on a 3σ level up to 7 GeV/c in this whole acceptance
- $\sim$20 ps timing reference for ePIC ToF subsystems in the barrel and the forward endcap by combining single photon signals from aerogel and signals from multi-photon flashes of Cherenkov photons produced by charged particles in HRPPD fused silica windows

  R&D effort: The pfRICH design is based mostly on proven technologies, therefore, the remaining R&D effort is limited to HRPPD aging studies, which will be performed at BNL, JLab, and INFN Trieste by the end of 2026.

  E&D status and outlook: Several engineering design activities and first article productions described earlier in the text in more detail have been performed in FY24/FY25, and will continue into FY26:

  - Full size mirror production and quality assessment
  - First article pfRICH vessel outer shell production
  - Adjustments of the production process of CFRP-based parts, mirror substrates and HRPPD pockets in the sensor plane in particular
  - Fine tuning of the aerogel refractive index and bulk uniformity measurement procedure
  - HRPPD sensor design modifications required after the first batch was produced
  - HRPPD performance confirmation in the $\sim$1.3 T magnetic field typical for a pfRICH location in ePIC

  Other activity needed for the design completion: The readout backplane design cannot be fully completed at this stage because of the unavailability of a final design iteration of the anticipated FCFD ASIC chip.

The performance of the pfRICH in its anticipated configuration needs to be confirmed in a beam test for both Cherenkov photon imaging and timing in the whole momentum range required for e/π, π/K and K/p separation. Such a beam test will be performed with electron and hadron beams at Fermilab in 2026 (contingent on facility availability), with an extensive use of first article components (outer vessel shell, aerogel, mirrors, HRPPDs).

Status of maturity of the subsystem: The design of the pfRICH subsystem is in a fairly mature state. As described in previous sections, the pfRICH consists of a cylindrical vessel with two endcap plates, an aerogel tile plane, an HRPPD sensor plane with onboard electronics, mirrors and a number of subsystems (HV and LV, cooling, gas, light monitoring). Engineering design of all of these components (except for the HRPPD ASIC backplane for the reasons stated above) is by now sufficiently advanced to be more than 60% ready by the CD-2 EIC Project phase at the end of FY26.

Environmental, Safety and Health (ES&H) aspects, Quality Assessment (QA), and Construction and assembly planning: The environmental, safety, and health impacts of the pfRICH subsystem are expected to be minimal. When installing and integrating the pfRICH into the overall detector, all applicable safety standards (i.e. OSHA, Critical Lift procedures, etc.) will be followed and adhered to. Furthermore, the composition of the vessel itself consists mainly of carbon fiber, epoxy, and plastic and any (small) excess can be retained for future use or disposed of via standard waste streams. The operation of the detector will require a modest 400 watts of cooling power and the working gas is pure nitrogen which does not pose any greenhouse concerns.

The individual HRPPDs, mirrors, and aerogel tiles used in the pfRICH will all undergo rigorous quality assessment (QA) checks to ensure that their operation and/or properties are within acceptable limits. Beyond the testing done by the manufacturer, the performance of individual HRPPDs will be evaluated using test stands located at BNL, JLab, and possibly Yale University. While the details of the test stands differ, they all consist of a light-tight enclosure to house the HRPPD, a fiber-coupled light source (either a pulsed laser or a monochromator), an optical assembly to focus the light onto the sensor, power supplies, and readout electronics, see Fig. 3.111 (left) as an example.

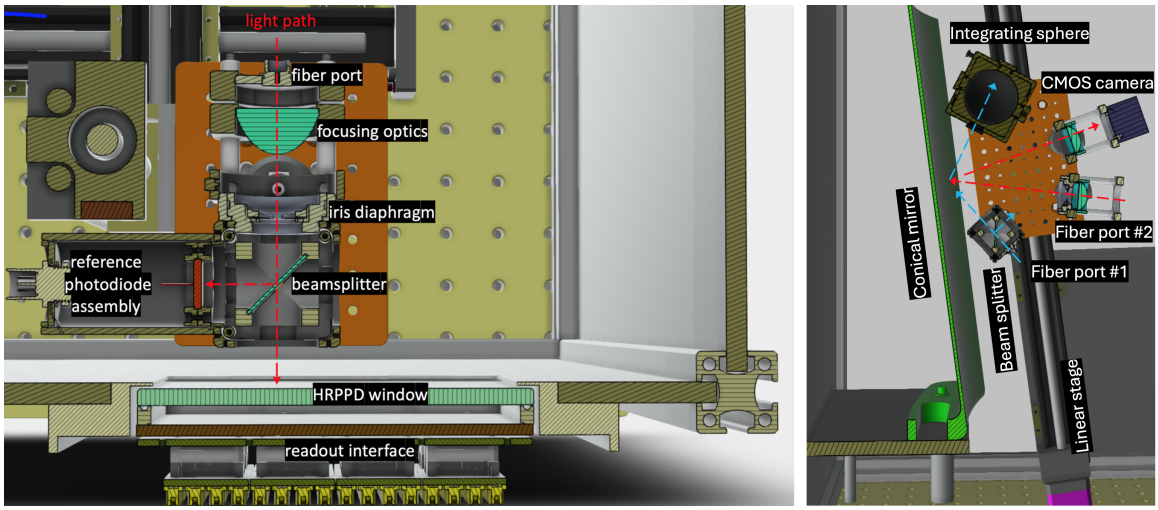

Figure 3.111: Left: optical setup of an existing HRPPD QA station at BNL. Right: optical table of the future full size mirror QA station at BNL. See text for more details. (Figure documentation)

The gain uniformity, quantum efficiency, photon detection efficiency, and dark count rates will be determined over the entire active photosensor area. In addition, the use of a Menlo Systems Elmo 780 femtosecond laser at BNL will allow precision determination of the timing characteristics of the sensors.

The reflectivity of the mirror samples produced at SBU will be determined using a dedicated test stand at BNL, see Fig. 3.111 (right). The setup will consist of a large dark box with a mirror sample stand, multi-functional optical table assembly and motion control hardware implemented as a combination of rotary and translation stages.

Blue arrows in Fig. 3.111 (right) show the light path of the reflectivity measurement setup. Light from a halogen/deuterium arc lamp source located outside of the dark box will be fed via fiber with a collimating lens to a beam splitter which directs a fraction of the light to a reference photodiode and passes the remaining beam to the conical mirror sector. Reflected light gets collected in the integrating sphere and then fiber coupled into a compact spectrometer, providing a capability to measure the whole wavelength spectrum of interest at once. The reflectivity will be determined by taking the ratio of the wavelength spectra of the conical mirror under study and a calibrated small flat stock mirror located next to it. Variations in the light source intensity will be corrected using the reference photodiode.

Red arrows show the optical path of a 2D surface mapping setup. A monochromatic light will be directed onto a focusing lens through a single mode fiber with a few micron diameter core. The image of this point-like source after a reflection off the conical mirror surface will be focused onto a CMOS camera sensor. Transverse displacement of this image when the optical head is moving along the mirror surface in azimuthal and lateral directions is a measure of deviation of the mirror surface from an ideal conical shape.

The aerogel quality assessment will be performed at Temple University and include assessments of the refractive index, transparency, uniformity and mechanical specifications. So far, the refractive index has been determined by measuring the deflection of the light passing through the corner of the aerogel tile, following the procedure described in Ref. [61]. Work is currently underway to develop a setup and approach that is based on measuring changes in the polarization between the light incident on the aerogel and the light that is reflected from its surface. This would allow for localized refractive index measurements to ensure not only the aerogel has the proper mean refractive index, but also its uniformity across the whole tile. Transparency QA will make use of wavelength dependent transmittance measurements carried out using a newly commissioned and validated UV/VIS LED-spectrometer system. The transmittance data will be fitted with the Hunt Formula [62] to extract aerogel properties such as the scattering surface coefficient and clarity, as well as the wavelength dependent properties which include the transmittance, transmission length, and scattering length. The density will be calculated by measuring the aerogel mass using a precision scale (100 μg) and volume via caliper and touch probe. Reference jigs can be made to ensure that the aerogel mechanical specifications such as the side-to-side length, tile height, and surface planarity variations are within acceptable ranges.

The structural components of the pfRICH including the cylindrical vessel, end rings, sensor plane and aerogel wall will undergo metrology evaluations during and after construction to ensure all dimensions are within tolerances. The pfRICH has been designed such that it can be fully assembled and inserted into ePIC in one piece. Individual components such as vessel walls, sensor and aerogel planes, mirrors, HRPPDs, and aerogel tiles will be manufactured and tested at various locations and then shipped to BNL for final assembly. It is envisioned that final subsystem assembly will take place in a cleanroom or dedicated lab space within the physics building at BNL. Once assembled, the pfRICH will be transported by truck roughly 1.3 miles to the experimental hall where

it will be integrated with the other ePIC subsystems.

The assembly of the pfRICH itself will proceed via the following general steps: (1) assemble the aerogel plane by fastening it to the outer and inner walls, (2) place the sub-assembly such that the upstream end is facing down, (3) add aerogel tiles and aerogel retaining system into the aerogel plane, (4) pre-assemble most of the sensor plane by affixing the inner and outer mirrors and any vessel services (i.e. inner gas tubing, laser monitoring system, etc.) to the sensor plane, (5) lift the sensor plane over the rest of the vessel and lower the sensor plane and mirrors into place, (6) fasten the sensor plane to the subassembly at the inner and outer walls, completing the cylindrical vessel, (7) systematically insert and secure the individual HRPPD modules into the back of the sensor plane, (8) lift the completed pfRICH, rotate it into its operating position, and install it onto the transportation/storage cart.

Collaborators and their role, resources and workforce: The pfRICH Detector Subsystem Collaboration (DSC) member institutions, as well as other affiliated groups are listed in Tab. 3.46, along with their anticipated commitments.

Table 3.46: Institutions contributing to the pfRICH effort and their roles and resources. Starred entries indicate no institutional commitment.

Institution	Nation	Activities	Resources for Construction / QA
Brookhaven National Lab	USA	Project Lead HRPPD and mirror testing Gas Systems DAQ Detector and physics simulation	HRPPD test stands (pico/femtosecond laser, dark box with translation stages, high-performance scope, waveform digitizers) Mirror test stands (monochromator, spectrometer) Sample temperature control chamber
Chiba University*	Japan	Connection to aerogel factory	Aerogel production equipment
Duke University	USA	Detector modeling	
INFN Genova*	Italy	HRPPD B-field studies	
INFN Trieste*	Italy	Detector modeling HRPPD aging and B-field studies	HRPPD test stand (laser, dark box, waveform digitizers)
Jefferson Lab*	USA	Mechanical design EIC Project support HRPPD testing	HRPPD test stand (laser, dark box, translation stages, digitizers)
Ljubljana University & JSI*	Slovenia	Expert input on detector design	
Mississippi State University	USA	Laser monitoring system	
Purdue University	USA	Vessel and mirror fabrication	Machine shop and fabrication lab
Stony Brook University	USA	Vessel fabrication Mirror coating	Mirror coating chamber Vessel form
Temple University	USA	Aerogel testing and QA	Aerogel test stand
University of Debrecen	Hungary	HRPPD backplane design and fabrication	
University of Glasgow	United Kingdom	MCP-PMT evaluation	MCP-PMT test stand (laser, dark box, cosmic ray stand, electronics)
Yale University	USA	Software support HRPPD QA	HRPPD test stand (dark box with translation stages, digitizers)

Technological Challenges and Path Forward: A reliable large area highly pixelated photosensor with a high quantum efficiency and single photon timing resolution better than $\sim$50 ps is a core component of the pfRICH design. The pfRICH team, together with the EIC eRD110 consortium (Photosensors) has been routinely working with one of the two manufacturers remaining

on the market (Incom Inc.) for several years to help the company re-design their HRPPD sensors so they fully meet EIC specifications. The ongoing evaluation of the first seven EIC HRPPDs produced in 2024 shows that overall quality, as well as reproducibility of parameters verified so far (quantum efficiency in particular) meet the requirements. As a fallback photosensor solution, we consider Photek Auratek MCP-PMTs.

Aerogel tiles of required quality can be produced in a very few places worldwide. The pfRICH team, together with the EIC Project, has been routinely working with the Aerogel Factory in Japan over the last two years, to make sure the quality and production capacity meet our requirements. A technical lead of the Chiba Aerogel Factory in Japan is also a member of the pfRICH DSC, see Tab. 3.46. Our simulations show, that in case Aerogel Factory cannot produce sufficiently large tiles to cover the whole front wall of the vessel in a configuration with three radial bands as shown in Fig. 3.105, one can resort to using tiles of a readily available size up to 145 mm in a four-band configuration, with an acceptable loss of performance caused by additional dead area introduced by an extra row of radial spacers between the tiles.

3.3.4.3 The high performance DIRC

Requirements

Requirements from physics: The PID system in the central section of the ePIC detector must provide at least 3 standard deviations of separation of π/K up to 6 GeV/c, and contribute to low momentum e/π identification.

Requirements from Radiation Hardness: The anticipated radiation dose in the hpDIRC optics and its potentially sensitive readout electronics are predicted to be modest. These estimates are based on minimum-bias 10×275 GeV e+p events from PYTHIA. The maximum machine luminosity over a six-month period of annual operation at 100% machine and detector efficiency for a total of 10 years was assumed. Under these conditions, the total dose from electromagnetic and hadronic radiation is expected to be less than 100 rad. The 1-MeV-neutron-equivalent fluence is expected to reach 10^{10} neutrons per cm^2.

Requirements from Data Rates: The expected hit rate of 25 kHz per cm^2 for the hpDIRC was estimated using detailed Geant4 simulations, incorporating the Pythia event generator. This estimation assumes the baseline MCP-PMT sensors, which typically have a dark count rate of approximately 1 kHz per cm^2, or 0.09 kHz per pixel.

Justification

Device concept and technological choice: A radially compact detector based on the DIRC (Detection of Internally Reflected Cherenkov light) principle, a specialized type of RICH counter, is appropriate. It employs solid, long, rectangular-shaped radiators made of synthetic fused silica, which also serve to guide the Cherenkov photons to outside the central region for readout. This design allows the active radiator section to remain radially compact, minimizing its impact on the performance of neighboring systems and simplifying the system integration.

The photons are recorded by an array of pixelated photon sensors mounted on the back of the expansion volume. As a result of the excellent optical finish of the optical components, the emission angle of Cherenkov photons with respect to the particle track is maintained during the photon transport via the total internal reflection. This angle can be reconstructed for each track from the measured position of the photon on the detector surface and the measured arrival time of each photon.

The general concept of a barrel DIRC detector was first successfully demonstrated by the BaBar DIRC and followed by several other experiments worldwide. The ePIC high-performance DIRC (hpDIRC) takes advantage of the lens-based focusing concept of the PANDA Barrel DIRC, and has also several other advancements to meet the performance requirements of the Electron-Ion Collider (EIC). The hpDIRC concept for ePIC was developed as part of the EIC generic R&D program performed by the EIC PID collaboration (eRD14) and direct EIC Project R&D eRD103 with the focus on extending the momentum coverage well beyond the DIRC counter state-of-the-art at that time.

Subsystem description:

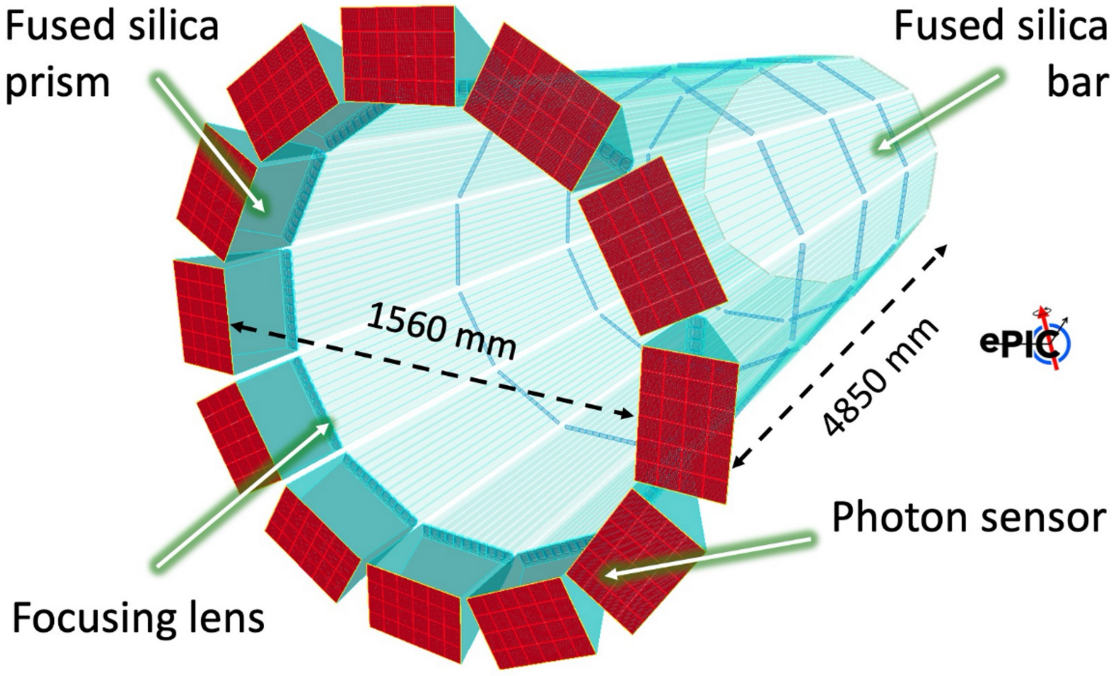

Figure 3.112: ePIC hpDIRC geometry in the Geant4 standalone simulation.

General device description:

The baseline design of the ePIC hpDIRC detector, as implemented in a detailed and test beam-vetted Geant4 simulation, is shown in Fig. 3.112. It is divided into twelve optically isolated sectors, each composed of a bar box and a readout box. These 12 sectors surround the beamline in a 12-sided polygonal barrel with an inner radius of about 760 cm. Each bar box includes ten radiator bars, each made of synthetic fused silica and with a length of 4850 mm and a cross-section of 17 mm $\times$ 35 mm. The bars are placed side-by-side, separated by small air gaps, inside the light-tight bar box. Mirrors are attached to one end of each bar to reflect the Cherenkov photons towards the other (readout) end. At the readout end they exit the bar and are focused by a 3-layer spherical lens on the back surface of the prism which serves as an expansion volume.

Bars:

The baseline ePIC hpDIRC design envisions that the 120 long bars needed will be composed of three refurbished BaBar DIRC bars and one shorter new bar manufactured by industry. The number of bar boxes and bars per box has been optimized to the width of the BaBar DIRC bars while maximizing the azimuthal acceptance of the hpDIRC. This approach assumes that the BaBar bars can be safely extracted from the Babar boxes without compromising their optical and mechanical integrity. The disassembly and evaluation of the BaBar bar boxes are currently underway. Final information on the availability of BaBar bars for ePIC is expected by 2026.

Lenses:

The 3-layer spherical focusing lens is a novel component of the hpDIRC and is essential for achieving the PID performance ePIC requires. The lens design, shown in Fig.3.113, avoids the dramatic photon loss caused by air gap transitions in standard lens systems. It does

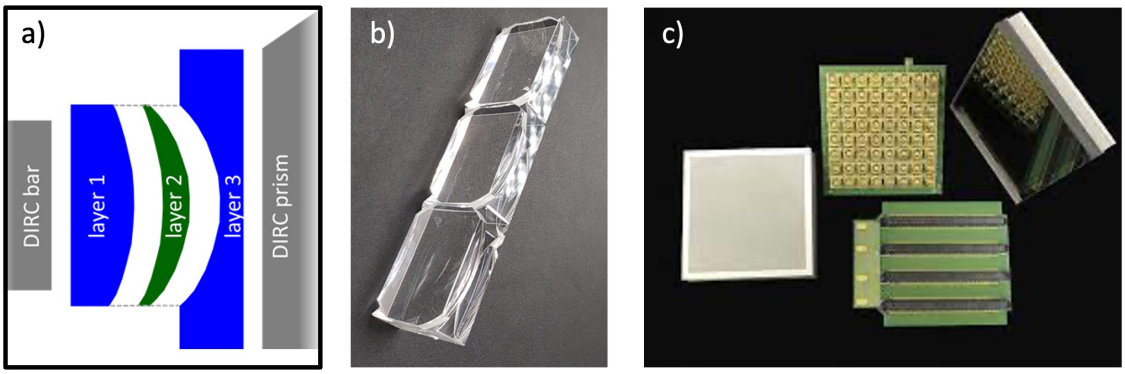

Figure 3.113: a) Schematic of the side view of one hpDIRC section and an exploded view of the 3-layer lens. b) Photo of prototypes of the 3-layer spherical lenses. c) Photec AuraTek MAPMT253 MCP-PMT.

this by focusing Cherenkov light through refraction at the interface between synthetic fused silica and a high-refractive-index material, such as sapphire or lanthanum crown glass. A thin layer of the high-refractive-index material is sandwiched between two layers of synthetic fused silica, with carefully optimized radii of curvature on all spherical surfaces. This design combines defocussing and focusing transitions to form a flat detector plane that accommodates a wide range of photon angles, matching the layout of the sensor array on the expansion volume prism. Several prototypes using different materials for the middle layer have been produced by the optical industry, and an example of a prototype lens is shown in Fig.3.113b.

Prisms:

The prism expansion volume is made of synthetic fused silica, has a 32° opening angle, and dimensions of 237 mm × 350 mm × 300 mm. The detector plane of each prism is covered by an array of 24 sensors shown in red in Fig. 3.112.

Sensors:

The photosensors attached to the rear of the prism record the positions and arrival times of the Cherenkov photons. In the baseline design of the hpDIRC, commercial microchannel-plate photomultiplier tubes (MCP-PMTs) with a pore size of 10 µm or smaller were assumed. A pixel size of 3.2 mm was chosen based on Geant4 simulations as a balance between cost, performance, and expected availability as the sensor technology for the hpDIRC. Lifetime-enhanced 2″ MCP-PMT tubes are commercially available from Photonis and Photek with suitable DC-coupled anode configurations. The simulation utilized Photonis Planacon XP85122 MCP-PMTs, incorporating realistic sensor characteristics including photon timing, collection efficiency, and quantum efficiency. With the termination of the production of the Photonis PMTs, the Photek MAPMT 253 sensors shown in Fig. 3.113, have been adopted as the baseline photosensor for the hpDIRC. These sensors share the same mechanical footprint and are expected to exhibit comparable performance characteristics to the Photonis tubes. High Rate Picosecond Photon Detectors (HRPPDs), currently under development by Incom, are the baseline sensor for the pfRICH detector in ePIC and are also being considered as an alternative option for the hpDIRC. Adopting a common sensor for both systems would offer significant advantages in terms of cost efficiency and streamlined integration efforts. To support an informed decision, several experimental setups are being used to conduct direct, side-by-side performance comparisons of the two sensor options, with the goal of selecting

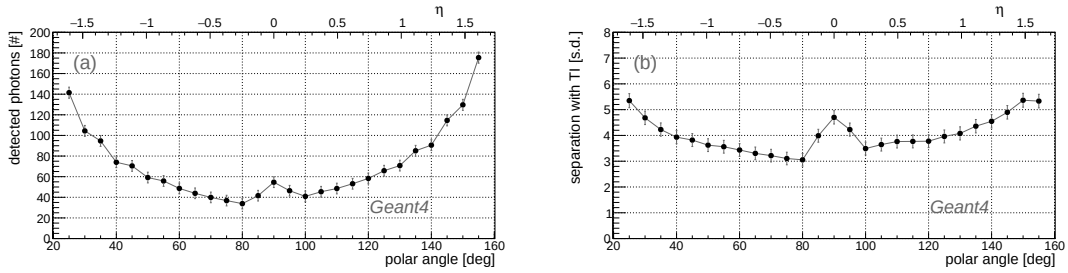

Figure 3.114: The expected performance of the hpDIRC as a function of the particle polar angle in terms of photon yield (a) for pions and π/K separation power (b). These results are based on a standalone Geant4 simulation of 6 GeV/c particles. Repository: https://github.com/rdom/eicdirc/tree/master/macro/tdr_hpdirc

a unified solution for both subsystems within ePIC. More details on the HRPPD option can be found in pfRICH section 3.3.4.2.

FEE: Fast ASIC-based readout systems are being developed by the EIC project to meet the demands of various ePIC detector systems. For the hpDIRC, the readout electronics must be capable of detecting small signals (on the order of a few millivolts) from MCP-PMTs while maintaining excellent single-photon timing resolution. Additionally, the electronics need to match the channel density and sensor footprint, as they will be directly coupled to the back of the sensor to minimize distance and achieve optimal timing precision. The leading candidate for hpDIRC readout is FCFD, which is discussed in detail in Section XXX.

Performance Figure 3.114 presents the expected performance based on standalone Geant4 simulation studies with a tracking angular precision of 0.5 mrad at 6 GeV/c. The plots illustrate particles that are fired over a range of polar angles but with an azimuthal angle fixed at zero degrees (so perpendicular to one of the middle bars). The points represent the photon yield and separation power for 6 GeV/c charged pions and kaons as a function of polar angle with the realistic ePIC magnetic field.

The number of detected Cherenkov photons per particle (Fig. 3.114a) ranges from 40 to 150, depending on the polar angle. The sharp increase in photon yield at steeper forward and backward angles is due to the longer track lengths in the fused silica bars, with an asymmetry in forward/backward yields resulting from photon loss due to longer propagation paths at smaller polar angles. The peak in the photon yield near a polar angle of 90° occurs because a larger fraction of the photons satisfy the total internal reflection criterion near perpendicular incidence, compared to slightly larger or smaller angles.

The "separation power" for both particle hypotheses (Fig. 3.114b) is obtained from Gaussian fits to the log-likelihood differences between pairs of particle hypotheses. It is calculated as the difference between the means of the two Gaussians divided by the arithmetic average of the two widths. The slightly improved performance for polar angles above 100° is due to shorter photon paths, resulting in higher photon yields and reduced chromatic dispersion in the bar material.

Similar studies were conducted for electron-pion (e/π) separation, which is primarily the responsibility of the Electromagnetic Calorimeter. However, the hpDIRC can further improve the performance at low momentum. At lower momenta, multiple scattering is severe, but assuming ePIC achieves the tracking resolution described in the Yellow Report, the hpDIRC can provide a 3 standard-deviation separation power up to 1.1 GeV/c.

The expected particle identification (PID) performance of the hpDIRC thus surpasses the ePIC PID goal, achieving more than 3 standard deviations of separation power for e/π identification up to 1.1 GeV/c and π/K separation up to 6 GeV/c across the entire polar angle range.

Performance Systematic Studies Most of the hpDIRC performance studies were conducted using a particle gun, providing precise control over the parameters under investigation while covering the entire required angular and momentum ranges. Detailed studies examined a range of azimuthal angles to measure the performance across the full width of the bar box. While a moderate performance deterioration was observed in some of the non-central bars, the system maintained the required 3-standard-deviation separation power. The effect of the magnetic field on hpDIRC performance was found to be negligible, as confirmed through simulations that incorporated a realistic ePIC magnetic field map.

Additionally, studies using PYTHIA-generated physics events were performed to assess the frequency and effect of multiple tracks per event within an hpDIRC module and with one bar. Even in the extremely rare cases where two or more particles are very close in momentum, polar, and azimuthal angles within a single event, the impact on performance was found to be moderate, demonstrating the robustness of the hpDIRC system.

Simulation tools and validation A detailed standalone Geant4 simulation, featuring realistic geometry and material properties, was developed in collaboration with the PANDA Barrel DIRC group and validated through modular prototype tests using particle beams at CERN. The simulation incorporates measured values for MCP-PMT quantum efficiency, collection efficiency, and timing resolution. It also accounts for the coefficient of total internal reflection of the DIRC radiator bars as a function of photon energy, the bulk transmission of the bars, glue, and lenses, as well as the wavelength-dependent refractive indices of the materials used, the photocathode, and the reflectivity of the mirrors. Background contributions from hadronic interactions and delta electrons in the bar, along with effects from MCP-PMT dark noise and charge sharing between anode pads, were also simulated.

All relevant resolution factors for hpDIRC performance are modeled using Gaussian smearing with conservative resolution assumptions. The total timing precision per photon, including sensor and readout electronics, is assumed to be 100 ps, and the angular resolution of the ePIC tracking system at the hpDIRC radius is assumed to be 0.5 mrad for particles with a momentum of 6 GeV/c for all studies. However, the simulation software is prepared to import and integrate a more detailed tracking parametrization when it becomes available.

Detailed hpDIRC PID Look-Up-Tables (LUTs), including the threshold mode, were generated using Geant4 simulations. These LUTs are now employed to streamline physics analyses without the need for full reconstruction.

Figure 3.115 presents photos of the modular PANDA Barrel DIRC prototype along with results obtained during the 2018 test beam campaign at CERN. Although the PANDA prototype differs significantly from the ePIC hpDIRC in terms of geometry (single bar), slower readout electronics, and lower-quality sensors with larger pixels, the studies and results are highly valuable for hpDIRC development. The same software used for all ePIC hpDIRC performance studies was employed to successfully reproduce the PANDA prototype test beam results. As shown in Fig. 3.115c and d, the agreement between the simulation and experimental data is excellent. Note that the same-size BaBar DIRC bar and the same 3- layer spherical lens prototypes were used as in ePIC.

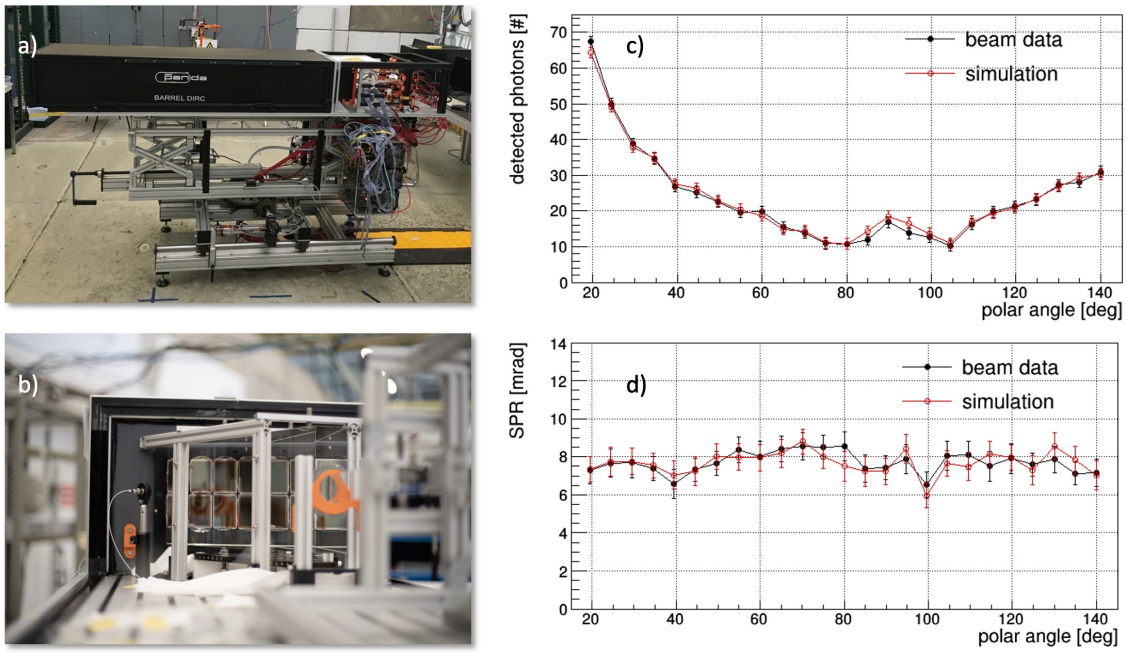

Figure 3.115: Photographs of the PANDA Barrel DIRC prototype (a), including a close-up of the readout section (b) taken during the CERN test beam. Performance plots illustrating the comparison between simulated and experimental data for photon yield (c) and single photon Cherenkov angle resolution (SPR) (d).

Reconstruction methods The hpDIRC utilizes two primary reconstruction methods for identifying particles based on Cherenkov photon detection: geometric reconstruction and time-based imaging reconstruction. These methods translate the detected photon patterns into meaningful physical information, particularly the Cherenkov angle, which allows direct particle identification.

Geometric reconstruction in DIRC detectors is based on determining the Cherenkov photon direction from the relative location of the radiator readout end and the pixel hit by the photon. This method allows direct reconstruction of the Cherenkov angle for each detected photon by utilizing both the photon direction and the beam particle direction. Photon directions in the prism are pre-calculated using full simulations, taking into account the optical materials, and stored in look-up tables (LUT). Discrete ambiguities arise due to photon reflections within the optical system, but these can be reduced by applying a cut on the difference between the expected and measured photon arrival times. The geometric method relies on the photon position, and only uses timing information to suppress ambiguities and background. The geomtrical method also provides key performance variables such as the single-photon Cherenkov angle resolution, and the number of signal and background photons.

The time-based imaging reconstruction method greatly enhances the particle identification (PID) by fully utilizing both the timing and position information of the detected photons. This method compares the measured photon arrival times to expected distributions for each particle hypothesis, stored as probability density functions (PDFs) derived from experimental or simulated data. For each photon, a time-based likelihood is calculated, which is then combined with the Poissonian PDF of the number of detected photons to provide the likelihood.

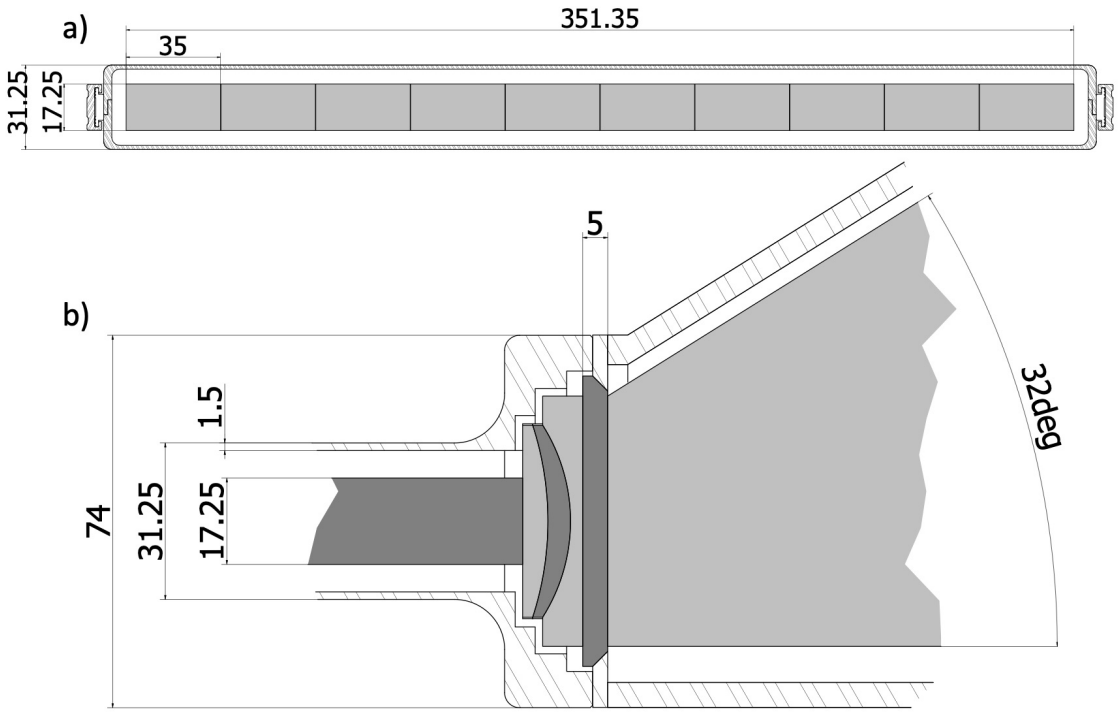

Figure 3.116: Technical drawings of the ePIC hpDIRC detector, showing the XY cross-section of the bar box (a) and the YZ cross-section of the connection between the bar box and the readout box (b).

Implementation

Subsystem mechanics and integration: The hpDIRC consists of two primary sub-assemblies: the readout section and the bar section. Both sections are composed of 12 boxes made of carbon fiber reinforced polymer (CFRP), with varying thickness depending on the stresses expected in different regions.

The readout section includes the fused silica expansion prism, readout sensors, and front-end electronics. The expansion prism has an angle of 32° and maximum dimensions of 300 mm in length, 352 mm in width, and 237.5 mm in thickness. The MCP-PMTs are coupled to the 352 mm x 237.5 mm back face of the prism using silicone cookies. The sensors and associated readout electronics are mounted onto a 3D-printed frame. The rear of the readout box is sealed with a light-tight plate with ports for cables, fibers for calibration lasers, and monitoring cameras. Dry nitrogen gas is flowed through the readout box to keep the prism surface clean and free from dust and condensation. To maintain stable temperatures and cool the electronics, water circulates through tubing thermally coupled to the heat sources.

The bar box is composed of a top and bottom shell with overall dimensions of 4627 mm in length, 368 mm in width, and 31.25 mm in height. Figure 3.116a shows a dimensioned view of the *XY* cross-section of the hpDIRC bar box. The thicker part of the carbon fiber shell on the sides will be used during installation to slide in the bar box and hold it in place. The carbon fiber thickness is 1.5 mm except for the 3 mm sides.

Each bar box contains 10 long radiator bars, lenses, and mirrors. The radiator bars are 35 mm wide, 17.25 mm thick, and 4580 mm long, spaced 0.15 mm apart using shims to ensure optical isolation. Each long radiator bar is made up of four shorter bars bonded together with an optically transparent adhesive, similar to the BaBar DIRC construction. Three of the shorter bars, each 1225 mm long, are repurposed from the BaBar experiment, while the fourth is newly manufactured to meet the ePIC total length requirement of 893 mm. The length of the light-guide can be adjusted, based on integration constraints with no impact on the hpDIRC performance.

At one end of each long bar, a 3 mm-thick flat mirror reflects photons back toward the readout end. At the opposite end, a three-layer lens is attached to the bar using the same adhesive used to join the short bars. The lens-mirror-bar joints are kept in compression by adjustable spring plungers located behind the mirrors, which reduce stress on the joints and prevent movement during installation, and operation. The spring system also compensates for differential thermal expansion and contraction rates between the bars and the bar box. Each short bar is supported by two pairs of fixed nylon buttons along its length, which minimize stress on the glue joints and reduce photon loss by reducing contact with the radiator surface. Eight support pairs are evenly distributed along each long bar's length, with adjustable spring buttons pressing the bars against the fixed buttons to maintain secure positioning while preserving the optical isolation. Similar support mechanisms are used for the 17.25 mm-thick end of the bars, where all 10 bars are pressed against a single set of fixed buttons. To handle the additional stress at the button locations and accommodate holes for the spring buttons, the CFRP is locally thickened at these points. Like the readout boxes, the bar boxes are also flushed with dry nitrogen to protect the radiator bars surfaces with nitrogen introduced at the mirror end and vented near the lenses.

The hpDIRC consists of 12 bar boxes and 12 readout boxes. The lenses at the bar box end are coupled to a thin window that seals the box, while this window is in turn connected to the prism in the readout box using an silicone cookies during final installation. The readout box, including the prism, is compressed against the bar box window to form a tight optical seal. Figure 3.116b is a dimensioned view of the XZ cross-section of the connection between the bar box and the readout box. The 5 mm-thick window between the 3-layer lens and the prism represents an initial design, which may be adjusted following further studies of strains and forces acting on the system.

The hpDIRC is positioned radially just inside the Barrel Electromagnetic Calorimeter (BIC) and just outside the outer Micro-Pattern Gas Detector (MPGD) within the ePIC detector. Both the bar boxes and the MPGD are supported by the EM Calorimeter via rails mounted on triangular brackets extending radially inward from the calorimeter's inner surface.

Installation: During installation, the bar boxes are placed on a specialized lifting fixture, allowing them to be rotated into their final orientation before being transferred along rails into their designated positions. The readout boxes are supported by an external ring attached to the Hadron Calorimeter via a series of legs. Each readout box is aligned with its corresponding bar box using specialized brackets and rails, which allow the readout box to be slid into position, compressing the optical interface and forming the connection. This rail system also enables the readout boxes to be removed without disturbing the bar boxes, if necessary.

Services: Gas and Moisture Control: To maintain a low-moisture environment for the bars, dry nitrogen gas from liquid nitrogen boil-off will flow through each box. The nitrogen gas will be monitored for humidity and filtered through a molecular sieve and mechanical filters to remove particulates.

Power Supply and Monitoring: High-voltage supplies will be provided for each MCP-PMT sensor.

A control and monitoring system will be implemented for the readout and bar box sections. The high voltage required for each MCP-PMT will be supplied by commercially available multichannel power supply modules in crates located outside the experiment.

The low-voltage power supplies, which regulate power to the front-end electronics (FEE), need to be placed as close as possible to the detector, in racks dedicated to the hpDIRC system. A modular, multichannel approach—similar to the high-voltage system, is planned for the control and monitoring of voltages, currents, and onboard temperatures for all FEE boards. The low voltage levels will be below 50 V, with currents reaching several Amperes.

Cooling System: The highly integrated FEE design generates a significant amount of heat in the compact readout unit. This heat will be extracted by a water cooling system, and the necessary supply lines are included in the mechanical design of the readout boxes, although further optimization is required.

Environmental Monitoring: Standard commercial devices will monitor environmental parameters such as temperature and humidity at various locations inside the hpDIRC volume to ensure optimal performance and safety.

Calibration, alignment and monitoring: Time Calibration: To achieve the time resolution required for the hpDIRC, it is essential to eliminate time offsets between pixels, which may arise from differences in cable lengths and pixel-to-pixel variations within the photon sensors. A laser monitoring system will be employed to provide channel-by-channel time-zero information, which will be stored in a database. This data will be used to accurately calibrate the photon arrival times for all pixels.

Optical Calibration and Alignment: The exact positioning of the optical components will be determined during the hpDIRC DIRC installation, using a laser and precise survey marks. The reconstruction of the Cherenkov angle, based on the hit pattern on the MCP-PMT array, depends on the accurate relative positions and orientations of all optical elements, including the photon sensors and their individual pixels.

In-Beam Calibration and Alignment: After installation in the ePIC detector, the alignment of the hpDIRC will be verified using beam data. Samples of muons, pions, kaons, and protons identified by other ePIC sub-detectors or through kinematic fitting will be used to calibrate the hpDIRC measured Cherenkov angles.

Geometric reconstruction will then be used to calculate the Cherenkov angle per photon for each track and sensor pixel. Any deviation between the measured and expected Cherenkov angles in the calibration samples will be utilized to develop a correction function or multi-dimensional lookup table. This information will be stored in the configuration database to correct for residual misalignment and optimize the performance. A similar procedure was successfully employed in the BaBar DIRC, where a 10% improvement in Cherenkov angle resolution was achieved by applying per-photon corrections based on a dedicated particle calibration sample.

Status and remaining design effort: Preparations for the hpDIRC are progressing in line with the overall project schedule. In the chart shown in Figure 3.117, the top lines highlight the major milestones of the project from the present day to the start of the experiment and CD-4 approval. Below these milestones is a detailed breakdown of key work packages, including the optical components, readout system, and mechanical design. The hpDIRC is expected to be fully ready in advance of the installation deadline, with a substantial time contingency built into the schedule.

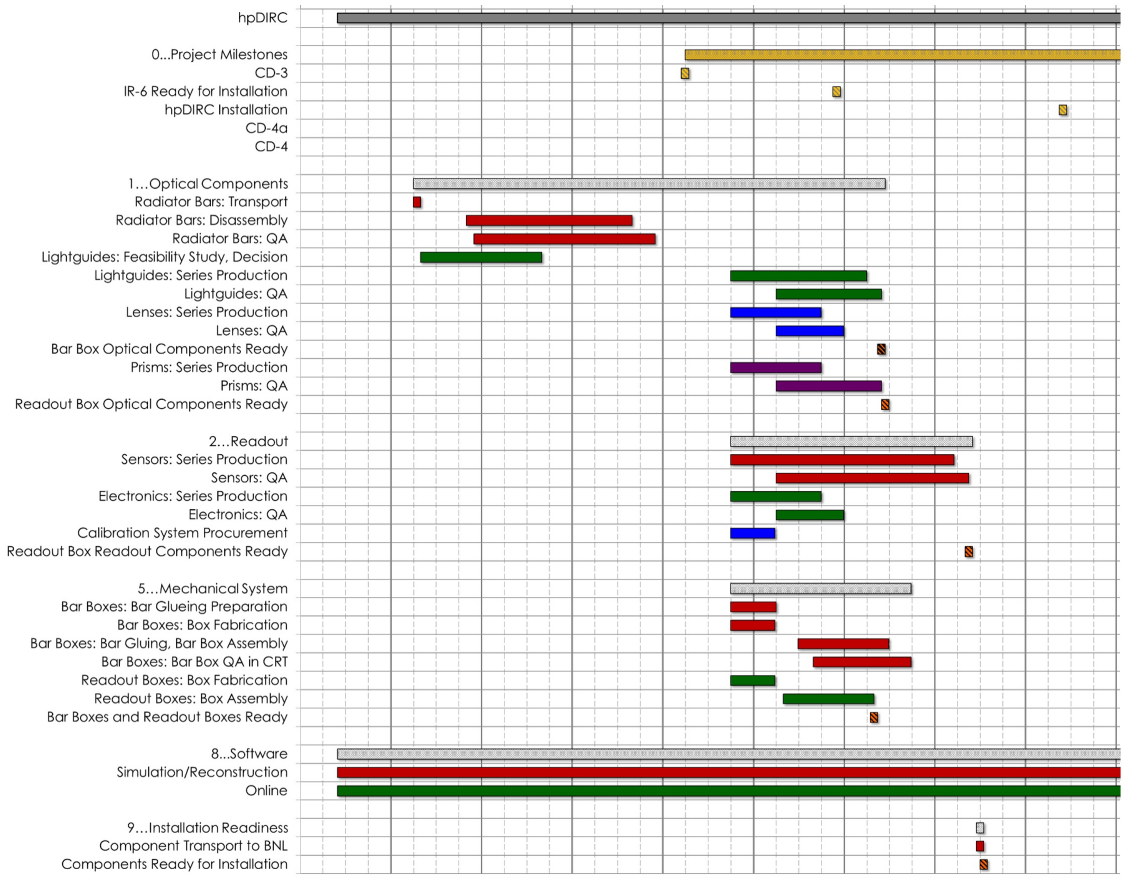

Figure 3.117: ePIC hpDIRC schedule chart alignment with EIC Project schedule

Remaining R&D effort: The primary objectives of the remaining hpDIRC R&D are to validate new components, ensure their successful integration into the hpDIRC system, and to optimize the final design. Ultimately, the goal is to achieve a validated, cost-efficient hpDIRC design for the ePIC detector, which will be demonstrated in the Cosmic Ray Telescope (CRT) setup. Several critical aspects of the hpDIRC design still require thorough study and verification to guarantee the necessary performance, mitigate risks, and explore new opportunities.

Ongoing R&D projects with a direct impact on the hpDIRC include eRD109 (focused on readout and ASIC designs) and eRD110 (focused on photosensors). The development of compact readout electronics for fast single-photon detection, using high-density sensors, must be completed and integrated into the hpDIRC prototype to validate the performance of a cost-optimized design for particle identification (PID).

The reuse of BaBar DIRC bars, another key cost-saving measure, is currently being explored with support from Jefferson Lab and the EIC Project, as discussed above.

Environmental, Safety and Health (ES&H) aspects The hpDIRC system is designed to operate without the use of any flammable gases or cryogenic liquids, which eliminates the risks associated with these hazardous substances. Both the bar boxes and readout boxes will be purged using boil-off dry nitrogen, which will flow at a rate of a few liters per hour per box. This method ensures

Figure 3.118: Photos of available setups developed during the hpDIRC R&D program that will be used for future QA of 3-layer lenses with laser setup at ODU (a), bars and other optics at Jefferson Lab (b) and readout chain including sensors and electronics and other hpDIRC components in hpDIRC prototype at CRT at SBU (c).

that the environment inside the boxes remains dry and free from contaminants, contributing to the system's safety and reliability.

In terms of electrical hazards, the sensors employed in the hpDIRC require high voltages, reaching up to 3 kV. To prevent the risk of electrical shock, the high-voltage (HV) connections will be inaccessible during normal operation. Furthermore, the HV module will be keyed off, and only trained personnel will be allowed to operate it, providing an additional layer of safety in the system's design.

The hpDIRC will also utilize a class 3B laser pulser for the calibration of sensors and electronics. Since lasers pose a radiation hazard, special precautions will be taken: the laser will be fully enclosed within optical fibers to prevent exposure, and only trained personnel will be authorized to operate the laser.

For the cooling of the readout electronics, a chilled liquid will be used, though the specific details of the liquid have yet to be determined. To avoid the risk of a chemical leak, the chilled water will circulate at sub-atmospheric pressure, which helps prevent potential leaks.

The entire hpDIRC system will comply with all applicable Environment, Safety, and Data (ES&D) standards and Occupational Safety and Health Administration (OSHA) regulations. This commitment to compliance ensures that the system adheres to the highest safety protocols, protecting both the equipment and the personnel involved in its operation.

Quality Assurance Plan The quality assurance (QA) plans for the hpDIRC components and modules prior to construction are centered around a combination of process control at the vendor sites and extensive in-laboratory measurements. The radiator bars and light guides will undergo

vendor-provided QA to assess their mechanical properties.

For newly built radiator bars and light guides, the initial QA tests will be performed by the vendors and certificates of compliance and QA data provided. The fabrication QA data for the refurbished BaBar DIRC bars is available.

For the sensors and electronics testing, laser pulser systems will be deployed at CUA, JLab, or USC (to be determined) to perform measurements including gain, quantum efficiency, collection efficiency, timing precision, and dark count rate. These tests will verify the operational integrity and performance of the sensors.

The lenses will be evaluated at the laser laboratory at ODU, where the shape of the focal plane will be analyzed to ensure proper optical alignment and focusing. Prisms will be subjected to vendor-provided QA, followed by further checks at WSU to confirm their specifications. Similarly, the bar boxes and prism boxes will undergo QA at the vendor sites, with additional testing and validation at SBU, prior to the module assembly.

Once the DIRC modules are fully assembled, including the coupling of the bar box to the readout box (a vertical slice), the Cosmic Ray Telescope at SBU will be used for testing. This will ensure that the assembled DIRC modules function as intended before final integration.

After installation of the DIRC module in ePIC, a picosecond laser pulser calibration system will be employed to fine-tune the system. Cameras will also be used to continuously monitor the optical coupling between the sensors, prisms, and lenses, ensuring that the entire optical system is correctly aligned and operational throughout the experiment.

Construction and assembly planning: In the current plan for the ePIC hpDIRC construction, the assembly will take place at three different locations. The bar boxes will be assembled at Jefferson Lab, utilizing the existing infrastructure developed for the disassembly of the BaBar bar boxes and the quality assurance of the bars. Short bars will be glued together to form ten long bars per bar box, with 3-layer lenses attached, and will then be mounted inside their carbon fiber shells. he readout boxes, along with the associated sensors and electronics, are first evaluated at multiple sites: the University of South Carolina (USC) characterizes the sensors and matches them with validated readout electronics before sending the paired sets to Brookhaven National Laboratory (BNL); Wayne State University (WSU) assesses the mechanical and optical properties of the newly acquired expansion volume prisms and ships them to BNL; and the carbon fiber reinforced polymer (CFRP) vendor inspects both the bar boxes and readout box structures before delivering them to Purdue University or Jefferson Lab (JLab). Final assembly of the readout box, including integration of the sensors and electronics, is performed at BNL. The completed readout boxes are then temporarily integrated with the corresponding bar boxes to verify light-tightness and ensure proper mechanical alignment prior to final installation.

Collaborators and their role, resources, and workforce: The hpDIRC system collaboration (DSC) consists of a core group of institutions that have long-standing experience with DIRC counters, having contributed to the BaBar, GlueX, PANDA projects, and the EIC DIRC R&D program. Many of these groups have been involved in these efforts since 2011, bringing a wealth of expertise to the development of the hpDIRC system for the ePIC detector. This collaborative network is expected to expand, with a few expressions of interest (EoIs) from various institutions interested in contributing to different aspects of the project closer towards construction. The process of aligning expertise and interest with system priorities is already underway, ensuring that the work is distributed efficiently.

Among the key collaborators, Jefferson Lab together with CUA have been handling the transport and disassembly of BaBar DIRC bar boxes and validation the quality of the disassembled bars. Future contributions are expected to include the QA of new bars for the light guide section as well as the gluing of the bars and lenses and the assembly of the bar boxes.

Stony Brook University (SBU) is preparing an important QA tool with their Cosmic Ray Telescope. The initial plan is to use it for incremental integration of new components into the hpDIRC prototype like disassembled BaBar bars, sensors, and electronics, but eventually, it will be used for validation of completed bar box modules. Old Dominion University (ODU) will contribute by evaluating the focal plane of the lenses and conducting QA procedures, ensuring the optical components meet the required standards.

On the sensor side, USC will handle QA and tests related to the readout chain, ensuring the sensors operate within specified parameters. Wayne State University (WSU) will oversee the assembly and QA of the readout boxes, another critical component of the system. Finally, institutions like CUA, GSI, William & Mary, and WSU are heavily involved in simulation and reconstruction efforts, which are essential for optimizing the performance and integration of the hpDIRC system into the overall ePIC detector framework.

This broad collaboration, with specific responsibilities assigned to various expert groups, ensures that all components of the hpDIRC system are developed and tested by specialists, assuming more junior workforce, like graduate students and postdoctoral researchers, can be added through external grants.

Risks and mitigation strategy: The disassembly procedure has been validated and is progressing successfully. The first bar box has been disassembled, with the short bars extracted, cleaned, and subjected to inspection. Preliminary measurements conducted in the laser QA laboratory confirm that these bars meet the performance criteria for use in ePIC. The optical quality of the remaining bars will be assessed following the disassembly of the remaining bar boxes. If the fabrication of new radiator bars or light guides is required, a vendor will need to be identified, and the procurement and production process initiated. Based on the current production timeline for PANDA Barrel DIRC radiator bars, the production of new bars for ePIC is still possible within the project schedule.

Both the baseline commercial MCP-PMTs and HRPPDs require testing and evaluation, which are being prepared by different groups. These tests will be conducted in parallel to ensure the necessary sensors are available within the required time before installation. The development of ASIC-based readout electronics is being coordinated by the EIC project.

Additional Material Add text here.

3.3.4.4 The dual radiator RICH

Requirements The dual radiator Ring Imaging Cherenkov (dRICH) detector is part of the particle identification system in the forward (ion-side) end-cap of the ePIC detector and complements the forward time-of-flight system and calorimetry, see Figure 3.85. The dRICH has to provide acceptance in the pseudo-rapidity range defined by the ePIC beam pipe and the barrel detector and to operate within the limited envelope allowed by the rest of the compact and hermetic ePIC detector. Distinctive features of the detector are: use of aerogel and gas radiators to extend the covered momentum range, usage of silicon photomultiplier (SiPM) to ensure single photon detection capability in high and not-uniform magnetic field, non-conventional optics with curved active surfaces and compact readout electronics to fit into ePIC.

Requirements from physics: The dRICH is required to provide continuous hadron identification from $\sim$ 3 GeV/c to $\sim$ 50 GeV/c, and to supplement electron and positron identification from a few hundred MeV/c up to about 15 GeV/c. Such an extended momentum range imposes the use of two radiators, gas and aerogel, with a common imaging system to ensure compactness and cost-effectiveness. The radiator gas must ensure π/K separation at 3-σ level up to 50 GeV/c in the most forward region, namely for $\eta > 2$. The aerogel radiator must cover the intermediate momentum interval, bridging the upper limit of the time-of-flight ($\approx$ 2.5 GeV/c) to the Cherenkov threshold of the dRICH gas ($\approx$ 12 GeV/c). The dRICH has to provide open acceptance in the ePIC forward pseudo-rapidity range $1.5 \lesssim \eta \lesssim 3.5$. To provide proper light focalization within the due volume, the dRICH active area is located behind the shadow of the barrel detector and its support ring, close to the MARCO solenoid coils. In this region, see Figure 3.86, the up to 0.6T not-uniform ePIC magnetic field imposes the use of unprecedented detectors (SiPM).

Requirements from Radiation Hardness: The radiation sensitive components (sensor and front-end electronics) of the dRICH detector are concentrated in a region of moderate radiation level, below O(10^{11}) cm^{-2} n_{eq} of maximum integrated fluence where n_{eq} is a 1-MeV neutron equivalent particle, see Figure 3.87. Close to the beam line, where the integrated dose can reach a value of 15 krad, only radiation tolerant materials reside like silica aerogel [63].

Requirements from 8xParticle Fluence: Data rates are expected to be dominated by the intrinsic significant dark count rate of the SiPM sensor, currently of the order of 50 kHz/mm^2 at room temperature, that indefinitely increases with the radiation damage. To mitigate this effect, the dRICH sensors are operated at low temperature (less than -30°C) and regularly annealed at high temperature (up to 150°C), in order to never exceed a maximum 300 kHz dark rate per channel. The latter value corresponds to a conservative limit taken to preserve the detector performance requirements for Physics and it is supported by present simulation studies that confirm the particle-identification capabilities of dRICH are unaffected. The corresponding maximum throughput rate of the whole dRICH is 1.3 Tbps assuming further data reduction. This will be achieved via a shutter signal on the front-end ASIC and/or via an external tagger or data reduction in dRICH DAMs using machine-learning techniques (see section 3.3.10).

Justification The specifications outlined above largely define the main technological choices: the momentum range dictates radiator refractive indexes that can be reliably met only by aerogel and gas, while the ePIC environment, space and magnetic field, imposes sensor characteristics that can only be met by SiPM.

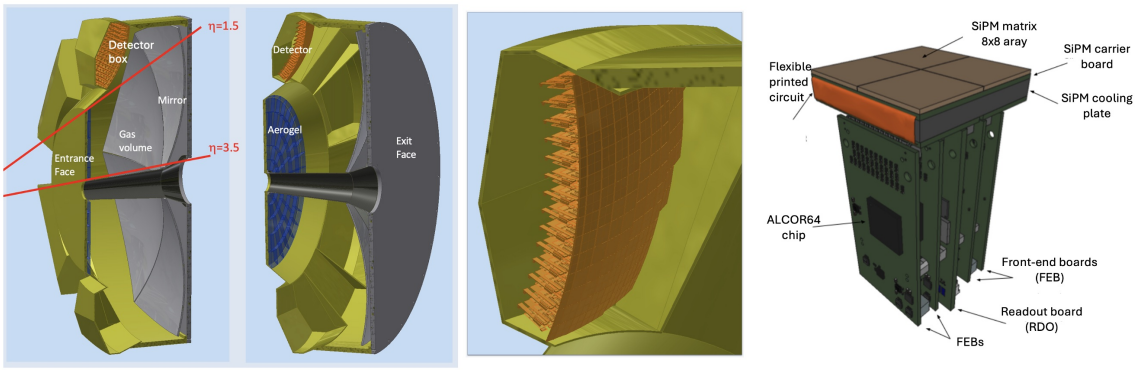

Figure 3.119: (Left) dRICH detector model with highlighted the major components. (Center) Model of the dRICH photodetector unit (PDU) module with its major components highlighted. (Right) dRICH detector box model with 208 PDUs forming a curved active surface.

Device concept and technological choice: The dRICH is a ring-shaped detector, with a length of 1.27 m and a diameter of 3.6 m, fitting inside the ePIC forward endcap, see left panel of Figure 3.119. The essential components are a layer of aerogel radiator, a volume of gas radiator, and an array of mirrors focalising the Cherenkov light into compact areas instrumented with photosensors. The detector is designed in a modular way, with 6 sectors around the beam line of equivalent mirror set and detection area.

The aerogel radiator is an amorphous solid network of SiO_2 nanocrystals whose density regulates the refractive index and chromaticity [64]. The current manufacturing methods succeeded in improving the attenuation length Λ ($\lambda = 400$ nm) up to 50 mm (e.g. aerogel for CLAS12 and BELLE-II). The selected aerogel radiator has refractive index n = 1.026 at $\lambda = 400$ nm. The chromatic dispersion has been measured during the R&D phase to be $dn/d\lambda = 6 \cdot 10^{-6}\,\mathrm{nm}^{-1}$ at 400 nm wavelength. Aerogel is produced in tiles of few cm thickness: in order to minimize edge effects, the dRICH tile side should be greater than 18 cm, approaching the word record value of 20 cm.

The selected reference gas radiator is hexafluoroethane (C_2F_6), which matches the requirements being characterized by refractive index n = 1.00086 at STP and excellent chromatic dispersion $dn/d\lambda = 0.2 \cdot 10^{-6}\,\mathrm{nm}^{-1}$ at light wavelength $\lambda = 350$ nm [65].

The selected refractive indexes dictates a minimum thickness of 4 cm for the aerogel and O(1) m for the gas in order to ensure enough photon yield. Mirror focalisation is necessary to minimise the consequent uncertainty on the Cherenkov photon emission point. Being inside the detector acceptance, the mirror structure is made of carbon fiber reinforced polymer (CFRP) to ensure the necessary stiffness while being light. In order to preserve the Cherenkov angle information the mirror surface should have excellent optical quality, i.e. few nm roughness and better than 0.2 mrad angular precision (reflecting in a point-like image with more than 90% of the light intensity concentrated in a disk smaller than 2.5 mm). The single mirror dimension is limited to a ≈ 1 m maximum diagonal when accounting for realistic forming mandrel and coating chamber dimensions. In the dRICH mirror array, the radius of curvature should be replicated within 1% of the nominal value and the reflectivity should be better than 90% in the 300-600 nm wavelength range of interest.

The dRICH photon detector surface is shaped over a sphere of radius ~ 110 cm to best approach the 3D focal surface of the mirror array, see Figure 3.119 (center). The Silicon Photomultiplier (SiPM) sensor technology is selected for the photon detector. It ensures superior single-photon counting capability inside the ePIC magnetic field and compact dimensions suitable for tessellat-

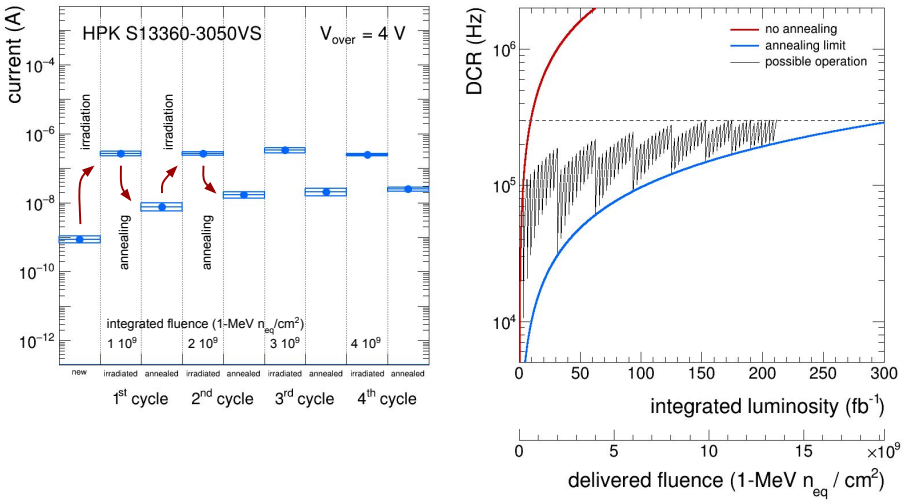

Figure 3.120: (Left) Dark current measurements on sample SiPM sensors for the studies of repeated irradiation-annealing . (Right) Projected increase of the DCR of SiPM as a function of the integrated luminosity (delivered fluence) for the PDU closer to the beam pipe (worst case scenario). The "no annealing" and the "annealing limit" curves show the limits of possible operations. The dashed line indicate the desired maximum DCR threshold.

ing a shaped active surface. The single SiPM sensor has a $3 \times 3\,\mathrm{mm}^2$ area to provide the necessary spatial resolution with an intrinsic time resolution better than 150 ps. The selected front-end ASIC is ALCOR [66], a 64-channel chip with coupling and rate capability optimized for SiPMs, and a ToT architecture with better than 50 ps (least significant bit) resolution in order the SiPM-ALCOR readout chain could achieve an overall time resolution better than 200 ps RMS. To minimize the volume within the dRICH envelope and to maximize the active area, the photodetector is organized in compact photodetector units (PDU). The PDU integrates 256 SiPM channels with the ALCOR TDC readout provided by four front-end boards (FEB), one readout board (RDO) to interface with the ePIC data aquisition (DAQ) and detector control (DCS) systems. In addition, the PDU is designed to allow sub-zero cooling of the SiPMs as well as high-temperature annealing operations. Figure 3.119 (right) shows the conceptual design of the PDU and its main components. The present dimensions of the PDU concept are approximately $52 \times 52 \times 140\ \mathrm{mm}^3$.

Subsystem description:

General device description:
Because at ePIC the electron and hadron beam collide at an angle of 25 mrad and acceptance should be provided to the far forward detectors, the common beam pipe cross-section is off-axis at the dRICH location and increasing in area with the distance from IP, imposing an asymmetric layout of the inner components. The aerogel wall is composed of five rings of tiles, each shaped in order to fit inside a 0.2 mm thin aluminum supporting structure. In each sector, focalization is provided by a compound of five mirrors covering a total area of about 2 m^2 with an optimized radius of curvature around 2200 mm. Six independent spherical active surfaces with curvature radius around 1100 mm, each made of 208 PDUs for a total of 53k readout channels, are mounted inside detector-boxes that provide thermal insulation, cooling for the electronics and connections to the services. Given the gas radiator open volume,

the Cherenkov photons can be reflected into different detectors depending on the parent charged particle kinematics. The aerogel and photo-detector are separated from the radiator gas by transparent septa, and immersed in a dry (e.g. purged N_2) atmosphere to minimize contaminant absorption and prevent moisture formation. The mirrors are supported by a light carbon fiber structure that is mechanically decoupled from the vessel and allows fine alignment adjustments by means of piezo-electric motors.

Sensors:
The silicon photomultiplier (SiPM) [67, 68] is chosen as the sensor technology for the dRICH photodetector. The main baseline specifications demand sensors with a 3×3 mm^2 single-channel active area, single photon detection over a broad spectral range from 300 to 900 nm and overall photodetection efficiency $> 40\%$ at the peak sensitivity wavelength $400 < \lambda_{\text{peak}} < 450$ nm. SiPMs fulfil the dRICH requirements as cost-effective and versatile devices with excellent photodetection efficiency (PDE) and time resolution. Their single-photon performance is unaffected by high magnetic fields [69, 70]. SiPM sensors on the other hand have very high dark count rates (DCR) and are not radiation tolerant. The DCR in SiPM is mostly of thermal origin and it reduces significantly by lowering the SiPM temperature, typically halving every 7-10°C in new sensors [71]. Radiation damage in SiPM is mainly due to displacement damage in silicon, which causes a significant DCR increase [72]. At the moderate radiation levels expected at the dRICH location, no significant change in the SiPM parameters (PDE, gain, quenching resistor R_{quench}, pixel capacitance C_{pixel}, breakdown voltage V_{break}) is observed [73]. SiPM cooling is important to keep the DCR low and it becomes crucial after radiation damage [74]. In the dRICH, the SiPMs will be operated at subzero temperature of T = −30°C, or lower. A cooling block is placed in thermal contact with the back-side of the printed-circuit board hosting the SiPMs (carrier board). Cooling fluid in the cooling block will be circulated through a closed loop by a circulating thermostat with dynamic temperature control to regulate and maintain the SiPMs at low temperature. The radiation damage on SiPMs increases moderately with the integrated luminosity. At the location of the dRICH photodetector a maximum (average) fluence of Φ_{eq} = 6.0 (3.6) 10^7 cm^{-2}/fb^{-1} 1-MeV equivalent neutrons (n_{eq} in the following) is expected from e+p interactions at the highest center-of-mass energy of the EIC (see left panel in Figure 3.121). Beam-induced background from proton beam-gas events at 35 kHz are expected to contribute bringing the total maximum (average) expected radiation damage to Φ_{eq} = 6.4 (3.7) 10^7 cm^{-2}/fb^{-1} n_{eq}. As shown by the "no annealing" curve in Figure 3.120 (right), the SiPM DCR is expected to increase with the integrated luminosity at a maximum (average) rate of 31.8 (18.6) kHz/fb^{-1}, reaching a DCR of 300 kHz after an integrated luminosity of approximately 9.5 (16.1) fb^{-1}. Annealing of SiPMs can be achieved exploiting the Joule effect [75]. When a SiPM is forward biased, the micro-cells composing the device behave as directly polarized diodes connected to their quenching resistors. The current flowing through the resistors eventually heats up the entirety of the sensor. In the dRICH, the circulating thermostat system used for low-temperature operation of the SiPM will be operated in heating mode to warm up the SiPM cooling plate (T = 100°C, or higher) during high-temperature annealing. Therefore a low-viscosity silicone fluid is particularly suitable for cold and heat transfer. Because a fraction of the heating power is delivered by fluid, a reduced current is required to perform the 'forward-bias annealing" to the SiPM. Nonetheless the required power to perform annealing at once over the full dRICH detector is excessively large and unpractical. Therefore annealing operations will be segmented in space and time across the dRICH detector and performed during periods with no Physics beam, and the temperature will be tuned up to T = 150°C, depending on the DCR reduction needs. During the R&D phase it was shown that the "forward-bias mode" approach can cure approximately 97% of the radiation damage. It is therefore expected that a residual irreducible radiation damage (residual DCR) will build up during the dRICH lifetime. As

can be see from left panel in Figure 3.121 the sensors closer to the beam line will experience a radiation damage almost a factor 3 times larger than those further from the beam line and will likely require a more frequent annealing. As shown by the "annealing limit" curve in Figure 3.120 (right), closer to the beam pipe (worst scenario) the SiPM residual DCR is expected to increase with the integrated luminosity at a rate of 950 (560) Hz/fb^{-1}, reaching a residual DCR of 300 kHz after an integrated luminosity of approximately 310 fb^{-1}. The "possible operation" curve shows a potential scenario for the DCR evolution for these SiPM sensors. This is based on an operation model where more frequent (every ~ 3 fb^{-1}) softer annealing cycles at lower temperature and/or of shorter duration, delivering a DCR reduction of 10 times, are interleaved by less frequent (every ~ 30 fb^{-1}) full annealing cycles to reduce DCR as much a possible. A limit in the operation scenario is reached when the annealing is not able to keep the DCR below the desired threshold or when the annealing frequency become too high. Beyond an integrated luminosity of ~ 200 fb^{-1} to keep the DCR below the 300 kHz threshold requires to perform full annealing cycles every ~ 5 fb^{-1}, which is not obviously a practical operation scenario anymore. Some of the SiPM sensors might be needed to be replaced at that stage with new ones or with SiPM sensors of improved performance and radiation hardness as a future upgrade of the dRICH photodetector. One has to keep in mind though that the 300 kHz limit is a conservative value that is connected to the present level of dRICH reconstruction and could be relaxed in future. Moreover, the model shown in Figure 3.120 (right) is based on measurement on Hamamatsu S13360-3050 sensors operated at V_{over} = 4 V in a climatic chamber at T = -30°C. Possible SiPM operation in ePIC at a lower V_{over} of 3 V and at a lower T of -40°C will allow one to achieve lower DCR overall.

FEE:
The ALCOR (A Low Power Chip for Optical Sensor Readout) ASIC, developed by the electronics laboratory of INFN Torino, is the baseline option for the readout of the dRICH SiPM sensors. The architecture of ALCOR and its key specifications are described in Section 3.3.10. The main goal of ALCOR is to provide single-photon time tagging of the incoming signals, while being able to cope with the SiPMs inherently high DCR: a maximum DCR value of 300 kHz/ch is expected before an annealing cycle is performed. A good time resolution, better than 200 ps RMS, is required to perform DCR suppression via time gating at both hardware and software levels. A programmable hardware shutter, implemented inside the digital logic of ALCOR, can be enabled to filter out-of-time DCR and provide a significant bandwidth reduction to the system. The time window of interest is controlled off-chip by the RDO FPGA and can be adjusted using in-pixel programmable delays to compensate timing offsets among the 64 channels. Note that the shutter may be needed only when DCR becomes significant due to SiPM integrated radiation damage over time. Therefore, the first period of ePIC data taking can be used to optimize the shutter calibration. The ASIC will be integrated inside a BGA package, providing a compact and robust solution to be assembled on the FEB. A 17×17 mm^2 flip-chip ball grid array (FC-BGA), with 256 balls and 1 mm ball pitch, is the option chosen for the ASIC packaging since it offers more interconnections and better performance w.r.t. standard packaging techniques and matches well with the pixel-matrix geometry of the ALCOR ASIC. Each FEB hosts one ALCOR BGA device and several components to ensure a stable and safe operation of the system. Linear regulators are employed to provide clean power supplies to the chip and are coupled to I2C interface and current monitors to control the regulators and prevent potential damage from over-current conditions. The FEB incorporates a dedicated PCB section for SiPMs bias voltage routing and also a circuit to enable the SiPM forward-biasing when annealing cycles are carried out. AC-coupling between the SiPM sensors and ALCOR inputs has been chosen to isolate them when the SiPMs are operated in forward bias.

Other components:

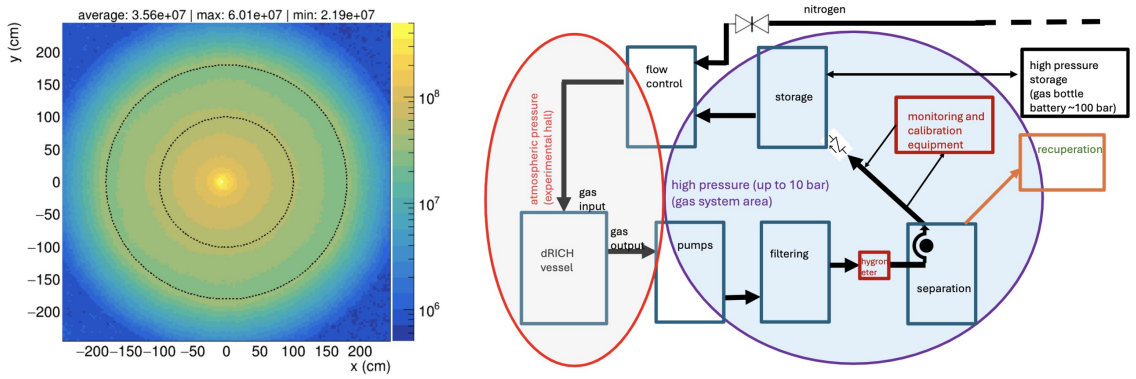

Figure 3.121: (Left) Transverse map of the expected 1-MeV equivalent neutron fluence per 1 fb^{-1} of integrated luminosity in e+p interactions at the maximum EIC center-of-mass energy at the location of the dRICH photodetector ($210 < z < 260$ cm). The average, maximum and minimum values within the region of the dRICH photodetector ($100 < R < 180$ cm, indicated by the dashed lines) are reported. (right) Block diagram of the dRICH gas system.

The radiator gas in the RICH vessel is controlled by the gas radiator system, see right panel in Figure 3.121. Its main tasks are, during detector operation, (i) providing well controlled pressure conditions in the 12 m^3 RICH vessel to avoid relevant pressure difference at the vessel walls and at the fused silica windows; (ii) removing oxygen and water vapor contaminates, in order to prevent building up impurities due to air leaks entering the gas system; (iii) performing detector vessel filling with hexafluoroethane before a data taking period and radiator gas recovery at the end of the period; the filling/recovery is from/to the storage tank. The main components of the radiator gas system are two oil-free compressors, working in parallel, which continuously extract gas from the vessel at constant rate in order to ensure the gas circulation, a pressure sensor installed on top of the radiator vessel for continuous monitoring of the internal relative pressure and to dictate the opening level of a flow control valve on the input line, adjusting the opening so to preserve the relative pressure inside the vessel. Oxygen and water vapor traces are removed by filtering cartridges with molecular sieves and Cu-catalyst, which are permanently in series in the circulation system, to maintain a contamination level better than 20 ppm (a value less stringent than for gas devices working in the VUV wavelength region). The gas temperature and pressure will be continuously monitored to correct the variation of the refractive index within an uncertainty below 0.1% in terms of (n-1). The vessel is flushed with nitrogen during the shutdown periods. Nitrogen and hexafluoroethane separation during filling and recovery is under study and two options can be envisaged: (i) the use of osmosis via dedicated membranes or (ii) via a two-step procedure: replacing nitrogen with carbon dioxide and then performing distillation at $-35°$C. Hexafluoroethane is a greenhouse gas and, therefore, the residual C_2F_6 present in the nitrogen/carbon dioxide cannot be vented out: it must be collected and trapped for disposal with a dedicated recovery system. The control of the whole radiator gas system is performed via a Programmable Logic Controller (PLC).

Performance

For each recorded dRICH hit, the photon path is reconstructed taking into account the charged particle trajectory and the focalising optics of the detector, in order to provide an estimate of the Cherenkov angle at the emission point. The combined information of all the Cherenkov photons

associated to a charged particle result in a precise determination of its velocity βc and, knowing the momentum from the ePIC spectrometer, its mass. The dRICH model is part of the ePIC simulation framework and allows complete performance studies taking into account quality of the track reconstruction, bent trajectories (by magnetic field) and multiple scattering. To bypass the complexity of such a framework, some specific study can be anyway performed with standalone simulation chains. The laboratory characterization and the numerous test-beams have provided detailed inputs for modeling in a realistic way the single components and global detector response. In the dRICH, the contributions to the single-photon (SPE) angular resolution have a different weight depending on the radiator. The dRICH has been designed in order to keep most of the contributions to the SPE angle resolution close or below 0.5 mrad, see Figure 3.122, a value dictated by the tiny Cherenkov angle difference between pions and kaons at 50 GeV/c in the radiator gas. The single SiPM readout channel has been limited to 3×3 mm^2 area. The MARCO coils and the dRICH position has been optimized in order to minimize the bending inside the radiator gas volume. The tracking resolution is assumed to cope with the same constrain. Note that combining N photons the angular precision scales with a maximum $N^{-1/2}$ factor only in case of a completely uncorrelated information, a condition that is not valid for the bending and tracking contributions. The uncertainty on the emission point is not an issue for a few cm layer of aerogel, but is critical for a 1 m long gas volume, expecially within the limited space available in ePIC for the optics: this remains the major contribution to the SPE resolution of the radiator gas despite the mirror focalization and the curved dRICH detector surface. Because the present model assumes a single radius for the dRICH mirros, optimized for the forward rapidity region to boost the high-momentum reach, the resolution worsens with the polar angle increase. This is not a problem, because the average particle momentum decreases as well loosening the performance requirement. The chromatic error is well under control for gas but is the largest contribution to the angular resolution for the aerogel. This derives from the intrinsic nature of the radiator in conjunction with the quantum efficiency characteristic of the photosensor. The chromatic uncertainty limits the aerogel momentum reach to something above 15 GeV/c, a value well above the Cherenkov threshold of kaons in gas, high enough to provide the wanted overlap between the measured ranges of the two radiators.

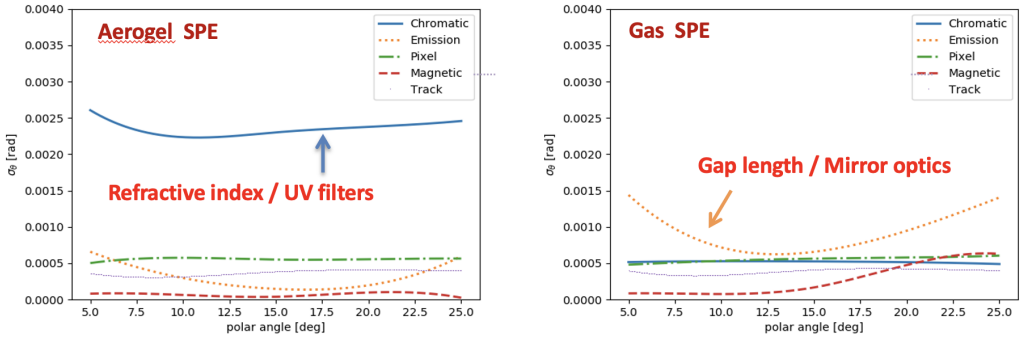

Figure 3.122: (Left) Contributions to the single-photon angular resolution for aerogel. (Right) Contributions to the single-photon angular resolution for radiator gas.

The number of emitted photons varies with the pseudo-rapidity due to the different path of the particle within the radiators. The mean number of recorded photons is about 18 for the radiator gas and 12 for the aerogel for a particle with momentum well above the Cherenkov threshold. In average, few charged particles per event are expected to hit the detector. With a proper pattern recognition and photon path reconstruction, the information of the two radiators can be combined to extend the hadron momentum coverage of ePIC PID from the TOF $\approx$ 2.5 GeV/c upper momentum limit to above 50 GeV/c, and support electron separation up to 15 GeV/c, see Figure 3.123. In

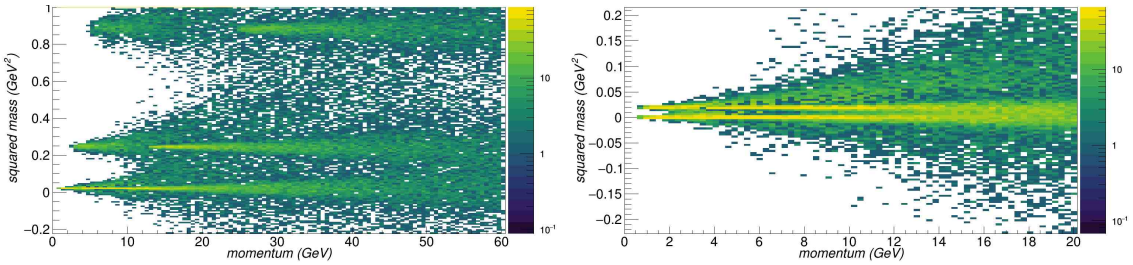

Figure 3.123: (Left) Reconstructed mass vs momentum for pions, kaons and protons. (Right) Reconstructed mass vs momentum for pions and electrons. Distinct values derived from aerogel and gas are shown, to highlight the complementary coverage and effective interplay of the two radiators. The study is performed at the large rapidity endpoint $3.2 < \eta < 3.5$.

the forward direction with optimized focalization, an identification efficiency greater than 95 % at a corresponding 5 % percent mis-identification probability, is achieved.

Implementation

Services:

The dRICH services are grouped into power lines for sensors, electronics and slow control monitors, gas lines for the radiator gas volume, the aerogel inert gas volume, and cooling lines for the sensors and electronics. Table 3.47 shows a list of the power services for the dRICH photodetector. Eighteen 19" wide/8U mainframes (approximately $50 \times 40 \times 70$ cm^2 each) capable to host 16 boards each are needed to accommodate the low-voltage and high-voltage boards. The primary power-supply channels will serve multiple modules at the same time, with a typical grouping of 1024 SiPM channels. Nonetheless, further segmentation is implemented on the detector electronics, reaching a low-voltage power segmentation of 64 SiPM channels and a high-voltage power segmentation of 32 SiPM channels. The circulating thermostat system should be capable of circulating approximately 50 l/min of fluid at a maximum pressure of 1.5 bar in a broad temperature range (from -60°C to 120°C). It is expected that a potential circulating thermostat system with the desired characteristics will require space in the experimental hall for a volume of approximately $1.3 \times 0.8 \times 1.6$ m^3. Manifolds are needed to split the fluid from the thermostat into 6 loops, each feeding one dRICH photodetector box. A solution without manifold and 6 smaller independent thermostat units for each dRICH sector will be investigated as a possible optimization. Insulated pipes will be needed to transport the fluid from the thermostat to the detector, and back. The insula-

Name	Voltage (V)	Current (A)	Channels	Boards	AWG gauge
Analog	1.4	10.0	312	39	10
Digital low	1.4	8.5	312	39	11
Digital high	2.7	6.0	312	39	12
Master panel	5.0	5.2	6	1	13
SiPM bias	64.0	1.3	12	2	19
Annealing	12.0	3.2	1248	156	15

Table 3.47: List of the voltage services to the dRICH electronics, indicating the number of primary power-supply channels and boards as well as the cross-section of the cables (AWG). The number of power-supply boards is defined assuming to use commercial 8-channel low-voltage boards.

tion must guarantee no frost and no water condensation on the pipes when operating at the lowest temperatures and is also required to limit transport losses in heating/cooling capacity. Cooling for the front-end electronics is required to remove the approximately 15 kW of heat generated by the dRICH photodetector ($\approx$ 2.5 kW in each of the six photodetector boxes). Forced-air circulation in the boxes with diffusers and heat exchangers are being studied as a possible effective solution. It is important that the air-cooling system for the FEE electronics provides dry air with a dew point well below the SiPM operating temperature. A system based on forced circulation of gaseous nitrogen might be well suited also to ensure an inert environment inside the detector boxes. Gaseous nitrogen will be used to maintain the aerogel in a clean and inert environment. The radiator gas system and its related monitoring equipment require a surface of about 15 m^2, in order to host 5 racks of instrumentation, the gas storage tank and a support for the spectrophotometer. Various sections of the gas system operate at a 2-3 bar pressure, while the cell to measure and monitor the gas transparency operates at 10 bar. Some gas bottles at typical high pressure (100-150 bar), organized in a battery, have to be included to provide the radiator gas at filling and house it when recovered. The pipelines connecting the gas system to the vessel can be 70 m long with a diameter of 10 cm.

Subsystem mechanics and integration:
The dRICH structure can be described by two disks, one entrance window of 0.9 m radius supporting the aerogel radiator and one exit window of 1.8 m radius mounting the mirror system, connected by two ring-shaped structures, an outer shell that mounts the six detector boxes and one inner pipe surrounding the ePIC beam pipe. All the elements are made in composite materials, see left panel of Figure 3.124. The pipe and shell are made by a carbon fiber reinforced polymer (CFRP) bulk to provide support strenght. The two windows are a sandwich of two thin carbon fiber skins and a core honeycomb to limit the material budget to about 1% of radiation length each. The shell and detector boxes are shaped in order to allow the passage of all the services of the inner barrel detectors, see central panel of Figure 3.124. The dRICH services are concentrated on the shadow of the detector boxes and do not interfere with the routing of the others. A dedicated scaffolding would be realized to allow the installation of the detector, and the roll-in and roll-out movements to the service position without interference with the beam pipe to preserve the beam vacuum, see right panel of Figure 3.124. The dRICH is suspended inside ePIC via brackets connected to the HCAL barrel.

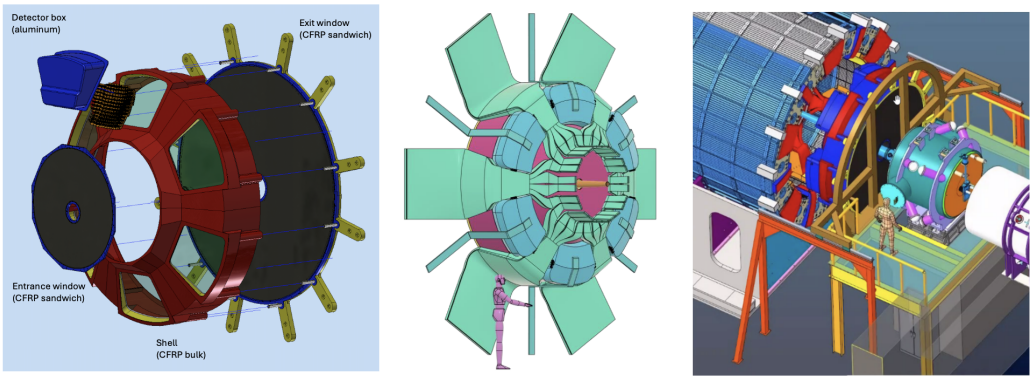

Figure 3.124: (Left) dRICH mechanical model. (Center) Service routing around the dRICH. (Right) Installation and exctraction tool.

Calibration, alignment and monitoring:

Dark counts in SiPMs are indistinguishable from photon-induced signals and owing to the large SiPM DCR there is no need of a dedicated system to evaluate the functioning of any given read-out channel. A measurement of the DCR as a function of the front-end electronics discrimination threshold can provide information on the actual single-photoelectron signal amplitude. Using solely the dRICH readout system it is therefore possible to measure the signal amplitude as a function of the bias voltage, hence to obtain information on sensor functioning, breakdown voltage and gain at different operation conditions. Timing calibration of the SiPM sensors can be achieved with a picosecond pulsed laser light system. The light from the laser is brought inside the dRICH volume via optical fibres. The light from the laser directly impinges on a diffuser that eventually illuminates the full area of one dRICH photodetector sector. At least one laser-fibre-diffuser system is needed for each dRICH sector. The time delay due to the different path of photons from the diffuser to the SiPM that detects the light is known and can be corrected to achieve a relative calibration of the times of SiPMs within the same sector. Absolute timing calibration can then be achieved with collision data. Sample particles from physics reactions can be used to perform fine adjustment of the calibration costants. Electron particles identified by other ePIC subsystems can be used to correct residual misalignment or calibrate the radiator refractive index thanks to the saturated Cherenkov rings. Known particles from meson decays (Λ, ϕ, K_S, ...) identified by kinematics criteria can be used to verify the parameters of the dRICH reconstruction and the consequent PID performance. The calibration and monitoring equipment of the radiator gas and gas system includes a set of temperature sensors placed inside the dRICH vessel and equipment on-line in the gas circulation loop. A commercial hygrometer and a commercial oximeter, a transparency measurement system by a commercial spectrophotometer equipped with a high pressure (≈ 10 bar) cell and a Jamin interferometer setup complete the set of the equipment. The interferometer, complemented with temperature and pressure sensors, will provide in real-time the refractive index of the gas in the vessel. The refractive index measurement has a twofold role: during filling/recovery, it monitors the hexafluoroethane level in the vessel, during operation it will provide in real time the refractive index of the radiator gas to make possible quasi on-line data reconstruction as foreseen in the ePIC streaming read-out model.

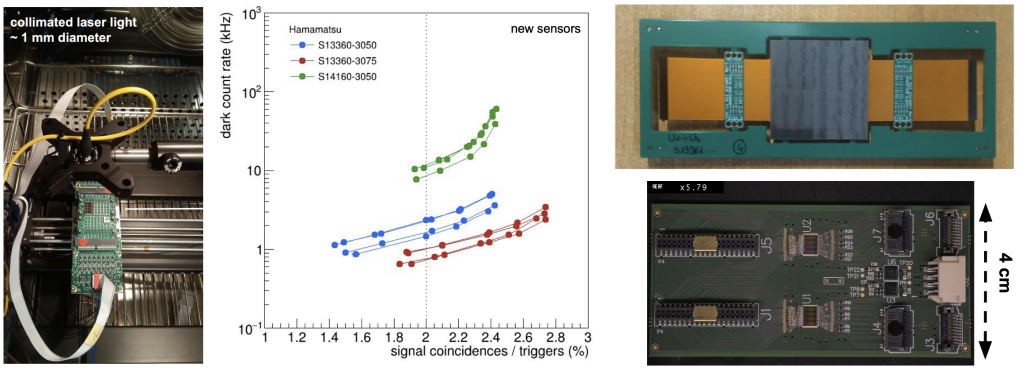

Figure 3.125: (Left) Test stand for SIPM characterization. (Center) Performance comparison between different SiPM models. (Right) Prototype version of the SiPM carrier board (top) and FEB (bottom).

Status and remaining design effort:

R&D effort:

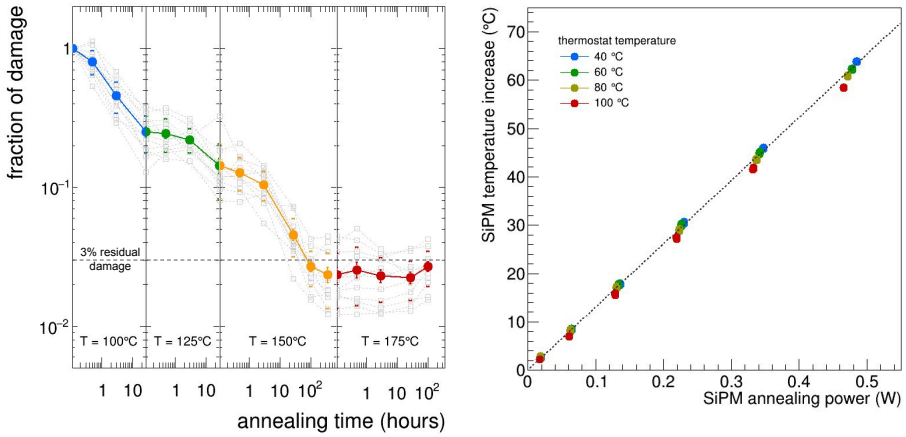

Figure 3.126: (Left) Fraction of residual irradiation damage measured on multiple SiPM candidate samples after "forward-bias annealing" cycles at increasing temperature and integrated annealing time. The measurements are shown for individual sensors (gray points) and as averages (coloured points, uncertainty of the average and RMS are indicated on the plot). (Right) Temperature increase of the SiPM sensor with respect to the temperature of the SiPM carrier board as a function of the "forward-bias annealing" power at different temperature values of the circulating thermostat system.

SiPM sensors. A station has been realized to characterize the SiPM sensors inside a climate chamber to control the working temperature, see left panel of Figure 3.125. The readout chain is based on ALCOR to reproduce the ePIC configuration. Such a station allowed detailed performance comparison between SiPMs of different manufacturers and types, see Figure 3.125 (central panel), and different ageing due to radiation and annealing. The R&D results on photosensors reported here are those obtained with Hamamatsu S13360-3050 sensors operated at V_{over} = 4 V in a climatic chamber at T = -30°C, unless otherwised specified. Nonetheless, the qualitative features of the results are valid also for other types of sensors. Irradiation tests performed to simulate a realistic experimental situation where SiPMs experience repeated irradiation and annealing cycles (see left panel of Figure 3.120) show that each irradiation cycle produces a consistent DCR increase (approximately 500 kHz for a 10^9 cm^{-2} n_{eq} irradiation) and the fraction of damage cured in the thermostatic chamber is approximately 97%. The 3% residual damage builds up after each irradiation-annealing cycle and seems to be irreducible within the details of this annealing protocol. Irradiation tests and laboratory measurements show that the "forward-bias annealing" mode can cure radiation-induced damage on SiPM (see left panel of Figure 3.126) to the same effectiveness level as the one measured for the "oven annealing" with a residual damage of approximately 3%. The benefit of the "forward-bias annealing" is significant: an extended SiPM sensors lifetime that can be achieved over the delivered radiation damage without the need to directly access the detectors in the experimental cavern. Higher temperatures and longer annealing times lead to more effective annealing. On the other hand, a limit seems to be reached already at T = 150°C as annealing at a higher temperature like T = 175°C does not lead to improved current reduction. Laboratory measurements performed so far show that the temperature of the SiPM increases with respect to the temperature of the SiPM carrier board proportionally to the power delivered by the forward-bias current. Figure 3.126 (right panel) shows that, as expected, the increase of SiPM temperature linearly depends on the annealing power and it is the same

at different values of circulating thermostat temperature. It is therefore sufficient to monitor the temperature of the SiPM carrier board and deliver the needed annealing power to have control of the SiPM temperature and keep the process safely under control. Laboratory measurements reported here are performed in an open environment at room temperature. With the circulating thermostat temperature set at T = 100°C, a SiPM annealing temperature of T = 150°C is reached with approximately a power of 0.5 W/sensor, which corresponds to a forward-bias current of approximately 60 mA/sensor. With the SiPM placed in a closed environment as the dRICH photodetector box, one would expect a lower power needed that will be measured during detector construction. Laboratory measurements show that for annealing temperatures up to T = 150°C there is no significant degradation of the PDE up to annealing times of 150 hours. More studies will be done, but at the time of writing annealing at T = 150°C can be considered safe for the expected dRICH operations.

FE Electronics. ALCOR has been extensively used within the ePIC dRICH Collaboration since 2021, testing it coupled to different SiPM models and assessing its single-photon time-tagging capability and time resolution. A prototype version of the SiPM carrier and FEB board have been developed, see right panel of Figure 3.125. The SiPM carrier provides electrical connections via thin kapton cables in order to bypass the sensor cooling plate. The prototype FEB hosts two 32-channel ALCOR chips which are directly wire-bonded on the PCB. It has been designed using specifications close to the ones for the final FEB, i.e. having the same dimensions and incorporating the same number of channels (64). It is served by a master-logic board that provide bias control and temperature monitor. These boards have been extensively used for the 2023-2024 dRICH activities, including two successful beam tests. ALCOR has been tested for radiation hardness with results showing only some small degradation on the TDC performance after a total ionizing dose (TID) of 300 krad, which is O(100) times the expected TID in ePIC. The single-event upset (SEU) cross section has been measured to be $3.3{\cdot}10^{-15}$ cm^2/bit, which corresponds to an expected mean time between failure due to SEU of about 190 hours for the entire dRICH detector. These results confirm that the technology is sufficiently radiation tolerant to be used in the ePIC dRICH environment.

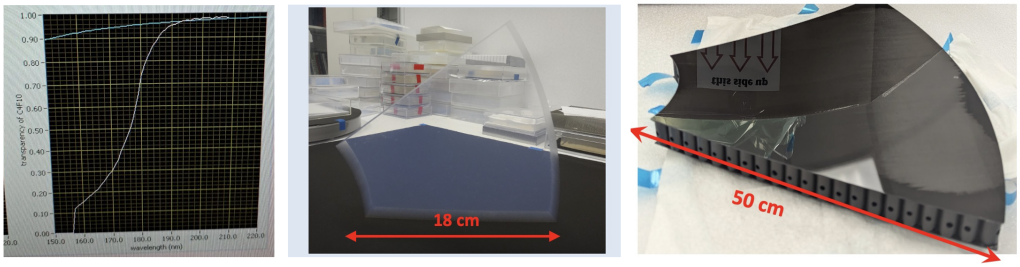

Figure 3.127: (Left) C_2F_6 measured transmittance in the near UV-region. (Center) Aerogel tile real-size demonstrator. (Right) Mirror demonstrator with an optimized dRICH core structure.

Radiator gas. The transparency in the near-UV benchmark region (most sensitive to the gas quality and contaminants) has been measured with a monochromator at CERN, resulting in values above 98% for a 1.6 m coloumn of gas at wavelengths grater than 200 nm, see left panel of Figure 3.127. The measurement has been done with a gas that was stored into bottles for about 4 years, indicating an excellent preservation with time.

Aerogel. The transparency of several aerogel samples from Aerogel Factory Co. Ltd (Chiba, JP) has been measured using a spectrophotometer at CERN and at INFN. Aerogel tiles with different refractive index (from n = 1.015 up to 1.05) and 2 cm in thickness have been tested. At the wavelenght of 400 nm, the transparency values are typically above 70% with a peak

at n=1.03. Real-size demonstrators have been realized with the baseline refractive index of n=1.026, see central panel of Figure 3.127. In general the tiles have the shape of a dome as a consequence of the production process. In the metrology laboratory at CERN, the thickness and flatness of the tile have been also measured. The measurement has been executed on a tile with n = 1.03 using the touch probe system (force applied = 2 g). The measuring system is the LEITZ PMMC with $\pm$ 0.3 μm of precision. There is a variation in thickness from the center to the edges, of the order of 0.4 mm, and a different planarity in the two faces, one 0.7 mm, the other 1.27 mm. These values are unexceptional but are not a reason of concern.

Mirror. A mid-size demonstrator (of 60 cm diagonal) has been realized with dRICH specifications, see right panel of Figure 3.127. The CFRP core structure has been optimized for preserving the surface shape accuracy and a light body: it adopts a light C-shaped cell structure (used by LHC-b) in the center, and a stronger cylindrical cell structure (used by CLAS12) on the edges. Before coating, the point-like source image test measures a D0 value, that represents a global surface quality estimator, of 1.8 mm, better than the specification of 2.5 mm. The same test indicates a radius of 2254 $\pm$ 5 mm, slight above the request to be within 1% of the nominal 2200 mm value.

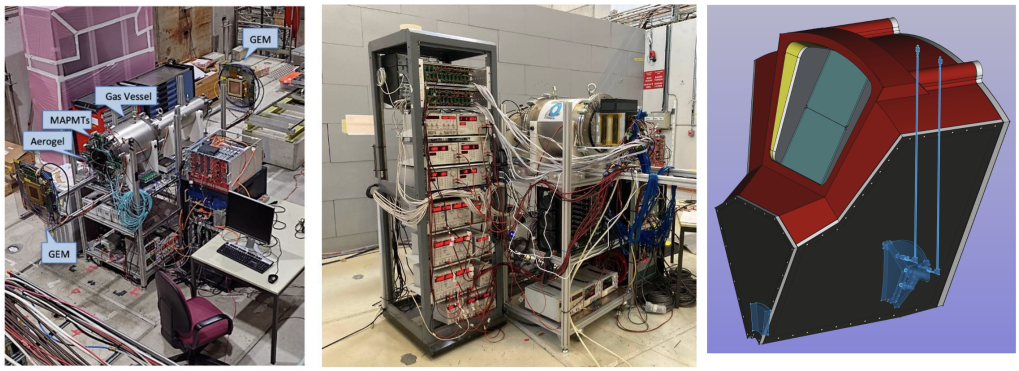

Figure 3.128: (Left) Baseline prototype with reference multi-anode PMT sensors at the SPS-H8 beam line of CERN. (Center) First ePIC-drive SiPM detector box under test at the PS-T10 beam line of CERN. (Right) Real-scale prototype model mimicking the basic dRICH construction unit (sector).

Prototyping. A baseline prototype has evolved in time to serve the dRICH R&D development for few years, see left panel of Figure 3.128. The gas vessel is a cylinder made of vacuum standards, to allow an efficient and safe gas exchange. The entrance flange can mount an external dark box separated from the inner gas volume by a UV-transparent lucite foil (or quartz window). An aerogel tile with possible additional UV filters, plus an array of alternative sensors and readout electronics, can be inserted into the dark box. Two mirrors inside the vessel have optimized focal lenghts to image the Cherenkov light from the two radiators onto the limited active surface. The major achievements obtained during several test-beams have been the validation of the dual-radiator concept, the validation of the C_2F_6 gas radiator (see left panel of Figure 3.129), the optimization of the aerogel refractive index (see central panel of Figure 3.129), the performance study of the SiPM-ALCOR readout chain (see right panel of Figure 3.129), and the development of an EIC-driven readout plane. A partially equipped EIC-driven plane has been realized in time for the October '23 test-beam with Hamamatsu S13360-3050 SiPM sensors of standard 50 μm pixel pitch, see left panel of Figure 3.130. The plane has been complemented for the test-beam in May 2024 with sensors of 75 μm pixel pitch, to verify the potential benefit in timing and photon detection efficiency.

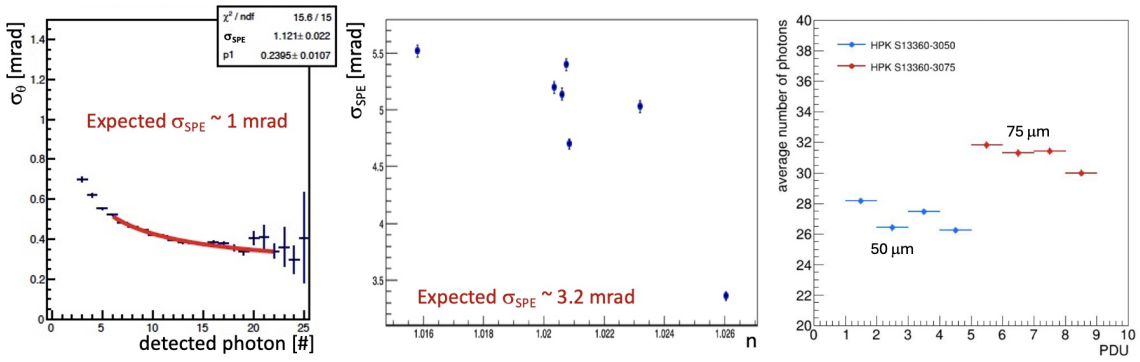

Figure 3.129: (Left) Cherenkov angular resolution obtained for C_2F_6 as a function of the recorded number of photons. The SPE values is consistent with expectations. (Center) SPE angular resolution measured on aerogel as a function of the refractive index. The expected resolution is obtained for an index greater than n=1.025. (Right) Comparison in photon yield of sensor with different SPAD size. All the measurements has been obtained with the dRICH prototype.

This has allowed for the first time a full ring coverage, an essential requirement for precise radiator performance study and effective signal over background study, see central panel of Figure 3.130. An effective interplay between the two radiators at intermediate energies has been demonstrated, see right panel of Figure 3.130. The new detector box has allowed a preliminary study of the thermal gradients and possible effects on the gas performance, indicating that the possible temperature gradient of few degrees induced into the gas volume by the cool sensor plane can be largely mitigated by a gas re-circulation or by a double window.

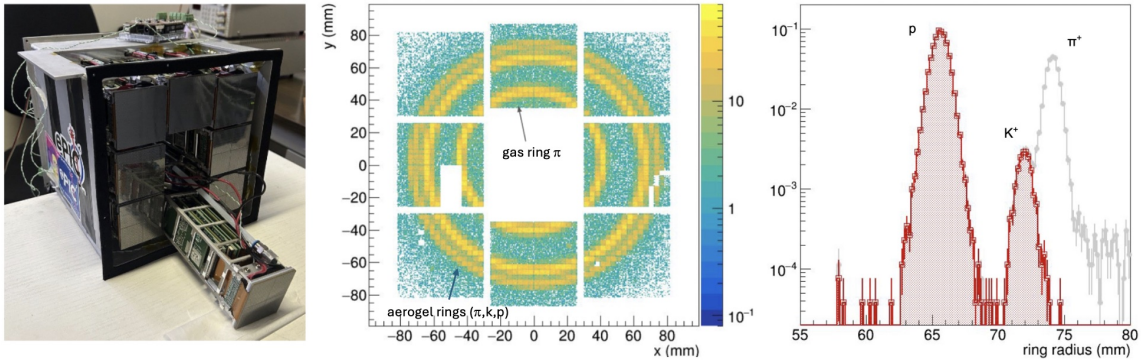

Figure 3.130: (Left) Prototype PDU and assembled detector plane. (Center) Cumulated ring imaging for a mixed hadron beam at 10 GeV/c. (Right) Dual-radiator interplay at 10 GeV/c: After the gas information is used to tag pions (clear histogram), an effective separation between kaon an proton is provided by the aerogel (shaded histogram).

E&D status and outlook: The study of SiPM performance continues with irradiation cycles of different particle type and more and more optimized annealing protocols to achieve the best PDE and time resolution preservation. A new version of the ALCOR ASIC has been designed to extend the number of channels to 64 and integrate the chip inside a BGA package with a tape-out in the first months of 2025. The design of the final version of the SiPM carrier, FEB and master-logic boards will be completed in 2025. For the radiator gas, it is required

to complete the design of the gas system and finalize the layout of the monitoring equipment. A dedicated system will be developed to measure the gas transparency in the visible wavelength range. The remaining E&D activity is expected to be completed by the end of 2026. An increase of the aerogel tile volume is instrumental to minimize the edge effects and contain the cost. During the R&D phase, tiles with side up to 15 cm and thickness up to 2 cm were realized. A feasibility study is ongoing to increase these limits towards a side of 20 cm or a thickness of 3 cm to maximize the photon yield. The aerogel production efficiency should be evaluated in conjunction with the optical quality and precise shaping obtained. This engineering work is expected to take time and not be completed before the end of 2026. Coating of the CFRP mirror substrate should be realized and compare with the benchmark performance obtained with the similar materials at CLAS12. This work will be completed by fall 2025. A real-scale prototype is being realized with composite materials and a realistic geometry (mimicking a dRICH sector). This is instrumental to validate the mechanical elements and study the assembling details (e.g. of transparent septa), the mechanical stability, the gas tightness, and the thermal aspects. One of the major goals of the real-scale prototype is also to reproduce the final ePIC working conditions, mount an extended readout plane with the designed RDO board, operate demonstrators of the optical components as results of the ongoing developments, and optimize the performance in a realistic off-axis optics configuration. To this end, a commissioning test-beam is planned for fall 2025 and a performance test-beam in spring 2026.

Other activity needed for the design completion:
Slow control, interlock and the calibration LED/laser system design is planned to start in 2026.

Status of maturity of the subsystem:
The R&D activity has been focused on the most innovative aspects of the detector that present technological challenges. These are the SiPM for single-photon detection in a strong and not-uniform magnetic field, a compact readout electronics to fit into the ePIC envelope and the use of two radiators to extend the momentum reach. The remaining effort is substantial, but is connected to more consolidated technologies, with possibly the only exception of the gas separation system for the peculiar C_2F_6 gas.

Environmental, Safety and Health (ES&H) aspects, Quality Assessment (QA), Construction and assembly planning:
Standard slow-control and interlock procedures will be implemented to control power and cooling while monitoring gas flow, humidity and temperature. The cooling system is complemented by a buffer tank to allow air flow and heat removal from the detector boxes in case of a failure of the recirculating system. Annealing of SiPM will be performed during technical stops and/or during the annual stops of the EIC machine. All the dRICH front-end electronics (FEE) will not be powered, with the exception of a few components needed to monitor and control the annealing operations. An interlock-based sistem will inhibit the FEE power-supply units during annealing. The circulating thermostat system used to cool the SiPMs will be switched to heating mode to reach a temperature of up to T = 100°C. A slow heating ramp of < 1 °C/minute will be employed to reduce thermal stress on the system. The dRICH photodetector boxes will be thermally insulated to control heat leaks into neighbouring detectors while performing annealing. It is expected that the inner volume of the detector box can reach a temperature of T $\lesssim$ 100°C and will be monitored with temperature sensors. Temperature sensors will be placed on the outside of the photodetector boxes to monitor the external environment. Only a fraction of the dRICH SiPMs will perform annealing at a given time, to limit the total amount of power needs to about 20-40 kW. This is a similar to the total power consumption of the FEE during normal operations and the same safety procedures

Component	QA station 1	QA station 2	QA detail and backup	QA Acceptance	In-depth
Aerogel	Temple U.	BNL	INFN-BA	100 %	5%
Gas	BNL		INFN-TS	2 %	2%
Mirror	JLab	Duke U.		100 %	10%
Sensor (SiPM)	INFN CS-SA-CT	INFN-TS	INFN-BO	100 %	1%
Readout	INFN-BO	INFN-FE	INFN-TO	100 %	1%

Table 3.48: Planned quality assurance (QA) stations, organized in order to provide redundancy and support specific characterization studies.

apply. Annealing power will be distributed evenly across the dRICH SiPM. In case of a power outage, the annealing current will be promptly removed from the SiPMs and their temperature will promptly drop to the temperature of the thermostat. The latter will eventually slowly cool down. The gas volume is maintained at +1 mbar with respect the atmospheric pressure on the top, with a consequent +5 mbar overpressure defined by the hydrostatic pressure of the radiator gas on the bottom, by means of pressure regulators connected to an UPS station and a two-way bubbler. Hexafluoroethane is non-flammable and it has limited toxicity, when below 1000 ppm level and for short exposure time [76]. In case of a major damage of the supply pipeline or of the vessel itself, 12 m^3 of hexafluoroethane at atmospheric pressure from the vessel (0.02% of the hall volume) will mix with the air present in the experimental hall, requiring the implementation of standard ODH procedures. Hexafluoroethane has a high Global Warming Potential (GWP): 12400 for a horizon time of 100 years [77] and it is, therefore, included in the group of GreenHouse Gasses (GHG). Environment protection imposes that such gases are not released in the atmosphere. This is obtained by using them in closed circuits, where leakages are minimized, and by collecting and sending for disposal the fraction of gas purged during circuit filling and gas recovery at the beginning and at the end of an operation period, respectively. Both closed circuit gas circulation and purged gas trapping are characterizing elements of the dRICH radiator gas system design. The maximum expected leakage rate during operation is about 20 m^3 / year assuming six-month operation.

Experience in quality assurance protocols has being gained in parallel with the R&D activity. For each critical component two stations are being organized to provide essential QA and redundancy, with a (third) station able to supports in-deep characterization on samples and serve as backup, see Table 3.48. The QA activity will be supported by workforce from all the dRICH groups. Essential QA parameters will be measured: integrity, refraction index, transparency, dimensions, and planarity of the aerogel; leak rate of the gas system (after completion); refractive index and transparency of the radiator gas (with the monitoring equipment of the gas system); dark count rate and PDE for the sensors; electrical connections, bias levels and data rate for the readout; dimensions, weight, reflectivity and D0 (point-like source image brigthness) for the mirrors.

The construction and assembling plan assumes to compress all the necessary tasks in a short time period in between the presently known EIC milestones: start with CD3 (late 2027) and completion 6 months in advance of installation (in October 2032), see Figure 3.131. The 6 months contingency time before installation will be used to perform functionality tests, and complete the services in the experimental hall at IP6. The assembling of 1248 PDUs comprising SiPM sensors and cooling, front-end electronics and RDOs, and their integration with the services inside six detector boxes will be staged over 2 years (mainly 2029 and 2030) by the dRICH DSC in Italy. This organized effort requires a timely procurement, starting with the ALCOR chip (wafer and packaging) followed by sensors, readout electronics, and box mechanics. Cooling infrastructure and DAQ system are expected to run in parallel to the detector box construction and be mainly covered by the EIC Project. First articles of DAQ, power supply and slow control could be used for the initial functionality tests of each single detector box, but the main effort on such services is concentrated on a later stage of the plan during assembling at BNL. The detector boxes will be completed in time to be shipped

to BNL and mounted on the dRICH in the second half of 2031. The dRICH vessel construction, a joint venture of the dRICH DSC and the EIC Project, will start in 2029 in order to be ready for detector assembly mid 2031. Mirror production is expected to take 2 years and is staged as soon as possible, subject to the funding profile of the EIC Project, to reduce the sole source risk. The engineering of the aerogel production is expected to extend beyond the TDR, with the consequent production led by the dRICH DSC not happening before 2029 and lasting for at least 2.5 years. An early procurement of the C_2F_6 gas by the EIC Project is planned in order to reduce the risk of a market price increase. The basic design of the radiator gas system will be completed by the end of 2026 by the dRICH DSC. The executive drawings and the system realization by the EIC Project engineering team supported by adequate technical personnel is expected during years 2029 and 2030. The layout finalization and validation of the monitoring equipment will be completed by the end of 2027, whit its realization by the dRICH DSC planned by the end of 2028. This equipment will be interfaced with the gas system in 2029, via synergistic effort between the EIC Project engineering team and the dRICH DSC. This combined group will perform the QA assessment of the gas system in 2030.

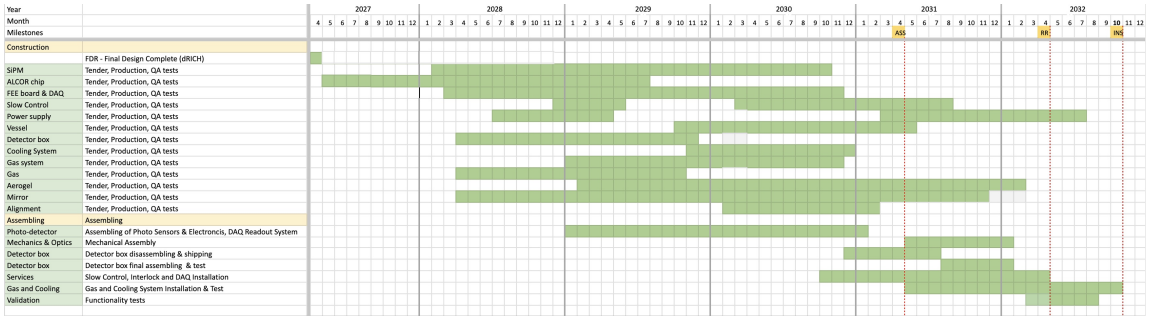

Figure 3.131: dRICH construction timeline

Collaborators and their role, resources and workforce:
The overview of the collaborating Institutes and their roles in the dRICH activity is presented in Table 3.49. INFN has agreed on a substantial in-kind contribution and the corresponding workforce has taken corresponding responsibilities in the construction within the DSC. The INFN in-kind will cover the design, production and quality assurance cost of the SiPM sensors, of front-end ASIC (ALCOR), of the front-end board (FEB), of the readout boards (RDO) as well as the assembly of the above components in a compact Photo Detector Unit (PDU), including the cooling circuitry and related mechanics. It will cover the cost of the realization of the six detector boxes (containing the 208 PDUs of each sector) with the control panels and the electronic services attached (for HV/LV/daq links routing). It will contribute to the design and realization of the main vessel, the design/supervision of the powering and monitoring systems, the dRICH tagging system and data filtering in streaming mode, see Sec. 3.3.10 , and to the definition of specifications and quality assurance (QA) of all the other components and services (i.e. gas, power and cooling plants). Secondments of personnel from all the DSC groups will be organized to support the QA activity in US and the assembling phase at BNL. The EIC Project is expected to cover the procurement effort that can be more efficiently based on US, and all the safety, infrastructural and integration aspect that require specific engineering background. This include the cost of the gas, of the mirrors, of the installation tools, of the power-supply systems , of the cooling plant and the gas plant, and of the FELIX cards receiving the data from the RDO.

Institution	Nation	Main Activity
INFN-FE	Italy	Mechanics, detector box and control panels
INFN-BO	Italy	Photosensors, photodetection unit PDU and readout board RDO
INFN-TO	Italy	ALCOR and front-end board FEB
INFN-BA	Italy	Aerogel radiator
INFN-CS-SA-CT	Italy	SiPM quality assurance
INFN-GE	Italy	dRICH tagger
INFN-LNS	Italy	Mechanical design
INFN-RM1-RM-TV	Italy	Online data reduction
INFN-TS	Italy	Radiator gas, gas system and software, SiPM quality assurance
DUKE-U,	USA	Mirror and mirror characterization
JLab	USA	Mechanical design and mirror characterization
BNL	USA	Mechanical design, integration, infrastructure
Temple U.	USA	Aeorgel quality assurance
M.S. Ramaiah U.	India	Simulations and performance study
NISER	India	Performance study
Central U. of Haryana U.	India	Performance study
Central U. of Karnataka U.	India	Performance study

Table 3.49: Overview of Institutes and roles in the dRICH activity.

Technological Challenges and Path Forward:
The dRICH gas radiator is a greenhouse gas with high GWP. A more severe restriction or ban on the usage of hexafluoroethane can result in an increase in cost or difficult procurement. The only alternative option to preserve the dRICH performance would be an eco-friendly gas with a very similar refractive index, an option not available in nature at atmospheric pressure. Argon at $\approx$ 3 bar absolute pressure mimics with great accuracy the hexafluoroethane characteristics. It is also non-expensive, non-toxic and non-flammable. R&D activity has been performed within the EIC generic R&D program and is now pursued within the DRD4 initiative (see below) to establish the validity of this approach. Radiation damage reduces the lifetime of the SiPM as good photodetector for the dRICH performance. Estimates of the radiation level on the dRICH photodetectors are expected to be accurate. The DCR model shown in Figure 3.120 (right) is for the sensors experiencing the largest radiation levels (closer to the beam line) and for detector operation at V_{over} = 4 V and T = -30°C. Operation at lower V_{over} = 3 V and/or lower temperature T = -40°C would reduce the DCR without loss in performance, hence allowing one to accommodate larger integrated radiation levels (up to a factor 2-3) than those reported in the figure. The addition of small thermoelectric cooling (TEC) modules will be evaluated as a potential approach to boost the cooling performance, allowing one to reach an even lower operation temperature of T = -50°C and avoid possible dishomogeneities. Current R&D on new SiPM technologies for improved performance and radiation hardness are being followed up as an optimization strategy and as a potential upgrade for the dRICH photodetector in the late 2030's or in the early 2040's. For two components, optical aerogel and carbon-fiber mirror, there is only one known supplier able to deliver the wanted specifications at the present stage. An early procurement should limit the risk of a market discontinuity. Within the ePIC RICH Consortium, the recently initiated R&D on mirrors at Purdue University are being followed up as potential sources of cost mitigation in the long term period, if the adaptation to the dRICH needs will be proven feasible. DSC members are part of the recent DRD4 initiative, that aims to create a worldwide collaborative environment to foster new technological breakthroughs in Cherenkov particle identification and photon detectors. Within DRD4, there are many development areas of interest for the dRICH program, in particular gasses or mixtures alternative to the greenhouse fluorocarbon gasses and radiation hard SiPM.

3.3.5 Electromagnetic Calorimetry

Add text here.

3.3.5.1 The backward endcap electromagnetic calorimeter

The concept of ePIC places the backward endcap electromagnetic calorimeter inside the central detector. The requirements from physics outlined below require a homogeneous scintillator material. The basic requirements on this scintillator material are compactness to minimize the radial thickness of the calorimeter, reasonably fast response, and high energy resolution and efficiency over a wide range of energies given by the physics program, and finally adequate radiation hardness. To fulfill these requirements even a compact geometrical design must provide high granularity resulting in a relatively large quantity of crystal elements. Their fabrication relies on existing proven technology for mass production to guarantee the necessary homogeneity of the whole calorimeter. Presently there is no alternative material available besides lead tungstate.

Requirements

Requirements from physics: The electron-end-cap calorimeter (EEEMCal) will cover a dynamic energy range of 0.5–18 GeV for electromagnetic showers of the scattered electron based on e+p Pythia simulations at 18x275 GeV^2. Detection down to 0.1 GeV is needed for decay photons and radiated photons that improve the scattered electron reconstruction. The EEEMCal is a high-resolution ECal designed for precision measurements of the energy of scattered electrons and final-state photons in the electron-going region. The requirements for energy resolution in the backward region is driven by inclusive DIS where precise determination of the scattered electron properties is critical to constrain the event kinematics.

An excellent energy resolution of $\sigma_E/E \approx (2-3)\%/\sqrt{E} \oplus (1-2)\%$ is required for the backward endcap electromagnetic calorimeter over a large dynamic range of photon energies [11].

Requirements from Radiation Hardness: The EEEMCal detector must operate at a radiation level of $\sim$3 krad/year (30 Gy/year) electromagnetic and 10^{10} n/cm^2 per year hadronic at the EIC top luminosity.

Requirements from Particle Fluence The high-resolution EEEMCal has the following basic requirement: Interaction rate capability up to 0.5×10^6 Hz requiring reasonably fast scintillation kinetics.

Justification

Device concept and technological choice: The EIC physics program requires high-precision detection and identification of the scattered electrons emitted in the electron-going direction, as well as final-state photons. The backward endcap electromagnetic calorimeter (EEEMCal) provides a compact solution with excellent energy resolution over a large dynamic range and with high granularity.

In general, for high-precision electromagnetic calorimetry, the following areas are of relevance: smaller radiation length for smaller longitudinal size, smaller Moliere radius allowing higher granularity, smaller decay time, better energy resolution and larger number of photoelectrons per MeV to reach higher resolution, smaller constant term contribution to energy resolution, mainly due to

Parameter/ Material	Density (g/cm^3)	Rad. Length (cm)	Molière Radius (cm)	Decay time (ns)	Light Yield (%)	dLY/dT (%/°C)	Rad. Hard. (krad)
NaI(Tl)	3.67	2.59	4.13	245	100	-0.2	1–2
CsI(Tl)	4.51	1.86	3.57	1220	165	0.4	1
CsI	4.51	1.86	3.57	35/6	3.6/1.1	-0.6/-1.4	1
BaF_2	4.89	2.03	3.1	650/0.9	36/3.4	-1.9/0.1	>50
CeF_3	6.16	1.70	2.41	30	5	∼0.1	>100
(BGO) / $Bi_4Ge_3O_{12}$	7.13	1.12	2.23	300	21	-0.9/-1.6	> 1000(recovery)
(PWO-II)/$PbWO_4$	8.3	0.89	2	30/10	0.6	-3.0	> 1000
SciGlass	3.7–4.5	2.2–2.8	2–3	20–50	0.3	None	> 1000

Table 3.50: Table of crystal properties.

non-uniformity and gaps or due to readout and noise, reasonable temperature dependence to light yield, and higher radiation hardness.

Lead tungstate meets the requirements of an extremely fast, compact, and radiation hard scintillator material providing sufficient luminescence yield to achieve good energy resolution. We are here referring to a new material labeled PWO-II available since the late 2010's, which provides improved luminescence compared to the PWO as developed for CMS. PWO-II with its increased structural perfection and optimized activation with luminescent impurity centers as well as reduced thermal quenching of the luminescence process meets all the requirements of the EEEMCal. Full size crystals with 200 mm length deliver an average light yield of 18 photoelectrons per MeV (pe/MeV) at 18 degrees Celsius measured with a photomultiplier with bi-alkali photocathode (quantum efficiency $\sim 20\%$).

The specifications are based on a large quantity of full-size crystals and are similar to those achieved with detectors at Jefferson Lab. Detailed specifications as well as a quality control program have been developed, taking into account the experience from CMS, PANDA, and the Jefferson Lab detectors.

The quality crystal can be provided at the moment by the Czech Republic manufacturer Crytur. The only alternative producer SICCAS in China has not yet succeeded producing full size PWO-II crystals.

The EEEMCal meets the experiment requirements of fast timing to handle an interaction rate up to 500 kHz and acceptable radiation hardness. Furthermore, the EEEMCal achieves the required clean electron identification for energies greater than 1 GeV with a rejection factor better than 10^4 when combined with other detector subsystems (tracker and pfRICH). The EEEMCal has been reviewed and passed the EIC Project Calorimetry Technical Review on December 2022.

A drawing of the EEEMCal mechanical design is shown in Figure 3.132. The EEEMCal will be located at a distance of 175 cm from the EIC interaction point where it is installed around the beam line in a roughly cylindrical geometry. It will cover a pseudo-rapidity range of $-3.5 < \eta < -1.5$. The particles of interest impinge on the front face of the detector and pass through a radiator with adapted geometrical dimensions to contain the major part of the electromagnetic shower. The produced scintillation photons are detected at the back of the radiator by means of an array of Silicon PhotoMultipliers (SiPMs) and their readout electronics. The entire detector is enclosed in a mechanical structure that also provides services such as thermal monitoring, cooling and light monitoring. The entire assembly weighs on the order of three metric tonnes, which is consistent with the specifications of the EIC experimental area at IP6.

Based on extensive simulation and experimental studies, the preferred material for the EEEMCal radiator is lead tungstate (PWO), an extremely fast, compact, and radiation-hard scintillator pro-

Parameter	Unit	EEEMCAL Required	Q&A Inform. Source
Light Yield (LY) at RT (for all sides polished crystals)	pe/MeV	≥ 15	Test with γ-source
LY(100ns)/LY(1μs)	%	> 90	Test with γ-source
Longitudinal Transmission at $\lambda = 360$ nm	%	≥ 35	Optical Measurement
Longitudinal Transmission at $\lambda = 420$ nm	%	≥ 60	Optical Measurement
Longitudinal Transmission at $\lambda = 620$ nm	%	≥ 70	Optical Measurement
Transverse Transmission and LY uniformity along crystal	%	10	Optical Measurement
Inhomogeneity of Transverse Transmission $\Delta\lambda$ at T=50%	nm	≤ 5	Optic. Measure.
Induced radiation absorption coefficient Δk at $\lambda = 420$ nm and RT, for integral dose > 100 Gy	m^{-1}	< 1.5	Irradiate with different sources
Mean value of dk	m^{-1}	≤ 1.0	Test
Tolerance in Length	μm	$\leq \pm 0, -100$	Measure.
Tolerance in sides	μm	$\leq \pm 50$	Measure.
Surface polished, roughness Ra	μm	≤ 0.02	Vendor
Tolerance in Rectangularity (90°)	degree	≤ 0.1	Measure.
Purity specific (raw material)			Vendor
Mo contamination	ppm	< 10	Vendor
La, Y, Nb, Lu contamination	ppm	?	Vendor

Table 3.51: PWO specifications.

viding sufficient luminescence yield (15 - 25 photoelectrons/MeV) to achieve good energy resolution. This material has been widely used for high-precision measurements of electromagnetic particles in a variety of experiments, such as at multiple setups at JLAB and also at PANDA/GSI. To achieve good energy resolution including the so-called constant term typically requires 20 or more radiation lengths (X_0). For PWO in the EEEMCal we have $22X_0$ (20 cm). The transverse block dimensions of 2×2 cm^2 are matched to the Moliere radius to capture the major part of the transverse shower. It has been shown that a PWO calorimeter can achieve an energy resolution $\sigma_E/E \approx 2\%/\sqrt{E} \oplus 1\%$ [78] when all the system parameters are carefully controlled. To pinpoint the electron scattering kinematics, the EEEMCal provides a position resolution of $\sim$2mm at 1-3 GeV. The technology for mass production of PWO crystals that guarantees the needed homogeneity of the whole calorimeter has been well established with recent experiments, most recently with the Neutral Particle Spectrometer at JLab [79, 80].

The relatively low energy threshold for the EEEMCal requires the usage of excellent photodetectors. The magnetic field of the EIC detector precludes the use of conventional photomultipliers. To solve this a photosensor insensitive to magnetic fields and with a small response to ionizing radiation has to be used. Furthermore, the photosensor should have an internal gain as PWO has a relatively

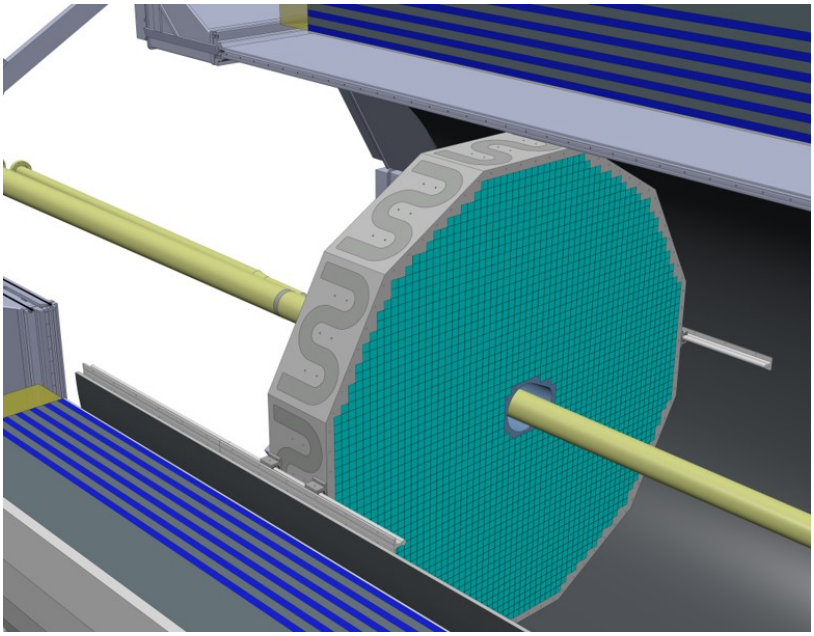

Figure 3.132: CAD drawing of the backward ECal attached to the Global Support Tube (GST) by means of rails. The outer structure shows the external cooling using Friction Stir Welding (FST) technology. The shape of the inner support structure is optimized to maximize the pseudo-rapidity coverage around the beam pipes.

low light output.

An effective way to read out the EEEMCal is through SiPMs that offer several advantages, e.g., a high gain and a medium photodetection efficiency of about 30%. Furthermore, SiPMs can be operated in the magnetic field of order few hundred Gauss expected at the location of the EEEMCal. Individual devices are grouped into an array to maximize surface coverage of the PWO blocks. In a recent beam test campaign, the readout concept was validated to work well with a Streaming Readout setup, the method of choice envisioned for the EIC [81].

Subsystem description:

General device description: In the EEEMCal the PWO crystals are arranged in the mechanical support structure (Fig. 3.133). This provides the infrastructure to attach the readout components, cooling system, and cables, as well as the installation fixtures to mount the detector in the experimental hall. The support for the crystals is provided by a frame that is installed in the mechanical structure. Photosensors are located at the backend of the crystals, and their photosensors are attached to a grating in the mechanical structure. The crystals are stacked with carbon fiber plates at front and back that allow one to guide the crystal into position. The cooling system provides thermal stabilization, which is important for crystal performance. Based on initial thermal calculations, this stabilization can be achieved with a combination of internal and external cooling aided by airflow.

Radiator: The radiation detectors are composed of lead tungstate scintillating crystals and thin reflector sheets.

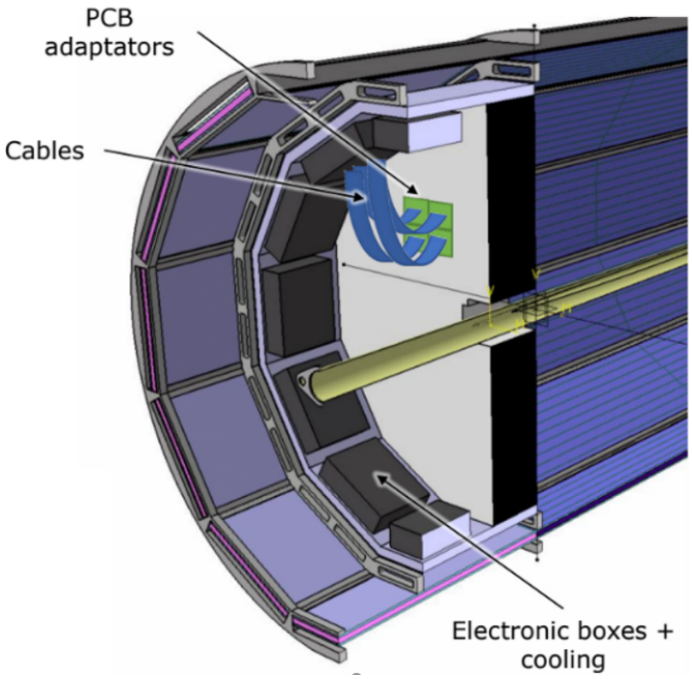

Figure 3.133: Conceptual design of the ePIC electron endcap electromagnetic calorimeter support.

Sensors: Hamamatsu S14160-3015 SiPMs have been identified as the optimal choice for the EEEMCal. Their gain of $3.6 \cdot 10^5$ and relatively low dark current rate (0.7 MHz) allow the measurement of very small signals, close to the single photo-electron (Fig. 3.134, left), while its high pixel density provided by a 15-μm pixel pitch provides very good linearity over several orders of magnitude (Fig. 3.134, right).

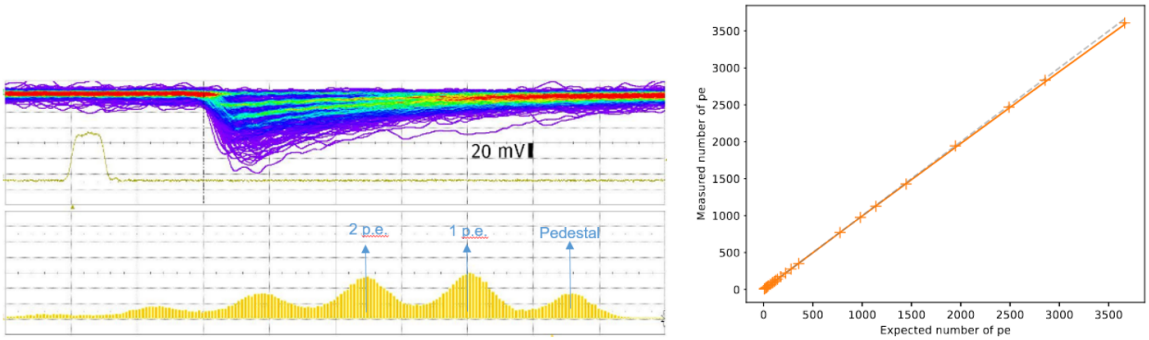

Figure 3.134: Left: waveform (top) and integrated signal (bottom) showing single photo-electron signals in Hamamatsu 15 um pixel SiPMs. Signals are produced with a low-intensity LED. Right: Linearity measurement, showing 2% linearity up to 3500 photo-electrons.

FEE: All calorimetry in ePIC will use SiPMs for their readout. However, the number of channels and input signals and capacitance varies greatly from detector to detector. The require-

ments of the EEEMCal are particularly stringent in terms of energy resolution, which in particular requires the detection of low energy signals (down to 5 MeV per crystal). The readout should provide sufficient dynamic range to accommodate for signals of energy up to 18 GeV.

A discrete readout solution based on commercial devices is currently the baseline for the forward and backward ECals. However, a readout based on the existing H2GCROCv3 chip (developed for the CMS HGCAL) is currently under investigation for the backward ECal. It presents many advantages, in addition to exploiting the synergies with most of the other calorimeters in ePIC. Using an ASIC in the readout of the calorimeter is a very cost effective, more radiation tolerant and cooler (i.e. consuming less power) solution. The H2GCROCv3 chip was developed by the Omega group for the primary use for the High Granularity Calorimeter (HGCAL) for the CMS detector at LHC, making it a great fit for any calorimeter readout. The ASIC requirements for the EEEMCal are very low noise level, low power consumption and very good ($< 1\%$) linearity throughout a very large dynamic range. The chip also has a current conveyor where each channel's bias voltage can be fine-tuned from the ASIC itself. A variation of the H2GCROCv3 chip (CALOROC) is currently under development by OMEGA in order to make it compatible with EIC.

A particular challenge for the EEEMCal (which is common for any readout solution) is the high capacitance of the photosensors (530 pF per SiPM; 8.5 nF if all 16 SiPM of a crystal are read in parallel). If we require to readout each SiPM individually in order to meet the energy resolution and time response of the detector, the number or readout channels for the EEEMCal will be $\sim$48,000.

LED monitoring system: the individual response of each calorimeter channel will be monitored using a dedicated LED light source integrated onto the PCB and positioned adjacent to the SiPM matrix of each crystal (see Fig. 3.135). These LEDs will provide a controlled light pulse that enables continuous monitoring of the channel gain and stability over time. By tracking the LED-induced signal over time, it is possible to detect and correct for variations due to temperature changes, radiation damage, or electronic drift. An effort is ongoing to identify an LED model that is radiation-hard and suitable for this purpose.

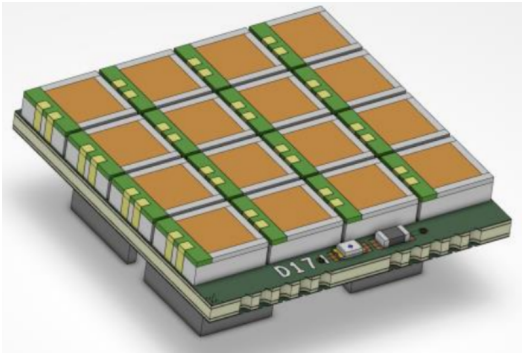

Figure 3.135: PCB holding the 16 SiPMs of a PWO-II crystal. An SMC LED is mounted on each PCB (the white component centered at the bottom of the board in this figure).

Performance Our group has performed extensive simulations of the detector performance in the ePIC geometry, including a realistic material budget in front of the detector, which directly affects its resolution and PID capabilities. Figure 3.136 shows the performance of two key parameters: the energy resolution and the pion rejection factor. For this resolution result, a conservative, energy-independent 2% smearing was applied on the simulated deposited energy values to account for

effects of digitization and randomness of the optical photon yield. Results fulfill the physics requirements as outlined in the Yellow Report [11] and NAS study [82].

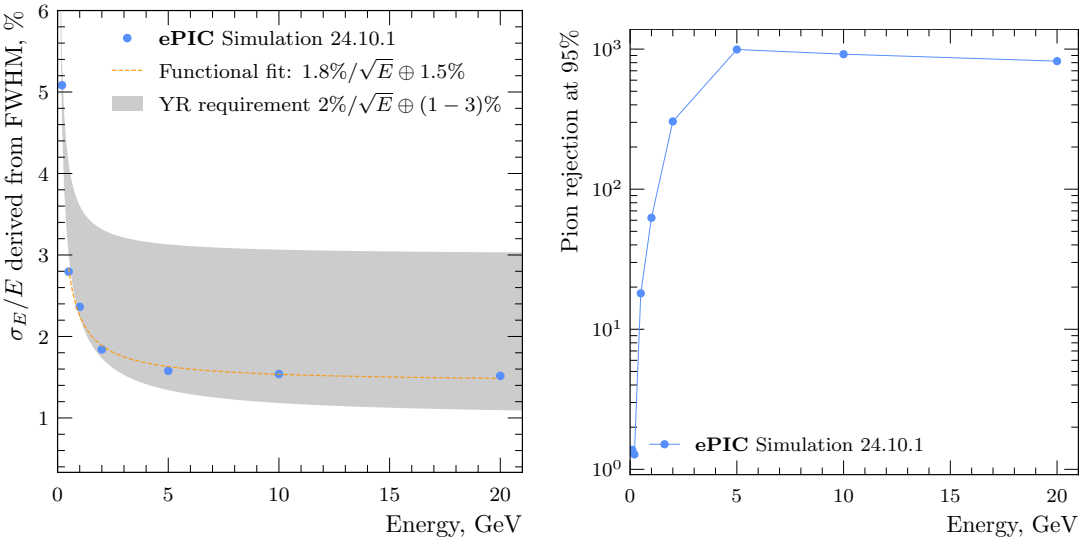

Figure 3.136: EEEMCal performance estimated from single particle simulations using the full ePIC detector geometry. Left: energy resolution as a function of the incident particle energy. Right: pion rejection factor as a function of energy and different values of electron efficiency. (Performance plots were produced by the backwards_ecal benchmark)

Implementation The EEEMCal project has been organized into a well-defined Work Breakdown Structure (WBS). The WBS contains the work necessary to complete the project scope and will form the basis of planning, executing, and controlling project activities. The WBS ensures that no portions of the estimate are omitted. The level of the WBS reflect a logical breakdown of the work by major system as shown in Table 3.52.

The EIC-DOE project dictates the window of installation of the EEEMCal. The EEEMCal assembly at BNL and full system cosmic tests are projected for 2029-2030. Installation in the ePIC detector is currently projected to be in the calendar year 2031.

Services: $PbWO_4$ crystals are sensitive to temperature changes with a variation of 2%/°C in light output. Thus, the specification is to keep the crystal temperature stable within ±0.1 °C. Temperature control is also needed for SiPMs, whose response is sensitive to temperature as well. To ensure temperature stability the additional heat generated by the electronics needs to be removed and the following cooling structures are being considered. As internal cooling structure several machined copper blocks with internal coolant circulation will be used around the beam pipe. To reduce the spatial extend support structures the EEEMCal consortium is moreover planning to use cooling plates in between the readout cables which are linked to the support structure surrounding the EEMC with tubes. This system is composed of 12 plates with a 5-8 mm spacing in which water can be circulated. The cooling near the crystals will likely not be enough to meet specification. These challenges could be overcome by outside cooling with standard cooling blocks with airflow in front of the electronics or additional cooling added at the back of the assembly.

ANSYS simulations are being performed to quantify the efficiency and guide the design of the

WBS	WBS Title	WBS description
2.00	EEEMCAL Project	Construct the EEEMCAL. The EEEMCAL is an electromagnetic calorimeter for measurement of the inclusive process physics in the electron-going direction at the EIC
2.01	Radiator	Radiation detectors consisting of scintillating crystals (PWO) and thin reflector sheets. These provide the detection of energetic electrons
2.02	Photosensor	Photosensors consisting of multi-pixel photon counters grouped into an array to maximize surface coverage of the PWO blocks.
2.03	Mechanical	Mechanical structure including installation fixtures and a cooling system providing thermal stabilization, which is important for crystal performance.
2.04	Signal Processing/DAQ	Signal Processing/DAQ providing the front-end electronics to transmit the signals to the data analysis modules
2.05	Simulation/Software	Simulations/Software providing the software libraries and infrastructure foundation for extracting the physics from the detector

Table 3.52: EEEMCAL WBS Structure

cooling system. Figure 3.137 show the temperature distribution of crystals in stationary state with room tempertaure at 26° C and cooling plates at 19° C assuming a uniform heat source of 1 kW behind the crystal, corresponding the current estimate of the FEBs power dissipation.

Steady-state simulation at different room temperatures have been performed to quantify the effect of the temperature fluctuation in IP6. Figure 3.138 shows the effect of a 3° C variation. Results of transient-state simulations are shown in Fig. 3.139 and demonstrate that crystal temperatures will remain within $\pm 0.1°$ C with the expected FEB power dissipation of FEBs and typical room temperature variations in IP6. This has also been confirmed experimentally by a recent and similar cooling-concept calorimeter built and operated by the EEEMCal consortium: the NPS calorimeter at JLab consisting of 1080 PWO crystals with readout electronics dissipating 500 W. Figure 3.140 show the crystal temperature variation within $\pm 0.1°$ C during a 24-hour period.

Subsystem mechanics and integration: The EEEMCal installation fixtures are shown in Fig. 3.141. They include a mechanical structure that mounts the detector and positions it in the EIC experimental hall at the appropriate height above ground. The structure is envisioned to ride on rails for the installation. The rails could be on the floor as shown, but could also be within the cylindrical structure. In the latter case the outer structure would be bolted to the floor. Having the rails extend from the cylindrical structure has the advantage that it would not require rails on the floor of the experimental hall, which could interfere with other hall infrastructure, e.g., the magnet.

Calibration, alignment and monitoring: To achieve the required energy and spatial resolution of the electromagnetic calorimeter it is essential to precisely calibrate the individual crystal

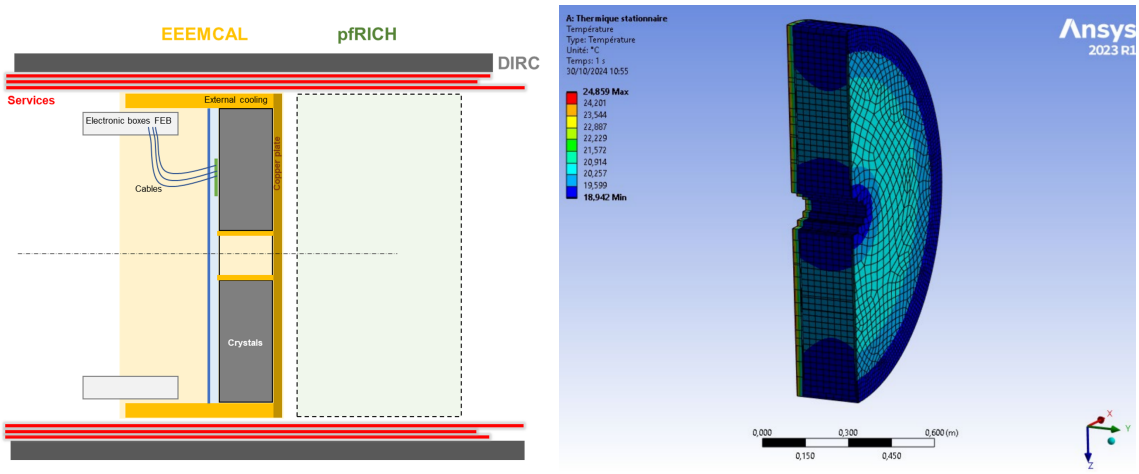

Figure 3.137: Left: Layout of the EEEMCal subsystem showing the external and internal cooling plates (yellow), a front copper plate, and some insulating barrier (blue) between the crystals and the heat source (FEBs, inside cooled boxes). Right: Simulated temperature distribution of crystals in stationary mode with plates at 19° C and room temperature of 26° C. A uniform heat source of 1 kW is assumed behind the crystals.

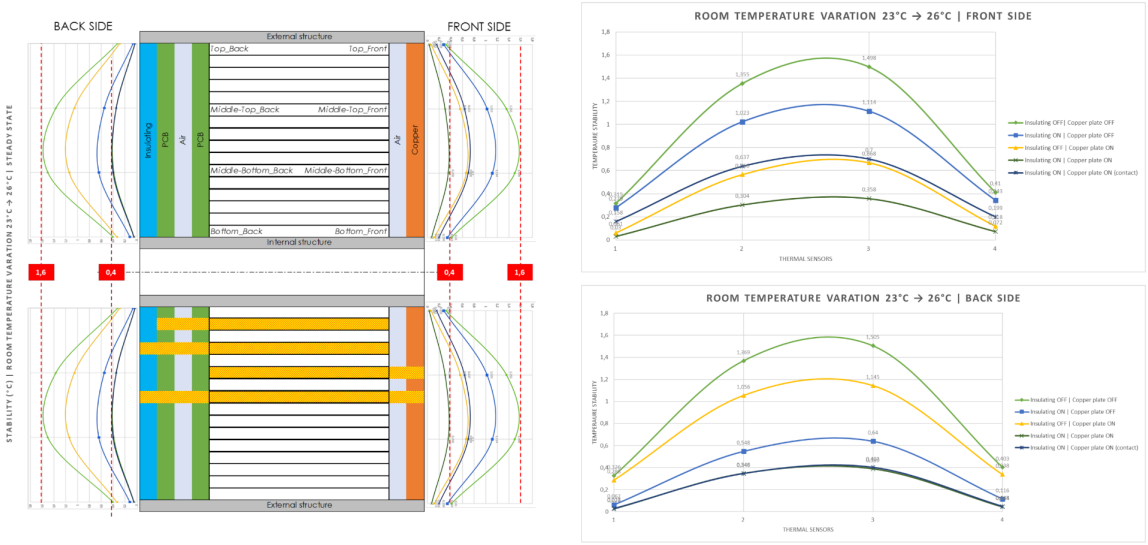

Figure 3.138: Steady-state simulation at 2 different room temperatures. Data show the temperature difference across the detector for different configurations of the cooling system. The nominal configuration (dark green) shows the best performance and yields a maximum temperature variation of 0.4° C in the central crystals.

channels. Time dependent variations of the calibration factors are expected due to several effects: change in light transmission, change in the coupling between the crystal and the photodetectors and variations in the photodetectors itself and the following electronics. Both the scintillation of the crystals and the amplification of the SiPMs depend on the temperature. Therefore stable cooling at the level of 0.1 degrees Celsius is required. Long term variations in the temperature need to

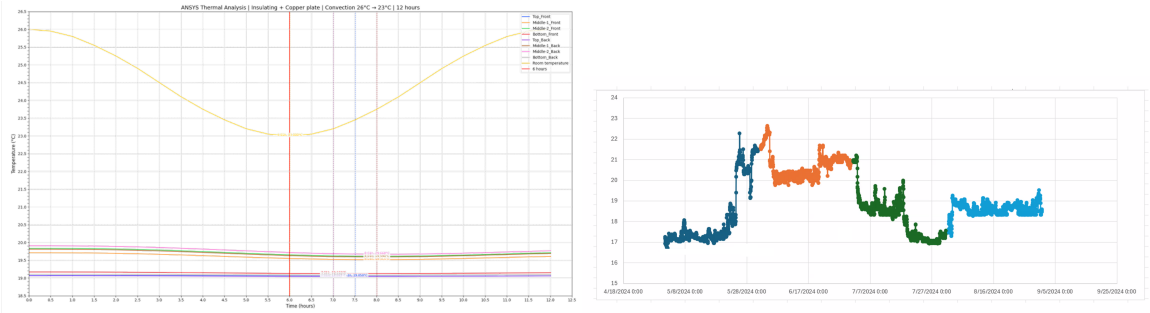

Figure 3.139: Left: Transient-state simulation showing the temperature variation of crystals as a function of time for a room temperature variation from 26° C to 23° in 6 hours. The thermal inertia of crystals is sufficiently high that the temperature variation of all of them is below 0.1° C. Right: typical temperature variations in IP6 as measured by the STAR experiment. Temperature is constant within ±1.5° C within a few hours.

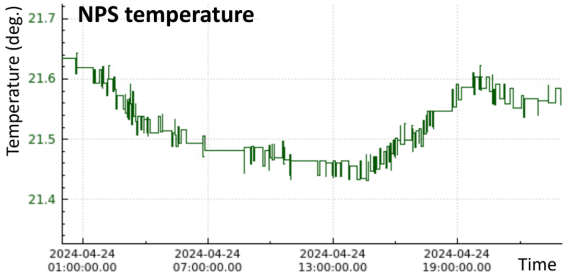

Figure 3.140: Temperature variation of PWO crystals measured in the NPS calorimeter, consisting of 1080 PWO crystals and 500 W FEBs. The cooling concept used for this detector is similar to the one planned for the ePIC backward ECal, and shows that the required crystal temperature stability is achieved.

be tracked by the calibration. Given an energy resolution between 1% and 2% at energies above 1 GeV, the precision of the calibration needs to be at the sub-percent level. For the calibration several methods performed in stages are planned: 1) Precalibration at test beams and with cosmic muons at the level of 10%, 2) In situ calibration with physics events (neutral mesons and electrons), 3) Continuous monitoring with a light-pulser system

Status and remaining design effort:

R&D effort: there are no ongoing R&D efforts for the EEEMCal.

E&D status and outlook: there are no ongoing efforts regarding the overall design choices. Ongoing activities relate to the integration and eventual impact on the design.

Other activity needed for the design completion: the test of engineering articles is required for the final choice of the readout electronics chain. Beam test campaigns are being prepared to address this.

Status of maturity of the subsystem: The EEEMCal subsystem is mature.

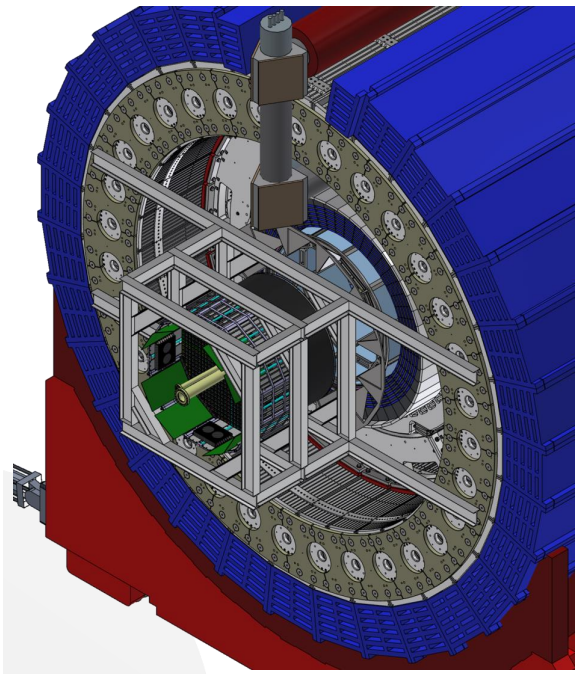

Figure 3.141: EEEMCal installation fixtures that allow for installing the detector safely into the ePIC detector barrel.

Environmental, Safety and Health (ES&H) aspects and Quality Assessment (QA), Construction and assembly planning Quality Assurance (QA) is an integral part of effective project management and will be employed throughout the design, procurement, and construction of the project. An EEEMCal Project-specific Quality Assurance Plan has been developed to establish all applicable QA requirements for the design, construction, and operation of the EEEMCal, consistent with the EIC Quality Assurance Plan that implements the ten criteria defined in DOE Order 414.1D.

Upon completion of its construction and initial testing, the EEEMCal will be situated at BNL. The EEEMCal collaboration leaders will coordinate the required equipment readiness for experiment and final integration of the EEEMCal into the EIC beamline with the EIC Project Management, the ePIC collaboration, and the BNL and JLAB Technical leads. This is necessary for successful integration. For example, a special external support frame will be provided, installed, and surveyed by the BNL technical staff for this purpose. All installations and the integration of the EEEMCal will be handled by BNL technical staff with expert's assistance to ensure appropriate interfacing of infrastructure and fulfillment of installation and operation protocols.

Once installed in the EIC experimental hall the EEEMCal will be operated and maintained by the EEEMCal team and its stakeholders in collaboration with technical teams at BNL. The normal operating resources will be provided by BNL. The physics resources to operate and maintain the EEEMCal will be provided through research grants. These resources are critical for tasks that are not directly related to the construction of the calorimeter, but instead to the integration of the EEEMCal into the ePIC detector. Examples include developing readout software and trigger algorithms, implementing online GUIs and the slow controls interfaces required to operate and monitor the detector during data taking, as well as designing clustering algorithms and calibration tools and integrating them into the ePIC workflow.

Collaborators and their role, resources and workforce: The participating institutions are briefly described and characterized by their expertise gathered in previous or ongoing research activities.

AANL (H. Mkrtchyan): the group has long-standing experience in constructing calorimeters and evaluating scintillating materials for different projects. For example, the group has built the lead glass based HMS and SHMS electromagnetic calorimeters in Hall C at Jefferson Lab.

ACU (L. Isenhower): the group has long standing experience with electronic signal digitization and readout systems.

Augustana (N. Grau)

Charles U./Prague (M. Finger): the group has long-standing expertise evaluating lead tungstate crystals for different projects.

CUA (T. Horn): the group has longstanding experience in crystal calorimetry. It has been leading the construction of the Neutral Particle Spectrometer at Jefferson Lab. In collaboration with Giessen U. the group contributed in the development of PWO-II

FIU (H. Szumila): the group has long-standing experience in running experiments at Jefferson Lab with focusing spectrometers and a variety of detectors including calorimeters. The group has experience with electronic signal digitization and readout systems.

JMU (I. Niculescu): The group has long-standing experience in the application of scintillation detectors and photo sensors.

Kentucky (R. Fatemi): the group has longstanding experience in experiments and detector construction at STAR. The group is leading simulation and software development efforts at the EIC.

Lehigh (R. Reed): the group performs research at BNL and has experience in detector construction and studies of photo sensors and readout systems.

MIT (R. Milner): the group has long-standing experience mounting large experiments and detector mechanical design and construction. The group has experience in response studies of scintillators using electron accelerators.

Orsay (C. Munoz-Camacho): the group has long-standing experience in mechanical and electronics engineering and the construction of large-scale detector systems. The group has played a leading role in the construction of the NPS.

LLR (M. Nguyen): the group has long-standing experience with readout electronics. The group has been strongly involved with the EMCal of CMS and, more recently, with the high granularity calorimeter upgrade for Phase-2 of the LHC.

OU (J. Roche, J. Frantz): the group's expertise covers many aspects of electromagnetic calorimeters, photo sensors, and readout systems.

W&M (C. Fanelli): the group has major experience in AI-assisted optimization of detector systems.

Technological Challenges and Path Forward Radiation exposure over time will induce damage in the SiPMs used for the backward ECal, leading to an increase in their dark current and associated dark rates. As dark rates rise, affected channels may begin to trigger more frequently, and in extreme cases, almost continuously, resulting in excessive data rates and potential degradation of overall detector performance. To mitigate this, it will become necessary to raise the discriminator thresholds for the noisiest channels, particularly those located at very high pseudo-rapidity, closer

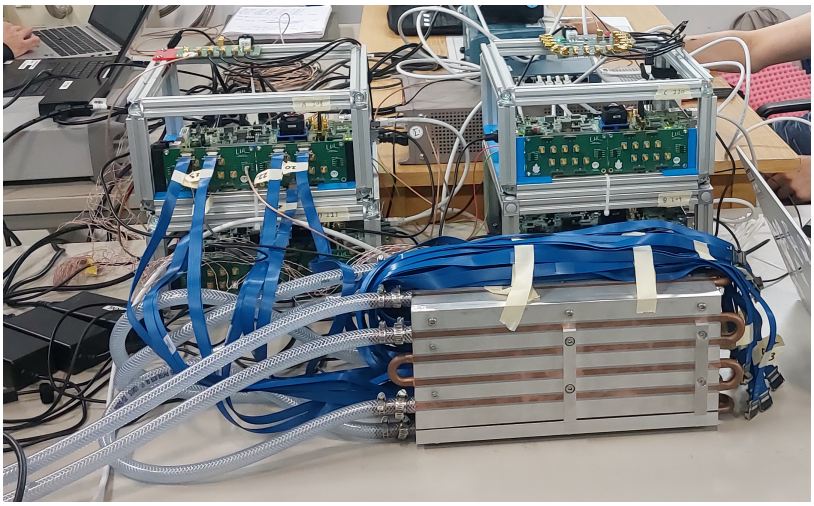

Figure 3.142: Backward ECAL 5×5 crystal prototype and full readout 400-channel electronic chain based on the HGCROC chip.

to the beam pipe, where radiation levels are highest.

We are also evaluating the impact of such threshold increases on the physics performance of the calorimeter. Raising thresholds can reduce sensitivity to low-energy deposits and may introduce non-uniformities in the detector response, which could affect energy resolution and reconstruction efficiency in certain regions. Quantifying these effects is essential to ensure that physics goals can still be met as radiation damage accumulates.

To inform our mitigation strategy, studies are currently underway combining irradiation campaigns on SiPM prototypes with simulations of trigger behavior as a function of dark current. These efforts aim to determine when performance degradation becomes significant and which channels are most vulnerable.

In the long term, the backward ECal has been designed with a modular architecture that enables targeted maintenance. Individual SiPMs can be accessed and replaced during scheduled shutdowns of the ePIC detector, allowing for restoration of performance in the most affected regions and ensuring the longevity and reliability of the calorimeter system.

Additional Material: prototype and beam tests After validation of the choice of scintillating material (PWO) and photosensor (Hamamatsu S14160-1315), a 5×5 prototype (Fig. 3.142) has been designed and built at IJCLab in order to test the full readout chain in a realistic experimental environment. It includes cooling plates to maintain crystals at constant temperature ($\pm 0.1^\circ$ C).

The readout chain is based on a protoboard developed within the EIC project R&D (eRD109) by the ORNL (Oak Ridge National Lab) group, driven by a Xilinx KCU105 board. The interface board between the ORNL board and the SiPMs was designed at LLR. It has been tested with LED signals injected into the crystals and more recently at CERN with electrons in the T09 line of the PS (see Figure 17). Figure 3.143 shows the waveforms of the 16 SiPM of a crystal as readout by the H2GCROCv3 chip. Signals show a rise time of 25-50 ns and a fall time of ∼100 ns (the scintillating PWO signal typically has a rise time of 20 ns with a fall time of ∼50 ns).

Additional beam tests were performed at DESY in 2025 and are currently under analysis.

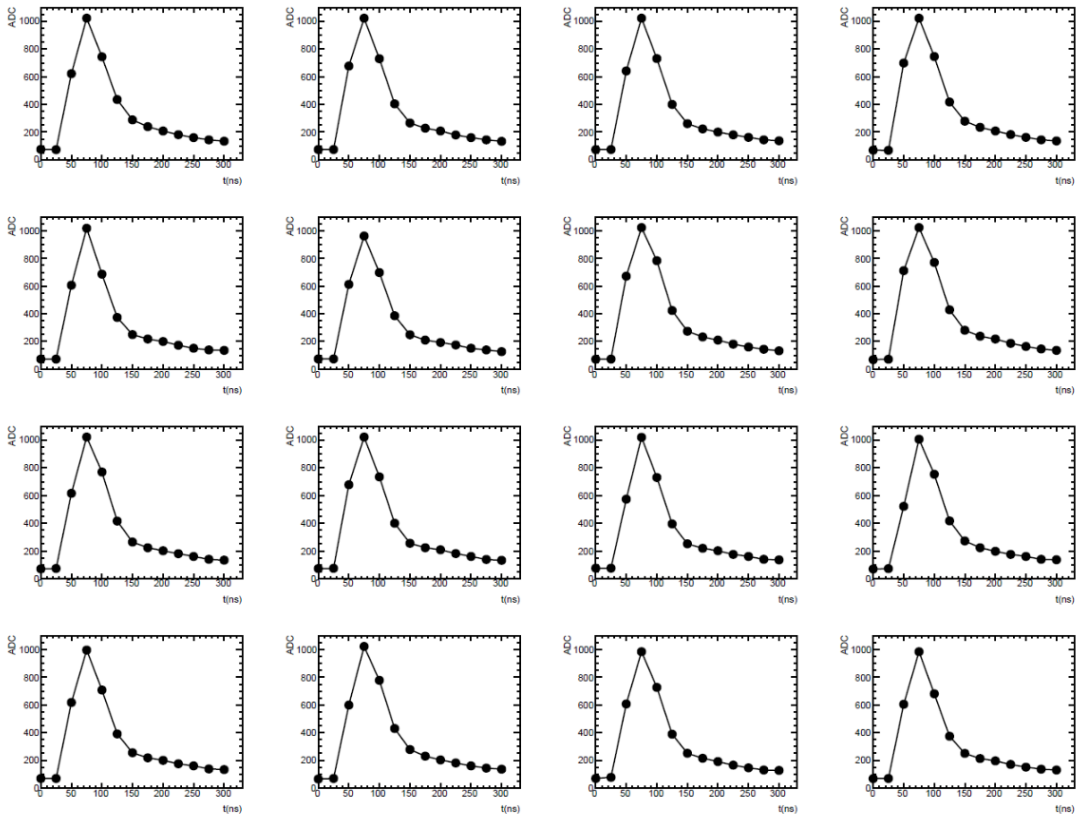

Figure 3.143: Waveforms for a 5-GeV electron in the 16 SiPM of a PWO crystal

3.3.5.2 The barrel electromagnetic calorimeter

Requirements

Physics requirements: The Barrel Electromagnetic Calorimeter (BEMC) must meet the following physics requirements: It needs to identify scattered electrons and measure their energy, particularly in high Q^2 events, and also detect decay electrons from vector or heavy flavor meson decays, and DVCS photons. Electron identification, including electron-pion separation, is required up to 50 GeV and down to 1 GeV, with an energy resolution better than $10\%/\sqrt{E} \oplus (2\text{–}3)\%$. Additionally, the BEMC must provide photon reconstruction from 100 MeV to 10 GeV. The system must also achieve photon-pion discrimination (γ/π^0 separation) up to 10 GeV, with the ability to distinguish two showers with an opening angle down to 30 mrad. Furthermore, the BEMC will assist with muon identification and provide a charged tracking point behind the DIRC to help with charged hadron PID, with a spatial resolution of less than 150 μm. Lastly, the system must have sufficient dynamic range to detect MIP signals, such as those from muons.

Radiation hardness requirements: The BEMC must be designed to operate in an environment where it may experience radiation levels of up to approximately 3.2×10^9 1-MeV neutron equivalent per cm^2 over the first 15 years of running (corresponding to 140 fb^{-1}), and ionizing doses of less than 1 krad over the BEMC's lifetime.

All components, including sensors, electronics, and structural materials, must be sufficiently radiation-hardened to maintain performance under these conditions. This includes ensuring that the sensor response, energy resolution, and position reconstruction capabilities remain stable throughout the detector's operational lifetime.

Data rate requirements: The BEMC and its readout technology must be designed to handle the high event rates expected at full luminosity, ensuring stable performance under expected background conditions, including radiation doses and neutron flux. The system must provide sufficient timing resolution to accurately discriminate between different bunch crossings, ensuring precise event separation. The chosen detector and readout technologies must be capable of processing the high data rates without compromising performance or data integrity. Furthermore, noise levels in the combined detector/readout system need to be low enough to enable detection of MIPs. The expected rates in the detector are presented under Performance and Readout Electronics and Data Acquisition.

Justification

Device concept and technological choice: The ePIC BEMC is called the Barrel Imaging Calorimeter (BIC). The BIC combines two proven technologies to meet the stringent requirements of the EIC physics program: The first is a lead-scintillating fiber (Pb/ScFi) sampling calorimeter read out with SiPMs, providing robust energy measurement through light collection, based on the well-established GlueX Barrel Calorimeter (BCAL) design [83]. This technology offers a reliable solution for high-resolution energy measurements, benefiting from its extensive use in other experiments. The second is a silicon tracker using AstroPix [84, 85] sensors, monolithic active pixel sensors (MAPS) based on HV-CMOS technology, interleaved with the Pb/ScFi layers to provide precise 3D imaging of calorimeter shower development. This hybrid approach delivers excellent

spatial resolution and position reconstruction, essential for separating particle showers and achieving accurate photon and electron identification, while preserving the superior energy performance of sampling calorimetry. The AstroPix sensors, developed for the NASA space mission AMEGO-X, offer low power consumption, radiation tolerance, cost-effectiveness, and scalability, making them ideal for large-area applications in a high-radiation environment. We selected the combination of Pb/ScFi for energy resolution and AstroPix for spatial resolution to balance performance, cost-effectiveness, and long-term reliability under the expected operational conditions at the EIC.

Subsystem description: The Barrel Imaging Calorimeter has a cylindrical geometry consisting of 48 trapezoidal sectors, with End-of-Sector Boxes (ESBs) at each end for services and readout, including the SiPMs for two-ended readout of the scintillating fibers and electronics front end boards. The trapezoidal sectors are fully active, with no dead areas of the Pb/ScFi matrix at their boundaries. This design allows the sectors to maintain a simple trapezoidal shape, projective to the solenoid axis, without requiring a tilt. The calorimeter spans approximately 17.1 radiation lengths (X_0) at central pseudorapidity, with the first layer consisting of an AstroPix imaging layer that provides a tracking point behind the DIRC. Each sector has six slots for AstroPix imaging layers, separated by about 1.43 X_0 of Pb/ScFi at $\eta = 0$. In the baseline configuration, slots 1, 3, 4, and 6—counting radially outward—are filled with AstroPix sensors, while slots 2 and 5 are designated for future upgrades. Figure 3.144 presents the overall structure of BIC and its sectors and Figure 3.145 shows the imaging AstroPix layers components. A sketch of the mechanical envelopes of the ESB is presented in Figure 3.146. Table 3.53 summarizes the main BIC detector parameters and Table 3.54 summarizes the structure of AstroPix and Pb/ScFi layers.

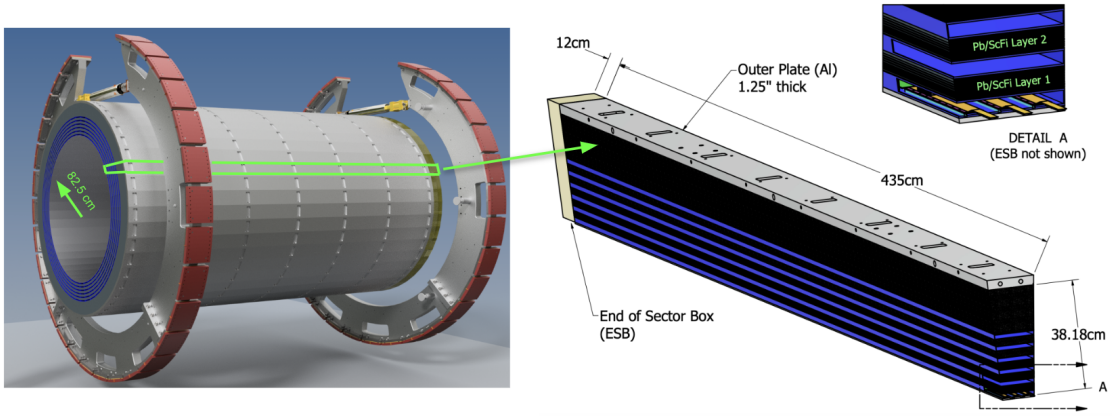

Figure 3.144: On the left, a 3D rendering of the Barrel Imaging Calorimeter with its 48 sectors. The central drawing shows the structure of a single sector, featuring interleaved Pb/ScFi layers and slots for trays holding AstroPix chips, followed by the Pb/ScFi bulk section. On the right, a zoomed view of the first radially layers is presented.

Scintillating fibers for Pb/ScFi: The Pb/ScFi calorimeter system, similar to the GlueX BCAL, has its fibers positioned parallel to the z-direction with 2-sided readout for energy measurement and position reconstruction along the fiber. We will use scintillating fibers with 1 mm diameter embedded in lead and glue to provide reliable energy measurement through light collection. For the scintillating fiber parameters refer to Table 3.57.

Sensors for Pb/ScFi: The light from the scintillating fibers is subdivided into 12 rows of 5 columns per sector-end by light guides, which are optically coupled with silicon rubber

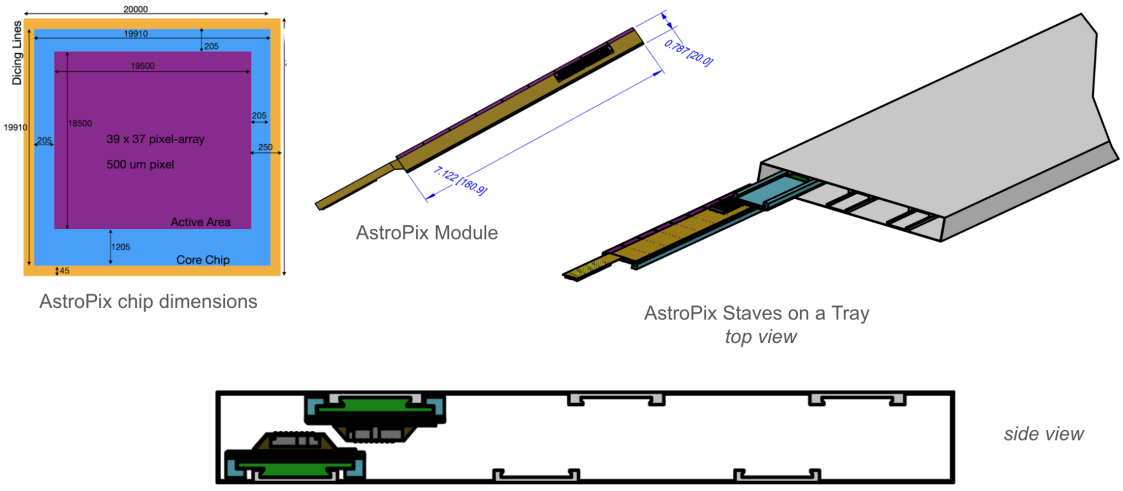

Figure 3.145: Components of Barrel Imaging Calorimeter imaging AstroPix layers. The side view shows a cross section of a single AstroPix layer viewed from one of the ESBs.

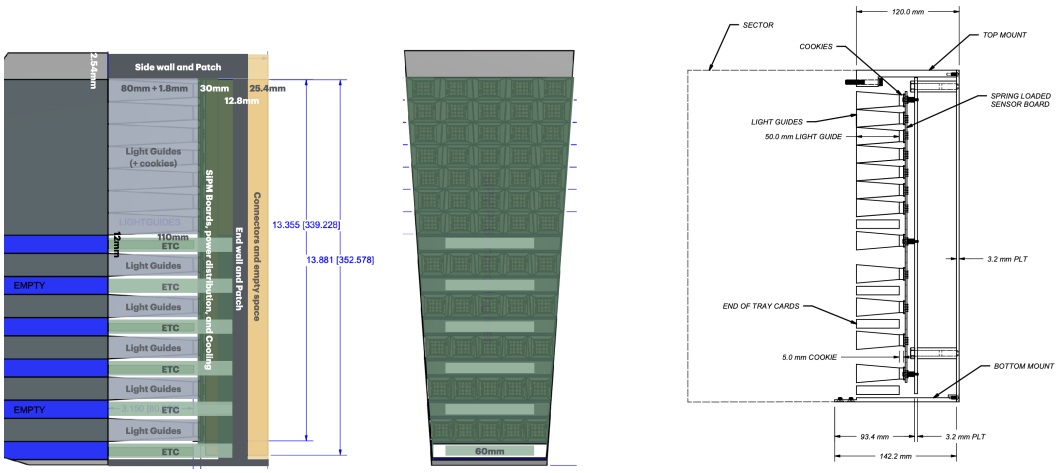

Figure 3.146: Sketch of the mechanical envelopes for the BIC ESB. Left: Side view at the end of a sector. Center: Rear view cutout at the SiPM PCB. Right: Engineering drawing showing the side view of the ESB.

optical interface (optical cookies) to the SiPMs. These sensors have a 50 μm pixel pitch to optimize dynamic range and photon detection efficiency. For the SiPMs parameters refer to Table 3.56.

FEE for Pb/ScFi: The FEE for the Pb/ScFi system, based on the CALOROC ASIC, processes the signals from the SiPMs. It provides sufficient time resolution for determining the z-position of events within the scintillating fiber, with position resolution of the order of 1 cm/$\sqrt{E}$, while maintaining low noise and high radiation tolerance.

Sensors and modules for imaging layers: The imaging layers use AstroPix monolithic silicon sensors with a 500 μm pixel pitch, interleaved with the Pb/ScFi layers. The 9 daisy-

chained AstroPix sensors are glued on a base plate and read out on a flexible PCB to form a module, providing high-resolution spatial information for 3D imaging and particle identification. For the AstroPix chip parameters refer to Table 3.55.

Staves and trays: Each stave is formed by daisy-chaining 12 AstroPix modules. A tray holds 6–7 staves based on the (radial) layer position, with each tray being half of the sector length and read out at its respective end in the ESB. This modular structure allows for flexible scaling and future upgrades to the system.

End-of-Tray Card (ETC): The ETC functions as the RDO unit in the ePIC DAQ scheme (see also RDO). Each ETC is responsible for a full tray of AstroPix staves. It manages signal processing, data formatting, and communication with the DAM, ensuring efficient and reliable data flow from the sensors. Note that within the module-stave-tray design, the ETC communicates directly with each 9-chip module.

Detector parameters	**Value**
Active length (z-direction)	435 cm
Inner radius	82.5 cm
Number of sectors	48
η coverage	$-1.71 \lesssim \eta \lesssim 1.31$
Radiation length X_0	1.45 cm
Total depth in X_0	between 17.1 ($\eta = 0$) and 42 ($\eta = -1.55$)
Molière radius	4.5 cm
Total sampling fraction of the entire Pb/ScFi system	about 9.5%, see Figure 3.147
Total sampling fraction of the entire AstroPix system	$< 0.4\%$
ScFi diameter	$\varnothing$ 1 mm
ScFi radial separation	1.22 mm (between fiber centers)
ScFi azimuthal separation	1.35 mm (between fiber centers)
Light guide length	5 cm
Number of light guides	60 per sector per side
Monitoring system	Blue LED, one LED per light guide
SiPMs	1.2×1.2 cm^2 arrays, 50 μm pixel
Number of SiPMs	60 arrays per side for each sector
Number of scintillating fibers per sector	about 20k

Table 3.53: Selected BIC Parameters.

Performance The BIC design meets the stringent energy and particle separation requirements for the EIC scientific program. We optimized the BIC design and validated its performance through a combination of detector simulations, beam tests, and bench measurements. We analyzed key metrics, including energy resolution, angular resolution, and particle identification, to ensure that the detector meets or exceeds the required specifications. The results presented here highlight the detector's capabilities and its ability to operate efficiently under EIC conditions. While the BIC may seem to exceed requirements in metrics such as energy and position resolution, this reflects a design

AstroPix layer (radially out)	Number of staves per sector-layer	Number of modules per sector-layer	Number of chips per sector-layer
1	6×2	144	1296
2	-	-	-
3	7×2	168	1512
4	7×2	168	1512
5	-	-	-
6	7×2	168	1512

Pb/ScFi layer (radially out)	Number of ScFi sublayers radially	Thickness in X_0	Readout channels per sector-layer
1–12	17	about 1.43	5×2

Table 3.54: AstroPix and Pb/ScFi layer parameters. The first table presents the parameters for the AstroPix layers, while the second table outlines the Pb/ScFi layer configuration. Radially outward, the calorimeter begins with AstroPix layer 1, followed by interleaved Pb/ScFi and AstroPix layers. Beyond AstroPix layer 6, the bulk section of the calorimeter consists of Pb/ScFi layers 6–12.

Parameter	Specification
Pixel size	500 μm x 500 μm
Power usage	< 2 mW/cm^2
Energy resolution	10% @ 60 keV
Dynamic range	25-700 keV
Passive material	$< 5\%$ on the active Si area
Design time resolution	3.125 ns
Si Thickness	500 μm
Active area per chip	2 cm x 2 cm

Table 3.55: AstroPix chip parameters for BIC.

tailored to meet more demanding performance needs, including electron-pion separation, neutral pion-photon separation, and the dynamic range required for detecting MIPs. These challenging requirements drive the superior energy resolution and the enhanced position resolution, which are critical for reconstructing event topologies where particles are closely spaced.

Energy resolution: We estimated the energy resolution of the Pb/ScFi layers based on detailed simulations in various rapidity ranges and photon/electron energies. Figure 3.147 (a) presents the energy resolution for photons, extracted from the Gaussian core of a Crystal Ball fit to the expected energy losses in Pb/ScFi. Table 3.58 shows the fitted stochastic and constant terms a and b of the energy dependence $\sigma/E = a/\sqrt{E} \oplus b$. The stochastic term, ranging from 5.8% to 6.6%/$\sqrt{E}$, and the constant term, between 0.6% and 1.2%, depending on rapidity, meet the detector's energy resolution requirement of better than 10%/$\sqrt{E}$ $\oplus$ 2–3%. Figure 3.147 (b) shows the sampling fraction, defined as the energy deposited in

Parameter	Specification
Active Area	3 mm x 3 mm (4 x 4 array) Preassembled array covering 1.2cm x 1.2cm
Pixel Size	50 μm
Package Type	Surface Mount
Peak Sensitivity	450 nm
PDE	$\sim$ 50%
Gain	$>\sim 2 \times 10^6$
DCR (Dark Count Rate)	Typ.: $\sim$ 500 kHz / SiPM Max: $<$ 1.5 MHz / SiPM (DCR applies to each SiPM in the 4 x 4 array)
Temperature Coefficient of Vop	$<$ 40 mV/C
Direct Crosstalk Probability	$<\sim$ 7%
Terminal Capacity	$\sim$ 500 pF / SiPM (Applies to each SiPM in the 4 x 4 array)
Vop Variation within a Tray	$<$ 200 mV
Recharge Time	$<$ 100 ns
Fill Factor	$>$ 70%
Protective Layer	Silicone (n $\sim$ 1.5-1.6)

Table 3.56: SiPM specifications for BIC.

Parameter	Specification
Light yield	$>$ 3.5 photoelectrons (measured using Sr-90 source with blackened opposite end)
Diameter	1.00 $\pm$ 0.01 mm (RMS $\leq$ 0.02 mm)
Attenuation length	$>$ 4 m (for blue light)
Batch-to-batch variation of light yield	$<$ 15%
Batch-to-batch variation of attenuation length	$<$ 10%
Emission spectrum	Blue-green light
Scintillation decay time	$<$ 3 ns
Total length	4900 km of fibers
Delivery method	In canes, length of fibers 4.55 meters $\pm$0.01 m

Table 3.57: Scintillating fiber specifications for BIC.

the scintillating fibers divided by the true energy of generated photons. Our energy performance results align well with beam test data using a positron beam at Jefferson Lab. See the Additional Material for more details, including results on the contribution of the low-energy tail of the energy loss.

Angular resolution: We estimated the angular resolution for photons using the AstroPix layers, based on detailed detector simulations for various rapidity ranges and photon en-

η range	$a/\sqrt{E}$ [%]	b [%]
$(-1.7, -1.3)$	6.60 ± 0.03	0.66 ± 0.04
$(-1.3, -0.88)$	6.11 ± 0.01	1.24 ± 0.01
$(-0.88, -0.4)$	5.91 ± 0.02	1.24 ± 0.02
$(-0.4, 0)$	5.85 ± 0.01	0.88 ± 0.02

Table 3.58: Fitted energy resolution parameters for photons in BIC for different η ranges.

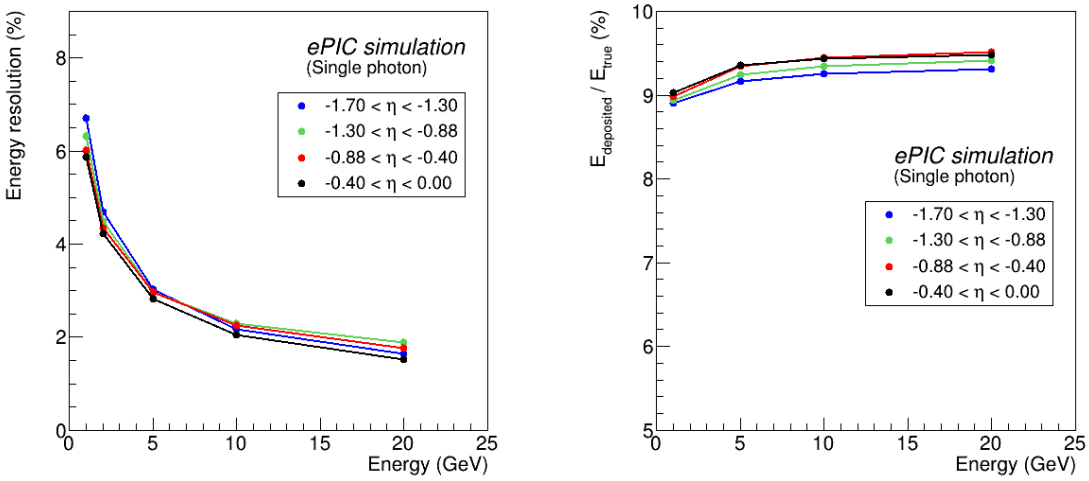

(a) (b)

Figure 3.147: (a) Simulated energy resolution from the Pb/ScFi calorimeter, extracted as the standard deviation (σ) of the Gaussian core of a Crystal Ball fit to the photon energy deposits in various rapidity ranges of the BIC. The performance in the positive η region is similar to that in the negative region; for clarity, only the negative region is shown. (b) Sampling fraction for photons, defined as energy losses in scintillating fibers divided by the true photon energy, as a function of photon energy in different rapidity ranges. Source code for figures

ergies. We extracted the difference between the true and reconstructed polar (θ) and azimuthal (ϕ) to estimate the FWHM resolution. In the current reconstruction algorithm, the angles are reconstructed from the hit with the maximal energy deposit in the AstroPix layer where the shower started. The resolutions for θ and ϕ are presented in Figure 3.148. The results indicate a small dependence of the angular resolution on η. In all regions, the angular resolution remains well below 0.1 degrees, which is on the level of single pixel resolution. The example fit of the θ resolution in the rapidity region of $-0.88 < \eta < -0.4$ gives (0.040 ± 0.004) deg$/\sqrt{E} \oplus (0.016 \pm 0.003)$ deg. The ϕ resolution is worse than the θ resolution due to the smearing of shower particles by the magnetic field. Overall, the results show significantly better performance than what can be achieved with any tower-like calorimetry systems and fulfills the requirements for the barrel electromagnetic calorimetry for the EIC.

Electron-pion separation: The design of the barrel calorimeter aims to provide high π^-/e^-

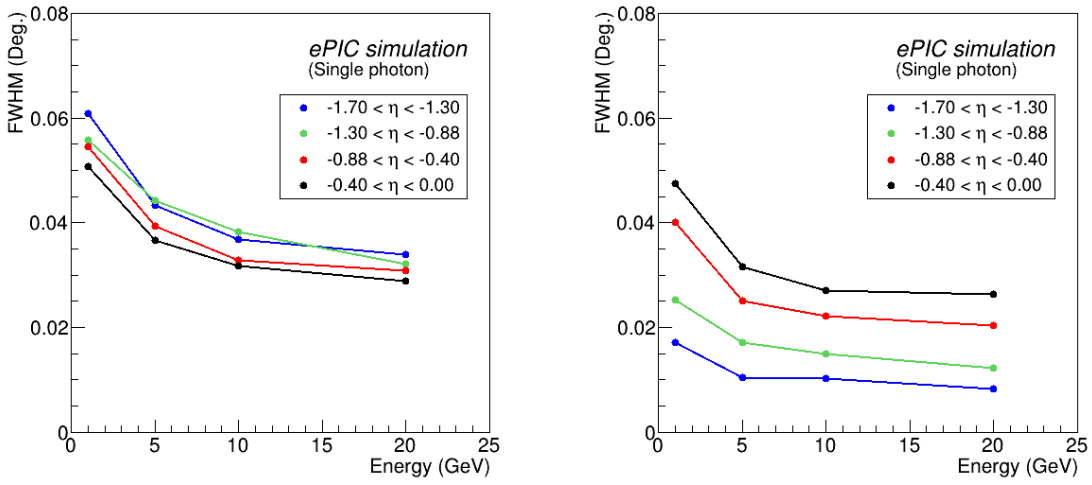

Figure 3.148: Simulated angular resolution for photons at different energies for the ϕ (a) and θ (b) angles reconstructed form the maximal-energy pixel from the first AstroPix layer where the shower started. The resolution is taken as FWHM from the distribution of the difference between true and reconstructed angle. Source code for figures

separation, particularly in the momentum region below 5 GeV. The AstroPix layers capture snapshots of electromagnetic and hadronic showers, allowing for the reconstruction of a 3-dimensional profile of the shower development, supported by the longitudinal energy profiles from the Pb/ScFi layers. Charged pion rejection is a two-step process. First, we apply an E/p cut to the cumulative energy deposit in the Pb/ScFi layers. This cut is deliberately loose to ensure high electron efficiency. The "cleaned" samples, following the E/p cut, are then fed into a classification neural network for inference. We used a 10-layer Visual Geometry Group-style Convolutional Neural Network [86] using the combined AstroPix and Pb/ScFi detector response. The network utilizes energy and position features from both technologies capturing energy and spatial shower details. Future improvements may come from using more advanced reconstruction techniques based on Graph Neural Networks [87] or Point Clouds [88]. Figure 3.149 (a) illustrates the charged pion suppression factor at $\eta = 0$ rapidity for a target 95% electron efficiency. The rejection exceeds 10^3 at low to mid energies, where it is most critical.

Photon-π^0 separation: Figure 3.149 (b) shows the upper limit of the probability of merging two γs from a π^0 decay into a single cluster at $\eta = 0$. Simulations were performed for neutral pions decaying into two γs with various momenta. For the calorimeter technologies based on tower geometry, as outlined in the EIC Yellow Report [11], the separation probability is defined by the criterion requiring the two γs to be separated by at least one tower size. In contrast, the BIC technology, leveraging granular position information from AstroPix, employs a different criterion. The probability of merging two γs was determined using a separation of six times the FWHM of the shower profile, measured at the third imaging layer. This layer registers at least one hit for more than 90% of photons with energies above 0.5 GeV, ensuring a conservative estimate. This limit for γ/π^0 separation is expected to be well above 10 GeV, based on studies incorporating AstroPix' position resolution and shower profile data. Addi-

tionally, initial results from a neural network approach for neutral pion identification, similar to the e^-/π^- studies but simplified, were applied using full detector simulations. These initial findings indicate a π^0 rejection of approximately 82% at 90% photon efficiency for 10 GeV particles, reflecting the current status of model training.

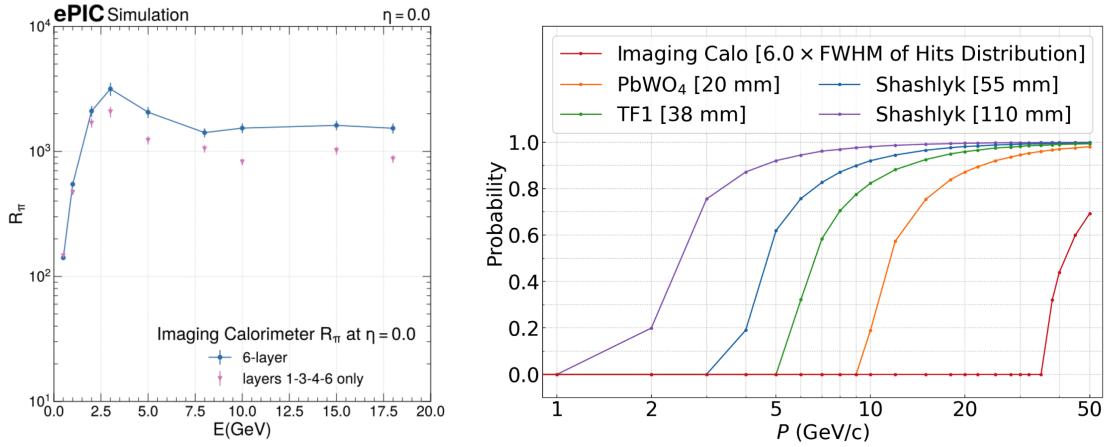

(a) (b)

Figure 3.149: Simulated performance on particle identification from BIC. (a) The charged pion suppression factor for $\eta = 0$ rapidity for 95% electron efficiency as a function of particle energy E. Pink points show the baseline performance where slots 1, 3, 4, and 6, counting radially, of imaging layers are filled with AstroPix trays, blue points show performance with 6 imaging layers. (b) Upper limit on cluster merging at $\eta = 0$ (shortest distance for particles to travel about 80 cm) from 2 photons from π^0 decay at particular π^0 momentum P. For calorimeter technologies based on tower geometry from [11] the separation by at least one tower size, marked in the plot legend, is required. For BIC the separation based on shower profile was assumed (see text). Source code for figures

Low-energy response: We evaluated the performance of the BIC for detecting MIPs through simulations using 5 GeV muons at various rapidities. The deposited energy per readout cell, represented by the most probable value of the MIP peak, was extracted from simulations with Kuraray fibers that meet the Final Design Review fiber specifications. This was compared against the 4-sigma pedestal peak from S14161-3050-04 SiPM array simulations, which is one of SiPM models that fulfill Final Design Review specifications. Even with the dark count rate corresponding to the irradiation level of 1×10^9 1-MeV neq/cm^2 (performed for ePIC by the INFN Bologna group) at 5°C, the MIP signal remains well-detectable with a 4-sigma cut on the pedestal. Figure 3.150 shows the extracted most probable value (MPV) of the MIP peak in terms of the number of photoelectrons (nphe) for muons at $\eta = 0$, which is the case where we observe the least photoelectrons from muons due to the combination of the distance the light has to travel in the fibers and the energy muons deposit at this angle in one Pb/ScFi layer. The pedestal 4-sigma value is marked in red and the electron-going and proton-going end results are presented. An example pedestal and MIP signal spectrum for 9 and 12 phe MIP signals assuming same sample size for the pedestal and the signal, showing the worst-case scenario for the back Pb/ScFi layer of the BIC, is also presented. The BIC demonstrates the capability to detect minimum ionizing particles for calibration purposes in the Pb/ScFi layers, with the MIP peak from 5 GeV muons remaining well-separated from

the pedestal, even after realistic irradiation doses. This separation is maintained through careful application of threshold cuts in each channel, ensuring that the MIP signal remains distinguishable from the noise. If necessary, we can lower readout thresholds, as the ASIC provides enough headroom, and employ a coincidence logic (e.g., requiring two neighboring readout cells to fire) for further zero suppression to ensure stable MIP performance over the lifetime of the detector.

We also evaluated the response to low-energy photons using simulations. For 100 MeV photons—the lowest energy required to be detected in the BIC according to the EIC detector requirements—we observe performance that meets the energy resolution requirement with high efficiency. The GlueX BCAL has demonstrated the capability to detect and reconstruct photons down to the nominal threshold of 100 MeV, with certain physics-channel analyses lowering it to 50 MeV for which typical clusters contain two fired readout cells [83]. Our simulations indicate that for 100 MeV photons, the energy resolution achieved will be approximately 15%, with an efficiency of firing at least two readout cells per shower on both sides of the calorimeter of 94% for photons at $\eta = 0$ and 73% at $\eta = 1$. See the Additional Material for more details.

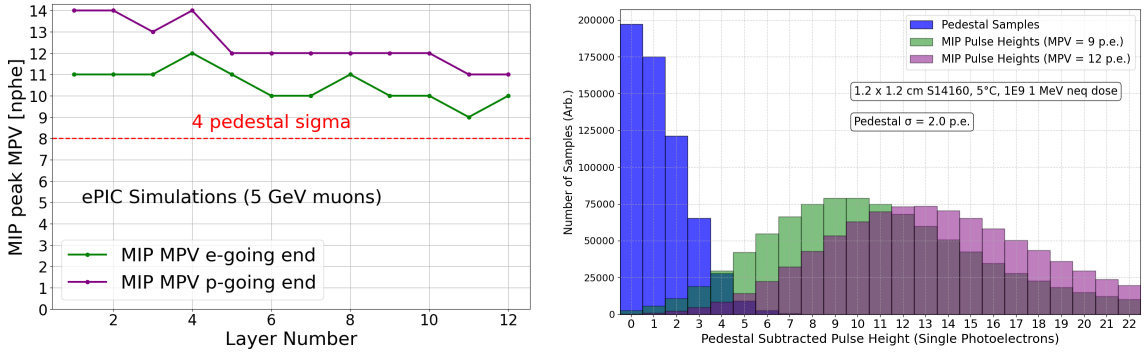

(a) (b)

Figure 3.150: Simulated performance on MIP response in BIC. (a) The most probable value of the MIP peak in terms of the number of photoelectrons for 5 GeV muons at $\eta = 0$ at each of the 12 BIC layers. The red line corresponds to 4 sigma of the pedestal simulated with realistic S14160 family SiPM responses at 5 degrees Celsius, irradiated with a dose of 1×10^9 1-MeV neq/cm^2. The green line corresponds to the electron-going end, while the purple line corresponds to the proton-going end readout cells. (b) An example spectrum of the pedestal and MIP pulses at 9 and 12 phe signals, showing the worst-case scenario from plot (a) for the back Pb/ScFi layer of the BIC at $\eta = 0$. Source code for figures

AstroPix sensor performance: The AstroPix chip has been extensively tested in both bench and beam environments. The AstroPix_v3, the first full-size chip with a 500 µm pixel pitch and row-and-column readout (35 rows and columns in a strip-like format), has demonstrated strong performance, as summarized, for example, in [85]. Key tests included a noise study and a radiation source test. In the noise study, less than 0.5% of the pixels exhibited a noise rate exceeding 2 Hz, at the threshold of approximately 25 keV. These results meet the BIC's requirements for low energy thresholds and masked pixel yield. The radiation source test, using isotopes with calibration points ranging from 22.2 keV to 122 keV, as shown in Figure 3.151, showed that 44% of pixels met the 10% energy resolution requirement at 59.5 keV, and 92.4% of pixels achieved the required 25 keV sensitivity for BIC. Although the AstroPix_v3 chip is not fully depleted, it demonstrated promising performance. The upcoming

AstroPix_v5, designed with a dynamic range extending to 700 keV, is expected to meet energy resolution requirements for all pixels.

AstroPix beam test results: We used beam tests at Fermilab Test Beam Facility (FTBF) to further validate the AstroPix_v3 chip in both single- and double-layer configurations. In the single-layer test, data collected with a 120 GeV proton beam was used to match corresponding row and column hits, using matching timestamps and ToT to reveal a hit map that showed the proton beam profile presented in Figure 3.151 (a). Although the AstroPix_v3 has a daisy-chained row and column readout and does not yet have an individual pixel buffer (which is implemented in AstroPix_v4 and higher versions), it demonstrated a precise hit-pixel reconstruction. In the double-layer configuration, two daisy-chained layers of AstroPix_v3 were tested, successfully reading events in coincidence and pinpointing hit-pixel locations, providing a proof-of-concept for layer integration in a beam environment.

In summary, the characterization of AstroPix_v3 is ongoing, with specific tests designed to meet the ePIC detector requirements. Remaining improvements, including enhanced dynamic range and energy resolution, will be addressed in the upcoming AstroPix_v5, which is expected to be fabricated by late 2025.

Simulation performance validation: The BIC performance results presented in this work are based on a full simulation of the system within the ePIC detector, using realistic geometry and a framework validated through bench tests and beam data from FTBF and Jefferson Lab Hall D (see [89] for FTBF results). The Pb/SciFi matrix was modeled in detail, with embedded scintillating fibers in lead and glue. AstroPix layers were implemented as realistic staves, accounting for dead areas and material contributions from sensors, electronics, cables, insulation, and support structures. Realistic digitization and reconstruction were applied throughout. For the Pb/ScFi component, we implemented an effective model incorporating fiber attenuation, photoelectron statistics, light guide efficiency, and SiPM thresholds, based on data and optical simulations. AstroPix digitization was modeled at the pixel level, while each Pb/ScFi readout unit corresponded to one light guide with an attached SiPM.

We present more details on select benchmarks of realistic simulation results against measurements in the supplemental material.

Expected Data Rates: Based on global ePIC studies of rates from signal and background [90], the channel maximum, channel average, and total data rates for the BIC are presented in Table 3.59. For the imaging layers, one channel corresponds to one chip, while for the ScFi/Pb layers, one channel corresponds to one SiPM array. For electron-proton DIS, rates have been estimated from the 18×275 GeV simulations, where $0 < Q^2 < 1$, and the collision rate has been scaled to the highest luminosity (500 kHz), corresponding to the 10×275 GeV beam energy configuration. In beam background simulations, the highest channel rates are achieved for the hadron and electron beam backgrounds at 10×275 GeV.

Implementation

Subsystem mechanics and integration: The 48 BIC sectors are arranged in a self-supporting Roman arch configuration. Once assembled, the full calorimeter rests on the solenoid cryostat support rings. In the hadron-going direction a small gap must be bridged between the end of the BIC and the support ring, while in the lepton-going direction the system slightly overhangs, creating a cantilevered structure.

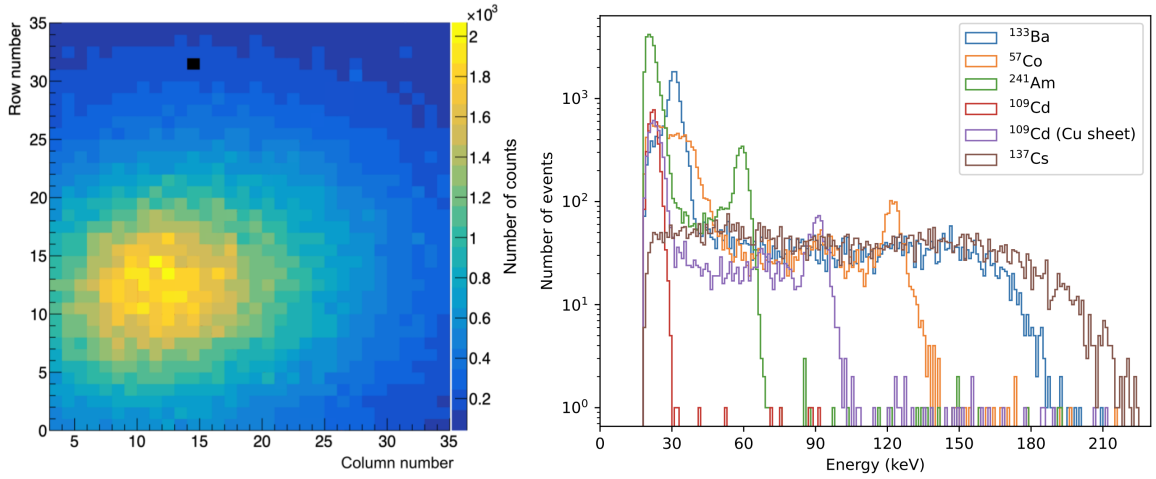

(a) (b)

Figure 3.151: (a) Beam hit map recorded in the 120 GeV proton run in Fermilab Test Beam Facility with a AstroPix_v3 chip. The masked pixel has been marked in black. Source code for figure. (b) Calibrated energy responses form an example pixel of a AstroPix_v3 chip. Plot from [85].

	DIS	Electron Beam Background	Proton Beam Background	All Sources
ScFi/Pb Layers				
Channel Max	7.4 kHz	8.8 kHz	430.0 Hz	15.2 kHz
Channel Avg	2.8 kHz	875.1 Hz	132.5 Hz	3.8 kHz
Total	16.1 MHz	5.0 MHz	763.4 kHz	21.9 MHz
Imaging Layers				
Channel Max	794.7 Hz	389.2 Hz	51.8 Hz	924.8 Hz
Channel Avg	179.9 Hz	36.8 Hz	7.8 Hz	224.5 Hz
Total	11.7 MHz	2.4 MHz	509.2 kHz	14.6 MHz

Table 3.59: Expected data rates for ScFi/Pb and Imaging layers of the BIC. For the imaging layers, one channel corresponds to one chip, while for the ScFi/Pb layers, one channel corresponds to one SiPM array.

A BIC sector consists of six carbon fiber frames for the imaging layers, interleaved with five single layers of a Pb/ScFi matrix (each 17 fibers tall), followed by a bulk segment consisting of seven Pb/ScFi matrix layers. The back of the sector consists of an aluminum support plate with connectors designed to link the sectors together, affix the ESB, and integrate with the global BIC support structure. The sector is constructed as a monolith, with all components epoxied together to ensure structural integrity.

The inner face of each BIC sector consists of a 0.5 cm thick aluminum plate, designed to connect the inner support rails to the detector. The inner support rails hold the inner detector support structure, maximizing the use of available space while avoiding obstruction of the ESBs (the readout boxes),

ensuring that individual imaging layers can be added or removed as necessary for future upgrades or servicing. Hence, the BIC plays a critical role in supporting the overall inner detector structure.

Detailed Finite Element Analysis to validate the mechanical integrity of the sector design is ongoing. The design of the support that connects the BIC to the solenoid cryostat support rings is still under development, ensuring it meets the mechanical stability requirements while maintaining accessibility to readout electronics and other critical components.

Calibration, alignment and monitoring: The BIC calibration approach treats the Pb/ScFi and AstroPix imaging layers as two separate systems, each calibrated independently. For the Pb/ScFi calorimeter, we will follow well-established in-situ calibration methods, starting with MIP-based calibration, then refining with meson decays, electrons, and kinematic techniques successfully used in many other experiments including experiences with GlueX and HERA experiments (See, e.g., [83]). The energy calibration is further refined using decay photons from neutral pion events ($\pi^0 \to \gamma\gamma$).

For the AstroPix layers, the calibration process occurs in three steps. First, an absolute pixel energy calibration is performed during stave assembly using a radioactive source. Next, in-situ position and alignment calibration will be conducted similarly to standard tracker procedures, utilizing cosmics. Finally, the overall imaging cluster energy calibration will be matched with the Pb/ScFi calorimeter, leveraging the energy reconstruction methods described above.

We will use metrology for alignment during installation, but precise alignment of the full BIC detector is not critical due to the calorimeter's purpose. Sub-millimeter physical alignment of the entire detector is unnecessary, except for potential requirements driven by the alignment needs of the inner detector, which the BIC supports. However, subcomponent alignment is more stringent: AstroPix modules and staves require alignment at the 100 µm level. The alignment requirements for the carbon fiber frames holding the AstroPix trays are still under evaluation but are likely to fall within a few hundred microns. We will calibrate the relative positioning of detectors and sensors using cosmic and physics events to ensure accurate reconstruction.

Calibration stability during operation for Pb/ScFi will be ensured by using LED-based relative light monitoring systems, along with additional checks on linearity and timing using both cosmics and dedicated calibration runs for both AstroPix and Pb/ScFi layers.

Services: The Pb/ScFi part of BIC, which utilizes SiPMs, requires two LV lines (plus ground) of 1.2 V and 2.5 V for each H2GCROC3-based front-end board (FEB), along with one HV line (plus ground) operating at less than around 50V for biasing SiPMs. The SiPM bias voltage is 38V and operating voltage is 38V+2.7V. In order to fill the LV needs, the current ESB design has a single 30 V line arriving at the FEB, where it will be stepped down to the required voltages for the SiPM board, AstroPix ETCs, and the FEB itself. The system features a total of 5,760 readout channels distributed across 48 sectors, with one FEB per sector per side, each managing 60 readout channels. Each FEB is connected to the RDO through four lines: two data lines, one clock line, and one slow control line, and 1 RDO maintains 24 FEBs.

For the AstroPix sensor layers, the LV services include two 1.8 V to power the analog and the digital part of the chip and the HV of 200-400 V distributed to each stave. Each stave within an AstroPix tray connects to the data acquisition system through an FPGA-based End-of-Tray Card (ETC, one per tray) connected to DAM via an optical link. In total, each sector will include 27 staves per side. Each ETC will receive power from the Pb/ScFi FEB.

The SiPMs require cooling to maintain a temperature of 7°C in order to keep the dark noise at an

acceptable level for detecting signals from MIPs. Refer to the simulations as detailed in the *Performance* section, which show that after radiation doses corresponding to about one year of running at top luminosity, MIP peaks remain distinguishable at temperatures around 5°C. Each ESB will have in/out lines for cooling water and a dry air or N_2 system to prevent condensation. The estimated heat load per ESB is projected to be under 100 W, necessitating effective heat management. Liquid water cooling will be utilized for the SiPMs, their readout boards, and the ETCs. AstroPix sensors are highly heat efficient, consuming less than $2\,mW/cm^2$. The baseline cooling strategy involves thermal coupling to dissipate heat through the staves and trays, with cooling occurring at the edges along with the ETCs. If additional cooling is required, circulating liquid through the staves will be employed as a mitigation measure. The ongoing PED program includes detailed thermal simulations toward a preliminary cooling design.

Status and remaining design effort: High-level schedule for the BIC design and production phase is available in Additional Material (SeeFigure. 3.152).

R&D effort: The R&D efforts for BIC focus on demonstrating the combined performance of Pb/ScFi and AstroPix in EIC-like environments. This involves measuring higher than GlueX energy response up to about 10 GeV, benchmarking high-energy electron and pion simulations, testing AstroPix in high-rate environments, and integrating the Pb/ScFi with AstroPix sensor layers. In FY23, responses to 6 GeV positrons in 60 cm long Pb/ScFi prototype (termed *Baby BCAL*) were measured in Hall D of Jefferson Lab, showing a constant term of about 2%, consistent with simulations. The Baby BCAL was commissioned with proton, pion, and electron beams during a June 2024 FBTF test, where data collected allowed for pion simulation benchmarking [89]. A proof-of-concept synchronization of AstroPix with Baby BCAL was achieved by triggering on the AstroPix analog signal. With extensive data from previous AstroPix tests in FY23, and the multi-layer Pb/ScFi and AstroPix bench tests, the R&D program has been concluded in FY25.

E&D status and outlook: The Project Engineering Design phase of our project that started with granting the funding to the participating institutions starting Q4 2024, encompasses a detailed roadmap for the design, testing, and integration of key components for BIC. Early milestones focus on the design and development of Pb/ScFi sectors, including short and long test articles and the structural framework needed for housing these components. Alongside this, efforts are directed toward the design and prototyping of the end-of-sector box, which includes light guide and light monitoring system integration. The tracking layer, which features AstroPix sensors, undergoes simultaneous development. This includes tracker mechanical design, cooling design, performance characterization of the AstroPix chips, module design and assembly, and testing of components such as bus tapes and end-of-tray cards. By mid-PED-phase, both the Pb/ScFi and tracking layers will undergo rigorous integration testing to ensure seamless functionality within the full detector system. The final phase focuses on validating the designs and performing full integration testing of staves, modules, and tracking layers. Quality control procedures will be established for each component, ensuring that everything meets performance specifications before final assembly. The PED phase is setup to exceed 90% design maturity by Q1-Q2 FY26.

Other activity needed for the design completion: Within the small-scale R&D and design funding in Korea, a focused effort is underway during the period from August 2024 to April 2027, covering the PED phase and pre-production phase. The primary objectives include the development of testing and assembly systems for the AstroPix chip, particularly emphasizing automatic wafer testing and module assembly. Additionally, this work involves

designing the readout box for the Pb/ScFi system and producing test modules to conduct performance studies.

Status of maturity of the subsystem: The maturity of BIC is currently estimated to be at least 60%, with some components, such as the scintillating fibers and SiPMs advanced beyond the final design review level. The entire BIC underwent an incremental Preliminary Design Review (PDR2) in September 2024. The Final Design Reviews for both the scintillating fibers and SiPMs were successfully passed in September 2023. The first and second batches the scintillating fibers were included in CD3a and CD3b. The vendor selection is complete and the contract for the scintillating fibers has been finalized.

Construction and assembly planning:

Pb/ScFi Sectors Construction: The production of Pb/ScFi sectors will take place at Argonne, where there will be two production lines. The sectors will be constructed by embedding scintillating fibers in lead sheets, arranged in a stepped "Mayan pyramid" configuration, following the GlueX model. Carbon fiber frames will be integrated with the sector as it is built, with each frame assembled from two C-channel-like sides and a top and bottom plate. The sector construction process will proceed at a pace of 0.5 to 1 matrix layer per day, with the ability to build two sectors in parallel. Once the matrix lay-ups have been completed, an external machine shop will trim and polish the ends and machine the sides to the desired trapezoidal shape. Upon return to Argonne, the sector will undergo metrology and QC before being prepared for shipment to BNL.

ESB Manufacturing: The construction process for the ESB is still in development. ESB construction will include large-scale SiPM testing, SiPM mounting, light-guide manufacturing, light-monitoring system integration, construction of structural and cooling components, and manufacturing of electronics boards. There will be likely two ESB production sites: one in Canada at U. Regina and one in Korea. After the ESB assembly is completed, they will be shipped to the production site at BNL for installation (see Assembly Planning).

AstroPix Sensors and Wafers: The AstroPix sensors were originally developed for NASA-GSFC's AMEGO-X mission. Although we collaborate closely with NASA-GSFC on AstroPix, the external dependency is minimal at this advanced stage of chip development. The AstroPix engineering runs are nearly complete, with the only remaining dependency being the AstroPix v6 engineering run, which is covered by NASA for the ComPair project.

The AstroPix sensors will be fabricated at the AMS foundry. Due to the large scale of the detector, automatic wafer-level testing will be conducted at two sites: PNU (South Korea) and Argonne. This testing will ensure the functionality of each chip before dicing, including IV-CV measurements, ASIC performance, noise levels, and defect detection early in the production process. After testing, the wafers will be diced into individual AstroPix chips.

AstroPix Modules and Trays: AstroPix chips will be assembled into modules at three production sites: Argonne, UC Santa Cruz, and PNU (South Korea). Each module will consist of nine daisy-chained AstroPix chips, readout on flexible PCBs. After assembly, each module will undergo initial testing to ensure proper chip-to-chip communication, pixel functionality, and noise levels. Modules that pass this stage will be integrated into staves, with 12 modules per stave. To keep the production process scalable and efficient, only one flavor of stave will be used across the entire system. The staves will then undergo additional QC testing. Once validated, the staves will be integrated into trays. There are two flavors of trays: one for the first imaging layer and the other for layers 3, 4, and 6. The hadron-going side and the lepton-going side trays of the detector are mirror images of each other. Each tray will contain

6 staves in layer 2 and 7 staves in the outer three layers. These trays will then undergo final QC prior to shipping to BNL. The entire production and QC procedure is designed to catch any defects early and ensure that the trays are fully operational before final integration into the BIC sectors.

Assembly Planning: The assembly of the BIC will follow a carefully planned sequence. Upon arrival at the integration site, the Pb/ScFi sectors will be unpacked and prepared for assembly. The first step will involve attaching the light guides to the sectors. Once the initial sectors have been prepared, we can begin the barrel assembly while continuing to unpack and attach light guides to the remaining sectors. The BIC barrel will be assembled next to the solenoid and then inserted into the solenoid using existing sPHENIX tooling. Following the installation of the barrel at BNL, the imaging layer trays will be inserted using specialized tooling that is still under development. After all trays are installed, the ESB will be mounted to complete the installation. This phased approach ensures that all components are properly integrated (and tested) prior to integration testing.

Quality Control (QC) Planning: QC will be implemented at multiple stages of the BIC production and assembly process to ensure system integrity and performance. The system, particularly the imaging layers, is designed with both modularity and scalability in mind, allowing for efficient production, easier upgrades, and reworkability. Key QC procedures include:

Pb/ScFi Sector Assembly: The Pb/ScFi sectors will undergo thorough inspection during assembly. Scintillating fibers and lead sheets will be inspected for defects before embedding. After each matrix layer is completed, visual and metrological inspections will ensure proper alignment and uniformity in matrix growth thickness (height of the build). Final metrology checks will be performed after external machining to confirm dimensions prior to shipment.

AstroPix Wafer Testing: Automatic wafer-level testing will be conducted to assess chip functionality, including chip performance, noise levels, and defect detection. Once tested, wafers will be diced, followed by additional metrology and electrical/non-electrical QC on individual AstroPix chips to ensure reliability before moving to the module assembly phase. We are currently exploring an alternative possibility to leverage experience in our collaboration in automated chip-level testing as part of our ongoing engineering design studies.

Module and Tray QC: Modules will be assembled from AstroPix chips and undergo functional tests to verify chip-to-chip communication, pixel functionality, and noise levels. Defective modules will be identified and replaced before progressing to stave assembly. Staves will be tested for electrical continuity, power consumption, and thermal performance under load. QC for staves and trays will use the actual End-of-Tray Card (ETC) readout electronics to perform these tests. Once integrated into trays, final testing will check for alignment, electronic connectivity, and cooling performance, ensuring that trays operate as intended under operational conditions.

ESB QC: SiPMs will undergo rigorous testing to ensure proper photon detection efficiency, dark count rates, and timing precision before being integrated into the ESB, while, component-wise optical tests will characterize the light guides and optical cookie system. Furthermore, the QC procedure at the production site will include a full system test of the electrical connections, readout electronics, cooling system, and light tightness. The full-chain tests will be repeated during installation at BNL.

Final Integration and Barrel Assembly at BNL: After attaching light guides to the Pb/ScFi sectors, alignment and metrology checks will be conducted during barrel assembly to ensure

sector and tray alignment within tolerances. Electrical and cooling system checks will be completed post-installation of the ESBs on assembled barrel to confirm proper functionality. System-wide tests, including cosmic ray runs and electronic readout, will validate the entire system before commissioning.

Environmental, Safety and Health (ES&H) aspects The BIC design incorporates standard safety and environmental practices across all production sites. We will strive for standardized safety protocols while adhering to internal work planning and control processes at each institution to identify hazards, implement mitigations, and document safety procedures. Main hazards associated with the BIC include:

Lead handling: The handling of lead sheets for the Pb/ScFi matrix requires careful consideration. We are working closely with experts to determine the appropriate safety steps. These steps may include specific protocols to mitigate any hazards and the potential enrollment of personnel in continuous health monitoring programs to ensure long-term safety.

Epoxy usage: Standard procedures for handling, mixing, and applying epoxy will be followed, with work conducted in fume hoods to ensure safety. Part of our PED work aims to deploy a custom mixing nozzle to reduce air contaminants and epoxy waste while improving consistency in the application process.

Scintillating fibers: The fibers are made of flammable polystyrene, and with the total fiber mass exceeding 3.9 tons, proper fire safety measures and storage protocols are essential.

Pinch/nip hazards: Automated systems, such as robots for wafer probing, pick-and-place, and glue application, present pinch hazards. Controls, such as PPE, gloves, guards, and procedures, will be in place to mitigate these risks.

Crush hazards: The use of presses and swaging equipment introduces crush hazards during assembly processes. Strict safety protocols, including the use of guards and operator training, will mitigate these risks.

Radioactive sources: The use of radioactive sources for calibration introduces additional handling requirements, and proper shielding and storage protocols will be implemented as necessary.

Electrical safety: Electrical safety procedures will also be applied for all electronics and power systems associated with the BIC production tooling and detector components.

Collaborators and their role, resources and workforce: The full BIC WBS org chart is available in Additional Material (see Figure 3.157). BIC is supported by a diverse and robust international collaboration, with institutions from the United States, Canada, Korea, and Germany. These collaborators bring together a wealth of expertise and resources, working collectively to advance the development of the BIC, and has the necessary workforce and expertise to execute the BIC design on schedule.

In the United States, several institutions play a key role across multiple aspects of the project. Argonne National Laboratory is leading several crucial areas, including the design and assembly of modules and staves, sector production, cooling systems, and system testing and QC, while also overseeing the software, simulation, and benchmarks. Oklahoma State University leads efforts on stave bus assembly, and the University of California, Santa Cruz (UCSC) supports module design and assembly efforts. NASA Goddard Space Flight Center (GSFC) contributes via the ETC components, ensuring that electronic testing is integrated into the system.

Canadian institutions play a critical role, especially in the production and quality control of ESB. The University of Regina contributes to multiple efforts, including the QC of scintillating fibers, SiPM integration, light guides, and electrical design, while also contributing to the system's demonstration and testing. The University of Manitoba provides leadership in cooling system development and supports the SiPM integration efforts. Mount Allison University focuses on ESB production, aiding in the overall electronics support infrastructure.

Korean institutions are heavily involved in various production, design, and testing processes. Collaborators from Kyungpook National University (KNU) support both electronics and SiPM integration. Yonsei University plays a key role in the sector production process and testing, while Sungkyunkwan University (SKKU) focuses on sector development and production. Pusan National University (PNU) leads efforts on wafer testing and supports software development and simulation. Additionally, Hanyang University, Korea University, and other Korean institutions provide significant contributions across assembly, installation, and testing.

The Karlsruhe Institute of Technology (KIT, Germany) is responsible for the AstroPix chip development, and provide essential chip support and communication with the foundry.

Risks and mitigation strategy:

A potential risk in the production of AstroPix chips is related to the feasibility of using 12-inch wafers, which offer a more modern and cost-effective solution. However, if this option proves unviable, we will need to use 8-inch wafers, increasing costs. This is budgeted in the risk registry.

The schedule has sufficient time built in to accomodate an additional iteration of AstroPix beyond v6 if needed.

Risks on production-delays due to the availability of scintillating fibers and SiPMs were mitigated through CD3a/b long-lead procurement ensuring the timely availability of these components.

As outlined in the Construction and assembly planning paragraph, in the default scenario, sector production will take place at Argonne using two production lines, with one staffed by Korean collaborators. ESB production and quality control will be managed by Canada and Korea. Wafer testing will occur in both Korea and the US. AstroPix module and stave production will be distributed across three or more sites in the US and Korea. The baseline plan includes producing four AstroPix layers, with the possibility to fill the two additional slots as a later upgrade. In the unlikely event of no in-kind funding from Canada and Korea, the project will cover all sector production labor costs, including Korean collaborators, and consolidate production to a single ESB site (Canada) and a single wafer testing site (US). AstroPix module/stave production will be limited to two sites in the US, requiring an increased workforce at each site or potentially facing a one-year delay to deliver the four baseline layers.

Additional Material

Schedule High-level BIC schedule can be found in Figure 3.152.

Performance

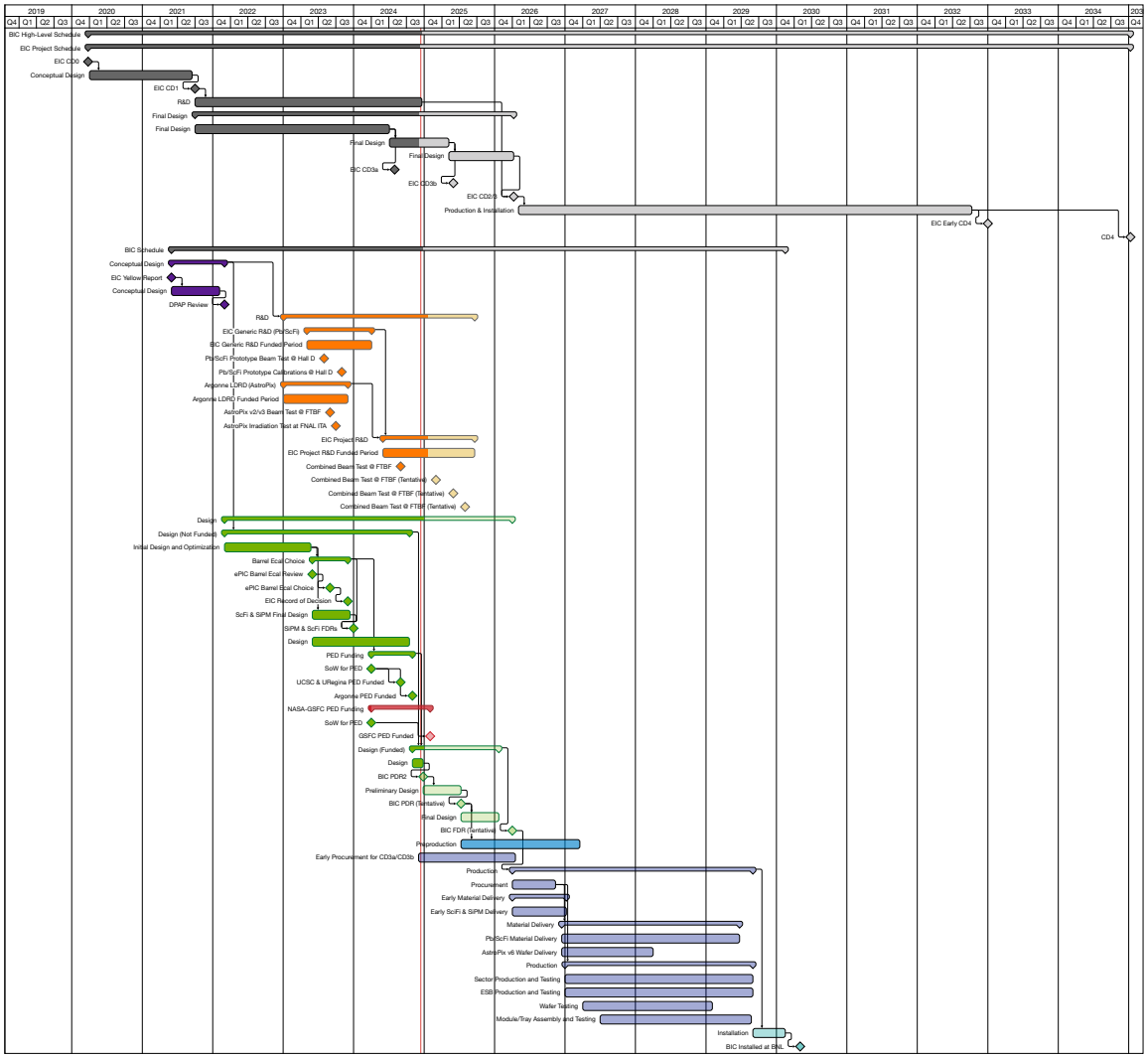

Figure 3.152: Barrel Imaging Calorimeter high-level schedule for design and production phases.

Energy Response Measurement and Simulations The realistic BIC geometry was implemented, including a detailed Pb/SciFi matrix with scintillating fibers embedded in lead and glue, following the GlueX model. The AstroPix layers were implemented as staves, with AstroPix chips placed in realistic dead areas, and materials accounted for the sensors, electronics, cables, insulation, glue, and support structure. Realistic digitization and reconstruction were applied. For the Pb/SciFi component, an effective model for light attenuation in the fibers, photoelectron statistics, light guide efficiency, and SiPM thresholds was implemented based on beam and bench measurements as well as optical simulations of the light guide response. For AstroPix, each digitized readout unit corresponds to one pixel, while for the Pb/SciFi component, each readout cell covers the area of one light guide with an attached SiPM.

The contribution of the low-energy tail of the energy losses was quantified by calculating the difference between the area under the fitted Crystal Ball function and that of its Gaussian core marked in

red in Figure 3.153 (a). The tail contribution to the overall energy loss area is shown inFigure. 3.153 (b) and (c) for electrons and photons, respectively. In addition to the energy resolution and total sampling fraction as a function of energy presented for photons in Figure 3.147, the results for electrons are presented in Figure 3.154.

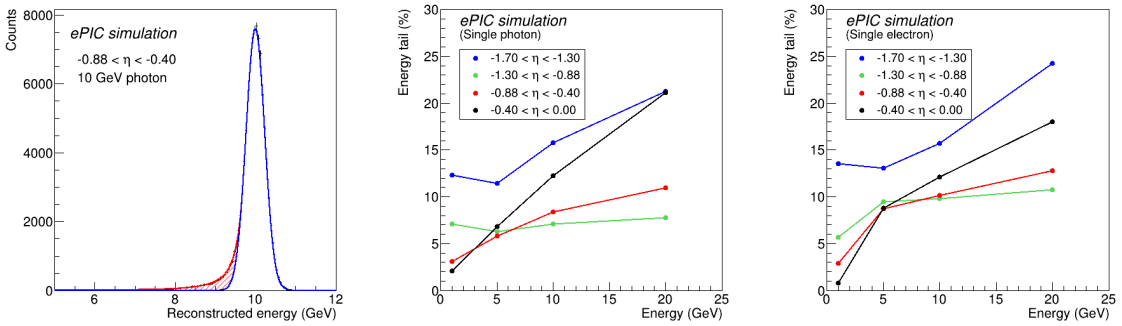

(a) (b) (b)

Figure 3.153: (a) Simulated energy losses in scintillating fibers of BIC for 10 GeV photons in the rapidity range $-0.88 < \eta < -0.4$. The distribution has been fitted with the Crystal Ball function; the Gaussian core of the function is marked in blue, and the power-law tail area is marked in red. (b) Percentage contribution of the low-energy tail–red area in plot (a)–to the overall area under the Crystal Ball fit to the energy losses of photon in Pb/ScFi as a function of photon energy and rapidity. (c) Same as (b) but for electrons. Source code for figures

The low-energy photon response has also been evaluated based on simulations, as described in the Performance section. Two example plots for low-energy photons at $\eta = +1$ are shown, which represent a highly asymmetric situation where the photon shower develops close to the p-going end of the BIC, far from the e-going end. As shown in Figure 3.155, left plot shows the number of fired readout cells for 100 MeV photons with a threshold of 6 phe, and right plot shows the energy resolution extracted from each end of the BIC and the combined resolution for photons below 0.5 GeV. We observe performance that meets the energy resolution requirement with high efficiency.

Energy response to both electromagnetic and hadronic showers has been tested in the beam test environment with a 60 cm long and 15.5 X_0 deep Pb/ScFi bulk-section prototype based on GlueX BCAL geometry, termed *Baby BCAL*. At Hall D of Jefferson Lab, Baby BCAL was exposed to 3-6 GeV positrons hitting it at different impact angle and position depending on beam energy. Figure 3.156 (a) presents the measured energy resolution measured in those conditions. Note that the highest energy points reflect positrons hitting the prototype close to the end and at the impact angle that causes partial shower leakage. At Fermilab Test Beam Facility, Baby BCAL was exposed to mixed electron-pion-muon beam at energies of 4, 6, 8 and 10 GeV. The energy response to pion beam has been benchmarked in simulation of Baby BCAL implemented in ePIC environment, same as used for the BIC simulations. Figure 3.156 (b) shows comparison between collected data and simulations benchmarking their realism.

Particle identification The following section provides details of the AI-based particle identification performance described in the Performance section.

For our π^-/e^- separation studies, we utilized a 10-layer Visual Geometry Group (VGG)-style Convolutional Neural Network (CNN) to process combined data from the AstroPix and Pb/ScFi parts

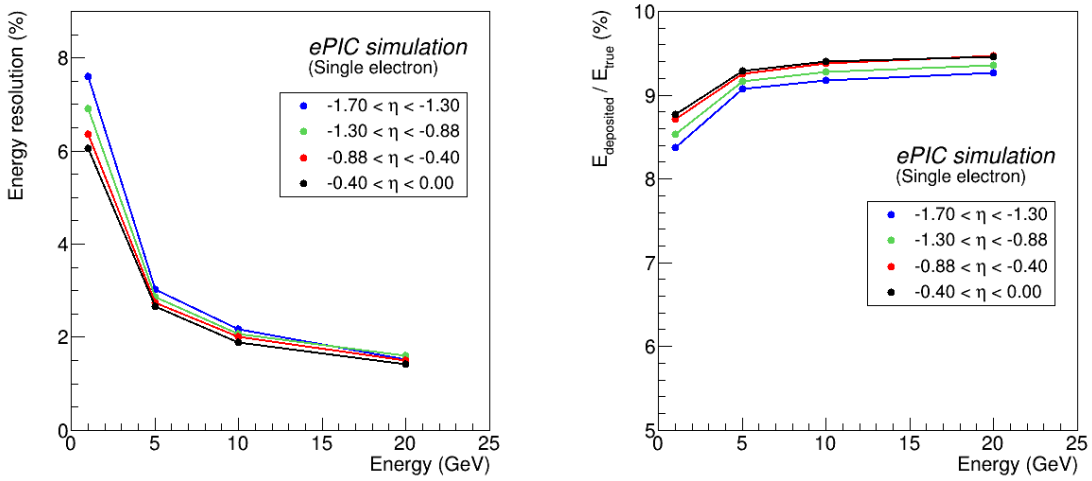

(a) (b)

Figure 3.154: (a) Simulated energy resolution in from Pb/ScFi extracted as a σ of the Gaussian core of the Crystal Ball fit to the energy deposits of electrons in different rapidity ranges at BIC. (b) Sampling fraction for electrons, defined as energy losses in scintillating fibers divided by the true electron energy, as a function of electron energy in different rapidity ranges. Source code for figures

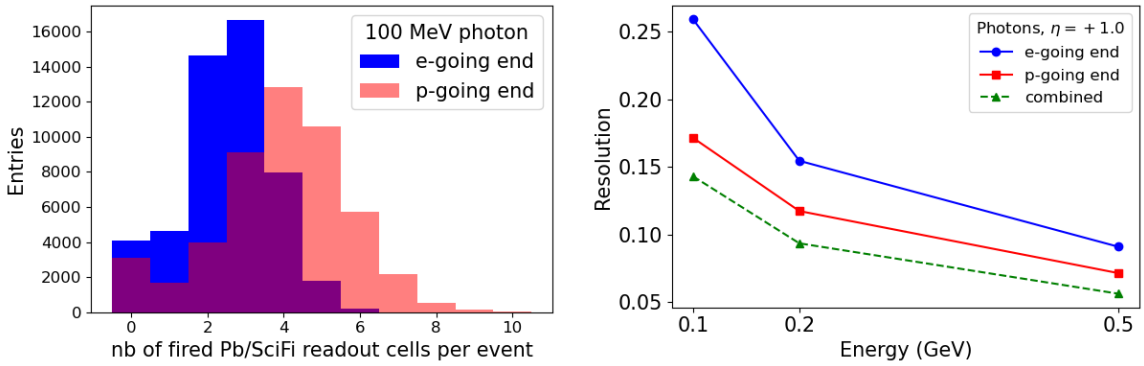

Figure 3.155: Simulated, low-energy photon response in BIC at $\eta = +1$. (left) Expected number of fired Pb/SciFi readout cells for 100 MeV photons with a threshold of 6 phe. (right) Energy resolution extracted for both ends of the BIC and the combined one for photons below 0.5 GeV. Source code for figures

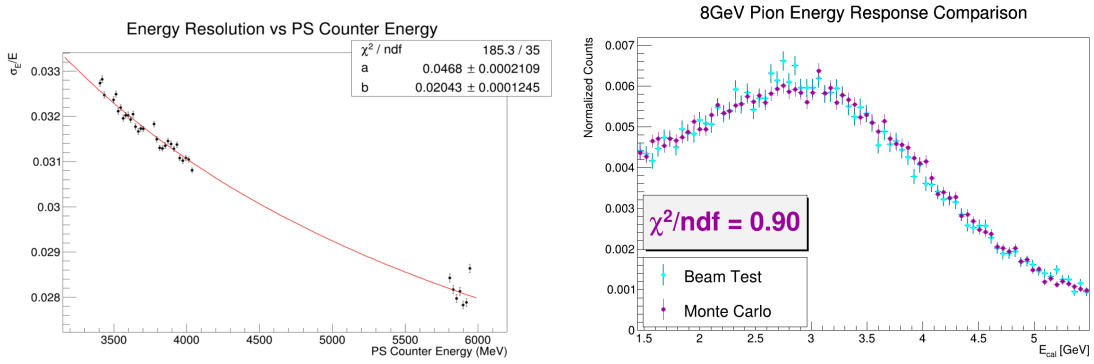

(a) (b)

Figure 3.156: (a) Preliminary energy resolution of Baby BCAL exposed to 3–6 GeV positrons at Hall D of Jefferson Lab, with varying impact angles and positions depending on beam energy. The highest energy points correspond to positrons striking near the end of the prototype and at angles causing partial shower leakage. Red line shows the fitted function $\sigma/E = a/\sqrt{E} \oplus b$. Repository to be added (b) Preliminary energy response of Baby BCAL to an 8 GeV pion beam at the Fermilab Test Beam Facility. The plot compares the collected data (light blue) with simulations (purple) implemented in the ePIC environment, as used for BIC simulations, benchmarking the realism of the simulation model. Source code for figures

of the calorimeter. This CNN architecture consists of 5 convolutional layers interspersed with 2 pooling layers, followed by 3 fully connected (dense) layers. Each event is formatted into an input array with dimensions $N_{\text{layers}} \times N_{\text{hits}} \times N_{\text{features}}$, where 4 primary features: energy deposit, η, ϕ, and radial position of the hit inside the calorimeter, to capture both energy deposition and spatial information about the particle shower.

We trained the network using supervised learning with a data set composed of a 10:1 ratio of pions to electrons. This ensured a sufficient number of pions remained after applying the energy-over-momentum (E/p) cut, which was crucial for training accuracy. Each training cycle consisted of 20 epochs, with data split into 70% for training, 10% for validation, and 20% for testing. On average, between 100,000 and 200,000 events were included in each training set, drawn from over 2TB of official singles productions simulations.

The CNN's performance is measured with uncertainties based on binomial statistics, providing robust estimates of classification accuracy. A similar but simplified approach was used for neutral pion identification. Initial results demonstrate promising pion rejection rates, which could be further enhanced by implementing algorithmic improvements. Future iterations of the model may explore Graph Neural Networks or Point Clouds to better capture the spatial and relational data inherent in these complex events.

Collaborators and their role, resources and workforce: The full org chart for the BIC Detector Subsystem Collaboration is presented in Figure 3.157.

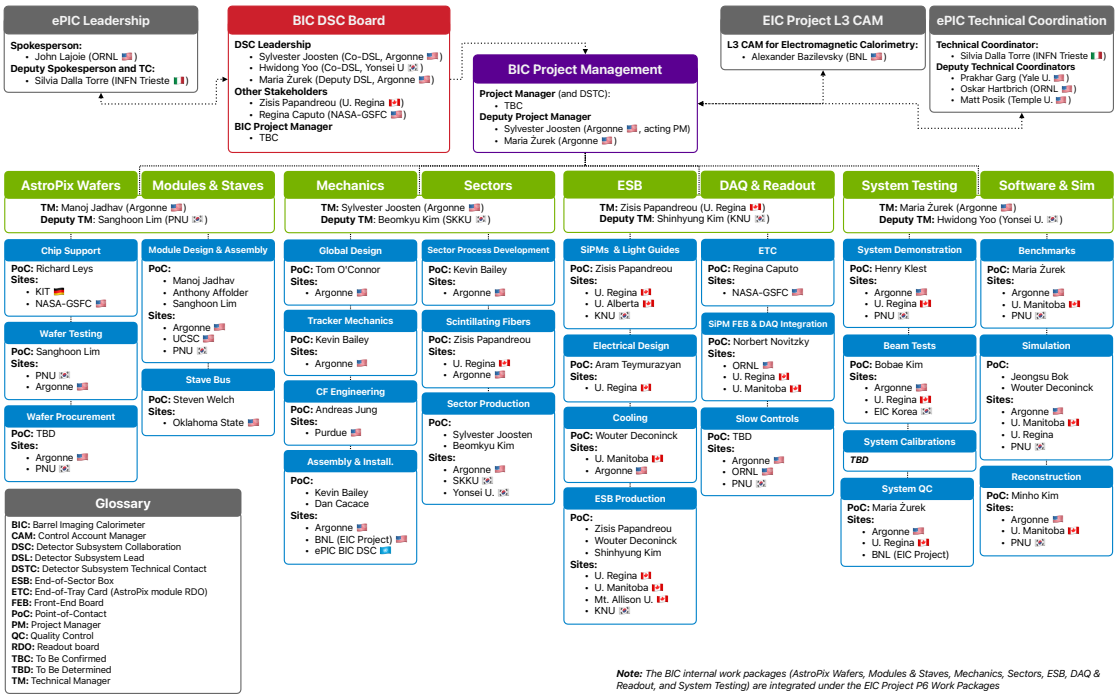

Figure 3.157: Barrel Imaging Calorimeter org chart.

3.3.5.3 The forward endcap electromagnetic calorimeter

Introduction The ePIC forward electromagnetic calorimeter (FEMC) is part of the hadron end-cap calorimeter system, complementing the forward hadronic calorimeter. Complete electromagnetic calorimetric coverage in ePIC is essential for detecting photons and electromagnetically decaying mesons, which are crucial for reconstructing parton-scattering kinematics through jets and to identify DVCS photons. FEMC provides full azimuthal coverage within a pseudorapidity range of approximately $1.4 \lesssim \eta \lesssim 3.9$. At lower pseudorapidity, FEMC overlaps with BEMC, ensuring continuous coverage by electromagnetic calorimeters in the hadron side of the ePIC detector. Coverage at higher pseudo-rapidity is restricted due to mechanical limitations (clearance required to accommodate the accelerator beam pipe).

The design requirements for the FEMC were established through extensive studies of various detector concepts proposed for the EIC over the past decade. These concepts originated from the designs presented in the EIC White Paper [91] and Yellow Report [11], evolving through the ECCE [92] and ATHENA [93] proposals and culminating in the ePIC detector concept discussed here. It was concluded that an energy resolution of approximately $12\%/\sqrt{E} \oplus 2\%$, along with high granularity needed to distinguish single photons from DVCS events and photon pairs from π^0 decays up to 50 GeV, would meet the EIC's measurement objectives.

Though numerous electromagnetic calorimeter technologies were considered, as noted in the EIC Yellow Report [11], the stringent space limitation in ePIC detector (an integration length of only 27 cm along the Z-axis for FEMC) ruled out all but one technology for the FEMC: WScFi. This technology, developed during the generic EIC detector R&D program [94], has also been successfully implemented in the recently constructed barrel electromagnetic calorimeter of the sPHENIX experiment [95], which is comparable in scope with the ePIC FEMC.

Some of the key requirements and parameters for the FEMC are summarized in Tab. 3.60. The most critical challenges include the limited integration space and the need for a very large dynamic range, approaching 7000:1. Radiation doses and neutron fluxes are not expected to pose significant challenges for current technologies. For instance, the forward calorimeter system (FCS) constructed for the STAR experiment at RHIC has been successfully operational since 2021 under conditions—both in terms of radiation and neutron flux—similar to those anticipated at the highest luminosities of the EIC. The choice of photodetectors and front-end readout electronics for the FEMC is partially based on the readout system developed for the STAR FCS.

Device concept and technological choice: Figure. 3.158 depicts the front face of the ePIC hadron end-cap in its closed position, which is divided into two halves to allow access to the inner ePIC detectors in its open position. The end-cap features 1,145 FEMC installation blocks, each of which is mounted to a one-inch-thick steel plate situated between the hadronic and electromagnetic calorimeters. Each installation block comprises 16 FEMC towers and weighs approximately 18 kilograms, bringing the total weight of the FEMC to around 21,000 kilograms. A 1.00 mm air gap separates each FEMC installation block to accommodate production and installation fixtures tolerances. The readout system for the FEMC is located at the front face of the blocks, ensuring easy access to the electronics. Cables and utilities run horizontally along each row of blocks to the perimeter of the FEMC, where they bunched and passed through few openings in the light-tight external shell and connected to the RDOs positioned on the sides of the hadron end-cap.

Each FEMC installation block is composed of four "production blocks," with each production block consisting of a 2×2 arrangement of towers. All production blocks are identical, and precise mechanical tolerances are ensured by using identical production molds fabricated to high tolerances,

Table 3.60: Some requirements on performance of FEMC and its parameters

Parameter	Requirements	Comments
Geometrical Acceptance	$1.4 \lesssim \eta \lesssim 3.9$	$R_{out} \sim 190$ cm, $Z_{frontface} \sim 341$ cm
		Hole for the beam pipe $30 \times 30\ cm^2$
Integration envelope	R_{max}=205 cm, Depth = 27 cm	
E_{min} in a single tower	100 MeV	Min. shower energy 100 MeV
E_{max} in a single tower	100 GeV	18×275 GeV, ep
Maximum rate in a single tower	10 kHz	E_{thr}=15 MeV, 10×275 GeV ep
		500 kHz collision rate
Radiation doses	15 kRad	Integrated over 10 years
Neutron fluxes	4×10^{11} n/cm^2	1 MeV eq, integrated over 10 years
Energy resolution	$\lesssim 12\%/\sqrt{E} \oplus (2)\%$	Verified in the test beams
γ/π^0 separation	up to 50 GeV	$\sim 5\%$ mis-identification at 50 GeV
Depth	23 X_0	Minimize leakages
Detector parameters	**Units**	**Comments**
X_0, R_m	7 mm, 19 mm	Rad. length, Moliere radius
f_{samp}	2%	e/h $\simeq$1 above 10 GeV
Scintillating Fibers	$\varnothing$ 0.47 mm	Single clad sc. fibers
Light yield	$\sim$ 1600 pixels/GeV	Test beam results.
Transverse size of tower	2.5 cm $\times$ 2.5 cm	Matches R_m
Transverse size of installation block	10 cm $\times$ 10 cm	Block of 16 towers
Total number of towers	18320	
Photodetector	S14160-6015PS	Four 6$\times$6 mm^2 SiPMs per tower
		15 um pixels size
Monitoring system	Blue LED	LED integrated on SiPM board.
		One LED per four towers

within a few tens of micrometers. The epoxy layer between production blocks is typically less than 100 micrometers thick. These thin epoxy layers, along with air gaps between installation blocks, represent the only dead material within the FEMC volume. These dead zones have a negligible impact on the overall performance of the FEMC.

The primary reason for using tungsten powder and scintillating fiber technology for FEMC is that it is the only practical method to meet the stringent requirements outlined in Tab. 3.60. Specifically, the desired energy resolution with extremely compact tower dimensions can only be achieved by combining a small sampling fraction with a high sampling frequency. This high sampling frequency is attained by using 780 thin, 0.47 mm diameter scintillating fibers in each tower, arranged in a staggered pattern with a center-to-center distance of approximately 0.955 mm. Both the fiber diameter and spacing were optimized through Monte Carlo simulations to ensure FEMC is nearly compensated and maintains the required energy resolution. Tungsten powder is used as the base material for the absorber structure to make the technology viable in practice. A set of specifications for tungsten powder and scintillating fibers for ePIC were established during generic detector R&D program for EIC and experience of constructing sPHENIX barrel EMCal utilizing WScFi technology.

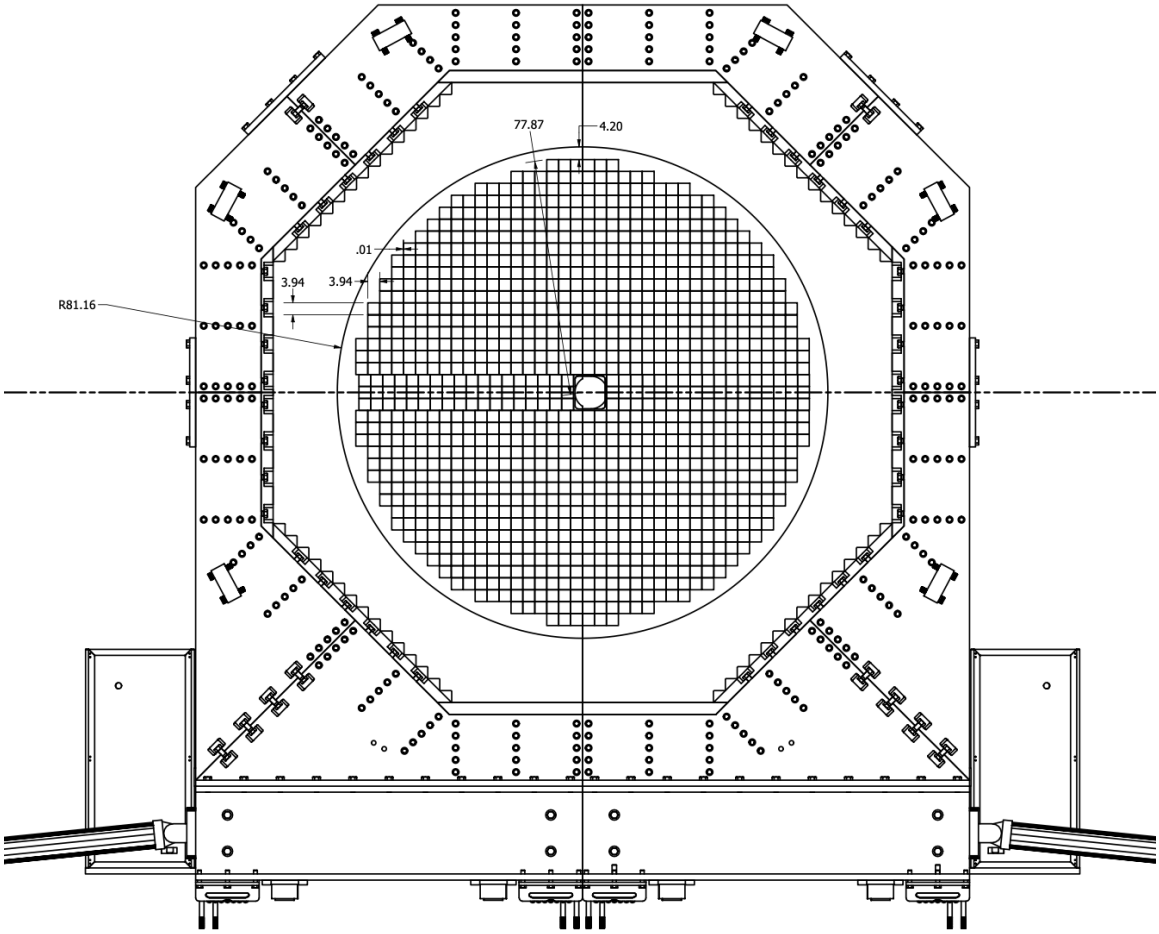

Figure 3.158: The front face of the ePIC hadron end-cap.

Despite the apparent simplicity of fiber calorimeters, constructing them is not straightforward. Detector components must be produced with extremely tight tolerances to maintain uniformity. Historically, techniques like extrusion, machining, or rolling were used to manufacture absorber plates, but these processes were complex and often required the creation of specialized machinery and tools. Building fiber calorimeters has traditionally been a labor-intensive process, with individual detector elements being handled one at a time, driving up costs compared to scintillating plate detectors. Moreover, traditional methods face challenges with increasing sampling frequency, as thinner absorber layers and fibers become more difficult to produce and manage. We refer to the example of the H1. Construction and assembly techniques for the H1 fiber calorimeter detailed in [96].

Our approach differs in that we first create a matrix of fibers and then pour the absorber material into the matrix. Unlike previous methods, this technique eliminates the need to handle individual calorimeter elements separately. Fig. 3.159 shows a matrix of scintillating fibers and image of tungsten powder used to build FEMC prototypes. This powder has a particle size distribution of 90% between 70 and 160 microns, a tap density of 11.5 g/cm^3, and a purity of W $\geq$ 99.9%, with Fe, Ni, and Co combined at $\leq$ 0.1%. Additionally, this tungsten powder demonstrates exceptional fluidity, a critical characteristic for our application. It is stored in a humidity-controlled environment prior

to its use in block production, as humidity can impact epoxy impregnation. The only other step required for the absorber material is accurately measuring the specified amount of powder before pouring it into the fiber matrix.

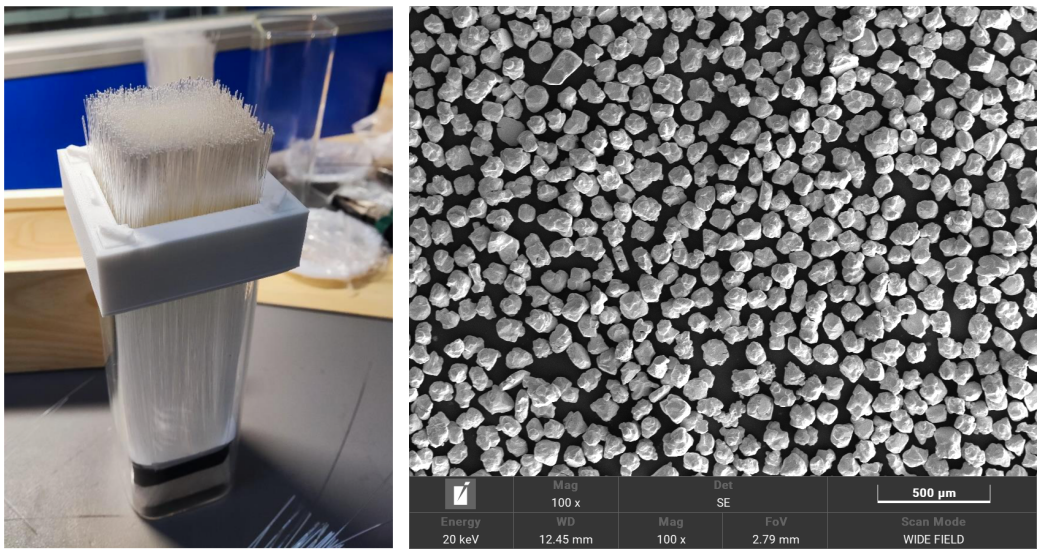

Figure 3.159: Matrix of scintillating fibers prepared to build production FEMC blocks and SEM image of tungsten powder.

The second key element is a straightforward method for forming the scintillating fiber matrix. This matrix is defined by a set of precision brass meshes produced via photo-etching. These meshes have mechanical tolerances of 30 microns on their overall dimensions for 300-micron thick meshes and about 15 microns for the center-to-center distances between the holes for the scintillating fibers. The fibers are cut to the desired length using a thermo-cutter, which melts the fiber ends to form small drops that act as stoppers, preventing the fibers from slipping through the mesh holes. Once the meshes are stacked, approximately 500 fibers at a time can be dropped into the container holding the meshes, and with slight tapping, the fibers will flow through the set in seconds. For our recent prototypes, a trained student could form a fiber matrix for a 2x2 tower production block with 3,120 fibers in around 30 minutes.

The total production volume of scintillating fibers for the forward EMCal (FEMC) is 3,000 km. Only two companies, KURARAY and Luxium (formerly St. Gobain, BICRON), are capable of producing the necessary fibers. Both companies' fibers were previously used to construct and beam-test several WScFI EMCal prototypes for the EIC, with St. Gobain fibers also utilized by the sPHENIX collaboration for their barrel EMCal. Recently, Luxium optimized the composition of their standard BCF-12 fibers specifically for the shorter 17 cm fibers required for FEMC, resulting in a 20% improvement in light yield compared to their standard fibers. This was achieved by adjusting the concentrations of primary and wavelength-shifting fluors, bringing them to the same performance level as KURARAY fibers. Tab. 3.61 outlines the technical specifications and requirements for the FEMC fibers.

To create a scintillating fiber matrix, it is essential that the fibers remain straight when placed into the mesh framework. Fibers processed from spools tend to retain a bend due to "memory," which leads to significant friction between fibers flowing through a set of meshes, which complicates the

Table 3.61: Requirements and Technical specifications for FEMC scintillating fibers.

Parameter	Requirements	Comments
Light Yield (LY)	$\geq$ 8000 photons per MeV	Acceptance QA with Sr90 source
		Compared to a standard sample
Nominal Diameter	0.47 mm $\pm$ 0.0094 mm RMS $\leq$ 0.02 mm	QA sampled on 10% boxes
		100% at ramp-up prod. stage
Attenuation Length	$\geq$ 3 m	QA with UV LED
Batch-to-batch LY variation	$\leq$ 10%	QA with Sr90
Emission spectrum	Blue-green light	To match QE of SiPMs
Scintillation Decay Time	$\leq$ 3 ns	Bunch structure at EIC
Delivery Method	In canes, length of fibers +2%, -0%	Length $\geq$ 1 m, increment 20 cm

assembly process. Among suppliers, only Luxium agreed to a delivery method that addresses this issue, making them the sole provider of fibers for the FEMC. These scintillating fibers are a long lead procurement item, with a pre-production batch delivered to UCLA early in 2025. Both the production and acceptance sites will adhere to agreed-upon QA and acceptance protocols to ensure that the fibers meet FEMC specifications. Some of these QA steps are outlined in Tab. 3.61.

The concept of using tungsten powder as an absorber was briefly explored by the UCLA group in 2003, when they constructed and tested a small electromagnetic prototype at SLAC. At the time, the tower structure required a thin-walled brass container to hold the dry powder and fibers in place. However, this assembly technique proved imperfect, leading to significant transverse non-uniformities in detector response due to variations in the sampling fraction and potential displacement of fibers during packing. A compact calorimeter demands strict mechanical tolerances and a highly uniform internal structure to achieve theoretical energy resolution. To address these issues, we introduced intermediate meshes to secure fibers along the towers and developed a vacuum-assisted method to infuse epoxy into the tungsten powder/fiber assembly. Once assembled, the structure becomes rigid, eliminating the need for external containers and dead material in the tower. The homogeneity of the WScFi structure was confirmed by cutting multiple samples into small pieces for analysis. The results showed a uniformity better than 1%, ensuring a negligible effect on energy resolution. The mechanical properties of the WScFi structure (Young's, shear and bulk modulus) were measured and they are comparable to construction steel.

This refined technique, with slight variations, was then employed in constructing the sPHENIX barrel EMCal and all recent FEMC R&D prototypes.

Light Collection scheme and Photosensors The light collection scheme and photosensor setup adhere to the general requirements outlined in Tab. 3.60. The back of each installation block features a thin layer of optical epoxy (1.8 mm thick) mixed with 10% TiO_2, which acts as a diffuse optical reflector for the scintillating fibers and provides a surface for bonding the 13 mm-thick aluminum "strong back." This strong back plate is then bolted to the steel interface plate connecting the EMCal and HCal. On the front side of the installation block, a 21 mm-long light guide (LG) plate is attached. Fabricated from a single piece of optically clear cast acrylic, this LG plate features 64 trapezoidal light guides designed to channel light from the fibers to the SiPMs. Specialized tools were developed and refined during the R&D phase to optimize the machining of these light guides. Additionally, a post-machining light polishing process, which enhances light collection efficiency by approximately 10% compared to non-polished guides, will be implemented during production. The front and back views of the LG plate with SiPMs attached can be seen in Fig. 3.160. The light

collection efficiency of this setup is approximately 80%, which is sufficient to detect 15 MeV in a single tower, corresponding to 24 fired pixels. However, due to the short length of the light guide (typically much longer in fiber calorimeters), light "mixing" from individual fibers is minimal, resulting in spatial non-uniformities in light collection at the 10% level, as measured with a point light source.

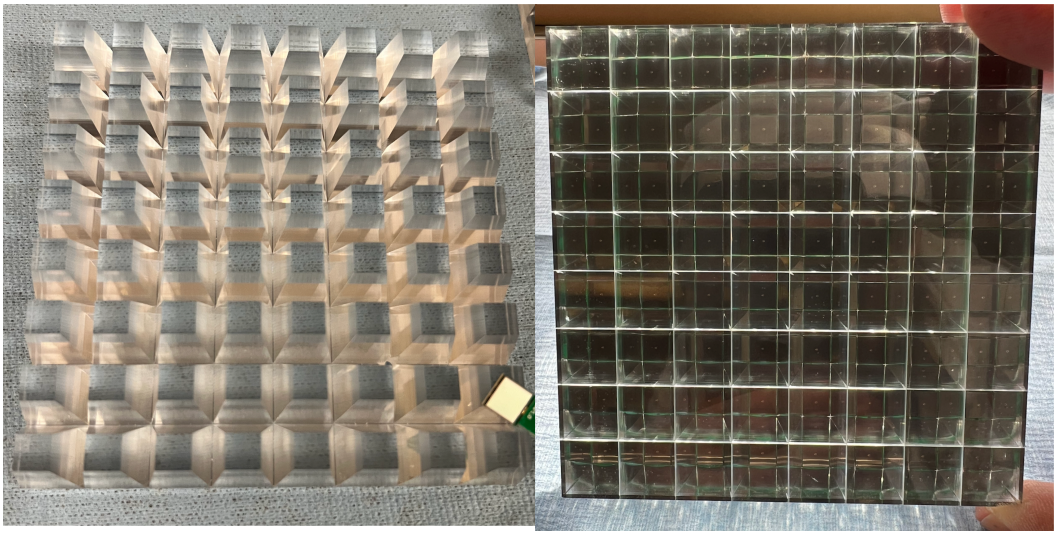

Figure 3.160: Front and back views of LG plates with installed SiPMs.

The chosen photodetector for the FEMC is the SiPM (Silicon Photomultiplier). Over the past 15 years, extensive R&D programs across the globe—including the generic detector R&D program for the EIC—have worked to bring SiPM technology to a mature and reliable level. Today, hundreds of thousands of SiPMs are in use in various high-energy physics and nuclear physics experiments. These detectors are extremely compact, robust, and well-suited for calorimetry readout in moderate radiation environments, such as the forward region of the ePIC detector, as shown in Tab. 3.60. The failure rates of SiPMs in calorimeter operations at facilities like JLab, BNL, and CERN have been remarkably low, typically less than $\approx 0.1\%$. Notably, the STAR Forward Calorimeter System (FCS) experienced zero SiPM failures (out of $\sim$ 10k SiPMs) during three years of operation under conditions similar to those expected in the high-luminosity EIC. Although neutron-induced damage will lead to increased leakage current and noise levels, these effects remain within tolerable limits. For example, it is anticipated that the equivalent noise level for FEMC at ePIC will rise to around ≈ 6 MeV after 10 years of operation, particularly in areas near the beam pipe. This projection is based on scaling from the results observed in the STAR FCS. After this period, replacement of some of the SiPM boards near the beam pipe may be necessary. These considerations guided the design of the FEMC readout system, ensuring simple and seamless integration with the detector, as well as facilitating maintenance of electronics and replacement of SiPM boards during shutdowns if necessary. The technical specifications and performance details of the SiPMs for the FEMC are summarized in Tab. 3.62.

Mechanical Integration The mechanical integration, installation procedures, and structural tests for the FEMC were validated using installation blocks at BNL. These blocks were produced following the final production protocols and using the same components that will be used for the

Table 3.62: Requirements and Technical specifications for FEMC SiPMs.

Parameter	Requirements	Comments
Active Area	6 mm × 6 mm	Efficiency of light collection, E_{min}15 MeV
Pixel Size	15 or 20 um	Dynamic Range, E_{max}100 GeV
Peak Sensitivity	$\sim$ 420 nm	Match scintillating fibers spectra.
PDE	$\geq$ 30%	Efficiency of light collection, S/N
Gain	$\sim 2\times10^5$	at 3 V overvoltage, S/N
DCR	$\leq$ 3000 kcps	at 3 V overvoltage, 25 C, S/N
Temperature Coefficient	$\leq$ 40 mV/C	Stability, Uniformity
Direct Cross Talk	$\leq$ 1%	
Terminal Capacitance	$\leq$ 2.5 nF	FEE coupling
Packing Granularity	Multiple of 4 per tray	4 SiPMs per tower at same V_{op}
V_{op} variation within a tray	$\pm$ 0.02 V	Uniformity of response

actual installation. Structural tests on smaller samples demonstrated that the safety factor for the proposed mounting scheme is greater than 48. A full structural test Fig. 3.161 was conducted by mounting an installation block on a mockup plate and applying five times the expected load. The deflections at the readout end of the FEMC block were measured to be less than 100 um, confirming that each installation block is self-supporting and does not exert any load on the blocks beneath it. Simple installation fixtures were designed, and the installation procedures were verified to ensure safety. Specifically, it was crucial to confirm that the FEMC blocks could be safely installed with the SiPM-carrying boards glued to the LG plates. The tests confirmed that the blocks can be safely mounted onto the hadron end-cap without causing any damage to the SiPM boards.

Figure 3.161: Structural and installation tests at BNL.

Performance The performance of the FEMC prototypes has been tested in several test beams at FNAL over the past few years, initially as part of the generic detector R&D for the EIC and later as part of the ePIC R&D program. In the summer of 2024, one installation block featuring the latest version of the light guide (LG) and SiPM readout was tested at FNAL. Energy scans were conducted at various impact angles covering the entire FEMC acceptance range. As expected, some variation in response across the surface was observed, as shown in Fig. 3.162, due to the compact nature of the LG. However, this variation represents an improvement compared to earlier versions [97]. Position-dependent corrections, based solely on the data from FEMC, were applied to account for non-uniformities. This method is similar to the approach used in the 2014 test [97] and for the sPHENIX barrel EMCal. As anticipated, the uniformity of response improves with shallower impact angles. The energy resolution, shown in Fig. 3.162, corroborates previous measurements with this type of electromagnetic calorimeter [97] and aligns with the performance requirements outlined in Tab. 3.60. The measured absolute light yield is 1580 pixels/GeV.

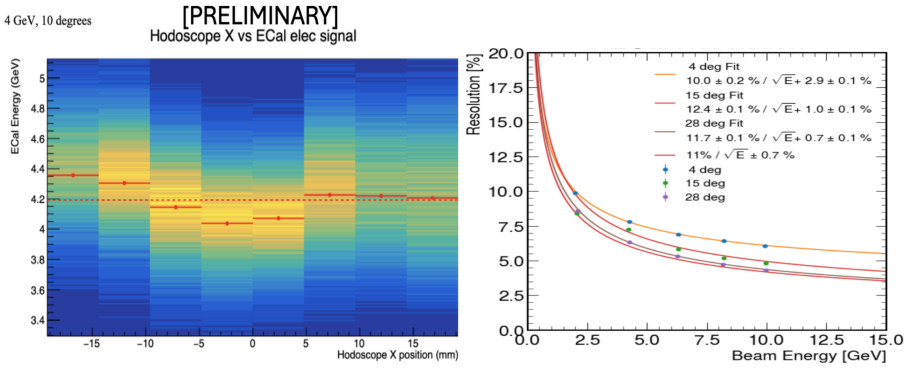

Figure 3.162: Response of calorimeter vs position in hodoscope (left panel). Energy resolution for different impact angles (right panel).

The remaining performance parameters were extensively tested using MC simulations, incorporating the full ePIC simulation chain with the latest detector geometry updates. A material scan indicated the presence of approximately 0.2 X_0 of "dead" material in front of the FEMC in ePIC, but its impact on performance was found to be negligibly small. Simulations conducted with PYTHIA8, using minimal Q^2 cuts for all energy configurations at the EIC, examined occupancy, rates, and dynamic range. These studies informed the set of requirements listed in Tab. 3.60.

An initial investigation into γ/π^0 separation, based on the traditional shower shape analysis method outlined in the EIC Yellow Report (Fig. 11.46, [11]), revealed potential for improvement. A significant enhancement in γ/π^0 separation was achieved by applying machine learning algorithms. As shown in Fig. 3.163 (left panel), the misidentification rate at 60 GeV dropped to approximately 10%, compared to 80% with traditional methods [11].

Readout Electronics The FEMC readout electronics face three primary challenges: achieving a large dynamic range of 7000:1, ensuring precise discrimination for streaming small signals (24 pixels) amidst dark counts of up to 45 GHz caused by radiation damage to SiPMs, and integrating everything within a compact space—around 5 cm for SiPM boards, front-end boards (FEBs), cooling, and cables. Tab. 3.63 summarizes requirements for the FEB.

Building on the successful design of the STAR FCS readout, FEMC's readout system transfers SiPM signals to a low impedance load, shapes and amplifies the resulting voltage, and digitizes the waveform. Hits are detected in the digital waveform via threshold crossing (which may be filtered). In

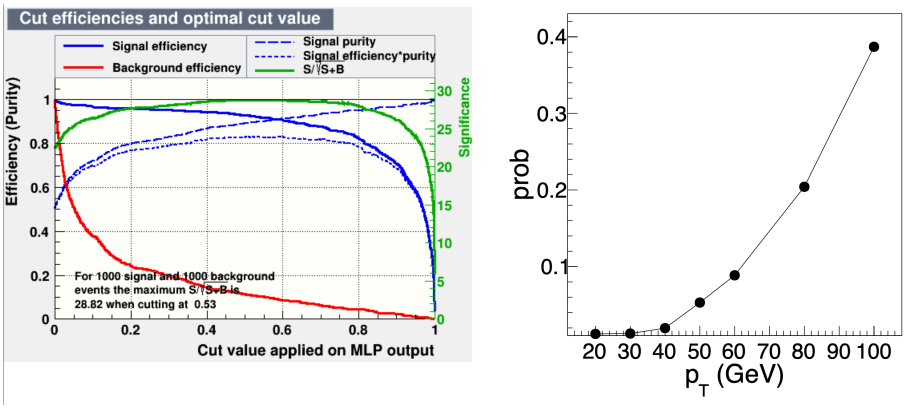

Figure 3.163: Signal (single photon) efficiency and background (merged di-photons) contamination for different cut value of the NN output for 60 GeV (left panel). Probability of misidentifying π^0 as a single photon vs energy (right panel)

Table 3.63: Requirements for the FEB

Parameter	Requirements	Comments
SiPM & overvoltage	4xS14160-6015PS, 2-3V	
Min signal	15 MeV (@ 1.6 pix/MeV)	
Max signal	100 GeV	
Hit rate	10 kHz	per channel
Charge reso.	$\sim 210\%/\sqrt{npix} \oplus (0.9)\%$	contribute $\leq$10% of FEMC resolution
Charge nonlinearity	$\leq 1\%$	
Time resolution	$\ll$ 10 ns	for $\geq$100 MeV signals only
SiPM bias voltage stability	$\leq$ 10 mV	including T compensation
Bias voltage setting range	33 to 47 V	sufficient for meaningful IV curve
Bias current range & mon. resolution	2 mA, $\leq$200 nA	4 SiPMs per tower at same V_{op}
LED drive control	var. amplitude, masks	fired by global command

streaming readout mode, regions of interest in the digital waveform are identified, timestamped, and sent to an output FIFO/merging scheme, before being transmitted to the readout (RDO) board. At the RDO, data from up to 16 FEBs are buffered, merged, and sent to the DAM. Feature extraction, converting raw waveform samples to estimated pulse amplitude and timing, may be done either at the FEB or RDO level to reduce data volume. If hardware feature extraction is not used, this will be performed during preliminary online analysis.

Waveform digitization for FEMC will operate at either 39.4 MSPS or 49.25 MSPS. The digitization clock must be phase-locked to the beam bunch crossing clock at 98.5 MSPS to extract hit timestamps in real-time within the streaming DAQ system. Sampling at 98.5 MSPS is not feasible due to power and FPGA resource constraints. To meet the 15 MeV readout threshold and achieve the dynamic range, the ADC resolution must be 14 bits. The analog waveform will be shaped before digitization to achieve a peaking time of approximately $2.8/f_{SAMPLE}$, which ensures less than 1% error in pulse amplitude measurement while minimizing noise from dark count pileups. For instance, a 57 ns peaking time is optimal at 49.25 MSPS.

The FEB will individually regulate bias voltage for each tower, providing temperature compensa-

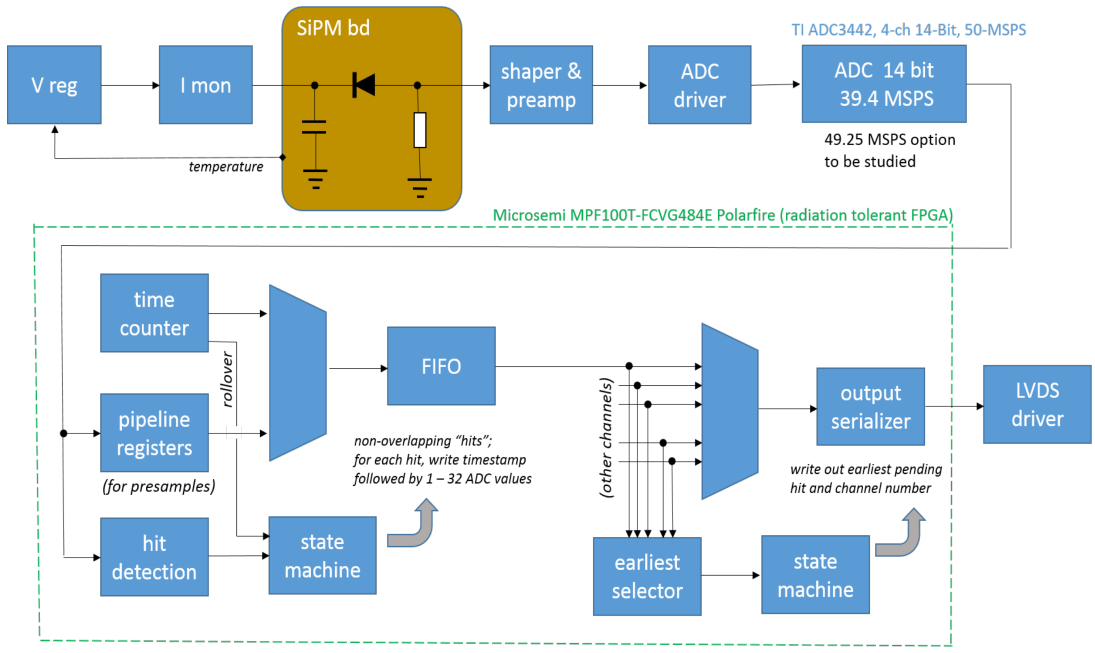

Figure 3.164: FEMC front end electronics.

tion for each SiPM board (covering 2 × 2 towers) and monitoring current with built-in protective current limits. Each tower's four SiPMs will be connected in parallel, sharing a common bias voltage, requiring precise matching of the breakdown voltages (V_{BR}) among the four SiPMs to ensure uniform gain. The bias regulation circuits, developed from the STAR Forward Calorimeter, have proven effective, though radiation sensitivity in a voltage reference IC was noted. To mitigate this, FEMC's bias regulator will use a remote reference on the power distribution boards, ensuring the required 0.03% stability. Less critical internal voltage references require only 1% stability. The bias regulation channels provide sharp current limiting to protect the SiPMs from overload, maintaining 10 mV bias voltage stability up to the current limit (2 mA).

Signal routing from the SiPM boards to the FEBs is achieved through board-to-board connectors, eliminating the need for cables. These connectors can accommodate mechanical tolerances of +/- 0.5 mm between the FEB and SiPM boards and overlap with space allocated for the cooling water tube. Should radiation damage impact the innermost FEBs, a backup plan would route SiPM signals via 2m coaxial cable bundles to FEBs mounted at the block periphery.

Connections between the FEBs and RDO will use shielded Cat6 Ethernet cables, routed horizontally through the FEB rows and out of the magnet to racks housing the RDOs. One rack will be placed north of the north detector half, and another south of the south detector half. Cable lengths are estimated at 15 meters, and it has been confirmed that LVDS signals can be properly received at 200 Mb/s over this distance, meeting performance requirements.

Each rack will also house a Wiener MPOD crate with low-voltage (LV) power supplies, with one crate serving the north half and one for the south half of the detector. Each FEB will require approximately 250 mA at +16 V, 180 mA at -2 V, and up to 67 mA (depending on SiPM radiation damage) at +50 V.

The FEBs will be cooled conductively via a copper bracket attached to the main board (housing the ADCs, FPGA, and power supply circuits) and connected to a water cooling line. The water line will

consist of standard 1/4" inch (potentially 3/16 inch) diameter copper tubing. A negative pressure system will mitigate the risk of water leaks. Two rows of FEBs will be served by a single water line in a U-shaped loop, with no fittings at each FEB, only at the loop ends. Reliable flare fittings will be used for the connections. Custom water manifolds, located in the "service gap" at the outer perimeter of the calorimeter blocks, will manage water distribution. The arrangement will likely consist of two supply and return manifold sets—one for the upper and one for the lower half of the detector.

Each water circuit will need to cool about 750 W of power from 148 FEBs, requiring chillers with at least 1.5 kW capacity for each half of the detector. One chiller will serve the north half and another the south, cooling two water circuits each.

Slow controls for FEMC will fall into two categories: hardware registers on the FEBs (communicated through DAQ software and the DAM/RDO) and controls for commercial equipment such as the water chillers and power supplies (Wiener MPOD), connected via Ethernet. SoftIOC interfaces will manage EPICS variables, providing GUI control, logging, and alarms.

Tab. 3.64 summarizes the control and status registers for the FEB.

Table 3.64: Control and status registers on the FEB

Function/description	Qty per FEB	R/W	Notes
SiPM bias voltage (base)	32	R/W	
Bias temp. comp. slope	1	R/W	
actual compensation	8	R	i.e. temperature
SiPM current monitor	32	R	extra diagnostic info
input LV supply monitor	2	R	
FEB temperature monitor	3	R	
FEB & SiPM board serial numbers	9	R	read once at startup
firmware revision	1	R	read once at startup
firmware update interface	1	R/W	maintenance use only
hit threshold channel mask	32	R/W	
hit detection options registers	4	R/W	
LED firing mask	1	R/W	
hit scalers	32	R	
fifo overrun scalers	32	R	
ADC configuration interface	1	R/W	might be internal use only

Calibration The FEMC faces the hadron beam, and at mid to high energies, its signals will predominantly come from photons produced by π^0 decays. Tower-by-tower absolute energy calibration of the forward electromagnetic calorimeter will be performed by reconstructing π^0 mesons through the invariant mass of two photons from π^0 decays. It is expected that π^0 calibration for each tower can be achieved in approximately one day of data collection, followed by semi-online analysis using only forward FEMC data. The method involves associating reconstructed π^0 mesons with the tower showing the highest response, adjusting the tower's gain based on the π^0 mass location, and repeating the process over several iterations. This technique has been successfully implemented in forward calorimeters at RHIC, including the STAR FCS.

Electrons from DIS events, combined with tracking information, can be used to cross-check the

calibration. However, this approach requires a large dataset and will be performed offline. Additionally, Minimum Ionizing Particle (MIP) signals from hadrons can be utilized for calibration at the low-energy end. For high energies, where the two photons from π^0 decays are too close together for the forward EMCal to distinguish them, η mesons can be used to verify energy non-linearity.

Monitoring system An LED system will be installed on the FEE boards to illuminate four towers using a trigger pulse. The LEDs will be preselected to provide equal light output to the towers, serving as a critical monitoring system. This will be essential for initial testing during installation, verifying mapping, and ensuring long-term stability of the detector, SiPMs, and FEE board gain, as well as detecting any potential radiation damage. A dedicated short LED run will be performed daily to monitor the calorimeter's performance.

Additionally, the current and voltage on the FEE boards will be continuously monitored. Periodic I-V curve measurements will be conducted, on a weekly or bi-weekly basis, to assess the health of the SiPMs and FEE boards.

Status and remaining design effort:

R&D effort: eRD106 was completed in 2025 with final analysis of the test beam data.

E&D effort: Detailing of mechanical design, and formalizing production drawings.

Other activity needed for the design completion: Produce and test first versions of final design FEB and SiPM boards.

Status of maturity of the subsystem: $\sim 70\%$

Environmental, Safety and Health (ES&H) The project will strictly adhere to all Environment, Safety, and Health (ES&H) regulations to ensure the safety of personnel, the integrity of the equipment, and the protection of the environment throughout the construction and operation phases. Specific hazards associated with production of FEMC blocks are:

Using epoxy, the work will be carried out in fume hoods.

The large volume of scintillating fibers is a combustible material that requires proper fire safety storage and handling protocols.

The use of a radioactive source Sr^{90} for fiber QA follows all radiation safety guidelines and appropriate training of personnel.

Comprehensive risk assessments will be conducted for all activities, including the handling of hazardous materials and electrical components, while implementing appropriate controls to minimize exposure to risks. The personnel will receive specialized training in safety protocols and emergency response procedures.

3.3.6 Hadronic Calorimetry

Add text here.

3.3.6.1 The backward endcap hadronic calorimeter

The backward hadronic calorimeter, here called **nHCal** (meaning Negative-eta/Neutral Hadronic Calorimeter), is a tail catcher calorimeter to be installed in the electron-going negative-z direction. As illustrated in the ePIC detector schematic 3.14, the nHCal is surrounded by an outer collar, backed by a flux return plate and has an oculus ring placed in front. Experience from the H1 experiment at HERA demonstrates the need for such a calorimeter for low-x measurements [98,99].

Requirements

Requirements from physics: The main requirements for nHCal originate from physics processes in events with low Q^2 and low $x \sim 10^{-3} - 10^{-2}$ as well as high inelasticity y. This requires the acceptance of $-4.14 < \eta < -1.18$.

The processes of interests include diffractive vector meson overproduction $J/\psi \rightarrow \mu^+\mu^-$, $\phi \rightarrow K_L K_S$, $\phi \rightarrow K^+K^- \rightarrow \mu^+\mu^-$ and diffractive dijets. It will be also used as a veto for jet studies with neutral energy component and help in scattered electron identification along with backward EMCal. Finally, it will be used as a hadron beam background veto for dRICH in conjunction with LFHCAL for which a good timing resolution is required. In order to measure vector meson production with muons a good μ/π separation of tracks with MIP signal in calorimeters is required. Low-energy neutron detection for neutral jet identification demands low hit thresholds to achieve greater than 90% detection efficiency for 2 GeV neutrons. Moreover, neutral clusters must be identifiable after charged hadron correction, necessitating track matching and cluster position resolution capable of distinguishing showers separated by 30 cm. This resolution is achievable with tiles of up to 25 cm size.

Requirements from Radiation Hardness: In general, the radiation dose in the electron endcap area is expected to be low. A study was performed and summarized by ePIC background study group [12].

The low radiation dose compared to the forward region makes the use of SiPMs and FEE safe. SiPMs are required to maintain a low dark count rate after 10 years of operation. This is possible with the selected Hamamatsu S14160-1315PS model. Radiation tests [100] show that non-avalanche starts to increase above the level of 10^{-10} MEQ neutron fluence, which is expected to be reached after 10 years of operation.

Requirements from Data Rates: Data rates were studied by considering the following sources:

- Deep Inelastic Scattering (DIS)
- Synchrotron Radiation
- Electron Beam Gas

bkg. type	hit rate in detector [kHz]	max single channel hit rate [kHz]
DIS	$\sim 10^3$	1.23324
Synchrotron rad.	$\sim 2 \cdot 10^1$	-
e+gas	403.899	6.6448
h+gas	$\sim 7 \cdot 10^2$	0.303781

Table 3.65: Maximum expected background rates for backward HCal. The assumed threshold is 170 keV.

- Hadron Beam Gas

The values are taken from background studies found here:

- https://wiki.bnl.gov/EPIC/index.php?title=Background

Justification

Device concept and technological choice: Sampling calorimeter design featuring 10 layers of steel absorber and plastic scintillator tiles was selected as nHCal, because of low cost and simplicity. SiPMs and WLS fibers are going to be used for the light collection. The design, similarly to LFHCAL, is inspired by CALICE [101] collaboration, which allows mass production and easy handling of same type of detector modules.

Subsystem description:

General device description:

The nHCal is planned to be a sampling hadronic calorimeter with 10 layers of alternating steel and plastic scintillator, 4 cm and 0.4 cm thick, respectively. This arrangement provides compensation. The structure of the calorimeter will be a flattened cylinder with an outer radius of 276 cm cm and an inner radius of 14 cm to accommodate the hadron and electron beam pipes. The total thickness along the beam direction will be 45 cm. The detector will be placed at a position of -395 cm from the interaction point in the electron-going direction. The plastic scintillator layer will consist of tiles with a size of 10 cm $\times$ 10 cm(TBD). Two light collection solutions are under consideration: either the use of WLS fibers with SiPM readout or the SiPM-on-tile design, similar to that used for the LFHCAL, which was developed by CALICE [101]. The SiPM-on-tile approach is feasible with smaller tiles near the beam ($\eta \sim -4$), while larger tiles will require the WLS+SiPM combination. Tiles and absorber plates will be assembled into modules inspired by LFHCAL modules, with dimensions of 10 cm $\times$ 20 cm $\times$ 45 cm in the y, x, and z directions, respectively.

Sensors:

The Hamamatsu S14160-1315PS SiPMs will serve as light sensors. They will either be connected to the WLS fibers or placed directly on the tiles.

FEE:

The HGCROCv3 will be used as a Front-End Electronics (FEE) system, similar to other calorimetry systems in ePIC. The FEEs will be placed in front of the modules.

Other components:

The nHCal will also feature a calibration system based on LEDs as well as a temperature monitoring via sparsely place temperature sensors. This is described in more detail in 3.3.6.1.

Performance: The performance of the nHCal was studied using single particle simulations in dd4hep with GEANT4 used for particle transport. Neutron detection thresholds were evaluated against kinetic energy and integration time. Figure 3.165 illustrates the neutron detection efficiency as a function of energy threshold and integration time. Good performance is achieved with 100 ns integration time, and further increases offer minimal improvement. Additionally, a low threshold of $0.25E_{MIP}$ already provides a good detection efficiency 70% at 300 MeV.

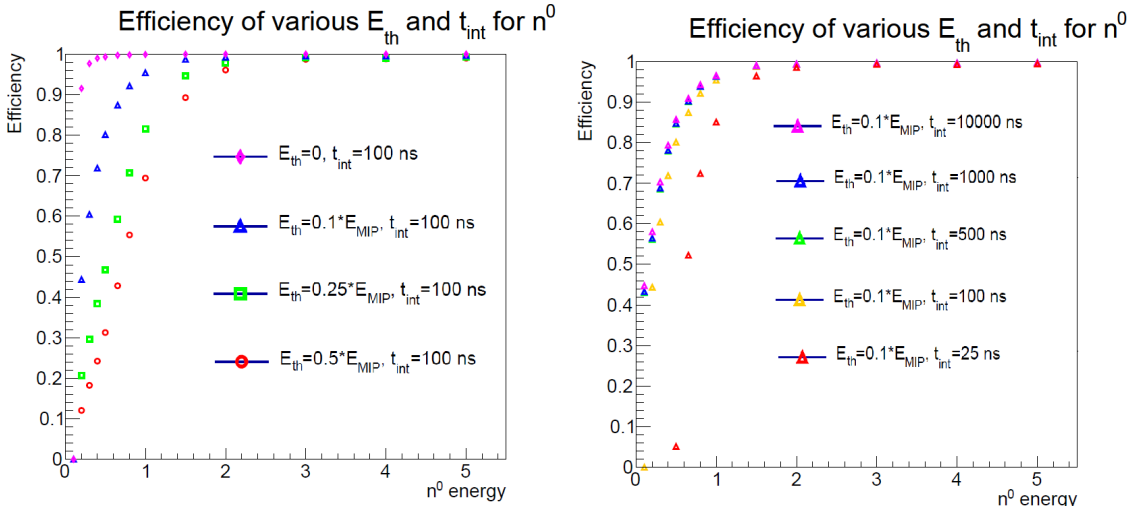

Figure 3.165: **Left:** Neutron detection efficiency vs. kinetic energy E_{kin}, dependence on threshold as a fraction of MIP energy deposit. **Right:** Same as left, but showing dependence on integration time. Repository: https://github.com/OSUNuclearPhysics/ePIC_preTDR_nHCal_thresholds

Studies of e/h response with e/π simulation show that the ratio of steel and scintillator achieves compensation within uncertainties as presented in Fig. 3.167.

Simulated DIS events: One of the basic studies is a check of energy and momentum distributions going into backward HCal. This study used DIS $e+p$ events at $18+275$ GeV with $Q^2 > 1\,\text{GeV}^2$. The Fig. 3.168 shows total energy E and p distributions of each particle species in the nHCal acceptance $-4.0 < \eta < -1.0$.

Energy and momentum distributions of particles within nHCal acceptance in $e+p$ DIS events at $18+275$ GeV with $Q^2 > 1\,\text{GeV}^2$ were studied using the full official simulation of the ePIC detector. These distributions are presented in Fig. 3.168 as well as versus η in Fig. 3.169, Fig. 3.170 and Fig. 3.171. This analysis was used to determine the average energy of neutrons and optimize the detector geometry and thresholds.

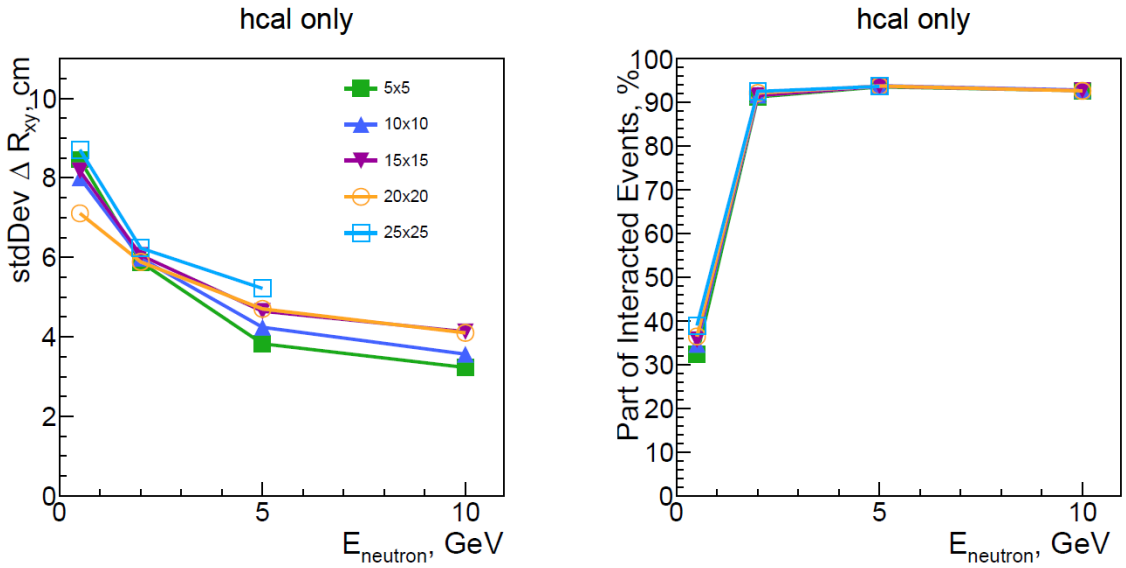

Figure 3.166: Position resolution R_{xy} and cluster efficiency vs. E for different tile sizes. Repository: https://github.com/OSUNuclearPhysics/ePIC_preTDR_nHCal_TileScaling

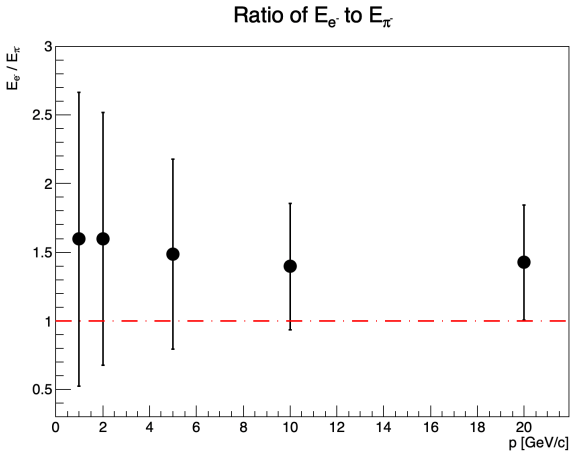

Figure 3.167: Ratio of e/π response vs. E. Repository: https://github.com/OSUNuclearPhysics/ePIC_preTDR_nHCal_eh-ratio

Vector meson reconstruction: Vector meson reconstruction and acceptance were studied in $e+p$ and $e+A$ events using a standalone Sartre simulation, focusing on exclusive diffractive production. A large fraction of the J/ψ cross section was found to be produced in the backward direction, highlighting its importance. It should be noted that the J/ψ study is one of the major goals of EIC, as listed in the Yellow Report [22]. The acceptance of J/ψ is shown in Fig. 3.172 versus $-t$, Bjorken x_{BJ}, and Pomeron x_P. The figure also illustrates the acceptance when decay daughters are measured in different hadronic calorimeters. A similar study was performed for $e+A$ collisions and is presented in Fig. 3.173. Studies of $\Phi \to K^+K^-$ were also performed as shown in Fig. 3.174

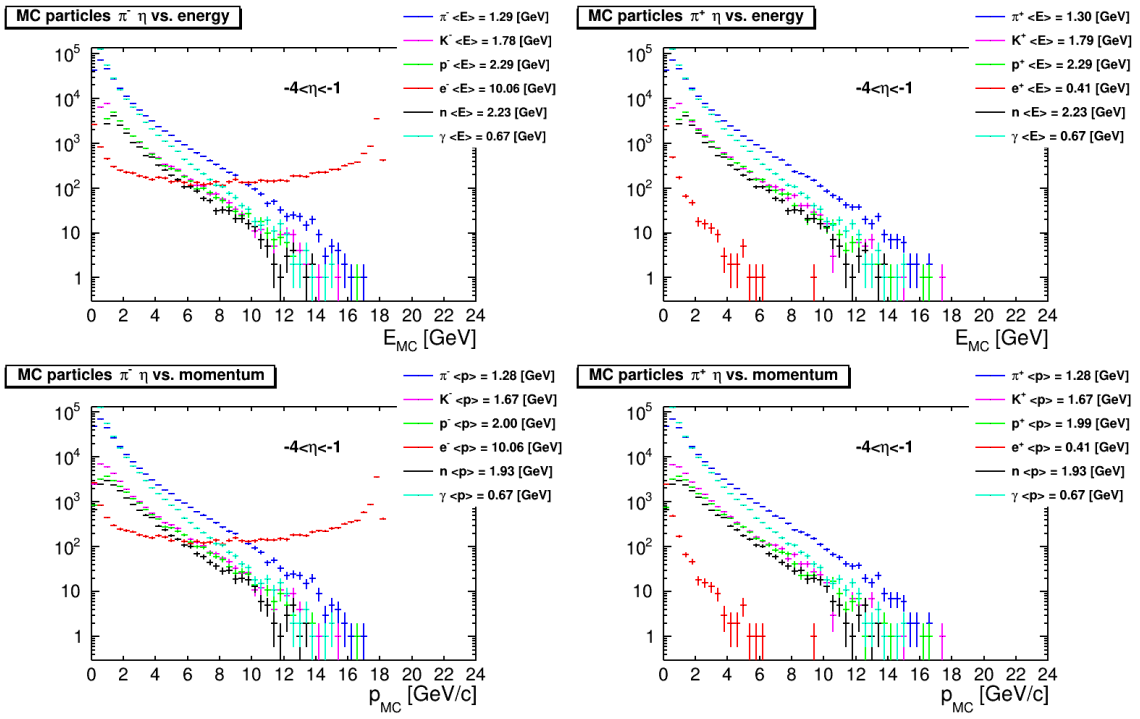

Figure 3.168: **Top:** Primary, generated particle E distributions in nHCal acceptance $-4.0 < \eta < -1.0$. **Bottom:** Primary, generated particle p distributions in nHCal acceptance $-4.0 < \eta < -1.0$. Repository: https://github.com/OSUNuclearPhysics/ePIC_preTDR_nHCal_DIS_MCPart

for $e + p$ and in Fig. 3.175 for $e + A$ collisions. These studies indicate that nHCal is needed to measure J/ψ and ϕ in events with $x \sim 10^{-3}$ and lower.

Vector meson reconstruction was also studied with Sartre and Pythia generated events with full EICrecon reconstruction output and ePIC geometry. The results are qualitatively consistent and are summarized in a technical report [102].

Jets with neutral component: Another purpose of the nHCal is to help identify jets with neutral energy component, especially low energy neutrons of around $E = 2.23\,\text{GeV}$ total energy. This is an average neutron energy as indicated by the DIS study mentioned above. By selecting charged only jets and vetoing those containing neutral hadrons, the jet energy resolution can be improved. This was studied with a full ePIC simulation and track matching to MC particles or clusters using MC information. The jet energy resolution for the cases of inclusive (squares) and charged-only jets (triangles) is compared in Fig. 3.176. Results show a $\sim$ 20% improvement in jet energy resolution with the nHCal present.

Diffractive dijet measurement: Diffractively produced dijets [103] are a key area of study for the nHCal. With integrated luminosity $10 - 100\,\text{fb}^{-1}/\text{year}$ it is expected that $10^8 - 10^9$ diffractive dijet events will be produced at ePIC. Preliminary studies indicate that 1.8% of diffractive dijet events contain one of the jets in the nHCal acceptance. This increases to 4.8% for jets shared between

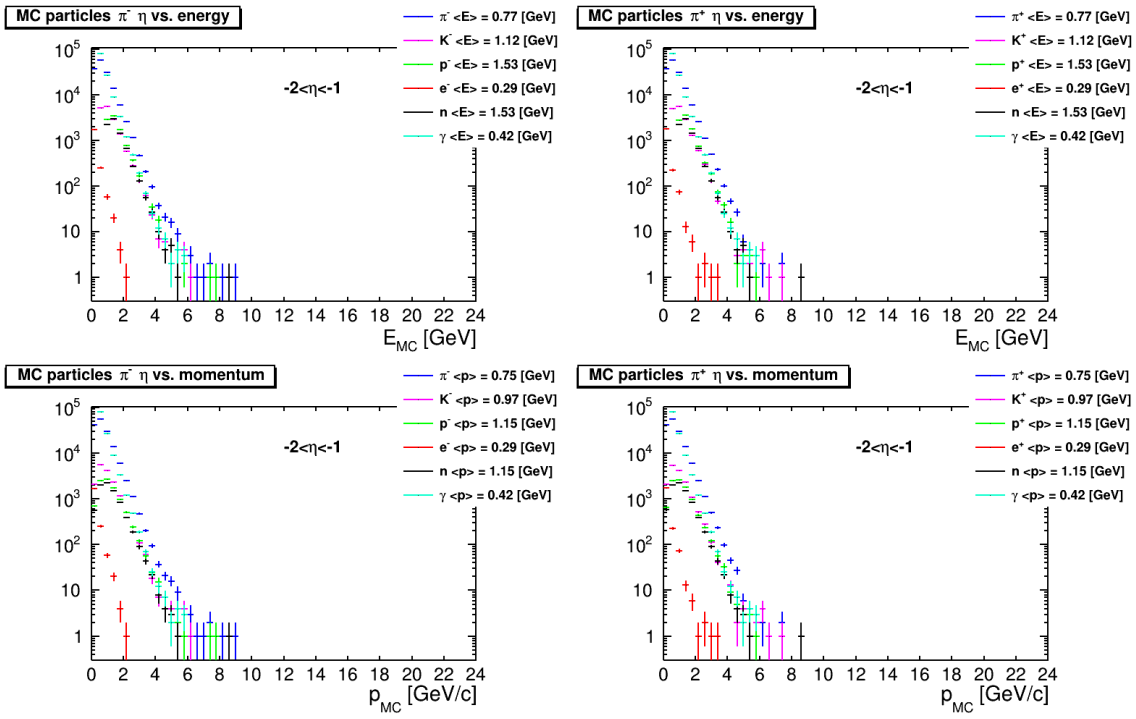

Figure 3.169: **Top:** Primary, generated particle E distributions in $-2.0 < \eta < -1.0$ range. **Bottom:** Primary, generated particle p distributions in $-2.0 < \eta < -1.0$ range. Repository: https://github.com/OSUNuclearPhysics/ePIC_preTDR_nHCal_DIS_MCPart

nHCal and barrel HCal. Such events have $x \sim 10^{-3}$, so are important to study the structure of protons and nuclei. This is illustrated in Fig. 3.177 vs. Bjorken x and inelasticity y for different number of jets with thrust axis in the nHCal acceptance.

In order to investigate the required position resolution to distinguish charged and neutral hadrons the momentum vectors of pairs of MC particles were projected onto the surface of nHCal and their separation was calculated. This provides an approximate estimate of the particle density per event in nHCal. A normalized distribution of the distances for all particle pairs is shown in Fig. 3.178 (left). The fraction of pairs that are separated by less than 30 cm is 1.8%. This includes secondaries produced in the detector material. On the other hand, the distance between neutron and any other particle is different and presented in Fig. 3.178 (right). The fraction of such pairs drops to 0.7%, which means it will be much easier to separate neutrons from other particles.

After full reconstruction with EICrecon it was possible to also investigate the distance (R_{xy}) between clusters of neutrons paired with clusters of any other particles (X). This provides constraints on the position resolution required to distinguish charged and neutral hadrons. Fig. 3.179 presents the dependence of the fraction of such cluster pairs per cm on the distance between their centers. The Fig. 3.179 (left) shows MC truth clusters, while Fig. 3.179 (right) shows reconstructed clusters. The effect of merging is visible for distances below 20 cm. On the MC truth level, a 22% of clusters fall below 30 cm, which provides an upper limit on the fraction of clusters affected by merging. On the other hand, only 5% of reconstructed clusters are within 30 cm. Overall this means that the nHCal will be able to separate clusters which are separated by 30 cm between their centers.

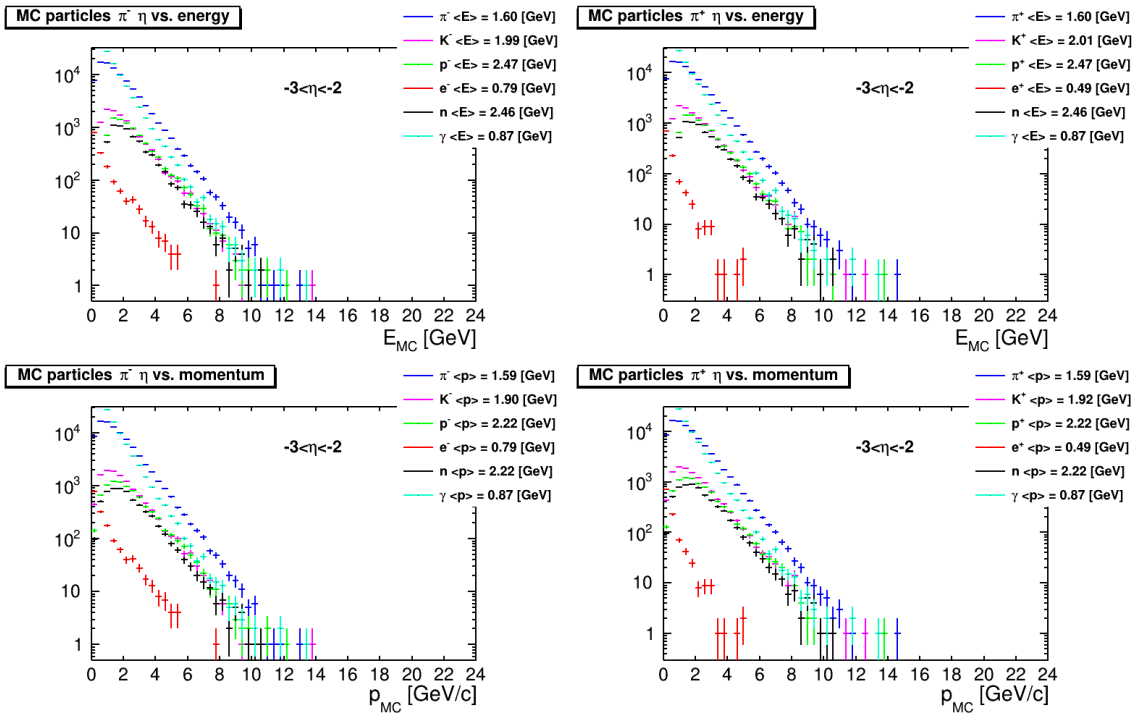

Figure 3.170: **Top:** Primary, generated particle E distributions in $-3.0 < \eta < -2.0$ range. **Bottom:** Primary, generated particle p distributions in $-3.0 < \eta < -2.0$ range. Repository: https://github.com/OSUNuclearPhysics/ePIC_preTDR_nHCal_DIS_MCPart

Scattered electron identification: The nHCal will augment the backward EMCal in scattered electron identification, by increasing the e/π rejection.

Hadron beam background veto for dRICH: Another important function of the nHCal is to serve as a hadron beam background veto along with the LFHCAL. Such background is problematic for dRICH. Experience from STAR experiment shows that 30% of events may be due to background. Further studies need to be performed in order to understand the impact of beam background.

Cluster reconstruction: Clusters are reconstructed using the standard island clustering algorithm [104, 105]. To distinguish between charged and neutral clusters, track-cluster matching must be employed. The neutral energy component is obtained by subtracting the expected energy of charged particles, determined from the momentum measurement via tracking. The overlap of clusters was studied using two-particle simulations of neutrons and pions with $E = 1$ GeV. This is illustrated in Fig. 3.180 as a function of x, y position of the reconstructed clusters. The legends indicate the emission angles of the neutrons and pions.

Initial studies show that neutron and pion clusters can be distinguished when separated by ≈ 30 cm or ≈ 4.5 degrees.

In order to check the performance of neutron energy reconstruction and isolation, a charged hadron correction was applied on the total reconstructed energy E^{reco}_{total}. This is done by subtracting the

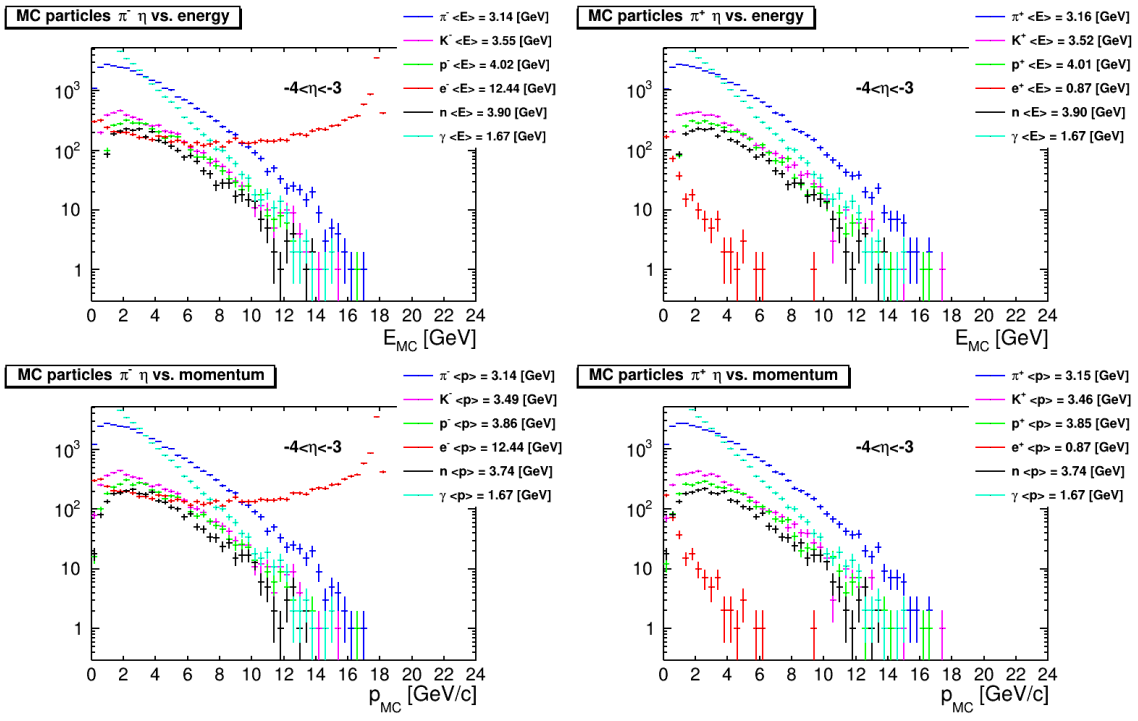

Figure 3.171: **Top:** Primary, generated particle E distributions in $-4.0 < \eta < -3.0$ range. **Bottom:** Primary, generated particle p distributions in $-4.0 < \eta < -3.0$ range. Repository: https://github.com/OSUNuclearPhysics/ePIC_preTDR_nHCal_DIS_MCPart

pion momentum with the formula $E^{reco}_{neutral} = E^{reco}_{total} - p_\pi$ when $|\frac{E^{reco}_{charged} - p}{\sigma_{E^{reco}_{charged}}}| > 3$ otherwise, just the energy of the isolated charged pion cluster $E^{reco}_{charged}$ is subtracted using $E^{reco}_{neutral} = E^{reco}_{total} - E^{reco}_{charged}$. The performance of neutral energy reconstruction is quantified by the ratio $\frac{E^{reco}_{neutral}}{E^{MC}_{neutral}}$ presented in Fig. 3.181 for different values of neutron and pion impact point separation. The overlap of the 2 showers starts impacting neutron energy reconstruction at a separation of 33.9 cm with serious effects below 25.6 cm. For distances smaller than 8.7 cm, the distribution is almost flat meaning that the energy is associated randomly between pion and neutron and the showers are not separable in this way. The distribution has a large tail at lower values due to shower fluctuations. This impacts the reconstruction performance depending on how much energy was deposited by neutron. This is visible in Fig. 3.182 when plotting $\frac{E^{reco}_{neutral}}{E^{MC}_{neutral}}$ as a function of $E^{MC}_{neutral} \times f$, which corresponds to the original neutron energy deposits in the scintillators by factoring out the sampling fraction f. As expected, the fraction reaches unity when the energy deposit is large, because it's easier to pass the thresholds and obtain a stronger signal.

This confirms that good neutral energy separation should be possible between clusters which are ≈ 30 cm apart.

Implementation

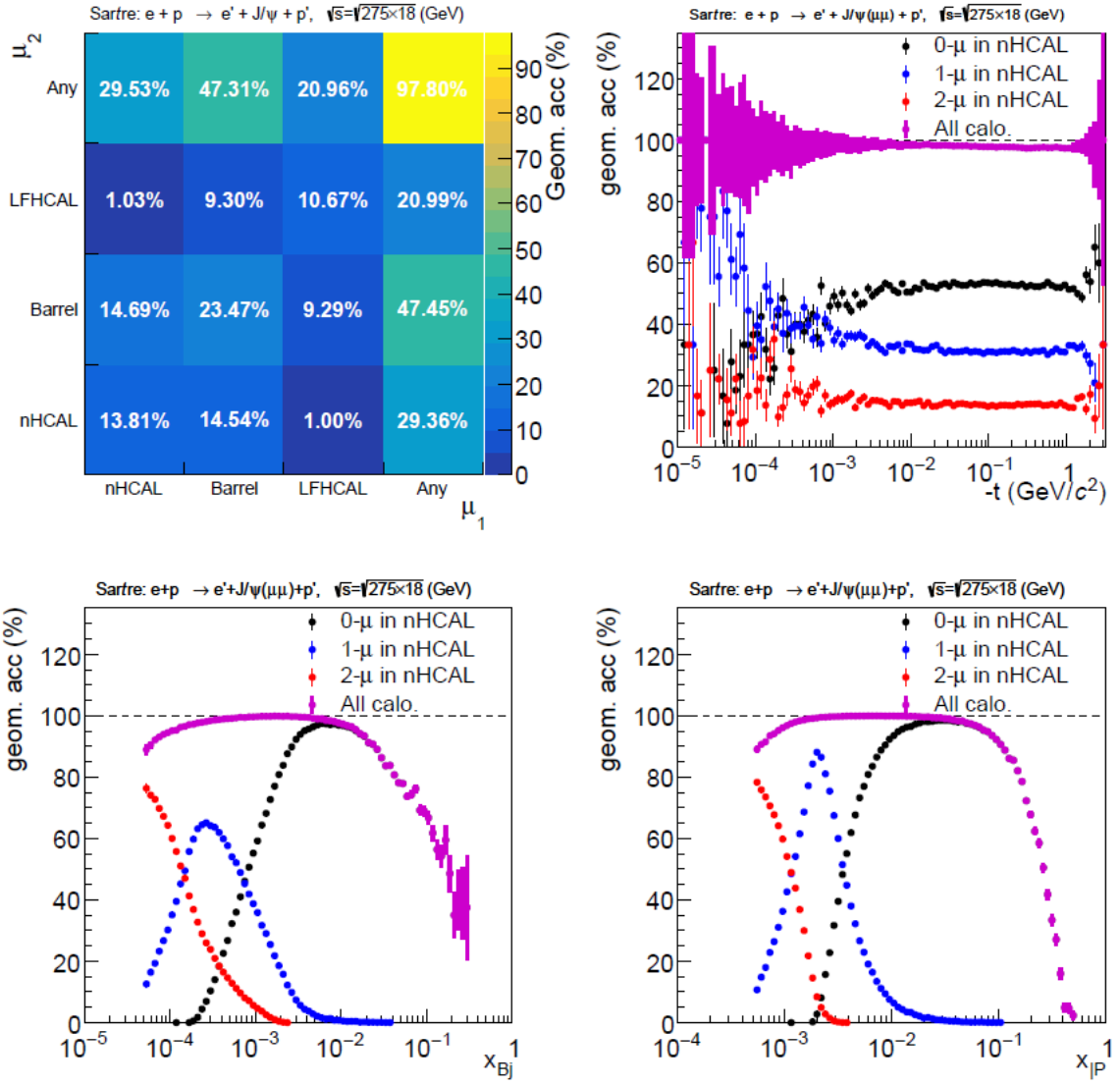

Figure 3.172: Acceptance of photoproduced $J/\psi \rightarrow \mu^+\mu^-$ in $e + p$ collisions at $18 + 275$ GeV. **Top left:** Acceptance vs. μ_1 and μ_2 hitting different HCals. **Top Right:** Acceptance vs. $-t$ for different number of μ in nHCal. **Bottom Left:** Acceptance vs. Bjorken x_{bj} for different number of μ in nHCal. **Top Right:** Acceptance vs. Pomeron x_P for different number of μ in nHCal. Repository: https://github.com/OSUNuclearPhysics/ePIC_preTDR_nHCal_VM_Sartre_kine

Services: All services will be provided through the service gap in front of the endcap, including power supply cables for the FEEs and SiPMs, as well as data connections to the FEEs. Depending on the final chosen granularity of the nHCal readout channels, it will have to be investigated whether a small cooling system to dissipate the heat produced by the ASICs will have to be integrated, similarly to the LFHCAL as described in Subsec. 3.3.6.3.

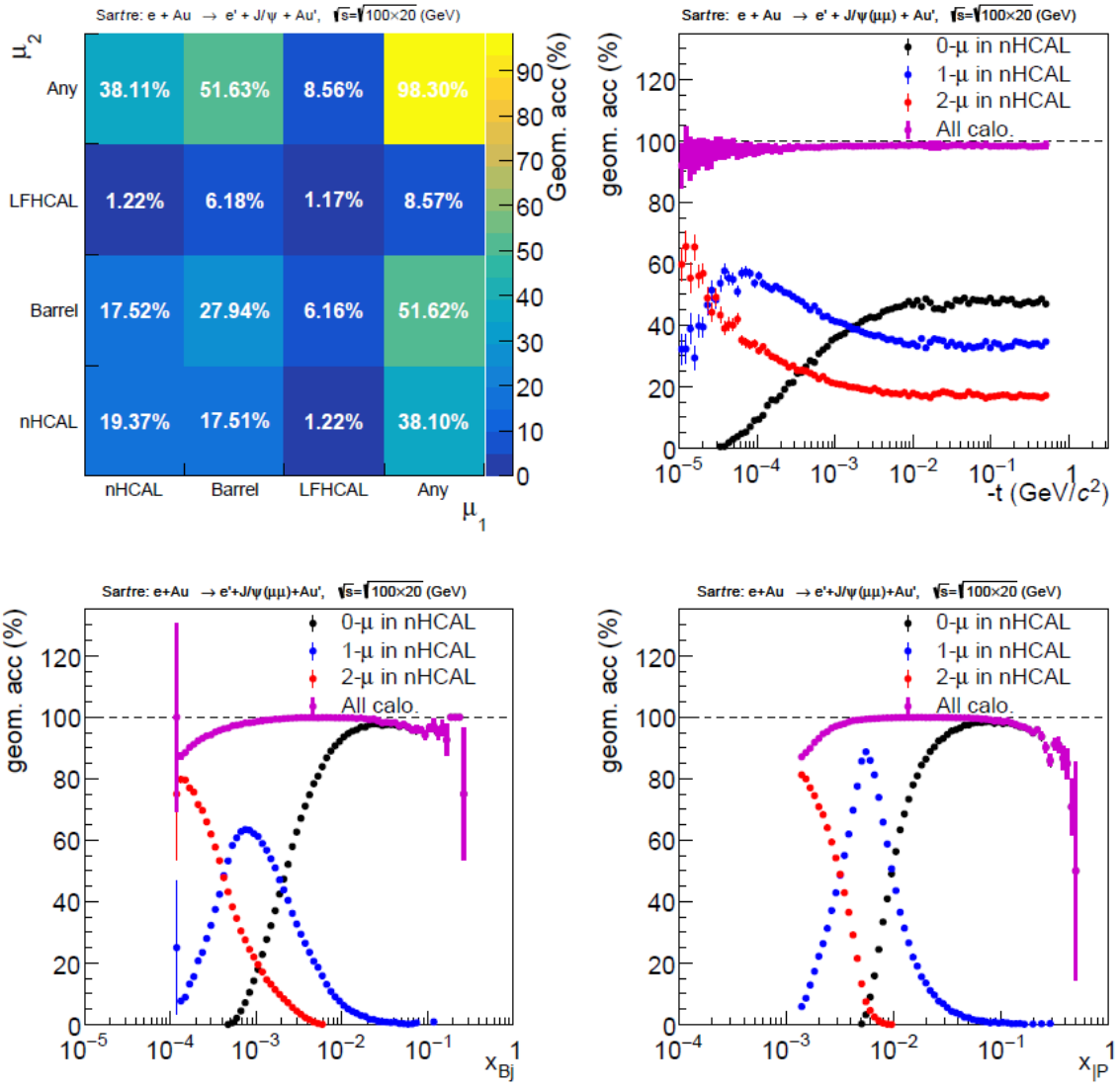

Figure 3.173: Acceptance of photoproduced $J/\psi \rightarrow \mu^+\mu^-$ in $e+p$ collisions at $20+100$ GeV. **Top left:** Acceptance vs. μ_1 and μ_2 hitting different HCals. **Top Right:** Acceptance vs. $-t$ for different number of μ in nHCal. **Bottom Left:** Acceptance vs. Bjorken x_{bj} for different number of μ in nHCal. **Top Right:** Acceptance vs. Pomeron x_P for different number of μ in nHCal. Repository: https://github.com/OSUNuclearPhysics/ePIC_preTDR_nHCal_VM_Sartre_kine

Subsystem mechanics and integration: The backward HCal modules will be stacked on top of each other similarly to the LFHCAL. Communication with the calibration system will be handled by the HGCROCv3 ASIC on FEE board through I^2C.

Calibration, alignment and monitoring: Calibration will be performed using LEDs on the tiles or additional clear fibers to guide laser/LED light (similar to the STAR EEMC calibration

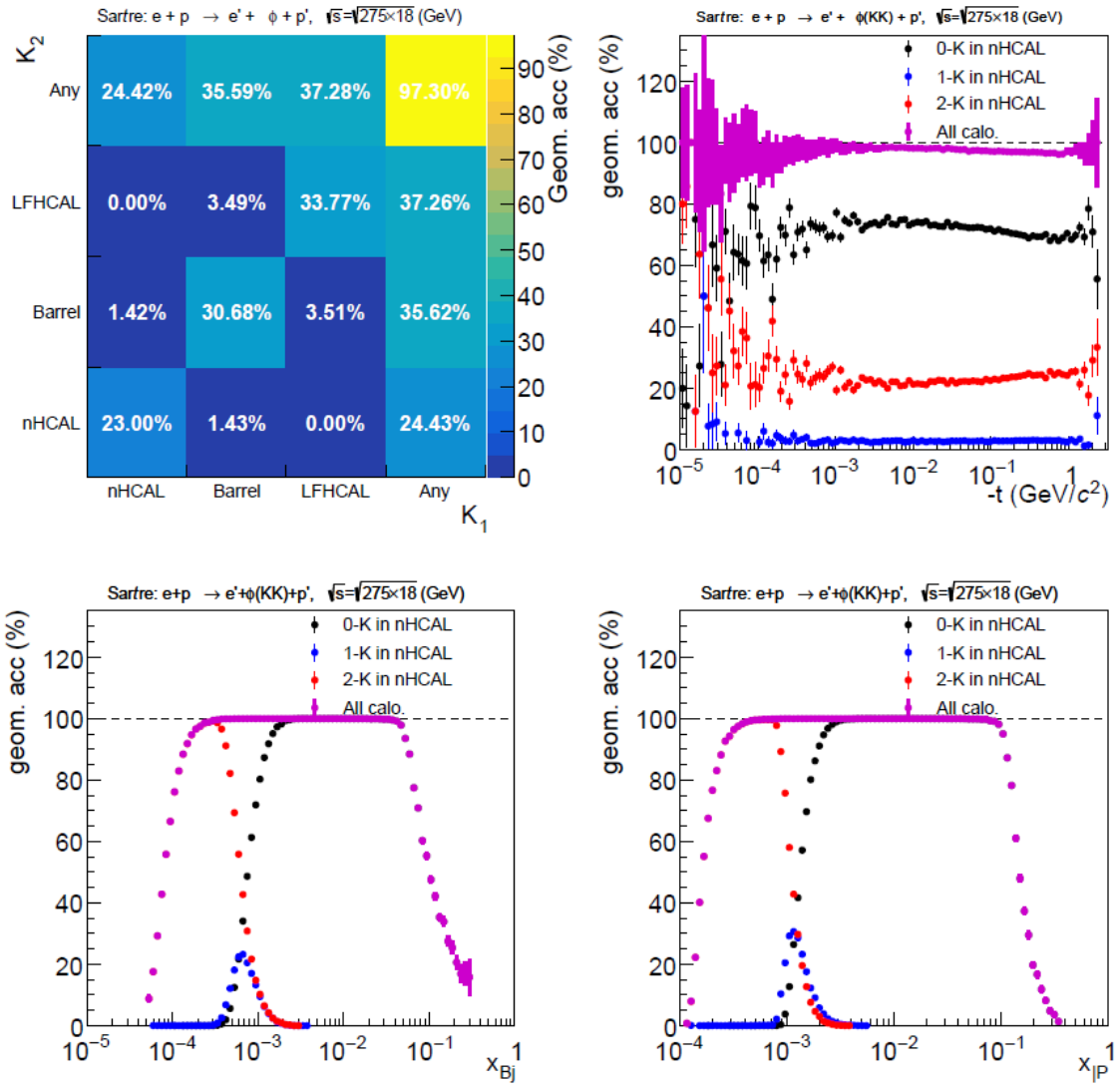

Figure 3.174: Acceptance of photoproduced $\Phi \to K^+K^-$ in $e+p$ collisions at $18+275$ GeV. **Top left:** Acceptance vs. K_1 and K_2 hitting different HCals. **Top Right:** Acceptance vs. $-t$ for different number of K in nHCal. **Bottom Left:** Acceptance vs. Bjorken x_{bj} for different number of K in nHCal. **Top Right:** Acceptance vs. Pomeron x_P for different number of K in nHCal. Repository: https://github.com/OSUNuclearPhysics/ePIC_preTDR_nHCal_VM_Sartre_kine

system) to the scintillator tiles. The system will enable the simulation of custom shower shapes, similar to the LFHCAL. The response will be studied and used to calibrate the SiPM gains by adjusting the bias voltage to compensate for variations in response, differences between SiPMs, and potential radiation damage to the SiPMs and tiles. This approach allows for system monitoring during operation.

Alignment will be performed during assembly. During operation, physics events and cosmic rays

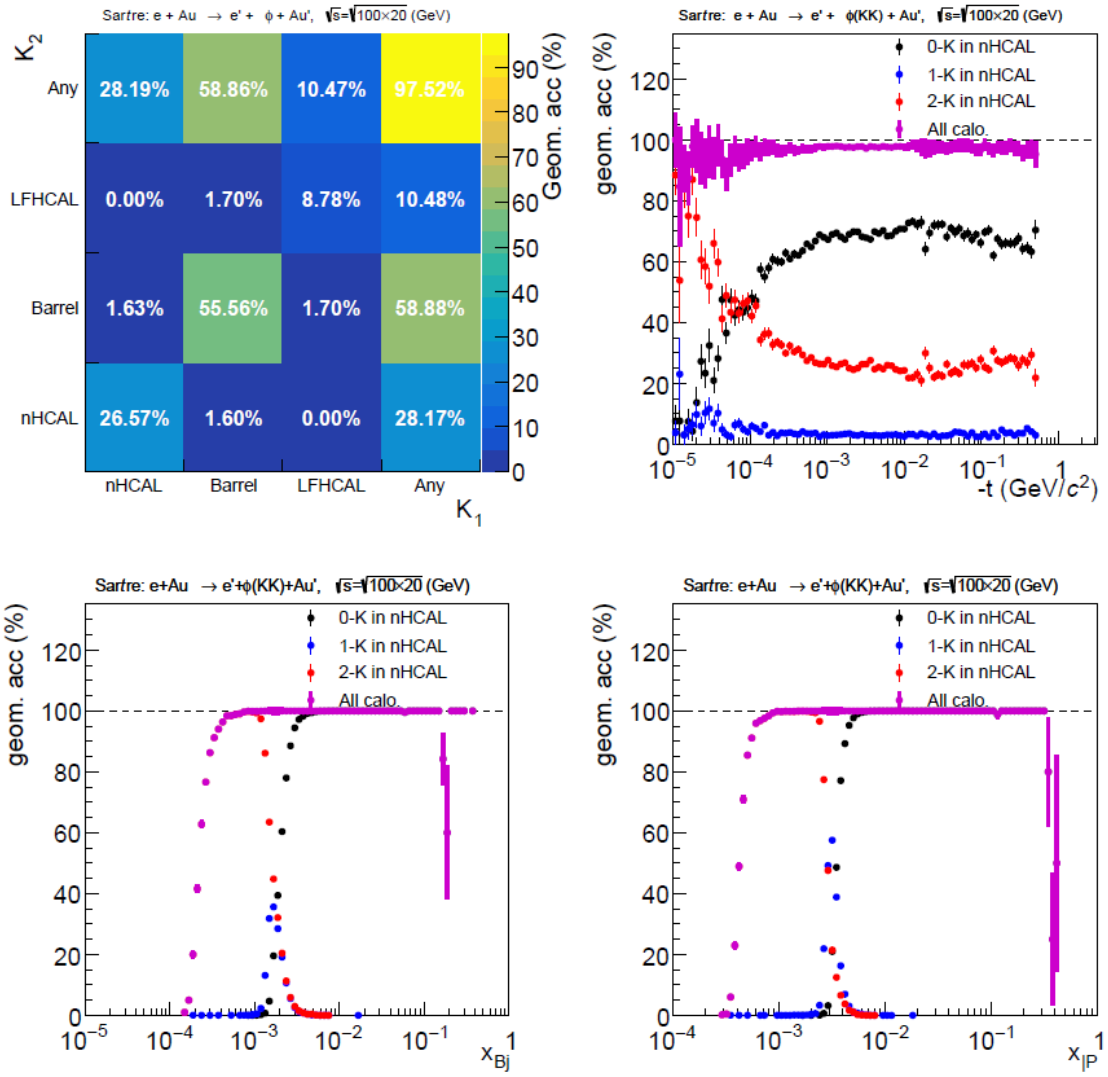

Figure 3.175: Acceptance of photoproduced $\Phi \to K^+K^-$ in $e+p$ collisions at $20+100$ GeV. **Top left:** Acceptance vs. μ_1 and μ_2 hitting different HCals. **Top Right:** Acceptance vs. $-t$ for different number of K in nHCal. **Bottom Left:** Acceptance vs. Bjorken x_{bj} for different number of K in nHCal. **Top Right:** Acceptance vs. Pomeron x_P for different number of K in nHCal. Repository: https://github.com/OSUNuclearPhysics/ePIC_preTDR_nHCal_VM_Sartre_kine

will be used to study the relative position of the calorimeter with respect to the trackers. We will follow standard alignment procedures used in many collider experiments.

Since SiPM gains are sensitive to temperature variations, a temperature monitoring system with thermocouples will be employed. These only need to be placed coarsely, as SiPMs generate very little heat. Additionally, the absorber steel, with its high thermal conductivity, will help distribute

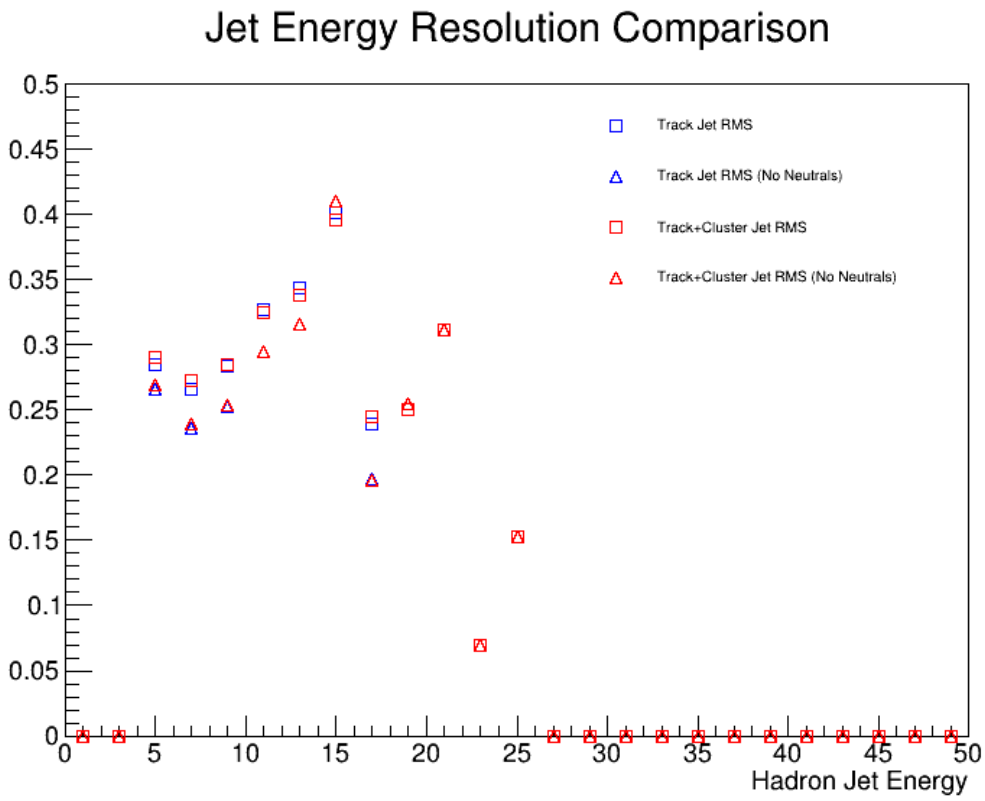

Figure 3.176: Energy resolution of jets vs. jet energy E compared for inclusive jets(squares) and jets with neutral veto(triangles). Track only jets(blue) are also compared to track and nHCal cluster jets(red). Repository: https://github.com/OSUNuclearPhysics/ePIC_preTDR_nHCal_neutralJetRes

heat over large volume.

Status and remaining design effort:

R&D effort: Finalize simulations and confirm optimal tile size.

E&D status and outlook: Design of support structures to follow the confirmed tile design.

Other activity needed for the design completion: Finalize simulations to confirm the tile size and design.

Status of maturity of the subsystem: Technologies and design are mature. Dependent on the outcome of performance simulations.

Environmental, Safety and Health (ES&H) aspects and Quality Assessment (QA planning): We will follow standard ES&H procedures observed at all participating institutions. Quality of the tile, fiber and SiPM interfaces as well as optical isolation will be tested after assembly of individual modules. This will be performed with the calibration system of the nHCal.

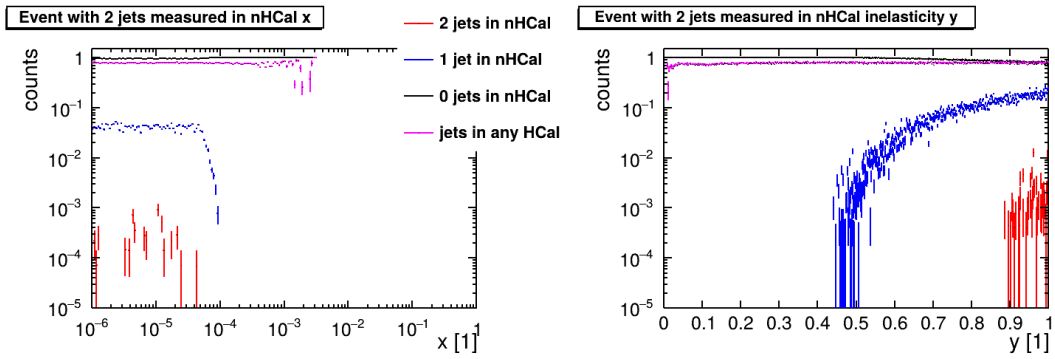

Figure 3.177: **Left:** Acceptance vs. x for 2, 1 and no diffractively produced jets with thrust axis in nHCal acceptance. **Right:** Acceptance vs. inelasticity y for 2, 1 and no diffractively produced jets with thrust axis in nHCal acceptance. Repository: https://github.com/OSUNuclearPhysics/ePIC_preTDR_nHCal_Diff2Jet_Pythia

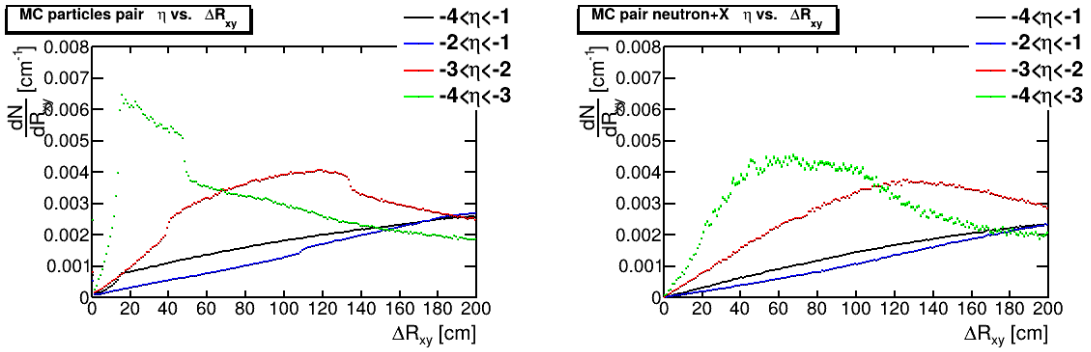

Figure 3.178: **Left:** Fraction of MC particle pairs per cm as a function of distance between straight line projections of particle pairs onto nHCal surface. **Right:** Fraction of MC particle pairs per cm as a function of distance between straight line projections of neutron paired with X(any particle) onto nHCal surface. Repository: https://github.com/OSUNuclearPhysics/ePIC_preTDR_nHCal_Diff2Jet_Reco

Construction and assembly planning: The 294 nHCal modules will each contain 2×10 scintillator tiles and 10 steel absorber plates. They will be produced using electron beam welding technique in a vacuum. The modules will be assembled in a similar way as it is described for LFHCAL.

The tiles will be wrapped in a highly reflective foil using a machine being developed for CMS collaboration or by hand with the help of students.

Collaborators and their role, resources and workforce: There are a few institutes participating in nHCal development and construction including The Ohio State University (OSU), Czech Technical University in Prague (CTU), University of Illinois Urbana-Champaign (UIUC). There is also help from Brookhaven National Laboratory (BNL) and Oak Ridge National Laboratory (ORNL). The organization structure of work is shown in the chart in the Fig. 3.183. The tasks la-

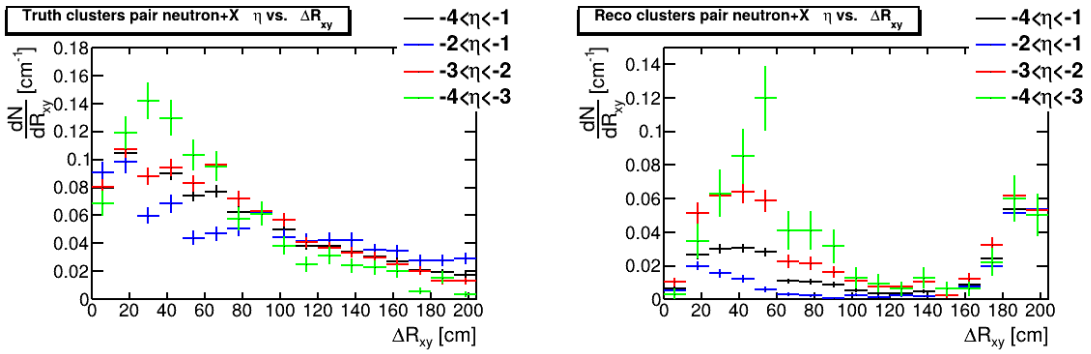

Figure 3.179: **Left:** Fraction of MC truth cluster pairs per cm as a function of distance between clusters created by neutron paired with X(any particle). **Right:** Fraction of reconstructed cluster pairs per cm as a function of distance between clusters created by neutron paired with X(any particle). Repository: https://github.com/OSUNuclearPhysics/ePIC_preTDR_nHCal_Diff2Jet_Reco

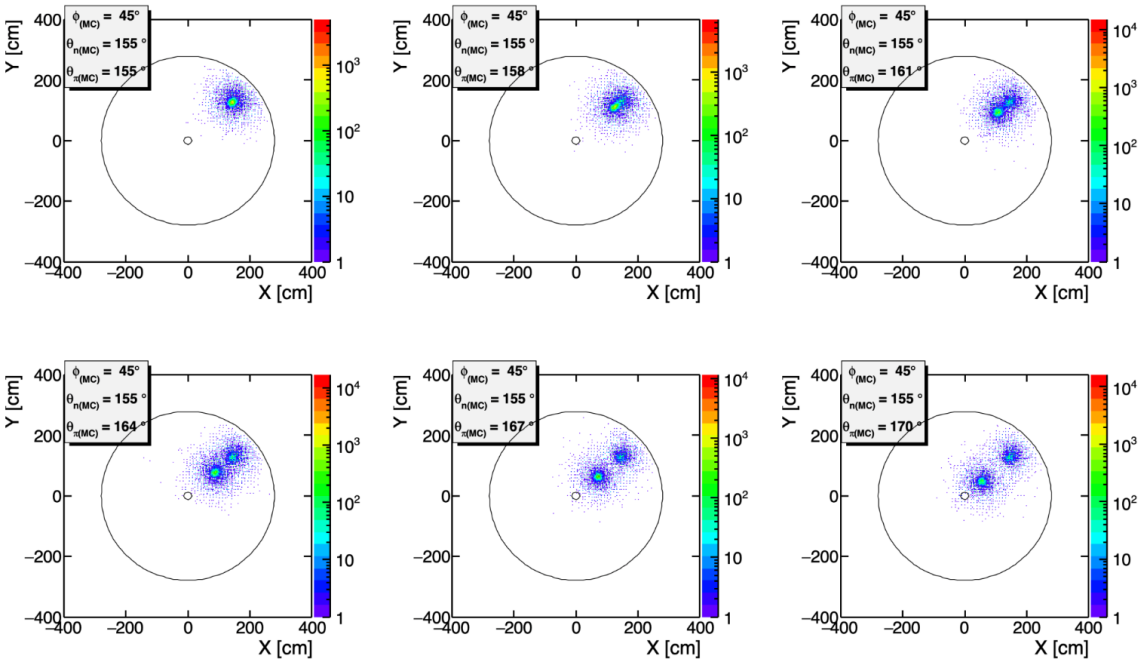

Figure 3.180: Position of the reconstructed clusters in x, y for 2-particle position resolution study. Repository: https://github.com/OSUNuclearPhysics/ePIC_preTDR_nHCal_PosRes

beled as TBD can be filled by additional institutions joining the effort or sharing work and expertise with other ePIC groups.

Risks and mitigation strategy: Each nHCal module needs to be tested before assembly to make sure that the LEDs, SiPMs and connectors work properly. Such work can be performed by

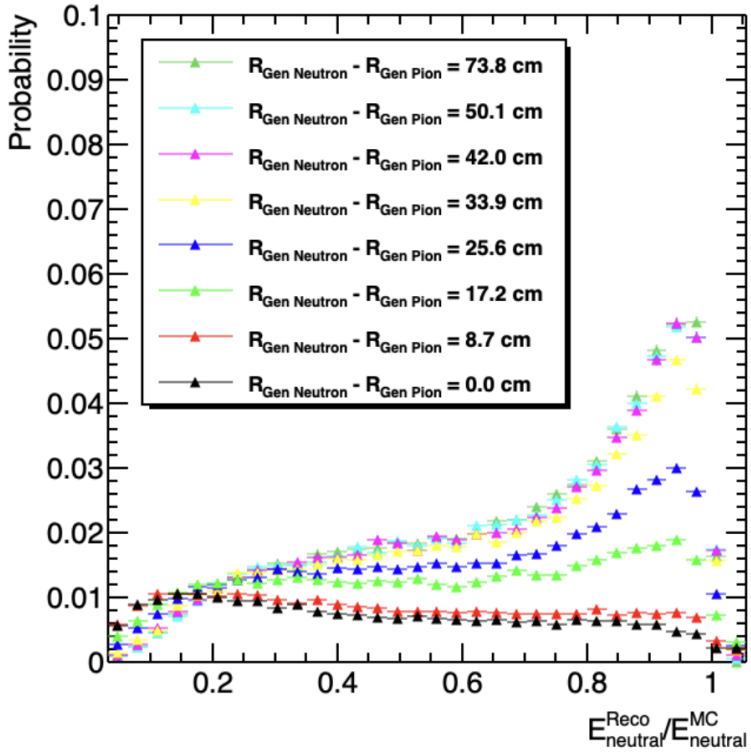

Figure 3.181: Ratio of reconstructed, charged hadron corrected cluster energy to the sum of neutron MC energy deposits for different values of the distance between neutron and pion impact points on the nHCal surface. Repository: https://github.com/OSUNuclearPhysics/ePIC_preTDR_nHCal_PosRes

experts with the help of students.

Additional Material Add text here.

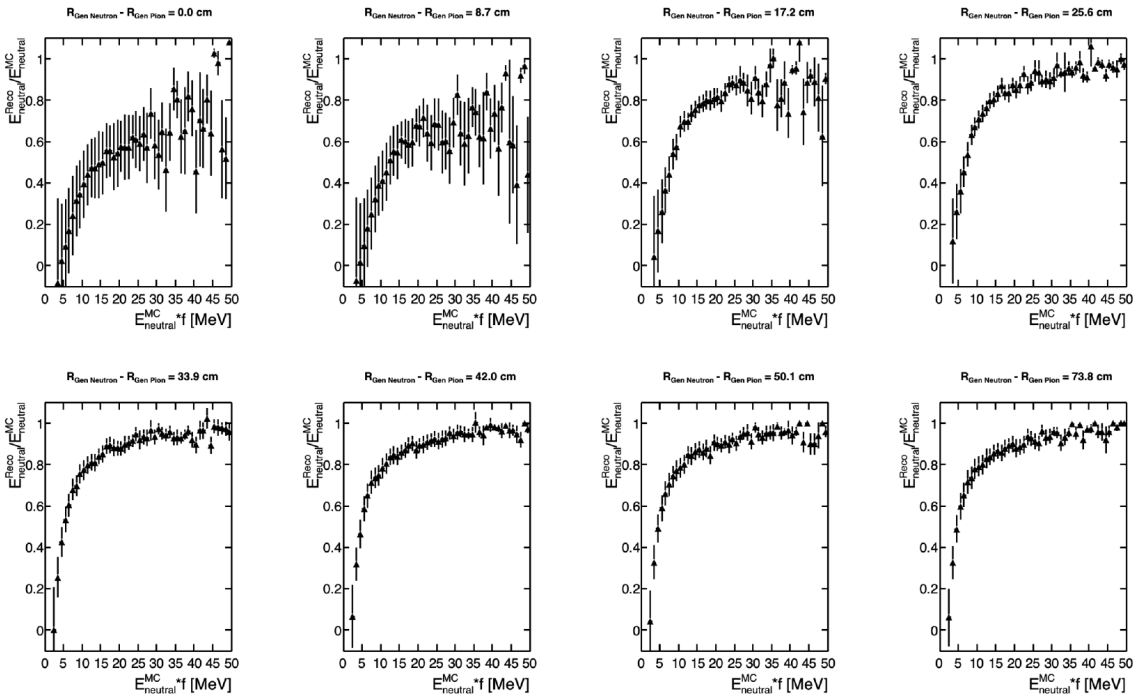

Figure 3.182: Ratio of reconstructed, charged hadron corrected cluster energy to the sum of neutron MC energy deposits vs. neutron MC energy deposits in scintillator tiles only. Comparison for different values of the distance between neutron and pion impact points on the nHCal surface. Repository: https://github.com/OSUNuclearPhysics/ePIC_preTDR_nHCal_PosRes

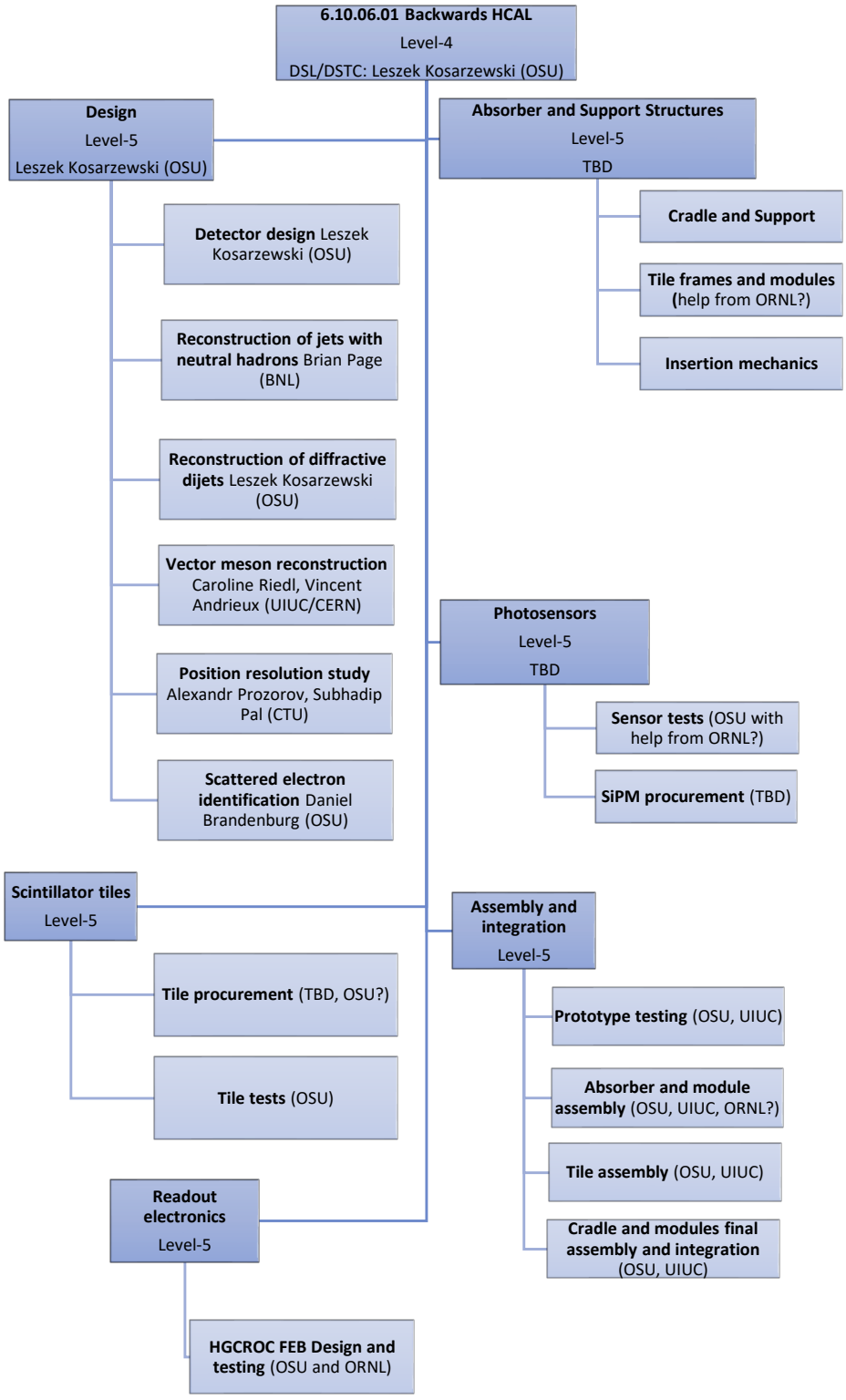

Figure 3.183: Work organization structure of nHCal project within ePIC.

3.3.6.2 The barrel hadronic calorimeter

Requirements The yellow report states the energy resolution of the mid-rapidity hadronic calorimeter should be $85\%/\sqrt{E/\mathrm{GeV}} + 7\%$, driven by single-jet measurements. Although approximately 90% of the jet energy will be measured using high-precision tracking and electromagnetic calorimetry, the hadronic calorimeter plays a critical role in measuring the neutral hadron component, which is otherwise inaccessible.

The importance of measuring this contribution at mid-rapidity is demonstrated in Figure 3.184, which shows the charged, neutral EM, and neutral hadronic momentum fractions of jets as a function of the pseudorapdity η in the lab frame. For $|\eta| < 1$, while sub-dominant, there is still a significant population of jets with a substantial neutral hadronic component.

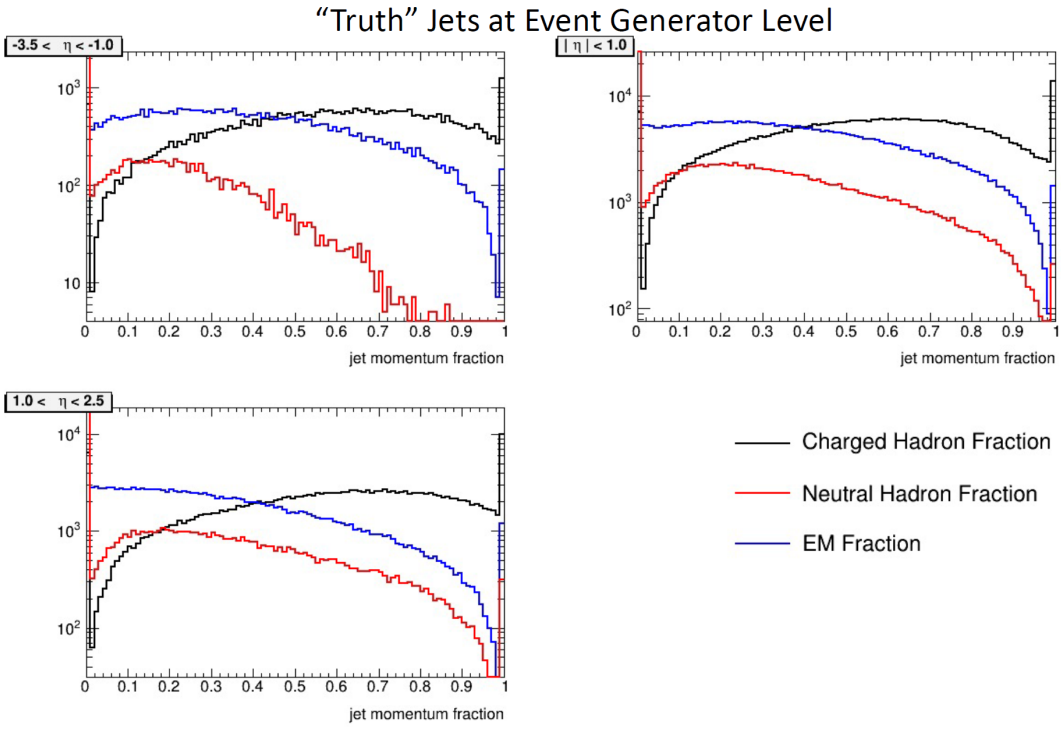

Figure 3.184: The charged (black lines), neutral EM (blue lines), and neutral hadron (red lines) fractions of jets at the truth level in $\eta \in (-3.5, 1.0)$ (upper left panel), $|\eta| < 1$ (upper right panel), and $\eta \in (1.0, 3.5)$ (lower left panel). Received from John Lajoie in private communication.

Requirements from Radiation Hardness: Compared to LHC detectors, the various subsystems of the ePIC detector have moderate radiation hardness requirements. The Yellow Report states that at the calorimeters, the radiation level will be up to ≈ 3 krad/year electromagnetic and $10^{11} n/\mathrm{cm}^2$ hadronic at top luminosity. At the BHCal, the radiation level will be orders of magnitude lower than, *e.g.*, at the fHCal. Figure 3.185 shows the results of ePIC simulations in the BHCal

region: the 1-MeV neutron equivalent (MEQ) fluence from all processes (DIS plus beam gas events) over 15 years of running (150fb^{-1}). The fluence drops as a function of radius until it plateaus at 240 cm, before the BHCal outer radius of 263.5 cm where the SiPMs are located. That means the fluence at the SiPMs will be between 5-7 $\times 10^8$cm^{-2}.
In comparison, sPHENIX expects $\sim$ 7×10^{10}cm^{-2} at its SiPMs over its operational lifetime. sPHENIX experience has shown that while increased leakage current from neutron damage does reduce the ability to observe single photo-electron peaks, it does not significantly impact the calorimeter's signal performance. Therefore, better behavior is expected for the BHCal in ePIC.

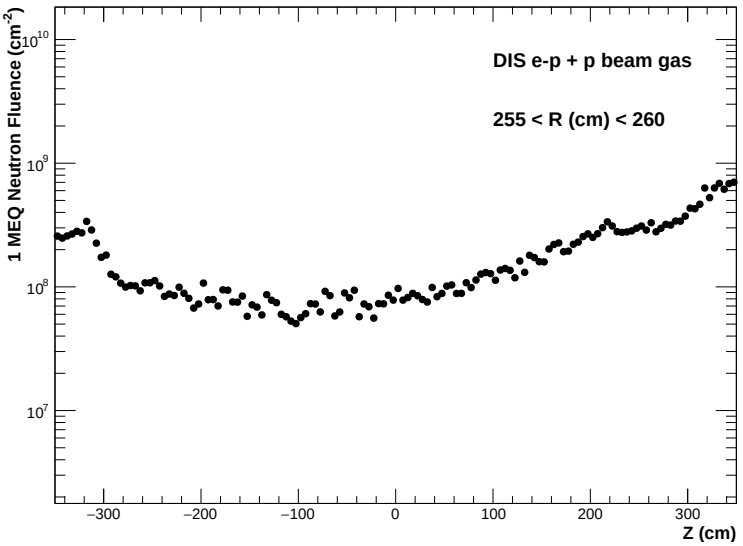

Figure 3.185: Results of ePIC simulations in the BHCal region: the 1-MeV neutron equivalent (MEQ) fluence from all processes (DIS plus beam gas events) over 15 years of running (150fb^{-1}).

The on-detector electronics (SiPMs, CALOROC) are radiation tolerant. While the read-out boards (RDOs) contain FPGAs and therefore are radiation sensitive, they will sit well outside the detector, and therefore there is no concern for single-event upsets (SEUs). Since the CALOROCs are used for the other calorimeter systems as well, there is no concern for the BHCal.

Justification

Device concept and technological choice: The sPHENIX outer HCal, which was demonstrated to have a single particle energy resolution of $75\%/\sqrt{E} \oplus 14.5\%$, will be repurposed for the EIC. It satisfies the requirements described in the previous section.

The absorber material for the central hadronic calorimeter will also serve as the flux return for the solenoid magnet.

Subsystem description:

General device description: The sPHENIX Outer HCal will be used as the basis of the ePIC Barrel HCal. The sPHENIX OHCal design was developed and optimized through a series of simulation and prototype studies. The sPHENIX hadronic calorimeter system consists of two longitudinal compartments of calorimeter, one inside the solenoid, filling the gap between the magnet and the electromagnetic calorimeter, and one outside the solenoid. In the ePIC design the electromagnetic calorimeter will fill the space before the magnet. Therefore only the sPHENIX Outer HCal will be adopted in ePIC.

The basic calorimeter concept is a sampling calorimeter with tapered absorber plates tilted from the radial direction to provide more uniform sampling in azimuth. Extruded tiles of plastic scintillator with an embedded wavelength shifting fiber are interspersed between the absorber plates and read out at the outer radius with silicon photomultipliers. The tilt angle is chosen so that a radial track from the center of the interaction region traverses at least four scintillator tiles as shown in Figure 3.186.

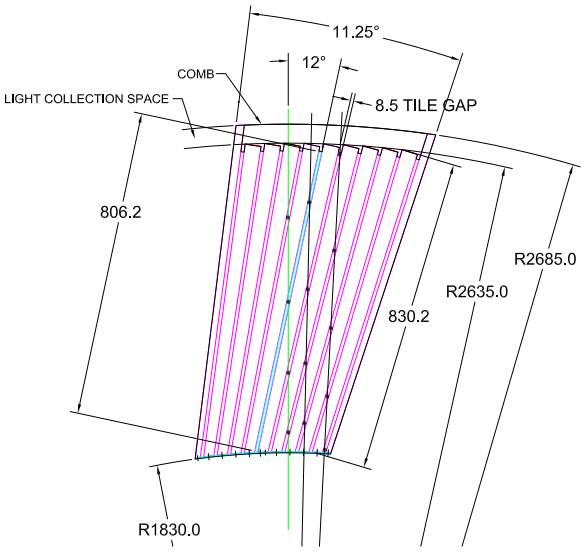

Figure 3.186: Transverse cutaway view of an sPHENIX Outer HCal module, showing the tilted tapered absorber plates. Light collection and cabling is on the outer radius at the top of the drawing.

Each tile has a single SiPM. In the sPHENIX design, the analog signal from five SiPMs are combined at a single preamplifier channel to form a calorimeter tower. In ePIC, each SiPM will be read out individually. Twelve tiles span 1.1 units of pseudorapidity in each direction as shown in Figure 3.187. Therefore the overall segmentation is $\Delta\eta \times \Delta\phi \sim 0.1 \times 0.02$.

Scintillator description:

The properties of the HCAL scintillating tiles are listed in Table 3.66. There are 12 different shaped tiles which span half of the η range of the detector. The detector is mirror-symmetric in η except in the region where the chimney for the cooling of the magnet reduces the depth of the HCal.

A wavelength shifting (WLS) fiber is embedded in the tile to direct the light to the SiPM. The Kuraray single clad fiber was selected due to its flexibility and longevity which are critical for the multiple fiber bends in the design. The routing of the fiber was carefully designed to maximize the uniformity of light collection across the various tile shapes and avoid light leaks in the bends. The properties of the HCAL wavelength shifting fibers are listed in Table 3.67.

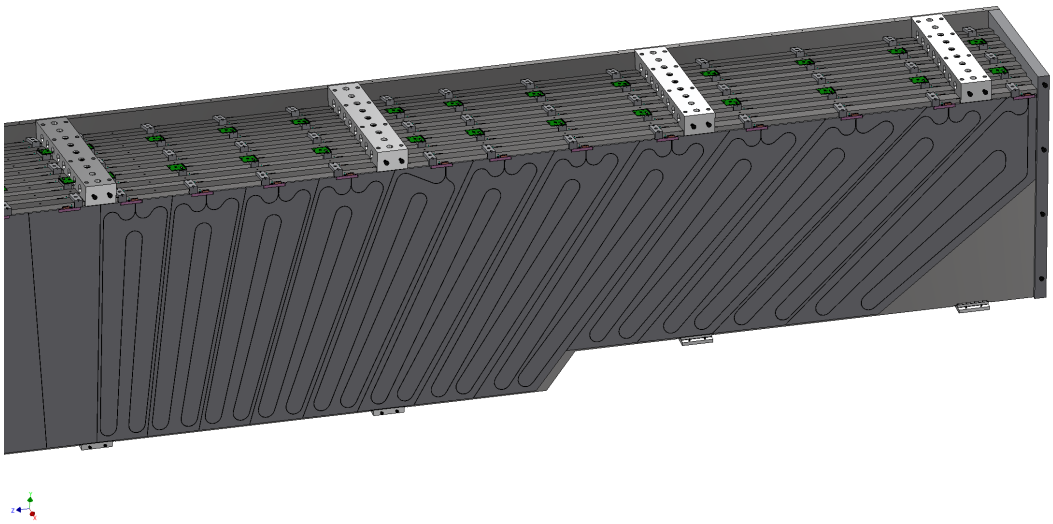

Figure 3.187: Scintillator tiles in a layer of the Outer HCal.

Component	Description
Plastic	Extruded polystyrene
Scintillation dopant	1.5% PTP and 0.01% POPOP
Reflective coating	Proprietary coating by surface exposure to aromatic solvents
Reflective layer thickness	50μ
Wrapping	one layer of 100 μ Al foil, one layer of 30 μ cling-wrap, one 100 μ layer of black Tyvek
Attenuation length in lateral (with respect to extrusion) direction	$\sim$2-2.5 m
Wavelength shifting fiber	Single clad Kuraray Y11
Fiber size	1 mm round
Fiber core attenuation length	$>$ 2 m
Optical cement	EPO-TEK 3015

Table 3.66: Properties of HCal scintillating tiles.

The fiber routing was designed so that any energy deposited in the scintillator is within 2.5 cm of a WLS fiber to minimize the pathlength of the light through the tile to the fiber and maintain uniformity in the response of energy depositions throughout the tile and across various tile shapes. In addition, the bend radius of any turn in the fiber has been limited to 35 mm. These parameters on the fiber routing where based on T2K and the sPHENIX R&D experience with test tiles. Since there are 12 different tile shapes, the routing for each tile shape was uniquely designed to satisfy these conditions.

The two ends of a fiber are brought to the outer radius of a tile where a small plastic holder

Property	Description
Fiber diameter	1.0 mm
Formulation	200, K-27, S-Type
Cladding	single
Cladding thickness	2 percent of d (0.02 mm)
Numerical Aperture (NA)	0.55
Emission angle	33.7 deg
Trapping Efficiency	3.1 percent
Core material	polystyrene (PS)
Core density	1.05 g/cc
Core refractive index	1.59
Cladding material	Polymethylmethacrylate (PMMA)
Cladding density	1.19 g/cc
Cladding refractive index	1.49
Color	green
Emission peak	476 nm
Absorption Peak	430 nm
Attenuation length	$>$ 3.5 m
Minimum bending radius	100 mm

Table 3.67: Properties of Kuraray Y-11 (200) wavelength shifting fibers.

carries a 3 mm $\times$ 3 mm SiPM at 0.75 mm from the end of the polished fibers.

Table 3.68 summarizes the major design parameters of the HCAL, which is illustrated in Figure 3.186.

The Outer HCAL SiPM sensors and electronics are to be arranged on the outer circumference of the detector which reduces the radiation exposure of the SiPMs.

Sensors: The SiPMs used in sPHENIX will be replaced with newer S14160-3015PS Hamamatsu SiPMs. The SiPMs are still 3 mm $\times$ 3 mm and will be attached to a board that will fit in the same plastic connectors used in sPHENIX to mount the SiPM to the tile. Each SiPM will be read out individually via the CALOROC. The electronics developed for the BHCal is similar to other calorimeters and are described in a separate section.

LED system: An LED system injects light into each tile. This allows for testing the entire functionality of the detector and read-out chain starting all the way from the SiPMs. The LED system can also be used to track time dependent changes of the SiPM gain. We will re-use the existing (from sPHENIX) fiber distribution system, which is comprised of five bundles of 25 fibers each (24 tiles per fiber bundle plus one spare) for each half sector. (The separation in five bundles, each driven by an individual LED, was necessary in sPHENIX to test each individual SiPM due to the read-out of towers consisting of five tiles. In EPIC, this is not necessary since each tile is read out individually. But the separation into five bundles does not constitute any disadvantage (except that five LEDs are needed instead of a single one) and allows for the re-use of the already installed fiber system. The polished fibers end in a ferrule plugged and held in place in the light blocker glued to the tile. A hole in the light blocker allows for the LED light to hit the diffusely coated surface of the tile. The CALOROC allows for LEDs to be pulsed at a defined rate. An LED board will be designed that will be driven by the CALOROC. One LED board per half sector will have five LEDs each in cans into which the fiber bundles plug in.

Parameter	Units	Value
Inner radius (envelope)	mm	1820
Outer radius (envelope)	mm	2700
Length (envelope)	mm	6316
Material		1020 low carbon steel
Number of tiles in azimuth ($\Delta\phi$)		320
Number of tiles in pseudorapidity ($\Delta\eta$)		24
Number of electronic channels		$320 \times 24 = 7680$
Number of modules (azimuthal slices)		32
Total number of absorber plates		$5 \times 64 = 320$
Tilt angle (relative to radius)	$^\circ$	12
Absorber plate thickness at inner radius	mm	10.2
Absorber plate thickness at outer radius	mm	14.7
Gap thickness	mm	8.5
Scintillator thickness	mm	7
Module weight	kg	12247
Sampling fraction at inner radius		0.037
Sampling fraction at outer radius		0.028
Calorimeter depth	λ	3.8

Table 3.68: Design parameters for the Barrel Hadronic Calorimeter w/o additional absorber, based on the sPHENIX Outer Hadronic Calorimeter.

Performance The performance of the BHCal for ePIC has been studied in simulation as well as tested through the experience of the HCals in sPHENIX. The sPHENIX HCal system has performed very well in Au+Au and p+p collisions. A key consideration when using SiPM sensors is their susceptibility to radiation damage in high-energy collisions. Radiation exposure can lead to increased leakage currents and elevated noise levels. However, measurements from the sPHENIX running indicate that leakage currents remain well below critical thresholds, even when extrapolated over time, as shown in Figure 3.188. This is attributed to the significant amount of material positioned in front of the SiPMs, which provides effective shielding and reduces radiation exposure.

Physics performance: As mentioned above, the yellow report requirements on the BHCal are driven primarily by single jet measurements. However, the BHCal will provide significant additional capabilities in terms of performance. These capabilities include:

- Identification of muons,
- Reconstruction of neutral hadrons such as neutrons,
- Constraining the jet energy scale and resolution by precise measurement of the jet neutral component,
- Reconstruction of event kinematics and the hadronic final state,
- And tagging of charged-current DIS events.

One way the BHCal can aid in muon identification is by the identification of MIPs as muons will

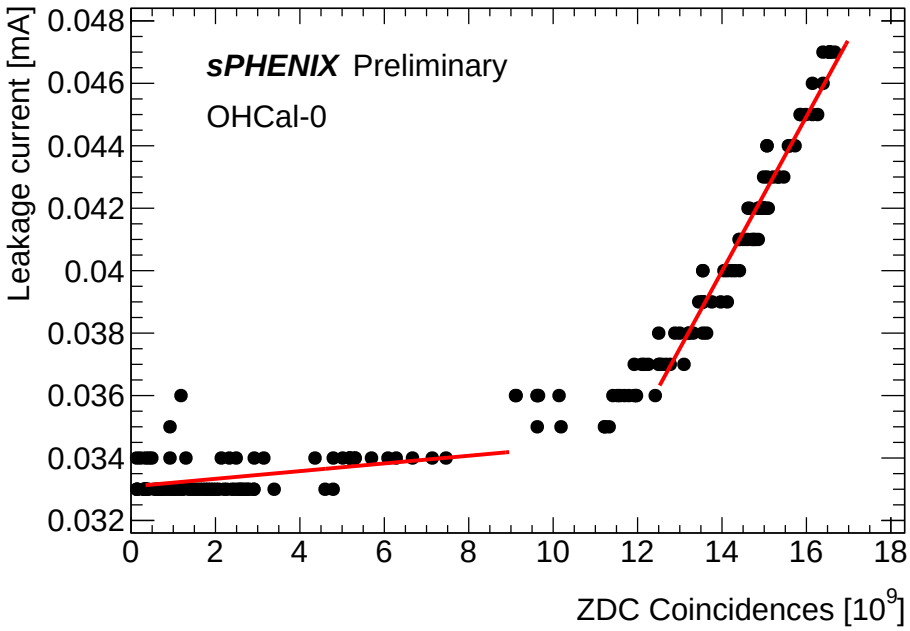

Figure 3.188: Leakage current in HCal measured once per fill as a function of total number of ZDC coincidence hits

typically MIP through both an EMCal and an HCal. Being able to reliably measure this signal is one motivation for reading out individual tiles rather than groups of tiles.

To assess the performance of the BHCal in this category, single $\mu^{\pm}$ with energies between 2 - 20 GeV were thrown with $|\eta| < 1$. Figure 3.189 illustrates the energy deposited on a given scintillator tile (i.e. the sum of G4 hits for a tile) and their reconstructed energies. A clear peak at 250 MeV can be observed in the reconstructed tile energies, well above the minimum energy anticipated to be measured by the BHCal.

To contrast this, the same quantities are shown in Figure 3.190 for all particles in NC DIS events for beam energies of 10×100 and 18×275. As one would expect, this sample is dominated by particles which do not MIP through both calorimeters, and the clear MIP peak in the reconstructed tile energies is washed out. This figure also demonstrates the typical reconstructed energies on a tile-by-tile basis.

To measure hadron energies, clusters are formed from individual tiles. Figure 3.191 shows the reconstructed energy of the leading (highest energy) cluster in single $\pi^{\pm}$ simulations of only the BHCal. Note that these energies are shown at the EM scale, i.e. are corrected for the sampling fraction. The pions were simulated with energies between 2 - 20 GeV, and clear gaussian peaks are observed for each pion energy. The solid lines in the figure are Gaussian fits to the main peak of the energy spectra. This demonstrates that the simulation of the BHCal produces reasonable hadronic energy spectra.

However, the reconstructed energy of a hadron in an HCal will be significantly smeared by energy loss in dead material and due to nuclear binding, fluctuations in the hadronic shower, and clustering inefficiencies. These effects can already be seen in the BHCal-only simulation of Figure 3.191.

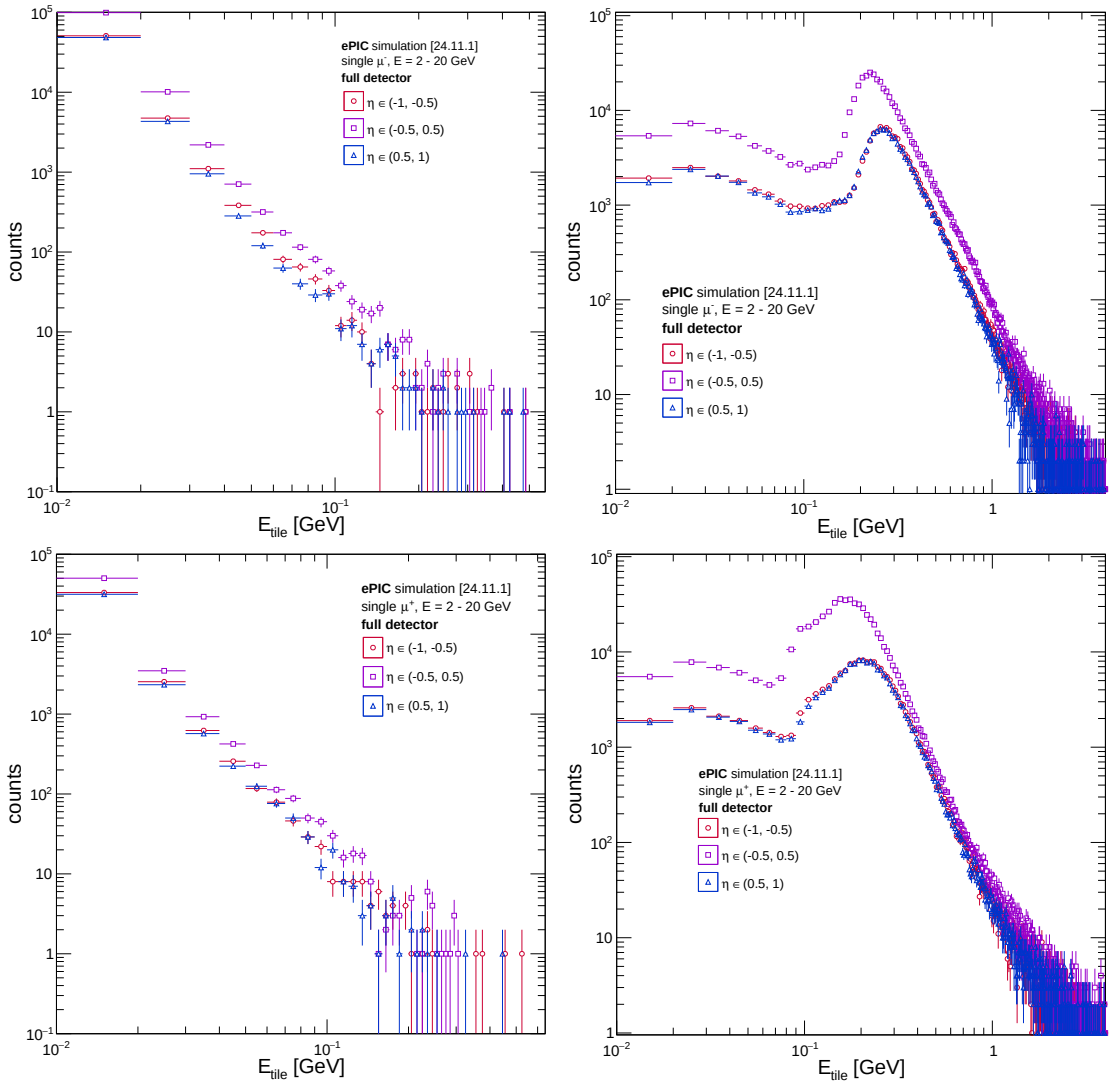

Figure 3.189: Energy deposited on BHCal tiles (left panels) and reconstructed tile energies (right panels) by single μ^- (top row) and μ^+ (bottom row) as a function of tile pseudorapidity. Muons were simulated using the 2024.11.1 simulation geometry with energies between 2 and 20 GeV. Repository: https://github.com/ruse-traveler/EpicBHCalPTDRStudies

These effects will be exacerbated when the full detector is present. This can be seen in the upper row of Figure 3.192, where the Gaussian peaks of the BHCal-only single $\pi^{\pm}$ simulations are washed out. Thus, hadron energies measured with the BHCal will need to be further calibrated from the EM scale to the hadronic scale utilizing information from additional subsystems. This calibration is carried out using two simple machine-learning models, a Linear-Discriminant (LD) and a Multi-Layer Perceptron (MLP), implemented in the ROOT TMVA package [106]. In both cases, the models are trained to perform a regression on the simulated particle energy using the leading BHCal and BIC (ScFi + imaging) cluster energy, and the sum of energy in the 6 imaging (AstroPix) and 12 ScFi layers of the BIC.

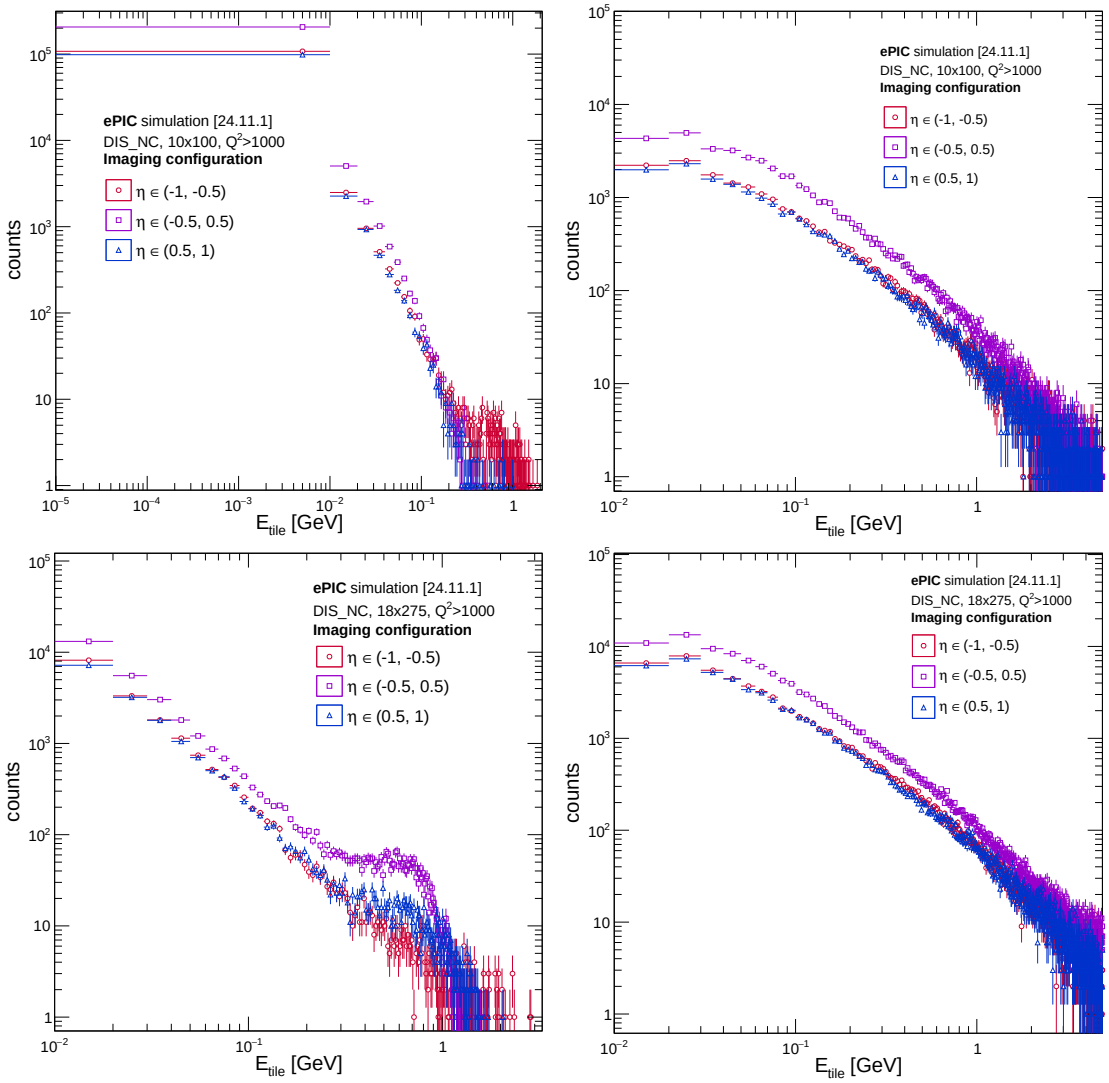

Figure 3.190: Energy deposited on BHCal tiles (left panels) and reconstructed tile energies (right panels) by all particles in 10×100 (top row) and 18×275 (bottom row) NC DIS events as a function of particle pseudorapidity. Distributions were simulated using the 2024.11.1 simulation geometry with $Q^2 > 1000$ GeV^2. Repository: https://github.com/ruse-traveler/EpicBHCalPTDRStudies

The single $\pi^{\pm}$ energies calibrated by the LD model and the MLP model can be seen in the middle and bottom rows of Figure 3.192, respectively. The Gaussian shape of the energy spectra is clearly recovered by the models, except for the MLP-calibrated 20 GeV π^- which displays some pathologies.

Figure 3.193 shows the linearity and energy resolution of the calibrated $\pi^{\pm}$. Also shown in Figure 3.193 is what the linearity and resolution would be if one simply summed all of the clusters in the BHCal. This illustrates the impact of the calibration and that the BHCal meets the yellow report requirement for energy resolution.

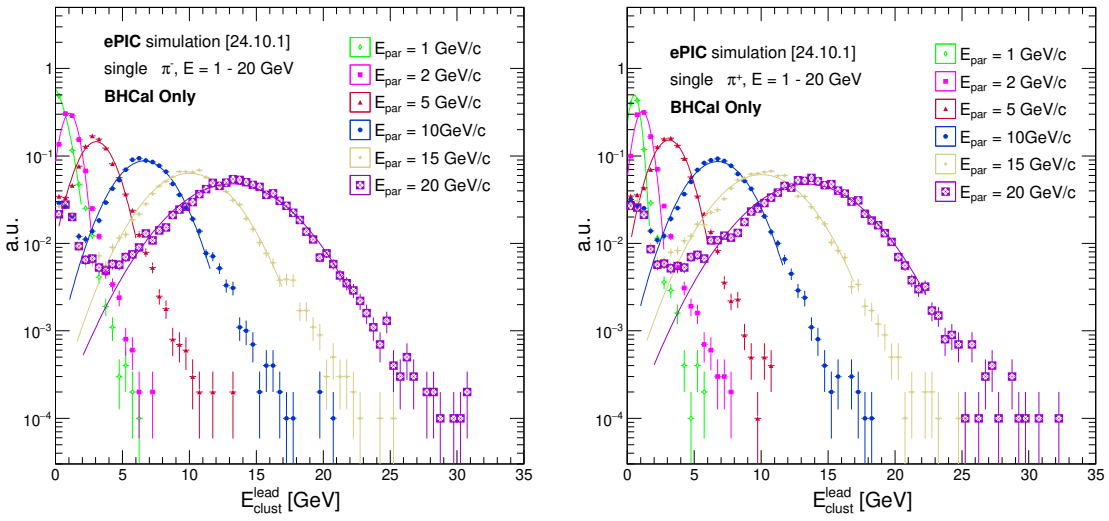

Figure 3.191: Reconstructed energy of leading BHCal cluster for 1 (green) - 20 GeV (purple) single π^- (left) and π^+ (right) in BHCal-only simulations. Pions were simulated using the 2024.10.1 simulation geometry. Solid lines are Guassian fits. Repository: https://github.com/ruse-traveler/EpicBHCalPTDRStudies

To gauge the performance of the BHCal in reconstructing neutral hadrons, the calibration procedure was repeated for single neutrons. Figure 3.194 shows the uncalibrated and calibrated neutron energies, and Figure 3.195 shows the linearity and resolution of the calibrated neutron energies. Note that even after calibration, there are distinct low-energy tails in the energy spectra. These could be due to cluster splitting, fluctuations in the hadronic shower, or inadequacies in the model. Efforts to understand and improve these tails are ongoing. Toward understanding the role of cluster splitting, Figure 3.196 shows the ratio of uncalibrated lead BHCal clusters to the sum of all BHCal clusters for single neutrons.

As discussed, the BHCal provides an additional handle of the neutral hadronic component of jets, and thus aids in constraining the jet energy scale (JES) and jet energy resolution (JER). This is illustrated in Figure 3.197. Furthermore, measurement of neutral hadrons will be crucial for precise measurements of the hadronic final state and of event kinematics, particularly in CC DIS. Figure 3.198 shows the DIS kinematic variables x, y, and Q^2 reconstructed using the Jacquet-Blondel method at the truth and reconstructed level for two different acceptances, $|\eta| < 3.5$ and $|\eta| < 4$. Lastly, Figure 3.199 shows the truth versus the missing reconstructed E_{T}, $E_{\mathrm{T}}^{\mathrm{miss}}$, a quantity that is relevant for event characterization. This observable could be particularly useful for tagging charged current deep inelastic scattering (CC DIS) events.

Implementation

Subsystem mechanics and integration: The BHCal is the outermost central detector and will need to be installed first. The steel serves as the flux return for the solenoid magnet.

Calibration, alignment and monitoring: The sPHENIX HCal was calibrated to the electromagnetic scale using cosmic ray muons by matching the the ADC distribtution in data to the energy deposition in a realistic simulation. To account for imperfections in the simulation from not including material outside the main sPHENIX detector, a tower slope method in collision data was used to symmetrize the response in ϕ η bin by η bin. Further, gain variations with time due to changing ambient temperature was corrected for by measuring the temperature as a function of time can applying the corresponding temperature dependent correction. Alternatively, the LED system can be used to correct for the time dependence of the gain. Currently, the calibration to the hadronic scale relies on HIJING simulations propagated through Geant, with reweighting of the HIJING particle spectra based on experimental measurements. In the future, the hadronic scale calibration will be further improved by photon (or high fragmentation z hadron)-jet balancing and studying the calorimeter response to isolated hadrons measured with the sPHENIX tracking system. In ePIC we plan to pursue a similar calibration strategy.

Status and remaining design effort:

R&D effort: The basic design is set by reusing the sPHENIX outer HCal. However, the electronics and details of the LED system are still being developed. There are plans to utilize the sPHENIX prototype, which was used to demonstrate the energy resolution from beam tests, to test the readout of individual tiles instead of tiles. Related simulation studies are also underway. Additional tests include measuring the potential noise for longer cables to transmit the signal from the SiPM to HGCROCs located at the end of the sector.

Environmental, Safety and Health (ES&H) aspects and Quality Assessment (QA planning:

Construction and assembly planning: Once RHIC operations conclude, the sPHENIX detector will be disassembled. During this process, each outer HCal sector will be removed from sPHENIX, and the SiPMs for each tile within the sector will be replaced with ePIC SiPMs. Following installation, the cables will be connected and integrated with a dedicated electronics test setup to verify that each tile can be read properly. To ensure accurate calibration, cosmic-ray tests will be performed on each sector. These tests will confirm the relative calibration factors on a tile-by-tile basis.

Currently, three test stands are being constructed at BNL, Georgia State University (GSU) and the University of New Hampshire (UNH). These facilities will be used to train students in the assembly and testing procedures. Following the disassembly of sPHENIX, the students will travel to BNL to perform these tests. The assembly process at BNL will be overseen by Stefan Bathe from Baruch College. Dr. Bathe previously served as the Level 3 Manager for the sPHENIX HCals and was responsible for the assembly of both the inner and outer HCals for sPHENIX.

Collaborators and their role, resources and workforce: There are several collaborating institutions working on the BHCal. The co-DSLs are Prof. Stefan Bathe and Prof. Murad Sarsour. Stefan Bathe is the PI of the Baruch College, CUNY, group. One postdoc in that group, Dr.Ànjaly Menon, works on testing the read out and setting up the prototype for test beam. Stefan Bathe has extensive experience with the sPHENIX HCal as former Lvl3 manager for the assembly and testing of the HCal in the sPHENIX project, Operations Manager for the sPHENIX HCal, and co-convenor

of the calorimeter calibrations group in sPHENIX. Murad Sarsour is co-PI at Georgia State University. GSU is a large group (with co-PIs Megan Connors and Xiaochun He) and several postdocs and graduate students. GSU was responsible for the tile testing in sPHENIX. Brookhaven National Lab is involved, mainly with Dr. Eric Mannel (former Lvl2 manager for the calorimeter electronics in sPHENIX) and Dr. Martin Purschke (data acquisition and calorimeter expert). The BNL group has extensive experience with the HCal, in particular with multiple test beam campaigns for sPHENIX. Groups not previously involved in sPHENIX are the University of New Hampshire with PI Prof. Nathaly Santiesteban, postoc Dr. David Ruth, and a graduate student. UNH is now leading the simulations effort (previously led by Dr. Derek Anderson (then ISU), who has recently moved on to a new position) David Ruth will join the University of New Mexico and start a new HCal group there, focusing on the design of the LED system and simulations. Oak Ridge National Lab is developing the electronics and collaborating on testing the electronics with the HCal prototype. The electronics development is led by Dr. Norbert Novitzky.

Risks and mitigation strategy: The BHCal depends on previously tested technologies which minimizes the risks associated with it. A limited number of spare tiles were stored at GSU; however, these tiles are currently being used in the HCal prototype that is being prepared for beam test. Therefore, it is essential to procure additional tiles to ensure replacements are available in case any tiles are damaged during the HCal refurbishment process. We anticipate needing 20 tiles of each shape, for a total of 240 tiles. There are two ways we can monitor the tiles once they are installed into EPIC. The LED system is useful for quickly testing the tiles on a regular basis while the cosmic ray studies require a long time to collect sufficient data.

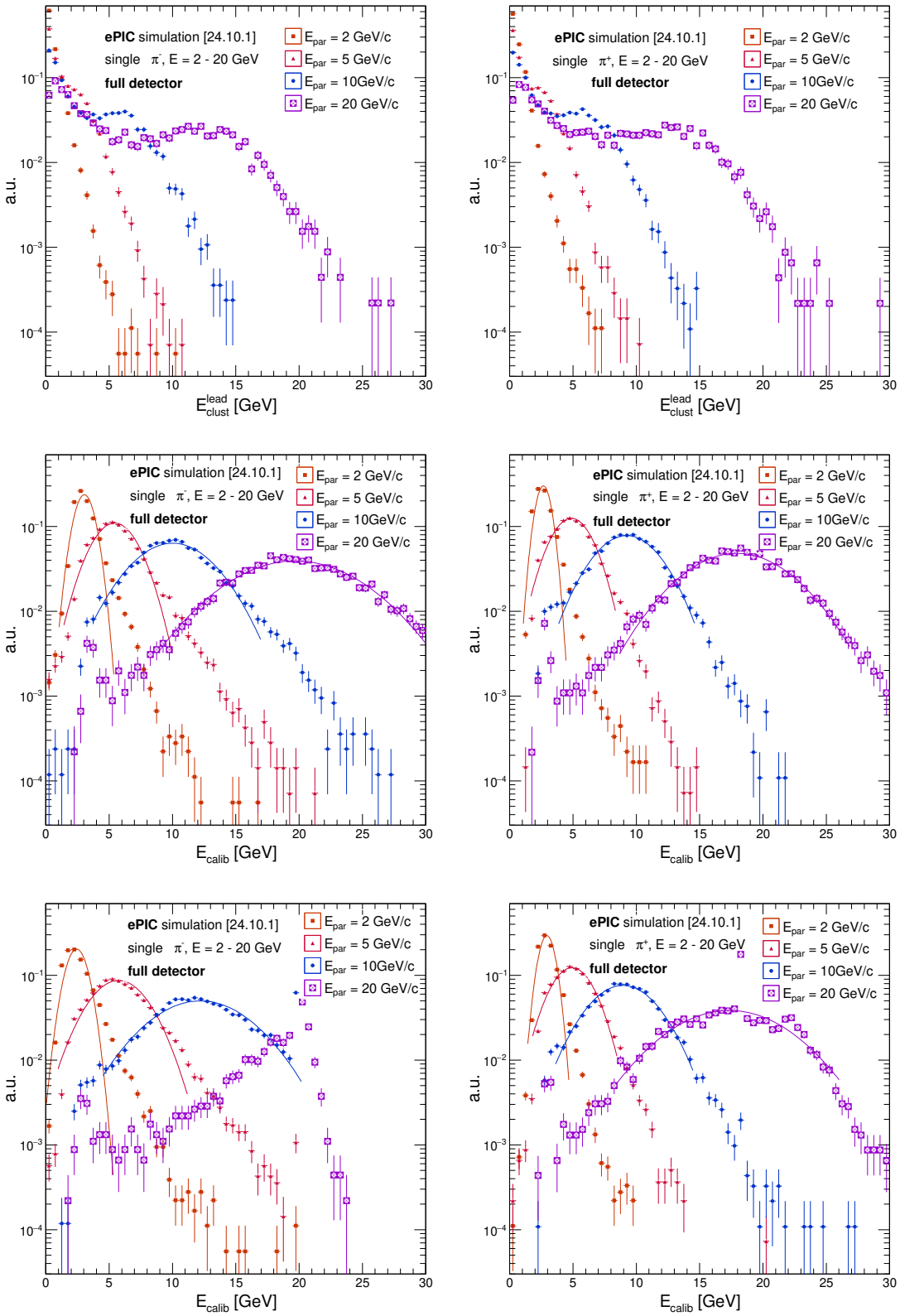

Figure 3.192: Uncalibrated (top row) vs. LD-calibrated energy (middle row) and MLP-calibrated (bottom row) of lead BHCal clusters for 2 (orange), 5 (pink), 10 (blue), and 20 GeV (purple) π^- (left column) and π^+ (right column). Distributions were simulated using the 2024.10.1 simulation geometry. Repository: https://github.com/ruse-traveler/EpicBHCalPTDRStudies

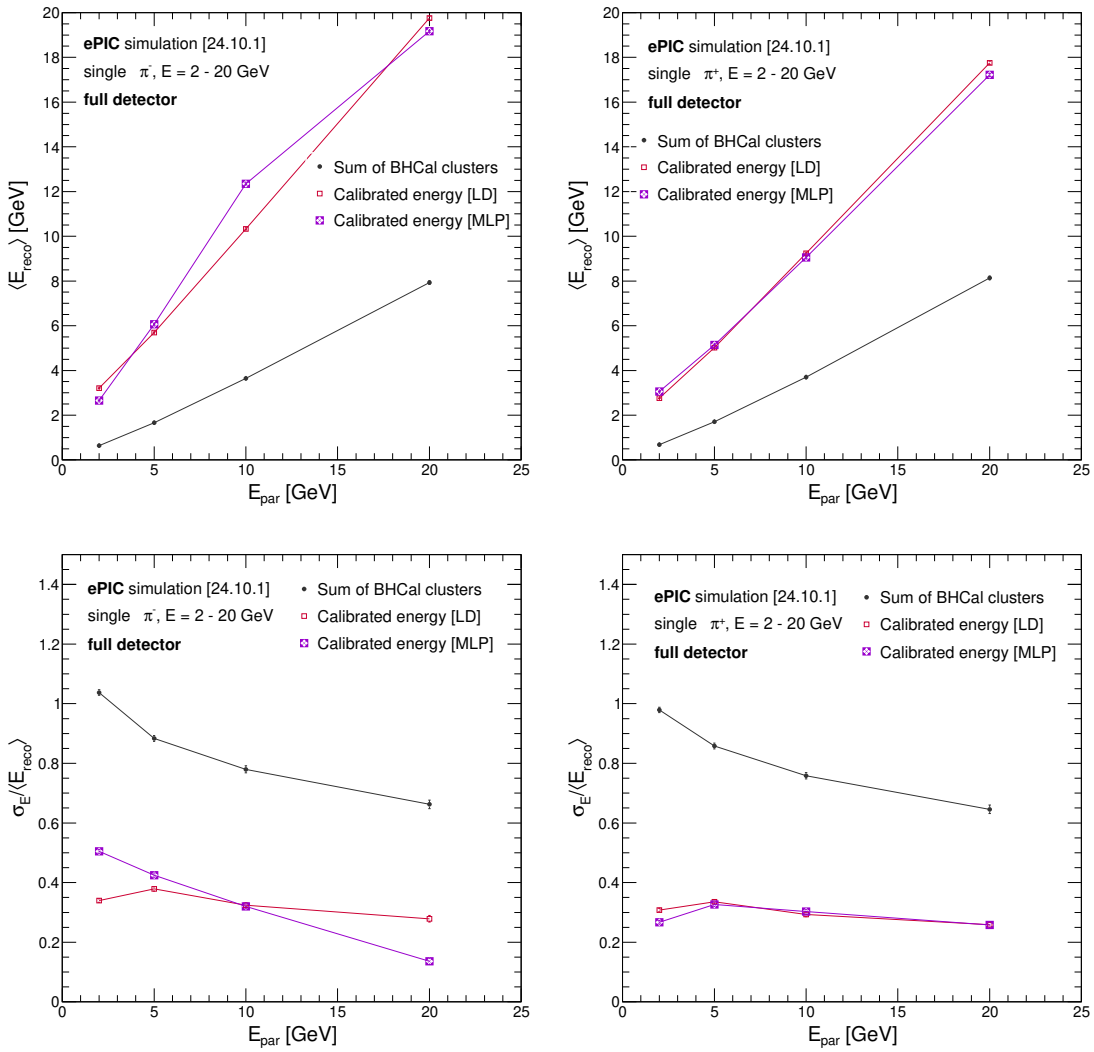

Figure 3.193: Linearity (top row) and energy resolution (bottom row) of calibrated single π^- (left column) and π^+ (right column). Red lines indicate LD-calibrated energies, purple lines indicate MLP-calibrated energies, black lines indicate the linearity, resolution of summing BHCal clusters without calibration. Distributions were simulated using the 2024.10.1 simulation geometry. Repository: https://github.com/ruse-traveler/EpicBHCalPTDRStudies

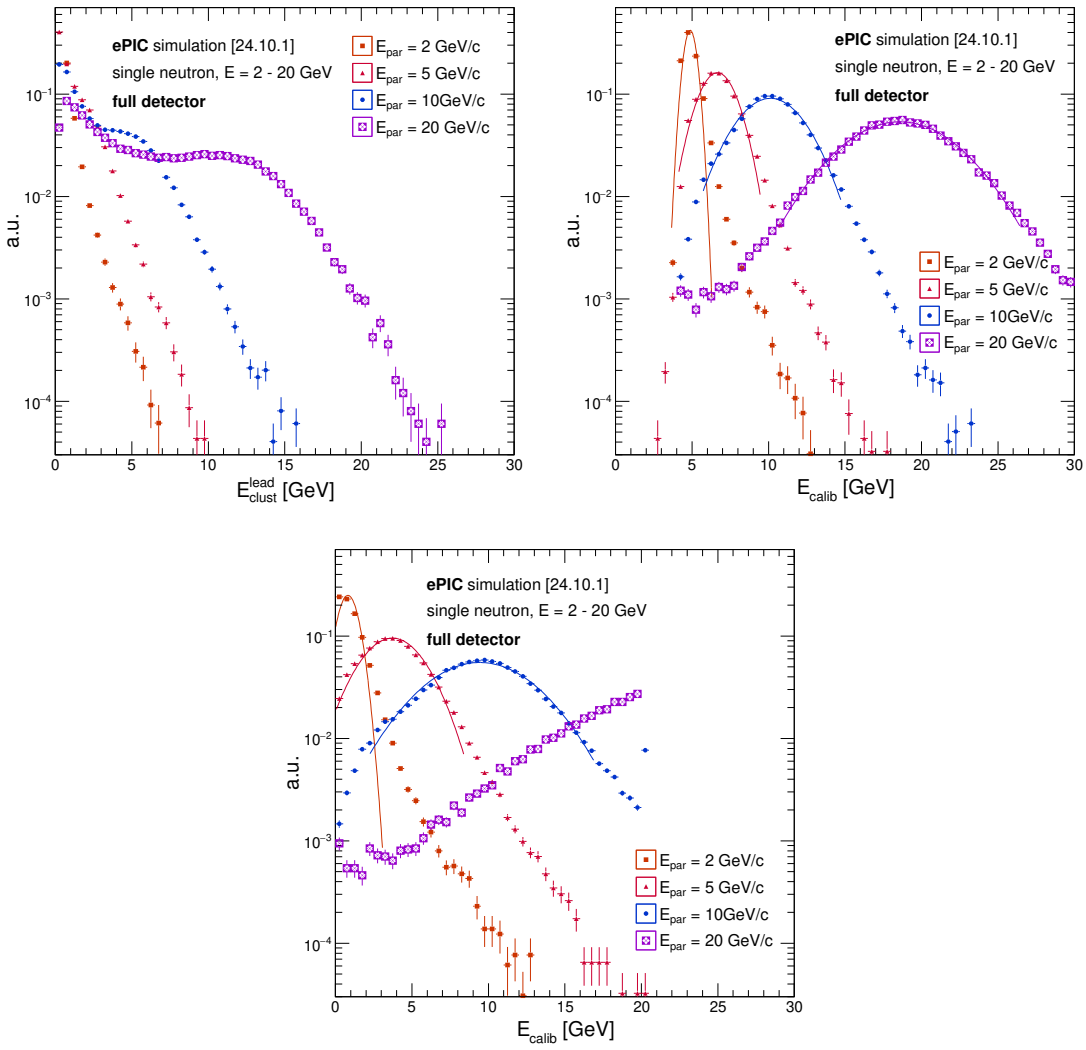

Figure 3.194: Uncalibrated (to left) vs. LD-calibrated energy (top right) and MLP-calibrated (bottom) of lead BHCal clusters for 2 (orange), 5 (pink), 10 (blue), and 20 GeV (purple) neutrons. Distributions were simulated using the 2024.10.1 simulation geometry. Repository: https://github.com/ruse-traveler/EpicBHCalPTDRStudies

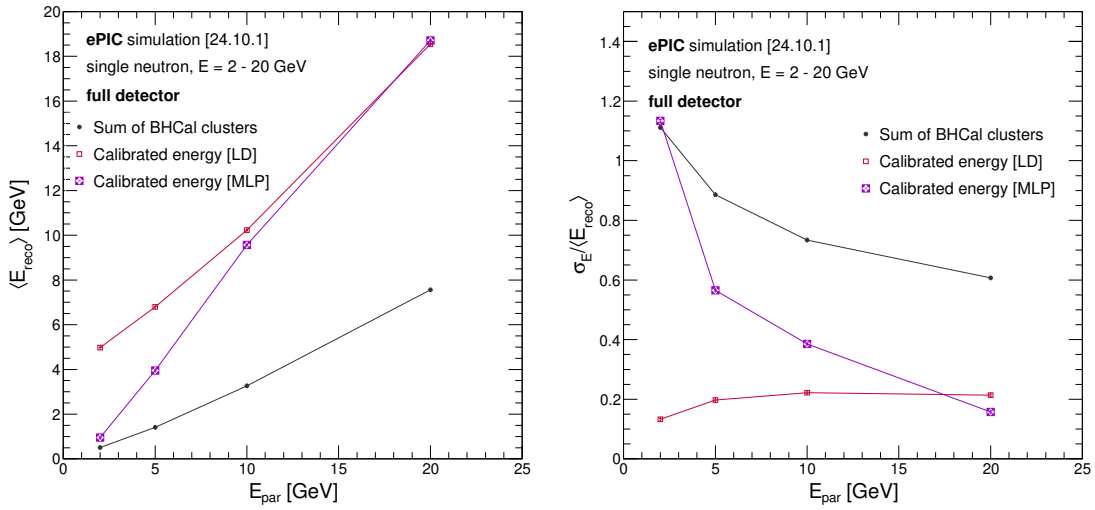

Figure 3.195: Linearity (left) and energy resolution (right) of calibrated single neutrons. Red lines indicate LD-calibrated energies, purple lines indicate MLP-calibrated energies, black lines indicate the linearity, resolution of summing BHCal clusters without calibration. Distributions were simulated using the 2024.10.1 simulation geometry. Repository: https://github.com/ruse-traveler/EpicBHCalPTDRStudies

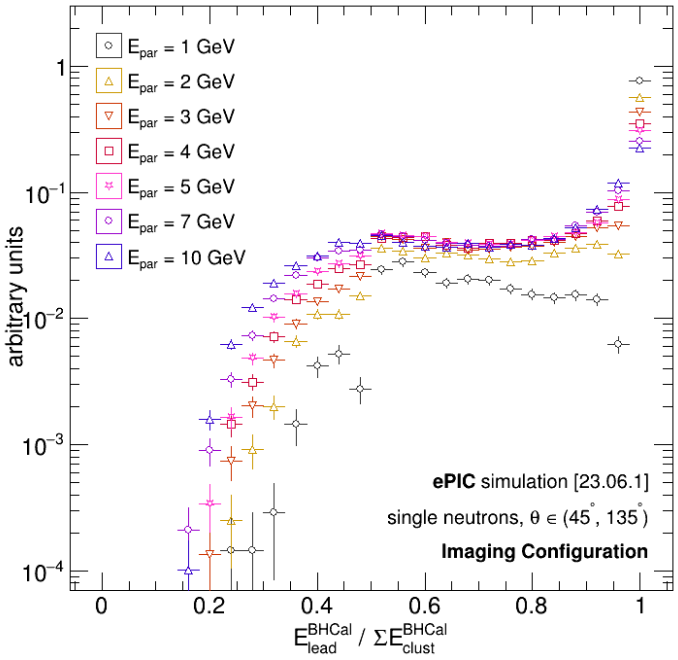

Figure 3.196: ratio of uncalibrated lead BHCal cluster to the sum of all BHCal clusters for 2 (grey) - 10 GeV (blue) single neutrons. Distributions were simulated using the 2023.06.1 simulation geometry. Repository: https://github.com/ruse-traveler/EpicBHCalPTDRStudies

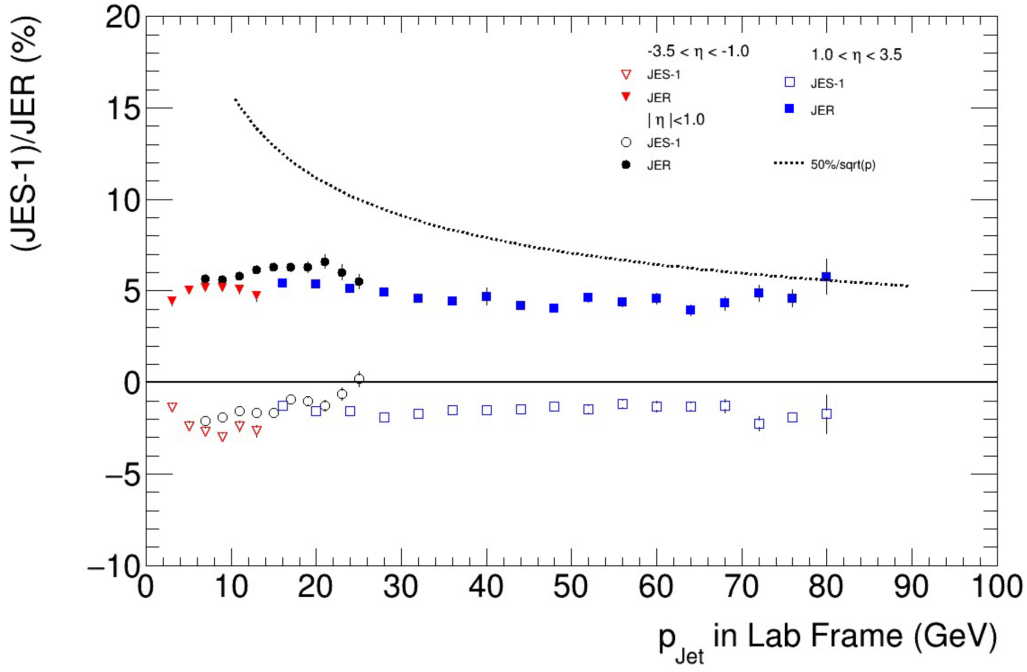

Figure 3.197: JES/R for full (tracks + ECal + HCal): The JES $-1 = \langle \Delta p/p \rangle$ (open markers) and JER (closed markers) plotted as a function of p_{jet} in the lab frame for jets in $\eta \in (-3.5, 1.0)$ (red points), $|\eta| < 1$ (black points), and $\eta \in (1.0, 3.5)$ (blue points). In the barrel region, jets are constructed from reconstructed tracks and ECal clusters *without* a nearby track. Neutral hadrons are included in the jets by smearing the particle energy by the measured energy resolution of the sPHENIX OHCal. Jets are reconstructed via the Centauro algorithm (R = 0.8) and transformed back into the lab frame. Jets are required to have at least 2 particles, and exclusively charged or neutral jets are rejected. From ECCE responses to the EIC DPAP Panel; received from John Lajoie in private communication.

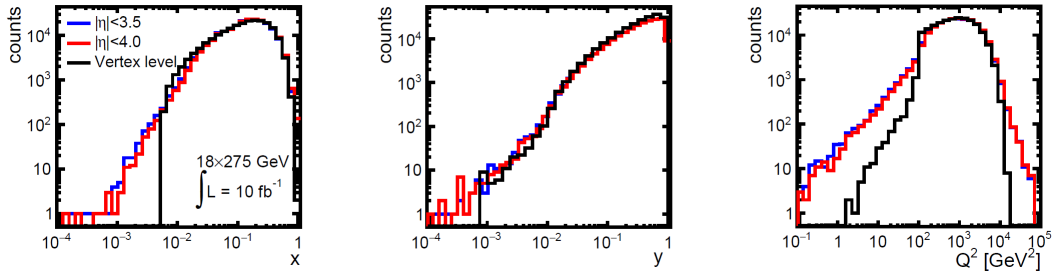

Figure 3.198: JB variables at truth ("vertex", black) and reconstructed level for particle $|\eta| < 3.5$ (blue) and $|\eta| < 4$ (red) in 18×275 CC DIS events. Detector simulation and reconstruction was carried out using a fast simulation using Delphes. Figure 8.21 from the EIC Yellow Report.

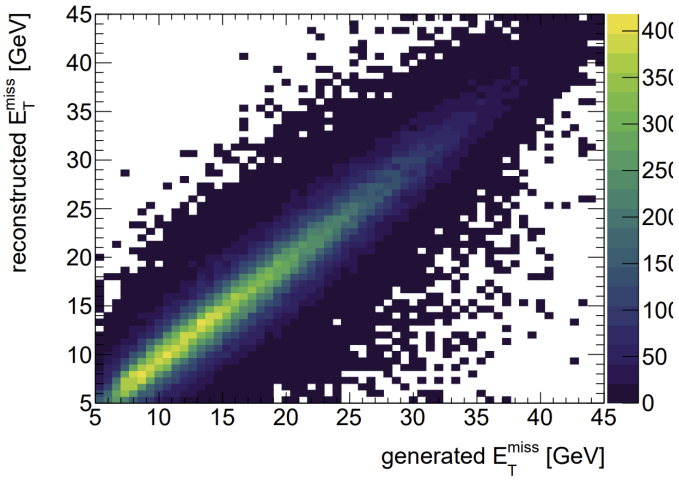

Figure 3.199: Truth vs. reconstructed $E_{\mathbf{T}}^{\mathbf{miss}}$: the truth (x-axis) vs. reconstructed (y-axis) $E_{\mathrm{T}}^{\mathrm{miss}}$ for 10×275 CC DIS events. Detector simulation and reconstruction was carried out using a fast simulation using Delphes. Figure 4 from arXiv:2006.12520.

3.3.6.3 The forward endcap hadronic calorimeter

Requirements

Requirements from physics: In electron-proton (ep) or electron-ion (eA) collisions, many highly-energetic hadrons are created in the process of probing the partonic structure of the target proton or ion using the electron. However, since the incoming proton/ion has a significantly larger kinetic energy than the incoming electron, most of the hadrons are emitted in the same direction as the hadron beam, into the hadron end cap, which is defined as the "forward" direction at the EIC.

Thus, jets of particles, with single-particle energies of up to 150 GeV, are expected to reach the forward hadronic calorimeter, e.g. based on simulated PYTHIA events for e+p collisions at 18×275 GeV^2. Typical jets consist of 10-12 particles contained within a jet radius of $R = 1$, with R being the angular distance $\sqrt{\eta^2 + \phi^2}$. These jets also contain nontrivial substructure within this cone, which carries important information about QCD dynamics. Unfortunately, the tracking momentum and angular resolution worsen rapidly above $\eta = 3$. Because of this, the hadronic and electromagnetic calorimetry in that region are required to provide both excellent energy resolution and sufficient spatial resolution to resolve particles within the jets. Thus, the forward calorimeter system has to be finely-segmented and built with minimal dead space in between the towers. This design will provide shower containment for highly energetic particles while still providing good energy resolution down to low energies.

Requirements from Radiation Hardness: In the forward region the radiation dose the detector is exposed to varies significantly as a function of radius. Three different regions are considered:

- **A:** $R > 1\,\text{m}$ which is exposed to less than $5 \cdot 10^9$ neq cm^{-2}year^{-1}
- **B:** $0.2\,\text{m} < R < 1\,\text{m}$ which is exposed to less than $10^9 - 10^{11}$ neq cm^{-2}year^{-1}
- **C:** $R < 0.2\,\text{m}$ which receives around 10^{11} neq cm^{-2}year^{-1}

The maximum radiation dose is received closest to the beam pipe and closest to the interaction point. Consequently, the primary concern will be the radiation hardness of the silicon photo multipliers (SiPM) within each layer and a secondary concern are the ASICs used to read out their signals and all other components for calibration or control, which will be sitting behind the calorimeter. It is not expected that the scintillator or steel will experience significant deterioration due to the radiation.

Requirements from Data Rates:

Justification

Device concept and technological choice: The ePIC forward HCal (LFHCal) will be a steel-plastic scintillator sampling calorimeter, read out in transverse and longitudinally separated segments. The design is based on the SiPM-on-tile concept first introduced by CALICE collaboration [107], which is now being further developed for the CMS HGCAL upgrade [108]. The SiPM-

on-tile concept allows for high readout granularities with low dead space between scintillator tiles in a design that enables largely automated assembly of individual layer modules.

The LFHCal baseline readout granularity has been adapted to satisfy the physics performance requirements of the EIC Yellow Report [11], leading to a readout granularity of 5x5 cm in transverse direction and about 10-20 cm in the longitudinal direction. The innermost section closest to the beam pipe will be populated by an high-granularity insert [109, 110] with geometry tailored to maximize acceptance up to $\eta = 4.0$.

Figure 3.200 shows an overview of the LFHCal design and the main parameters are given in Table 3.69.

parameter	**LFHCal 8M & 4M modules**	**insert modules**
inner x,y (R)	-20 cm $> x >$ 40 cm, -30 cm $> y >$ 30 cm	$R >$ 17 cm
outer R (x,y)	$R <$ 270 cm	-20 cm $> x >$ 40 cm, -30 cm $> y >$ 30 cm
η acceptance	$1.2 < \eta < 3.5$	$3.5 < \eta < 4.4$
tower information		
x, y	5 cm	$\approx$ 4.2 cm (layer 1-20) $\approx$ 6.5 cm (layer 21-60)
z (active depth)	120 cm	120 cm
z read-out	$\approx$ 8.4 cm	$\approx$ 8.4 cm
# scintillator plates	60 (0.4 cm each)	60 (0.3 cm)
# absorber plates	60 (1.52 cm)	60 (1.52 cm)
interaction lengths	5.8-6.5 λ/λ_0	5.8 λ/λ_0
# towers	8752	
# modules		2
8M	1058	
4M	72	
# read-out channels	7 x 8752 = 61264	$\approx$ 7000

Table 3.69: Overview of the calorimeter design properties for the LFHCal.

Subsystem description:

General device description: The LFHCal is positioned at $z = 3.68$ m from the interaction point, with a radius of about 2.7 m and a total depth of $\Delta z = 1.32$ m. It is constructed in alternating layers of 1.52 cm steel absorber and 0.4 cm plastic scintillator, see details in Table 3.69.

The LFHCal is largely constructed from mechanical assemblies housing 60 layers of 2x4 ("8M" modules) or 2x2 ("4M" module) tile layers. Alongside each assembly module, a multi-layer PCB picks up the analog pulses from each SiPM and passively transports them towards the end-face of the LFHCal. This analog signal transport approach differs from the latest CALICE/CMS designs, where the signal is digitized with ASICs placed near the SiPMs. Similar to the approach first proposed in Ref. [109], it simplifies the SiPM-carrying boards, saves longitudinal space in the detector's active area, and eliminates the need for cooling to counteract heat generated by the ASICs. In order to reduce the number of readout channels of the

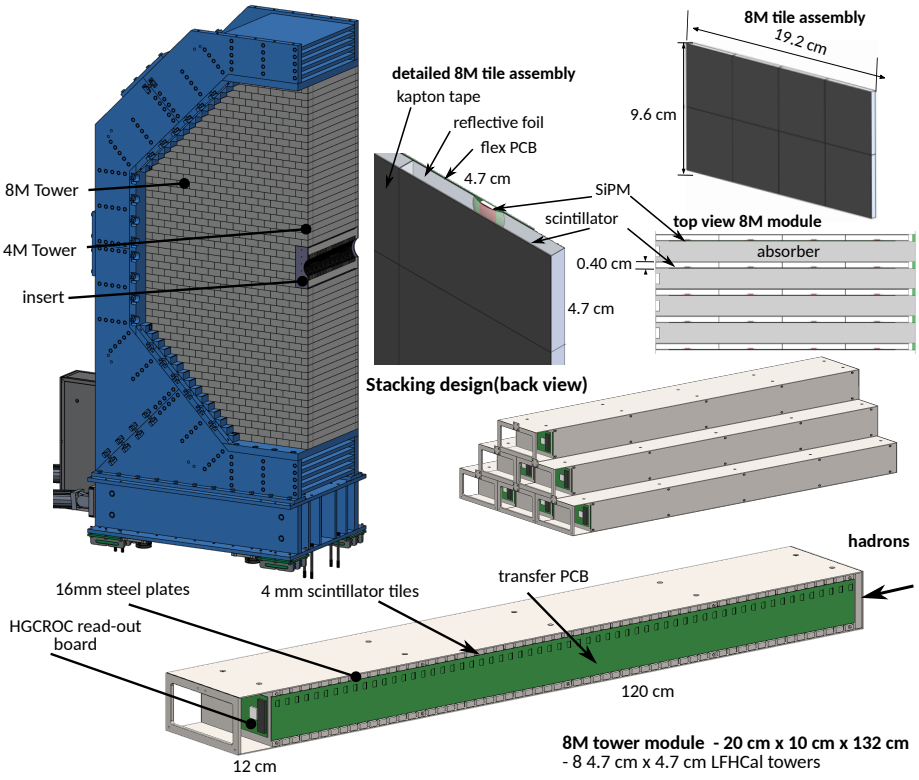

Figure 3.200: Renderings of the forward calorimeter assembly (top left), tile assembly of 8 scintillator tiles of the LFHCal with the SiPMs sitting in a dimple on each tile, detailed stacking example (middle right) and 8-tower module design (bottom).

LFHCal, SiPM signals from tiles in 5-10 consecutive layers are summed up before digitization by the readout electronics placed on the rear end of the LFHCal, facing away from the interaction point. Following [109], to increase the geometrical acceptance around the beam pipe and allow access to the scintillator layers during extended shutdowns for SiPM replacement or annealing, the modules surrounding the beam pipe are designed to be larger and include a conical cut-out for the beam pipe, as shown in Figure **??** (left).

The majority of the active scintillator layers are segmented into $5 \times 5 \times 0.4$cm tiles, individually wrapped in reflective foil, as depicted in Figure 3.202. The scintillation light generated in each tile is detected by a SiPM placed inside a circular "dimple" depression in the center of the tile. Tiles and SiPMs are assembled on thin, flexible printed circuit boards which carry the electrical signal of each SiPM to the side of an assembly module. In the insert region hexagonal tiles of two different sizes are used in order to maximize the acceptance and simultaneously reduce the number of read-out channels Consequently, the first 20 layers are equipped with hexagonal tiles of 4.2 cm width which are arranged in a staggered pattern repeating every four layers and the subsequent layers are tiled with hexagonal tiles of 6.5 cm width. This staggering pattern creates overlaps among neighboring cells, which can improve position resolution for hadronic showers when applied in sub-cell reweighting algorithms, such as HEXPLIT [111], or with AI/ML methods. In the insert region, each tile is read out separately to maximize the position resolution of individual showers and to facilitate cell-by-cell calibration and monitoring in high-radiation environments, where radiation levels are expected to be inhomogeneous in both radial and longitudinal positions.

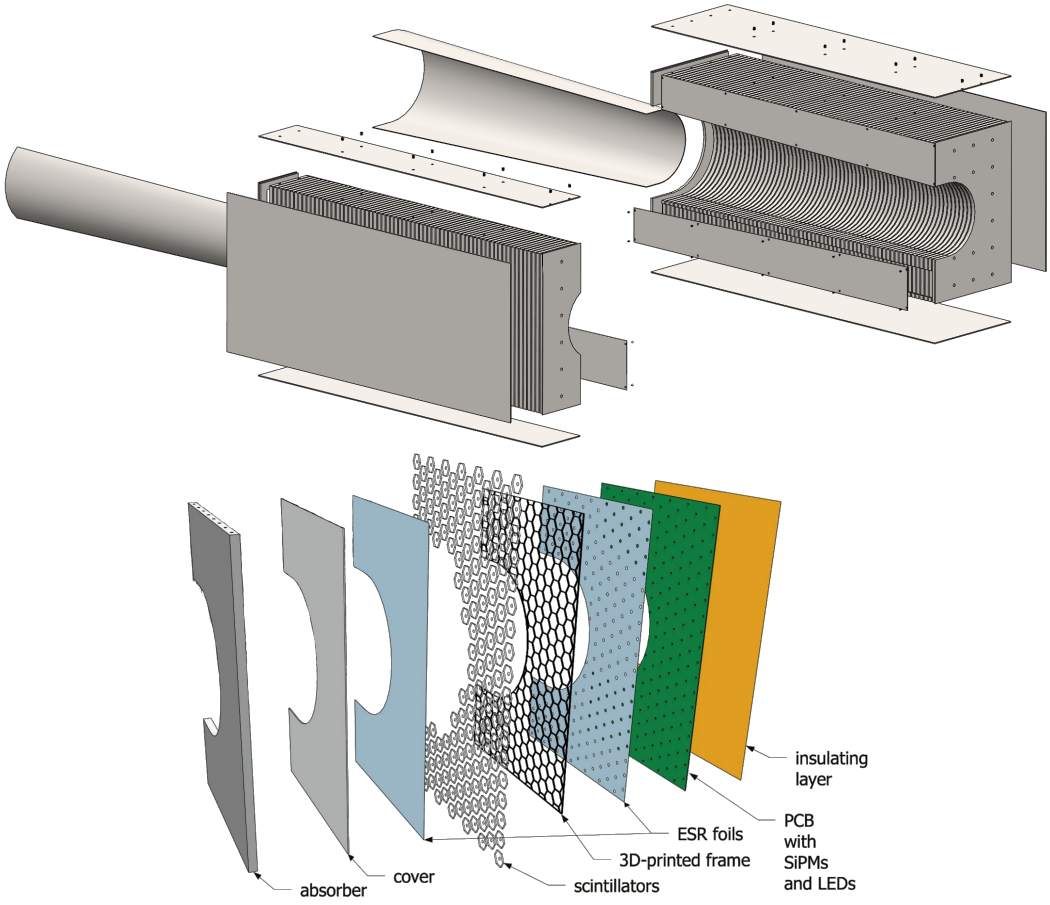

Figure 3.201: Renderings of the absorber structure for the insert modules surrounding the beam pipe (top) and their individual layer composition (bottom).

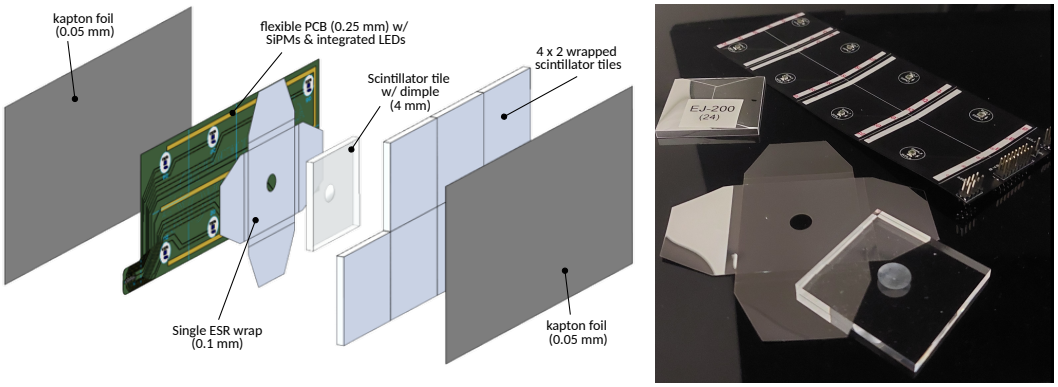

Figure 3.202: Left: Visualization of 8M-scintillator assembly with its individual components. Right: Samples of the individual components used for the 2024 test beam campaign.

The full LFHCal consists of 68264 readout channels. Out of these about 7000 channels are located in the insert modules and the remaining channels are contained in the 1058 "8M" modules and 72 "4M" modules. They are grouped into 8752 towers of 5×5 cm^2 transverse size with each 7 read-out segments.

Scintillator: The majority of the LFHCal will be instrumented with injection molded plastic scintillator tiles developed and produced by the Fermilab Scintillator Manufacturing Facility. While the light yield of injection molded plastic scintillator is found to be 20-25% lower than that of otherwise comparable commercially available cast sheet plastic scintillators, injection molded scintillator tiles are at least one order of magnitude more economical on the scale of the full LFHCal.

Only for the LFHCal segments that will be exposed to the highest radiation doses ($R < 1$ m) and inaccesible during the yearly maintainance intervals tiles machined from cast plastic scintillator stock will be used to increase the light yield in order to maintain enough signal-to-noise ratio to distinguish single MIP signals from the background noise.

Sensors: Simulations and test bench studies have shown that SiPMs with an active area of 1.3×1.3 mm^2 and pixel sizes around 20 µm (i.e. Hamamatsu S13360-1325PE or S14160-1315PS) will yield enough light yield, gain and dynamic range even after full irradiation over the whole projected lifetime of the LFHCal. However, as neither the scintillator tiles nor the SiPMs are accessible after assembly, larger SiPMs with an area of 3×3 mm^2 (ie. Hamamatsu S13360-3025PE or S14160-3015PS) for radii below 1 m in order to provide an additional operational safety factor in the S/N ratio towards the end of its lifetime. For example, Ref. [112] demonstrated that an S14160-3015PS, operated at 40.5 V ($\approx$ 2 V over-voltage), yields a most-probable value of approximately 60 photoelectrons per MIP when coupled with an EJ-212 scintillator cell with an area of 8 cm^2.

FEE: The electrical signals from all SiPMs in the LFHCal are routed towards the end-face of the LFHCal using a passive transfer board, where they are picked up by a summing board that forms analog sums of $5-10$ channels located consecutive layers of the same position. The following text will need to be adapted with the details of the CALOROC. The summed signals are then digitized by an ASIC based on the CMS HGCROC chip designed and produced by OMEGA. Each HGCROC can read out up to 72 individual SiPM channels. It features a 12bit ADC for low amplitude hit digitization, complemented by a 16bit time-over-threshold counter for larger amplitude signals. Individual signal arrival times are tagged with a 20 ps time-of-arrival counter. The HGCROC chip family features trimmable bias voltage in the range $0-2.5$ V for each input channel, greatly reducing the number of required high voltage power supply channels to operate the LFHCal.

While the HGCROC chip family is well advanced in its design, it is designed for the externally triggered environment of the CMS experiment. A self-triggered variant of the HGCROC concept named CALOROC will be developed for the use in ePIC, which will natively support the ePIC streaming readout model. [108].

Performance The minimum requirements for the LFHCal performance are driven by the energy and position reconstruction of hadronic particles within a jet of $5-250$ GeV. These requirements, however, must be evaluated as a combined resolution of the electromagnetic and hadronic calorimeter responses, as a significant fraction of the energy may already be deposited in the electromagnetic calorimeter, which has an equivalent depth of one interaction length. Since these two calorimeters have different e/h values, their combination must account for this to achieve a linear response with optimal resolution. Moreover, as the hadronic calorimeter is not compensated at the hardware level (i.e., given its Fe/Sc design, the response differs for electromagnetic and hadronic

depositions, with $e/h \approx 1.2$), optimal energy reconstruction requires a shower-by-shower weighting approach. This is necessary because the electromagnetic content of hadronic showers varies on a shower-by-shower basis on an energy-dependent manner. This weighting procedure, dependent on particle energy and angle, is commonly referred to as "software compensation" or "offline compensation". As noted in Section 11.4.1 of the Yellow Report [11], this approach requires fine granularity in the hadronic calorimeter, including in the longitudinal direction. This was demonstrated in previous experiments, such as H1 at HERA, which used a Pb/Fe liquid argon calorimeter, and in test beams with the CALICE Fe/Sc calorimeter.

Rather than following a traditional minimization approach to achieve the weight functions to implement software compensation, we rely on AI/ML methods, which provid a more efficient and optimal way. Specifically, we used a graph neural network approach, following the method applied in EIC calorimetry studies in Refs. [2, 6], which builds on prior work by the ATLAS collaboration [113]. Similar advancements were recently presented by the CALICE collaboration using test beam data [4]. This graph network approach effectively implements software compensation through shower-by-shower weighting at the cell level, using the shower structure encoded in graphs to achieve a linear response that is independent of both energy and the electromagnetic energy fraction of the hadronic shower, thereby yielding optimal energy resolution.

Figure 3.203 shows the combined energy resolution of the forward electromagnetic and hadronic calorimeter for single pions within the primary acceptance of the LFHCal as a function of η, obtained using the aforementioned graph network approach. The resulting combined energy resolution of $\sigma_E/E = 27\%/\sqrt{E} \oplus 3\%$ surpasses the required resolution of $\sigma_E/E = (35-50)\%/\sqrt{E} \oplus (7-10)\%$, as specified in the Yellow Report [11].

The combined position resolution of the LFHCal and forward electromagnetic calorimeter for single pions can be found in Figure 3.204. Both the φ and θ resolution are found to be better than 4 mrad for pions with an energy larger than 5 GeV within the full acceptance. A mild energy dependence can be observed for the θ resolution increasing as a function of energy down to 2.5 mrad. For the φ no clear energy dependence can be claimed. While the θ resolution appears to be largely η independent, the φ improves with increasing η to better than 2.5 mrad

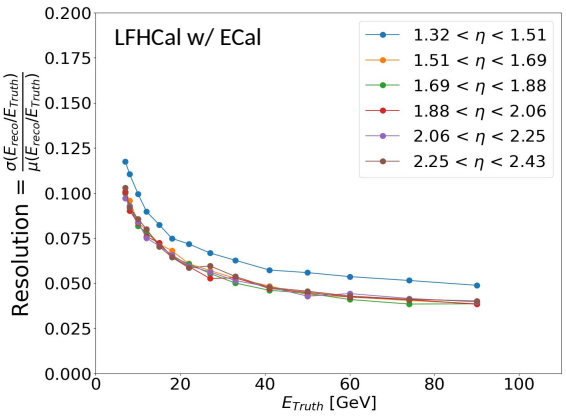

Figure 3.203: Combined energy resolution of the forward calorimeter system as a function of pseudo rapidity η for single pions, evaluated within the primary LFHCal acceptance. These results are obtained using the graph-neural network approach described in Ref. [2].

Implementation

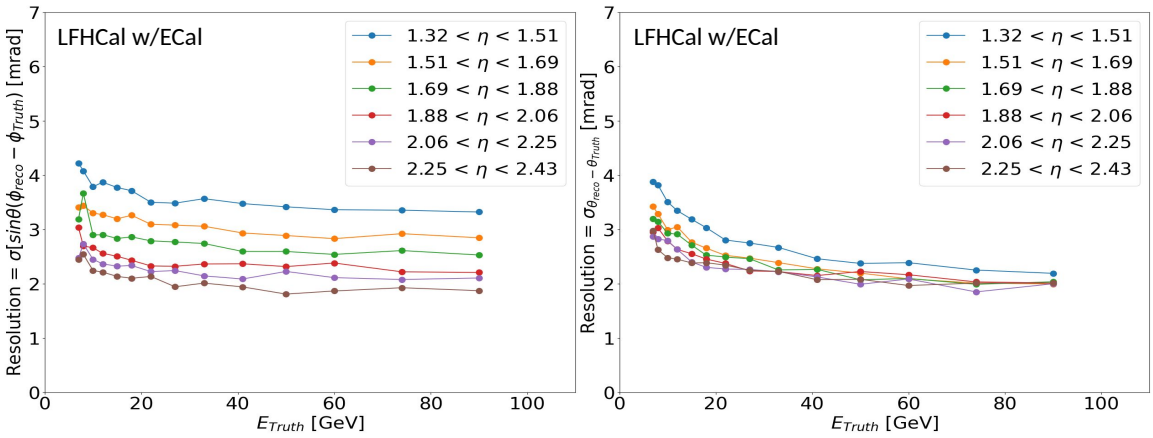

Figure 3.204: Combined position resolution of the forward calorimeter system as a function of pseudo rapidity η for single pions, evaluated within the primary LFHCal acceptance. These results are obtained using the graph-neural network approach described in Ref. [2].

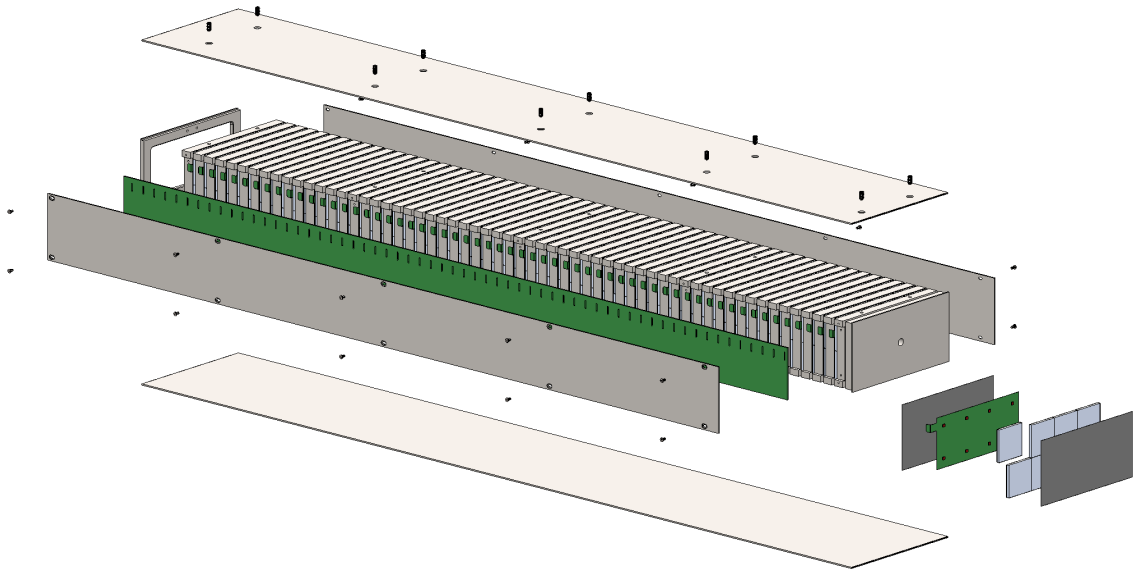

Figure 3.205: Visualization of the individual components of an 8M module.

Subsystem mechanics and integration: The primary construction component of the LFHCal are the 1052 8M modules, as depicted in Figure 3.205. These modules are constructed out of an electron beam welded and nickel-plated absorber structure out of AISI-1020 carbon steel, consisting of the 60 absorber plates, the front and back plate and the top and bottom plate. Inside the resulting slots inbetween the absorber plates 8M scintillator assemblies (Figure 3.202) are placed, which are connected to a long transfer PCB running along the side of the 8M module. The module is closed by two screwed side panels out of AISI 304 stainless steel. The read-out electronics is placed in a rear compartment of about $19.5 \times 9.5 \times 8.5$ cm^3, which is accessible from the rear though a cut-out window in the back plate.

The individual absober plates are welded on the top and bottom using alternating stich welds of

two times 63.5 mm and 88.78 mm length with a minimum penetration depth of 0.5 mm over the full length. For the front and back plates, as well as, the those plates to which the strong back for transportation is anchored the available maximum weld length is used to ensure maximum stability. Afterwards, the fully welded structure is nickel electroplated to reduce the effects of corrosion and the stainless steel side covers are installed. This production mechanisms allows for minimal distortions during construction and thus allows for a maximization of the available active detector surface.

The active layers are inserted and tested together with the long transfer board at the various assembly locations. The FEE-cards at the rear of each module can be installed during the same assembly process or could be mounted prior to installation at Brookhaven National Laboratory depending on the production readiness of the CALOROCs.

A similar construction procedure will be followed for the half sized 4M modules, where the staggering of the welds will not be necessary. For the two individual modules we envision the same construction technique, however, due to is weight and corresponding necessary rigidity it will most likely need to be welded also on the outer straight edge of each module to correctly disperse the load of the modules stacked on top of the respective inserts.

The LFHCal will be stacked in two half shells surrounding the beam pipe, as shown in Figure 3.206 (top), which are situated on rails and movable using Hillman rolers and linear actuators, which are detailed in the same drawing on the bottom. During assembly each module is lifted into place and then adjusted horrizontally and vertically using different sized stainless steel shims. Afterwards it is fixated in place using bracket at the rear of each module as seen in the detailed stacking pictures in Figure 3.200. Moreover, each module is bolted to the 2.54 cm plate covering the full front face of the each half of the LFHCal. This steel plate will simultaneously serve as mounting plate for the forward electromagnetic calorimeter.

Services: Apart from the SiPM sensors integrated into each scintillator tile layer, all active LFHCal electronics are located on the end-face of the LFHCal, fully accessible in between active beam runs of the EIC. As such, there are no significant bottlenecks in terms of maximum permissible occupied cross section of service channels.

The total number of readout ASICs is expected to be around 1000 at a power dissipation of an estimated 2 W per ASIC distributed over the entire end-face of the LFHCal, which is cooled with a small liquid cooling system.

The overall cross section of low voltage supply cable conductors is estimated to be around 1000 mm^2 from the required current rating (up to 1kA at 2.5V), which can be supplied by a few units of off-detector low voltage power supplies in a common crate area with the appropriate air flow, mains power connection and electrical safety facilities.

The HGCROC readout ASIC supports channel-individual trimming of SiPM bias voltages, reducing the overall number of required high voltage bias supply channels. For the start of the operation of ePIC, we expect not more than 16 channels of high voltage supplies in the voltage range 50-80 V. When more significant adjustments to the bias voltages will have to be made due to the varying effects of radiation damage across the LFHCal volume, more channels might have to be added.

Since the LFHCal is planned to be assembled in two individual half-discs, all cables and other services are separated along the same axis and cannot reach across the central separation gap of the LFHCal, which is either reflected in individual cable trees from the power supplies to individual halves of the LFHCal, or potentially entirely separate power supplies located on different sides of the experimental hall.

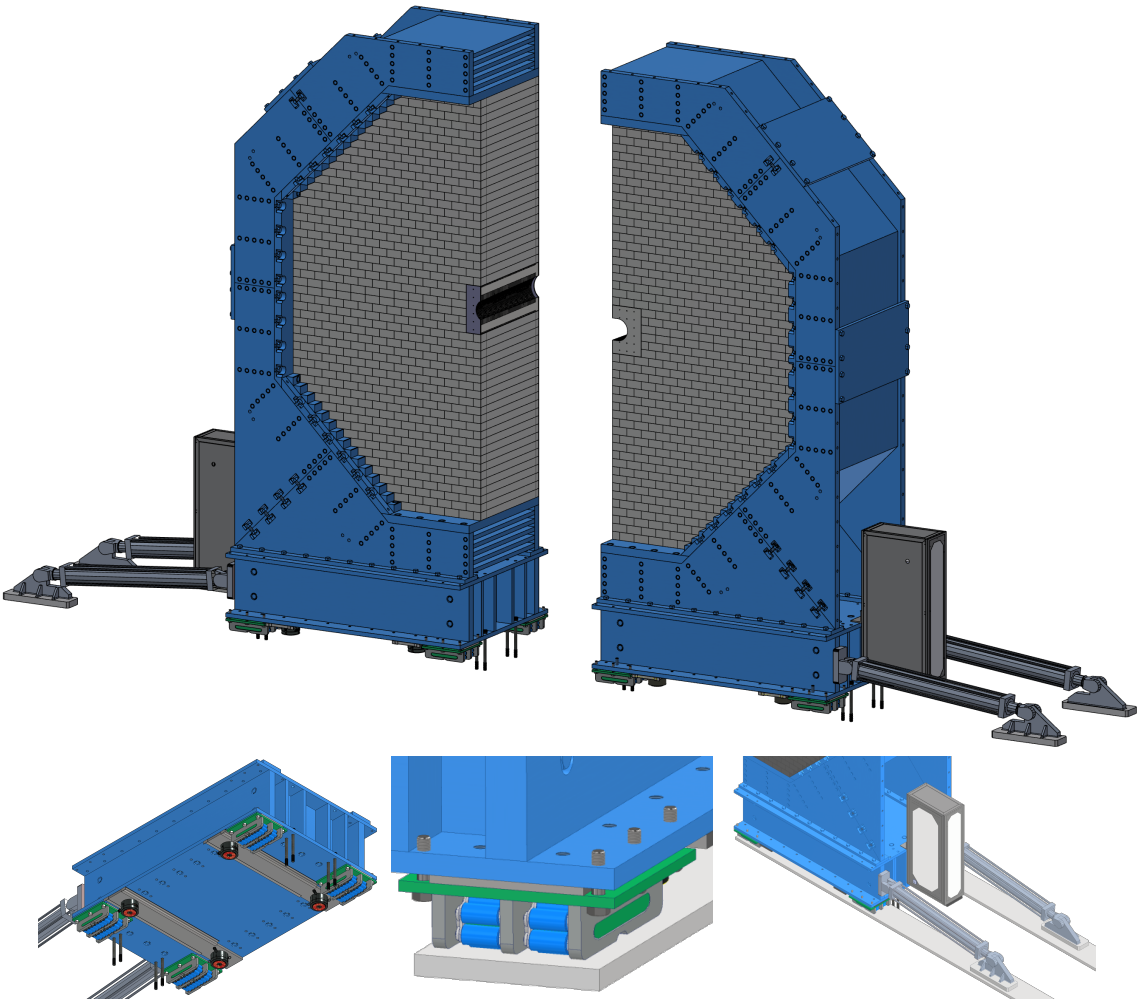

Figure 3.206: Visualization of the full LFHCal in its cradle (top) and details of its moving mechanism (bottom).

Calibration, alignment and monitoring: The gains of individual SiPMs will be monitored and calibrated by means of an integrated LED calibration system providing short, low amplitude flashes of light into each sensor. This gain calibration scheme does not depend on the exact amplitude of each LED pulse and is thus robust to changes in ambient conditions and very cost effective. The front-end electronics include a charge injection mechanism that can calibrate its own ADC and ToT scales with respect to each other.

Using the calibrations in sensor gain and readout electronics scales, the light yield of each tower of summed scintillator tiles will be monitored from the deposits of minimum ionizing tracks produced in EIC collisions during the operation of the accelerator, as well as with cosmic muons in between run periods.

Initial parameters for module alignment will be provided from the metrology during and after the stack-up of the LFHCal modules into the full LFHCal detector. No significant relative movement of LFHCal modules is expected during its lifetime, however the absolute position of each half-cradle will need to be validated each time the cradles are moved out and back into their positions.

Status and remaining design effort:

R&D effort and status: The primary R&D efort for the LFHCal has been concluded in 2024. The remaining activities focus on the readout electronics as well as the analog summation of the signals for consecutive individual layers and the long passive tranfer board. First protoypes of a summation test board have been received and are currently being tested. The long transfer board is in its design phase and a first protoype should become available middle of 2025.

Other activity needed for the design completion: To validate the simulated performance of the different LFHCal module types several test beam campaigns are planned during 2025-2028 with increasingly larger protoypes. The first of which have been completed in 2023 and 2024 with particle or single modules.

Status of maturity of the subsystem: The a large fraction of the LFHCal components has reached 90% design maturity and thus the steel structures for the 8M- and 4M-modules as well as the necessary SiPMs have been included in CD3-A as part of the long lead procurement items. The first preproduction items are evaluation and are largely complacent with the given specifications. The remaining mechanical components, as well as, the SiPM carrier boards are currently under evaluation and are being considered for inclusion in the CD3-C procurement, as the assembly of the 8M- and 4M-modules will take about 2 years after receiving the various components.

Quality Assessment (QA) and Control (QC) planning: The quality assessment of the LFHCal components will be structured similarly to the construction process. The following processes are currently foreseen:

Absorber structure: During the production of the absorber structures of the 8M and 4M module, at random 5% of the modules will be inspected with full GD&T, while for the remaining modules only the external dimensions will be inspected and the slots cross-checked using a go-no-go-gauge after welding. The subsequent nickel plating thickness will be evaluated at for a random 5% of the modules following standard industry techniques. For the insert modules full GD&T will be performed on both individual modules and the thickness of the nickel plating will be evaluated. Should any of these evaluations be outside the specified limits the module badge of modules will be rejected and the production parameters adjusted as necessary.

Silicon photomulipliers: The quality control of the SiPMs will be performed in a two step process. The vendor guarantees that within one badge of about 520 SiPMs a maximum variation of the break down voltage of 0.1V for the 8M and 4M-modules can be expected, whilst for the $\sim$20k SiPMs necessary for the insert a variation of 0.05V will be guaranteed. Out of each badge 5% of the SiPMs are tested at random and their break down voltage is measured as well as their gain dependence and noise levels. Should the respective SiPMs fail to comply with the desired specifications the full badge shall be rejected and replaced by the vendor.

Assembled SiPM-flex boards: As per industry standard connectivity tests for all SiPM-flex board assemblies will be performed by the vendor.

Assembled Scintillator layers: All assembled scintillator layers will be visually inspected regarding light tightness by flashing the internal LEDs. These will be followed by a go-no-go gauge approach for checking the external dimensions. Moreover, connectivity tests as well as single photon spectra measurements will be performed for every assembly, prior

to installation in the absorber structure. Each assembly will receive a unique identification number and the collected data will later be used as basis for the calibration of the full module.

Long-transfer-board: Each long-transfer board will be tested for connectivity as well as level of cross talk among the different lines.

FEE-card: Each FEE-card will be exposed to a series of functionality tests prior to installation in the module.

Full Modules: After the assembly of each module first electrical connectivity test for each SiPM layer will be performed and afterwards cosmics data will be taken in order to assess the performance of the module. The same procedure will be repeated once the modules are put in place in the experimental hall prior to installing the next layer.

Environmental, Safety and Health (ES&H) aspects: The LFHCal design follow the best practices established within the national laboratories regarding standard safety and environmental concerns. We will strive to implement these practices at all production sites by standardizing the safety protocols, while adhering to local constraints and control processes specific to each institution. Consequently, for each site the potential hazards will be identified, mitigation strategy will be developed and the appropriate safety procedures will be documented.
The primary hazard during construction of the LFHCal have been identified as:

Handling of absorber structure: The different modules of the LFHCal range in weight from 74 kg up to 1.3 t. None of them should be lifted without a lifting fixture (strongback) and the appropriate lifting equipment for the respective weight. They will need to be uncrated for assembly and lifted on top an appropriate assembly table which can support the respective weight during installation and testing of the individual components. In particular, for the lifting operations specific protocols in compliance with the local safety rules will need to be established in order to prevent accidents.

Storage of absorber structure during assembly: While the modules are being assembled a large fraction of the 8M modules will need to be stored at the different assembly sites. Thus in order to mitigate excessive space requirements a storage solution which allows stacking of crate modules (2-3 crates) or similar solutions will need to be pursued. This will require additional safety measures to prevent collaps of the crates or other stacking previsions as well as lifting the modules accordingly in their crates.

Laser operation hazards: The ESR foil wraps will need to be cut with a laser-cutter. Controls and measures will be implemented to ensure the corresponding device cannot be operated without interlocks and following the laser safety guidelines of the respective institution.

Pinch/nip hazards: Automated systems, such as robots for wafer probing, pick-and-place, and glue application, present pinch hazards. Controls, such as guards and procedures, will be in place to mitigate these risks.

Crush hazards: The use of presses and swaging equipment introduces crush hazards during assembly processes. Strict safety protocols, including the use of guards and operator training, will mitigate these risks.

Radioactive sources: The use of radioactive sources for calibration introduces additional handling requirements, and proper shielding and storage protocols will be implemented as necessary.

Electrical safety: Electrical safety procedures will also be applied for all electronics and power systems associated with the LFHCal production tooling and detector components.

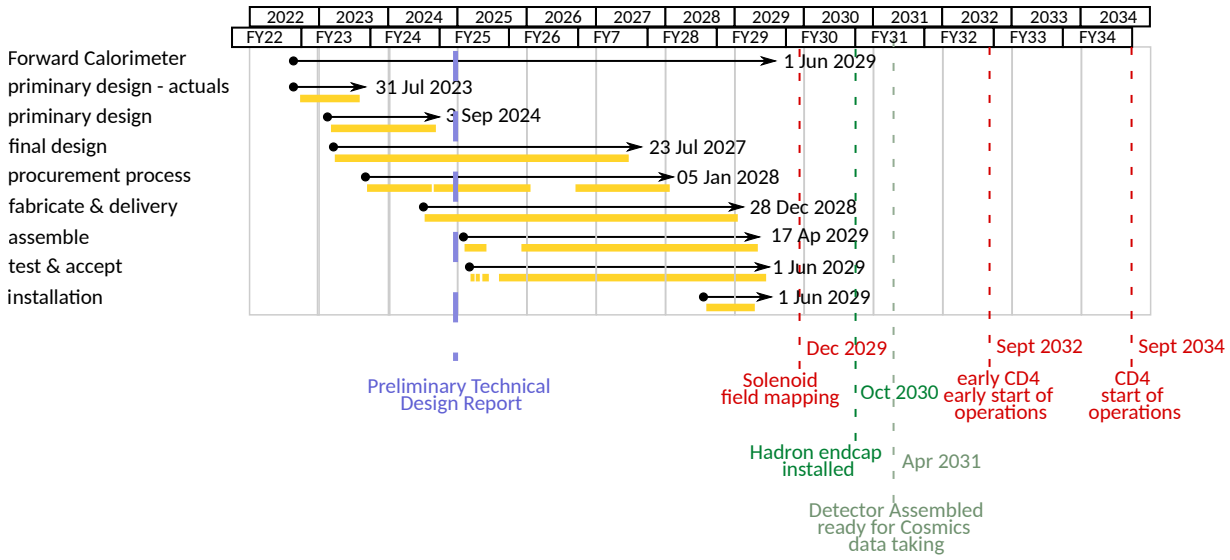

Figure 3.207: General timeline of the LFHCal design, construction and assembly.

Flammable liquid handling: For cleaning the different electrical components ethanol might be used, these bottles will need to be handled with care and their storage will follow the institutional safety protocols. Handling will only be done with appropriate gloves.

Construction and assembly planning: The LFHCal construction is divided into several phases, which are partially happening in parallel:

Absorber structure fabrication: The individual 8M, 4M and insert module absorber structures are assembled out of 66 individual pieces each, excluding screws, as seen in Figure 3.205. Out of these 64 pieces are welded together using electron-beam welding after having been preassembled and fixated in a specially designed jig for the weldment. It has been currently estimated that a maximum of 12-20 8M modules and 4M modules could be produced within a 5-day work week. The limiting factor being the availability of the large vacuum welding chamber and a full weldment cycle lasting about 2/hour per weldment. The weldments are afterwards electroplated with nickel to prevent corrosion and reduce the wearing on the outer surface due to transportation and handling. At full capacity this would require a full year of production time for the 1058 8M weldments not factoring in any delays in the supply chain. With the LFHCal also serving as flux-return for the MARCO magnet and the need to be available for the powering tests currently scheduled for December 2029, has led us to acquire the LFHCal modules as part of CD3-A and CD3-B long lead procurement starting in fiscal year 2024. In order to reduce the storage needs at the respective vendors and allow for a staggered further assembly the delivery of these modules will be done in badges of 50-100 modules during 2025 and 2026.

Scintillator layer assembly: The assembly of the individual scintillator layers for the 8M and 4M modules can be completely decoupled from the absorber structures fabrication. In order to assemble a single 8M-scintillator layer one fully equipped flexible SiPM-carrier board, 8 wrapped tiles and two layers of Kapton foil will be needed. For the main body of the LFHCal (1058 8M and 72 4M) modules a total of 63480 8M scintillator layers and 4320 4M scintillator layers will be required, leading to at least 525120 wrapped scintillator tiles.

About $10 - 12\%$ of the tiles will be produced out of cast sheets, while te remaining $\approx 90\%$ of the tiles will be injection molded out of scintillator plastic using the facilities at Fermilab. Producing all tiles out of cast material is cost and schedule prohibitive, despite having an about 20% higher light yield. The production time at Fermilab has been estimated to be about 6/month of nominal operations, which can be done in batches in order to reduce the storage overhead. The tiles produced using injection molding have to be degrated and subsequently wrapped in highly reflective foil (i.e. ESR foil). Given the tight tolerances of the LFHCal modules and the amount of tiles to be wrapped it is currently envisioned to perform the wrapping using a specifically designed tile-wrapping setup similar as for the CMS HGCAL.

Afterwards, the wrapped tiles are assembled into 4×2 or 2×2 scintillator assemblies backed by a flexible SiPM-carrier board and sandwiched into two adhesive sheets fo thin capton foil, as seen in Figure 3.202. The assembled layers are subsequently tested and packaged into groups of 60 assemblies to ease storage and assembly during the module assembly.

For the two insert modules each layer will need to be assembled individually due their unique shape and hexagonal tile arrangements. The around 7000 hexagonal will need to be painted on their edges individually with TiO_2-paint and then subsequently embedded in their 3D printed frame for each layer. The frame is mounted to a kapton backed SiPM carrier board which is covered with a precut ESR sheet in order to accomodate the SiPMs and LEDs for each tile. After installing another sheet of ESR-foil ontop of the scintillator layer the assembly is completed by a thin cover. Do due to their uniqui shapes and placements the insert module layers have to be assembled manually and then tested. These layers are constructed with a significantly larger rigidity than the 8M assemblies in order to allow for removal during the extended year end shutdowns and possible replacement of annihilation.

Module assembly and testing: The assembly of the individual 8M- and 4M-modules requires: 1 steel absorber structure, 60 tile-assemblies, 1 long-transfer-board and 1 FEE-card. For the assembly the absorber structure will be placed on a flat surface using its lifting fixtures and afterwards the 60 tile assemblies will be inserted in the corresponding slots. They are then connected to the long-transfer-board by connecting the 60 individual latches with the connectors through the prepared slots in the long tranfer board. Afterwards, the FEE-card is connected in the rear of the module and a connectivity test for all layers is executed. Then the side-panels are installed and the module can be place on its front face for cosmics testing in a vertical position. Should the FEE production be delayed a test board instead of the final FEE-could be installed for the tests and removed afterwards. In this case the final FEE's would be installed prior to installation in the experimental hall at BNL.

The insert module assembly follows a similar procedure except that each layer of tile assmeblies is uniques and thus should be placed in the correct order for these two modules.

LFHCal assembly: The LFHCal assembly will be done in the Point 6 experimental hall at BNL in its support cradle. Each half of the LFHCal is going to be assembled separated by placing one module at a time with a crane and chiming it in place using the prepared chims, layer by layer. At the same time the cradle is growing around it as the number of layers grows. The large front plate to mount the ECal is installed simultaneously to anchor the LFHCal modules in place in front.

Collaborators and their role, resources and workforce: The full LFHCal WBS organizatorial chart is available in the additional material (Figure 3.208). The LFHCal consortium consists of a diverse list of institutions under the leadership of Oak Ridge National Laboratory (ORNL). Currently the majority of the leadership team is situated at ORNL, in particular regarding mechanical, electrical and read-out design as well as scintillator testing. System testing and Software and

Simulation design are headed by Brookhaven National Laboratory (BNL) and the University of Riverside, respectively.

Risks and mitigation strategy:

Each LFHCal scintillator tiles has to be wrapped in a suitable foil, ensuring the wrapping fulfills the requirement in light-tightness as well as geometric tolerances after wrapping. The LFHCal tiles for lab tests and testbeam studies so far have been wrapped manually. The CMS collaboration is developing an automated wrapping machine, following two similar concepts at Northern Illinois University and DESY, Germany. We are in close contact with these groups and plan to adapt one of their designs to the needs of the LFHCal design. If their final designs turns out to be unsuitable to wrap LFHCal tiles, we will require additional R&D efforts to adapt the existing design to the LFHCal or potentially develop our own. If all automated wrapping developments fail to produce reliable results, all tiles can be manually wrapped with the help of already existing 3d-printed and a sufficient number of e.g. students to perform the wrapping under supervision.

The readout ASIC of the LFHCal (as well as other ePIC detectors) is expected to be based on the HGCROC design with modifications enabling a self-triggered streaming readout named CALOROC. In case the CALOROC developments are not successful, HGCROC can be operated to be quasi self-triggering by adding additional FPGA logic close to the readout electronics that locally generates external triggers based on the streaming trigger output that already exists in the HGCROC. This mitigation would require additional electronics on the LFHCal end-face and greatly increase the number of differential data links required, which increases system complexity and cost.

Stacking the 1168 LFHCal modules into two coherent half-discs requires each module to adhere to the defined tolerances after assembly. Ongoing tests of the electron-beam welding procedures achieve tolerances very close to the requirements, but scaling the production to the required volume still needs to be demonstrated and validated. If the tolerances for individual modules can not be ensured, more shimming is required during the module stackup.

A number of critical components of the LFHCal are not accessible after the modules are stacked up into the full LFHCal. All connectors and PCBs buried into the LFHCal volume must thus be throughly validated for electrical and mechanical functionality and longevity. If certain connector types are found to be unsuitable e.g. in past and future testbeam campaigns, different connectors need to be selected or, if not possible, additional fastening mechanisms need to be introduced to ensure no readout channel is lost to bad or worsening connectors over the lifetime of the LFHCal.

Additional Material

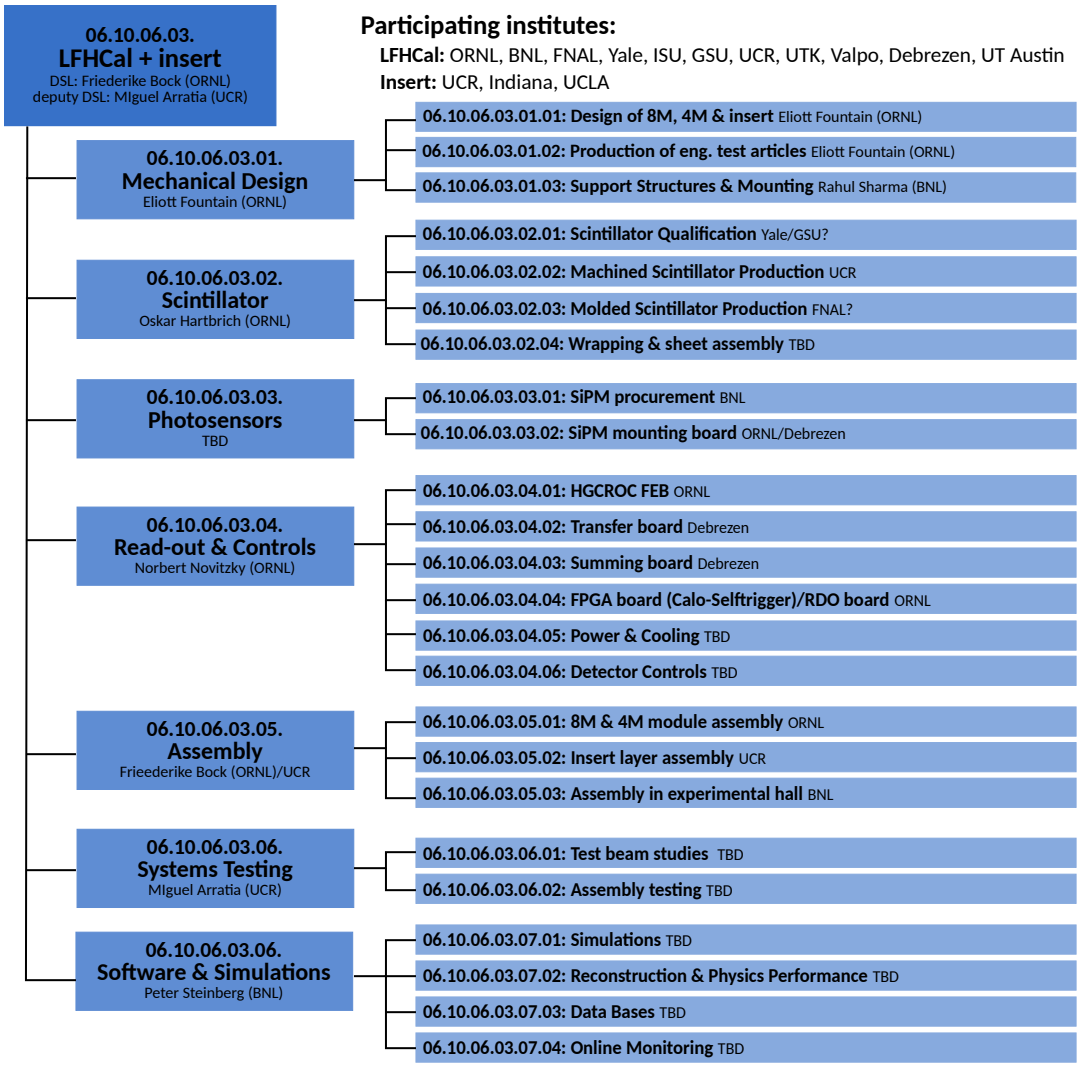

Figure 3.208: Organizatorial chart of the LFHCal & insert consortium, indicated by the numbers are the associated WBS structures.

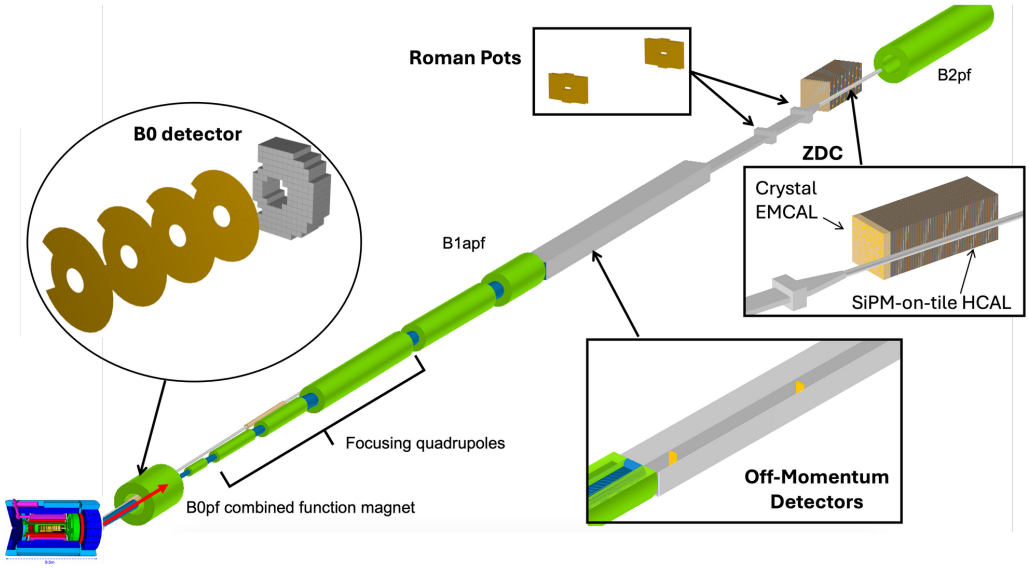

Figure 3.209: All four far-forward subsystems in the outgoing hadron beam direction. The green cylinders are accelerator dipole and quadrupole magnets.

3.3.7 Far-forward detectors

The ePIC far-forward detectors are required to enable essentially the entirety of the exclusive physics program at the EIC, where final-states involve protons, neutrons, photons, and various other particles at $\eta > 4.5$. There are four subsystems, all integrated with the outgoing hadron beamline between ∼5.5 and 39 meters from the interaction point. The far-forward subsystems are summarized in Fig. 3.209, and details are presented in subsequent subsections.

3.3.7.1 The detectors in the B0 bending magnet

Requirements

Requirements from physics: The B0 magnet bore will contain two detectors: a charged particle tracker and an electromagnetic calorimeter. Both will have acceptance covering the angular region from 5.5 to 20 mrad. Given the mechanical constraints imposed by the detectors' location in the magnet (and respecting the beam lines themselves) the detectors will be highly asymmetric for angles greater than ∼13 mrad. To maximize acceptance it's required that there be minimal dead areas in the instrumentation especially for angles less than ∼13 mrad. The tracker should have momentum resolution up to 6% for protons, and timing precision sufficient to properly associate tracks with their vertex, ∼ 35 ps. The calorimeter should have a large dynamic range with sensitivity to both soft, O(100 MeV), and hard, O(100 GeV), photons. The energy resolution should be less than $8\%/\sqrt{E} \oplus 4\%$, with position resolution $\lesssim 10$ mm. We note that for some analyses the calorimeter will function as a photon 'tagger' rather than an actual calorimeter, and so in some regions of acceptance (where the mechanical constraints are acute) this resolution may not be achieved but having the acceptance instrumented is still valuable to tag the event as containing a forward photon even with only imprecise knowledge of the photon's energy.

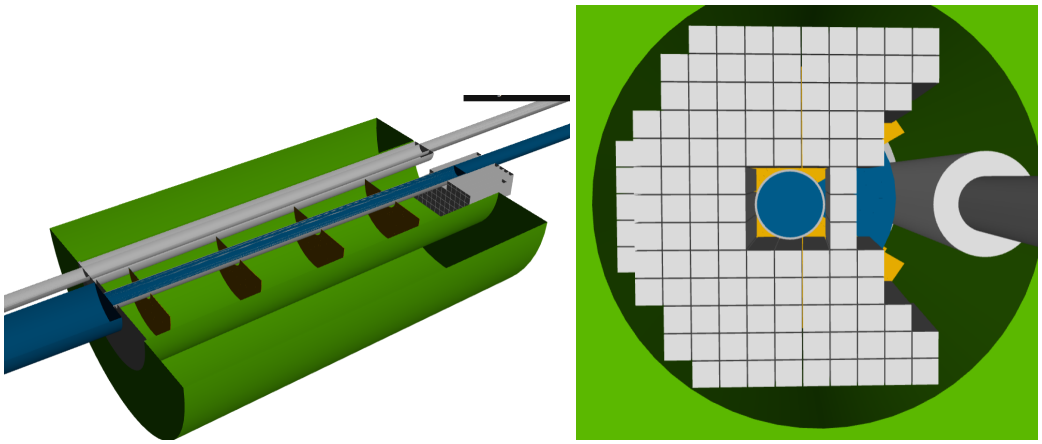

Figure 3.210: Left: A cutaway view of the detectors in the B0 magnet. The beampipes are shown in blue and gray, the four tracking detectors are dark brown and the calorimeter is gray (the figure orientation is such that IP is to the left of the magnet). Right: The transverse profile of the calorimeter in the B0 magnet. Both figures are from the DD4HEP implementation of the detectors.

Requirements from Radiation Hardness: The expected non-ionizing radiation dose at a longitudinal distance of 692 cm from the interaction point (near the fourth tracking layer and the front of the calorimeter) is approximately 3.1×10^{11} 1 MeV neutron equivalent per square centimeter for 100 fb^{-1}. At this location the ionizing dose can reach $\sim$ 100 kRad.

Justification

Device concept and technological choice: The charged particle tracker will be composed of four layers instrumented with silicon. The layers are approximately equidistantly placed at distances between 590 and 690 cm from the interaction point, to enable measurement of the protons with resolution $\lesssim$ 6%. The electromagnetic calorimeter is composed of 112 scintillating $PbWO_4$ crystals, each 2 x 2 x 20 cm^3 (the long direction is on the z axis). We note that the crystals are the same as those used in the EEEMCal as discussed in Section 3.3.5.1.

Subsystem description:

General device description: Each tracking layer has a transverse layout to cover as much of the angular acceptance as possible given the mechanical constraints. The transverse geometry of each layer may be very roughly thought of as a ring with inner radius of 5 cm and outer radius of 15 cm, however there is a significant "cut-out" of the ring to accommodate the beam pipe as well as other deviations from the radial geometry due to mechanical constraints inside the magnet. The crystals of the calorimeter are arranged in a similar transverse geometry. A cutaway view of the detectors in the magnet as well the transverse profile (shown for the calorimeter) are illustrated in Figure 3.210.

Sensors: For the tracking detectors AC-coupled low-gain avalanche diodes (AC-LGADs) are chosen for their capability to provide both high-precision space and time information. To meet the momentum resolution performance requirements a spatial resolution of $\sim$20 μm. To

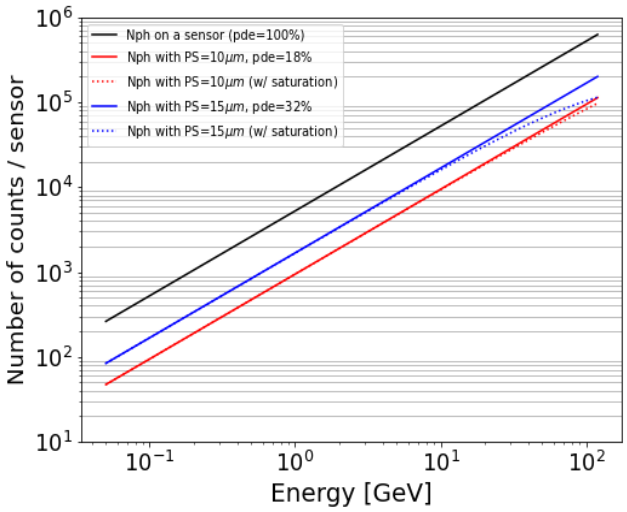

Figure 3.211: A simulation of the expected number of pixel hits for a 6x6 mm^2 SiPM coupled to a $PbWO_4$ crystal as function of the energy of a photon impinging on the crystal. An ideal SiPM response is shown as well as the response of a 10 μm pitch SiPM with 18% photo-detection efficiency and a 15 μm pitch SiPM with 32% photo-detection efficiency (matching the specs of S14160-6010PS and S14160-6015PS). The realistic SiPM responses are shown with and without occupancy effects.

achieve this with the AC-LGADs charge sharing must be implemented in the reconstruction. We note that this technology is broadly in use within ePIC, and its particular implementation for the B0 detectors is very similar to the Roman Pots/Off Momentum Detectors and a more detailed description of the sensors may be found in Section 3.3.7.2. Assuming identical or similar staves as those used in the Roman Pots/Off Momentum Detectors, each tracking layer will be composed of approximately 30 staves with 4 modules per stave. The tiling scheme has not yet been fixed.

For the calorimeter the $PbWO_4$ crystals produce light peaking at $\sim$ 420 nm, which will be read out by SiPMs. Unlike most scintillating crystal calorimeters the light will be read out from the front face of the crystal. Either four 6x6 mm^2 SiPMs or sixteen 3x3 mm^2 SiPMs will be used per crystal. The sensors will be a mixture of 15 μm pitch and 10 μm pitch SiPMs (likely Hamamatsu S14160-6015PS and S14160-6010PS or S14160-3015PS and S14160-3010PS), in a ratio of 3:1. Compared to the higher pitch SiPMs the larger pitch SiPMs have higher efficiency but fewer pixels, and are thus more prone to non-linearity due to occupancy as shown in Figure 3.211. Given this the the smaller pitch SiPMs are appropriate for smaller signals, whereas the smaller pitch SiPM will be utilized for the higher energy particle signals. Using them together provides energy resolution in line with the requirements (as shown in Figure 3.215 below).

FEE: Following the Roman Pots/Off Momentum Detectors, the ASICs will be readout using lpGBT in-place of FPGAs due to the high-radiation environment in which these detector will be located. AC-LGAD + ASIC modules will be connected to the lpGBT, which will be coupled to a VTRX+ to convert the signals to a fiber to send off to the DAW system. The electronics to process the SiPM signal are still to be worked out but expected to follow closely the scheme of the EEEMCal.

Other components: For both detectors the front-end board, power distribution, and cabling schemes are all still in development.

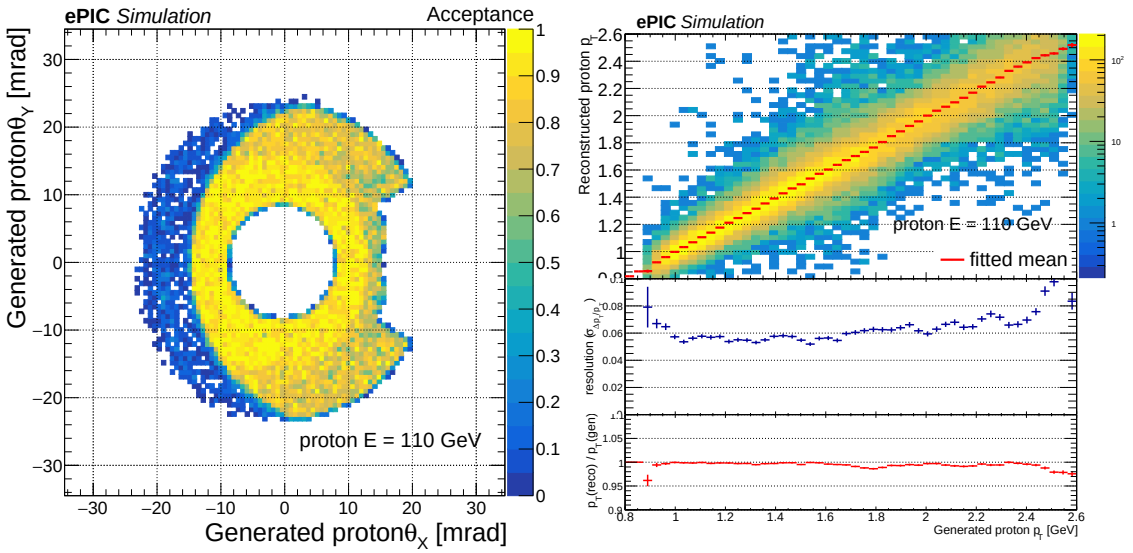

Figure 3.212: Left: The B0 tracker's acceptance of protons (E=110 GeV), as a function of θ_x and θ_y. Right: The top panesl shows the reconstructed vs generated proton p_T. Each slice of this distribution is fit to a Gaussian function and from this fit a resolution (middle panel) and bias (bottom panel) are extracted.

Performance The key physics task of the B0 tracker system is the measurement of protons, and this is summarized by the acceptance and transverse momentum resolution shown in Figure 3.212. We note that the precise longitudinal position and transverse acceptance of each layer is not finalized, and so the figure should be considered a tentative performance estimate. To contextualize the B0 tracker's proton measurements in the larger ePIC context, Figure 3.213 shows the acceptance for forward protons as a function of psuedo-rapidity in the central tracker, B0 tracker, and Roman Pots. The B0 calorimeter's acceptance for photons is shown in Figure 3.214. The calorimeter seeks to measure photons over a very large range. The performance of the detector, in particular the energy resolution, is shown separately for low and high energy photons in Figure 3.215. The higher energy photons are evaluated based on a signal to a single 6x6 mm^2 SiPM with 10 μm pitch, whereas the lower energy photon performance assumes readout of the light using three 6x6 mm^2 SiPMs with 15 μm pitch.

Implementation

Services: For the trackers low voltage (∼3V) and high voltage (∼150V) supplies for the operation of the ASICs and the bias supply, as well as slow controls for the voltages and the DAQ system. We assume The SiPM for the calorimeter need a bias of (∼5V) .The cooling system is still to be worked out, but is expected to be air based (unlike the in-vacuum challenge of similar instrumentation for the Roman Pot/Off Momentum Detectors). Temperature stability

Subsystem mechanics and integration: The integration of the detectors into the B0 magnet bore is a significant undertaking. The space for the detectors (and services) is quite limited and the installation procedure introduces more constraints. After the vacuum valve is closed there is only about 10 cm of clearance in front of the magnet and this precludes installation of the 20

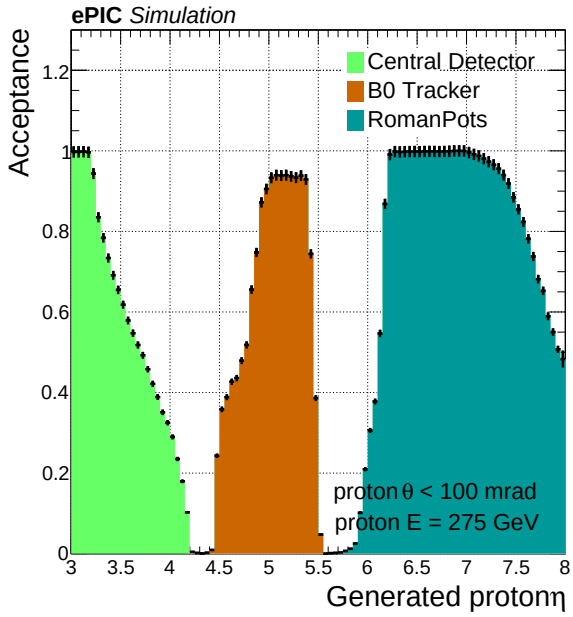

Figure 3.213: Proton acceptance as a function of η spanning the central tracker, B0 tracker, and Roman Pots.

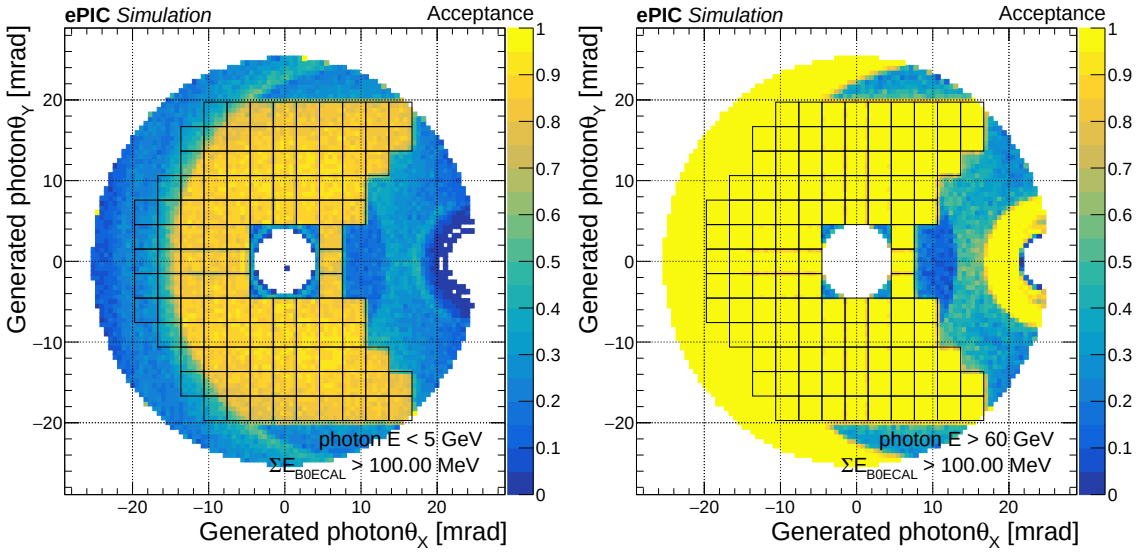

Figure 3.214: The B0 EM calorimeter's acceptance of photons shown for soft (less than 5 GeV) and hard (greater than 60 GeV) photons. Acceptance is defined as more than 100 MeV deposited in the calorimeter. The position of the calorimeter crystals is indicated as a grid. The un-instrumented regions which nevertheless high nominal acceptance, correspond to upstream interactions whose shower products are visible in the B0 calorimeter.

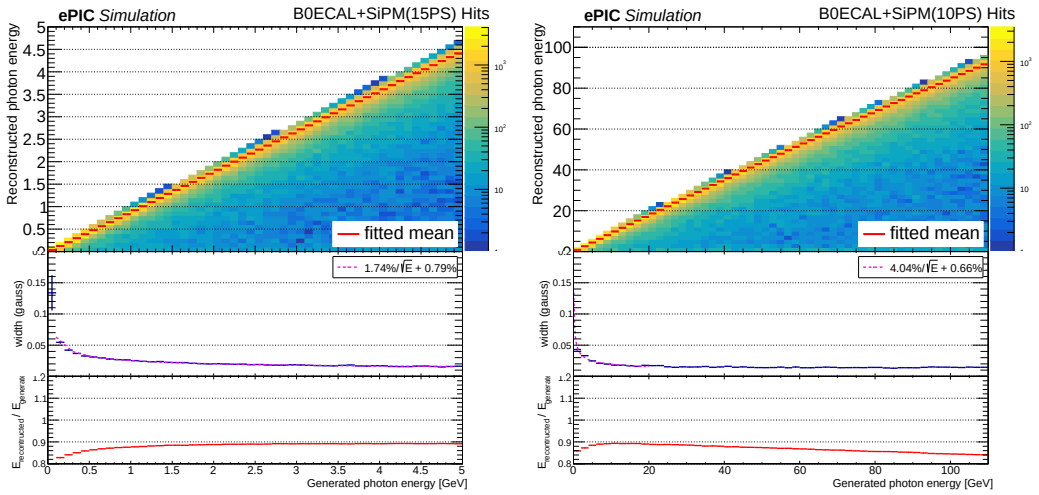

Figure 3.215: The energy reconstructed and associated resolution for the B0 EM calorimeter of photons with $\theta < 13$ mrad in the soft (left) and hard (right) energy reconstruction regimes. The top panels show the reconstructed photon energy vs the generated energy. Each slice of this distribution is fit to a Gaussian function and from this fit a resolution (middle panels) and energy scale shift (bottom panels) are extracted.

cm crystals. To address this difficulty, the crystals -themselves less radiation delicate than other components - will be installed prior to the valve closing and the beam commissioning. At this point *only* the crystals will be installed to avoid the risk of damaging other components during the commissioning. The crystals themselves are Following this, the SiPMs and electronics of the calorimeter will be installed. Both installations, as well as the final positioning of the detectors, will be via a rail system: detector components will be loaded onto the rails system outside the magnet and inserted in to it. We note that each tracking layer and the calorimeter is composed of multiple components installed individually.

Calibration, alignment and monitoring: During operation an in-situ calibration based on pions and/or rho mesons will be employed. The calorimeter will utilize LED signals shined onto the crystals and a thermistor, both integrated into the front end board, for monitoring.

Status and remaining design effort:

R&D effort: There is still work to be done for full detector operation. For the trackers especially, demonstrating effective reconstruction using charge sharing and for the calorimeter the multi-SiPM readout. For both the trackers and calorimeter this includes optimizing the acceptance in concert with the installation procedure.

E&D status and outlook: Engineering design is still very preliminary, but necessary design choices are being evaluated as engineering support becomes available. A full thermal and mechanical study is still needed for both detectors.

Other activity needed for the design completion: Completion of the mechanical rail system and an installation procedure is underway. For both the tracker and the calorimeter the front

end electronics are still being finalized (with as much overlap as possible with other subsystems).

Status of maturity of the subsystem: Both detectors in the subsystem have (intentionally) large overlap with other subsystems and the maturity of the B0 detectors thus follow to a large extent this common development. There are, of course, particulars of the implementation for the B0 detectors and these are progressing in line with the shared development.

Environmental, Safety and Health (ES&H) aspects and Quality Assessment (QA planning): The detectors placement inside the magnet bore as well as the staged installation procedure will require somewhat special considerations for integration with the accelerator complex. All the detector component and services must be coordinated with the magnet.

Construction and assembly planning: The tracking system should benefit from the local BNL expertise, production capabilities for AC-LGAD, and from there 'directly' to installation readiness. The calorimeter sub-components may be prepared either on or off site, but in any case the final assembly can not be separated from the installation procedure.

Collaborators and their role, resources and workforce: The Israeli ePIC consortium, in particular BGU and TAU, are playing the main role in the detector development and this will continue through installation and operation. Both the BGU and TAU groups have one PI, several graduate students and postdocs expected to contribute. Local resources in both groups allow in lab testing but not significant fabrication capabilities. There is also very significant participation from BNL generally and especially for the common AC-LGAD instrumentation.

Risks and mitigation strategy: For the trackers the largest risk is the necessity to utilize charge sharing in the reconstruction to obtain the needed momentum resolution. Other detection technologies have been considered to mitigate this risk (with smaller pixels) but to this point none have been identified as an appropriate alternative. For both detectors, and even more acutely for the calorimeter, the installation challenge risks limiting the detector acceptance.

3.3.7.2 The roman pots and the off-momentum detectors

Requirements

Requirements from physics: The Roman pots (RP) and off-momentum detector (OMD) subsystems are both intended to tag far-forward protons and reconstruct their momenta. These detectors are based on the same technology and are implemented in a very similar way, so throughout this subsection they will often not be differentiated unless an aspect of the discussion is specific to one of the two subsystems.

Measurement of protons with scattering at angles < 5 mrad requires tracking detectors integrated directly into the outgoing hadron beamline. In previous and current experiments, silicon detectors meeting these basic criteria have been implemented in the form of Roman pots (RP) subsystems, and the EIC will take a similar approach. However, since the EIC will also aim to tag and reconstruct protons which arise from the breakup of light nuclei (deuterons, helium-3, etc.), another

set of silicon detectors which are optimally placed for capturing these protons is required. These off-momentum detectors (OMD) enable tagging and reconstruction of spectator protons whose momentum is significantly smaller than that of the hadron beam itself. We classify the various far-forward protons based on their magnetic rigidity, which determines their trajectories through the seven magnets (four dipoles for bending/steering; three quadrupoles for focusing) between the interaction point and the drift region where the RP and OMD systems are located. For the sake of simplicity, the ratio of the longitudinal momentum of the proton with the total momentum of the beam itself is used to determine if the proton is within the RP or OMD fiducial acceptance, and defined as $x_L = p_{z,proton}/p_{beam}$. As an example, a proton from the breakup of a deuteron has an $x_L \sim 50\%$, on average. The RP acceptance is for $x_L > 65\%$, while the OMD covers a region between $25\% \lesssim x_L \lesssim 65\%$, with the lower bound being determined heavily by the scattering angles in question, since low-x_L particles will not follow the design beam orbit and will often be lost in the magnets before reaching the OMD. The RP and OMD are placed to have a small overlap in x_L to aid in alignment of the detectors, and calibration of the matrices used to reconstruct the particle's momentum. Figure 3.216 shows and illustration of the proton envelopes relevant for the RP and OMD placement.

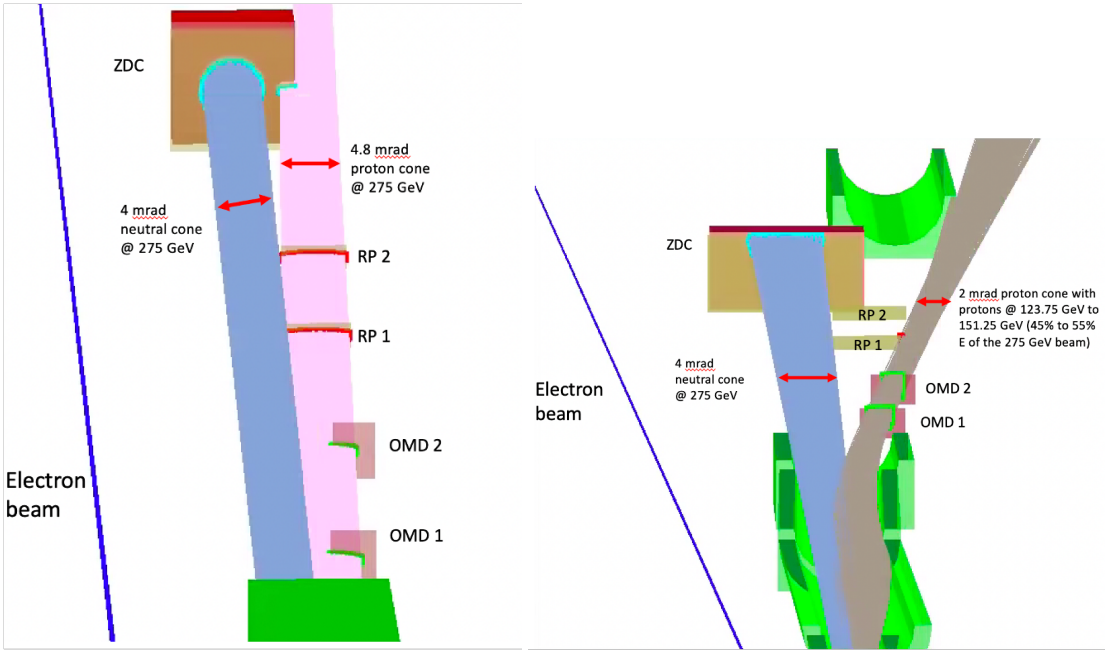

Figure 3.216: Depiction of the envelopes from protons with $x_L \sim 1.0$ (left) and with $x_L \sim 0.5$ (right). The RP and and OMD systems are placed to obtain an almost-continuous acceptance of protons across a broad range of proton rigidities.

A particular challenge for the Roman pots (true for any Roman pots detector) is achieving acceptance down to 0 mrad (or, $x_L = 1.0$). This is impossible due to the presence of the hadron beam itself, so the low-θ (low-p_T) acceptance is essentially entirely driven by the focusing quadrupoles (driven by the choice of machine optics) before and after the interaction point. If the RP sensor planes approach too close to the core of the beam, they would see an extremely high particle incidence and be rapidly damaged (the beam itself would also not be able to operate with the detectors that close to the beam core).

For IP-6, the choice of low-β^* optics to maximize luminosity (so-called "high divergence") means

the transverse beam size, $\sigma_{x,y} \approx \sqrt{\beta_{x,y}(z_{RP}) \times \epsilon_{x,y}}$, where $\beta_{x,y}(z_{RP})$ are the beta-functions in (x,y) at the Roman pots location and $\epsilon_{x,y}$ is the emittance for the machine, is larger, providing maximal luminosity at the expense of lowp_T acceptance at the Roman pots. Generally, $10\sigma_{x,y}$ is the average "safe distance" for the Roman pots to operate and is used as the assumed "nominal" position for data-taking, although this distance is adjusted based on operation beam conditions, in reality. For reference, at the top hadron beam energy, these translate to $10\sigma_x = 1.6$ cm and $10\sigma_y = 0.27$ cm. Conversely, a choice can be made to reduce luminosity to improve low-θ (low-p_T) acceptance at the Roman pots location, normally referred to as "high acceptance" optics. Given this set of operational parameters for the machine itself, it is required that the sensor packages have minimal dead area at the edges to take maximum advantage of the machine optics during data taking runs.

It should be noted that the OMD don't suffer from the same trade-off between luminosity and acceptance, because they are centered on the location for a $x_L = 0.5$ proton with a 0 mrad scattering angle, which places them at more than 20σ from the core of the beam. This means that off-momentum protons can be tagged at 0 mrad (or, $p_T = 0.0$ GeV/c), allowing for tagged-DIS measurements to be carried out to arbitrarily low-p_T.

For momentum resolution, the detectors must deliver p_T-resolution better than 10% for $p_T \sim 1$ GeV/c. These requirements are detailed on the EIC Wiki page [114], along with numerous links to supporting studies done for ePIC.

Requirements from Radiation Hardness: Maximal radiation doses for the RP and OMD are shown to be $< 10^8$ cm^{-2} 1 MeV neutron equivalent for NIEL fluence per fb^{-1} of integrated luminosity, while total ionizing doses are $\sim 10 - 100$ Rads for the same integrated luminosity, for a combination of minimum-bias and hadron beam+gas events. It should be noted that these numbers do not include estimates from the hadron beam halo, as no simulations are yet available to study the impact of this source of background. These doses and fluences are far below the operating limits of the AC-LGADs, but these doses and rates will need to be assessed further with simulations that can approximate the beam halo.

Requirements from Data Rates: Rates during normal operations, with expected vacuum of 10^{-9} mbar, are a few Hz/channel. However, the beam halo could potentially provide rates of 30-50kHz at $\sim 10\sigma$ from experience of Roman pots at STAR. While the EIC hadron beam will have many differences to the RHIC hadron beam, it's hard to estimate the full rate impact of the beam halo without an appropriate simulation. This is something to be done in the coming year as the machine develops.

Justification

Device concept and technological choice: The basic concept of Roman pots detectors for measuring protons near the beam is not new and has been employed at HERA, RHIC, and the LHC, among other collider facilities. In the case of the EIC, the Roman pots (and OMD) need to be able to make measurements with challenges different to those in previous facilities. Studies from the EIC generic R&D program [115], in particular eRD24, demonstrated that the RP detectors need to have both high spatial ($\sim 140\mu$m) and timing ($\sim$35ps) resolutions, a challenge to deliver with one subsystem. In previous studies, the beam effects (e.g. angular divergence, beam-momentum spread, vertex smearing from crab cavity rotation) were shown to be the dominant source of smearing for momentum reconstruction. The spatial resolution requirement for the RP and OMD is chosen such

that when the effects are separated and added in quadrature, the smearing coming from the detector spatial resolution is subdominant. It should also be noted that there are various different optical configurations for the machine, as noted above, and as the smearing components driven by the beam are decreased, the detector-driven portion becomes dominant and can be a limiting factor for momentum reconstruction. This is something unique to the beamline detectors, where normally negligible beam smearing effects become a major factor impacting momentum reconstruction. Finally, the B0 tracking system has the most-stringent requirement for spatial resolution to meet the physics requirements, and the RP and OMD need to use the same sensor as the B0 to ensure efficient cost savings and the ability to use the same ASIC for reading out the sensor.

The silicon detector technology which meets our requirements is the AC-coupled low-gain avalanche diode (AC-LGAD), an evolved version of the DC-coupled Low Gain Avalanche Diode (DC-LGAD) sensor, normally used for high-resolution timing detectors. The AC-LGADs allow for finepixilization and can meet the requirements of the RP and OMD subsystems, as was the goal of eRD24.

An additional challenge with operation of the RP and OMD systems is the usage of these detectors in vacuum. The subsystems themselves are large enough to prohibit use of the conventional "pot" vessels used to protect the detectors in other colliders, and therefore necessitate the inclusion of the sensor planes directly into the machine vacuum, providing unique challenges for cooling and shielding.

Subsystem description:

General device description: The Roman pots and off-momentum detectors are both vacuum-based silicon sensors arranged into two stations for fully reconstructing protons at various magnetic rigidities, where rigidity here refers to the fraction of the momentum the proton has with respect to the steering dipoles design orbit momentum.

Sensors: AC-LGADs are the technology of choice for these two subsystems due to their capability to provide both high-precision space and time information [40]. These sensors were originally introduced into the EIC efforts with an expected application to beamline detectors.

FEE: ASICs will be readout using low-power gigabit transceivers (lpGBTs) in-place of FPGAs due to the high-radiation environment in which these detectors will be located (as stated aboved, the radiation doses calculated are based collision rates, not on the beam halo and other backgrounds which are not yet simulated). Up to sixteen AC-LGAD + ASIC modules will be connected to a single lpGBT, which will be coupled to a VTRX+ to convert the signals to a fiber to send off to the data acquisition system. The stave design is aimed to have a minimal amount of components inside the vacuum to ensure smooth operations and ease of access during maintenance periods.

Other components: Design of the front-end board and power distribution is still in a very early stage for the RP and OMD systems. The current plan is to reuse as much of the design for the forward time-of-flight as is possible to reduce costs.

Performance The performance of the Roman pots and Off-Momentum Detectors is summarized in Fig. 3.217. The overall momentum resolution is also affected by the detailed understanding of the hadron magnet lattice, which is used to be able extract the normal transfer matrices used to reconstruct momenta in Roman pots detectors. There is also a software solution in place using deep neutral networks to further improve the momentum resolution performance, especially for

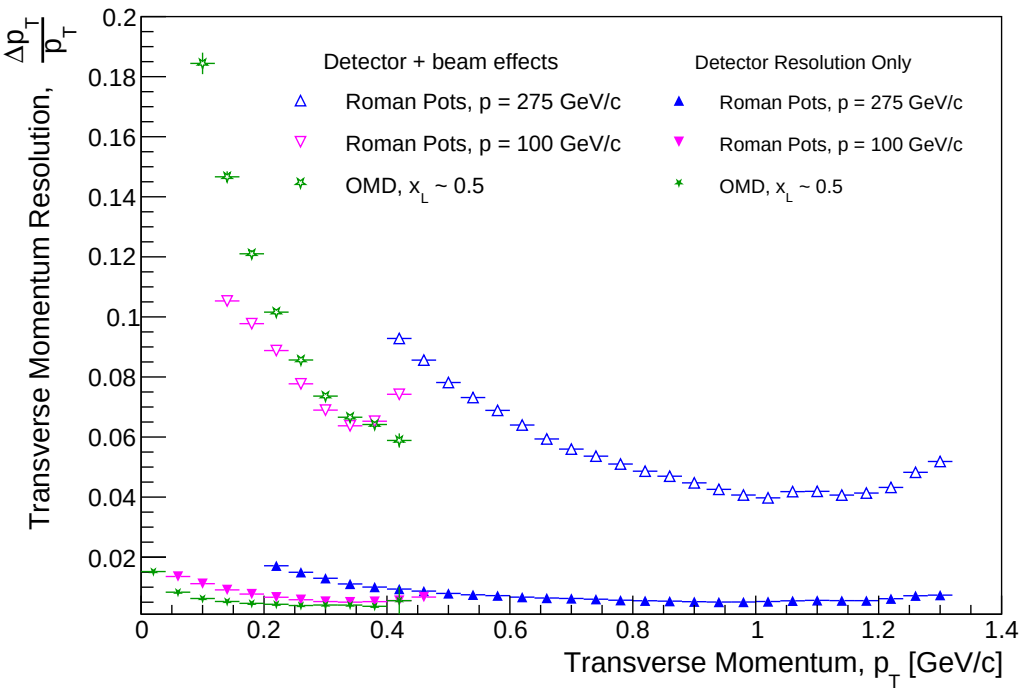

Figure 3.217: Summary of transverse momentum resolutions for the Roman pots and off-momentum detectors using stand-alone detector simulations. Contributions are separated by those induced by intrinsic detector choices (e.g. pixel sizes) and those from beam effects (e.g. angular divergence), which have an outsized impact on momentum measurements at very-forward rapidity.

the off-momentum detectors. This solution is presently being integrated into the ePIC software framework.

Implementation The basic detector component will be a "stave" which contains 3 "modules" consisting of bump-bonded AC-LGADs and ASICs attached to a PCB, arranged in a 1x3 layout with modules on either side of the PCB to enable partial transverse overlap of the sensors to cover the dead area at the edges (e.g. guard ring location). The staves only contain the sensors and ASICs, plus cooling services, with all other services coming from a readout board placed outside the vacuum which contains the lpGBT and VTRX+ components and power distribution. The details of the this concept still need to be properly worked out with engineering support, but strawman versions of these concepts can be found in Figs. 3.219 and 3.220. A full layout of the sensors in the 1x3 stave configuration is shown in Fig. 3.221, while the DD4HEP implementation for the "high acceptance" optics configurations for the three proton beam energies is shown in Fig. 3.222. The RP and OMD subsystems will both be immersed directly into the machine vacuum to maximize acceptance and minimize impact to the machine. This technically makes the name Roman pots incorrect to describe these detectors, since they are literally potless tracking systems operating in vacuum.

The OMD system will be much simpler than what is needed for the Roman pots, with the staves

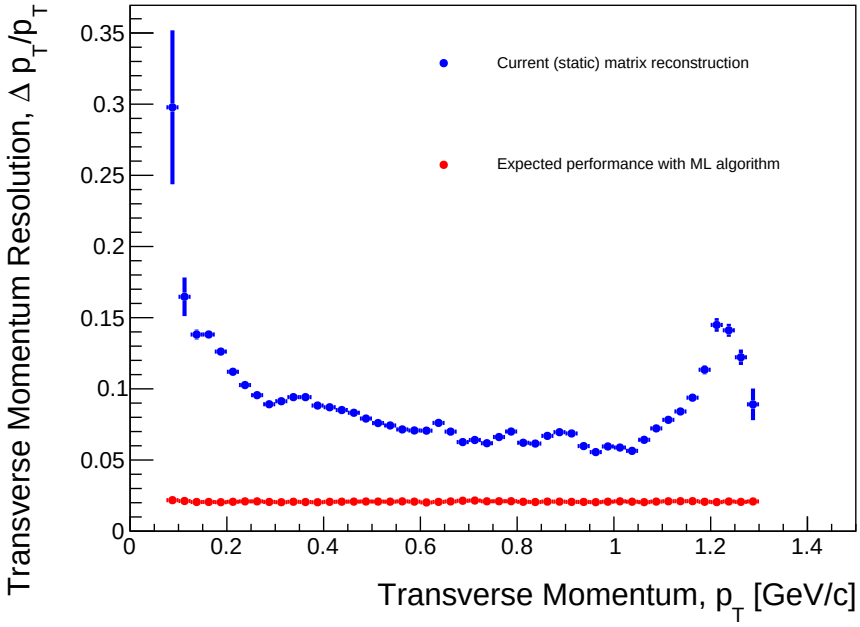

Figure 3.218: Transverse momentum resolution for Roman pots using the full ePIC simulation framework. This plot is from the ePIC framework, where Fig. 3.217 shows performance from standalone simulations which include beam effects and optimized matrix reconstruction, shows both the nominal performance with the current reconstruction algorithm (in blue), and (in red) the expected improvement from the machine learning model which has been developed and tested in standalone simulations. This ML algorithm (based on deep neural networks) is currently being implemented in ePIC. A presentation on this work and the resulting performance of the model was presented at the Deep-Inelastic Scattering conference in 2023 [3]. Work is underway to integrate this model into the ePIC framework for RP and OMD reconstruction.

arranged into a rectangle with the dimensions 10cm x 20cm and insertsed horizontally into the vacuum of the beamline.

Services: The Roman pots and OMD have the same essential needs for services, which include cooling using conductive strips coupled to an external chiller to allow cooling in-vacuum, low voltage (∼3V) and high voltage (∼150V) supplies for the operation of the ASICs and the HV bias supply for the sensor, and slow controls to control both voltages and the DAQ system, and also to control the moving stages necessary for the detector operations. There will also need to be communication between the slow controls and the machine for safety interlocks for fast beam abort systems, and for permits to enable motion control of the detectors when beam conditions are stabilized.

Subsystem mechanics and integration: The primary support systems only need to be able to support very light staves with 3-4 modules per PCB. However, the entire subsystem needs to be on a motor-driven rail system to enable movement near the hadron beam, especially in order to achieve acceptance at very low $p_T \sim 0.2$ GeV/c.

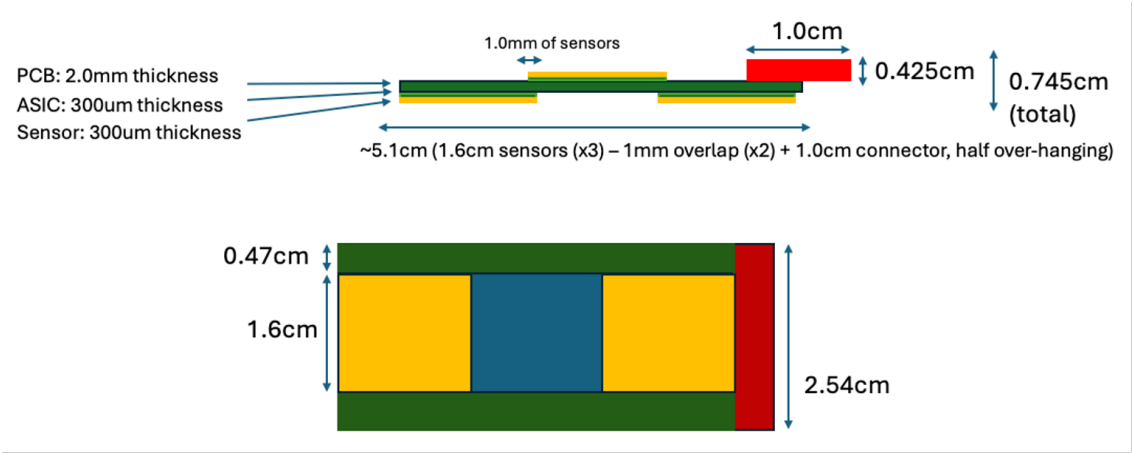

Figure 3.219: Strawman concept for the layout of the RP and OMD sensor staves. Work is ongoing to get the necessary electronics engineering support to design the final PCB. The connector on the end of the PCB is presently assumed to be a TE connectivity Erni 354096-E 32 pin serial connector. Work is still needed to understand how to apply thermal cooling to the staves without using compressed gases or liquids (not allowed in the primary machine vacuum). Presently, cooling plates/heat sinks which are thermally coupled to outside the vacuum and cooled with an LN2 chiller are assumed, but only preliminary thermal analysis has been carried out.

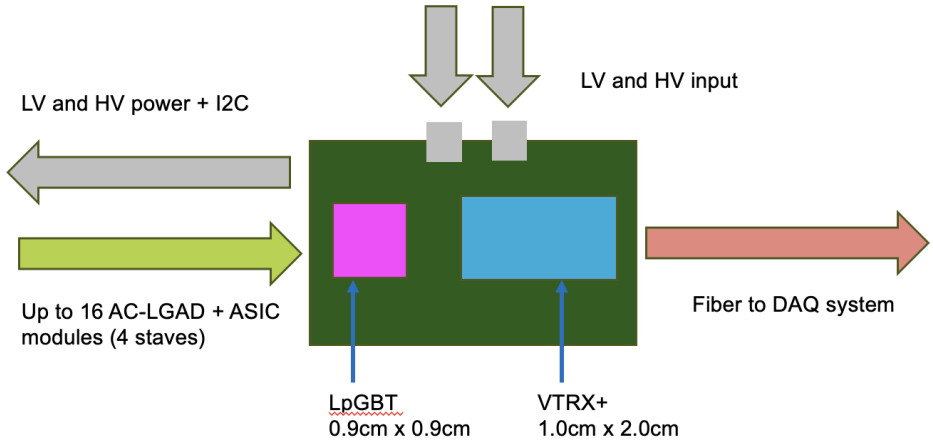

Figure 3.220: Strawman concept a readout board concept to communicate with and readout RP and OMD sensor staves. Work needs to be done to solve the issue of power distribution, and to ensure the EICROC ASIC can indeed be readout by the lpGBT.

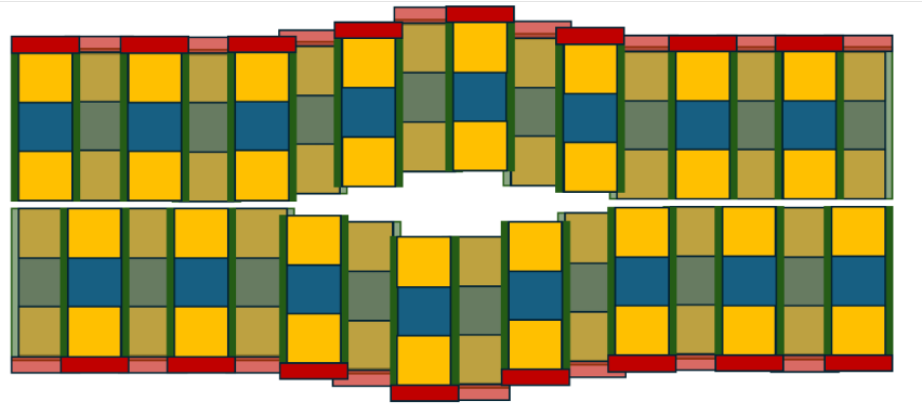

Figure 3.221: Current layout of a single RP layer using a 1x3 stave configuration, with the staves following the concept shown in Fig. 3.219. This configuration leads to a full detector layer with dimensions $\sim$ 26cm x 10cm, with some work to be done to finalize the exact amount of overlap between individual staves to provide uniform acceptance in the transverse plane.

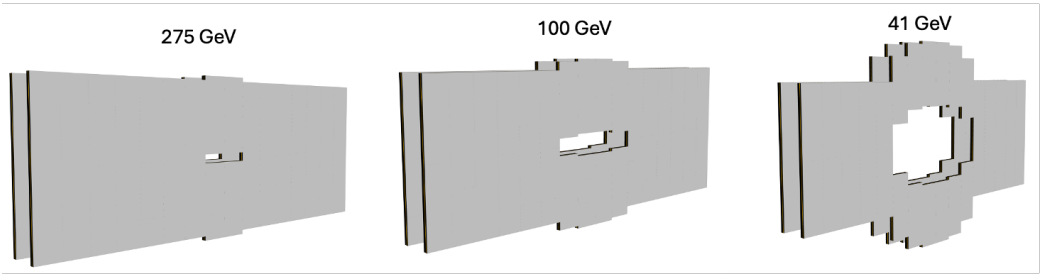

Figure 3.222: Depiction of the location of the RP sensor packages for the three different "main" EIC hadron beam energies, all in the optics configuration with the maximal low-p_T acceptance. Optimization of the stave layout and movement stages is still underway to ensure best fiducial acceptance.

Calibration, alignment and monitoring: AC-LGAD sensors will be calibrated with MIPs, while alignment of the detector systems will need to be carried out using beam-based alignment with dedicated, short, very-low luminosity runs, which enable the detectors to approach the beam much closer than the standard 10σ distance such that the beam halo itself can be seen on the sensor planes. This, combined with conventional survey information used to align the motion system to the machine should enable alignment at a level much less than 1mm, where 1mm is the minimum precision required to avoid introducing additional smearing effects competitive with those from other sources.

Status and remaining design effort:

R&D effort: Much work is still needed to demonstrate full system operations with full size sensors + ASICs, and the cooling concept using conductive strips. As of now, only 4x4 channel versions exist and have been tested, but 32x32 channel versions of the ASICs necessary to perform tests of AC-LGADs with the same channel count are expected in Fall 2025. These

versions will not have the fully optimized digital backend or power consumption, but will still enable most of the tests needed for necessary design maturity, and will allow for close to final design of the carrier PCB for the sensor modules to be completed.

E&D status and outlook: Engineering design is still very preliminary, but necessary design choices are being evaluated as engineering support becomes available. This is especially needed for the stave design to carry the sensor modules, and for the support substrucutre and cooling for both subsystems.

Other activity needed for the design completion: The design of the front-end PCB which carries the sensors, ASICs, and necessary services needs to be carried out. Presently, only a strawman concept which will meet our requirements exists.

Status of maturity of the subsystem: The design of the RP and OMD subsystems are aimed for 60% design maturity by end of calendar year 2025. The main components which need to be developed to realize that timeline are the PCB design for the stave, a cooling solution for the staves, and more-advanced design of the vacuum system and support structure for the two subsystems. The first two items are already in-progress, while the final item is in-progress, but still needs several iterations, as it does not concern just the RP and OMD subsystems, but also the HSR machine design in that region 30 meters from the IP.

Environmental, Safety and Health (ES&H) aspects and Quality Assessment (QA) planning: Since these detectors are embedded directly into the machine vacuum, special considerations must be made for integration with the machine. We expect that the detectors will be interlocked against operation until permits are received from the machine, pending stable operations of the machine in terms of stable beam losses, collisions at the IP, and background conditions. The cooling system will also have to be integrated with the machine envelope, which requires coordination with the machine group.

Construction and assembly planning: AC-LGAD sensors and EICROC ASICs will be manufactured in different foundries, but bump-bonding of the sensors + ASICs can be done for the far-forward subsystems at BNL, since these detector subsystems are very small compared to other ePIC subsystems. The assembly will have to take place in stages which include the following steps. First, preparation of stave PCBs will be carried out, which will include the production of the bump-bonded sensor + ASIC assemblies, adhesion of these modules to the PCB, and the wire-bonding of the ASICs to the pads on the PCBs. Each stave will then need to be integrated into the support structure for the RP and OMD detector layers, and tested. These final modules would then be installed into the respective motor-driven insertion systems for usage. It should be noted that these detectors will not be installed on "day one" since the machine will need to be commissioned and stabilized before detectors approaching so close to the beam can be installed and tested safely.

Collaborators and their role, resources and workforce: BNL and JLAB will take the primary role in constructing the Roman pots and off-momentum detectors, with engineering support for cooling design supplied by IJCLab in France. The RP and OMD subsystems will leverage the work on AC-LGAD development which originated from efforts to apply this technology to these detectors (EIC generic R&D project 24), and have grown to include applications to time-of-flight subsystems and generic particle tracking in ePIC. The larger AC-LGAD effort covers several subsystems, and includes work from collaborators from Los Alamos National Laboratory, Hiroshima University, Rice University, the Univseristy of Illinois at Chicago, Lawrence Berkeley National Laboratory, and the University of California at Santa Cruz. While these groups will not participate

in the construction of the RP and OMD subsystems, they are instrumental the overall AC-LGAD efforts. The work on the EICROC ASIC development is lead by OMEGA and IJCLab in France, and testing is done by all institutions listed.

Risks and mitigation strategy: The primary risks to the successful construction of the Roman pots and OMD are late receipt of the final 32x32 channel EICROC ASICs and issues with the bump-bonding and construction of the final staves. These risks are fairly minor given the large interest in in successful implementation of AC-LGADs in ePIC, and given the small size of the RP and OMD subsystems. Much of the contruction work can take place with a small laboratory space at BNL. There are additional risks related to machine integration, which are hard to fully quantify at the present moment, but will be better understood in the coming year (e.g. operating and cooling the detector in the machine vacuum). These risks are all under evaluation and work is being done to develop studies to identify solutions to outstanding problems.

Additional Material Extra details, including links to numerous studies on aspects of the far-forward detectors can be found on the ePIC Wiki page [114] for the far-forward detectors. This material is being migrated to the ePIC Zenodo page.

3.3.7.3 The Zero Degree Calorimeter

Requirements

Requirements from physics: The ZDC must achieve energy and polar-angle resolutions for neutron showers better than $50\%/\sqrt{E}$ and $3\,\text{mrad}/\sqrt{E}$ as specified in the Yellow Report [116]. For electromagnetic showers, it must achieve $20\%/\sqrt{E}$ resolution [117,118]. The ZDC also needs to tag photons in the $\mathcal{O}(10\text{–}100\,\text{MeV})$ range in eA collisions.

These requirements originate from the extensive physics program enabled by the ZDC in ep, ed, eH^3 and eA collisions that need measurements of neutral particles such as neutrons, photons, neutral pions, neutral lambda baryons, and other neutral mesons and baryons at near-zero polar angle with respect to the hadron beam. Table 3.70 summarizes the reactions that yield these signatures; they are briefly discussed below.

Reactions in ep collisions that produce signals in the ZDC include various channels. The highest cross sections are for inclusive processes involving leading neutrons (e.g., $ep \to eXn$), which were measured at HERA to be about 10% of all DIS events [119]. Leading neutrons can originate either from scattering off the pion cloud (the Sullivan process) or from regular beam fragmentation in DIS, which serves as a background to the Sullivan process that probes pion structure.

In contrast, inclusive Lambda production ($ep \to eX\Lambda^0$), predicted to have a cross section about five times smaller than that of leading neutrons, can probe the kaon cloud and enable measurements of kaon structure, although target fragmentation in DIS also contributes to the inclusive reaction. The Lambda channel was not measured at HERA.

Channels with lower cross sections include exclusive processes such as deeply exclusive meson production (DEMP), e.g., $ep \to e\pi^+ n$ and $ep \to eK^+\Lambda(n\pi^0)$; backward u-channel DEMP (e.g., $ep \to e\pi^0 p$); and DVCS ($ep \to e\gamma p$) [117,118].

Table 3.70: Examples of reactions that yield high-energy neutral particles within the ZDC acceptance. In each case, the leading particle's energy and polar scattering angle are used to constrain the Mandelstam variables t or u. The azimuthal angle can also be exploited for spin-dependent modulation measurements and for studying Λ^0 polarization and deuteron structure. While these reactions are labeled as having an electron in the final state, it should be understood that they can correspond to either the electroproduction (large Q^2) or photoproduction ($Q^2 \approx 0$) regime. The references provided are representative of the literature discussing the corresponding channel, although they do not constitute an exhaustive list.

Name	Refs.	Reaction	Signal in ZDC	E of interest
Inclusive leading n	[119–121]	$ep \to eXn$	n	10–275 GeV
Inclusive leading γ	[122]	$ep \to eX\gamma$	γ	10–275 GeV
Inclusive leading Λ	[123]	$ep \to eX\Lambda$	$\Lambda^0 \to n\pi^0 \to n\gamma\gamma$	10–275 GeV
t-channel DEMP	[116]	$ep \to e\pi^+ n$	n	10–275 GeV
	[124]	$ep \to eK^+\Lambda^0$	$\Lambda^0 \to n\pi^0 \to n\gamma\gamma$	10–275 GeV
	[124]	$ep \to eK^+\Sigma^0$	$\Sigma^0 \to \Lambda^0\gamma \to n\gamma\gamma\gamma$	10–275 GeV
u-channel DVCS	[118]	$ep \to e\gamma p$	γ	10–250 GeV
u-channel DEMP	[118]	$ep \to e\pi^0 p$	$\pi^0 \to \gamma\gamma$	10–275 GeV
	[117]	$ep \to e'\omega^0 p$	$\omega^0 \to \gamma\gamma\gamma$	10–275 GeV
Sullivan DVCS off π^+	[125]	$ep(\pi^+ n) \to e\gamma\pi^+ n$	n	10–275 GeV
Sullivan DEMP off π^+	[125,126]	$ep(\pi^+ n) \to e\rho\pi^+ n$	n	10–275 GeV
	[127]	$ep(\pi^+ n) \to e\phi\pi^+ n$	n	10–275 GeV
	[127]	$ep(\pi^+ n) \to eJ/\psi\pi^+ n$	n	10–275 GeV
Sullivan DIS dijet off π^+	[128,129]	$ep(\pi^+ n) \to ejjXn$	n	10–275 GeV
CC DEMP	[130]	$ep \to \nu_e\pi^0 n$	n	10–275 GeV
n-tagged DIS	[131]	$ed \to eX(n_s)$	n (spectator)	10–135 GeV
Di-tagged J/ψ	[132]	$ed \to eJ/\psi pn$	n (active or spectator)	10–135 GeV
Di-tagged DVCS	[132]	$ed \to e\gamma pn$	n (active or spectator)	10–135 GeV
p-tagged DEMP	[133]	$ed \to e\pi^0 n(p_s)$	n (active)	10–135 GeV
		$ed \to eK^0\Lambda^0(p_s)$	Λ^0 (active)	10–135 GeV
n-tagged DEMP	–	$ed \to e\pi^+ n(n_s)$	$2n$ (active and spectator)	10–135 GeV
	–	$ed \to eK^+\Lambda^0(n_s)$	Λ^0 (active) and n (spectator)	10–135 GeV
Quasi-coherent J/ψ	[134]	$eA \to eA^* J/\psi$	γ emission from A^*	$\mathcal{O}(100)$ MeV
Incoherent J/ψ	–	$eA \to eXJ/\psi$	n and γ de-excitation	$\mathcal{O}(100)$ MeV to $\mathcal{O}(100)$ Ge
eA DIS (centrality)	–	$eA \to eX$	Spectator neutrons	$\mathcal{O}(1)$ TeV

For all these measurements, the ZDC must provide a standalone determination of the energy and angle of the particle in question, which is used to constrain the Mandelstam variables t or u.

A parallel set of measurements to those described above can be carried out with deuteron beams to probe e.g. neutron structure. This relies on the "spectator tagging," technique. For example, inclusive DIS on a deuteron with spectator tagging [131] can be performed with proton tagging (in trackers) to yield "free-neutron" structure measurements, albeit with theoretical extrapolations. This method can be validated by the neutron-spectator case, which yields "free-proton" struc-

ture measurements that can be compared with proton-beam data. Neutron tagging requires the ZDC: measurements of the spectator neutron constrain the proton's momentum in the deuteron-rest frame, and low-momentum configurations approximate a "free-proton" structure. Differential measurements at higher neutron momentum select specific nucleon configurations or studies of short-range correlations and modified bound-proton structure, which also serve as references for studies in eA scattering.

Similarly, spectator tagging with deuteron beams can be used for diffractive or exclusive channels. In the method of Tu et al. [132], a "double-tagging" approach is proposed in which both the proton and the neutron from the deuteron breakup are measured to reconstruct t. This is necessary because, unlike in a proton beam, the incoming momentum of the proton bound in a deuteron is not known from the beam momentum. For example, Tu et al. apply this method to study incoherent diffractive J/ψ production off a deuteron, with either a proton or neutron spectator. They further argue that it can be used to study incoherent DVCS off a deuteron—probing bound neutron or bound proton structure depending on which nucleon is the spectator. A conceptually similar approach, with both proton and neutron tagging, was first performed by the CLAS collaboration to study neutron DVCS [135]. The same concept of double-tagging could be extended to DEMP off a neutron with proton spectator, which in the neutral-meson channels (π^0, K^0, etc.) yields neutron signals in the ZDC [133].

The ZDC has also an important role as veto detector for the study of production of exclusive vector mesons in diffraction processes from eA collisions. For the coherent processes, where the nucleus remains intact, the t- dependent cross section can be related to the transverse spatial distribution of gluons in the nucleus, which is sensitive to gluon saturation. In this case, however, the coherence of the reaction needs to be determined precisely. Incoherent events can be isolated by identifying the break-up of the excited nucleus. The evaporated neutrons produced from the break-up in the diffraction process can be used in about 90% of the cases to separate coherent processes. In addition, photons from the de-excitation of the excited nuclei can help identify incoherent processes even in the absence of evaporated neutrons. Therefore, to identify coherent events over a wide t range, neutrons and photons must be accurately measured near zero degrees.

An interesting limiting case that bridges coherent and incoherent diffraction is the "quasi-coherent" process, in which the final-state nucleus remains intact but is excited and then de-excites via photon emission [134]. In the nucleus rest frame, these photons have very low energies ($\mathcal{O}(1)$ MeV or lower), but the Lorentz boost to the laboratory blue-shifts them to $\mathcal{O}(100)$ MeV—within the range measurable by the crystal section of the ZDC. Tagging specific photon energies (i.e., γ-spectroscopy) could identify the lowest excited states and thus link coherent and incoherent measurements. This process lies beyond the traditional Good–Walker paradigm and is currently in theoretical limbo [134]. Moreover, in principle, γ-spectroscopy could support additional programs in nuclear fragmentation studies.

Another key role of the ZDC is to measure the number of spectator or evaporated neutrons from eA DIS. Each of these neutrons carries similar energy (around 110 GeV for the case of 250 GeV Pb beam). Thus, overlapping showers from several or even dozens of neutrons can produce large energy depositions, reaching up to the TeV scale. These measurements can be used to constrain the geometry of the collision, which is important for understanding the characteristics of each event in eA collisions. It has been proposed that collision geometry can be studied by tagging it with the multiplicity of forward neutrons emitted near zero degrees. Determining the geometry of the collision, such as the "travel length" of the struck partons in the nucleus, which correlates with the impact parameters of the collision, is very useful in the study of nuclear matter effects. Determining the geometry of the collision will allow us to understand the nuclear structure with greater accuracy.

Requirements from Radiation Hardness: In the ePIC radiation doses and particle fluences, the ZDC neutron fluence is smaller than 10^{12} 1-MeV equivalent neutron/cm^2 for 6 month operation. At this fluence degradation may occur for crystals due to radiation. The SiPMs are expected to suffer a considerable increase in the dark current [136]. This consideration is addressed in the design, which ensures adequate light yield for an acceptable signal-to-noise ratio and allows for high-temperature annealing of SiPMs to mitigate neutron fluence effects [136].

Requirements from Data Rates:

Justification

Device concept and technological choice: The ZDC system consists of two subsystems: a crystal calorimeter and a sampling calorimeter. The crystal calorimeter measures low to medium energy photons (0.1 GeV to 10 GeV) during eA running for tagging and vetoing purposes, while the sampling calorimeter covers high energy (10 to 250 GeV) neutrons, photons, neutral pions, and neutral lambda baryons, and can detect multiple neutrons from eA collision remnants.

Because the crystal calorimeter is not required for every run, it is mounted on a retractable table and can be removed when not needed.

The crystal calorimeter is constructed from $PbWO_4$ crystals. The sampling calorimeter is a high-granularity iron–scintillator detector with SiPM readout, often called "SiPM-on-tile." Both the crystal and sampling calorimeters are employed in larger ePIC systems: the crystal calorimeter in the backward electromagnetic calorimeter and the sampling calorimeter in the forward hadronic calorimeter, respectively.

The high granularity of the sampling section is motivated by the requirements associated with high energy neutrons and neutral lambda baryons in DEMP, which enable measurements of the momentum transfer variable t.

Subsystem description:

Crystal calorimeter

General device description: The first section of the ZDC is designed with a layer of crystal calorimeter towers, each with 8 radiation lengths (X_0) thick. This layer is composed of 2×2 cm^2 crystals arranged in a 30×30 grid. LYSO is chosen as the crystal material for its high light yield and suitability for measuring low energy photons.

Sensors: The gain of SiPMs is on the order of 10^5 with an operational bias of 25–30 V, while for APDs (avalanche photodiodes), the gain ranges from 1 to 50. Given the high light yield of LYSO crystals, APDs are a more suitable choice to avoid signal saturation. However, an operational bias of 150-200 V is required. If SiPMs are selected as the photodetector, a filter would need to be installed between the crystals and photodetectors to reduce the light yield and prevent saturation.

FEE: Under consideration.

Other components: Under consideration.

Sampling calorimeter The design and simulated performance of the sampling-calorimeter section of the ZDC is described in Ref. [6] and is briefly summarized here.

This ZDC section uses SiPM-on-tile approach, in which SiPMs directly couple to tile in the active layers of the calorimeter. This technology is used in the forward HCAL. The absorber structure, which is self-supporting, is composed of iron-blocks whereas the active layers correspond to tiles of plastic scintillator of size 50x50 mm^2 mounted on PCBs with SiPMs and no other component besides capacitors for passive filtering and connectors for flat cables.

One or more active layers will be placed in front of the first iron blocks to serve as a hodoscope for vetoing charged particles produced, for example, by neutrons interacting with upstream material. Charged-particle veto capabilities were also used in conjunction with the HERA ZDCs [119, 120]

Sensors: The SiPMs to be used are Hamamatsu 3 mm size, model S14160-3015PS, which are among the models to be used in the forward HCAL and Insert.

FEE: The raw analog signals from the SiPMs are transported to the back of the calorimeter to FEE boards using flat cables. The FEE boards will be identical to those used in the forward HCAL.

Other components:

Performance Crystal section performance:

The first test beam experiment for crystal calorimeter prototype was performed in February 2024 using 50 to 800 MeV positron test beam at the ELPH facility (now the RARiS facility) in Tohoku University in Japan and its data analysis is underway. The prototype modules have been made by the Taiwan group. Two simulation calculations and evaluations are ongoing; Λ identification and low energy photon identification. Angular resolution is a common thread. It has been less emphasized early on, but absolute requirements for successful exclusive physics program should be given.

Sampling calorimeter section performance:

The standalone performance of the SiPM-on-tile section of the ZDC has been simulated for the following single-particles: neutrons, lambda baryons, photons and neutral pions. The range of interest for all of these is 10–250 GeV. Studies have been published elsewhere, and are reproduced here in a summarized fashion. All performance studies below reflect the performance of the SiPM-on-tile system without the crystal calorimeter in front, since this will be removed when not needed.

Arguably, the most challenging channel for ZDC reconstruction is the neutral-decay channel of neutral lambda baryons: $\Lambda^0 \to n\pi^0$ (branching ratio 36%). As depicted in Figure 3.230, this measurement necessitates estimating the Λ^0 displaced vertex, which is expected to range from meters to tens of meters. We addressed this challenge using an iterative method that explicitly estimates the displaced vertex, called IDOLA [5], as well as a graph-neural network approach that resolves it implicitly.

Implementation The ZDC implementation will benefit from a creative approach; for example, non-static configurations which can adapt to different running conditions. The crystal-calorimeter needs depend on physics channel. Some level of conflict in the final states and associated require-

Figure 3.223: SiPM-on-tile ZDC.

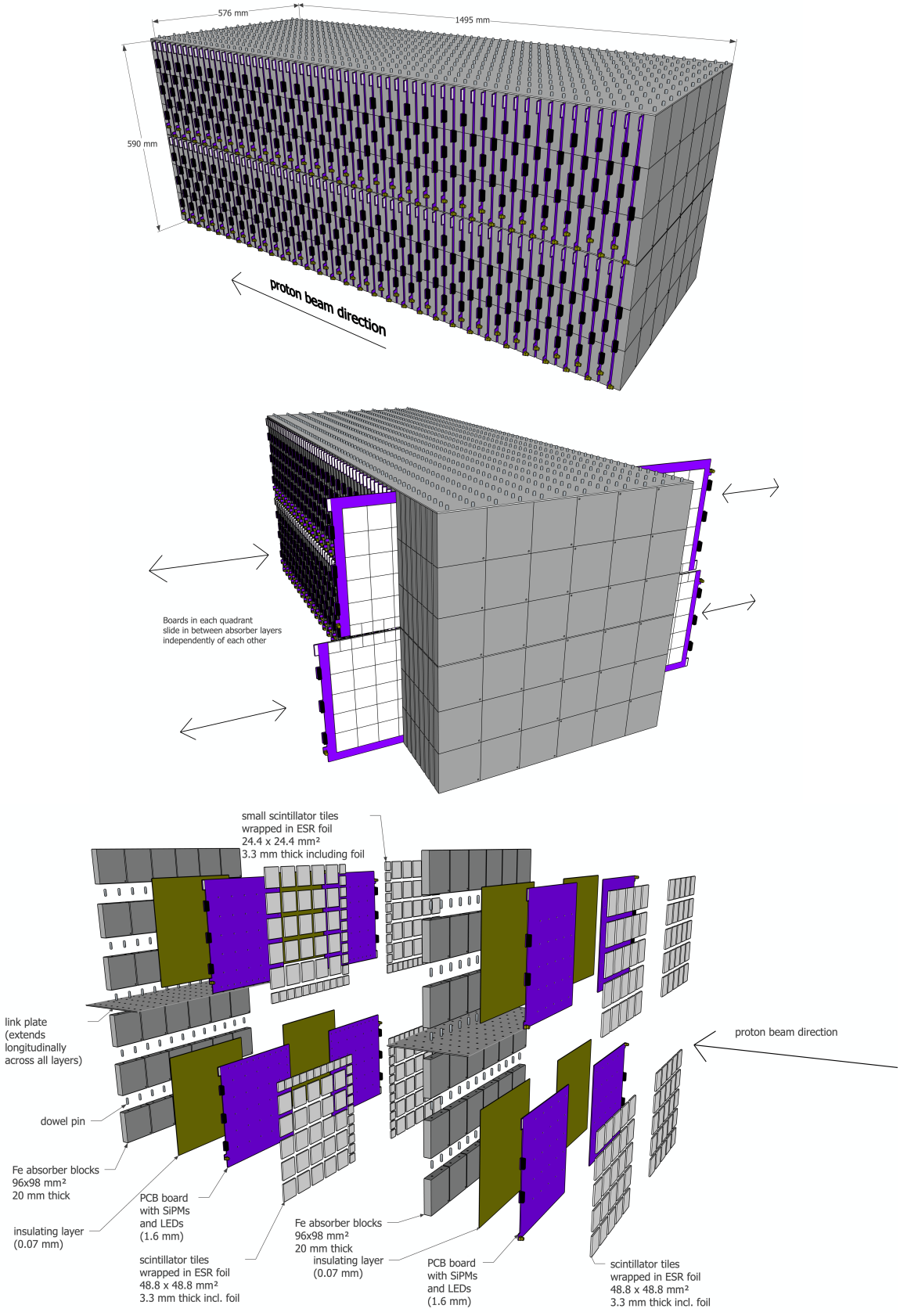

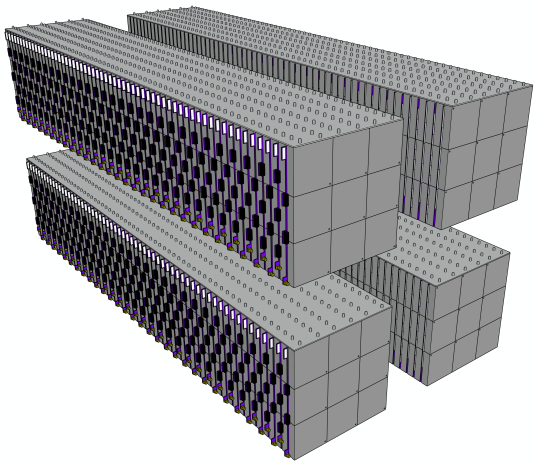

Figure 3.224: SiPM-on-tile ZDC modular design is composed of quadrants.

Figure 3.225: ZDC mechanical

ments. Having the ability to bring the crystal calorimeter in and out of configuration as needed, would provide clear benefit to specific physics needs.

Services: Add text here.

Subsystem mechanics and integration: Each LYSO crystal will be wrapped in ESR, a high-reflectivity foil. Each crystal tower, composed of a 5×5 array of crystals, will be either wrapped in aluminum foil or placed into an aluminum support structure to ensure stability. In total, there will be 36 towers. An additional thin aluminum support structure will be added around the crystal calorimeter for extra reinforcement.

The assembled crystal calorimeter will be housed in an aluminum container, which will be securely mounted to the table in the ZDC area using screws. This design allows for easy removal of the crystal calorimeter when necessary.

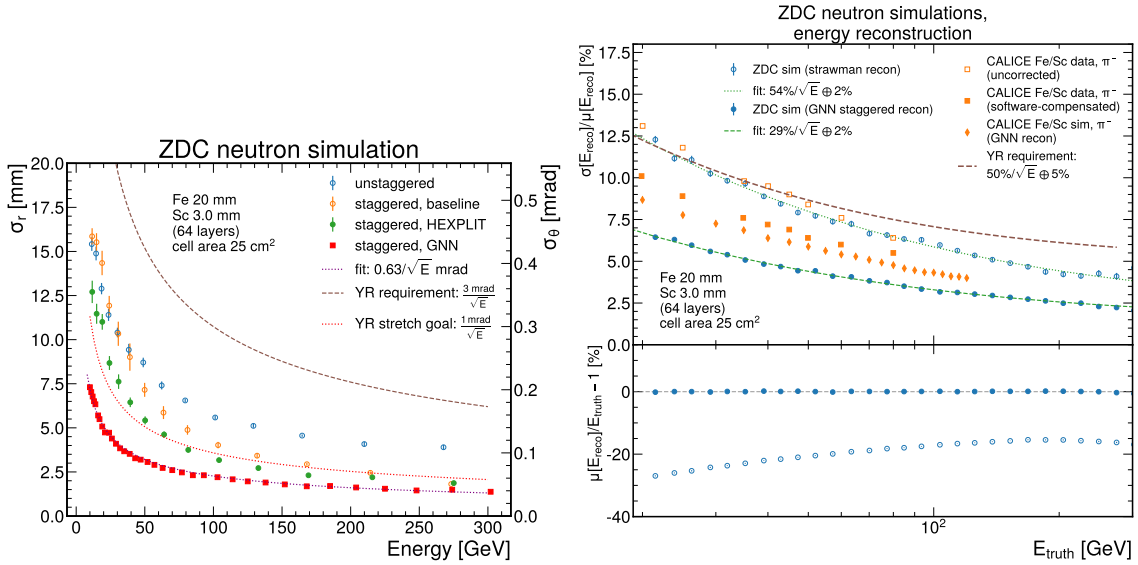

Figure 3.226: Left: ZDC neutron-shower position resolution for neutrons as a function of the generated energy. Results are shown with an unstaggered layout (blue) and staggered layout with the positions reconstructed with the baseline (orange), HEXPLIT (green), and GNN (red) reconstruction algorithms. Right: Energy resolution (top row) and scale (bottom row) obtained with the strawman (open symbols) and GNN (filled symbols) for simulated single neutrons. The resolutions are compared to those of the CALICE beamtest [**?**] (orange squares) with (filled) and without (open) software compensation, as well as the CALICE GNN reconstruction (orange diamond) [4].

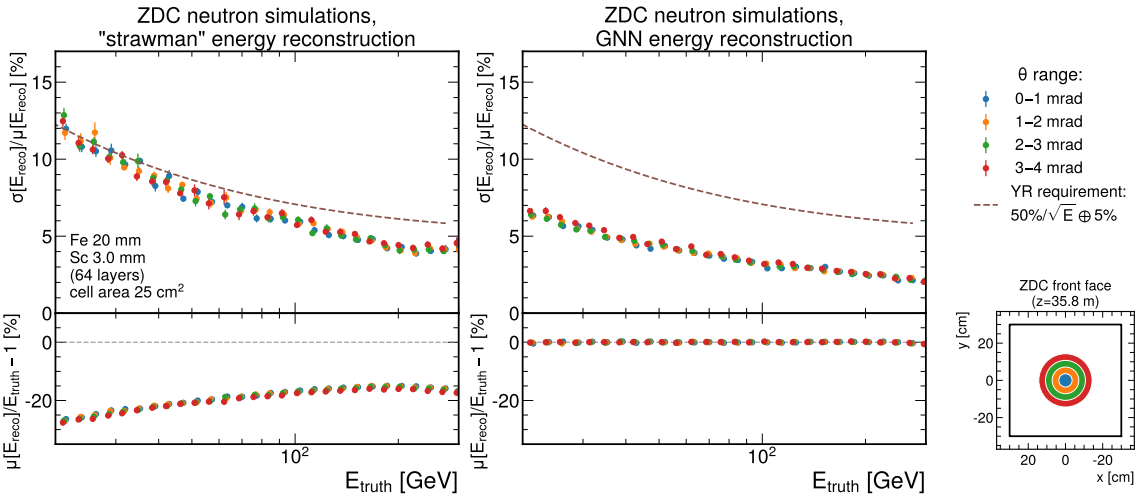

Figure 3.227: Energy resolution (top row) and scale (bottom row) obtained with the strawman (left) and GNN (right), at various ranges in θ. The positions on the face of the detector corresponding to each color are visualized in the inset.

Calibration, alignment and monitoring: Crystal subsection:

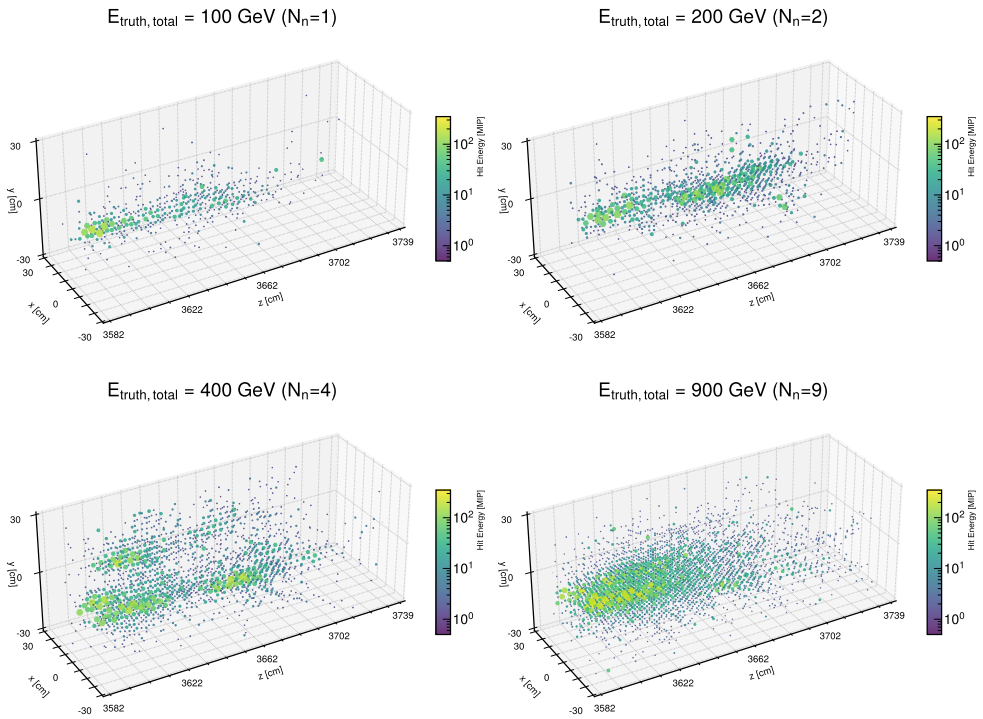

Figure 3.228: Examples of 4 reconstructed 3D shower shapes in the ZDC for events with 1 neutron ($N_n = 1$), 2 neutrons ($N_n = 2$), 4 neutrons ($N_n = 4$), and 9 neutrons ($N_n = 9$). The color code represents hit energy in terms of E_{MIP}. The marker size is displayed proportionally to hit energy for display purposes.

Precision cooling for the crystals and power cooling for the electronic readout will be achieved using water-cooling circuits. The cooling needs for individual crystals will be addressed through a thermal conduit extending from the crystal's rear face, through metal inserts, to the interface plate and support elements. A front thermal screen will also be installed to maintain the crystals at a controlled temperature.

The crystals will undergo pre-calibration using beam test facilities. In-situ calibration with physics events will be conducted using the process $\pi^0 \to \gamma\gamma$.

A light monitoring system will be implemented to continuously measure the relative light transmission and the full photodetector gains across all channels. Light pulses will be injected into each crystal to assess the optical transmission near the scintillation spectrum peak of LYSO crystals.

Sampling section:

The calibration of the detector is carried out with MIPs channel by channel. The self-supporting mechanical structure of the detector.

Status and remaining design effort:

R&D effort:

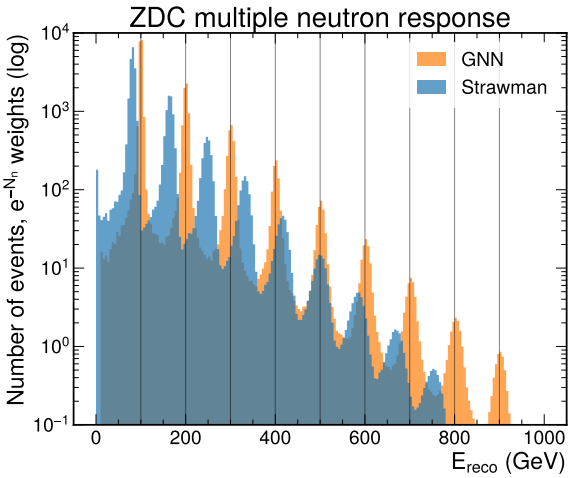

Figure 3.229: Energy measured for each integer number of neutrons with energy equal to 100 GeV, reconstructed with GNN (orange) and strawman (blue). The events are weighted by a factor of e^{-N_n}. The black, vertical lines are drawn at the total true energies of events with different numbers of neutrons. Here we show events containing up to nine neutrons. This performance illustrates just instrumental effects, excluding nuclear effects like smearing caused by Fermi motion and fission. In the laboratory frame, these nuclear effects would contribute in quadrature about 5 GeV per 100 GeV neutron, according to BEAGLE [**?**], which happens to be similar to the widths of the strawman reconstruction shown here.

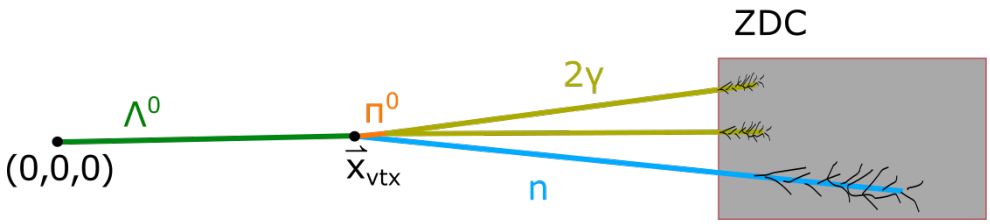

Figure 3.230: Topology of Λ^0 decay in neutral-channel decay. Not shown to scale. Figure reproduced from Ref. [5].

E&D status and outlook: Add text here.

Other activity needed for the design completion: Add text here.

Status of maturity of the subsystem: Add text here.

Environmental, Safety and Health (ES&H) aspects and Quality Assessment (QA planning): The quality assurance for each crystal and the assembly of each crystal tower will be conducted in Taiwan. Each tower will undergo pre-calibration using beam test facilities before being assembled into the final detector in Japan, after which it will be shipped to BNL for in-situ installation.

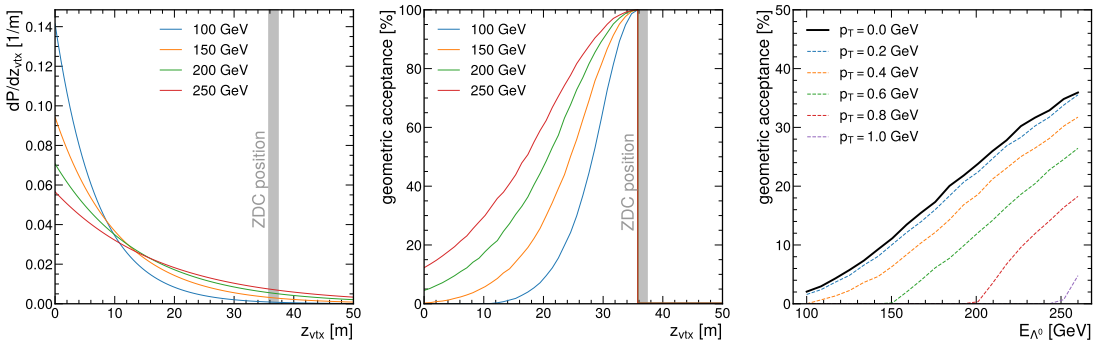

Figure 3.231: Left: Decay position distribution, for different Λ^0 energies. Middle: acceptance as a function of energy and decay position. Right: Acceptance as a function of energy, integrated over decay position, for Λ^0s along the proton axis (black solid curve) and with varying amounts of transverse momentum (colored dashed curves). Figure reproduced from Ref. [5].

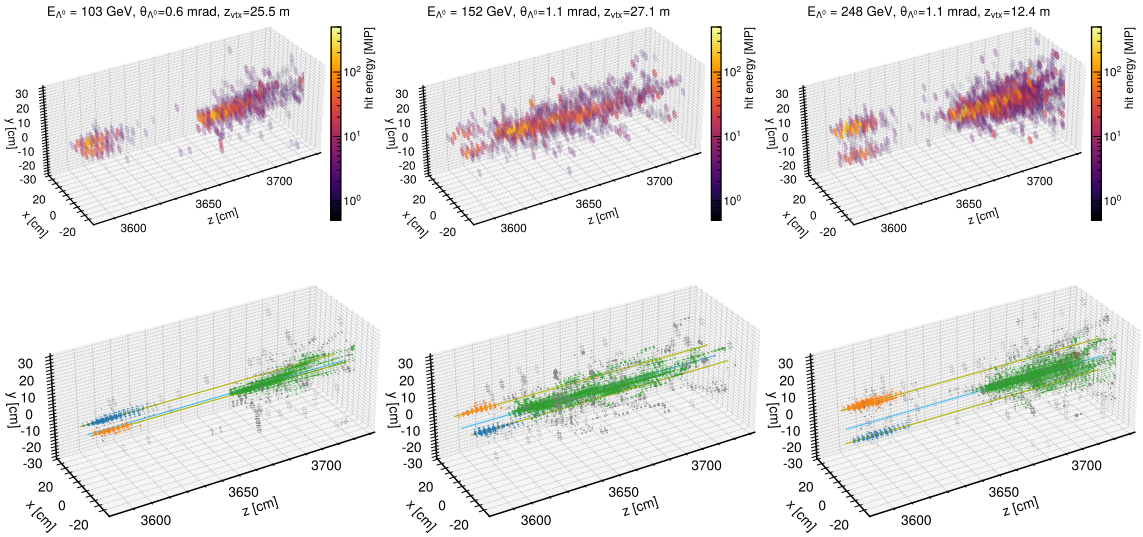

Figure 3.232: Top row: event display for example events, with the hits color coded by energy deposited, in units of MIPs. Bottom row: the same events, with subcell hits from HEXPLIT algorithm color-coded by which cluster the subcell hits have been assigned to by the 3D topological clustering algorithm. The olive (cyan) line(s) represent the truth-level trajectories of the incident photons (neutron). Figure reproduced from Ref. [5].

Construction and assembly planning: The self-supporting mechanical structure of the SiPM-on-tile section will be assembled at BNL. The construction process will follow a method similar to that shown in Figure **??**, which depicts a prototype with an area one-quarter that of the full ZDC and a depth of 23 layers. This prototype includes a total of 575 channels, representing approximately 10% of the total number of channels in the full-size ZDC.

In this modular assembly method, a baseplate with drilled holes serves as the mounting surface, where Fe blocks are connected using dowel pins. Each Fe block on the baseplate supports two additional blocks stacked above, also linked with dowel pins. Thin aluminum sheets are then used

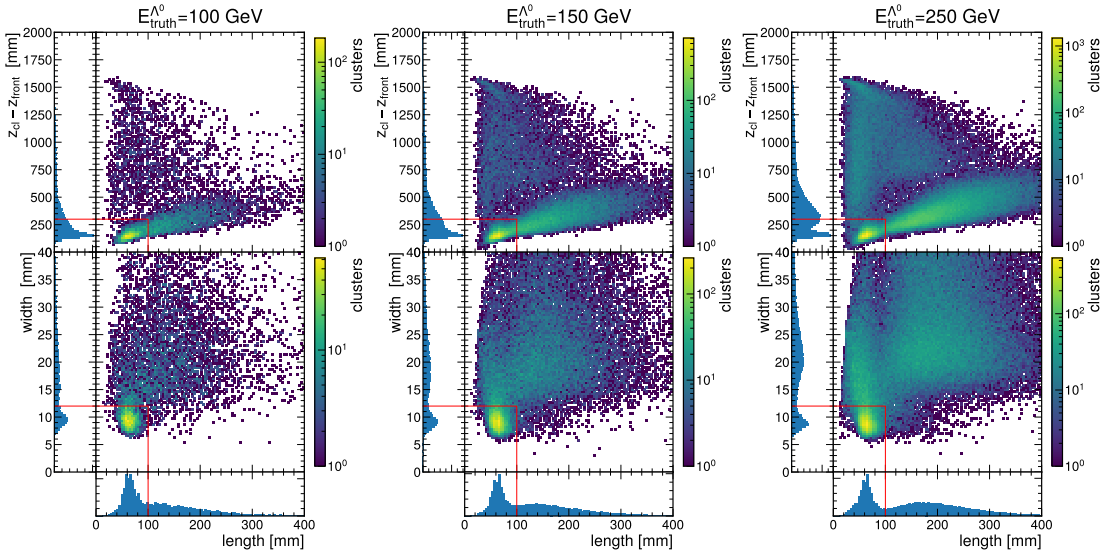

Figure 3.233: Distribution of the cluster shape parameters, at three different Λ^0 energies. The red lines show the cuts used to identify the photon clusters.

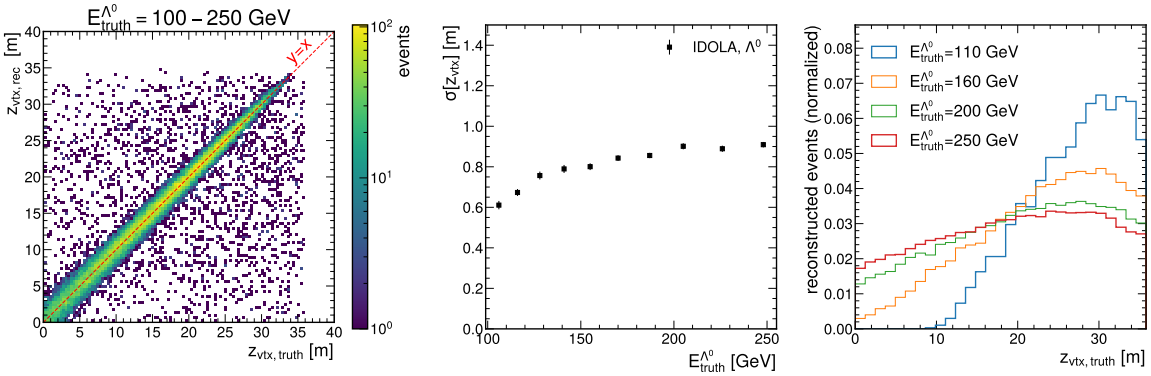

Figure 3.234: Left: truth decay position of Λ^0 (x axis), compared to the reconstructed values (y axis). A thin red dashed line is shown at $y = x$. Middle: the decay position resolution as a function of the Λ^0 energy. Right: distribution for the decay positions of reconstructed events for different Λ^0 energies. Figure reproduced from Ref. [5].

to connect the vertical 3×3 columns. This modular process is repeated until the entire 6×6 array and all 64 layers of the ZDC are completed.

The modular construction design was adapted from the successful design and deployment from the STAR forward HCAL construction.

Collaborators and their role, resources and workforce: Academia Sinica and National Central University in Taiwan, RIKEN, Kobe University, Shinshu University, University of Tsukuba, Tsukuba University of Technology and Nihon University in Japan, and Sejong University in Korea will contribute to the R&D, assembly, beam tests, and operation of the ZDC crystal calorimeter. The Taiwan team will collaborate with a crystal producer in Taiwan for LYSO crystals and develop

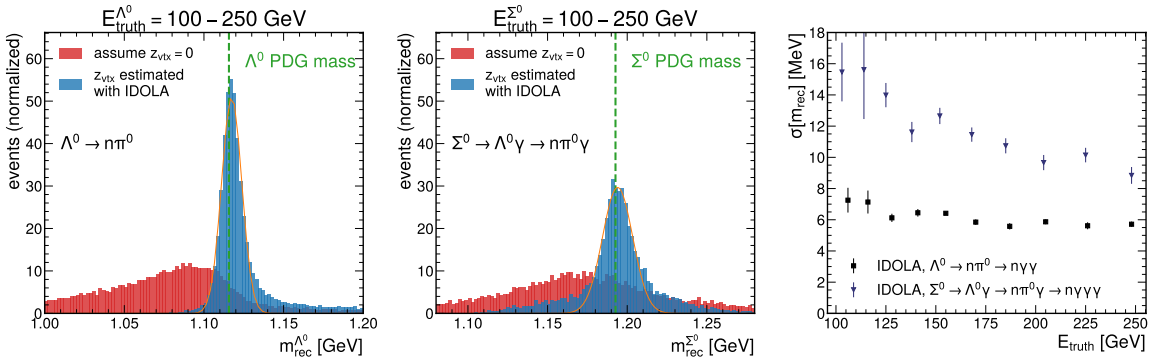

Figure 3.235: Left: distribution for the reconstructed Λ^0 mass before (red) and after (blue) fitting the vertex position with the IDOLA algorithm. Middle: Same for the reconstructed Σ^0 mass. Right: the Λ^0 (Σ^0) mass resolution as a function of the Λ^0 (Σ^0) energy. Figure reproduced from Ref. [5].

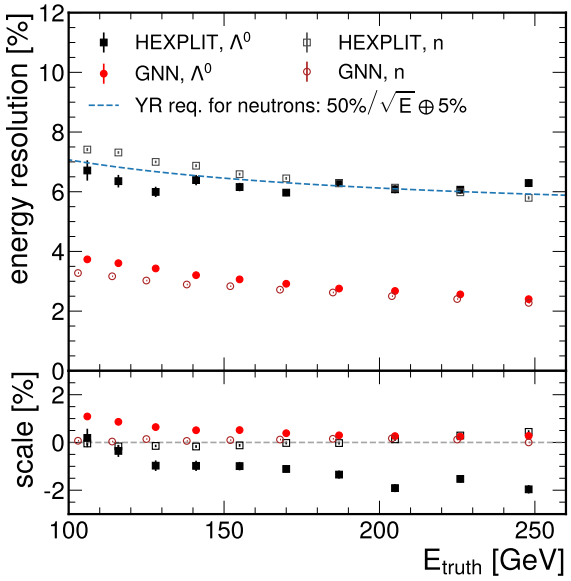

Figure 3.236: Energy resolution as a function of the Λ^0 energy. For comparison, the values obtained in Ref. [6] for single neutrons are shown in gray. Figure reproduced from Ref. [5].

electronic readout circuits and mechanical support. Currently, the Taiwan team consists of three faculty members, five postdoctoral researchers, and three students.

University of California, Riverside, University of Kansas, University of Connecticut, and Jefferson Laboratory in US will contribute to the R&D, assembly, beam tests, and opperation of the ZDC SiPM-on-tile section.

Risks and mitigation strategy: Radiation damage to the SiPMs poses a risk to the performance of the ZDC and must be mitigated. The expected dark current has been measured for the specific SiPMs intended for use in the ZDC [136]. The primary mitigation strategy involves high-

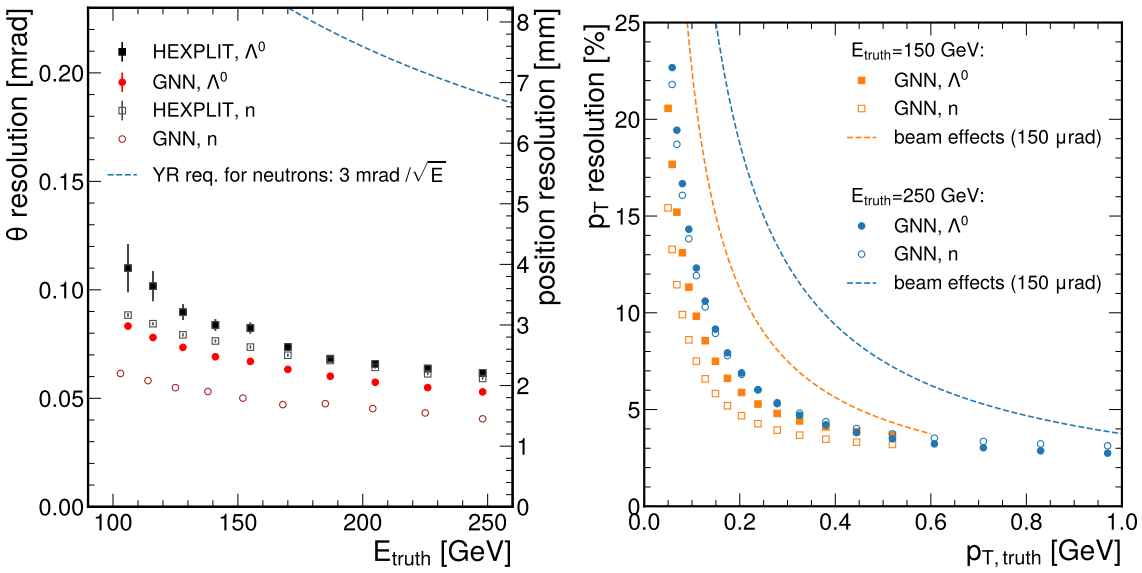

Figure 3.237: Left: Polar angle resolution for Λ^0 (filled symbols) and neutrons (open symbols) with baseline reconstruction and GNN reconstruction. Right: The resolution for reconstructing the transverse momentum for Λ^0 (filled symbols) and neutrons (open symbols) using a GNN at 150 GeV (blue) and 250 GeV (orange). These values reflect the resolution without beam effects. The beam effects terms for σ_{beam}=150 μrad are shown as dashed curves. Figures reproduced from Ref. [5].

temperature annealing of the SiPM boards. For these SiPMs, a 20-hour annealing session at 120°C reduces the dark current by a factor of two [136].

The design of the sampling section allows the SiPM boards to be removed from the mechanical structure for annealing treatment, which will be carried out in an environmental chamber in a BNL lab. High-temperature annealing can therefore be performed as needed between runs. This process requires removing the plastic scintillator tiles from the boards, as they would be damaged by the high temperature. Although delicate and labor-intensive, the procedure for removing and reattaching the scintillator tiles is straightforward.

From a mechanical standpoint, appropriate risk mitigation strategies include using a weight-rated table to support the detector and a crane if needed. The self-supporting structure closely follows that of the STAR forward HCAL, minimizing risks related to construction tolerances and structural integrity. Nevertheless, appropriate checks will be conducted, and custom support materials may be implemented to bracket the ZDC structure and provide additional reinforcement if necessary.

Additional Material Add text here.

3.3.8 Far backward detectors

The luminosity system at the Electron-Ion Collider plays a critical role in achieving high-precision measurements in nuclear physics experiments. By determining, monitoring and optimizing the number of particle collisions, the luminosity system ensures that the collider operates at peak per-

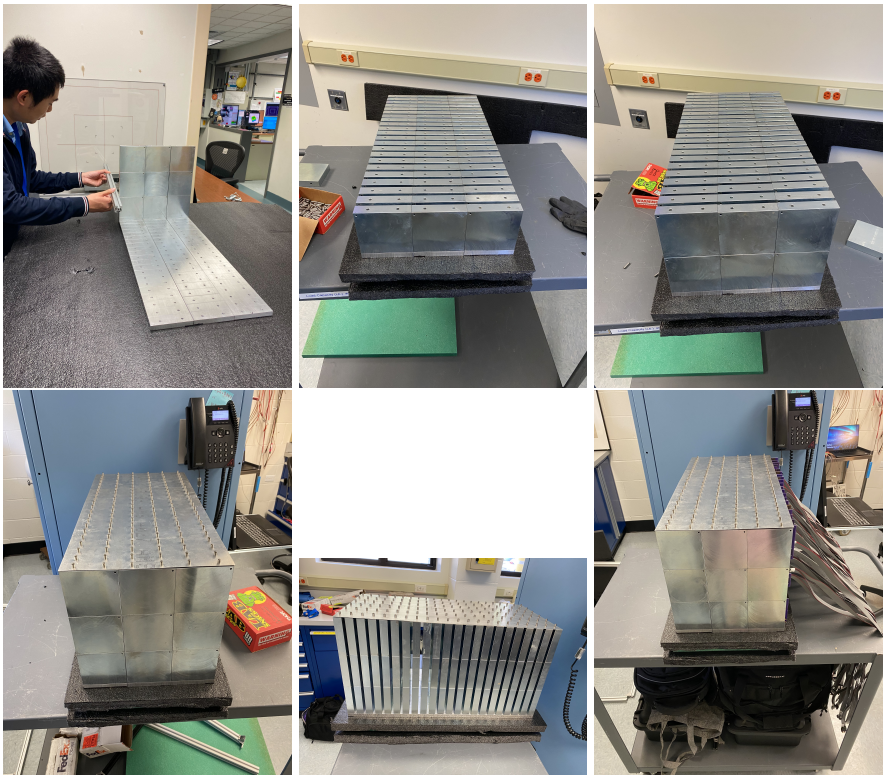

Figure 3.238: Assembly of a ZDC prototype representing approximately 10% of the full ZDC size.

formance, enabling detailed exploration of the structure of matter. When electrons collide with protons or nuclei, Bremsstrahlung (BH) photons are generated, with a well know cross section []. This process thus provides us with the mean to indirectly determine the luminosity by accurate and precise determination of the Bremsstrahlung photons generated in the interaction region of the collider.

Accurately determining luminosity is essential for addressing the fundamental physics questions that underpin the construction of the Electron-Ion Collider. The Yellow Report specifies the EIC requirements for luminosity determination to be 1% in absolute uncertainty and 10^{-4} in relative luminosity [11]. This requirement will be fulfilled by two complementary detectors in the luminosity monitoring system: the Pair Spectrometer (PS) and the Direct Photon Detector (DPD). It was demonstrated at HERA – the first electron-hadron collider – that the bremsstrahlung process can be successfully used to precisely measure the luminosity of high-energy ep collisions (ZEUS achieved an absolute uncertainty of 1.7% [**?**, **?**]). The luminosity monitors designed for the EIC utilise the same approach with implementation that mitigates large systematic uncertainties.

The two subsystems, Pair Spectrometer, and Direct Photon Detector, are sensitive to different systematic effects; on one hand the Direct Photon detector is placed downstream the photon beam with full acceptance, but within the synchrontron radiation fan and needs to be shielded. In addition, at nominal luminosities planned for the EIC several photons will hit the DPD in each bunch crossing. Thus the counting of bremsstrahlung photons is done through the total energy determination deposited in DPD and is associated with systematic uncertainties related to gain stability. On the other hand, the PS is outside the synchrontron radiation fan and overall rates can be controlled

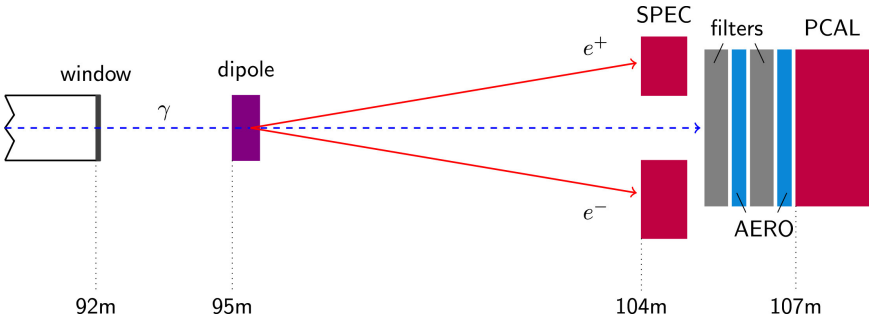

Figure 3.239: The layout of the luminosity monitor in the ZEUS experiment [**?**].

with a dedicated converter. The luminosity determination from the PS is sensitive to systematic effects related with the acceptance determination.

The PS and DPD detectors in the ZEUS luminosity monitor are shown in figure (3.239). The PS system consists of an analysing dipole magnet and two electromagnetic calorimeters, while the DPD system includes absorbing plates and an electromagnetic calorimeter. BH photons generated in the interaction region exit the vacuum chamber through a thick exit window. About 10% of these photons (depending on the window's thickness) undergo pair conversion into electron-positron pairs, which are then detected by the PS calorimeters. The remaining unconverted photons are detected by the downstream DPD. Additionally, the luminosity monitor includes a collimator positioned just after the exit window to produce a uniform, narrow cone of photons and pair-converted particles. This simple steel block also protects the PS system components from direct synchrotron radiation (SR), BH radiation, and unwanted stray particles.

The PS was needed at ZEUS due to challenges introduced by upgrades to the HERA accelerator, which significantly increased luminosity and, consequently, the rate of BH events [**?**]. The stronger beam focusing and increased synchrotron radiation (SR) — radiation resulting from the bending of electrons by the magnet—led to a higher pile-up of photons in the DPD, increasing the uncertainty in luminosity measurements from 1% to 3% [**?**]. The PS, positioned outside the SR fan and unconverted photon flux, experienced a lower pile-up due to fractional pair conversion. This introduction reduced the uncertainties in rate measurement to 2% [**?**], and additionally both detectors were utilized to monitor real-time detector inefficiencies and manage systematic uncertainties.

3.3.8.1 The luminosity system

Introduction The luminosity system at the Electron-Ion Collider plays a critical role in achieving high-precision measurements in nuclear physics experiments. By determining, monitoring and optimizing the number of particle collisions, the luminosity system ensures that the collider operates at peak performance, enabling detailed exploration of the structure of matter. The luminosity measurement provides the required normalization for all physics studies, allowing us to determine absolute cross sections and the proper scaling for different polarisation states enabling precise asymmetry measurements.

When electrons collide with protons or nuclei, bremsstrahlung (BS) photons are emitted, with a well known cross section due to Bethe-Heitler [**?**]. Thus, this process provides us with the means to indirectly determine the luminosity by accurate and precise determination of the bremsstrahlung photons produced in the interaction region of the collider. This approach was successfully implemented at HERA, measuring the luminosity of high-energy ep collisions [**?**, **?**]. The experimental

conditions at the EIC (expected luminosities of 10^{33} cm^{-2}s^{-1}), with a wide range of electron beam energies, and a variety of (polarized) targets complicate the precise determination of the luminosity. For example, beam-size effects suppress the bremsstrahlung process due to the finite transverse size of the beam overlap relative to the typical impact parameter [**?**]. In addition, the large cross section of the Bethe-Heitler process, which increases with Z^2 of the target for nuclear beams, results in a large amount of photons (over 20 for electron-proton scattering), complicating the determination of the rate of generated photons, which is also sensitive to event pileup. This direct measurement of the rate of generated photons at the interaction region is further affected by the strong synchrotron radiation background, which has a similar angular distribution as bremsstrahlung.

Beam Size Effects: The Bethe-Heitler process in electron-proton collisions is notable for its extremely small momentum transfers between the radiating electron and the proton. It is kinetically possible for both particles to continue along their initial paths without angular scattering, while the Bethe-Heitler photon is emitted in the direction of the electron's momentum. This specific configuration results in the smallest virtuality (Q^2_{min}) of the exchanged photon [**?**]. At high-energy colliders, this minimal photon virtuality becomes very small. For instance, at HERA, the Q^2_{min} for a photon energy of 1 GeV the photon virtuality can be as low as 10^{-8} eV^2. Consequently, the typical transverse momentum transfer ($q_\perp$) reaches values around 10^{-4} eV/c. Since the Bethe-Heitler differential cross section is proportional to Q^{-4}, photon virtualities near Q^2_{min} dominate the process and allows for the approximation,

$$Q^2 = Q^2_{\text{min}} + q^2_\perp.$$

Analyzing the process in impact parameter space reveals that these small $q_\perp$ values correlate to large impact parameters ($b = \hbar/q_\perp$), explaining the precision of Bethe-Heitler cross-section calculations in the Born approximation.

The derivation of the two-particle rate (R) relation with the collision luminosity (L) and cross-section (σ)

$$R = L\sigma, \tag{3.1}$$

assumes both beams to be modeled as simple plane waves with a uniform impact parameter distribution. However, this assumption falls short when beams are strongly focused at the interaction point, since focusing suppresses large impact parameters. Consequently, for the head-on collisions the Bethe-Heitler differential cross section is predominantly "over-sampled" at low impact parameters where the cross-section value is smaller. This results in an effective suppression of the Bethe-Heitler process. This is particularly pronounced at lower photon energies, since typical $q_\perp$ is proportional to E_γ.

Relative corrections to the standard Bethe-Heitler cross-sections due to the beam-size effects is shown in Fig. 3.240. The observed suppressed Bethe-Heitler cross-section is related to the Bethe-Heitler cross-section as $(d\sigma_{obs}/dy) = (d\sigma_{BH}/dy) - (d\sigma_{corr}/dy)$. It is worth noting that the beam-size effects will be higher at EIC as compared to HERA due to the stronger focused beam evident from the beam-size parameters. In a recent study, the understanding of corrections due to the beam-size effects is proposed to be verified by a precise measurement of the Bethe-Heitler spectra as a function of lateral beam displacements (indirectly the impact parameter) at the interaction point. This will be achieved using Van der Meer scans, commonly performed at hadron colliders. This involves systematically varying the beam positions to find the L as a function of lateral beam displacement, which can be described by the formula

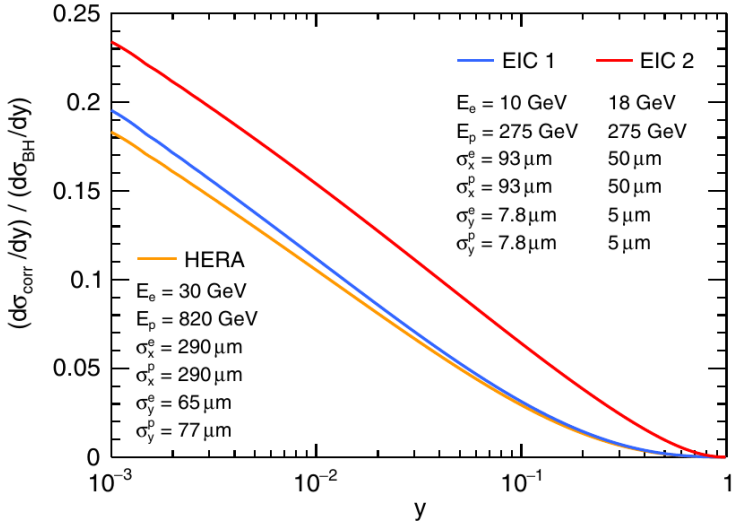

Figure 3.240: Relative suppression due to the beam-size effects $(d\sigma_{corr}/dy)/(d\sigma_{BH}/dy)$ is shown as a function of $y = E_\gamma/E_e$ for three cases of collider parameters, HERA, EIC 1 & EIC 2. The corresponding beam energies and Gaussian lateral beam sizes at the interaction point are listed. Figure from Ref. [**?**].

$$L(B) = L(0)\exp\left(-\frac{B}{2(\sigma_1^2+\sigma_2^2)}\right).$$

Here, B represents the lateral displacement of one of the beams within either the horizontal or vertical plane, σ_1 and σ_2 are the two Gaussian widths in a given plane, often assumed to be equal, and $L(0)$ corresponds to the luminosity of nominal, head-on collisions. However, in the case of Bethe-Heitler, its photon spectrum will also be modified in a very specific manner, reflecting the beam size effects.

Beam Polarisation: The electron and light ion beams at the EIC will be polarized both longitudinally and transversely. A recent study investigated the impact of longitudinal beam polarisation on the bremsstrahlung cross-section in the low-Q^2 region [**?**]. Calculations revealed that the polarised component is very strongly suppressed compared to the unpolarised component, by a factor of about $m_e^2/(E_eE_p)$. Figure 3.241 illustrates the unpolarised component first calculated by Bethe-Heitler, alongside the polarized component. Studies that extend this calculation to transversely polarised beams, including nuclear recoil effects need to also be performed to ensure negligible contributions.

Bremsstrahlung event rates: The Bethe-Heitler process is associated with high rates. Table 3.71 shows the ep bremsstrahlung cross sections in mb (and the corresponding event rated in GHz for the nominal EIC luminosities) for different selection criteria. Taking into account the bunch crossing rates, one gets about 20 photons per bunch crossing, with this number scaling with Z^2 for collisions with heavy ions. These high rates result in significant power deposited in the calorimeter that detects the bremsstrahlung photons. This also means that the counting of bremsstrahlung pho-

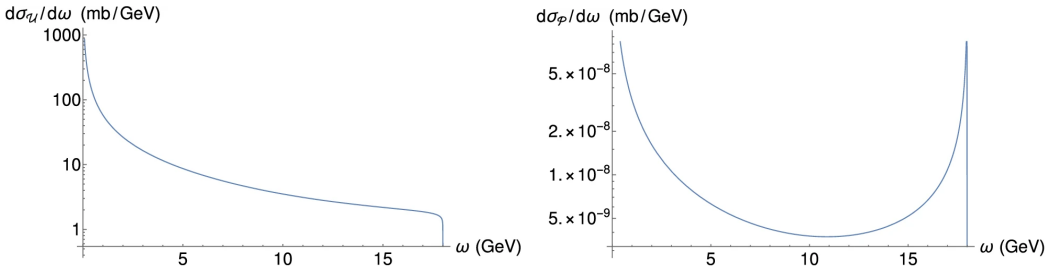

Figure 3.241: Unpolarised Bethe-Heitler cross-Section (left panel) and the polarised component (right panel), calculated in Ref. [**?**]

E_e	E_p	$E_\gamma/E_e > 0.01$	$1 > E_\gamma/E_e > 0.7$	$0.1 > E_\gamma/E_e > 0.1$
18	275	237 (0.36)	11.6 (0.018)	65.2 (0.10)
10	275	230 (2.3)	11.1 (0.11)	63.2 (0.63)
5	100	209 (0.77)	9.81 (0.036)	57.1 (0.21)

Table 3.71: Bethe-Heitler ep bremsstrahlung cross section in mb (and the corresponding event rates in GHz, for the nominal EIC luminosities), for various beam energies in GeV and three selection criteria. Table from Ref. [**?**].

tons effectively becomes an energy measurement in the photon calorimeter with all of the related systematic uncertainties (e.g. gain stability).

Synchrotron radiation: The magnet which bends the electrons away from the hadron beamline, serves as an analyzing magnet for forward scattered electrons and is a source of a large synchrotron radiation flux. Synchrotron radiation is emitted at very small angles ($\sim m_e/E_e$) and has a similar angular distribution as bremsstrahlung. This means that the dedicated system for the direct bremsstrahlung photon measurement will be exposed to this synchrotron radiation fan.

Luminosity monitors at the EIC The challenging conditions at the EIC dictate a complementary approach to the determination of the luminosity. A method that utilized the pair production from bremsstrahlung photons on a thin converter was also effectively employed at HERA [**?**]. This indirect approach that utilizes the detection and energy reconstruction of the e^+e^- pair, results in lower rates, which can be controlled from thin converters and an analyzing magnet. This approach is less sensitive to event pileup and insensitive to synchrotron radiation. This is due to the reduced rates ($\sim 1\%$) from pair production (conversion foil of 1% radiation length) and the placement of the pair spectrometer calorimeters, which will be installed outside the primary synchrotron radiation fan. On the other hand, a detailed knowledge of the detector acceptance and the conversion rate is needed for a precise determination of the luminosity. A direct photon detector, which sits in the direct synchrotron fan, provides a full acceptance of the bremsstrahlung photons but is also exposed to high rates and sensitive to event pileups. At the EIC, the luminosity will be determined using both approaches – direct photon detection (Direct Photon Detector, DPD), and detection of pair-produced photons (Pair Spectrometer Calorimeter, PSCal) – allowing us to reduce the associated systematics.

Requirements

Requirements from physics: An accurate determination of luminosity is essential for addressing the fundamental physics questions that underpin the construction of the Electron-Ion Collider. The Yellow Report specifies the EIC requirements for luminosity determination to be 1% in absolute uncertainty and 10^{-4} in relative luminosity [**?**]. Proper figure from Physics studies that highlight the requirement.

Requirements from Radiation Hardness: The DPD, which is exposed to the direct synchrotron radiation fan and the high bremsstrahlung rates has more stringent requirements than the PSCal, which sits outside the synchrotron radiation fan and only sees ∼1% of the events in the DPD. Geant4 simulations were performed to study the 3D distribution of doses due to bremsstrahlung only, which estimated a maximum annual local dose of about 7 MGy (assuming 100 fb^{-1}). Furthermore, a special ultra-fast synchrotron radiation event generator was developed to simulate hard part of synchrotron radiation spectra ($E_\gamma > E_{cr}$). It was found that for an 18 GeV bean a 35 cm of graphite (which is less than 2 radiation lengths), would be sufficient in shielding the DPD.

Requirements from Data Rates: The high cross-section of the Bethe-Heitler process drives the data rate requirements. As discussed above, the DPD will be exposed to high rates of about 20 photons per bunch crossing (at nominal luminosities) for ep collisions, with the rates scaling with Z^2 for heavy ion collisions. The requirement for the PSCal, is much less stringent as rates are expected to be much lower and can be controlled with the position of the calorimeters, the analyzing magnet, and the converter. The vertical position of the PSCal is as such that it does not affect the acceptance of the DPD (at least 5σ of the beam size at the position of the calorimeters).

Systematic Uncertainties - Past experience from ZEUS dictate that efforts to reduce/minimize systematic unceratinties in our system are needed. The systematic uncertainty in the ZEUS luminosity measurement at HERA II was 1.7 %, and our goal is to reduce this value to below 1 %. Table 3.72 summarises the main systematic uncertainties that contributed to the ZEUS luminosity determination. In our current design, we ensure we mitigate the largest of these sources with the introduction of trackers for the PS, that would enable an accurate determination of the detector acceptance and beam size effects, and a sweeper magnet that allows us to have more control on the converted pair rates in the PS.

Source	DPD detector (%)	PS detector (%)
Acceptance	1.0	1.0
x-position of photon beam	1.2	1.2
Pair conversion in EW		0.7
RMS Cut Correction		0.5
Pedestal Shifts	1.5	
Pile up	0.5	
Total	2.2	1.8

Table 3.72: Summary of systematic uncertainties at ZEUS DPD and PS detector. [**?**]

Justification The detector and beamline component layout for the luminosity system is illustrated in Fig. 3.242. A sweeper magnet is utilized to remove pair conversions primarily from the

Figure 3.242: Luminosity system layout showing the Direct Photon Detector and Pair Spectrometer, as well as the sweeper and analyzing magnets.

relatively thick exit window and conversion in air between the exit and sweeper magnet. This reduces the systematic uncertainty related to the photon conversion rate and allows us to control the rate at the PSCal and estimate systematics. A vacuum beam pipe also minimizes photon conversion in air. Converter foils will be located between the analyzing and sweeper magnet. The analyzing magnet bends the e^+e^- pairs away from the photon beam direction so that they can be detected by the PSCal. A set of trackers (PSTrack) is positioned in front of the PSCal and enables the detailed determination of the detector acceptance as well as the reconstruction of the beam spot profile. The DPD sits just behind the PSCal. Graphite absorbers are placed in from of the DPD to shield the detectors from the low-energy synchrotron radiation. The luminosity system described here would allow us to determine the luminosity at the required precision, minimizing contributions from systematic uncertainties.

Device concept and technological choice: Below we provide a description of each detector subsystem and the technology of choice that would enable us to meet all requirements as set above.

PSCal Subsystem description:

General device description: The Pair Spectrometer Calorimeters are based on the same technology as the fEMCal, and builds upon R&D studies []References from https://arxiv.org/html/2408.11075v1and applied in the sPHENIX experiment []References from https://arxiv.org/html/2408.11075v1. The calorimeters are composed of 20 layers, with the fibers oriented in alternate directions – parallel to either the x-direction or y-direction in the transverse plane. This alternating orientation and the orientation of the fibers perpendicular to the beam direction aids in reconstructing the shower profile of hits in all three dimensions, thereby enhancing the position resolution of hits and enabling the detection and reconstruction of multi-hit events. This feature becomes more important for the DPD (lower rate) and low-Q^2 taggers where multi-hit events are obtained even at low luminosities. Each layer has a thickness of 0.9 cm and a transverse size of 18.06 × 18.06 cm^2. Additionally, the layers are segmented into three modules, each with a width of 6.02 cm. This is illustrated in Fig. 3.243, where the two PSCal are illustrated with their layers and components. The location of the two calorimeters are :Top (0.0, 15.76, -6408.6) and Bottom (0.0, - 15.76, - 6408.6). Each module contains 448 scintillating fibers, grouped in bundles of 16 (4×4). All production modules will be identical, and precise mechanical tolerances are ensured by using production molds fabricated to high tolerances.

Sensors: Each bundle of 16 fibers are read out by 3×3 mm SiPMs (Hamamatsu S14160-3015PS). Each module is read out by 28 SiPMs providing us with information on the shower profile as a function of debth allowing for position resolution. This additional information allows the reliable reconstruction of multi-hit events.

FEE: A bespoke PCB board that host the 28 SiPM has been designed. Each PCB board provides individual bias to each SiPM and host a temperature sensor for correcting gains. Connectors between this sensor PCB and a bespoke ASIC is implemented. Details on the ASIC will be finalised and provided at a later stage.

Other components: A light-tight enclosure is designed to hold all modules at position and provide support for the PCB and ASICs.

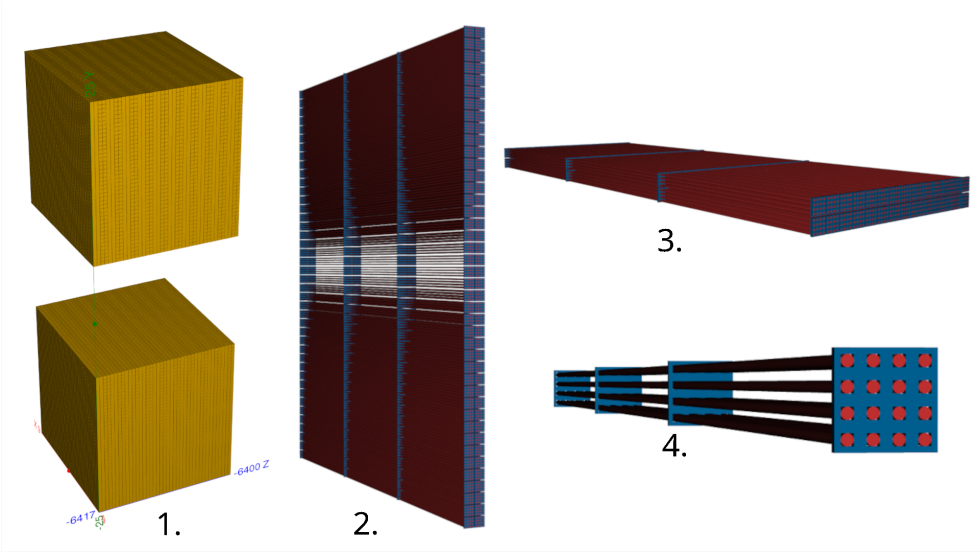

Figure 3.243: Pair Spectrometer calorimeters and their components: (1) The two Pair spectrometer calorimeters; (2) one layer, made out of three modules, with the fibers oriented perpendicular to the beam direction (the orientation of the fibers alternate from horizontal to vertical); (3) one module; (4) zoomed-in view of a set of 16 fibers which are read out by a SiPM.

PSTrack Subsystem description:

General device description: Two layers of AC-LGADs with pixelated sensors, for each calorimeter, constitute the Pair spectrometer trackers. The trackers adopt the technology of FTOT trackers and a detailed description can be found in that section. The pitch between the readout pads, set at 500 μm, is expected to provide approximately 70 µm position resolution at the detector plane and around 2 mm at the vertex (conversion foil).

Current estimations indicate that, in order to achieve acceptance uncertainties below 1%, the vertex resolution in the dispersive direction must be less than 6 mm. With a 500 μm pitch, the number of readout channels is estimated to be about 130,000 per plane. To minimize the number of DAQ channels, the number of pixels in the non-dispersive direction could be combined.

Their location is: Module 1 : Top (0.0, 15.76, - 6397.6) and Bottom (0.0, - 15.76, - 6397.6), and for Module 2 : Top (0.0, 15.76, - 6407.6) and Bottom (0.0, - 15.76, - 6407.6). Their dimensions are (18.06, 18.06, 0.044), covering the full front face of the PSCal, with a thickness of around 2% radiation lengths.

Sensors: Sensor, and FEE information for the trackers is provided in the FTOD section.

DPD Subsystem description:

General device description: Details on the DPD will be given by the Krakow group. Two detector systems, one for nominal luminosities and one for low luminosities, will comprise the Direct Photon Detector systems. The low luminosity calorimeter will be of the same technology of the Pair spectrometer, utilizing its capabilities for multi-hit reconstruction.

Sensors: Add text here.

FEE: Add text here.

Other components: Add text here.

Performance The performance of the PSCal has been evaluated and tested using MC simulations. These simulations utilized the ePIC DD4HEP framework with the full geometry of the luminosity system, including analyzer and sweeper magnets, in place. The field map for these magnets was also incorporated. Simulations were conducted by generating a bremsstrahlung photon spectrum, applying beam effects, and then propagating this photon to the conversion foil and converting it utilizing a photon splitting function (see Eq 34.31 of the PDG [**?**]). Converting the photons in this manner significantly reduces computation times for this simulation.

MC simulations for the PSCal demonstrate that the current design will meet design requirements. Simulations indicate that the design achieves a uniform sampling fraction of ∼2%, as seen in Fig. 3.244. The sampling fraction is defined as the total energy deposited in sensitive elements of the calorimeter divided by the total energy of the incident particle. Figures 3.245 & **??** also demonstrate that energy resolutions of 5 to 8% – stochastic term of 10% – (in the 3 to 18 GeV electron energy range) are also achievable with the current design. The energy resolution is about (stochastic term).

Figure 3.244: PSCal sampling fraction as a function of incident electron energy. Events incident on the top or bottom 2cm of the front face of the calorimeter have been excluded in this sample. This selection cut removes events where the full shower is not contained within the calorimeter.

Figure 3.245: PSCal energy resolution as a function of generated electron energy. In this study, monoergetic electrons (at the discrete values shown) were generated at the front face of the calorimeter.

Figure 3.246 shows the expected rates at the Pair spectrometer detector subsystems for different ion and energy combinations. The highest rate of coincidence events, at the highest luminosity runs, is approximately one coincidence event for every ten bunch crossings, or every 100 ns [**?**], with single hits having slightly higher rates.

The current design, which allows the 3D shower reconstruction allows us to further increase these rates, by reducing the magnetic field of the analyzing magnet while still being able to reconstruct the photon energy spectrum from multi hit events. This additional information allows us to better understand systematic uncertainties and constrain them.

Test beam runs to evaluate the performance of detector electronics and the uniformity of the calorimeter blocks are planned for late 2024/early 2025. Initial testing is planned at the Mainz A2 facility followed by tests in Jefferson Lab Hall D. Testing of individual module responses using cosmic ray data is already underway at the University of York.

The PSTrackers are capable of providing very precise position resolution for electron/positron tracks. This exceeds the required position resolution and utilizes technology (AC-LGAD) from other detector subsystems.

Studies that would estimate systematic uncertainties and how the current design meets all requirements will be provided at a later stage (currently investigated).

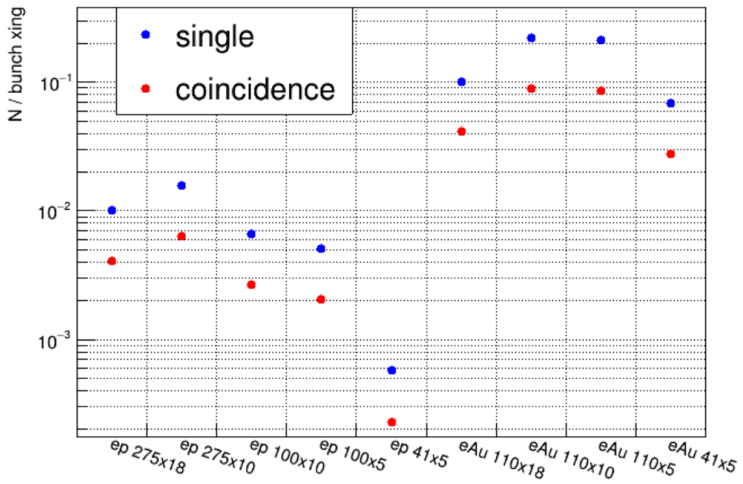

Figure 3.246: Rate of single and coincidence events for the PS detectors.

Implementation

Services: Subsystem services information will be provided at a later stage.

Subsystem mechanics and integration: Subsystem mechanics and detector integration is being prototyped and will be provided at a later stage.

Calibration, alignment and monitoring: Calibration of the PSCal is required for the accurate determination of the energy of the electron-positron pair and from that the energy of the bremsstrahlung photon. Corrections will have to be made to account for non-uniform SiPM responses to the same photon load, and other irregularities that might arise from the construction of the detector. Whilst initial calibration can be done on individual SiPMs and sections of the detector before installation in the beam enclosure, this will not be sufficient to ensure optimal performance of the detector. Further calibration will have to be carried out in dedicated calibration runs, as well as during regular operation of the machine.

The detectors are to be built in modules or tiles, with sixty of these tiles making up a single detector. Each module will be tested individually using cosmics, allowing for the characterization and correction of non-uniform SiPM responses. SiPMs are grouped in each module based on the operating voltage, and visual inspection will be carried out before their installation. Fibers will also be inspected.

LED benchmark tests will be carried out to characterize the module response before installation and compared with a reference module. These initial tests will be carried out at the University of York. The PSCal will be calibrated using dedicated runs and a tight collimator, allowing us to select electron-positron pairs with a well-defined energy. This can then be used to calibrate the detector response.

In-operation calibration will make use of the bremsstrahlung electron, as well as the photon. This electron will be detected by the low Q^2 taggers, and coincidences between the two systems al-

low us to continuously monitor the detector response. The pointing and position resolution of the PSTrackers also allows us to continuously monitor the PSCal detector response and provide continuous calibrations.

Status and remaining design effort:

R&D effort: Curr.

E&D status and outlook: Add text here.

Other activity needed for the design completion: Add text here.

Status of maturity of the subsystem: Add text here.

Environmental, Safety and Health (ES&H) aspects and Quality Assessment (QA planning): ES&H aspects from construction and use. QA testing - Test beams for uniformity, signal baseline from cosmics at York/BNL?

Construction and assembly planning: The construction of the calorimeters for the PS and DPD systems will involve plastic scintillating fibers embedded in a mix of tungsten powder and epoxy, this technique was developed by Prof. Tsai [**?**]. Fibers will be threaded through four thin brass meshes, which will hold them at even distances apart, shown in Fig. 3.247. The fibers and meshes will be placed in a mould with the meshes separated to form three sections of equal length. Tungsten powder will then be poured into the mould and leveled using weights and a vibrating table to ensure the mould is filled evenly and packed well. Epoxy will then be slowly poured into the mould before the mould and contents are placed into a low-temperature oven to cure the epoxy. A test module, consisting of only tungsten powder and epoxy is shown in Fig. 3.248a, with Fig. 3.248b showing a cross-section of a broken piece. The epoxy permeates well through the module, forming a solid and durable brick. A larger amount of force, applied with a hammer, was needed to produce the piece seen in the figure.

Figure 3.247: Multiple fibers threaded through a pair of brass meshes.

(a) **(b)**

Figure 3.248: (a) Tungsten powder and epoxy-only test module. (b) A section of another test module showing the interior.

Collaborators and their role, resources and workforce: The main collaborating institutions for the PS calorimeter are York and Houston. The roles of each institution are outlined below -

- University of York, United Kingdom
  - Design and construction of calorimeters
  - Calorimeter simulation
  - Calorimeter reconstruction and analysis

- DAQ and electronics for calorimeter
- University of Houston, Texas, USA
  - Calorimeter simulation
  - Calorimeter reconstruction software
  - Calorimeter design support
- Tel Aviv University, Israel
  - Design and integration of PS trackers.
  - Simulation.

Additional workforce is required for the detailed design of the two magnets, collimators, and exit windows, as well as the beam pipe and support structure.

The workforce at each institution comprises -

- University of York, United Kingdom
  1. Dan Watts, academic staff (20-25 % FTE)
  2. Nick Zachariou, academic staff (25-30% FTE)
  3. Mikhail Bashkanov, academic staff (10-15% FTE)
  4. Stephen Kay, PDRA (100% FTE)
  5. Alex Smith, PG Student (100% FTE)
  6. Pankaj Joshi, academic support staff (5% FTE)
  7. Julien Bordes, Geant4/simulation support (10-15% FTE)
  8. Technical Support Staff
     - Electrical engineer
     - Mechanical engineer
     - CAD support
- University of Houston, Texas, USA
  1. Aranya Giri, PG Student (100% FTE)
- Tel Aviv University, Israel
  1. Igor Korover, academic staff (15% FTE)
  2. Avishay Mizrahi, Mechanical engineer (50% FTE).

Risks and mitigation strategy: Add text here.

Additional Material Add text here.

3.3.8.2 The low Q^2 taggers

Requirements The Low-Q^2 Tagger is required to measure the momentum of low-angle scattered electrons. The Tagger sits close to the electron beamline and consists of two modules, each with silicon trackers and a calorimeter. This is shown in Figure 3.249.

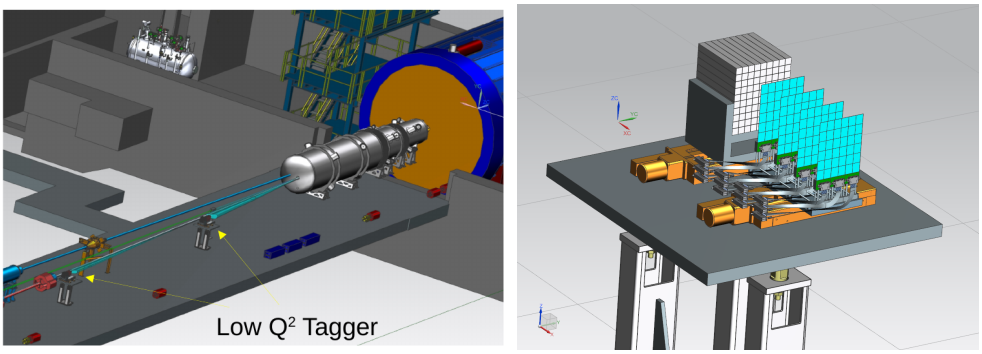

Figure 3.249: Left: Low-Q^2 taggers in relation to beamlines and central detector. Right: Tagger module with calorimeter and tracker from recent CAD model.

Requirements from physics: The acceptance for the low-Q^2 tagger should complement the central detector to reach the coverage close to the limits given by the divergence of the beam and beamline magnets. Low-Q^2 tagger will have one or more stations to cover the maximum momentum acceptance.

The Low-Q^2 tracking system shall have a spatial resolution providing a momentum resolution $<$ 5% with Q^2 acceptance between 0 and 0.1 GeV². The acceptance ranges of the Central Detector and Low-Q^2 Trackers as function of Q^2 and Bjorken x are shown in Figure 3.250, and the positions and angular acceptances of the tracker are illustrated in Figure 3.251.

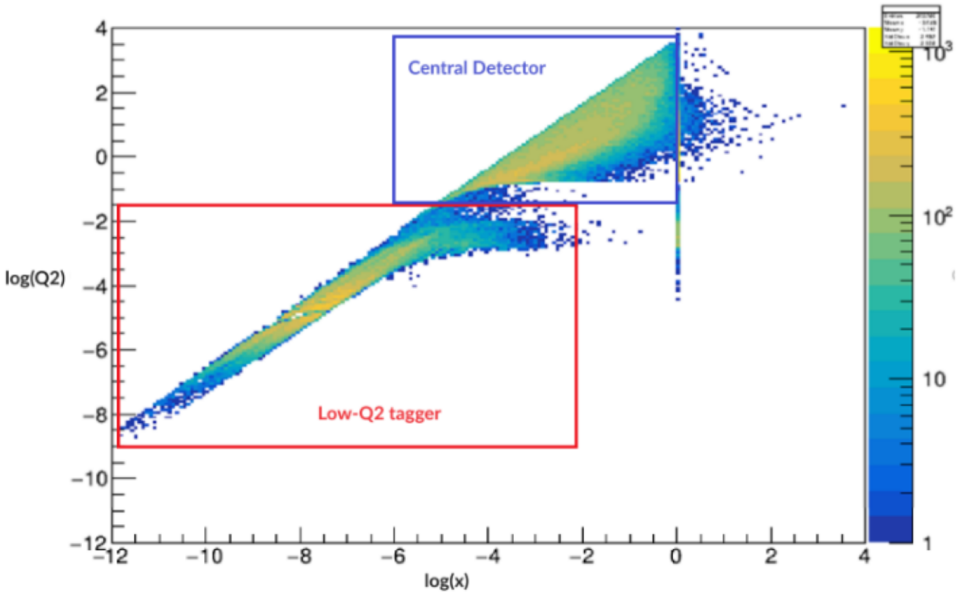

Figure 3.250: Acceptance ranges of the Central Detector and Low-Q^2 Trackers as function of Q^2 and x.

More on resolution here? Too much here on spectroscopy - maybe reduce and more from the ArXiv paper blurb. Or add other sections with other physics titles. I added two.

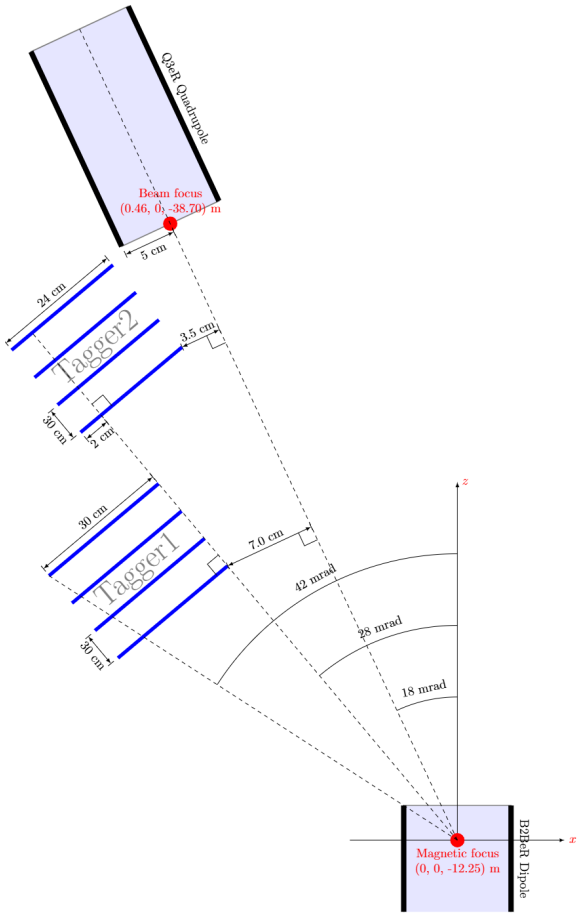

Figure 3.251: Low-Q^2 tagger coverage.

TCS Add text

Vector Meson production Add text

Spectroscopy Reduce - only want to know how it influences the detector requirements. Electron-ion collisions, where the electron is scattered through a very shallow angle, correspond to the case where the exchanged photon is almost real. Such photoproduction processes are of interest in their own right, but also can enable a program of hadron spectroscopy. Furthermore, as the virtual photon flux is highest in this region, yields may be relatively high or rare states may be searched for.

A topic of particular interest is the photoproduction of exotic charmonium-like mesonic states. Commonly refered to as XYZ spectroscopy, these states were originally seen in decays containing J/ψ mesons and additional products. Despite there being many missing charmonium states these states do not fit the quark model expectations in terms of numeracy, masses or widths. While the Z_c^+ states were manifestly exotic as their charge required additional constituent quarks to a $c\bar{c}$ pair.

The production cross section of these states is expected to be low, of order 1 nb and branching ratios

to particles that can be detected can also be small. Therefore tagging a large fraction of the virtual photon flux is essential for making measurements of exclusive production of these states. The energy of the tagged photon can be used to determine the reaction invariant mass, W, and provide exclusivity discrimination when combined with the measured meson state from the central detector and hadron from the far-forward region.

Reconstruction of the azimuthal angle for the electron would provide an effective linearly polarised photon beam, with polarisations up to 1 when the tagger electron energy is close to the beam energy. Reconstructing this angle will be challenging and probably only possible with sufficiently high scattering angles. Provided this information alongside the virtual photon degree of polarisation, which will mainly depend on the measured energy, would allow additional constraints to be used in partial wave analysis of the meson decay allowing the production amplitudes to determined.

The Q^2 of the scattering is not directly of use for these reactions, however ultimately it can be used to reject bremsstrahlung electrons which would improve the analysis.

Count rate estimates were performed for a number of exotic states in [**?**] including branching ratio through to detected particles and using the models developed in [**?**] . To summarise for the charmonium-like XYZ states they are expected to be of the order 1000 per day at luminosities of $10^{34} cm^2 s^- 1$, while for double J/ψ or Z_b decays there may be 10s per day.

Given just providing evidence of the existence of these states in photoproduction would be a great result, as few of these states have been seen in more than one production mechanism, tagging efficiencies of 10% would be sufficient. However to perform detailed physics studies to determine quantum numbers and production amplitudes, which may provide insight into their exotic nature, or to measure rarer states such as the Z_b, large data samples would be required.

Requirements from Radiation Hardness:

The Low-Q^2 trackers are in the far backward region, where the incident flux is predominantly from bremsstrahlung electrons (MIPS). This means there is no requirement for a radiation hard classification for the trackers. However, the intensity is focused on a narrow band in the bend plane (see Figure 3.252), particularly close to the beam line, and trackers should be designed to *spread the load* by period vertical translation, and exchange of modules.

Requirements from Data Rates:

The Low-Q^2 system must operate at a full projected EIC luminosity.
The Low-Q^2 system must operate in extreme background conditions (synchrotron radiation, bremsstrahlung events and beam gas) at the levels specified by the simulation studies.
The Low-Q^2 trackers shall provide timing resolution sufficient to resolve 10 ns beam buckets.
The Low-Q^2 tagger will be able to measure the momentum of more than 10 electrons per bunch crossing.

The rate distributions, based on simulation, are illustrated in Figure 3.252. It is clear that the raw rates on the detectors are dominated by bremsstrahlung, with increasing intensity closer to the bend plane, and to the beam line. These results can be used to calculate the integrated data rates for DAQ and storage, and the bottom right plot can be used to estimate the maximum rate which the tracker must be able to handle, in terms of pixel, column, sensor and board. The rates are summarised in Figure 3.253.

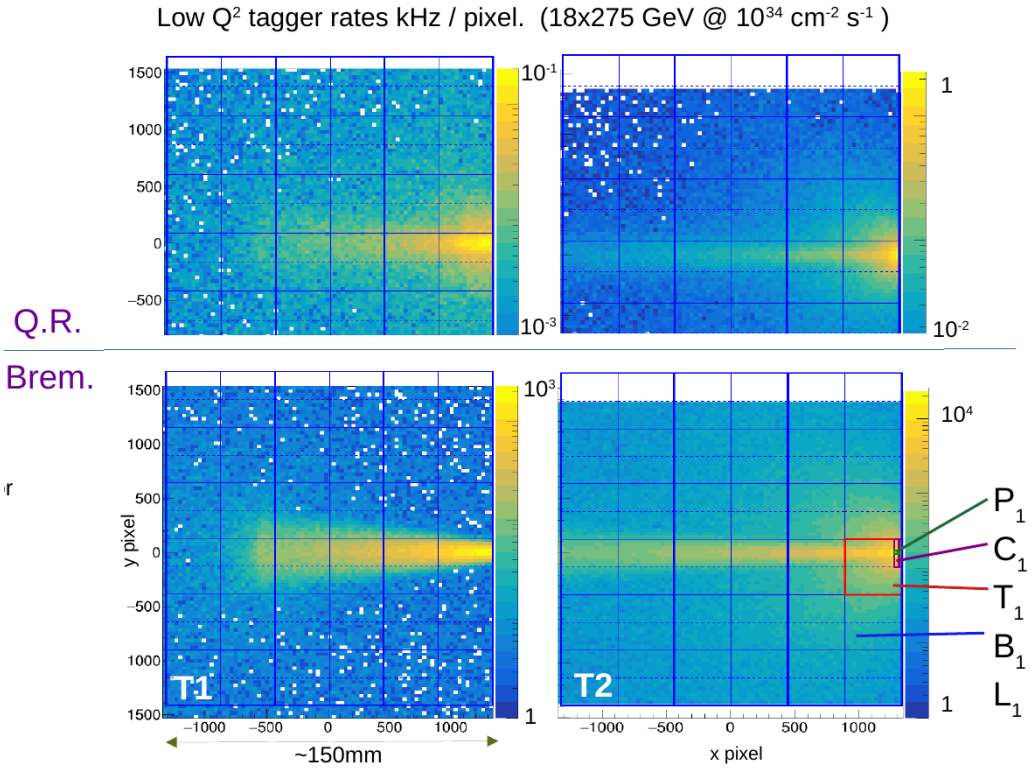

Figure 3.252: Hit rates on tracker layers for Quasi Real (Top) and bremsstrahlung (bottom) electrons, incident on Tagger 1 (left) and Tagger 2 (right), This design is based on layers with three carrier boards, each containing twelve Timepix4 hybrid sensors. The dashed lines indicated the centre lines of the Timepix4 ASICS, where the vertical columns terminate.

Justification

Device concept and technological choice: As described above, the Low-Q^2 detector will consist of two separate taggers, each with a silicon tracker and a calorimeter. For the trackers, the positions and layer spacing are still to be optimised on the basis of simulations. The essential characteristics are angular resolution (since all other quantities are derived from polar and azimuthal angles), rate capability and background rejection. For pixel detectors, the angular resolutions relate to pixel size, or, more precisely, to the position resolution of the centroids of pixel clusters. From the simulations it is clear that 55 μm pixels (Timepix4 pixel size) would provide very good resolution. Bigger pixels would still provide acceptable resolution, but high segmentation is even more important for rate capability, where the efficiency for separating multiple tracks within a single event needs to be as high as possible: For an electron-proton collision event, at maximum lumonisity there are typically ten background bremsstrahlung electrons within the same beam bucket, each passing though all layers of a tagger and creating hits. Furthermore, in each layer there will be *singles* resulting from rescattering, or synchrotron radiation, together with hits from detector noise. However, we already have enough information to set some constraints on detector and readout technologies. We have used Timepix4 as the template for much of the development, and have had its dimensions, readout and rate capabilities as a strong influence in the development of the current design. However, where possible, we used *generic* pixel detectors - particularly in the Geant4

Maximum rates		
Pixel (P1)	70 kHz	
2 column (C1)	8 MHz	
Tpix4 (T1)	600 MHz	38 Gb/s
Board (B1)	1500 MHz	96 Gb/s
Layer (L1)	2500 MHz	160 Gb/s

Total integrated rates		
Tagger 1	2 GHz	130 Gb/s
Tagger 2	7 GHz	480 Gb/s
Total	**9 GHz**	**600 Gb/s**

Data buffered & filtered:	need a hadron in main detect	
Trigger rate: 500 kHz:	99.4% rejection (brem only)	
Data rate (signal):	4 Gb/s	
Data rate (incl BG and rand sample)	**<20 Gb/s**	To tape

Figure 3.253: Maximum and integrated rates for Low-Q^2 trackers.

simulations, with the aim of being able to evaluate other current, or emerging, technologies.

It is already clear, both from a basic knowledge of the kinematics of bremsstrahlung and quasi-real events, and from preliminary simulations, that the intensity of electrons passing through the trackers will be distributed in a highly non-uniform way, with the bulk of the events close to the plane of the accelerator, and the flux increasing strongly towards the electron beamline. In particular, the rates on Tagger 2 are significantly higher than Tagger 1, with the hottest zone closest to the beamline (Figure 3.253). For an estimate of the relevant rates we focus on the bremsstrahlung distribution in Tagger 2 and superimpose a tracking layer geometry based on three boards, each consisting of 12 Timepix4 hybrids, as shown in Figure 3.252. The six Timepix4 detectors running across the centre of Tagger 2 take the bulk of the events, with the very highest on the one closest to the electron beam (T1). The small vertical offset between the centre of the board and the accelerator plane is to ensure that the centre line (dashed), where the top and bottom vertical 255 pixel columns meet, does not coincide with the very high rate band. The maximum rate estimates can be obtained by integrating over the relevant bins of the 2D histogram, and are shown in Figure 3.253. Although the dimensions of pixels and sensors are from Timepix4, these rates are *detector agnostic*, in the sense that they merely quantify numbers of electrons passing though the 55μm pixels in the tracking plane. After comparison with other technologies with other technologies proposed for the ePIC detector (MAPS, AC-LGAD) is became clear that Timepix4 is the only solution which can provide the required combination of rate capability, timing resolution and position resolution. The calorimeter ..... paragraph.

The final configuration and position of the Low-Q2 tagger is still to be decided, since it depends on the position and structure of the magnets and beamline configuration in the backward regions. These are not yet finalised.

Subsystem description Tracker :

There are two trackers, each consisting of four layers on pixel sensors. The sensors are mounted on carrier boards (12 sensors per board) which connect to a readout modules. Read-

out modules perform some presorting and pass data to cluster and tracking modules and data buffers. Tracks which are in coincidence with a hadron in the central detector are saved in the main DAQ readout.

Sensors: Timepix4 ASIC with Silicon sensor.

FEE: SPIDR4 readout to custom FPGA clustering and tracking modules.

Other components: Frame / infrastructure with cabling and cooling for layers with removable carrier boards. Cabling from boards to readout modules (housed below on platform).

Subsystem description Calorimeter: Main purpose of the calorimeter is direct energy measurement for cross check with energy obtained from trackers, where it is measured indirectly via ML methods. Also alignment and fake-track reduction will benefit from the use of the calorimeter.

General device description: In the initial running at lower luminosity when in-bunch pileup from Bethe-Heitler bremsstrahlung is relatively small it is assumed to share the same technology as luminosity pair spectrometer, i.e. scintillating fibers embedded in tungsten-powder epoxy (SciFi), read-out by SiPMs. General layout of the SciFi calorimeter is indicated in Fig. 3.254, giving tower arrangement of 4 layers. Total perpendicular size is given by the trackers. The towers are arranged perpendicular to shower axis. Fibers inner radius is 0.25 mm, fiber spacing is 1 mm. Optical photons are detected by SiPMs, shown as yellow rings at the end of each fiber. It is assumed that groups of 4x4 fibers in the same cell act as a single SiPM. Opposite ends of the fibers are ended by aluminum mirrors, shown as green caps.

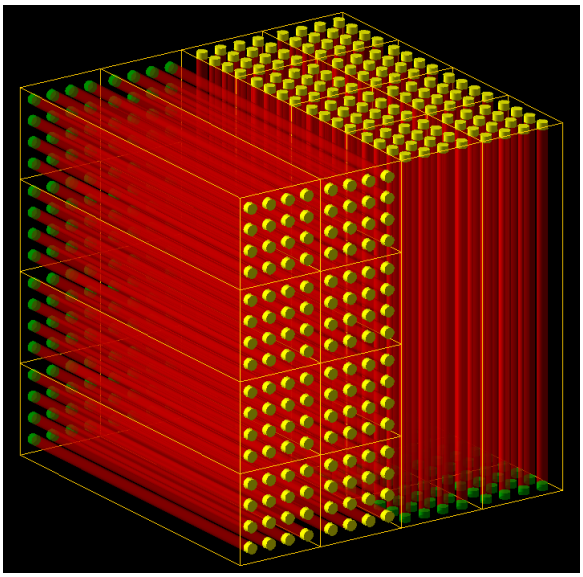

Figure 3.254: Layout of SciFi calorimeter.

For the case of nominal collider luminosity, reached in later runs, the in-bunch pileup from Bethe-Heitler bremsstrahlung will cause calorimeter rates to reach bunch crossing frequency, giving some signal every 10 ns at top luminosity for 10x100 GeV beams. Calorimeter technology will be shared with luminosity direct photon detector, where only Cherenkov fibers can fulfill the rate requirement. Expected energy resolution is shown in Fig. 3.255

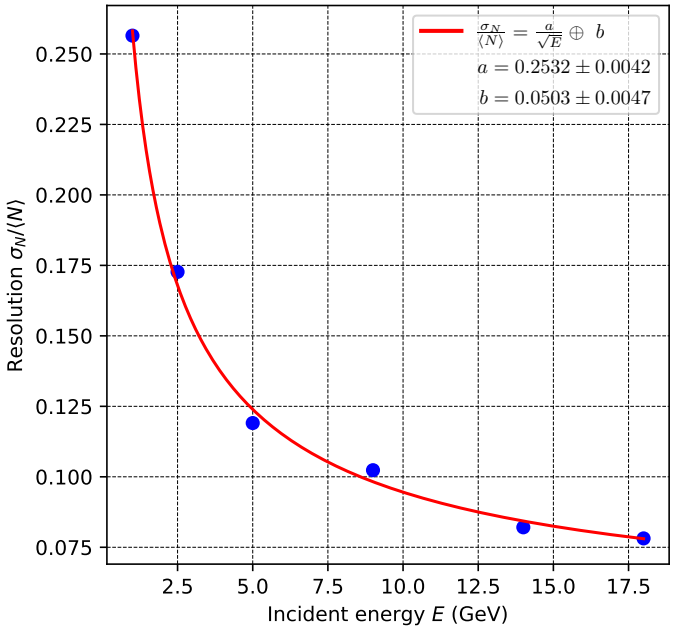

Figure 3.255: Energy resolution for Cherenkov fiber calorimeter.

Diameter for quarts fibers 1.5 mm, fiber spacing is 2.5 mm. The resolution is mainly driven by limited Cherenkov photon yields. Photon detection efficiency of 0.41 is included.

Sensors: SiPM, specific SiPM with fast capacitive coupling is required for nominal luminosity, possible example is Onsemi 30035 series.

FEE: fADC250 (flash ADC, 250 MSPS, 12 bit) for nominal luminosity

Other components: Add text here.

Performance Figures 3.256, 3.257 and 3.258 show the performance of the Trackers based on current simulation.

Implementation

Services: No special services.

Subsystem mechanics and integration: The taggers are housed on platforms which need to be movable in vertical and horizontal (towards beamline) directions. Lower platform for readout modules in close proximity for readout modules. Bias and LV per board (24 total). Chiller (800W) per tagger.

Calibration, alignment and monitoring: Procedures for calibration and equalisation of individual sensors are already well established within the Medipix collaboration. These will be mapped

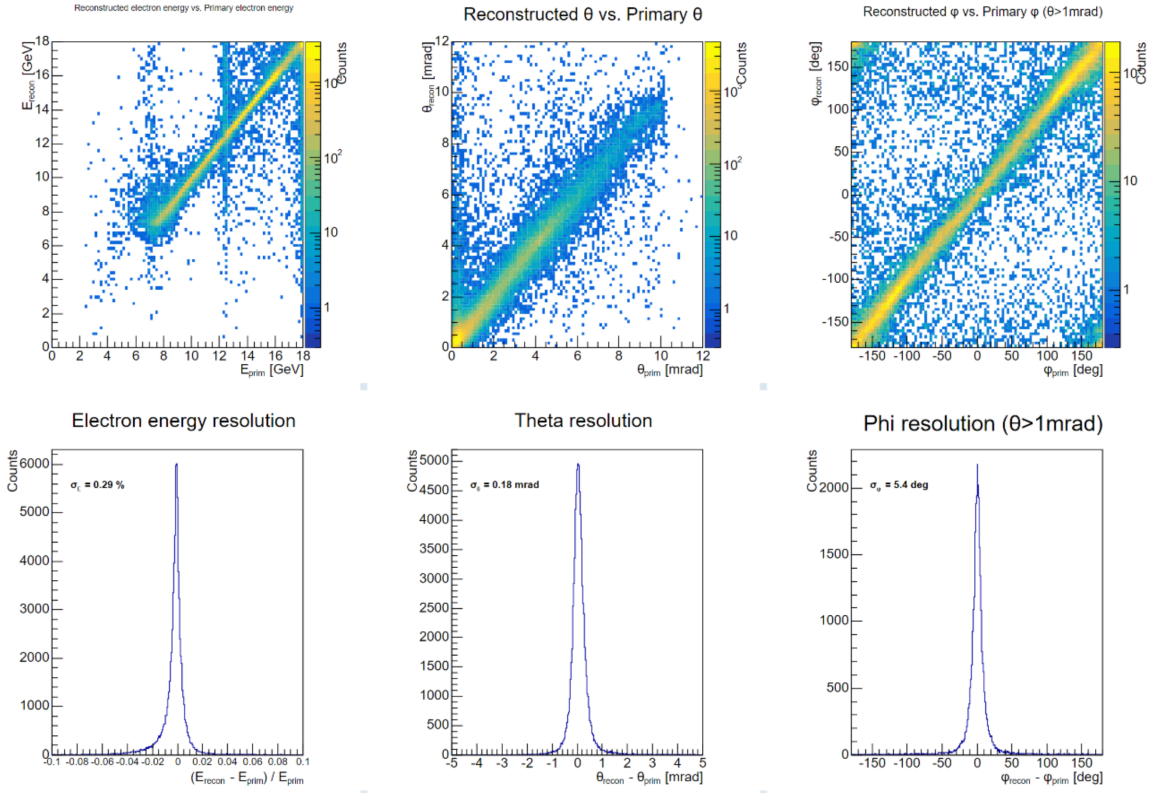

Figure 3.256: Top - Reconstruction of the initial electron energy, θ and ϕ angles from fitted tracks. Bottom - Integrated reconstruction difference.

to a dedicated Slow Controls interface for the tracker. Alignment and timing calibrations require tracks; they can be developed locally using cosmic rays and more rigorously tested in beam at Jlab or one of the European facilities.

Status and remaining design effort:

More a total effort not just R&D

R&D effort:
Electron tracker
Total expected from UK Infrastructure project in FTE years:
Academic 1.5
Senior Researchers 2.5
Postdocs 10.0
Technical 3.0
PhDs 10
Additional Requirement: Postdoc 6 FTE Years

R&D status and outlook:
Electron tracker:

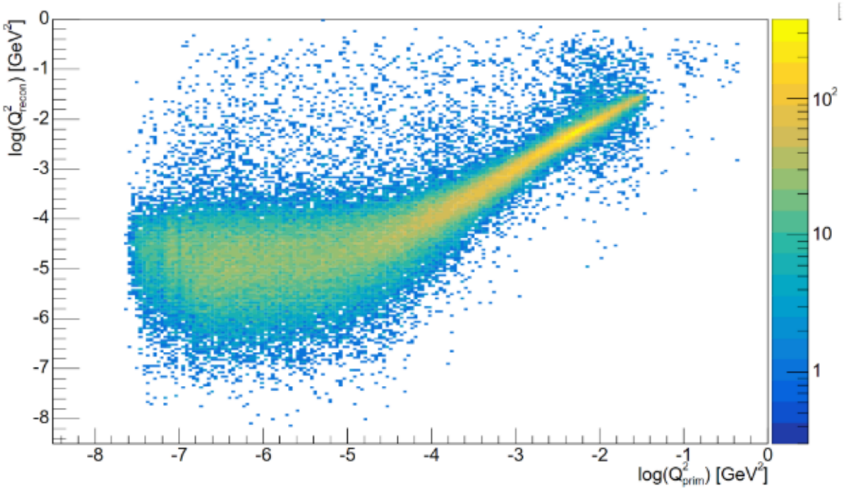

Figure 3.257: Reconstruction of the initial electron as a function of Q^2.

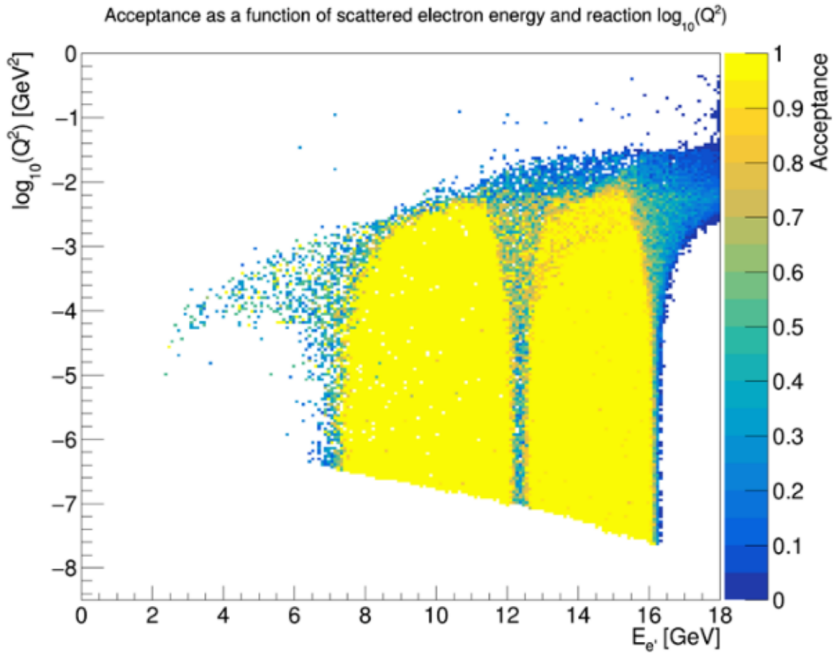

Figure 3.258: Acceptance as a function of Q^2 and $E_{e'}$.

A test rig with SPIDR4 and Timepix4+Si sensors is complete, and fast readout tested. The development of prototype tracker with single sensor layers in progress. To be tested in stand-alone mode in Mainz, Dec24, with a further test using preliminary ePIC DAQ at Jlab in 2026. Carrier board for 12 x Timepix4 sensors to be developed and approved by Dec 2027. Procurement and fabrication of layers from Jan 2028 - 2030. Completion of taggers including

mechanical infrastructure, cooling, readout to be completed in Glasgow by Dec 2030 with delivery to BNL Jan 31.

Other activity needed for the design completion
Final decision on positioning, layer dimensions and spacing is still to be made. The requires completion of designs for magnets, beamline and vacuum windows in the backward region.

Status of maturity of the subsystem:
Electron tracker
The Timepix4 sensor is well established, and is the latest in a series of detectors by the CERN Medipix collaboration. Current applications used the wire-bonded readout mode, but the TSV (through silicon vias) mode is in fast development, and we anticipate having a test setup within the next few months. The TSV mode is required to allow 4-side buttability, and fabrication of the layers with no dead space. The current readout uses SPIDR4 from the NIKHEF group in Amsterdam. We will collaborate with the developers to make an upgraded version of their carrier boards and readout to handle the data from the 12 sensor layer modules.

Environmental, Safety and Health (ES&H) aspects and Quality Assessment (QA planning): We will follow all procedures laid out by BNL and other labs where production test and development are carried out. During the engineering design phase, we will include production of mockups and engineering test articles to insure the proper functionality and quality, and will have full production chain tests for each sub-system.

For operation with HV and cooling we will ensure that these are mechanically secure and not a trip hazard, have proper warning signs and follow the lab procedures for electrical safety, and for operation near the beam-pipe and vacuum, anyone working near the far-forward/backward detectors will wear ear protection, and will post signage to that effect.

Construction and assembly planning: The tracker modules will be constructed assembled and tested in Glasgow as Work Package 2 (WP2) of the UK's EIC Infrastructure project. We will follow closely the fabrication and quality control procedures developed for the LHCb Velopix and ATLAS ITK detectors by the Glasgow experimental particle physics group.

Collaborators and their role, resources and workforce: The electron trackers are a *deliverable* within the UK's EIC Infrastructure project. The resources for constructing and delivering the trackers are expected to be mostly met by this. However, the project is still to be passed through a peer review panel and the costings for the tracker work package officially approved. As outlined above, we anticipate that we need and additional 6 FTE postdoc years for simulation, analysis and thermal modelling relating to detector development.

Risks and mitigation strategy: The Timepix4 tracker is being developed in close collaboration with colleagues in the Medipix collaboration. We will use suppliers and services recommended by them for wafers and production. For local production, fabrication and testing we have a team trained in bonding and quality control in case of staff changes. Our maximum rates have been calculated on the basis of EIC maximum proton luminosities, so in the initial running we will be well below capacity.

Additional Material Add text here.

3.3.9 Polarimeters

3.3.9.1 The electron polarimeters

The electron polarization will be measured in two locations in the EIC accelerator complex. The first polarimeter will be in the Rapid Cycling Synchrotron (RCS) and will be primarily used for setup of the accelerator, and hence has rather modest performance requirements. The second will be in the Electron Storage Ring (ESR), near the ePIC detector. The performance requirements for this polarimeter are more challenging. Both systems will employ Compton backscattering and will be described in the following sections.

Requirements

Requirements from physics: The measurements made using the ePIC detector will require high-precision, non-destructive measurement of the electron beam polarization. In particular the, Compton polarimeter in the ESR will measure the electron beam polarization with systematic uncertainty of $dP/P < 1\%$. This implies that the measurement must be made for each electron bunch in the ring individually (since the polarization can vary bunch-to-bunch) and that the polarimeter must measure both the longitudinal (P_L) and transverse (P_T) components of the beam polarization (since the polarimeter cannot be located between the spin rotators due to space constraints). Due to the short amount of time that bunches will be stored in the ESR at the highest energy, the system must also be able to make polarization measurements of a single bunch within ≈ 2 minutes. The need to measure the polarization bunch-by-bunch also places challenging requirements for the detector and electronics response time due to the small time (10 ns) between bunches at 5 and 10 GeV.

The primary purpose of the RCS polarimeter will be to monitor the evolution of the electron polarization between the electron source (which injects electron bunches into the RCS) between the injection energy of 3 GeV and the ESR energies of 5, 10, or 18 GeV. The required absolute systematic uncertainty requirements are less challenging ($dP/P < 2-3\%$) and the measurement need not be made for each bunch separately. In addition, since bunches are injected into the RCS at 1-2 Hz, the detector rate requirements are much easier to meet.

Justification The most commonly used technique for measuring electron beam polarization in rings and colliders is Compton polarimetry, in which the polarized electrons scatter from 100% circularly polarized laser photons. The asymmetry from this reaction is measured via the scattered electrons or high energy backscattered photons. A brief review and description of several previous Compton polarimeters can be found in [137]. A particular advantage of Compton polarimetry is that it sensitive to both longitudinal and transverse polarization.

The longitudinal analyzing power depends only on the backscattered photon energy and is given by,

$$A_{\text{long}} = \frac{2\pi r_o^2 a}{(d\sigma/d\rho)}(1-\rho(1+a))\left[1-\frac{1}{(1-\rho(1-a))^2}\right], \tag{3.2}$$

where r_o is the classical electron radius, $a = (1+4\gamma E_{\text{laser}}/m_e)^{-1}$ (with the Lorentz factor $\gamma = E_e/m_e$), ρ is the backscattered photon energy divided by its kinematic maximum, E_γ/E_γ^{max}, and $d\sigma/d\rho$ is the unpolarized Compton cross section. In contrast, the transverse analyzing power depends both on the backscattered photon energy and the azimuthal angle (ϕ) of the photon (with

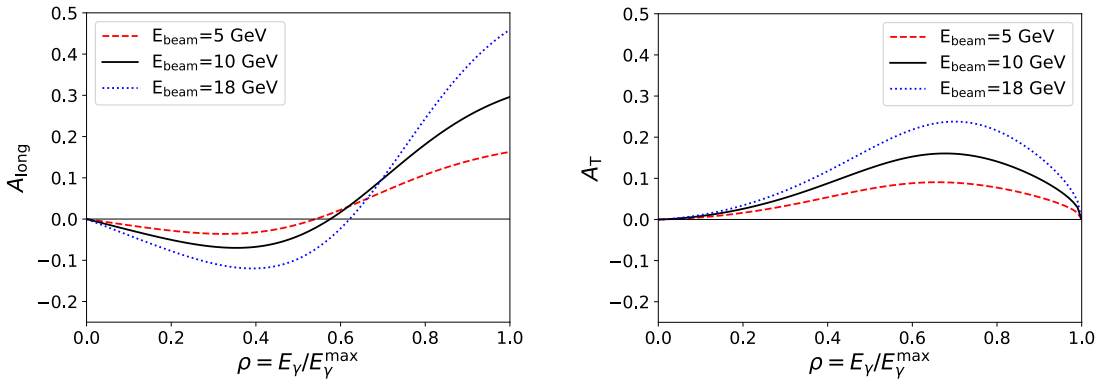

Figure 3.259: Longitudinal (left) and transverse (right) analyzing powers assuming a 532 nm wavelength laser colliding with an electron beam at 5 GeV, 10 GeV, and 18 GeV. The transverse analyzing power is shown for the case $\phi = 0$, i.e., the backscattered photon angle is in the same plane as the (transverse) electron polarization direction.

respect to the transverse polarization direction);

$$A_{\mathrm{T}} = \frac{2\pi r_o^2 a}{(d\sigma/d\rho)} \cos\phi \left[\rho(1-a) \frac{\sqrt{4a\rho(1-\rho)}}{(1-\rho(1-a))} \right]. \tag{3.3}$$

This azimuthal dependence of the asymmetry results in an "up-down" asymmetry (assuming vertically polarized electrons) and requires a detector with spatial sensitivity. Both the longitudinal and transverse analyzing powers are shown in Fig. 3.259.

The ESR Compton Polarimeter is designed to be able to determine both the longitudinal and transverse electron polarization simultaneously with high precision, while the polarimeters for the RCS will primarily determine the transverse polarization.

Subsystem description: ESR Compton Polarimeter

Performance The ESR Compton Polarimeter will measure the electron beam polarization bunch-by-bunch with a systematic uncertainty of $dP/P \leq 1\%$. It will also be able to measure both the longitudinal and transverse polarization. These requirements determine the configuration of the polarimeter, the performance of the polarimeter detectors, as well as the required properties of the Compton laser system.

Implementation The primary components of the ESR Compton are:

- Laser system to provide the photon "target" for the electron beam. The ESR Compton laser system will be a pulsed laser with repetition rate equal to the bunch frequency.
- Photon detector system: the photon detector system will consist of an electromagnetic calorimeter to provide event tagging and total energy measurement of the backscattered photons and a position-sensitive detector to measure the transverse position dependence of the asymmetry for measurement of the transverse beam polarization.

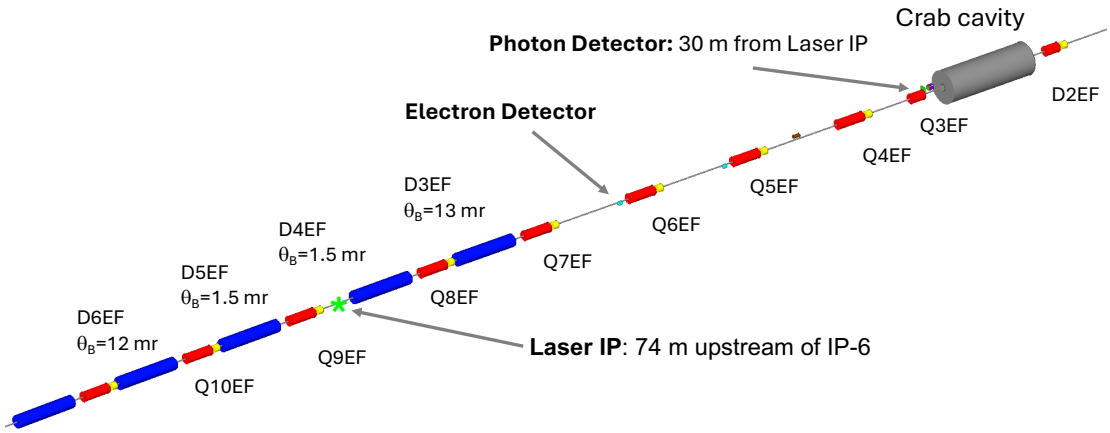

Figure 3.260: Layout of the Compton Polarimeter in the ESR. The collision point between the laser and electron beam is about 74 m upstream of the ePIC detector IP.

Beam energy (GeV)	P_L (%)	P_T (%)
5	99.1	13.2
10	96.5	26.2
18	89.0	45.6

Table 3.73: Beam polarization components at the ESR Compton laser IP for the EIC nominal electron beam energies.

- Electron detector: the electron detector system will consist of position sensitive detectors to measure the asymmetry vs. energy of the momentum-analyzed scattered electrons.

Subsystem mechanics and integration

Polarimeter layout in ESR The layout of the Compton Polarimeter in the Electron Storage Ring is shown in Fig. 3.260. The Compton interaction point is $\approx$ 74 m upstream of the EPIC IP. This location is downstream of the spin rotators which convert the vertical electron polarization direction to horizontal. The total in-plane spin-precession is such that at the ePIC IP, the electron polarization is purely longitudinal, but at the Compton IP it will be a mix of longitudinal and in-plane transverse. The expected polarization components are summarized in Tab. 3.73.

A key feature of the ESR beamline in the vicinity of the Compton Polarimeter is the introduction of a pair of "weak" dipoles ($\theta_{bend} \approx 1.5$ mrad, more typically, the dipoles bend the beam by about 14.5 mrad in that area) around the laser IP. These weak dipoles bend the beam just enough to mitigate the flux of synchrotron radiation incident on the polarimeter detectors. Fig. 3.261 shows simulations of the expected synchrotron radiation before and after the introduction of these dipoles.

Custom vacuum chambers will be needed in the laser IP and for extraction of the backscattered photons and scattered electrons. These chambers will be designed in a manner to minimize impact on the beamline impedance, yet allow unimpeded transport of the laser and scattered particles in and out of the vacuum system.

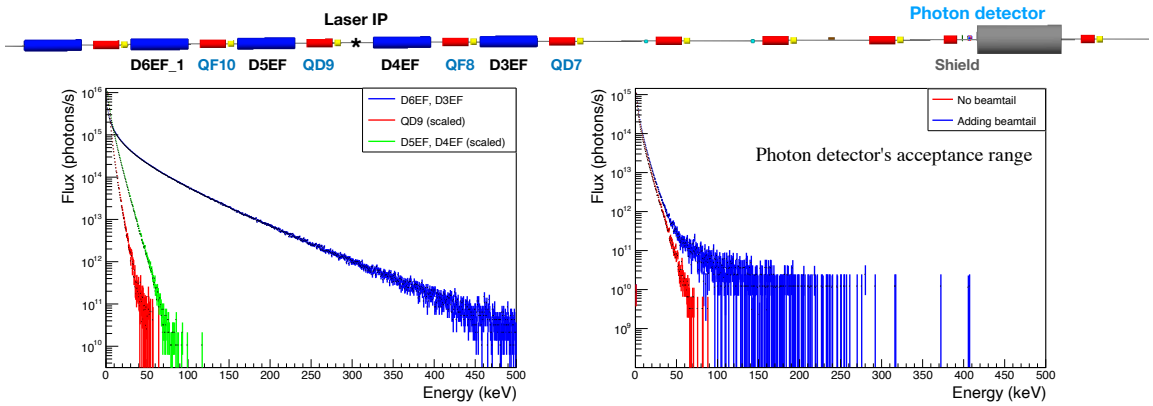

Figure 3.261: Simulated synchrotron radiation in the ESR Compton Polarimeter photon detector at 18 GeV without (blue curve) and with (green curve) the "weak" dipoles introduced around the Compton IP. GeV

Laser System The requirement to measure the polarization for each bunch in the storage ring sets the requirements for the polarimeter laser system. A pulsed laser system with repetition rate at the electron bunch frequency is required to unambiguously identify a given event with a particular electron bunch. In addition, at the highest energy (18 GeV), a given bunch will only be stored in the ESR for 1-2 minutes, meaning that the laser system must have sufficient power to provide measurements of statistical precision better than 1% in that time period.

The luminosity (per bunch) for a pulsed laser colliding at an angle α_c with an electron bunch is give by,

$$\mathcal{L} \approx f N_\gamma N_e \frac{\cos(\alpha_c/2)}{2\pi} \frac{1}{\sqrt{\sigma_{x,\gamma}^2 + \sigma_{x,e}^2}} \frac{1}{\sqrt{(\sigma_{y,\gamma}^2 + \sigma_{y,e}^2)\cos^2(\alpha_c/2) + (\sigma_{z,\gamma}^2 + \sigma_{z,e}^2)\sin^2(\alpha_c/2)}} \tag{3.4}$$

where f is the collision frequency (=73 kHz for a single bunch in the ring), $\sigma_{x(y)}$ are the transverse sizes of the electron and photon bunches, σ_z is the longitudinal bunch size and $N_\gamma = \frac{P_{laser}}{(hc/\lambda)f_{laser}}$ and $N_e = \frac{I_e}{ef_e}$ are the number of photons and electrons in bunch, respectively. In the vicinity of the Compton IP, the electron beam transverse beam size is expected to be on the order $\sigma_{x,y} =$ 300 μm and the longitudinal bunch length about σ_z = 0.7 cm. The laser system will have a smaller transverse size (100 μm) to allow measurement of the polarization profile of the electron beam and comparable longitudinal profile (a 30 ps pulse width). Tab. 3.74 shows the expected rate of backscattered photons from a single electron bunch assuming a 532 nm wavelength laser with average power 5 W colliding with the electron beam at a crossing angle of 2.5 degrees. It's worth noting that the laser power is chosen give 1-2 backscattered photons per bunch, to allow a counting-mode measurement of the asymmetry.

The time needed for a measurement of a given precision depends on the square of the relevant analyzing power as noted in the equation below:

$$t^{-1} = \mathcal{L}\sigma P^2 \left(\frac{\Delta P}{P}\right)^2 A_{method}^2 \tag{3.5}$$

where $\mathcal{L}\sigma$ is the luminosity and total cross section, $\frac{\Delta P}{P}$ is the relative precision of the measurement and A_{method}^2 is the analyzing power (squared) for the relevant measurement technique. In

E_e (GeV)	I_e (A)	Rate	$A_{L,diff}$	$t_{L,diff}$	$A_{L,Ewgt}$	$t_{L,Ewgt}$	$A_{T,diff}$	$t_{T,diff}$
5	2.5	116.7 kHz	7.8%	28.9 s	7.4%	31.9 s	5.5%	58.1 s
10	2.5	103.2 kHz	13.7%	10.6 s	12.3%	13.1 s	9.6%	21.6 s
18	0.26	9.2 kHz	20.3%	53.5 s	16.6%	80.3 s	13.9%	113.7 s

Table 3.74: Backscattered photon rates, analyzing powers and measurement times (per electron bunch) for the beam and laser parameters described in the text. The beam polarization is assumed to be 70%.

this discussion, A^2_{method} can be $A^2_{diff} = \langle A^2 \rangle$, where the spectrum of the asymmetry is measured, $A^2_{Ewgt} = \left(\frac{\langle EA \rangle}{\langle E \rangle}\right)^2$, where the energy-weighted asymmetry is measured, or $A^2_{avg} = \langle A \rangle^2$, where the simple average asymmetry is used. In general, the energy-weighted and differential measurements have the highest figures of merit so will be used here.

Tab. 3.74 shows analyzing powers and ideal measurement times for a 1% (statistics) measurement of the electron beam at 5, 10, and 18 GeV using the beam and laser properties assumed above for the longitudinal polarization using the differential and energy-weighted techniques, and for the transverse polarization using just the differential technique. In all cases, the measurement times meet the requirements dictated by the bunch lifetime in the storage ring.

The laser system for the ESR Compton Polarimeter will be housed in a dedicated laser room outside ring and transported to the laser IP via fiber optic cable The system will utilize a gain-switched seed laser with wavelength of 1064 nm operating at the electron bunch frequency (100 MHz or 25 MHz). The gain-switched seed laser will be amplified to 10-20 Watts using a fiber amplifier, then frequency-doubled to 532 nm using a PPLN doubling crystal. The conceptual layout of the laser system is shown schematically in Fig. 3.262. Of note is the partially reflective window at the beamline exit, that will allow continuous monitoring of the laser polarization at the collision point using the back-reflection technique implemented in [138]

Photon Calorimeter: The photon calorimeter for the ESR Compton Polarimeter will be used to measure the energy of the backscattered photons and will use one of the forward EMCAL modules, a 5 x 5 x 17 cm^3 tungsten-scintillating fiber calorimeter. The forward EMCAL is described in detail in Sec. 3.3.5.3 and is expected to have an energy resolution of $\frac{\sigma_E}{E} \approx \frac{10\%}{\sqrt{E}} \bigoplus 1-3\%$. With the reduction of the synchrotron radiation background due to the addition of weak-bending dipoles near the laser IP, we expect to operate the photon detector in threshold-less, energy integrating mode, rather than measuring the energy spectrum. This results in relaxed requirements for the detector energy resolution. The forward EMCAL will silicon photomultipliers for extracting the light yield from the calorimeter modules, however, we plan to use instead a single photomultiplier tube, which is easier to interpret for energy-integrating measurements.

An LED system similar to that described in [139] will be used to determine the linearity of the photon detector system. In the threshold-less, energy-integrating technique, it is not crucial that absolute detector response be known, but the linearity directly impacts the measured asymmetry so must be determined. A collimator will be placed upstream of the detector to help reduce backgrounds and unabmiguously define the detector accetpance.

In addition, the photon detector system will set on a movable detector stand, which will enable centering of the detector on the backscattered photon cone, reducing systematic uncertainties due to misalignment of the collimator relative to the backscattered photon cone.

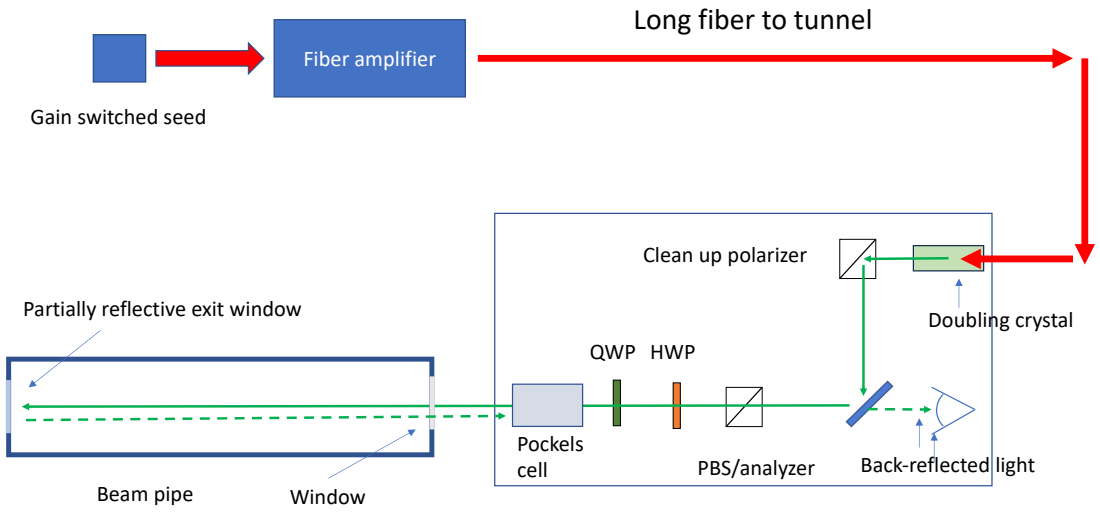

Figure 3.262: Schematic layout of the ESR Compton Polarimeter laser system. The gain-switched seed and fiber amplifier will be housed in a dedicated laser room outside the ring and transport to the Compton IP via fiber. A laser table under the beamline at the IP will include the frequency doubling crystal, beam focusing and polarization optics.

Position Sensitive Detectors: Position sensitive detectors will be used to measure the spatial dependence of the transverse Compton asymmetry at the photon detector as well as for measuring the longitudinal asymmetry for the scattered electrons. Diamond strip detectors will be used for systems, due in large part to their radiation hardness and fast response times.

The photon detector will use 2 planes of diamond strips, each 5 cm long x 1 cm wide with a piece of tungsten one radiation length (3.5 mm) thick to convert the backscattered photons to electrons. On plane will be oriented vertically to measure the vertical beam polarization and the other horizontally to measure the horizontal components. Note that the vertical component is expected to be zero, but it will be measured to verify that the spin-rotating solenoids upstream of the Compton are performing as expected.

The detector length is chosen to match the size of the photon calorimeter and the detector pitch (strip size) is dictated by the shape of the asymmetry. The size of the backscattered photon cone is smallest at the highest beam energy, so the 18 GeV requirements determine the detector pitch. Fig. 3.263 shows a simulation of the extracted asymmetry from a diamond strip detector with strip size of 100 μm vs. horizontal position at the photon detector. Both the "true" (generated) and reconstructed positions are shown. The asymmetry for the reconstructed photon position case is very similar to that for the "known" position, indicating that a segmentation of 100 μm is appropriate and will not require significant corrections to the measured asymmetry.

The size of the scattered-electron diamond strip detector is determined by the scattered electron spectrum at the highest energy. The highest precision can be achieved when both the kinematic endpoint asymmetry as well as the zero crossing can be measured. At the planned position of the electron detector (just upstream of quadrupole Q6EF as shown in Fig. 3.260) the difference in deflection from the nominal beam path for the scattered electrons at 18 GeV is about 5 cm. The detector pitch is determined by the desire to have at least 30 strips between the endpoint and zero-crossing. At 18 GeV, this would be 1.7 mm, but the separation between the beam and scattered

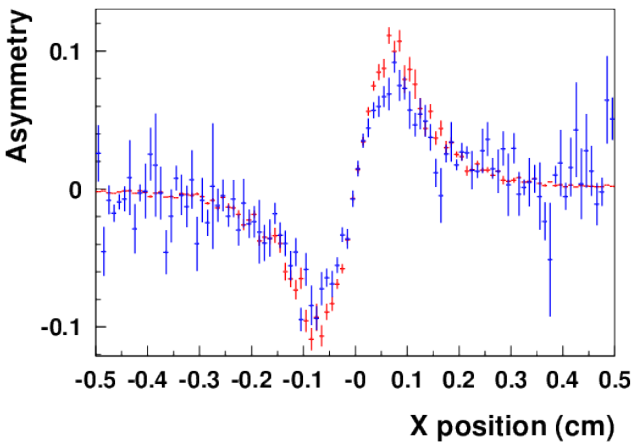

Figure 3.263: Simulated asymmetry from a diamond strip detector for Compton scattering from a transversely polarized electron beam at 18 GeV. The red points show the asymmetry vs. the generated x position, while the blue use the reconstructed value.

Beam energy (GeV)	Δx_{max} (mm)	Δx_0 (mm)
5	23.0	11.2
10	44.6	21.5
18	101.4	46.3

Table 3.75: Deflection from nominal beam path for the Compton scattered electrons at the position of the diamond strip detector for electrons at the kinematic endpoint (Δx_{max}, where the asymmetry is largest) and at the zero-crossing of the asymmetry (Δx_0).

electrons decreases with decreasing beam energy (see Tab. 3.75). At 10 GeV, the required strip pitch would be 0.77 mm, and at 5 GeV, 0.39 mm. The Compton asymmetry vs. position at the diamond strip detector is shown in Fig. 3.264. Unfortunately, at 5 GeV, the electrons at the zero crossing of the asymmetry are too close to the nominal beam path (11.2 mm) to be extracted from the beamline vacuum and detected in the diamond strips. Rather, only about half the desired spectrum will be available at 5 GeV. Nonetheless, we will use a strip pitch of 400 μm for the electron detector. The limited electrum spectrum at 5 GeV may result is larger systematic uncertainties for the measurement of the longitudinal asymmetry.

As noted earlier, a key benefit of using diamond strips is the fast response time, needed to measure the beam polarization for each bunch separately. However, the small signals characteristic of diamond detectors requires a custom ASIC capable of providing the amplification required without introducing noise. A new ASIC has been developed for use with a new diamond detector in experimental Hall A. This ASIC, the so-called FLAT32, is a higher channel-density version of the CALYPSO electronics used at LHC. Both CALYPSO and FLAT32 were developed by SenseICs, a small business in Columbus, OH. The FLAT32 is capable of producing fast, low-noise output in the form LVDS digital pulses from diamond strips. Fig. 3.265 shows a photo of the FLAT32 on a prototype board as well as the signals resulting from the ASIC. Of note is that this chip is capable of pulse-widths smaller than 10 ns, the bunch spacing at 5 and 10 GeV at EIC. This ASIC, or a slightly modified version, is an excellent candidate for use with the ESR Compton diamond detectors.

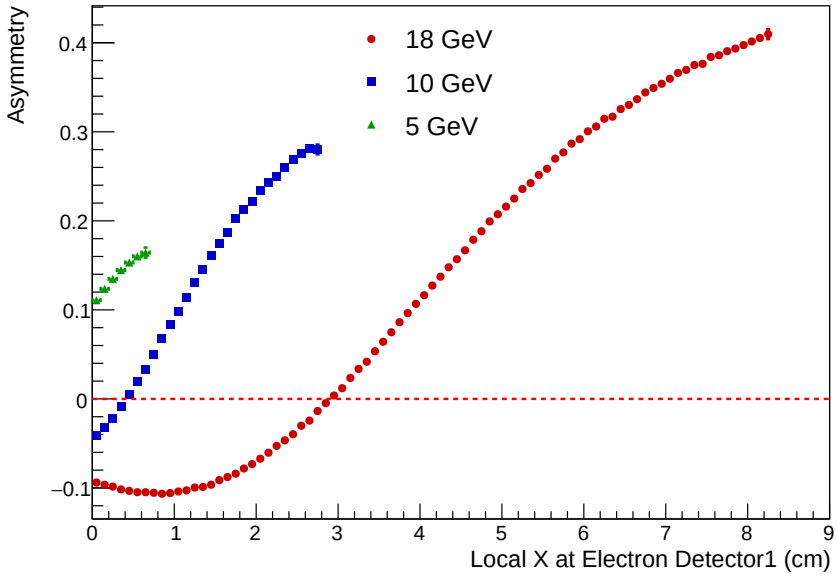

Figure 3.264: Asymmetry vs. scattered electron position at the Compton diamond strip electron detector position for the three ESR beam energies (5, 10, 15, GeV). Only the part of the scattered electron spectrum 1.8 cm or farther from the beam is shown (1.8 cm from the beam corresponds to 0.0 on the plot).

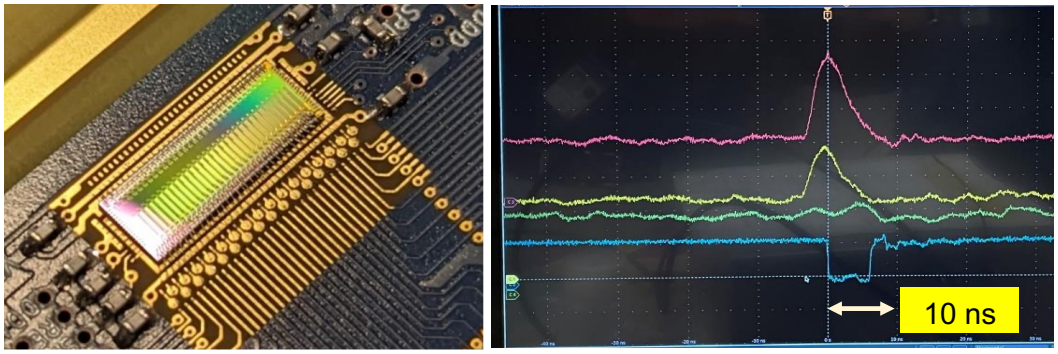

Figure 3.265: (left) Photograph of FLAT32 ASIC developed for Hall A at Jefferson Lab mounted on a test PCB. (right) Analog pulses and LVDS output from an initial prototype of the FLAT32 ASIC. The LVDS pulse width is less than 10 ns.

Data Acquisition The ESR Compton Polarimeter will use a stand-alone data acquisition system, separate from the ePIC DAQ. The rather simple detectors and modest channel count imply that a fairly simple DAQ setup can be used. Key components will include:

- A flash ADC for the photon calorimeter. This ADC will have a custom firmware for operation in threshold-less integrating mode, and will also be able to extract the pulse-height/pulse-integral for a subset of events. An FADC similar to the JLAB FADC250 is adequate for this application.

- A digital logic module or TDC will be used for reading out the LVDS (or other logic) pulses resulting from the diamond strip detectors. A module similar to the JLAB VETROC modules is appropriate for this application.
- An LVDS repeater is required to propagate the output of the diamond ASICs to the DAQ.
- Signals from the laser system (polarization state, etc.) will be incorporated in the DAQ via additional channels in the digital logic/TDC. A signal tagging the bunch number in the ring is also required.

One challenge is that although the data volume will not be extremely large, the data rate (100 MHz) will be. One proposal is to accumulate detector counts, integrated energy, etc. in a buffer for each of the $\approx$1000 bunches separately, and read out out these accumulated quantities during intervals when the laser helicity is flipping, which will take on the order of 1 ms.

Status and remaining design effort:

E&D status and outlook: While the fundamental concept for the ESR Compton Polarimeter beamline integration exists, detailed design activities for the interface between the laser and beamline, as well as the scattered electrons and backscattered photons must be completed. In addition, minor design effort is need for the detector stands for both the photon and electron detector.

Other activity needed for the design completion: In addition to mechanical design work, the impact on the beamline impedance must be checked for the ESR Compton interface designs. The data acquisition must also be specified in more detail (specific modules, etc.), but the requirements for the polarimeter DAQ are not considered very challenging.

Status of maturity of the subsystem: The conceptual design for the ESR Compton Polarimeter is mature, with only detailed design work required.

Environmental, Safety and Health (ES&H) aspects: Beyond the typical ES&H considerations for nuclear physics detectors (HV, etc.), the polarimeter will require dedicated laser areas both inside and outside the storage ring. These areas must adhere to all DOE laser-safety standards and include an interlock system with crash buttons and smoke detector connected to the interlock system (the latter is required for Class IV lasers).

Collaborators and their role, resources and workforce: At this time, the ESR Compton Polarimeter is being developed and constructed by the workforce at Jefferson Lab and BNL.

Technological Challenges and Path Forward: No technological challenges in the construction of the ESR Compton Polarimeter are expected. Near-term plans are to develop detailed designs for mechanical and storage-ring interface components.

Subsystem description: RCS Compton Polarimeter

Performance The RCS Compton Polarimeter will measure the electron beam polarization averaged over several bunches with a systematic uncertainty of dP/P=2-3%. It will primarily measure the transverse electron polarization, but it will have the capability to measure the longitudinal polarization.

The RCS operates in a fundamentally different mode than the electron storage ring, which impacts the design and operation of the polarimeter. Electron bunches of up 28 nC are injected into the RCS at 750 MeV, with a frequency of 1-2 Hz. Each bunch is ramped from the injection energy to the operating energy of the ESR (5, 10, or 18 GeV) in 100 ms. This mode of operation makes it impossible to measure the polarization of each electron bunch. A single bunch will interact with the laser system at a given energy (for example, 4.1 GeV) a single time. This makes it impossible to measure an asymmetry from that bunch at fixed energy. It would be possible to measure an asymmetry from a single bunch, but over many different beam energies. Since the analyzing power for Compton scattering depends on beam energy, this would make it exceedingly complicate to extract a meaningful beam polarization. Rather, the RCS Compton polarimeter will measure the beam polarization *at a given energy*, averaged over several injected electron bunches. Such a measurement, when combined with the polarization measurement in the injector via Mott polarimetry, will be sufficient to determine the polarization transport performance of the RCS.

Implementation The primary components of the RCS Compton are:

- Laser system to provide the photon "target" for the electron beam. The RCS laser system will be a low duty cycle, large pulse energy (10-40 mJ) laser. Such lasers are commercially available from several vendors.
- Photon detector system: like the ESR Compton, the photon detector system will consist of an electromagnetic calorimeter to provide event tagging and total energy measurement of the backscattered photons and a position-sensitive detector to measure the transverse position dependence of the asymmetry for measurement of the transverse beam polarization.
- In contrast to the ESR polarimeter, no electron detector will be used.

Subsystem mechanics and integration A schematic of the RCS along with the planned location of the Compton Polarimeter is shown in 3.266. The laser system will located about halfway through the first straight section after the electron injector with the photon detector after the arc bend, about 20 m downstream of the Compton IP. Like the ESR polarimeter, the RCS laser system will require a custom vacuum chamber for the laser to enter and exit the beampipe. This vacuum chamber will mimic the design for the ESR chamber as much as possible. In addition, a special section of beampipe will be needed to allow the backscattered photons to exit the vacuum system.

Laser System The laser system for the RCS Compton Polarimeter will be an off-the-shelf, low duty-cycle, pulsed laser with pulse energy 20-40 mJ. To make polarimetry measurements in a reasonable amount of time, the RCS polarimeter will need to operate in "multi-photon" mode, in which each laser-electron bunch crossing will result in many backscattered photons. The estimated rate can be calculated using Eq. 3.3.9.1, using 1-2 Hz for the nominal collision frequency, 8 ns for the laser pulse length. We assume the same collision angle since we plane to use the same design for the Compton interaction point vacuum chamber. The resulting rates and measurement times are shown in Tab. 3.76. Although the measurement will be made in multi-photon mode, using the differential, transverse analyzing power is most appropriate since the total energy deposited in the

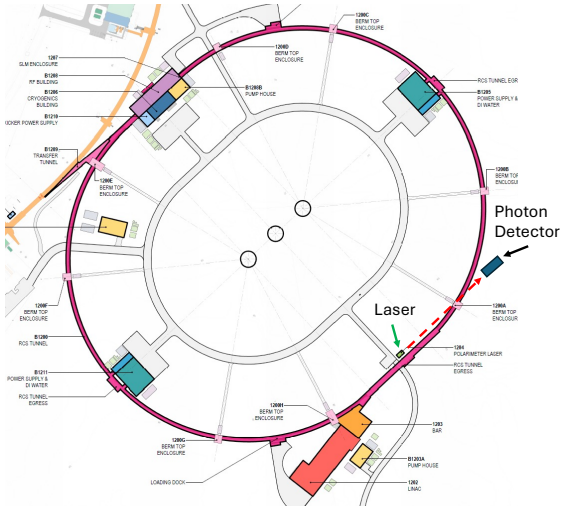

Figure 3.266: Layout of the Rapid Cycling Synchrotron. The RCS Compton Polarimeter laser will be located about halfway through the first straight section after the electron injector with the photon detector after the arc bend, about 20 m downstream of the Compton IP.

E_e (GeV)	Rate	N_γ/bunch	$A_{T,diff}$	$t_{T,diff}$
5	10.3 kHz	5178	5.5%	655.0 s
10	9.2 kHz	4600	9.6%	243.8 s
18	7.9 kHz	3932	13.9%	133.2 s

Table 3.76: Backscattered photon rates, analyzing powers and measurement times using the RCS Compton. We assume a 28 nC electron bunch colliding with 40 mJ laser pulse at 2 Hz. Measurement time is calculated for a beam polarization of 70% and a statistical uncertainty of $dP/P = 1\%$.

position sensitive detectors will be proportional to the number of backscattered photons (i.e., each photon will deposit about the same amount of energy in the thin strip detectors).

The measurement times range from about 2 minutes (at 18 GeV) to 11 minutes (at 5 GeV).

Due to the low average current of the electron beam in the RCS, radiation levels are not expected to be high. The will allow the placement of the laser system in the RCS, near the interaction point. A special, laser-safe enclosure will be required where the laser enters the beamline, and the laser itself will be housed in the same location

Detectors The RCS Compton polarimeter will use the same detectors as the ESR polarimeter. The photon calorimeter will be a 5 x 5 x 17 cm^3 tungsten-scintillating fiber, forward EMCAL module. As in the ESR, the signal will be collected using a single PMT to allow easy measurement of the energy-weighted asymmetry. Note that the calorimeter will primarily be used as a trigger for the position sensitive detectors since the polarization will be transverse. However, extraction of the energy-weighted asymmetry in the calorimeter will provide verification that there is no longitudinal beam polarization. Like the ESR system, the RCS calorimeter will be mounted on a movable table to allow centering the detector on the backscattered photon cone.

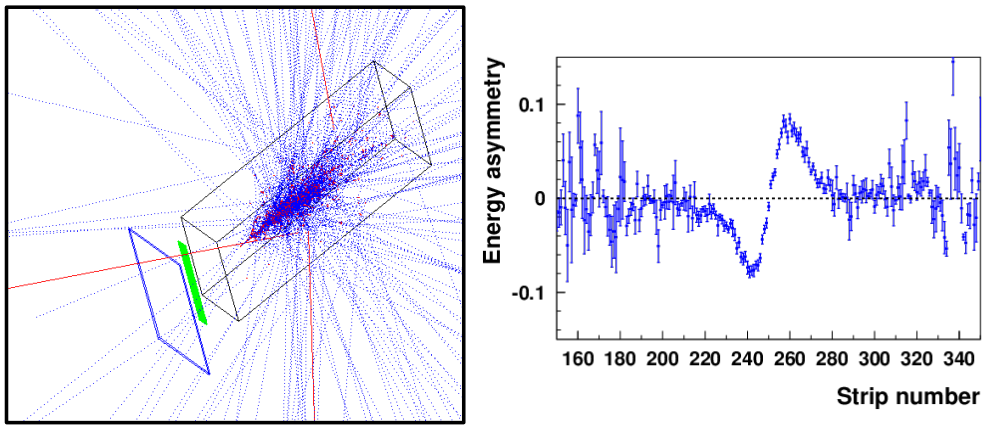

Figure 3.267: Simulation of photon detector system for the RCS Compton Polarimeter. (left) The photon calorimeter (black box) is shown along with a 5 cm tall diamond strip detector (green) with 1 RL tungsten radiator (blue). (right) Simulation of energy-asymmetry for each strip of the diamond strip detector. 10 laser pulses were simulated with an average of 10,000 backscattered photons per pulse.

The RCS Compton Polarimeter will also use diamond strips to make measurements of the position dependence of the transverse asymmetry. However, since the RCS polarimeter will operate in multi-photon mode, the readout will have to be adapted. Rather than a single digital output for hit in a given strip, the RCS diamond detector must provide an analog signal from each strip to provide the total energy deposited in a strip for each collision. Fortunately, the FLAT32 ASIC developed for JLab can be programmed to provide the analog pulse in place of the digitized LVDS output. To send the signal more than a few meters, a stand-alone amplifier or repeater will be needed.

As in the ESR, the segmentation required for the diamond detectors is determined by the shape of the asymmetry at 18 GeV. In Fig. 3.267, a simulation of the asymmetry measured from a diamond strip detector with a strip-width of 0.1 mm is shown. The simulation assumes ≈10,000 backscattered photons per laser pulse, and was run for 10 pulses. The asymmetry is calculated in terms of the energy deposited in each strip, i.e., $A_{strip} = \frac{E^+_{strip} - E^-_{strip}}{E^+_{strip} + E^-_{strip}}$. A radiation length piece of tungsten is placed just upstream of the diamond detector to convert the backscattered photons to charged particles. As seen in the figure, a strip pitch of 0.1 mm is clearly adequate for determining the shape of the asymmetry spectrum.

Data Acquisition The RCS Compton Polarimeter will use a stand-alone data acquisition system. As is the case for the ESR polarimeter, the rather simple detectors and modest channel count imply that a fairly simple DAQ setup can be used. Key components will include:

- Flash ADCs for the photon calorimeter and the diamond strip detectors. The flash ADCs will be triggered by the laser pulse and will provide the pulse integral from each channel. An FADC similar to the JLAB FADC250 is adequate for this application.
- An analog signal amplifier or repeater is required to propagate the output of the diamond ASICs to the DAQ.
- Signals from the laser system (polarization state, etc.) will be incorporated in the DAQ via additional channels in the digital logic/TDC. A signal tagging the bunch number in the ring

is also required.

Status and remaining design effort:

E&D status and outlook: The fundamental concept for the RCS Compton Polarimeter beamline integration exists. Detailed design activities for the interface between the laser and beamline, as well as the backscattered photons must be completed. In addition, minor design effort is need for the detector stand for the photon detector.

Other activity needed for the design completion: The data acquisition must also be specified in more detail (specific modules, etc.), but the requirements for the polarimeter DAQ are not considered very challenging.

Status of maturity of the subsystem: The conceptual design for the RCS Compton Polarimeter is mature, with only detailed design work required.

Environmental, Safety and Health (ES&H) aspects: Beyond the typical ES&H considerations for nuclear physics detectors (HV, etc.), the RCS polarimeter will require a dedicated laser area inside the RCS. This area must adhere to all DOE laser-safety standards and include an interlock system with crash buttons and smoke detector connected to the interlock system (the latter is required for Class IV lasers).

Collaborators and their role, resources and workforce: At this time, the RCS Compton Polarimeter is being developed and constructed by the workforce at Jefferson Lab and BNL.

Technological Challenges and Path Forward: No technological challenges in the construction of the RCS Compton Polarimeter are expected. Near-term plans are to develop detailed designs for mechanical and storage-ring interface components.

3.3.9.2 Hadron polarimetry systems

Overview and Requirements The Electron-Ion Collider physics program requires hadron beam polarimetry with unprecedented precision to extract spin-dependent observables from electron-hadron collisions [22]. The polarimetry system must deliver absolute beam polarization measurements exceeding $P = 0.7$ with a relative uncertainty of $\delta P/P \leq 1\,\%$, representing a five-fold improvement over current RHIC capabilities [140]. This stringent requirement necessitates a hierarchical measurement approach combining absolute calibration through the Hydrogen Jet Target (HJET) polarimeter with fast relative measurements from proton-carbon (pC) polarimeters distributed along the accelerator.

The physical basis for hadron polarimetry at EIC energies relies on Coulomb-Nuclear Interference (CNI) in elastic scattering at small momentum transfer [7, 141, 142]. In this kinematic regime, electromagnetic and hadronic amplitudes interfere constructively, producing analyzing powers of $A_y \approx 0.046$ at $t = 0.003\,\mathrm{GeV}^2$ for, e.g., proton-proton elastic scattering, as shown in Fig. 3.268. The electromagnetic contribution to this interference arises from the same anomalous magnetic moment that determines the proton g-factor, $g_p = 2(1 + G_p)$, where $G_p = (g_p - 2)/2$ is the anomalous gyromagnetic ratio [143]. At EIC energies ranging from 23.5 GeV injection to 275 GeV storage, no scattering processes exist with analyzing powers known to the required absolute accuracy [8]. This

fundamental limitation drives the requirement for a polarized hydrogen jet target with precisely determined nuclear polarization measured via the Breit-Rabi polarimeter [144, 145].

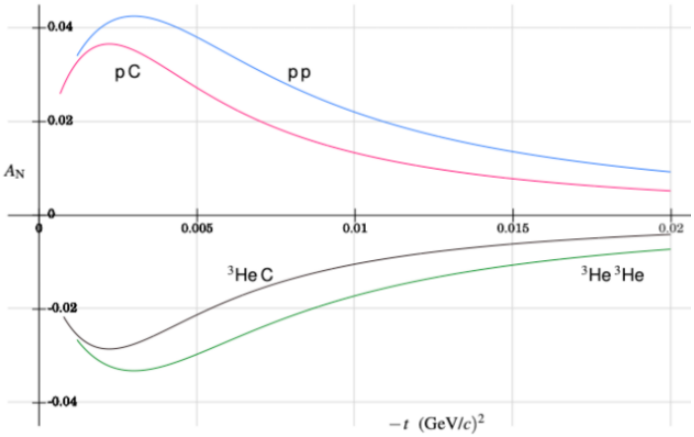

Figure 3.268: Coulomb-nuclear interference (CNI) analyzing power A_N versus $-t$ for pp, pC, ^{3}HeC, and ^{3}He ^{3}He. (Figure taken from [7].)

The fundamental challenge for absolute beam polarimetry at EIC energies is that no scattering process exists with analyzing powers known to the required 1% precision [8]. This necessitates the use of a polarized hydrogen jet target with precisely determined nuclear polarization. The measurement principle relies on the relationship,

$$P_{\text{beam}} = \frac{\varepsilon_{\text{beam}}}{\varepsilon_{\text{target}}} \cdot Q_{\text{target}}\,, \tag{3.6}$$

where ε represents the measured left-right scattering asymmetries with respect to beam and target, and Q_{target} is the precisely known target polarization determined by the Breit-Rabi polarimeter.

The asymmetry measurements form the core of the calibration procedure. When the polarized beam scatters from the polarized hydrogen target, silicon strip detectors positioned symmetrically on the left and right sides of the beam measure recoil protons in the CNI kinematic range. The target asymmetry is determined from the accumulated detector counts via $\varepsilon_{\text{target}} = (L - R)/(L + R) = A_y Q_{\text{target}}$, where L and R are the left and right detector count rates and A_y denotes the analyzing power. The sign of the target polarization Q_{target} is periodically reversed to eliminate systematic asymmetries from detector geometry or efficiency differences [146]. A corresponding measurement with the circulating beam yields $\varepsilon_{\text{beam}}$, and since the analyzing power A_y is identical for elastic scattering of identical particles regardless of which is polarized, the beam polarization is extracted through the ratio of asymmetries. This approach transfers the precision from the well-understood atomic physics of hydrogen to the beam polarization measurement, enabling the stringent systematic uncertainty control required for EIC physics [144, 145].

The polarimetry system must characterize the complete beam polarization vector $\vec{P} = (P_x, P_y, P_z)$ throughout the acceleration cycle and during physics stores. Measurements are required at injection energy where a 30 min electron cooling period provides optimal conditions for absolute calibration, and continuously at storage energy during typical 8 h stores. The system must resolve transverse polarization profiles across the beam to identify depolarizing resonances and betatron coupling [147], provide bunch-by-bunch measurements at the $\approx$ 90.7 MHz bunch frequency, and track polarization lifetime to quantify depolarization rates [148].

Operating parameters differ substantially from RHIC experience, with the EIC featuring a tenfold increase in bunch frequency ($\approx$ 90.783 MHz versus $\approx$ 9.4 MHz), bunch intensities ranging from 6.9×10^{10} protons at flattop to 2.76×10^{11} at injection, and transverse beam sizes varying from $\sigma_r = 1.57$ mm at injection to 0.66 mm at flattop. These parameters drive fundamental design modifications including increased magnetic holding fields for the HJET to avoid beam-induced depolarization [10], enhanced thermal management for carbon targets, and new detection electronics capable of sub-nanosecond timing resolution.

Beyond the baseline proton program, the polarimetry system must anticipate future measurements of polarized light ions including $^3He^{++}$, deuterons, and potentially ^6Li and ^7Li beams [149]. Each species presents unique challenges in atomic beam source development, analyzing power determination, and detection optimization. The ^3He program, scheduled for early EIC operations, requires development of a cryogenic atomic beam source operating at 1 K to achieve the necessary target thickness and polarization [150]. Deuteron polarimetry must address both vector and tensor polarization components characteristic of spin-1 systems [151]. Future lithium beams will require entirely new polarimetry approaches adapted to their nuclear structure and available atomic physics techniques.

Proton beam polarimetry The proton polarimetry system employs a two-tier measurement strategy combining absolute calibration from the Hydrogen Jet Target (HJET) polarimeter with continuous fast monitoring from proton-carbon (pC) polarimeters. The HJET provides the fundamental calibration standard with target polarization determined by the Breit-Rabi polarimeter [144, 145], which in principle can achieve systematic uncertainties below 0.5 % for the atomic polarization. However, careful attention must be paid to molecular hydrogen contamination in the atomic beam, as the nucleons inside H_2 molecules are unpolarized and dilute the effective target polarization. The pC polarimeters enable rapid polarization profile measurements and bunch-by-bunch monitoring throughout physics stores [147, 152–154]. This hierarchical approach ensures both the accuracy required for systematic uncertainty control and the time resolution necessary for operational optimization.

HJET absolute polarimeter The HJET polarimeter, shown in Fig. 3.269, measures the absolute beam polarization through elastic proton-proton scattering between the circulating beam and a polarized atomic hydrogen target. The system comprises three integrated components: a polarized atomic beam source generating hydrogen atoms in specific hyperfine states, a scattering chamber where the atomic beam intersects the circulating hadron beam within a precisely controlled magnetic holding field, and a Breit-Rabi polarimeter that determines the atomic target polarization through Stern-Gerlach analysis [144, 145].

The most critical modification for EIC operation involves increasing the magnetic holding field from RHIC's 120 mT to approximately 400 mT. This change addresses beam-induced depolarization arising from the EIC's tenfold increase in bunch frequency [10]. At $\approx$ 90.7 MHz bunch repetition rate, the frequency spectrum of beam-induced electromagnetic fields extends to harmonics that resonantly drive hyperfine transitions in hydrogen atoms at the lower field. Analysis of the photon emission rate shows that at 120 mT, essentially all hyperfine transitions fall within populated beam harmonics, with the spectral cutoff occurring at $f_{\text{cut}} = \approx 5060$ MHz (harmonic number $n_{\text{cut}} \approx 56$). The resonance spacing narrows to approximately 1.5 mT compared to 4 mT at RHIC, making atoms susceptible to depolarization even from transient field variations.

Operating at 400 mT, as discussed in Ref. [10], shifts all hyperfine transition frequencies above potentially depolarizing harmonics, specifically placing the lowest dangerous transition $f_{13}/f_b \approx$

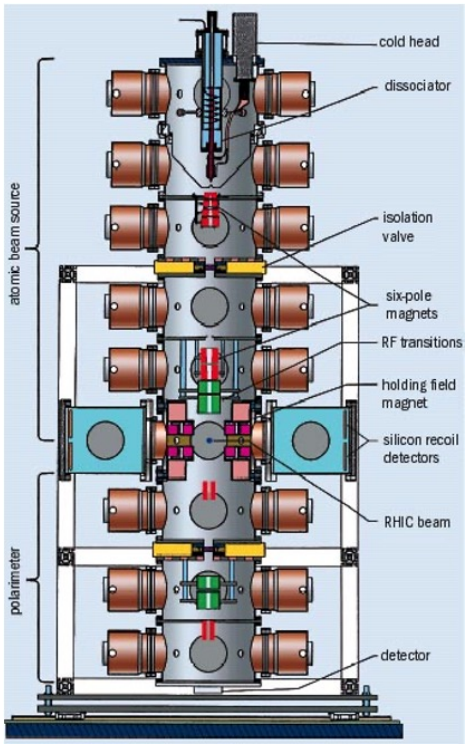

Figure 3.269: Schematic layout of the HJET polarimeter, taken from Ref. [8], showing the atomic beam source, the scattering chamber, and the Breit–Rabi polarimeter.

$125/n_{\text{cut}} \approx 2.2$ times above the spectral cutoff. This safety factor ensures robust operation even accounting for power broadening effects and spatial field variations across the atomic beam. Quantum mechanical analysis confirms that transitions which would cause depolarization at 120 mT become negligible at the higher field [10].

A critical systematic uncertainty that directly impacts the absolute polarization determination arises from molecular hydrogen contamination in the atomic beam. While recent analyses have claimed total systematic uncertainties below 0.5 % [155], the methodology used to determine the H_2 fraction – measuring with the dissociator turned off – does not accurately represent operational conditions [10]. In actual operation, hydrogen atoms that are defocused by the sextupole magnets recombine on the magnet surfaces, creating an effusive molecular beam that accompanies the atomic beam to the target region. Analysis of data from similar atomic beam sources demonstrates that 3 % to 4 % molecular contamination is typical [156,157]. This molecular fraction fundamentally limits the polarimeter's accuracy because H_2 molecules contain unpolarized nucleons that dilute the effective target polarization. The effective target polarization per nucleon is reduced by twice the molecular fraction: if 4 % of the target consists of H_2 molecules, the true nucleon polarization is 8 % lower than what the Breit-Rabi polarimeter measures for the atomic component alone. The upgraded Breit-Rabi polarimeter will incorporate a quadrupole mass analyzer for continuous H_2 monitoring, reducing the associated systematic uncertainty.

The system design modifications include a new target chamber accommodating the larger holding field magnets, upgraded vacuum systems, and new detector systems positioned for EIC beam conditions. The detector configuration and technology selection remain under development, with options including silicon strips, diamond detectors, or alternative technologies to be determined

based on radiation tolerance and timing requirements for bunch-by-bunch measurements. These detectors will measure recoil protons in the CNI kinematic range, providing the asymmetries that determine beam polarization.

For the EIC, the HJET shall deliver a statistical precision of the beam polarization $\delta P/P \approx 3\,\%$ per 4 h integration, assuming an atomic flux of $12.4(2) \times 10^{16}$ atoms/s and an areal target thickness of $\sim 10^{12}$ atoms/cm^2. The apparatus provides an absolute calibration for both transverse polarization components through appropriate detector configurations. The overarching objective is an *absolute* systematic uncertainty on the beam polarization of $\delta P/P \leq 1\,\%$; the time required to reach a given total uncertainty is then dominated by counting statistics. The Breit-Rabi polarimeter (BRP) supplies essentially instantaneous measurements of the target polarization with sub-percent systematic control, consistent with this 1 % beam-polarization goal. At present, the RHIC HJET readout provides sensitivity to the vertical component P_y of the beam polarization. With suitable upgrades, all three Cartesian components (P_x, P_y, P_z) can be determined by (i) increasing detector acceptance to sample the needed azimuthal harmonics and (ii) implementing a flexible magnetic guide-field system so that the quantization axis of the target polarization $\vec{Q}$ can be oriented along $\vec{e}_x$, $\vec{e}_y$, and $\vec{e}_z$. This approach – using controlled guide-field orientations to access and exploit the full set of spin-dependent asymmetries – has been demonstrated at the IUCF Cooler [158] in polarized pp scattering, see Ref. [159, 160].

The planned HJET upgrades for the operation of the system at the EIC include:

1. Holding-field system design and installation; target-chamber redesign accommodating the holding field.
2. BRP upgrade with a mass analyzer for quantitative determination of the H_2 admixture in the target gas.
3. Detector-system modernization for operation at the EIC bunch frequency. Development towards full $\vec{P}$ sensitivity – i.e., holding-field orientation selectable along $\vec{e}_x$, $\vec{e}_y$, and $\vec{e}_z$ – and operation at the EIC bunch frequency.
4. Impedance evaluation following finalization of the holding-field and chamber concepts.

The overarching aim of these modifications is to reduce systematics of the beam polarization determination to $\Delta P/P \leq 1\,\%$. As a next step, the HJET system will be relocated to a suitable BNL lab space in early 2026 to execute items 1–4 when the engineering resources become available.

pC fast polarimeters The proton-carbon (pC) polarimeters provide rapid relative polarization measurements through periodic scans using ultra-thin carbon ribbon targets inserted temporarily into the circulating beam [147, 152]. Each scan, involving a single traversal of the carbon fiber through the stored RHIC beam, achieves statistical precision of $\Delta P/P \approx 1\,\%$ and enables identification of depolarizing resonances during acceleration as well as mapping of polarization profiles across the beam cross-section. Multiple scans performed throughout typical 8-hour stores provide polarization lifetime measurements, while the fast measurement capability supports accelerator operations and beam optimization.

The pC polarimeters exploit Coulomb-Nuclear Interference (CNI) scattering on ultra-thin carbon ribbon targets, read out by six silicon-strip detectors positioned at different azimuthal angles around the beam pipe at radius $\sim 18\,\text{cm}$ [152] (see Fig. 3.270 for the vacuum chamber with in-beam target ladders and Fig. 3.271 (a–d) for the detector system, Si detector, carbon ribbons, and

target ladder). The carbon ribbons measure $w \approx 10\,\mu\text{m}$ width, $t \approx 50\,\text{nm}$ thickness, and $\ell \approx 25\,\text{mm}$ length, with recoil particles detected in the CNI kinematic range. The azimuthal detector arrangement enables measurement of both transverse polarization components P_x and P_y, while remaining insensitive to the longitudinal component P_z. The CNI analyzing power provides sensitivity to beam polarization through azimuthal asymmetries in the scattering distribution [141,142,152]. Absolute polarization calibration is provided by cross-referencing with HJET measurements [145,155].

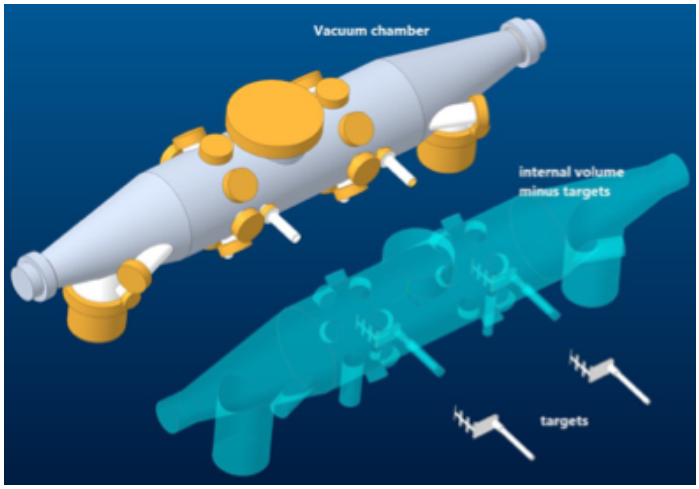

Figure 3.270: One of the pC polarimeter vacuum chambers presently used in RHIC with in-beam target ladders installed inside the beam pipe. There are two target holders that are moved horizontally (shown) and two more (not shown) that are moved vertically, such that the chamber can hold 4×6 carbon-ribbon targets in total.

Detailed thermal modeling based on a code developed by Peter Thieberger (BNL) [9] indicates that target heating remains manageable at EIC conditions when realistic beam sizes are considered (Table 3.77). The calculations show that despite EIC's higher beam energy (275 GeV vs 250 GeV) and increased total beam current from more bunches (1160 vs 120), the larger beam sizes at the polarimeter location ($\sigma_x^{95} = 3.9\,\text{mm}$, $\sigma_y^{95} = 0.7\,\text{mm}$ at EIC flattop vs $\sigma_r^{95} = 0.6\,\text{mm}$ at RHIC [10]) distribute the heat load sufficiently to maintain similar peak temperatures (Fig. 3.272). The modeling predicts maximum target temperatures below the carbon sublimation threshold of approximately $2200\,^\circ\text{C}$, with heating profiles showing gradual temperature rise and decay as the beam traverses the ribbon. This analysis led to a reduction of the target heating risk (ID #128) to low priority in the project risk registry. Independent modeling approaches and experimental validation [161] are currently being developed to validate these thermal calculations and ensure robust target survival under EIC operating conditions.

The comparison in Table 3.77 reveals a significant challenge for EIC polarimetry operations. While RHIC maintained uniform coverage ratios of 11.2 for both orientations, the planned 50 mm carbon targets at EIC provide substantially reduced coverage depending on ribbon orientation and beam energy. As shown in the table, the coverage ratio for horizontal ribbons drops to just 1.45 at injection energy, indicating that the target length barely exceeds the beam width with minimal safety margin. This marginal coverage could lead to reduced counting statistics, and beam offset could result in partial beam loss, causing operational difficulties during polarization profile measurements. To maintain reliable horizontal polarization measurements, particularly at injection energy where absolute calibration occurs during the 30-minute electron cooling period, target lengths significantly longer than 50 mm will likely be required, potentially approaching 100–150 mm to achieve reasonable coverage ratios above 3–4. Longer targets would also benefit thermal management by

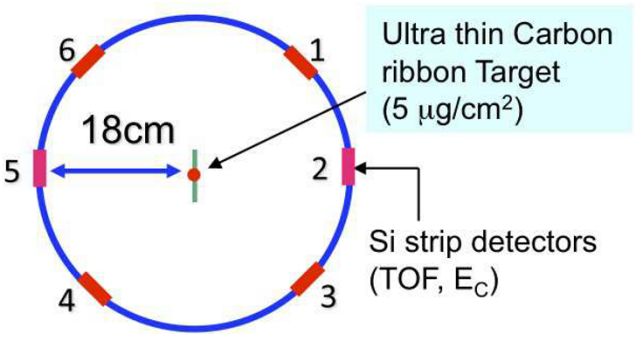

(a) Six-telescope ring (∼18 cm radius).

(b) Silicon-strip detector mounted on a vacuum flange.

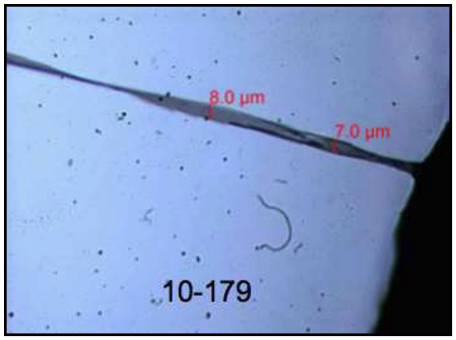

(c) Carbon ribbon ($w \approx 10\,\mu$m, $t \approx 50$ nm, $\ell \approx 25$ mm).

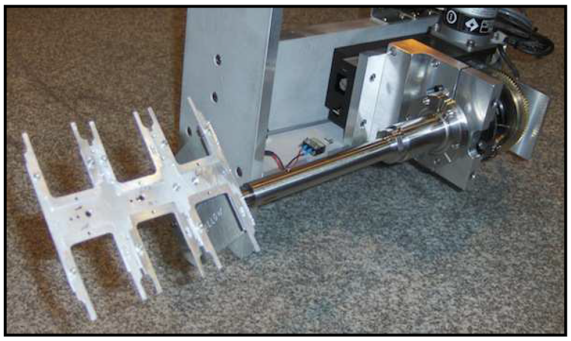

(d) Multi-position target ladder (six ribbons).

Figure 3.271: Present pC polarimeter: detector system and targets. Panels show (a) the azimuthal detector placement, (b) a Si-strip detector package, (c) a carbon ribbon target, and (d) the multi-position ladder.

distributing the heat load over a larger surface area, reducing peak temperatures. Recognizing these fabrication challenges, commercial suppliers of ultra-thin carbon targets have been engaged to develop manufacturing processes capable of producing the longer ribbon geometries required for EIC operation.

Operation at the EIC presents significant technical challenges for the pC polarimeter system due to higher beam intensities and reduced bunch spacing. The threefold increase in beam current and 10 % energy increase require enhanced thermal management to prevent target damage, addressed through enlarged beam sizes via increased vertical beta functions and longer target ribbons ($\ell \approx 50$ mm compared to 25 mm at RHIC). The $\approx$ 11 ns bunch spacing precludes temporal separation of recoils from adjacent bunches, necessitating new detection schemes with waveform digitization and pattern recognition algorithms. Additional modifications include dielectric target holders to reduce wake impedances, vacuum transfer systems for target exchange without breaking vacuum, and RF shielding to suppress higher-order modes at the increased bunch frequency.

Electromagnetic simulations[1] demonstrate that wakefield effects[2] pose manageable challenges for EIC operation with appropriate design modifications. The analysis compared target holder

[1] conducted by A. Blednyk, G. Wang, and M. Sangroula (all BNL).

[2] The wake potential describes electromagnetic disturbances created when charged particle bunches pass through accelerator components [162, 163]. When a bunch of protons travels through the beam pipe, it gener-

Table 3.77: Comparison of carbon target coverage for pC polarimeters at RHIC and EIC. The coverage ratio indicates how many times longer the target is compared to the beam width ($4\sigma_{95}$). Values below 2 indicate marginal coverage with limited safety margin for beam positioning and alignment tolerances. EIC beam parameters from Ref. [10].

Parameter	RHIC	EIC Injection	EIC Flattop
Beam Parameters			
Number of bunches	120	290	1160
Protons per bunch ($\times 10^{10}$)	20.0	27.6	6.9
Beam Sizes (95%)			
Horizontal σ_x^{95} (mm)	0.56*	8.60	3.94
Vertical σ_y^{95} (mm)	0.56*	1.69	0.66
Equivalent round σ_r^{95} (mm)	0.56	3.81	1.61
Full Beam Width ($4\sigma_{95}$)			
Horizontal $4\sigma_x^{95}$ (mm)	2.24	34.4	15.8
Vertical $4\sigma_y^{95}$ (mm)	2.24	6.76	2.64
Target Length			
Length ℓ (mm)	25	50	50
Coverage Ratio			
Horizontal ribbon ($\ell/4\sigma_x^{95}$)	11.2	1.45	3.16
Vertical ribbon ($\ell/4\sigma_y^{95}$)	11.2	7.40	18.9

*RHIC approximated as round beam. Equivalent round beam size calculated as $\sigma_r^{95} = \sqrt{\sigma_x^{95} \times \sigma_y^{95}}$ for thermal modeling comparisons.

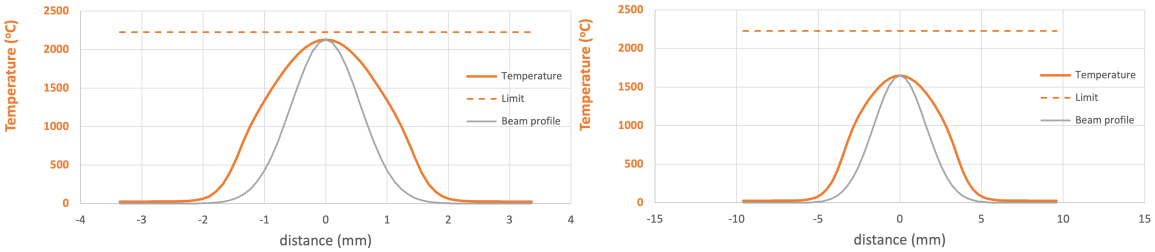

(a) RHIC conditions: 250 GeV, 111 bunches, 16×10^{10} protons/bunch, $\sigma_r^{95} = 0.68$ mm.

(b) EIC conditions: 275 GeV, 1160 bunches, 6.9×10^{10} protons/bunch, $\sigma_r^{95} = 1.2$ mm.

Figure 3.272: Thermal modeling results for carbon ribbon targets showing temperature profiles during beam passage. Despite higher beam energy and total current at EIC, the larger beam size distributes the heat load sufficiently to maintain peak temperatures below the carbon sublimation threshold. (The modeling calculations use a framework developed by Peter Thieberger [9].)

materials including aluminum, stainless steel, and dielectric options such as aluminum oxide (Al_2O_3), revealing that dielectric target holders significantly outperform metallic alternatives in wake impedance reduction (Fig. 3.273). The wake potential amplitude decreases substantially when dielectric holders are positioned downstream of the interaction region, with simulations showing improved accelerator performance when dielectric materials replace metallic components. To prevent electrostatic charging, a thin 10 nm gold layer will be applied to the dielectric surfaces.

The study also examined the effects of multiple target positions on the same holder, finding that wakefield amplitude decreases systematically as target holders are shifted further downstream from the beam interaction point (Fig. 3.274). These results validate the mechanical design approach of operating with one target in the chamber at a time and support the development of a vacuum transfer chamber system for target exchange without compromising beam conditions due to breaking the ring vacuum, presently required to install targets. Higher-order mode generation requires RF shielding of all pumping ports and feedthroughs to suppress electromagnetic coupling at the increased EIC bunch frequency of ≈ 90.7 MHz.

The planned pC polarimeter upgrades for EIC operation include:

1. Enhanced thermal management through increased vertical beta functions and longer carbon ribbon targets ($\ell \approx 50$ mm to 150 mm).
2. Dielectric target holders (e.g., Al_2O_3) with 10 nm gold coating to reduce wake impedances and prevent electrostatic charging.
3. Vacuum chamber system redesign incorporating:
   (a) Vacuum transfer chamber enabling target exchange without breaking ring vacuum, supporting one-target-at-a-time operation.
   (b) RF shielding of all pumping ports and feedthroughs to suppress higher-order mode generation at ≈ 90.7 MHz.
4. Waveform digitization and pattern recognition algorithms for bunch-by-bunch measurements at ≈ 11 ns spacing.
5. Commercial development of ultra-thin carbon ribbon manufacturing for extended target geometries.

The overarching goal is to maintain polarization measurements throughout the acceleration cycle, including polarization lifetime tracking and profile mapping capabilities, while addressing the threefold increase in beam current and reduced bunch spacing at EIC. As a next step, the pC target chambers will be relocated to a suitable BNL facility for refurbishment and upgrades when engineering resources become available.

Light ion polarimetry The EIC polarimetry system must accommodate polarized light ions as part of the baseline physics program and future beam species development. Following the same fundamental principle established for proton polarimetry, absolute polarization calibrations for light ions rely on elastic scattering of identical particles: ^{3}He-^{3}He, deuteron-deuteron, and Li-Li

ates electromagnetic fields that can affect following bunches. The wake potential $W(s)$ measures the voltage experienced by a trailing particle at distance s behind the leading bunch along the orbit path, where s represents the longitudinal position measured around the accelerator's circular trajectory. The units are V pC^{-1} to normalize the effect per unit charge of the driving bunch. Lower wake potentials indicate less electromagnetic interference with the beam, which is crucial for maintaining stable operation in high-intensity accelerators like the EIC where many bunches circulate simultaneously around the ring.

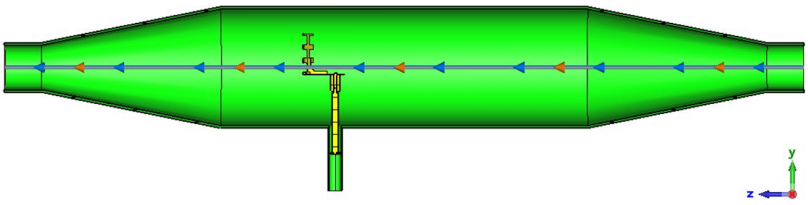

(a) pC polarimeter vacuum chamber with target positioning system showing electromagnetic field interaction regions.

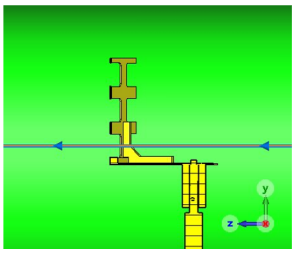

(b) Target holder geometry when the proton beam intercepts the C target.

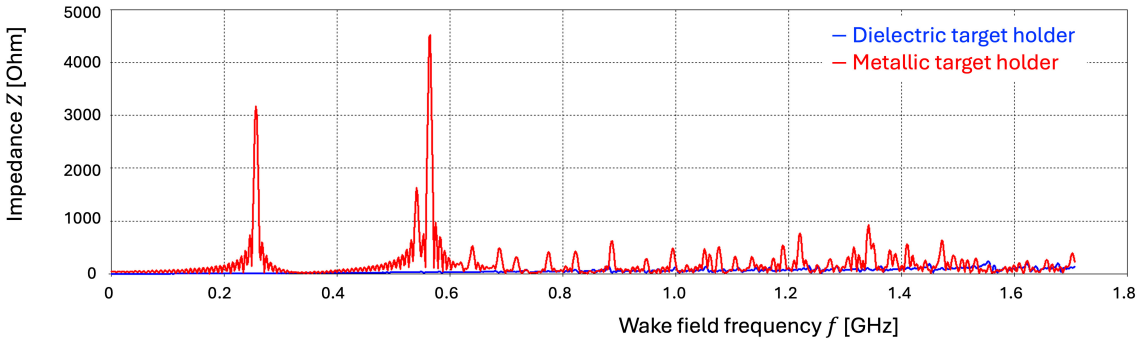

(c) Wake impedance Z as function of frequency comparing metallic aluminum target holder in a stainless steel vacuum chamber versus dielectric (Al_2O_3) target holders.

Figure 3.273: Wakefield analysis for pC polarimeter target systems. Electromagnetic simulations demonstrate superior performance of dielectric target holders compared to metallic alternatives, validating the design choice for EIC operation.

scattering. This approach ensures that the analyzing power cancels in the asymmetry ratio, requiring only precise knowledge of the target polarization. The identical-particle scattering method minimizes systematic uncertainties since the same CNI analyzing power governs both beam and target asymmetry measurements.

Helium-3 polarimetry The ^{3}He program, integrated into the baseline EIC physics program, requires development of a polarized ^{3}He atomic beam target for absolute calibration measurements through ^{3}He-^{3}He elastic scattering. Development is led by a collaboration from MIT under P.T. MohanMurthy and R.G. Milner, leveraging technology and expertise developed for the neutron Electric Dipole Moment (nEDM) experiment at Oak Ridge National Laboratory. This prior work with polarized ^{3}He systems provides the foundation for adapting the atomic beam source technology to EIC polarimetry requirements.

The technical approach centers on a cryogenic atomic beam source operating at 1 K to achieve the necessary target density and polarization for EIC conditions. Building on the nEDM experimental experience, the system utilizes quadrupole magnetic focusing to select nuclear spin states, with energy splitting $\Delta E = \mu_n \approx 67\,\mathrm{neV\,T^{-1}}$ enabling state selection at the required operating temperature. The cryogenic operation at 1 K provides atomic flux $\geq 10^{14}\,\mathrm{s^{-1}}$ suitable for EIC polarimetry requirements. Alternative approaches under consideration include polarized ^{3}He storage cells –

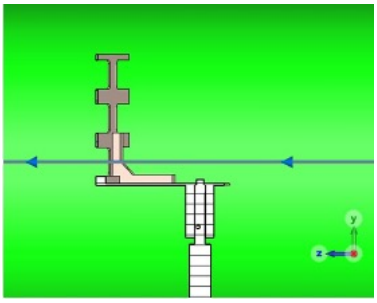

(a) Target holder at 0 mm displacement.

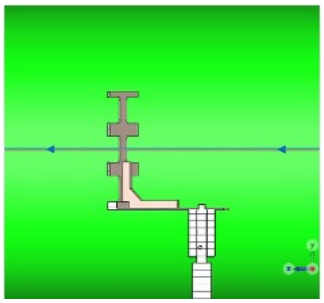

(b) Target holder at 38.1 mm displacement.

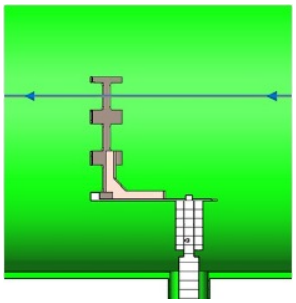

(c) Target holder at 76.2 mm displacement.

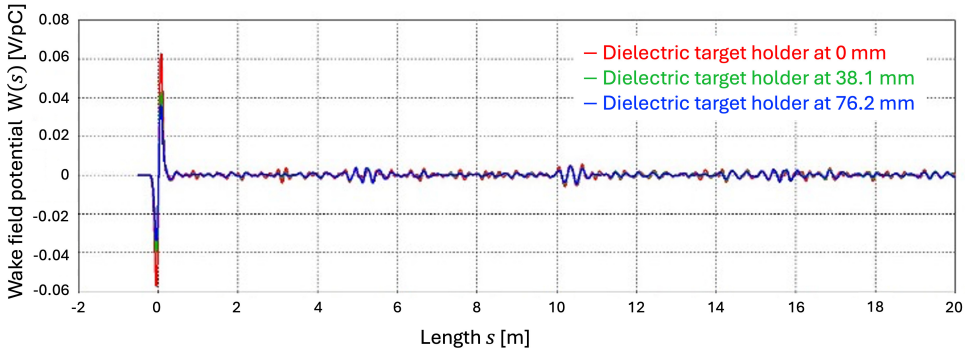

(d) Wake field potential showing systematic amplitude reduction as dielectric target holders are positioned further downstream from the beam interaction region.

Figure 3.274: Effect of target holder positioning on wakefield characteristics. The three target geometries (a-c) demonstrate different displacement positions, with corresponding wake potential calculations (d) showing reduced electromagnetic interference when holders are shifted downward toward the chamber wall.

demonstrated at HERMES [164] and at IUCF in the 1990s [165, 166] – can raise target densities by increasing the atomic dwell time in the vicinity of the stored beam.

Future light ion extensions Deuteron polarimetry requires development of a polarized deuteron target for absolute calibration through deuteron-deuteron elastic scattering, with additional complexity from both vector and tensor polarization components characteristic of spin-1 systems. The existing HJET can be adapted for deuteron operation with appropriate upgrades, thus the primary equipment for polarized deuteron atomic beam production is essentially available. Detection systems must be enhanced to resolve tensor polarization states beyond the baseline program scope. Potential ^{6}Li and ^{7}Li beams represent longer-term extensions requiring development of polarized lithium targets for Li-Li elastic scattering calibrations. These programs depend on advances in polarized atomic beam source technology and specialized target development for the lithium species.

System integration

IP4 configuration: The integration of all hadron polarimetry systems at Interaction Point 4 (IP4) represents a strategic design choice driven by both technical requirements and operational efficiency. The location selection is primarily determined by the need for a $\approx 20\,\text{m}$ drift space required for the tagger system used in light ion polarimetry, particularly for ^{3}He-^{3}He elastic scattering measurements. Unlike proton-proton elastic scattering where no nuclear breakup occurs, ^{3}He nuclei can fragment during collisions, creating ambiguity between elastic scattering events and breakup processes. The tagger system identifies and excludes breakup events by detecting recoil particles in the drift region, ensuring measurement of true elastic scattering for absolute polarization calibration. Co-locating the carbon fiber polarimeters, ^{3}He jet target, and hydrogen jet target systems at a single interaction point minimizes spin rotations between polarimeter measurements, facilitates reduction of systematic errors, and enables efficient use of common infrastructure.

The component arrangement follows the hadron beam direction through the High-energy Storage Ring (HSR), with systems positioned sequentially: CNI polarimeter (pC system), ^{3}He jet target, HJET polarimeter, two warm D0 dipoles, longitudinal superconducting pickup, four horizontal and four vertical superconducting kickers, the HJET tagger drift/tagging system, vacuum and ion pump sections, and the final focus quadrupole Q4, as shown in Fig. 3.275. This layout ensures optimal measurement conditions while maintaining accelerator performance requirements.

Infrastructure integration encompasses coordinated services and controls, unified detector readout architecture, and power and cooling systems coordination. The counting house at IP4 is anticipated to be realized from an assembly of prefabricated and wired containers, allowing for modular integration as control systems for different polarimeters can be added when they become available. The facility must accommodate control racks and equipment for all three baseline polarimeter systems (HJET, pC, and ^{3}He), along with detector electronics for comprehensive system operation and stepper motor logistics for carbon target positioning in the pC polarimeters. Additionally, a dedicated polarimeter control room at IP4 is required for operational oversight and coordination. This modular and centralized control approach facilitates synchronized measurements, reduces operational complexity, and provides flexibility for phased system commissioning.

A critical technical requirement for HJET integration involves the 400 mT holding field system and its impact on beam orbit dynamics. Ideally, the magnetic compensation scheme should ensure zero integrated $\int B\,dl$ along the hadron beam direction for all field orientations ($\vec{B}_x$, $\vec{B}_y$, $\vec{B}_z$), whether implementing full three-dimensional sensitivity or initially deploying only $\vec{B}_y$ orientation. The compensation system should achieve transparent operation where machine control systems do not recognize HJET holding field activation, preventing any transverse beam kicks during polarimeter operation.

IP6 configuration: The placement of a 2nd pC polarimeter (same as shown in Fig. 3.270) at IP6 serves multiple operational functions beyond providing measurement redundancy. The primary physics motivation involves monitoring spin evolution between IP4 and IP6 locations, enabling detailed understanding of polarization transport through the hadron storage ring arc spanning from 4 o'clock to 6 o'clock positions. This capability proves essential for systematic uncertainty control and verification of spin dynamics calculations throughout the accelerator lattice. Temperature estimates for carbon targets under beam conditions at IP6 remain to be completed to validate thermal management strategies at this location.

Layout and space allocation: The IP4 configuration detailed in Fig. 3.275 demonstrates the comprehensive integration of hadron polarimetry systems within a single straight section of the EIC storage ring. The sequential arrangement maximizes operational efficiency while maintaining

the precision required for systematic uncertainty control at the 1 % level.

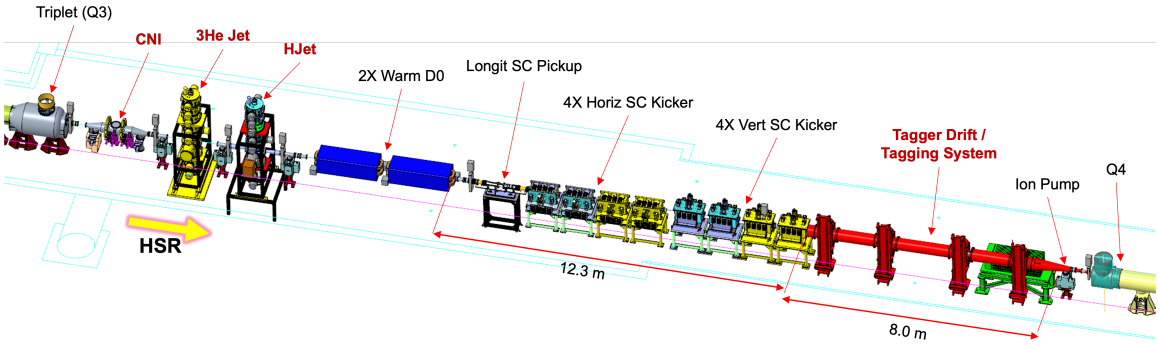

Figure 3.275: Hadron polarimetry instrumentation concentrated at Interaction Point 4 (IP4) of the EIC high-energy storage ring (HSR). From left to right along the beam direction (yellow arrow): CNI polarimeter; ^{3}He jet target; hydrogen-jet (HJET) polarimeter; two warm D0 dipoles; longitudinal superconducting pickup; four horizontal and four vertical superconducting kickers; HJET tagger drift/tagging system of length 7.5 m; vacuum/ion-pump section; and quadrupole Q4. Co-locating these devices in a single straight section provides shared infrastructure, common alignment, and efficient absolute/relative beam polarimetry, and minimizes spin rotations between polarimeters.

Critical technical developments

Solved challenges:

HJET beam-induced depolarization: The EIC's tenfold increase in bunch frequency creates electromagnetic harmonics that resonantly drive hyperfine transitions in hydrogen atoms at RHIC's 120 mT holding field. This challenge has been resolved by increasing the HJET holding field to 400 mT, ensuring robust operation against beam-induced depolarization [10].

pC target heating: EIC's higher beam energy and increased total beam current initially raised concerns about carbon target survival in the pC polarimeters. Thermal modeling demonstrates that the larger beam sizes at the polarimeter location distribute the heat load sufficiently to maintain peak temperatures below the carbon sublimation threshold. This analysis led to reduction of the target heating risk (ID #128) to low priority in the project risk registry.

pC wakefield effects: Higher bunch frequencies create electromagnetic disturbances that could affect beam stability through the carbon target holders. CST electromagnetic simulations[3] demonstrate that dielectric target holders (e.g., Al_2O_3) for the pC polarimeters significantly outperform metallic alternatives in wake impedance reduction, with a thin 10 nm gold coating preventing electrostatic charging.

Ongoing developments:

[3]CST Studio Suite is a commercial electromagnetic simulation software package widely used for accelerator physics calculations, including wakefield and impedance analysis. See https://www.3ds.com/products-services/simulia/products/cst-studio-suite/.

HJET holding field system: The challenge of beam-induced depolarization from EIC's tenfold increased bunch frequency has been analyzed, with the solution requiring an upgrade from RHIC's 120 mT to 400 mT holding field [10]. The design and implementation of this new magnetic system, including target chamber modifications and magnetic compensation schemes, remains under development.

Bunch-by-bunch polarization measurements: The EIC physics program demands individual bunch polarization determination at $\approx$ 11 ns spacing. Detector technology options under evaluation include fast silicon detectors with individual bunch triggering, diamond detectors with inherent sub-nanosecond response, and time-of-flight discrimination synchronized with accelerator timing. The goal is detectors fast enough that each 11 ns window sees essentially only one bunch's recoils, eliminating complex waveform analysis. This requirement applies to all polarimetry systems (HJET, pC, ^{3}He). The readout/detector choice must be finalized before the Final Design Review.

H_2 background systematics: Molecular hydrogen contamination of 3 % to 4 % in the HJET atomic beam dilutes the effective target polarization since H_2 molecules do not contribute to the CNI analyzing power. A quadrupole mass analyzer is being integrated into the upgraded Breit-Rabi polarimeter for continuous H_2 monitoring, targeting reduction of the associated systematic uncertainty from approximately 2 % to below 0.5 %.

Target thermal validation: Experimental verification of carbon target temperatures under beam conditions complements theoretical thermal modeling. Direct temperature measurements of carbon targets at CNI polarimeters in RHIC when hit by the proton beam are ongoing [161]. Additionally, temperature estimates for carbon targets at the IP6 pC polarimeter location remain to be completed to extend the thermal analysis beyond IP4 conditions.

Vacuum transfer chamber: Current pC polarimeter operation requires breaking ring vacuum for target installation. A vacuum transfer system is under development where carbon targets remain outside the ring vacuum chamber when not in use. When measurements are needed, a gate valve opens to insert a single target holder into the beam interaction region, then retracts and closes to maintain ring vacuum integrity. This approach eliminates beam interruption, enables rapid target exchange without compromising accelerator operation, and allows outgassing of target holders and carbon targets in vacuum before insertion, reducing ring vacuum contamination. The system would eliminate the need to vent the pC chamber for target maintenance.

^{3}He atomic beam source development: Development of the cryogenic atomic beam source operating at 1 K is in progress at MIT, with the timeline aligned to EIC ramp-up and commissioning schedule to ensure readiness for early light ion physics operations.

Schedule and milestones The polarimetry system development follows a structured timeline aligned with overall EIC project milestones. The Second Preliminary Design Review (2nd PDR) is scheduled for Q1 FY26, followed by the Final Design Review (FDR) in Q1 FY27. The construction and installation phase spans FY28-FY30, encompassing procurement, fabrication, installation, and testing of infrastructure, accelerator systems, and detector components.

Polarimeter systems will be ready for beam development by FY31, coinciding with the L2_0600 Construction of Components Complete milestone. Final commissioning extends into FY31-FY32, with full operational capability targeted for early FY32. This timeline provides approximately five years from the 2nd PDR to beam-ready systems, accounting for the complexity of integrating multiple specialized polarimetry technologies within the accelerator environment.

Quality assessment and workforce

QA procedures: Quality assurance protocols for hadron polarimetry systems build upon two decades of operational experience with pC and HJET polarimeters at RHIC. Established procedures encompass component fabrication standards following ISO 9001 protocols with documented material traceability, vacuum qualification testing to 10^{-10} Torr levels, and magnetic field uniformity verification to 0.1 % precision. Detector module acceptance testing includes cosmic ray validation and integration testing to verify interface compatibility before installation. The proven RHIC QA framework provides the foundation for enhanced procedures meeting EIC's more stringent 1 % systematic uncertainty requirements.

Assembly protocols require Class 10,000 cleanroom environments with continuous particulate monitoring during detector integration. Silicon strip detector modules undergo thermal cycling and bias voltage stress testing to validate long-term stability under EIC operating conditions. The magnetic field systems require field mapping validation and stability testing over extended periods to ensure systematic uncertainty control.

Collaborative effort: Brookhaven National Laboratory leads system integration, HJET modifications, and pC polarimeter development, leveraging institutional expertise from RHIC operations. MIT contributes ^{3}He atomic beam source development through their nEDM experimental program under P.T. MohanMurthy and R.G. Milner. International collaborations provide specialized detector development and testing capabilities, with coordination through the EIC project structure.

Environmental and safety considerations After 20 years of operating experience with pC and HJET polarimeters at RHIC, environmental safety and health (ES&H) protocols have been thoroughly established and validated. All systems comply with Brookhaven National Laboratory ES&H standards and DOE requirements, with proven procedures adapted for EIC-specific conditions.

Radiation safety protocols address handling of activated components following beam exposure, with established procedures for detector replacement and maintenance. The magnetic field systems require standard safety protocols for personnel protection near high-field regions, with exclusion zones clearly marked during operations. Oxygen deficiency hazard (ODH) analysis addresses areas with cryogenic systems, particularly for the ^{3}He atomic beam source operating at 1 K. Electrical safety procedures cover high-voltage detector bias systems and magnetic field power supplies, with established lockout/tagout protocols.

Environmental controls maintaining temperature stability are essential for detector alignment stability and systematic uncertainty control. The proven operational procedures from RHIC provide a solid foundation for safe and reliable EIC polarimetry system operation.

3.3.10 Readout Electronics and Data Acquisition

3.3.10.1 Requirements

The electronics and data acquisition systems are required to digitize and readout the data provided by the sensors of all ePIC detectors. The electronics must tag hits with a time resolution sufficient to

identify the bunch crossing (10.16 ns) and provide high resolution time reference. The most stringent timing requirement is 5 ps of clock jitter in order to meet the 25 ps overall timing requirement for the forward TOF (see section 3.3.4.1). The readout system must provide high data volume links to read data from the front end electronics up to 10 Gb/s for selected components. The readout system must provide very high live times, with the goal of zero system-wide deadtime in normal operation, despite the possibility of by-channel deadtime according the specific readout technology of each detector.

The Data Acquisition will group streaming data into time frames of O(600 ns). The readout systems are expected to digitize up to O(2 Tb/s) and must be capable of reducing this data volume to an output rate of O(100 Gb/s) using techniques to compress signal and remove noise with minimal impact to signal integrity. The data from all running detectors for each time frame will gathered together in a single buffer for transfer to the Echelon 1 computing facilities located at BNL and JLAB for archive and analysis.

3.3.10.1.1 Requirements from Physics The requirement for the ePIC readout system is to successfully collect data at the Electron Ion Collider for physics analysis. In turn, the expected performance and mode of operations of the collider impact the design of the readout system. The collision and background rates are detailed in section 3.2.2. The maximum event rates are expected to be as high as 500 kHz for DIS, 3.2 MHz for electron beam gas, and 32 kHz for hadron beam gas. These rates are of primary interest within DAQ to estimate the data volumes and will be discussed in section 3.3.10.1.3.

A second consideration is that individual bunch crossings can have different polarization states. This implies that the luminosity and polarization of the beams must be tracked by bunch and produces the requirement that events must be associated to the bunch crossing from which they originated.

Each ePIC detector has its readout organized into Front-End Boards (FEB) hosting ASICs to provide digitization, Read-Out Boards (RDO) providing aggregation and transmission of FEB data to the central DAQ system, and Data Aggregator and Manipulation Boards (DAM) (This scheme is further detailed later in section 3.3.10.2, see Figure 3.279). The scale and technology of the different ePIC detectors is summarized in Tables 3.276 and 3.277, where the large channel counts combined with low occupancy lead to the need for multiple levels of aggregation.

3.3.10.1.2 Requirements from Radiation Hardness The electronics installed in the ePIC detector will be subjected to significant radiation doses. Radiation doses are described in section 3.2.2. Electronics placed in the central detector (SVT, eTOF, bTOF, and MPGDs) will utilize radiation hard components to minimize the effect of radiation.

Electronics must be chosen and placed to minimize failure rates. The electronics must be tested against Single Event Latchup and the power system must have built-in protection mechanisms against latchup. There are commercial IP cores available for FPGAs that can support recovery from single event upsets (SEUs). Transient failures due to radiation remain possible, so automatic failure sensing must be implemented to allow recovery procedures such as automated reset and reload for FEBs and RDOs.

3.3.10.1.3 Requirements from Data Rates The triggerless readout of the ePIC detector uses zero-suppression to help manage the volume of data read out. The streaming model's sensitivity to noise, beam background, and collision data make the understanding of these effects critical.

Detector System		Channels	ASIC	FEB	RDO	Gb/s (RDO)	Gb/s (Tape)	DAM Boards	Readout Technology	Notes
Si Tracking:	Inner Barrel (IB)	1.8B Pixels	160	592*	24	2.36	2.36	1	ITS-3 sensors &	ASIC corresponds to VTRX+ counts
	Outer Barrel (OB)	5.0B Pixels	495	1870*	55	3.52	3.52	2	ITS-2 staves / w	FEB corresponds to detector fiber
	Backward Disks (EE)	4.7B Pixels	462	1744*	52	4.68	4.68	2	improvements	RDO is off detector Fiber aggregator
	Forward Disks (HE)	4.7B Pixels	462	1744*	52	4.68	4.68	2		
MPGD tracking:	Electron Endcap	16,384	256	64	16	2.86	0.58	1	uRWELL / SALSA	VTRX+ based FEB
	Hadron Endcap	16,384	256	64	16	4.01	0.80	1	uRWELL / SALSA	
	Inner Barrel	32,768	512	128	32	4.10	0.82	1	MicroMegas / SALSA	
	Outer Barrel	98,304	1536	384	96	15.81	3.16	2	uRWELL / SALSA	
Forward Calorimeters:	LFHCAL	63,280	1130	1130	74	18.54	2.47	2	SiPM / CALOROC	CALOROC:
	HCAL insert	8k	142	142	9	17.72	2.36	1	SiPM / CALOROC	56 Ch/CALOROC
	ECAL W/SciFi	18,320		574	72	14.75	7.36	2	SiPM / Discrete	16 CALOROC / RDO
Barrel Calorimeters:	HCAL	1,536	28	28	2	0.87	0.12	1	SiPM / CALOROC	
	ECAL SciFi/PB	5,760	102	102	4	11.45	1.52	1	SiPM / CALOROC	Discrete:
	ECAL ASTROPIX	500M pixels			340	1.25	1.25	8	Astropix	32 Ch/FEB,
Backward Calorimeters:	NHCAL	3,256	58	58	4	3.46	0.47	1	SiPM / CALOROC	8 FEB/RDO conservative (16 estimate).
	ECAL (PWO)	2,852		102	13	2.00	0.99	1	SiPM / Discrete	
Far Forward:	B0: Crystal Calorimeter	135		5	1	2.3	2.3	1	SiPM/APD / Discrete	
	4 AC-LGAD layer	688,128	672	168	42	12.75	2.1	1	AC-LGAD / EICROC	4 layer x 42 module x 4 EICROC x 1024 ch
	2 Roman Pots	524,288	512	128	32	14.53	2.1	1	AC-LGAD / EICROC	2 stations x 2 layer x 32 module x 4 EICROC x 1024 ch
	2 Off Momentum	294,912	288	72	18	3.53	0.7	1	AC-LGAD / EICROC	2 stations x 2 layer x 18 module x 4 EICROC x 1024 ch
	ZDC: Crystal Calorimeter	900		30	4	2.30	4.5	1	SiPM/APD / Discrete	
	HCAL	9,216	165	165	11	0.22	.22	1	CALOROC	
Far Backward:	2 x Low Q Tagger	66M pixels	3456	288	24	37	.3	10	Timepix4	Firmware Trigger to reduce output rate
	2 x Low Q Tagger Cal	420			1	-	-	1	SiPM / CALOROC	Low Q Calorimeter doesn't run at high luminosity
	2 x Lumi PS Calorimeter	3,360			1	19	7	1	SiPM / Discrete	
	2 x Lumi PS tracker	128k	1000	250	64	45	2	2	AC-LGAD: FCFD or EICROCx	
	Direct Photon Lumi Cal	100		24	24*	200	7	1	SiPM / fADC250	Direct Photon: commercial digitizer, no RDO
PID-TOF:	Barrel	2,359,296	18,432	288	288	15.95	4.79	8	AC-LGAD: FCFD or EICROCx	bTOF 128 ch/ASIC, 64 ASIC/RDO
	Endcap	3,719,168	3,632	212	212	33.92	7.34	6	AC-LGAD: EICROC	eTOF 1024 pixel/ASIC, up to 28 ASIC/RDO
PID-Cherenkov:	dRICH	317,952	4968	4968	1242	1240	13.5	30	SiPM / ALCOR	Worse case after radiation. Includes 30% timing window. Requires further data volume reduction
	pfRICH	69,632	544	68	17	24	12.5	1	HRPPD / FCFD or EICROCx	Firmware trigger
	DIRC	73,728	576	144	24	11	6	1	MCP-PMT / FCFD or EICROCx	

Figure 3.276: ePIC DAQ component counts

Detector Group	Channels					Det Fiber Down	Det Fiber Up	RDO	Fiber Pair (DAQ)	DAM	Data Volume (RDO) (Gb/s)	Data Volume (To Tape) (Gb/s)
	MAPS	AC-LGAD	SiPM/PMT	MPGD	HRPPD/ MCP-PMT							
Tracking (MAPS)	16B					183	5863	183	183	7	15	15
Tracking (MPGD)				164k		640	2560	160	160	5	27	5
Calorimeters	500M		100k					522	522	17	70	17
Far Forward		1.5M	10k					80	80	6	36	12
Far Backward	66M	128k	4k					60	82	14	301	16
PID (TOF)		6.1M				500	1364	500	500	14	50	12
PID Cherenkov			318k		143k			1283	1283	32	1275	32
TOTAL	**16.6B**	**7.7M**	**432k**	**164k**	**143k**	**843**	**9,787**	**2,788**	**2,810**	**95**	**1,774**	**109**

Figure 3.277: ePIC DAQ component count summary

Detector	Channel Max Hit Rate (Hz)	Noise To RDO (gbps)	Noise Per RDO (gbps)	Noise To Tape (gbps)	RDO (max) (gbps)	RDO_max / with Noise (gbps)
SiBarrelTracker	4.13E-04	3.25	0.06	3.25	0.00	0.06
SiBarrelVertex	5.22E-03	1.15	0.05	1.15	0.17	0.21
SiEndcapTracker	2.78E-03	6.02	0.06	6.02	0.23	0.29
BackwardMPGDEndcap	2.19E+02	1.74	0.11	0.35	0.42	0.52
ForwardMPGDEndcap	4.44E+02	1.74	0.11	0.35	0.86	0.97
MPGDBarrel	8.67E+01	3.26	0.10	0.65	0.04	0.14
OuterMPGDBarrel	1.29E+01	15.23	0.16	3.05	0.01	0.17
LFHCAL	2.10E+04	10.33	0.14	1.38	1.30	1.44
HcalEndcapPInsert	6.18E+04	1.31	0.15	0.17	2.78	2.93
EcalEndcapP	1.51E+05	0.78	0.01	0.35	2.69	2.70
HCcalEndcapN	7.81E+04	0.53	0.13	0.07	2.64	2.77
EcalEndcapN	8.07E+04	0.14	0.01	0.06	1.06	1.07
HcalBarrel	1.30E+03	0.25	0.13	0.03	0.08	0.21
EcalBarrelImaging	2.92E-02	0.32	0.00	0.32	0.01	0.01
EcalBarrelSciFi	1.52E+03	0.94	0.07	0.13	2.69	2.76
TOFBarrel	1.74E+00	13.59	0.05	4.53	0.01	0.06
TOFEndcap	8.34E-01	32.13	0.15	7.14	0.07	0.22
hpDIRC	2.35E+02	3.22	0.13	1.07	0.00	0.13
pfRICH	4.99E+02	3.05	0.18	1.02	0.00	0.18
dRICH	1.09E+02	1220.94	0.98	6.10	0.00	0.98
B0 Crystal Calorimeter	2.66E+05	0.00	0.00	0.00	0.00	0.00
B0 AC-LGAD	1.72E+01	5.95	0.20	1.32	0.00	0.20
RP	3.31E+01	4.53	0.21	1.01	0.00	0.21
OM	5.93E+00	2.53	0.21	0.56	0.00	0.21
ZDC Crystal Calorimeter	7.81E+04	0.02	0.00	0.02	0.00	0.00
ZDC HCAL	3.39E+01	0.20	0.02	0.20	0.00	0.02
DirectPhoton	2.00E+08	0.00	0.00	0.00	0.00	0.00
LowQ2Tracker	8.76E+00	0.04	0.00	0.04	0.00	0.00
LowQ2Calorimeter	0.00E+00	0.01	0.01	0.01	0.00	0.01
PairSpectrometerTracker	2.44E+02	0.74	0.07	0.25	0.00	0.07
PairSpectrometerCalorimeter	3.26E+04	0.07	0.07	0.07	0.00	0.07
Total		1334.01		40.67		

Figure 3.278: Maximum data volume per RDO with noise estimates by detector. (Data Rate evaluation: https://github.com/jml985/epicJTools)

Collision, synchrotron radiation and beam gas backgrounds from both the electron and hadron beams have been studied extensively by the ePIC collaboration, and the methods are presented in section 3.2.2. The hits have been converted to data volumes using our current understanding of zero suppression and data formats of each detector readout. Furthermore, the distribution of hits to each component has been estimated by arbitrarily assigning readout components to the sensitive planes of the detectors in order to estimate the impact of potential bottlenecks.

The hit rate for the collision signal is taken from simulated hits for DIS events generated by the ePIC

Detector	Noise (Hz/channel)
ITS3, ASTROPIX, TIMEPIX	0.01
AC-LGAD	30
HRPPD	230
dRICH(initial)	3000
dRICH(Max)	300,000
All Others	4.5σ = 340

Table 3.78: Noise Estimates

	Noise (Gb/sec)	Synchrotron Radiation (Gb/sec)	Electron Beam Gas (Gb/sec)	Proton Beam Gas (Gb/sec)	Collision Signal (Gb/sec)	Aggregate (Gb/sec)
Digitized	1,600	tbd	48	40	530	2220
To Tape	32	tbd	4.5	1.0	62	109

Table 3.79: Expected worse case data rate contributions for the ePIC detector. (https://github.com/jml985/epicJTools)

physics and detector simulations. The simulated data set was taken for 18x275 GeV collisions with $Q^2 > 0$ with luminosity $1.54x10^{33}$ cm^2s^{-1}. The hit rates were scaled to the maximum rate of the EIC collider of 500kHz. Hadron and electron beam gas events were generated using the simulated vacuum profile after 10,000 Ah of pumping.

Noise calculations are currently based on the ePIC detector group expert estimates and shown in table 3.78. Generally, the noise level can be controlled with thresholds. The thresholds for each detector will be set according to the physics requirements as balanced against bandwidth limitations.

One additional factor that must be considered is dark currents in the SiPM detectors which increase with radiation damage. In particular, this issue affects the dRICH, in which the SiPM threshold must remain low enough to be sensitive to single photons. There are several features planned to reduce these dark currents including annealing, and implementation of timing windows to synchronise readout with collision times. These are described in section 3.3.4.4. The DAQ system must be designed with the capability to manage the highest rates expected by the dRICH and must also apply filters to reduce the dRICH noise, either by applying high level selection criteria or by using specialized AI algorithms to determine which hits correspond to a dRICH physics signal.

The expected maximum data contributions of data digitized and stored to tape are summarized in table 3.79. The data volume expected, including collisions, background and noise for the worse case RDO by detector, is shown in Figure 3.278.

3.3.10.2 Device Concept and Technological choice: Streaming Readout

The ePIC readout system will implement a flexible, scalable, and efficient streaming DAQ as outlined by the EIC Yellow Report [22]. This design will provide the advantages of streaming include the replacement of custom L1 trigger electronics with commercial off-the-shelf (COTS) computing, virtually deadtime-free operation, great flexibility in event selection using full event data along with offline analysis, and the opportunity to study event backgrounds in detail. These advantages

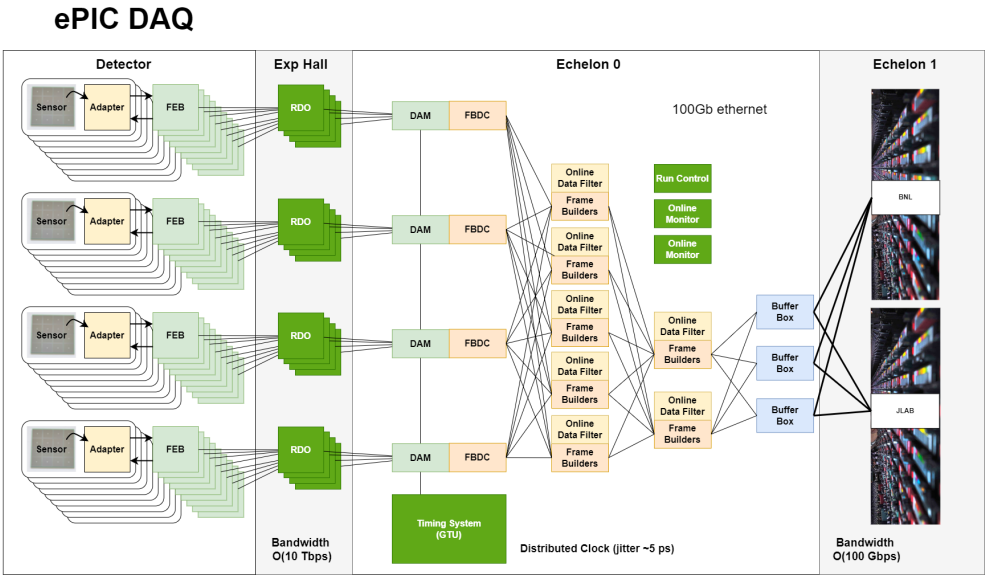

Figure 3.279: Schematic of the ePIC Streaming DAQ

come at the cost of greater sensitivity to noise and background. A schematic of the readout system is shown in figure 3.279.

Readout will be accomplished using detector specific front end sensors and adaptors. Even though the organization of the front end electronics varies by detector needs the custom electronics of each system generically referred to as Front End Boards (FEBs). There is no global trigger system in ePIC, instead each FEB is required to self-trigger, providing a stream of hit data. Digitization and zero-suppression is typically handled with ASIC support. Each FEB has similar needs for clocks, configuration, and serial data links. These needs are provided by Readout Boards (RDOs). In some cases the RDO-FEB link is direct using LVDS signals, and in other cases the transmission is accomplished by lpGBT serializer/deserializer devices [167] over fiber. The RDOs also aggregate data from the FEBs. The RDO serves as an interface between custom, technology driven, readout schemes of specific detectors and the ePIC DAQ. While there are a number of variations of the RDOs depending upon the FEB technology, all of the RDOs support a unified ePIC DAQ fiber protocol. They distribute high-resolution time reference, configuration, and control to the FEBs and transmit hit data and monitoring information to the Data Aggregation and Manipulation Boards (DAM).

The DAM boards have significant processing available for implementing high level data selection criteria and other data reduction algorithms. They also provide further aggregation and function as the interface between the electronics and the first level of COTS computers called the Frame Builder Data Collectors (FBDC). The farm of COTS DAQ computers dedicated to readout, data reduction, logging, monitoring, QA, data buffering, and data transfer to data centers is integrated in the ePIC computing model and referred to as Echelon 0.

Synchronizing the front end electronics and providing high resolution time reference to beam crossings is an important requirement of the streaming DAQ. The Global Timing Unit (GTU) is the interface to the EIC collider controls. It receives the 98.5Mhz bunch crossing clock, orbit information, and beam polarization information and distributes it via the DAM boards to the RDOs and FEBs. The GTU is the only global source of real time information provided to the FEB/RDOs, so it must

Implementation	Detector/Sensor	Key Attributes
Discrete	Calorimeter/SiPM	COTS devices, 14-bit digitization
CALOROC	Calorimeter/SiPM	ASIC, 10-bit digitization
EICROC	AC-LGAD, pixel	ASIC, High-precision timing for Cd < 5 pF
FCFD	AC-LGAD, strip	ASIC, High-precision timing for Cd < 10 pF
ALCOR	dRICH/SiPM	ASIC, uses shutter for 1 p.e. sensitivity
SALSA	MPGD	ASIC, peaking time to 50 ns, includes DSP

Figure 3.280: ePIC Electronics and ASICs summary

	# Ch	# Ch/ Unit	#ASICs/ Wafer	#Wafers	Node (nm)	Package	Institution
Discrete/COTS	24 k	32	NA	740 Digitizers	COTS	NA	IU
CALOROC	97 k	64	480	5	130	BGA	OMEGA/IN2P3/IJCL/ORNL
EICROC	5.2 M	1024	160	42	130	Wafer Bump	OMEGA/IN2P3/IJCL/CEA-IRFU/AGH
FCFD	2.6 M	128	180	149	65	Wire Bond	FNAL
ALCOR	318 k	64	800	8	110	BGA	INFN
SALSA	202 k	64	500	9	65	BGA	CEA-Saclay/U of Sao Paulo

Figure 3.281: Scope of the electronics and ASICs developments

provide information a trigger system would normally provide. These functions include the ability to synchronize data from different detectors, to send flow control signals, to pass bunch information such as spin orientations and bunch structure, the ability to provide user defined signals for signaling special data formatting or calibration needs, and the ability to implement a hardware trigger for debugging or as a fallback option to solve unforeseen readout issues.

The communication between the RDOs, DAM, and GTU will use an unified ePIC data protocol to coordinate data transfer. This protocol will be discussed in more detail in section 3.3.10.3.6.

3.3.10.3 Subsystem Description (components)

3.3.10.3.1 ASICS and digitization PCBs Readout electronics are being developed based on the sensor technologies. Common requirements among various sub-detectors have been identified to maximize synergy. In most cases the digitization solutions take the form of ASICs, but we also use PCB solutions with COTS components. Each component supports the ePIC streaming readout model with triggerless operation and serial interfaces. To facilitate calibration and debugging, capability for triggered operation is also implemented. The solutions and their characteristics are summarized in figure 3.280.

The scope of each project is summarized in figure 3.281, which shows the number of readout channels, technologies employed and institutions developing these readout solutions.

It is noted that the pfRICH and the hpDIRC detectors benefit from the FCFD and the EICROC developments due to their timing precision requirements. The FCFD is, however, the nominal choice due to its lower channel density packaging for these applications with higher detector capacitance, which enable tailoring their timing performance via detector bias adjustment.

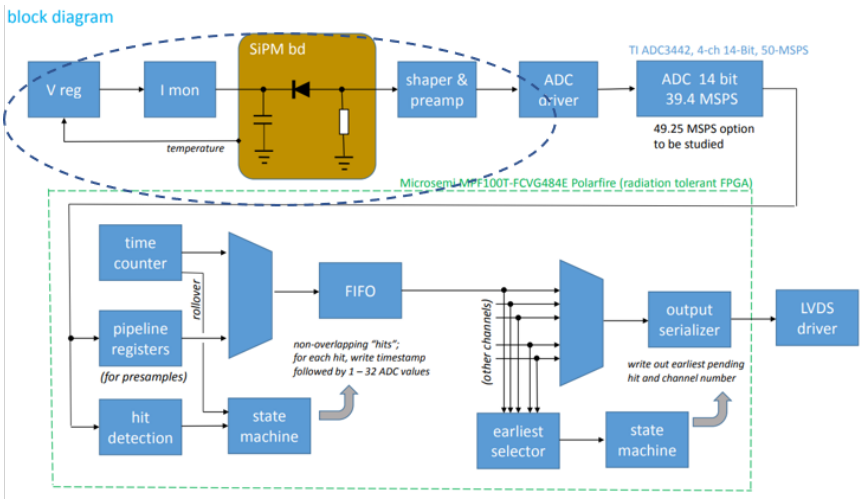

Figure 3.282: Discrete block diagram

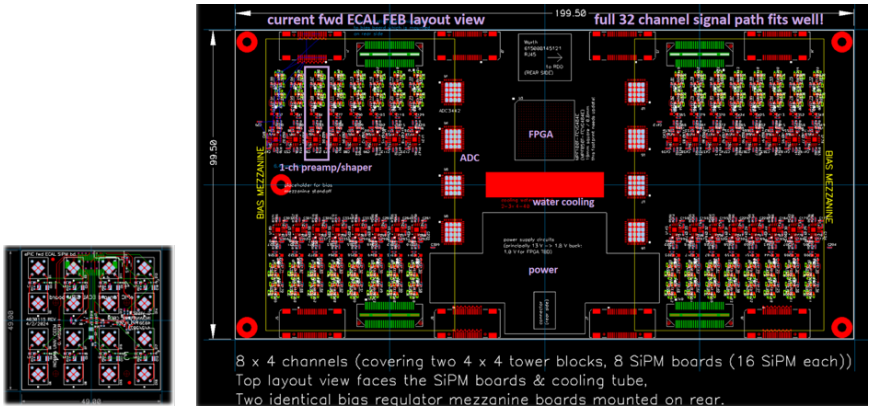

Figure 3.283: Discrete Adapter (left) and digitizer FEB PCBs

Discrete The Discrete readout refers to custom PCBs using commercial (COTS) components. Discrete readout addresses calorimeters with SiPMs where high resolution digitization (14 bit) is required.. The design and technologies will be validated for the radiation level expected in the specific positions of readout electronics within the ePIC detector. The block diagram is shown in figure 3.282.

The circled area in fig. 3.282 delineates the Adapter section with SiPMs and bias circuitry; the remaining parts make up the FEB PCB, which includes signal conditioning, ADCs and readout logic. The Adapter and FEB PCBs are located at the detector, as a stack, and CAT6 cables are employed for serial interfaces. Key specifications are shown in figure 3.284. Prototypes of the Adapter and FEB PCBs are shown in figure 3.283.

CALOROC The CALOROC ASIC is being developed from the H2GCROC (HGCROC-SiPM) [168]. The CALOROC will address readout from calorimeters with SiPMs and for which a 10-bit resolution digitization with wide dynamic range capabilities is applicable. The H2GCROC ASIC digitizes SiPMs with similar characteristics as needed in ePIC. But the CALOROC updates

Function	Waveform digitizer with COTS devices
Channels	32
Digitizer	TI ADC 3422
Resolution	14-bit (12-bit also available)
Shaping	80 ns peaking time
FPGA	Microsemi MPF100T-FCVG484E Polarfire (Rad Hard)
Power	DC-DC converter (bPOL12V, bPOL48V, LTC36xx)
Cooling	Liquid
Cabling	CAT6

Figure 3.284: Discrete key specifications

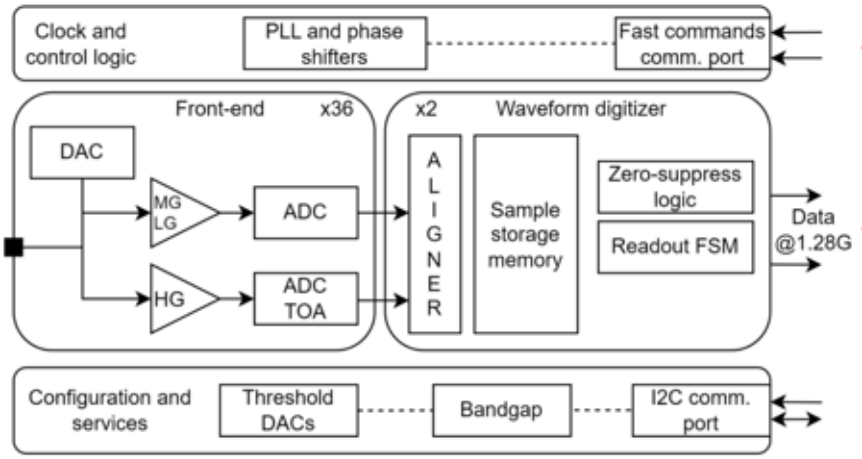

Figure 3.285: CALOROC block diagram

the digital backend with interfaces, conforming to the needs of the streaming readout approach at the EIC. In parallel, tests with the H2GCROCv3 chip continue to provide input and validation into the design of the CALOROC ASIC. There are, however, two frontend variants being considered: CALOROC1A uses an ADC, a TOA and a TOT for wide dynamic range, similar to the H2GCROC; CALOROC1B uses a different frontend architecture making use of dual gain switching techniques to extend its dynamic range. The CALOROC block diagram is shown in figure 3.285 and its specifications summarized in figure 3.286.

Function	Charge and timing digitization from SiPMs
Tech Node	130 nm CMOS
Channels	64
Cdin	500 pF – 10 nF
Digitization	Charge: 10-bit ADC, 15-bit TOT; Timing: <500 ps TOT (1 MIP)
Dynamic Range	Up to 12 nC
Clock	39.4 MHz operation from BX 98.5 MHz
Links	1260.8 Mbps @ 39.4 MHz, multiple
Power	10 mW/ch
Package	BGA
Rad Tolerance	Radiation hard

Figure 3.286: CALOROC Key Specifications

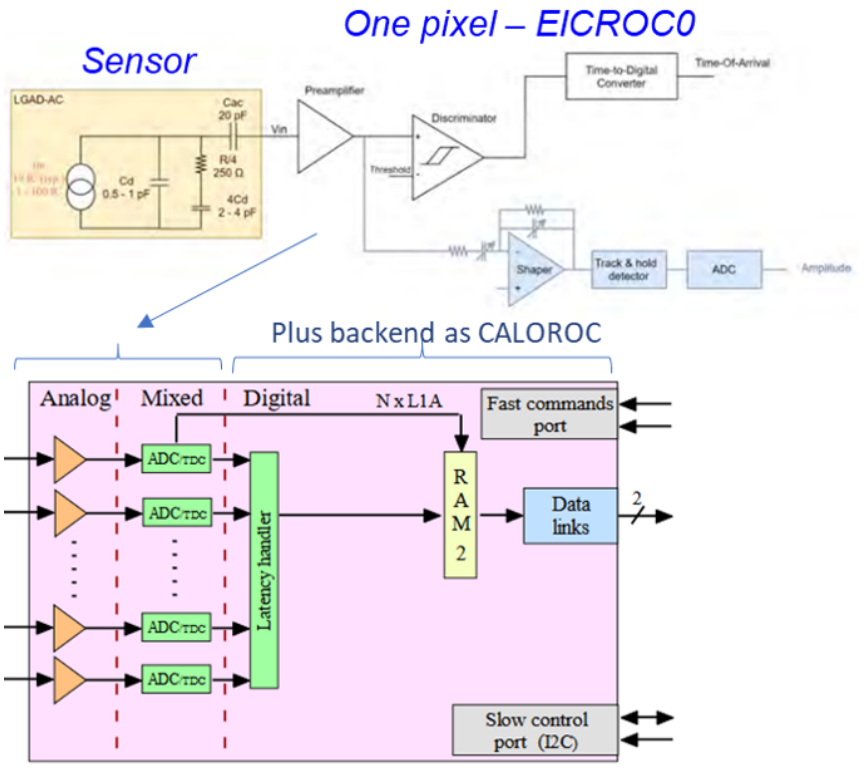

Figure 3.287: EICROC block diagram

EICROC The EICROC ASIC will address readout from AC-LGAD pixel detectors with low detector capacitance (Cdin) and very stringent timing precision requirements. The EICROC design is based on the existing HGCROC-Si ASIC [168] for Si and PMTs with similar characteristics and timing requirements as the AC-LGAD pixel sensors. The EICROC updates the digital backend with interfaces conforming to the needs of the streaming readout approach at the EIC. The same digital backend is already being designed for the CALOROC. Main IP blocks consist of preamp, discriminator, TOA, ADC and TDC. The EICROC block diagram is shown in figure 3.287 and its specifications are summarized in figure 3.289. Figure 3.288 shows the EICROC timing performance with varying charge from input signals.

FCFD The FCFD ASIC is currently under development to address readout from AC-LGAD strip detectors with medium detector capacitance (Cdin) and very stringent timing precision requirements. The FCFD design implements the constant fraction discriminator technique for high precision timing without time-walk corrections. The backend, which is currently being considered, may be based on the existing ETROC ASIC [169] or the EICROC development. The FCFD block diagram is shown in figure 3.290 and its specifications are summarized in figure 3.292. Figure 3.291 shows the FCFD timing performance with varying charge from input signals.

ALCOR The ALCOR ASIC is currently under development specifically for the readout of the dRICH detector with SiPMs due to its single photo-electron sensitivity requirement. The ALCOR design includes trans-impedance amplification (TIA) with regulated common gate (RCG) bias for

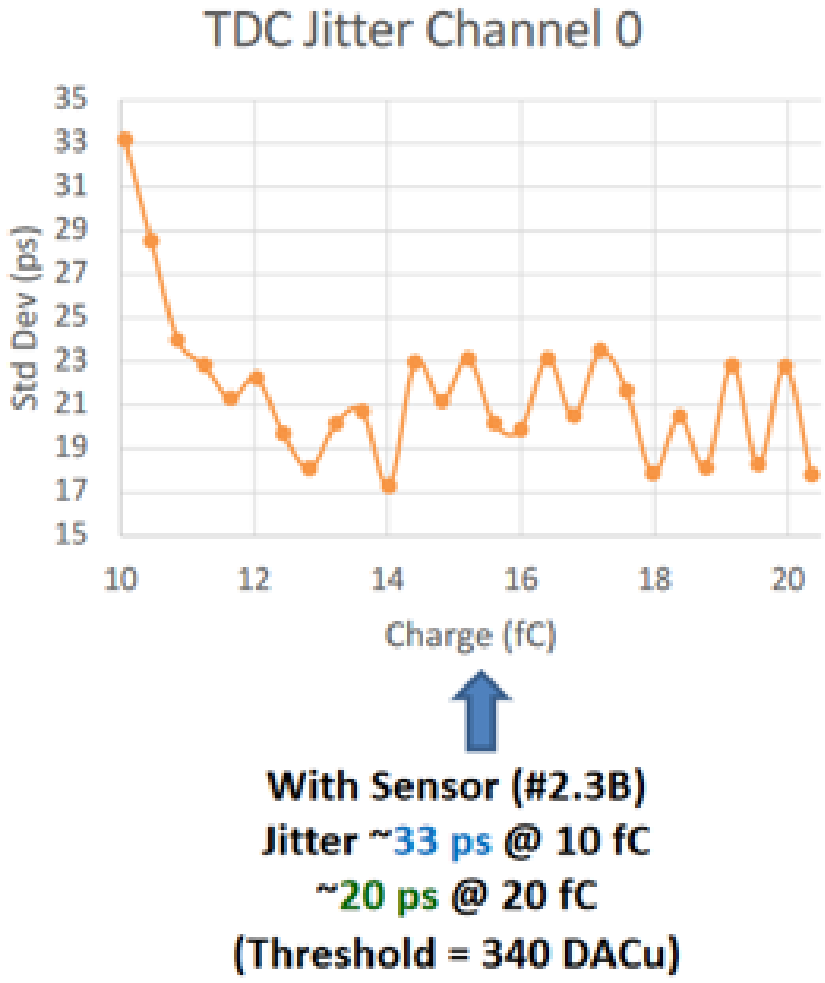

Figure 3.288: EICROC timing performance

Function	Timing digitization from AC-LGAD pixels
Tech Node	130 nm CMOS
Channels	1024 (32x32)
Cdin	1 – 5 pF
Digitization	ADC: 8-bit, TDC: 10b; Timing: 30 ps
Dynamic Range	1 – 50 fC
Clock	39.4 MHz operation from BX 98.5 MHz
Links	1260.8 Mbps @ 39.4 MHz, multiple
Power	<2 mW/ch
Package	Bump + wire bonds
Rad Tolerance	Radiation hard

Figure 3.289: EICROC Key Specifications

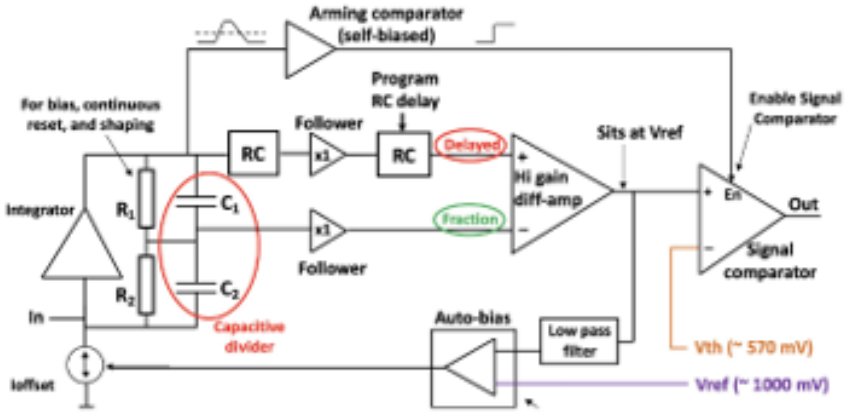

Figure 3.290: FCFD block diagram of the frontend

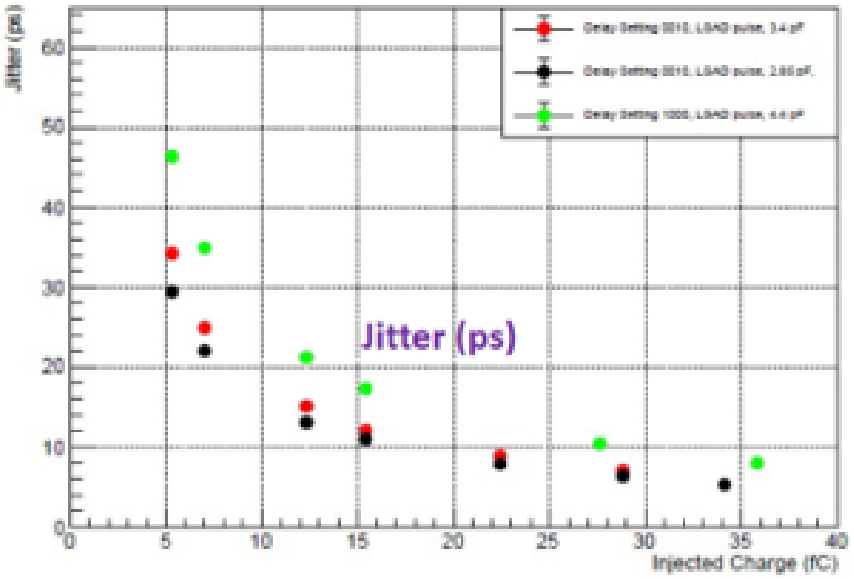

Figure 3.291: FCFD timing performance

Function	Timing digitization from AC-LGAD strips
Tech Node	65 nm CMOS
Channels	128
Cdin	<15 pF
Digitization	TBD; Timing: 10 - 30 ps
Dynamic Range	5 – 40 fC
Clock	39.4 MHz operation from BX 98.5 MHz
Links	1260.8 Mbps @ 39.4 MHz, multiple
Power	<2 mW/ch
Package	Bump + wire bonds
Rad Tolerance	Radiation hard

Figure 3.292: FCFD Key Specifications

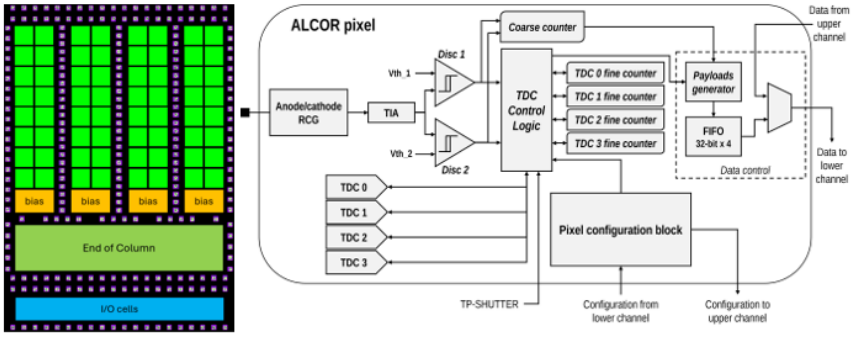

Figure 3.293: ALCOR Si Die (left) and block diagram

Function	Digitization from SiPMs with 1 p.e. sensitivity
Mode	Single-photon tagging or time and charge
Tech Node	110 nm CMOS
Channels	64 (8x8), dual polarity
Cdin	<1 nF
Digitization	20-40 ps TDCs, TOA + TOT; Timing <150 ps
Shutter	Width: 2–3 ns, programmable latency
Input Rate	<2.4 MHz (up to 5 MHz on single channel)
Clock	394.08 MHz operation from BX 98.5 MHz
Links	788 Mbps LVDS, SPI configuration
Power	12 mW/ch
Package	BGA
Rad Tolerance	Radiation hard

Figure 3.294: ALCOR Key Specifications

low noise, inhibit or shutter operation to limit contribution from dark-rate SiPM noise and TDCs to allow for single-photon tagging or time and charge digitization. The shutter function is a critical aspect of this ASIC and it is programmable for width and latency. The ALCOR die and block diagram are shown in figure 3.293 and its specifications are summarized in figure 3.294.

SALSA The SALSA chip is an ASIC being developed based on the SAMPA [170], [171]. It will readout the MPGD trackers, namely the barrel cylindrical Micromegas, the barrel μRWELL and the end-cap μRWELL detectors. The purpose of SALSA is to amplify, shape and digitize signals coming from the MPGD detectors, and then perform basic data processing on the digitized samples before to transmit them to the next element of the data acquisition chain. It gathers in a single die a CSA pre-amplifier, a shaper and an ADC for each of the 64 channels, followed by a DSP which performs baseline corrections, digital shaping and a zero-suppression in order to reduce the output data bandwidth. Furthermore, to reduce data output even more, a peak finding algorithm is implemented to extract from samples information like amplitude and time of detected hits. It will be able to work both in the streaming readout environment foreseen at EPIC, and in a triggered environment.

The characteristics, performances and configurability of SALSA are designed to make the ASIC very versatile, being able to be adapted to several kinds of MPGD detectors and to several applications. It will be able to work with a large range of signal amplitudes, a large range of electrode capacitance and large range of signal rise times. Its target specifications are summarized in the

Table 3.80.

Specification	Values	Remarks
Number of channels	64	
Input capacitance	50-200 pF	Reasonable gain up to 1 nF
Peaking time range	50 - 500 ns	
Max gain range	50 fC to 5 pC	
Max input rate	100 kHz/channel	Fast CSA reset
Signal polarity	Negative and positive	
ADC max sampling rate	50 MS/s	
ADC dynamics	12 bits	More than 10 effective bits
DSP processing	Baseline correction, filter, zero-suppression, peak finding	
Readout modes	Streaming readout, triggered	
Output data links	4 Gigabit links	1 only used at EPIC
Die technology	TSMC 65nm	
Die size	$\sim$1 cm^2	
Power consumption	$\sim$ 15 mW/channel	
Radiation hardness	Up to 300 Mrad and 10^{13} n_{eq}/cm^2	

Table 3.80: Main specifications of the SALSA chip.

3.3.10.3.2 FEB The Front End Boards (FEB) are customized to the space, power, radiation load, and cooling requirements of each detector. However each FEB has similar needs for clocks, serial links, power, configuration, and control. The FEB usually uses ASICs to provide functionality, so efforts related to the FEB design has focused primarily on components to be shared by most or all FEBs.

FEB Components: DC/DC converters DC/DC converters are employed throughout ePIC for the efficient distribution and regulation of the various sub-systems. The bPOL12V and bPOL48V DC/DC modules are selected for their radiation hardness and high magnetic field tolerances. Designs based on the LTC36xx family of devices will also be employed after proper validation.

FEB Components: lpGBT In some cases the serial links from the FEB to the RDO is direct, using Low-Voltage Differential Signaling (LVDS) or SPF+ fiber links. However, in the central detector region where radiation load is highest, and space and material budgets are most constrained the links will be accomplished using the low power Giga-Bit Transceiver devices (lpGBT) [167]. These devices operate at the 40 MHz LHC clock which has consequences for the ePIC fiber protocols (See sections 3.3.10.3.6 and 3.3.10.3.5) The lpGBT is a radiation hard part with Serializer/Deserializer (SERDES) functionality. The downlink transceiver operates at 2.5 Gbps, whereas the data uplink transceiver operates at 10.24 Gbps.

Target Detector	Input	Output	technology
TOF Pre-Prototype, Calorimeters	copper	SFP+ fiber	FPGA
dRICH	copper	VTRX+ fiber	FPGA
Fiber Aggregator (SVT, MPGD, AC-LGAD)	fiber	fiber	FPGA
Imaging Calorimeter	copper	fiber	FPGA
Low Q^2 Tagger	copper	up to 12 fiber	FPGA
Direct Photon Detector	copper	fiber	Flash ADC250

Table 3.81: Types of RDO

FEB Components: VTRX+ The VTRX+ [172] module is an electro-optical receiver/driver used to interface to multi-mode optical fibers with MT optical connectors. The VTRX+ is radiation hard and it is tolerant to high magnetic fields; it has a small footprint, has low power consumption and interfaces directly to the lpGBT transceiver devices. One (1) receiver Rx (2.5 Gbps) and four (4) transmitters Tx (10 Gbps) are implemented.

3.3.10.3.3 RDO

The RDO aggregates digitized ASIC data from the multiple front end boards, and ships this data to the DAM Boards. The RDO also has the function of delivering a high resolution clock (<=5 ps jitter) to the front end boards. This clock is reconstructed from the data on the downlink fiber. The final function of the RDO is to act as the interface between the detector specific function of the ASICS to the global ePIC DAQ fiber protocol (See section 3.3.10.3.6).

Several detectors — the SVT, the MPGD based detectors, and all AC-LGAD based readouts — will make use of lpGBT or lpGBT-like aggregation using VTRX+ transceivers. The lpGBT aggregates ASIC information, deliverers a high resolution reconstructed clock, and gives a transparent, simplified interface to the ASICs via serial links. It does not have, however, the capability of implementing the full ePIC protocol. For these RDOs the protocol will be implemented at the next level, either inside the DAM board or in a second level fiber to fiber RDO.

There will be several versions of the RDO depending on the needs of the specific detectors. The different RDO types are summarized in table 3.81

RDO Subtypes: TOF pre-prototype The TOF pre-prototype RDO was designed to use elements common to most ePIC detector RDOs. These elements include Xilinx Ultrascale+ Artix FPGA, SFP+ fiber optics interface, clock cleaner PLLs, and clock recovery. The pre-prototype has been produced and is undergoing measurements of power usage and clock jitter. The board is shown in figure 3.295.

RDO Subtypes: dRICH The dRICH RDO is part of the dRICH Photo Detector Unit PDU (see section 3.3.4.4, 1248 PDUs will serve the dRICH). It provides read-out of four 64-channel ALCOR ASIC, installed each on a separate FEB. The space constraints are particularly demanding: the total RDO area is 40x9 mm^2 - quite similar to a credit card - requiring a devoted design, given the high integration of data buses and services within the PDU. The FPGA providing readout of the ALCOR is an AMD Artix Ultrascale+ AU15P-SBVB484, complemented by a PolarFire FLASH-based FPGA MPF050T-FCSG325. The latter will support remote programming and continuous scrubbing of configuration bits of the SRAM-based AMD FPGA, to protect against SEU. Given the space constraints and the need to curb power consumption (total RDO power is expected $\approx$ 4 W)

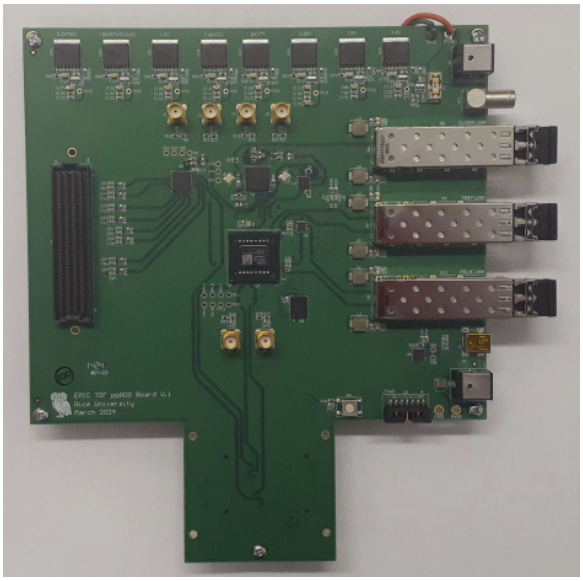

Figure 3.295: TOF pre-prototype RDO

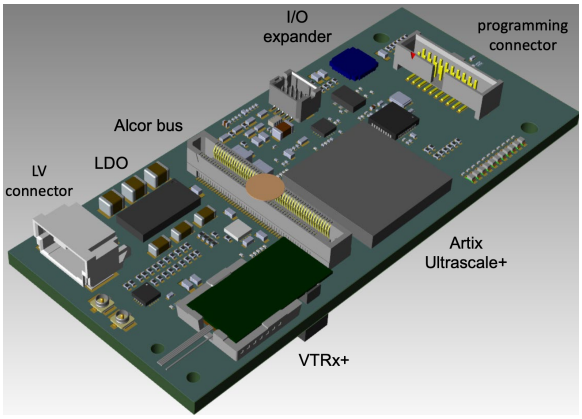

Figure 3.296: 3D model of dRICH RDO

the VTRX+ optical transceiver has been selected, directly connected to the AMD FPGA SERDES. The maximum throughput per link (reached at maximum radiation damage before annealing) is expected to be about 1 Gbps, safely within VTRX+ specifications. The ALCOR will be read out at 394 MHz, with a clock multiplier and jitter-attenuator (Skyworks Si5326) deriving this clock from the reconstructed EIC clock. A Microchip microcontroller provides power management and acts as watchdog against SEL. The first prototype of this card is under production and will be intensively tested during 2025, including irradiation tests. A 3D-rendering of the card is shown in Fig. 3.296.

RDO Subtypes: Fiber Aggregator The fiber to fiber RDO is to be used with lpGBT-like FEBs to convert the transparent ASIC interface to the ePIC DAQ protocol. They are also necessary to further aggregate the fibers, particularly in the case of SVT and bTOF large numbers of low-data utilization fibers are required.

RDO Subtypes: Astropix End of Stave Card This RDO is to be used by the Barrel Imaging Calorimeter. It is expected to be an updated version of the Astropix end of stave card developed by NASA.

RDO Subtypes: Low Q^2 This is a RDO specifically for the low Q^2 taggers. It is expected to be an updated version of the Spyder3 board. These use the timepix sensor and have high potential data volumes, requiring several uplink fibers per RDO.

RDO Subtypes: Direct Photon Detector The Direct Photon RDO is a specialized interface expected to use the JLab Flash ADC250. This detector has only about 100 channels, but is expected to have very high occupancy, and as such the appropriate technology is to digitize all channels at 200 MHz and stream it directly to the DAM boards which will summarize the information, writing out only the summed energy deposited each bunch crossing, or histograms of the bunch crossing energies according to bunch number.

3.3.10.3.4 DAM - Data Aggregation and Manipulation Hardware

For the ePIC DAQ system the DAM boards will be used as the primary aggregation point for the "raw" detector data streams. Because these boards are also the final aggregation points for the front-end (hardware managed) DAQ, there will need to be some well-defined but configurable algorithms for merging streams and managing potential congestion and data loss both for the incoming detector streams and the outgoing aggregated streams being queued up for online processing.

In Addition, the DAM boards will interface with the Global Timing Unit (GTU) hardware via a proprietary communication protocol that supports a synchronized EIC clock distribution to all subsystems and general DAQ/Run control and configuration. Finally, the DAM will act as the slow control interface for configuration and monitoring of all detector subsystem front-end boards (e.g. ASICs and other digitizing electronics).

We have identified an ideal candidate for the DAM hardware. An updated version of the FELIX board [173] (Model FLX-155) is currently being developed at BNL for ATLAS at the HL-LHC. The board is show in figure 3.297. The features and updated components ensure a longevity of production, performance, and support that match very well with the EIC timeline. The board is built around the Xilinx Versal ACAP. This will facilitate using the board both as a PCIe device (supporting both PCIe Gen4 and Gen5 standards) in a server or as a standalone "smart" "aggregation" switch running a Linux OS. It can support up to 48 serial links to RDOs at the front-end running at speeds up to 25 Gbps as well as an LTI interface (8 fibers) supporting a high-resolution direct clock along with our GTU-DAM communication protocol. There is also a separate 100 Gb ethernet link off the board. A DDR4 RAM slot is available to support buffering and more complex algorithms for data reduction or interaction tagging. The board supports JTAG and I2C communications.

We expect to procure several FLX155 boards for testing and software/firmware development in 2025.

3.3.10.3.5 GTU - Global Timing Unit

The design of the global timing distribution system (GTU) will be central to the operation of the streaming readout model. The timing system must provide signals to ensure that the data from different detectors can be synchronously aggregated. It must provide a copy of the accelerator bunch crossing clock (running at 98.5Mhz) to all front-end systems. A subset of these systems (e.g. TOF) will require a phase aligned system clock with a jitter of <5 ps in order realize required timing resolutions for these detectors (20-30 ps).

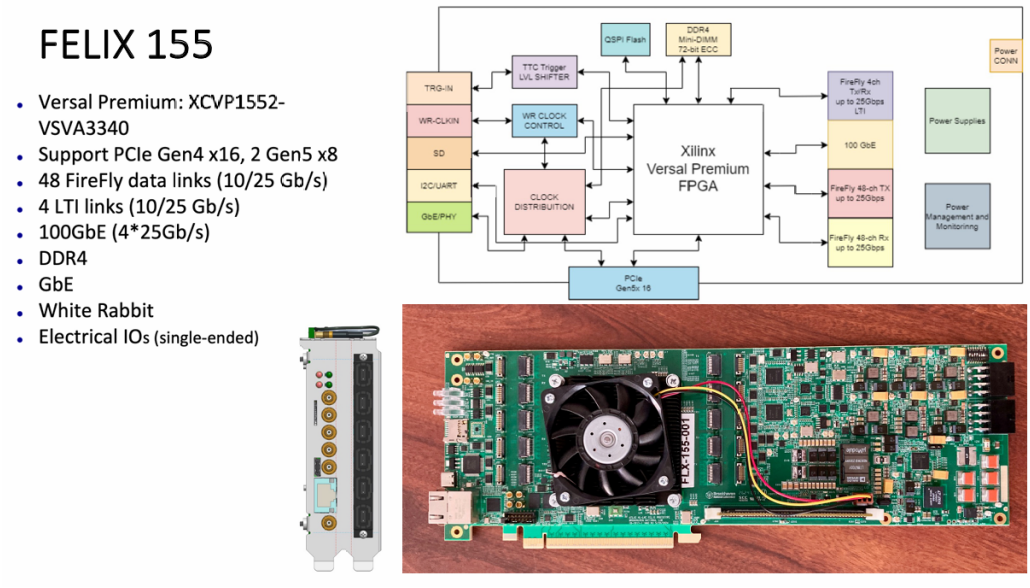

Figure 3.297: The FLX-155 board identified for use as a DAM board

The GTU is also the only source of real time information provided to the FEB/RDOs, so it must provide information a trigger system would normally provide. These functions include the ability to synchronize data from different detectors, to send flow control signals, to pass bunch information such as spin orientations and bunch structure, the ability to provide user defined signals for signaling special data formatting or calibration needs, and the ability to implement a hardware trigger for debugging, calibration or as a fallback option to solve unforeseen readout issues.

Precision Clock Distribution The ePIC clock distribution must support both 98.5 MHz and 39.4 MHz components both of which will reconstruct their clock from the data transferred on the fiber and require < 5 ps jitter and phase stability. In order to naturally support both frequencies the GTU will distribute clock synchronized to 10 bunch crossings at 9.85 Mhz to all DAM boards. The DAM boards will recover 98.5 MHz and 39.4 MHz clocks by multiplying by 10 and 4 respectively. The frequency multiplications will be done synchronously (i.e. the clock edge should be aligned with the 9.85 MHz clock).

We tested this scheme using the Si5344H evaluation board (Skyworks) to emulate the ePIC clock source (EIC common platform), Jlab's Trigger Interface board with Analog Devices' AD9510 chip to emulate the GTU, Finisar's FLT410 optic transceiver for the dedicated optical fiber distribution, and the Si5394A evaluation board (Skyworks) to emulate the DAM clock recovery.

We re-synchronize the clock divider (AD9510) and the clock recovery (Si5394A) every 1,073,741,830 (98.5 MHz) clock cycles. The recovered clocks (98.5 MHz and 39.4 MHz) are always phase aligned with the original clock (before the clock divider and multiplication). The measured phase difference uncertainty for this is about 1.5 ps (std). This uncertainty includes the recovered clock jitter, and the clock phase shift.

For the 98.5 MHz clock distribution, from DAM to RDO, our tests with the ppRDO shows that the jitter of the MGT recovered clock is less than 3 ps (std) and the phase can be aligned to picosecond precision with the pseudo clock technique.

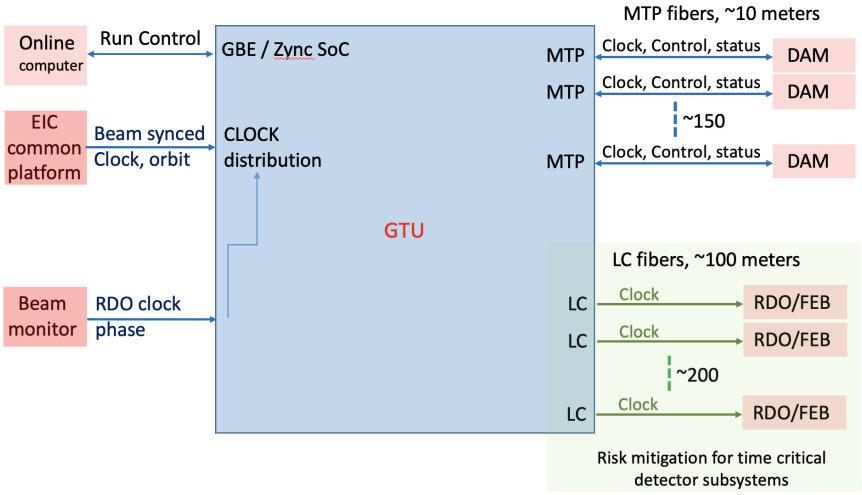

Figure 3.298: Schematic layout based for the GTU

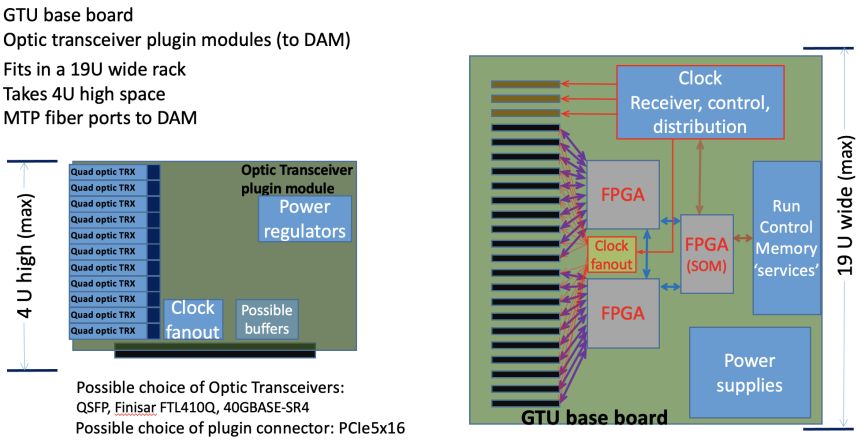

Figure 3.299: Physical concept for the fiber distribution for the GTU

For the 39.4 MHz clock distribution, from DAM to lpGBT, both the lpGBT ASIC production tests and our tests using a VLDB+ board (a CERN development board with VTRx+ optical receiver and lpGBT) show that the lpGBT recovered clock is phase aligned with the DAM (emulated by the kcu105 FPGA evaluation board from AMD, and the Si5344H evaluation board from Skyworks). The source clock and the lpGBT recovered clock have very low jitter. The uncertainty of the phase difference (including the clock jitter and the phase shift) is less than 2 ps (std).

GTU hardware design Figure 3.298 shows a schematic layout based on required functionality of the GTU. The physical concept is shown in figure 3.299. The GTU will be custom rack-mounted hardware in the DAQ room with a base board and multiple plug-in optical interface modules. It will be based on a multi-FPGA architecture including a single Zync SoC FPGA supporting gigabit ethernet and a full Linux OS to facilitate both ePIC Run Control and other user-based applications. It will include an interface for the EIC Common platform (Clock, beam orbit and other collider information) and an interface for feedback from the local IP-6 beamline to support bunch crossing

type	**clock (MHz)**	**downlink rate (Gb/s)**	**downlink word length** (ns)	**downlink word width** (bits)
Standard	98.5	10	10.15	64
VTRX+	98.5	2.56	10.15	16
VTRX+	39.4	2.56	25.375	64

Table 3.82: RDO downlink words

Decoded Synchronous Command Structure							
[0:7]	[8:15]	[16:23]	[24:31]	[32:39]	[40:47]	[48:55]	[56:64]
Flexible Command Data Encoding					FAST CMD		Comma
type	type specific				FAST CMD		Comma

Table 3.83: DAM/RDO Decoded Synchronous Command Structure. This structure is defined to allow continuous availability of the critical beam related bits and more rare commands. The data in the 40 bits worth of flexible command data encoding remains flexible but must contain enough control bits to select what structure it has. The ”type”, ”type specific” division is an potential holding this flexibility

clock phase corrections

The jitter-cleaned and phase corrected clock then is fanned out for distribution to all DAM boards via a multi-fiber communications link (We intend to support up to 150 of these links for current needs as well as potential future requirements). In addition we plan to support up to 250 direct clock links to the RDO/FEB electronics. This is to mitigate potential limitations with the distribution of the low jitter (<5 ps) clock via the DAM path communication protocol.

3.3.10.3.6 Protocols The ePIC fiber protocol is used to communicate information between the GTU, DAM and RDO boards. The DAM to RDO communications are limited by the type of interface, and can be described in three categories as shown in table 3.82.

The ePIC fiber protocol depends upon a synchronous command structure (table 3.83). The need for links with separate clock rates and with separate downlink speeds requires careful attention to the encoding of commands, which to the extent possible will share the same synchronized command format among all detectors. Detectors with faster links can support additional features and higher bandwidth for configuration and ASIC control. In order to synchronize data in all detectors it is necessary to demand that synchronous commands are sent on 5 bunch crossing (50.75 ns) intervals when the 98.5 MHz and 39.4 MHz clock edges coincide.

The protocol will deliminate streaming data into timeframes. The maximum length, in bunch crossings will be defined to fit within 2^{16}, which implies a time frame length of ∼600 us. This is also a convenient time as it corresponds to a manageable maximum time frame size of ∼10 MB.

The bandwidth available for transmitting data from the FEBs to the DAM depends upon adequate zero-suppression. This implies the potential for data loss if the front ends produce unexpected levels of data. This potential must be mitigated by sensing, and tagging any data loss, by implementing flow control mechanisms, and by providing mechanisms for resetting and disabling

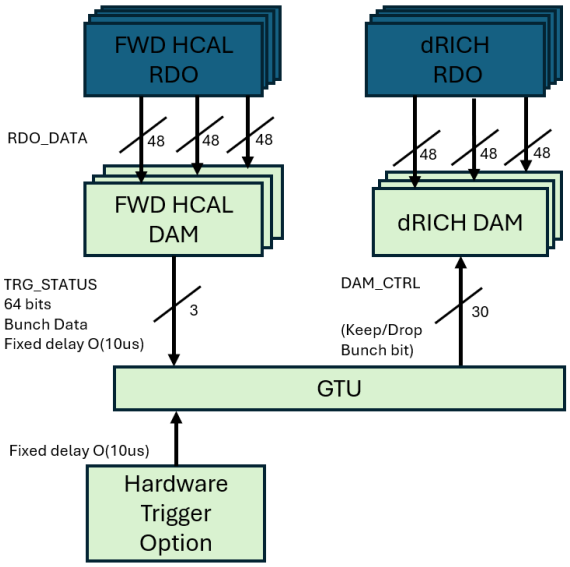

Figure 3.300: Operation of firmware trigger under assumption that the trigger decision for the dRICH depends upon data from fHCAL

problematic FEBs and RDOs.

The features that must be encoded in the Synchronous command protocol are

- The distribution of real-time control information to the RDO and FEBs.
- The distribution of a high-resolution beam crossing timing signal to the RDO and FEBs.
- Synchronize and verify synchronization of bunch counters among all detector readouts
- Define the time frame boundaries
- Provide RDO and DAM Data processing flags
- High performance ($\sim$ 10 Gbps) transfer of hit data and monitoring information from the FEBs and RDO to their DAM boards.
- The distribution of configuration information to the RDOs and FEBs.
- Firmware based high level selective readout
- Flow control
- Error detector and recovery
- Transfer Slow Controls Data from the FEB to soft IOCs in the DAM board or readout computer to pass slow controls information to Slow Controls.

High Level Selective Readout One example of the operation of the protocol is to allow a high level trigger criteria to reduce dRICH noise. This is not a global trigger to exclude events from the readout of the ePIC detector. Instead, this trigger criteria will be used to selectively omit data from particular detectors with unusually high data volumes. In this example, the dRICH.

The path of the commands sent is show in figure 3.300. Data arrives at DAM boards with 10us from digitization. It is stored in the DAM boards. After 10us FPGA based algorithms provide a description of the data (for example number of hits above a specified threshold) from each fHCAL DAM board. This information is encoded into 64 bits and sent to the GTU which aggregates data from fHCAL DAM boards and sends the keep/drop bunch bit to the dRICH DAM boards. The dRICH DAM boards drop or transmit data based upon this message. The decision comes after a fixed latency of about 11us which is very small compared to the buffering available on the DAM board.

Note that a similar approach can be implemented with a hardware signal into the GTU. In this case a fixed delay is applied to the hardware signal, but the decision mechanism uses the same data path.

dRICH data algorithms There are also additional schemes for implementing dRICH data reduction using only dRICH data or aggregated data from different sub-detectors. This is currently under investigation by the dRICH groups at INFN. One possibility would be to perform such reduction on the network of interconnected dRICH DAMS using the APEIRON framework [174], which implements a multi FPGA ML algorithm with deterministic time. The results of this calculation are transmitted to the GTU in the same manner as for cross detector selection criteria. The DAM buffering capacity is exploited in this scheme. Another possibility is to use instead, Online Data Filter algorithms in the servers receiving the aggregated data (see Fig. 3.279), exploiting xPU resources. Given the noise rate in the dRICH will increase with the radiation damage (see section **??**), this will provide an opportunity to develop and test carefully such systems.

Resource	Totals
DAM/FELIX boards	136
EBDC Servers	92
DAQ Compute Nodes	108
File Servers (Buffer Box)	6

Table 3.84: DAQ Computing Resources

3.3.10.3.7 DAQ/Online Computing - Echelon 0

Table 3.84 outlines the planned resources for the ePIC detector DAQ and Online computing needs. This is based on the elements shown in the DAQ schematic in Figure 3.279. Several thousand fibers from the RDOs will be aggregated in the DAM boards and presented to the Online Farm. To be clear each online farm node represents one multi-core server. The expectation is that they will minimally support 32-64 cores, and selected nodes will support PCIe-based GPUs and/or FPGAs in addition to the DAM boards in the FBDC (Frame Building Data Concentrator) nodes. The high performance DAQ network is expected to support 100/400 Gbps bandwidth connections. As the majority of the Online computing is expected to be COTS hardware, much of it will be acquired as late as is reasonable in the construction phase.

All Echelon 0 resources are fully dedicated to operation of the ePIC Detector and are included as part of the EIC Project. One open question under consideration, however, is to split these resources between the DAQ Room at IP-6 and the SDCC (BNL main data center) and to integrate them as a single enclave under ePIC control. There are several advantages to this configuration. First it will reduce the overall cost of infrastructure upgrades to the DAQ Room cooling systems. Also, having a subset of ePIC computing resources available in the SDCC will allow better network

access to DAQ and electronics labs during construction (when the DAQ Room will not be available. Finally, during operations having DAQ tiered storage of production data in the SDCC will facilitate distribution of that data to both Echelon 1 processing sites (BNL and JLAB).

At the DAM stage the aggregated data streams will have substantial buffering and available network bandwidth for online processing that will be primarily focused on event identification and background/noise reduction. While we do not currently have solid estimates on the necessary computing resources to complete the required tasks, we have tried to provide conservative estimates of computing resources that would allow a full reconstruction of a 500 kHz event rate of events from similar scale detectors that exist now (e.g. GlueX and CLAS12 at Jefferson Lab and sPHENIX at RHIC). More likely the necessary computing resources for online filtering to get the expected data rates of O(100 Gbps) to files will be somewhat smaller.

Time Frame Building In the streaming model, the primary consideration is ensuring that enough bandwidth and buffering will be available to handle the digitized data at each stage of the DAQ. At the front-end stage time frames for the individual streams are created, managed and aggregated. Given current background and noise estimates the planned bandwidth off the detector to the DAM boards O(10 Tbps) should be more than sufficient.

Streams at the DAM boards will support time frames using a 16 bit bunch crossing counter which would represent a configurable time window of up to 65536*10.15 ns = 665 us. Although the front-end DAQ will be synchronized using a single common clock from the EIC, not all ASICS/digitizers at the FEBs will be running at the same frequency. Hence the timestamps coming from hits in different detectors will need to be wrapped in smaller "time slices" within the full time frame to establish an absolute time for each hit.

Time frames buffered at the DAM boards will be able to utilize the online farm to complete a full build of complete time frames with data from all detectors. Effectively N streams from the DAM boards will generate M<N streams of time frames containing the time frame fragments from the N original streams. This will greatly facilitate additional event identification and processing at both the Echelon 0 and Echelon 1 stages.

Data Processing The ePIC readout system must support data reduction techniques. The implementation of high level selective readout has already been described, but there are many additional techniques that might be implemented in Echelon 0. These include zero loss techniques like aggregation of headers from ASICs or DAM board data. It could include standard or ML based compression techniques. It could involve analysis techniques such as cluster finding or track reconstruction. There could also be ML based noise reduction techniques. And there could be analysis done for specific purposes such as the creation of scalers for monitoring or collider feedback.

The framework for the code generating these features must allow the code to be shared with the offline software, for operational transparency, and for algorithm evaluation.

The results of the code must be incorporated into the time frame data using data formats that allow for independent data banks to co-exist. The policy of ePIC is expected to be to avoid dropping any data unless data volumes make it necessary. There should also be a sample of unprocessed data even if the readout of raw data banks are suppressed due to data volume limits. This implies that the write out of specific data banks be controlled by configurable prescales.

Configuration Databases Configuration information must be stored and made accessible to the ePIC Collaboration.

Slow controls interface to RDOs/FEBs The primary configuration and slow control communications interface to all the ASICs and other digitizing electronics (FEBs) will be through our proprietary data link between the DAM board and the RDOs. Our current plan is to take advantage of the Versal SoC FPGA dual-core ARM CorteX processor. All DAM boards will support a full LinuxOS and gigabit ethernet access. This will facilitate running an EPICS soft IOC as well as user-based server applications for local and remote communication with the front-end electronics.

Slow control communication on the DAM-RDO link must be bidirectional which means that slow control communications must share the link with streaming data coming from the detectors. The protocol must ensure that adequate bandwidth is available for digitized hits from the detector and slow controls readouts. The flow control provisions must enforce this requirement.

Software and firmware development of drivers and libraries necessary to access all the FEB "flavors" is supported as part of the Project. The majority of the FEBs will support standard I2C/SPI control communications.

Monitoring / Logging A unified system for centralized logging of informational and error messages is required. These messages should be ideally be available and archived in web-accessible form.

A unified system for monitoring of the real time behaviour and utilization of online components is also needed.

Interface to Echelon 1 As will be discussed in Section 3.3.11, the ePIC DAQ (Echelon 0) is an integral part of the computing system, and the output of the DAQ data triggers the calibration and reconstruction pipeline in Echelon 1, located at the computing centers of the host labs. From the DAQ buffering disks, two identical copies will be sent to the buffer file system at the BNL SDCC via a dedicated fiber link and at the JLab Data Center via the 400 Gbps ESnet link, respectively. Each data center's data buffer has the capability of about three weeks' ePIC data taking to allow for multiple iterations of calibration jobs and reconstruction passes. Data will also be copied to permanent archival storage (presumably HPSS-like tape system), one copy at each site, which allows for reprocessing of the data in the future in case a problem identified in the prompt reconstruction pass or an improved reconstruction becomes available in the future. Nevertheless, in a steady state, the prompt calibration and production are expected to make the final analysis-ready data for physics working groups within days of the data taking, significantly expedited compared to many ongoing Nuclear Physics experiments.

3.3.10.3.8 Slow Controls

There will be a myriad of slow controls information associated with both the EIC collider and the ePIC detector. These include various systems associated with the beamline, magnets, detector biases, gas flows, temperatures, pressures, etc... While the design and implementation of these slow control systems will be driven by the relevant subsystems they are associated with, it is the defined responsibility of the DAQ to provide software tools to facilitate the integration of all this information with the streaming physics data. This will include synchronizing the times associated with readout of slow control systems and the bunch-crossing clock that will be driving the DAQ system. Online slow control databases to support calibration and reconstruction processing will also be developed. Finally, a general network infrastructure in the experimental

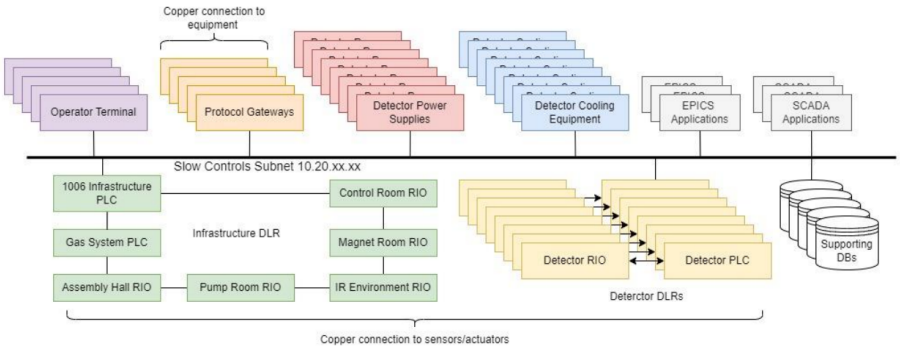

Figure 3.301: Proposed ePIC slow controls network topology

Scenario	Yearly Database Storage (TB)	Network Traffic (Mbps)
estimated	53.9	22.8
worst case	173.5	73.4

Table 3.85: Slow Controls data volume and network traffic

hall and control room, independent of the high performance DAQ network, will be provided to support integration of all slow control systems

A schematic of the proposed slow controls network topology is shown in figure 3.301. The implementation uses EPICS 7 on an ethernet network to control detector operation and read and archive conditions information. Allen-Bradley PLCs are to be used for controlling power to racks in the IR and for detector interlocks.

Resource requirements for the slow controls system were obtained by surveying detector managers. These resulted in approximately 500,000 channels to be read and stored. The yearly storage estimates and network traffic estimates are show in table 3.85.

3.3.10.4 Implementation

3.3.10.5 Calibration, alignment and monitoring:

During run time, predetermined calibration and alignment will be used in configuring the readout electronics and data reduction computing tasks. These calibration and alignment are managed by detector groups, extracted from dedicated prior-to-beam calibration runs, such as pedestal runs and zero field runs. When necessary, such as changes in detector condition, new calibration will be extracted and updated to be used in data taking. The calibration constant used will be archived in the run database and made available for reference in the offline analysis.

Constant monitoring for detector status and data pipeline healthiness is key to high-efficiency data taking and a successful run. We expect a multi-level of monitoring that includes monitoring the metrics on (1) detector statues (2) each stage of the data pipeline (3) sampled data content for decoding and analysis. In addition, in the Echelon 1 computing facility, full reconstruction will be performed for a small fraction of time frames expediently to provide holistic feedback of the experiment capability down to analysis level observable such as pi0 and K0s.

Figure 3.302: DAQ/Computing schedule

3.3.10.6 Status and remaining design effort:

R&D effort: ASIC R&D to continue through 2025

E&D status and outlook: The bulk of the engineering design efforts still required for the readout electronics are centered around the development of RDO and FEB designs needed to support all the detector subsystems. This information is needed to establish baseline costs and better define construction and testing schedules. Project Engineering design for a GTU engineering article can be completed prior to CD2/3. Finally, we expect to procure several FLX155 engineering articles in 2025 to support further timing and communication protocol testing and initial firmware development.

Status of maturity of the subsystem: Electronics and DAQ held a second PDR in June 2024. We expect to hold a third PDR in 2025 on track to an FDR in 2026. There are CD-3B items in the Electronics for VTRX+ and lpGBT. The FDR was held in June 2024, and will be presented during the CD-3B review in January 2025.

3.3.10.7 Environmental, Safety and Health (ES&H) aspects and Quality Assessment (QA planning:

3.3.10.8 Construction and assembly planning:

Figure 3.302 shows the current project schedule for DAQ/Computing. It is broken down into four general categories: Design/Procurement, Fabricate and Delivery, Test and Accept and Installation. Early in the construction phase there is a heavy focus on building and testing custom hardware (GTU, DAMs, RDOs) in order to facilitate detector subsystem testing and DAQ firmware/software development.

Once IP-6 infrastucture upgrades have been completed (DAQ and Control rooms, Wide Angle Hall), we can begin the main trunk fiber pulls into the hall and tunnels and install required patch panels and terminate fibers. At this time we can also start installation of the general IP-6 network infrastructure in the Hall, DAQ and Control Rooms.

Computing hardware procurement and installation are scheduled in three phases during the course of construction. Phase I at the beginning of construction will be for a small subset of machines for development and evaluation. They will be placed in both the DAQ/Electroncs development labs as well as in the SDCC. Phase II will be primarily in the DAQ Room as part of the DAQ subsystem installations and will provide the opportunity for full chain large scale testing of the DAQ as well as for detector subsystems as they begin to be installed at IP-6. Finally Phase III will be implemented at the end of the full ePIC detector installation as we have a better understanding of the required resources needed for inital Physics operation. This hardware will be installed at both the DAQ Room and in the SDCC which will define the full Echelon 0 enclave.

Detector System		Channels	SensorTechnology	Redout Technology	Institution
Si Tracking					
	3 vertex layers	7 m^2	MAPS	lpGBT, VTRX+	STFC, UK, ORNL
	2 sagitta layers	368 pixels	MAPS	lpGBT, VTRX+	STFC, UK, ORNL
	5 backward disks	5,200 MAPS sensors	MAPS	lpGBT, VTRX+	STFC, UK, ORNL
	5 forward disks		MAPS	lpGBT, VTRX+	STFC, UK, ORNL
MPGD Tracking					
	Barrel, e & H Endcaps	202 k	uRWELL, MicroMegas	SALSA	CEA, OMEGA, JLab
Forward Calorimeters					
	LFHCAL	63,280	SiPM	CALOROC	ORNL, Debrecen
	HCAL Insert	8 k	SiPM	CALOROC	ORNL, Debrecen
	pECAL W/SciFi	16,000	SiPM	Discrete	IU
Barrel Calorimeters					
	HCAL	7,680	SiPM	CALOROC	ORNL, Debrecen
	ECAL SciFi/Pb	5,760	SiPM	CALOROC	U Regina, ORNL
	ECAL Imaging Si ASTROPIX	500 M pixels	Astropix	Astropix	KIT,NASA (GSFC), ANL
Backward Calorimeters					
	nHCAL	3,256	SiPM	CALOROC	ORNL
	ECAL (PWO)	2,852	SiPM	Discrete	IU, EEEMCAL Consortium
Far Forward					
	B0: 3 Crystal Calorimeter	135	SiPM/APD	Discrete	IU, JLab
	B0: 4 AC-LGAD layers	688,128	AC-LGAD Pixel	EICROC	IJCLab, OMEGA, BNL, ORNL, Rice
	2 Roman Pots (RP)	524,288	AC-LGAD Pixel	EICROC	IJCLab, OMEGA, BNL, ORNL, Rice
	2 Off Momentum (OMD)	294,912	AC-LGAD Pixel	EICROC	IJCLab, OMEGA, BNL, ORNL, Rice
	ZDC: Crystal Calorimeter	900	SiPM/APD	Discrete	IU, JLab
	ZDC: HCAL	9,216	SiPM	CALOROC	ORNL, Debrecen, JLab
Far Backward					
	Low Q Tagger 1	33,030,144	Timepix4	Timepix4	U. Glasgow
	Low Q Tagger 2	33,030,144	Timepix4	Timepix4	U. Glasgow
	Low Q Tagger 1+2 Cal	420 (2x210)	SiPM	CALOROC	U. York
	2 Lumi PS Calorimeter	3,360 (2x1680)	SiPM	Discrete	U. York
	2 Lumi PS Tracker	128,000 (2x64,000)	AC-LGAD Strip	FCFD/EICROCx	FNAL, OMEGA, Hiroshima, NTU, ORNL, UIC, UH, Rice, KSU, Tokyo
	Lumi Direct Photon Calorimeter	100	SiPM	Flash250	AGH Krakow, JLab
PID-TOF					
	Barrel bTOF	2,359,296	AC-LGAD Strip	FCFD/EICROCx	FNAL, OMEGA, Hiroshima, NTU, ORNL, UIC, Rice, BNL, KSU, Tokyo
	Hadron Endcap fTOF	3,719,168	AC-LGAD Pixel	EICROC	IJCLab, OMEGA, BNL, ORNL, Rice
PID-Cherenkov					
	dRICH	317,952	SiPM	ALCOR, VTRX+	INFN (BO, FE, TO)
	pfRICH	69,632	HRPPD	FCFD/EICROCx	BNL, FNAL, JLab
	hpDIRC	73,728	MCP-PMT or HRPPD	FCFD/EICROCx	BNL, FNAL, JLab

Figure 3.303: Electronics and DAQ Resources

3.3.10.9 Collaborators and their role, resources and workforce

The institutions specifically developing the readout electronics and ASICs are listed under the electronics section. Figure 3.303 lists the institutions which have expressed interest in participating in the design of various other parts of the readout chain. Formal agreements committing engineering and technical personnel have not been officiated.

3.3.11 Software and Computing

This section provides an overview of the ePIC computing model, as presently conceived many years before datataking begins. Although ePIC datataking is distant, software and computing is an active and vital part of the ePIC development program today, supporting ongoing detector design optimization, studies of detector and physics performance, and the development of reconstruction and analysis software that will be the foundation for the ePIC physics program. A well-developed software stack and computing capability is also needed early in order to develop an understanding of the complete workflows and their operating scales sufficient to deliver the ePIC physics program, thereby establishing the S&C requirements for the experiment. A capable S&C infrastructure is also needed to support a steady R&D program such that when ePIC datataking begins, it will be with a modern, sustainable software stack that is effective and economical in using the computing facilities of the day; that effectively utilizes the globally distributed computing resources available to the Collaboration; and that strongly leverages the available community software within and

beyond nuclear and particle physics. This section addresses these aspects of the computing model and use cases for the present and near term, and the longer term towards datataking. In a future revision, details regarding the software, as well as the preservation of data and analysis, will be included.

Computing Use Cases In this section, we outline the computing use cases for the Streaming Computing model. In Sec. 3.3.11, the use cases are associated with the four tiers of the ePIC Streaming Computing Model computing fabric, Echelons 0 through 3. Echelon 0 refers to the ePIC experiment. Echelon 1 pertains to the host labs. Echelon 2 encompasses global processing and data facilities. Echelon 3 concerns home institute computing.

Interface between DAQ and Computing Where the interface lies between "online" and "offline" in the ePIC streaming data and processing flow is still a matter of discussion. The working definition for the purposes of this document is the point at which data flows to archival storage. In aspects both technical and sociological, this is the point at which substantial differences exist on the two sides. All processing prior to delivering the archival stream is at risk of permanently losing data in case of error or reduced live time. Post archival, the requirements and latencies are less stringent, the environment is more open.

This Section describes the computing use cases on the offline side of this definition, beginning with the stored data stream and its associated monitoring.

Stored Data Streaming and Monitoring The first and foremost responsibility of the data stream processing as it receives archive-ready raw data from DAQ is to archive it. ePIC's butterfly model provides for geographically separated replicas of raw data as it is archived, by symmetrically receiving the raw data stream at both BNL and JLab facilities, and archiving to tape at both sites. The data is also retained on disk at both sites for near real time workflows such as calibration and prompt processing, discussed below. Monitoring of the raw data stream and other data and metadata received from DAQ provides for examination, validation and alarming of the data stream, both by automated means and via UI. Monitoring can also consume the reconstructed objects produced by prompt reconstruction. Background analysis and subtraction can take place to ready the data stream for subsequent processing.

Alignment and Calibration ePIC aims for rapid turnaround from datataking to full calibrated reconstruction, making a prompt alignment and calibration loop vital. It will operate off the same buffered raw data stream (and prompt reconstruction data set) that is available at each site, and will be as automated and autonomous as possible in its operation. Workflows may ingest raw data or (by definition incompletely calibrated) reconstructed data as input. Alignment and calibration data products as used in the reconstruction and other downstream workflows are delivered to a conditions database available globally, and refined until final, ready for final reconstruction. Initial prompt reconstruction based alignment and calibration is restricted to Echelon 1 (like prompt reconstruction itself). Refinements towards a final calibration can proceed elsewhere as well.

Prompt Reconstruction A defining characteristic of ePIC's streaming data model is the events are reconstructed in near real time from the streaming data, modulo time varying calibrations that will require later reprocessing for a final fully calibrated reconstruction. The prompt availability of reconstructed data, and concurrent calibration cycle consuming it, is a crucial element of ePIC's

objective to have a rapid, near real time turnaround of the raw data to production, as expressed in the software principles [**?**]. The stringent low latency and high availability requirements of prompt reconstruction, together with the locality of its inputs at the Echelon 1 sites, makes this a processing activity limited to Echelon 1. Prompt reconstruction uses streaming based processing described in Section 3.3.11 below, taking time frames as produced by the DAQ as input and producing event (single interaction) based data as output, for processing by analysis software.

First Pass Reconstruction It is expected that the Echelon 1 facilities will have insufficient compute resources to perform the complete first pass reconstruction for incoming data. The prompt reconstruction workflow at Echelon 1 will process, at a minimum, the sample necessary for monitoring, diagnostics, quick-turnaround calibration and so on. The remaining first pass reconstruction processing will be shared with Echelon 2 facilities. The maximum acceptable completion time is about 2-3 weeks. This timescale is driven by calibrations. Given the expectation of relatively low data rates during commissioning and early running, and the need to commission, validate and stabilize the use of Echelon 2s for first pass reconstruction, it is likely that Echelon 2s will be integrated after the first pass reconstruction workflow at Echelon 1 is operating smoothly and Echelon 2s are validated as ready.

Reprocessing The reprocessing use case can take several specific forms: full reprocessing from time frames (expected to be infrequent, after commissioning), re-reconstruction of event-factorized data with updated reconstruction and calibration (as soon as calibrations are available, plus a few more times per year), and regeneration of analysis object data as selections against the full data sample evolve (frequent). The analysis object data will be compact enough to "take home". All reprocessing workflows are amenable to batch style processing and can utilize Echelon 1-2 and opportunistic resources.

Simulation Monte Carlo simulation in ePIC will encompass physics simulation (event and background modeling) and (with physics simulation as input) detector simulation, both fully detailed (Geant4) and fast (parameterized, ML based). At least one order of magnitude more simulated events than data will be needed for ePIC's various run configurations in order to estimate systematic uncertainties, ensuring simulation will remain a substantial production workload and resource consumer after datataking is underway. The output of simulation and subsequent digitization will have the frame-based streaming structure matching that of real data, such that the reconstruction operates on simulated data exactly as it does on real. (This is not yet implemented.) However in its production, simulation data has more in common with conventional batch processing than streaming. That said, we aim to set up the simulation workflows to mimic streaming data production workflows in an active attempt to gain experience with these workflows prior to datataking.

From a workflow and resource utilization perspective, reconstructing the simulated data within the same workflow is preferable, e.g. avoiding a storage-consuming output stage after the simulation, and avoiding the complication of distinct MC simulation/production workflows. Technical and sociological considerations may however separate these workflows at certain times, for example if the lifetime of simulated data (slow release cycle, determined mainly by experimental setup changes and major software releases) is substantially longer than for reconstructed data (fast release cycle determined by rapidly evolving reconstruction algorithms). Both workflow configurations should be foreseen. Simulation workflows can utilize Echelon 1-2 and opportunistic resources.

Analysis The EIC has a broad science program. The analysis effort in ePIC categorizes its studies into inclusive, semi-inclusive, and exclusive measurements, the investigation of jet and heavy-flavor physics, and the exploration for physics that goes beyond the standard model. Each category encompasses numerous observables under examination. The feasibility of analysis prototyping and some types of analysis aligns with the capacities of Echelon 3. Nonetheless, many studies, such as imaging the quark-gluon structure of the nucleon, necessitate the computing resources of Echelon 2 or 1. The traditional approach for these analyses is rooted around immediate data reduction of large amounts of detected particles into multi-dimensional histograms. Corrections for experimental effects, such as background effects, limited detector acceptance and resolution, and detector inefficiencies can then be deconvoluted from the observable of interest through simple arithmetic and matrix transformations. This procedure of deconvoluting experimental effects from histogrammed observables is referred to as unfolding. In contrast, there are emerging analysis techniques at the event level. The event-level approach requires a reversal of the traditional procedure of correcting and unfolding measured histograms: here, idealized events from theory have to be folded with the relevant experimental effects. After folding, the theoretical calculations can then be directly compared with the experimental events at the detector level. The accuracy and precision of these methods depend on intricate simulations in the unfolding scenario and detailed modeling of experimental effects in the folding scenario.

Modeling and Digital Twin The streaming data will be used as input for modeling the background for detailed studies of the background under various conditions of the EIC and ePIC detector. Furthermore, ePIC plans to use the complete information from the experiment to create a digital twin of the experiment. This digital twin will complement the detailed detector simulations. It will provide a model of the experiment to be used as input for experimental control in situations where immediate feedback from the model is necessary. The digital twin also offers a model that can be easily shared, facilitating the reproduction of results without the necessity of running computationally intensive detector simulations. The digital twin also allows for the exploration of different scenarios, providing complementary information to gain deeper understanding and optimization of experimental conditions. This, along with the data analysis and detector simulations, will offer valuable insights into improving run plans and potential upgrades for the experiment. Modeling workflows can utilize Echelon 1 and Echelon 2.

Computing Resources

The Computing Model's Resource Requirements Figure 3.304 shows the Butterfly Computing Model that will be used for ePIC. In this model the detector together with the DAQ system constitute Echelon 0. Two Echelon 1 sites are located in the computing centers of the host labs BNL and JLab, with the capability to serve as functional peers for host-site ePIC computing, both providing storage and processing resources. Echelon 2 sites contribute processing resources and may also provide storage resources convenient for access by distributed collaborators (see Section 3.3.11 for details).

The computing resources needed for all phases of data processing after the raw stream leaves Echelon 0 will be distributed across multiple facilities. The overall resource requirements are therefore cumulative among them, together with the networking required for robust distributed operation.

Overall, Echelon 0 will need to send raw data at 200Gbps and each Echelon 1 site will need to be able to receive data at 100Gbps. Additional bandwidth will be needed at the Echelon 1 sites to send data to Echelon 2 sites for processing and to receive the results. Storage bandwidth and volumes

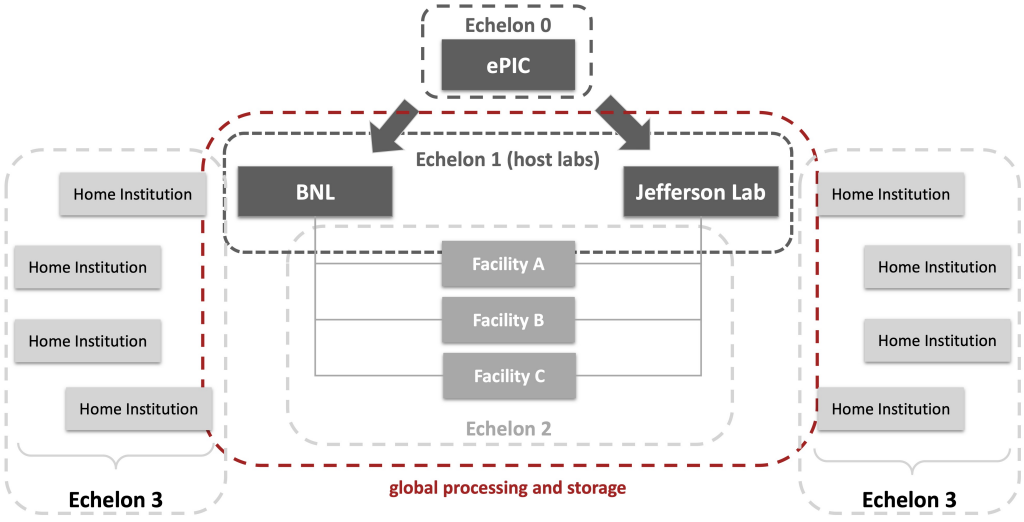

Figure 3.304: Butterfly Computing Model *see text for details).*

are driven by these rates and are detailed in the following sections.

The resource requirement estimates are based on the EIC/ePIC timeline and expected luminosity ramp as of Fall 2024. The expected maximum luminosity of the EIC for ePIC is $\approx 10^{34} cm^{-2} s{-}1$. It will take some years beyond the start of physics operations to attain this level. Present planning puts the luminosity target for initial 'Phase 1' physics operations at $\approx 10^{33} cm^{-2} s{-}1$. The resource estimations below are based on this Phase 1 scenario, unless specified otherwise, taking 2034 as a nominal Phase 1 datataking year. The computing model is designed to ultimately serve the full luminosity delivered by the EIC, while tailoring the deployed scale to current needs at any given time, thereby gaining cost savings from computing cost reductions over time.

Echelon 0: The Stored Data Stream The maximum EIC luminosity of $10^{34} cm^{-2} s{-}1$ is expected to correspond to a nominal data egress rate from DAQ of ≈100Gbps (see sec. **??**). During early Phase 1 running at lower luminosity the rate is expected to be circa 1/3 of that, the lower luminosity counterbalanced by a larger volume of detector data used for debugging and developing a detailed understanding of detector behavior. Given the uncertainties, for the purposes of resource estimation we use the full 100Gbps rate.

This is an instantaneous rate that will be reduced to the average rate via a data buffer in Echelon 0 just prior to the exit. While the average rate may be around 50% of the maximum, the system will be designed to accommodate the full 100Gbps bandwidth between Echelon 0 and each of the Echelon 1 sites. This will allow for closer to real-time processing of the data offsite. Both of the host labs will therefore receive the full storage-level data stream in real time.

Thus, Echelon 0 will use 200Gbps of outgoing bandwidth. A small amount of additional outgoing bandwidth will be needed for monitoring streams, slow controls data, and misc. metadata artifacts. These are expected to contribute $\leq 1\%$ to the total. The utilized bandwith on the network should not exceed 50% of the maximum throughput, putting the network bandwidth requirement out of Echelon 0 at 400Gbps.

A summary of the Echelon 0 rates can be seen in Table 3.86.

The incoming bandwidth to Echelon 0 is expected to be small by comparison to the total outgoing bandwidth. This will include incoming monitoring data from higher Echelons and relevant calibration values.

The Echelon 0 storage will be primarily short term disk in the form of the output Data Buffers. The buffers will serve to smooth out fluctuations in the DAQ rate as well as provide a means to store data for a short period of time in the event of a temporary loss of communication to the Echelon 1s. The buffer will be sized to hold at least 24 hours of raw data produced at the full 100Gbps rate, corresponding to on the order of 1PB.

Resource	**Type**	**Amount**
Outgoing bandwidth	raw data	200Gbps
	Monitoring, slow controls, misc. meta data	$\leq$ 1Gbps
	Capacity headroom	$\approx$ 200Gbps
	TOTAL	**400Gbps**
Incoming bandwidth	monitoring, calibration	$\leq$ 1Gbps
Storage	Disk (outgoing data buffer w/ 24hr)	1PB

Table 3.86: Echelon 0 networking and storage requirements.

Echelon 1: ePIC Computing at the Host Labs The host labs at Echelon 1 will each receive a full copy of the data. Current planning calls for the bandwidth, storage and compute requirements to be the same for both Echelon 1 sites. An Echelon 1 site will need to be capable of receiving 100Gbps and permanently storing both the raw data and the reconstructed data for the full data set.

The following Subsections describe the computing resource requirements for networking, storage and processing at Echelon 1, necessarily describing also the proportion of computing not done at Echelon 1. Processing not performed at Echelon 1 will primarily be done at Echelon 2s, described in the next Section. The ePIC Collaboration will also draw on opportunistic resources for computing needs that can be met away from the Echelon 1 centers; opportunistic and special resources are discussed in a later Section. -

Echelon 1 Networking The Echelon 1 sites will require sufficient incoming bandwidth to receive 100 Gbps of raw data and outgoing bandwidth to serve the Echelon 2 sites they connect to.

Preliminary plans have the near real-time computing for reconstruction of the raw data stream ('prompt processing') being split equally between each of the Echelon 1 sites. Over time, prompt processing is likely to be shared also with Echelon 2 sites. At any rate, Echelon 2 sites will also collectively host some number of raw data copies for reprocessing and calibration. This means each Echelon 1 site will need additional outgoing bandwidth at a level of at least 1/6 of the total raw data stream or $\approx$ 35Gbps with capacity headroom for steady state running.

The calibration, monitoring, and slow controls data will be needed by each Echelon 2 site. While the bandwidth for all of these combined is small relative to the full raw data stream, the Echelon 1 sites will need to supply multiple Echelon 2 sites with copies of those values.

The bandwidth requirements for each Echelon 1 site to the Echelon 2 sites it serves is shown in Table 3.87.

Resource	Type	Amount
Outgoing bandwidth	Raw data -*immediate* ($\frac{1}{6}$ of total)	17Gbps
	Raw data -*replay* (contingency)	50Gbps
	monitoring, slow controls, misc. meta data	1Gbps
	TOTAL	**68Gbps**
Incoming bandwidth	monitoring, calibration, slow controls *(from E0, E1, and Echelon 2)*	1Gbps

Table 3.87: Echelon 1 networking requirements. Values shown are for a single E1 site.

Echelon 1 and 2 Storage Each Echelon 1 site will require enough archival and disk storage to hold the entire raw data set as well as the Echelon 1's share of downstream data processing and simulation. The estimated raw data size for one year of running during Phase 1 is ≈70PB. The total Echelon 1 storage required across all workflows for a year of data is ≈200PB. This assumes that the Echelon 1s between them hold a complete simulated data sample (≈100PB), a complete first full reconstruction dataset and one re-reconstruction dataset (each ≈10PB).

Fast disk access will be needed to store raw data while calibrations are done and data is processed at either an Echelon 1 or 2 site. Raw data files will not be deleted from disk until their corresponding reconstruction artifacts are stored in both Echelon 1 tape archives. This process is currently estimated to take up to 3 weeks allowing for an extended calibration period. The prompt processing sample, currently estimated (conservatively) as 50% of the full sample, also will have a steady-state disk presence. These disk resident samples are expected to total about $5 - 10$PB in Phase 1.

The raw data as well as simulation and reconstruction data may be primarily tape resident in order to economize on disk, with a 'data carousel' workflow used to dynamically orchestrate the placement of a sliding window of tape-resident data on disk for processing. This approach has been used successfully for many years at RHIC and ATLAS, for example.

Additional disk space will be required for individual user analyses. Some of this will be distributed throughout the Echelon 2 sites, but it is anticipated that the Echelon 1 sites will also be used for this purpose. To estimate this, we assume these analyses will require an additional 10% of the reconstructed data volume (1% of the raw data volume) and that it will be distributed amongst the Echelon 1 and 2 sites in the same proportions. This is considered negligible for the purposes of this estimate, smaller than the uncertainties.

Echelon 2 sites will be important contributors to all workflows apart from raw data streaming and (at least in early running) prompt reconstruction. We use the following estimates of their participation share for the purposes of this resource estimation.

Fraction of alignment/calibration done outside Echelon 1	50%
Fraction of first full reco done outside Echelon 1	40%
Fraction of reprocessing reco done outside Echelon 1	60%
Fraction of simulation done outside Echelon 1	75%

Table 3.88: Fractions of production workflows performed outside of Echelon 1 sites (i.e. at Echelon 2 and opportunistic sites)

Storage resource requirement estimates are summarized in Figure 3.305.

Storage Estimates by Use Case [PB]	Echelon 1	Echelon 2
Streaming Data Storage and Monitoring	71	35
Alignment and Calibration	1.8	1.8
Prompt Reconstruction	4.4	-
First Full Reconstruction	8.9	3.0
Reprocessing	9	9
Simulation	107	107
Total estimate storage	**201**	**156**

Figure 3.305: Storage resource estimates aggregated over Echelon 1 and Echelon 2 sites, for a nominal Phase 1 datataking year.

Echelon 1 and 2 Compute Determining the scale of the ePIC Streaming Computing and planning for computing resource needs during the commissioning and operation of the experiment are essential. For a dependable estimate, a prototype for the holistic reconstruction of physics events from time slices is required. This reconstruction needs to include jet reconstruction and the identification of leptons and hadrons using all PID systems in the ePIC Detector. It is important to have reliable estimates of the fraction of background events in the data stream and their impact on the reconstruction performance in the time slices, and to understand how quickly these background events can be discarded without the need for full reconstruction. Defining the alignment and calibration methods for each subsystem and having detailed discussions about fast alignment and calibration techniques are crucial to estimate the computing resources required for alignment and calibration.

Substantial progress has been made in the year since the first release of this report, and while much work remains to be done and the uncertainties remain large (and will remain so for many years), we provide here a first estimate of the processing resources required by ePIC. Important steps during the year making this estimate possible were the implementation of time slice based track reconstruction; a careful examination of the physics and background rate environment; a similar examination of the data and processing flow of the raw stream from DAQ; and a detailed survey of alignment and calibration methodologies and timelines (during datataking) across ePIC's detector subsystems. As for the storage estimates above, the benchmark is a nominal Phase 1 year, $10^{33} cm^2 s^{-1}$ luminosity, circa 2034.

Processing resource requirement estimates are summarized in Figure 3.306. Raw data streaming to storage and real-time monitoring requires a relatively small amount of processing, smaller than the uncertainties. Alignment and calibration processing is estimated based on a 50/50 participation of E1 and E2; this is very approximate, the main point is that calibration and alignment processing will engage both Echelons. Prompt reconstruction will take place at Echelon 1 only in the early years, potentially extending to Echelon 2s later. The capacity estimate includes a factor of two for headroom sufficient to catch up if prompt processing is interrupted. The Echelon proportions for first full reconstruction, reprocessing and simulation are as for the storage case above. Note that the total processing numbers are an overestimate given that not all workflows are active at any given time, and all available computing resources will be applied to active workflows.

Echelon 2: Global ePIC Computing The ePIC Collaboration is international and its computing will be as well. This is expressed in the computing model as soon as it extends beyond the

Processing by Use Case [cores]	Echelon 1	Echelon 2
Streaming Data Storage and Monitoring	-	-
Alignment and Calibration	1,182	1,182
Prompt Reconstruction	11,820	-
First Full Reconstruction	14,184	9,456
Reprocessing	9,456	14,184
Simulation	24,280	72,839
Total estimate processing	**60,921**	**97,661**

Figure 3.306: Processing resource estimates aggregated over Echelon 1 and Echelon 2 sites, for a nominal Phase 1 datataking year.

Host Labs to become global, at Echelon 2. An essential component of ePIC computing, relied upon to achieve the computational scale necessary to meet the experiment's scientific goals, will be the resources contributed formally by ePIC's collaborating institutions around the world, which represent the Echelon 2 component. The computing model must be designed to effectively integrate these resources and manage their productive use, wherever they may be located, dependent of course on factors such as network connectivity.

The dual Echelon 1 structure of the ePIC computing model, the "butterfly model", already places distributed computing requirements on the model. Effectively integrating and leveraging globally distributed resources at Echelon 2 extends this requirement. The experience of the LHC experiments, well represented within the ePIC Collaboration, is relevant and applicable to developing an effective model for ePIC. Because Echelon 2 resources will be formally relied upon to meet computing requirements, they must come with appropriate MOUs specifying service requirements and assuring technical implementations compatible with the ePIC computing model. The ePIC Collaboration for its part commits to a joint effort on facility integration, and the provisioning of sufficient testing/validation protocols, monitoring and diagnostics to convey to the Echelon 2 facility, in sufficient detail to guide remediation, the faults and performance lapses that occur.

Connectivity of the Echelon 2 sites to Echelon 1 will be the same to both Echelon 1 sites (Host Labs). The connectivity will ultimately be to the ESnet network backbone to which the Host Labs are both connected. Echelon 2 sites will not have connectivity just to one or the other Echelon 1. Similarly, the Echelon 2 sites themselves will be interconnected as determined by their network environment, and these connections will be exploited by the computing model, e.g. for data replication among sites. A clear lesson from the LHC, which evolved from a hierarchical model to an interconnected mesh as experience was gained, is that the latter is far more effective.

Echelon 3: Home Institute Computing The Echelon 3 component of the computing model is where the ePIC collaborator doing analysis or developing software directly encounters the computing system. People will access ePIC computing from their institutional cluster, their work desktop, their personal laptop, and so on. Serving these use cases is the role of Echelon 3, and the Echelon 1 and 2 based services that support the Echelon 3s (like access to data). Like Echelon 2, Echelon 3 resources are global, as well as local to the user. These resources are numerous, diverse, often volatile and opportunistic, restricted in their use, and not suited to be managed as Collaboration resources. Rather the Collaboration will provide the tools, interfaces, connection points, data ac-

cess mechanisms and support mechanisms to make such resources effective portals and analysis processing resources for ePIC analysis.

Opportunistic and Special Resources Among the software and computing principles [**?**] guiding ePIC are those expressing the importance of leveraging as many computing resources for the collaboration as is possible and practical. ePIC software should be able to run on the architectures and platforms available, effort permitting, while leveraging system characteristics such as the presence of accelerators (GPUs, TPUs, etc.), again effort permitting. ePIC S&C should support distributed workflows on the computing resources available to the worldwide EIC community, leveraging not only conventional cluster "high throughput computing" (HTC) but also high performance (HPC) systems with good usability and thereby a rewarding cost/benefit calculation.

The most productive computing resource currently used by ePIC is the Open Science Grid (OSG), where a concurrent core count of 5-10k is stably attainable. As ePIC builds up its own computing resources we expect opportunistic resources like the OSG to continue to play a role, in particular for simulation production (detector and physics simulation). Simulation is a relatively simple workflow that puts moderate demands on resources (storage needs, I/O intensity, memory), steady state processing, and a relatively relaxed time to complete requirement. While ePIC's essential simulation requirements should be accommodated by planned and assuredly available resources, anticipating that ePIC science will be compute limited the exploitation of opportunistic resources should be foreseen. OSG has its origins as the US component of the Worldwide LHC Computing Grid (WLCG). The WLCG is evolving to also support non-LHC experiments (e.g. DUNE, SKA) and we can anticipate that opportunistic resources will be available to ePIC internationally as well.

Commercial clouds are being actively used by science communities (Rubin Observatory and ATLAS are examples) with their capabilities and cost models under study. Opportunistic (preemptible) usage modes together with workflows that elastically spike into the resource to support fast-turnaround use cases such as analysis are the most promising in terms of cost effectiveness. In ePIC we will monitor such developments and participate as we are able, and will decide at a later date whether such resources will have a role in our computing model.

Special resources include non-x86 processor architectures such as ARM, accelerators such as GPUs and TPUs, and no doubt others yet to emerge over the next decade. A requirement on ePIC S&C infrastructure is to have the flexibility and extensibility in the software and CI to add support for architectures of interest as they appear. The ARM architecture is already supported, and we anticipate it will have an important role in coming years given its cost effectiveness per dollar and per watt, and the relative ease of the port. FPGAs are used in the Streaming DAQ for low-level data processing and reduction. GPUs are highly likely to play a role online; whether the same is true offline is unclear. Nonetheless support for high concurrency in the software will be needed, with requirements such as multithreading support, and advantages such as efficient memory utilization. The rise of AI/ML and accompanying proliferation of specialized accelerators such as TPUs makes it probable we will exploit them, perhaps largely transparently behind software APIs. We will track the technologies as we pursue our own AI/ML R&D and applications.

Large supercomputers such as the leadership class facilities (LCFs) developed by the DOE and NSF are most often constituted by what we've called special resources. Whether such machines are effective for ePIC use will be a case by case evaluation. Today's GPU based machines offer limited potential given the dearth of GPU-capable workloads in ePIC (a common situation in NP and HEP), though we are doing R&D in GPU-amenable areas such as Cherenkov detector simulation. The US will have its first leadership class ARM machine in 2026, at the NSF's TACC facility, with Japan and Europe hosting others; such machines we would already be able to use effectively. LCFs are increasingly being designed as AI/ML factories; such machines we will assuredly be able

to use for at least training and optimization. We have since Sep 2023 an R&D project underway to leverage large scale resources for the processing-intensive AI application of EIC detector design optimization.

Authorization and Access Authorization and access mechanisms are evolving both in their technical aspects and the institutional policies that govern their use, thereby impacting the accessibility for users. The foremost priority of the ePIC Collaboration is to ensure that every collaborator has access to the resources of the collaboration, including data, websites, collaborative tools, information systems, document repositories and so on, today and reliably in the future. This consideration can be a leading or determining factor in the tools and services we use, and where they are hosted. It has been a factor in choosing GitHub as code repository and a cloud-based Mattermost instance, for example. We will continue to make this a requirement.

Distributed Computing The ePIC collaboration consists of a globally distributed community of scientists engaged in the experiment's data and compute intensive scientific program. Section 3.3.11 described the use cases and workflows that the ePIC computing infrastructure must support. Section 3.3.11 described the computing resources of ePIC from the detector to the host labs and on to the globally distributed data and processing centers providing the collaboration with resources, and finally to the local resources used by analysts at their institution or from their laptop. This Section describes the distributed computing software and services that will be needed in order to knit these resources into a coherent computing fabric for ePIC that serves the full spectrum of use cases.

The ePIC experiment follows a lineage of "big science" collaborations using computing resources on a global scale, the most prominent example to date being CERN's LHC experiments, which in their development towards the High Luminosity LHC (HL-LHC) are also preparing for a rich and data intensive physics program in the 2030s. The LHC's ALICE and LHCb experiments have further commonality with ePIC in having introduced streaming computing models for the LHC's present Run-3. The LHC experiments and their collaborators in the WLCG community have built and continue to develop expertise, tools and global infrastructure that the proliferating big science community can draw on. The ePIC approach to distributed computing described here is built on leveraging and collaborating with this community, bootstrapping our distributed computing infrastructure from existing components and approaches where possible so our own efforts can focus on the extensions and tailoring needed to support the unique aspects of ePIC's streaming computing model and global collaboration.

Processing Requirements for ePIC Streaming Data The processing of ePIC streaming data has characteristics that are markedly different from the workflows commonly found in NP and HEP experiments to date. Current convention is that data is acquired in online workflows that deliver the data to hierarchical storage as large files, and then processed by offline workflows with a typically substantial latency period after acquisition (apart from promptly processed subsets for monitoring, data quality and possibly calibration purposes). In this scenario the offline processing maps readily onto the batch queue based resource provisioning mechanisms of computing centers. Offline processing payloads are sent to batch queues and consume input files distributed appropriately for resource locality. Keys to the applicability of this straightforward approach are the discrete, coarse grained processing units in the form of files and collections of files (datasets), and the decoupling of processing with respect to real time data acquisition. The case of ePIC streaming data processing, however, has neither of these characteristics.

In ePIC streaming data processing, a quasi-continuous flow of fine-grained data must be processed promptly with the dynamic flexibility to match in near real time the inflow of acquired data to processing resources that stand ready to consume it. Prompt processing is necessary to ensure data quality and detector integrity during datataking, and while processing of a subset could achieve those aims, processing the full dataset quickly is necessary to minimize the time required for calibrating the detector and delivering analysis-ready reconstructed data promptly, a primary goal of ePIC. For ePIC data processing, with the two host labs symmetrically serving as Echelon 1 processing centers, the processing resources used at any given time must be transparent to the workflow engine, effectively a requirement that a distributed processing capability be an integral part of the system. The data sources are distributed as well; in a streaming computing model that dissolves much of the distinction between online and offline, the system must be flexible towards decisions as to the parallelism of data delivery received from the DAQ, i.e. where the event builder function occurs. The system must support processing parallel streams of data from subdetector, accelerator, beamline and other sources, augmented by sufficient metadata to make their association and merging fault-proof. The minimized latency and high system complexity require that a high level of automation and resilience to changing conditions be built into the streaming processing system, necessary also to keep the operations effort at a manageable level.

Summarizing the driving characteristics of ePIC streaming data processing, it is time critical, proceeding in near real time; it is data driven, consuming a fine-grained and quasi-continuous data flow across parallel streams; it is adaptive and highly automated, in being flexible and robust against dynamic changes in datataking patterns, resource availability and faults; and it is inherently distributed in its data sources and its processing resources. This model presents challenges for an infrastructure based on batch jobs and coarse grained files. However, the safe assumption for the infrastructure of the 2030s is that batch-style processing and coarse grained files – particularly as they map onto archival storage – will remain. A robust approach to building the ePIC streaming computing model and system will be to accommodate, but effectively hide, those underlying characteristics of the infrastructure. We may ultimately not need to accommodate them, for example Kubernetes or similar mechanisms of dynamic processing resource provisioning may displace the batch model. We should accommodate both and be resilient against technology evolution.

Workflow Management As described, the requirements of ePIC's streaming based prompt reconstruction are distinct from the typical workflow management practices of contemporary experiments. Streaming is however a fertile and rapidly evolving field, in our community and well beyond. Many streaming data processing frameworks and tools exist and evolution is rapid. ePIC should be ready both to take judicious advantage, and avoid technology lock-in. The tools generally share a fundamentally similar distributed parallel model, and have common features that do not risk lock-in such as the use of standard workflow descriptions (e.g. DAG, CWL). Some systems directly manage the processing resources, such as Apache Storm and Spark, others can overlay on conventional batch or dynamic resources (such as Kubernetes); HEP/NP's own PanDA is such a system. The underlying facilities must support high availability and service quality, though a distributed system mitigates against very stringent requirements on a single facility. The facility and the streaming workflow management system in tandem must support data flow optimization in real time.

Resources should be flexible across use cases and workflows, readily usable for other purposes when datataking is not active. For example, applications should be able to scale elastically and exploit heterogeneous hardware such as an AI/ML application spiking into an accelerated resource for low-latency turnaround. Some workflows such as simulation and reprocessing are served well by conventional batch processing, lending advantage to all ePIC's major resources supporting batch.

The international nature of the ePIC Collaboration and its computing makes it essential that workflow management tools support the use of computing resources around the world, for essentially all managed workflows apart from prompt reconstruction, and for physics analysis.

Data Management and Access Prompt processing of data streaming from the detector will yield file based data suitable for consumption by hierarchical storage and by file-based data management tools. Raw data copies will be written to archival storage at the two host labs, with the expectation that retrieval is rare. (Under normal operation, no production workflow involves archival data retrieval.) Data management tools must support the distribution and use of data around the world, serving ePIC's global processing resources and community of analysts. Disk resident replicas at Echelon 1 and 2 sites will be managed by the data management system. Client tools for accessing and storing data at managed data stores will be usable at all Echelons including local/personal computers with appropriate authentication. Authentication and authorization (AA) mechanisms must support access for all ePIC collaborators globally.

The broad acceptance of the Rucio data management system as a standard, within HEP and increasingly within NP, makes it the likely system for ePIC datataking use, in its evolved 2030s form. Rucio is being integrated and tested in ePIC now, and ePIC will engage with and contribute to the (very open) Rucio community. Rucio and the distributed computing community is migrating to SciToken based AA mechanisms which enable a federated ecosystem for uniform authorization across distributed scientific computing infrastructures, and should be capable of meeting the collaborator access requirement.

Data movement tools are in a state of flux. The long-used third party copy tool gridftp was recently retired, with http chosen as the basis for replacing it. XRootD is a powerful community-standard tool with data movement functionality tuned to the needs of HEP/NP (e.g. efficient handling of ROOT based data, in terms of both movement and caching). FTS is the data mover underpinning Rucio as used by the LHC experiments. Object store based data storage and movement (supporting the S3 API) are increasingly common. Some DOE computing facilities require the use of Globus data mover tools. Fortunately Rucio can hide much of this fragmentation (Rucio is not in itself a data mover, it interfaces with them). ePIC will leverage this encapsulation and avoid lock-in.

Project Organization and Collaboration

Organization of DAQ and Computing in ePIC The scientific management of the ePIC collaboration is organized in three efforts that report to the spokesperson and deputy spokesperson: an analysis effort with currently two Analysis Coordinators, a technical effort with a Technical Coordinator, and a software and computing effort with a Software & Computing coordinator (SCC). The SCC oversees all aspects of software and computing in ePIC and has three deputies sharing the responsibilities for development, operations, and infrastructure.

Development currently has two active working groups: Physics and Detector Simulations as well as Reconstruction. Another working group on Analysis Tools is being planned. Operations comprises three active working groups: Production, User Learning, and Validation. Among the Infrastructure working groups, which consist of Streaming Computing Model, Multi-Architecture Computing, and Distributed Computing, only the Streaming Computing Model group is active at present, the others not being an immediate priority. Moreover, there is a planned cross-cutting working group on data and analysis preservation. The activation of the working groups will depend on the number of people actively participating in software and computing.

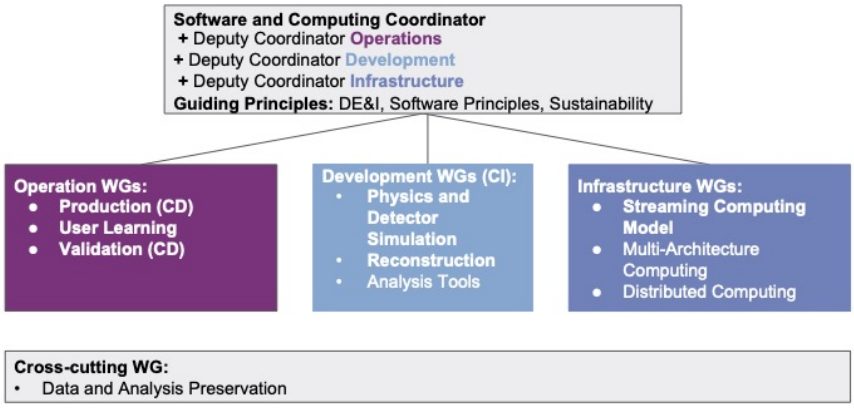

Figure 3.307: Organizational chart of the Software and Computing Effort in ePIC. The Streaming Computing Working Group is joint with Electronics and DAQ Working Group in the Technical Effort to ensure that DAQ and Computing are developed together.

Two of the three conveners of the Streaming Computing Model WG are also conveners of the Electronics and DAQ WG that is part of the technical effort. Both working groups have regular meetings, and a significant fraction of the attendees of these meetings are the same. This ensures that the DAQ and Computing are developed together with well-defined and well-understood interfaces, and ePIC builds a group of experts familiar with data processing from the DAQ to the analysis.

Long Term Software and Computing Plan

Timeline and High Level Milestones ePIC Software & Computing has developed closely with the collaboration and with input from the EIC project a timeline of high level milestones, including the long-term. The milestones are grouped by the anticipated date for CD-2 approval, the detector construction phase, and the commissioning and operations phase. Priority is always given to meeting near-term needs, with the longer range timeline progressively exercising the streaming computing model to deliver for the needs of the CD process, for specific applications (e.g. test beams), for scaling and capability challenges, and ultimately for the phases of datataking. The series of milestones ensures that the agile development process is continuously confronted with real world exercising of the software and the developing realization of the computing model.

Preparations for CD-2 and the Technical Design Report ePIC is providing support to the EIC Project in the preparations for CD-2 decision process and the Technical Design Report for the detector, both of which are due in November 2024:

- Software and simulation readiness for TDR preparation (and subsequent phases of the CD process).
- Provide for each use case Sec. 3.3.11 detailed estimates on the compute resources; update the networking and storage estimates according to format of streaming data format that is currently being defined.

Detector Construction Phase The subsystems of the ePIC Detector must be constructed by 2030. During the construction, the detector designs will be further optimized, considering changes in costing and the availability of materials. Additionally, prototypes of the various detector systems will undergo testing. This will facilitate software testing and provide an opportunity for validation of the simulations based on the results from the test-beam measurements. The relatively extended duration of the construction phase presents an ideal timescale for the further development and implementation of the ePIC Streaming Computing Model:

- Provisioning DAQ and software sufficient for test beams, which can serve as small scale real-world testbeds for the developing DAQ and software.
- Streaming challenges exercising the streaming workflows from DAQ through offline reconstruction, and the Echelon 0 and Echelon 1 computing and connectivity.
- Data challenges exercising scaling and capability tests as distributed ePIC computing resources at substantial scale reach the floor, including exercising the functional roles of the Echelon tiers, particularly Echelon 2, the globally distributed resources essential to meeting ePIC's computing requirements.
- Analysis challenges exercising autonomous alignment and calibrations.
- Analysis challenges exercising end-to-end workflows from (simulated) raw data to exercising the analysis model.

Detector Commissioning and Early Datataking Phase In approximately a decade, when the ePIC Detector is completed, the experiment's commissioning phase will commence. This phase will come with distinct expectations and requirements in comparison to steady-state operation. For instance, it will involve the utilization of semi-triggered data-taking modes, initial calibrations, introduction of zero suppression, and the gradual extension of near real-time processing from Echelon 1 to Echelon 2, among other tasks. Successful software and computing efforts during the commissioning phase will necessitate careful planning, drawing from the experience gained in the data and analysis challenges during the detector construction phase.

During the initial data-taking phase, immediately following the commissioning phase, simpler and more conservative approaches will be adopted as the ePIC Streaming Computing Model is gradually being deployed and validated.

Data and Analysis Preservation A guiding principle [**?**] of ePIC S&C is that data and analysis preservation (DAP) will be an integral part of EIC software and workflows, aiming for analyses that are fully reproducible, re-usable, and re-interpretable, based on reusable software and amenable to adjustments and new interpretations.

The ePIC Collaboration is planning to incorporate DAP into its software and computing from an early stage. A cross-cutting working group is foreseen in the org chart and will be activated during the next year. It will address DAP requirements and a timeline for DAP developments, prioritizing those with value for ePIC computing and analysis in the near as well as the long term, such as a robust and user friendly infrastructure for containerization in analysis, which is already well advanced in ePIC.

The S&C infrastructure that ePIC is establishing now will facilitate DAP, including containerization of the ePIC software stack, automation of well defined workflows using workflow definition languages (currently used in GitLab based CI), centralized workflow and metadata management

(supporting distributed production on OSG), a curated and sustainable code repository and web presence (GitHub and its website publishing tools), and data management supporting the full data life cycle and provenance (Rucio integration is in progress). A prominent missing component at present is document management, being addressed at the Collaboration level.

3.4 Detector Integration

Facilities: The EIC detector will reside in building 1006 at BNL. Since the building was previously used for the STAR Experiment there are many accommodations already in place for EIC. Figure 3.308 shows building 1006's layout.

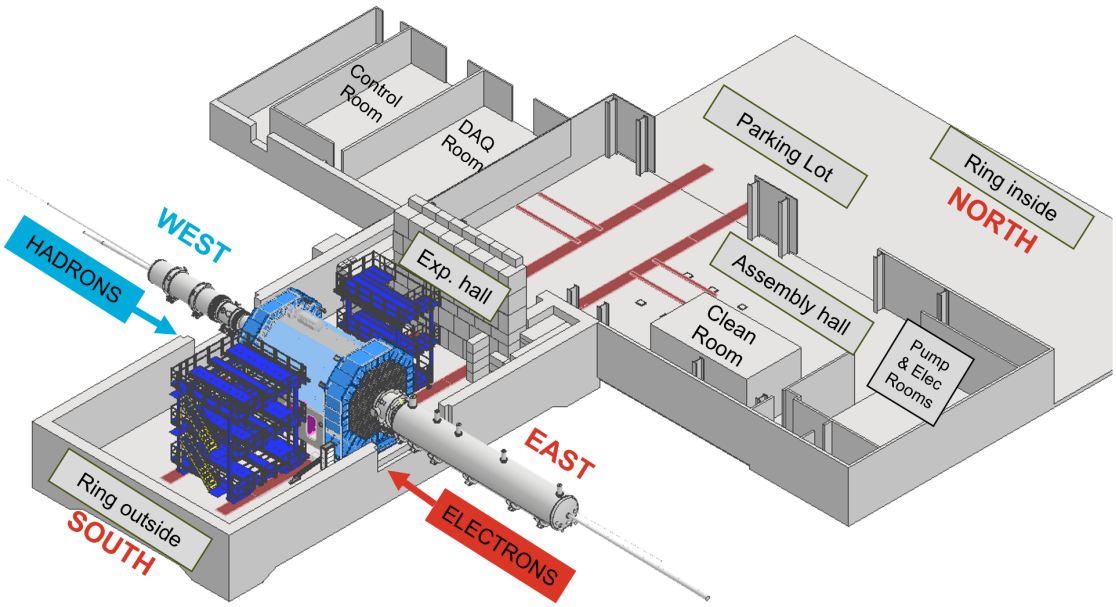

Figure 3.308: An isometric section view of building 1006, showing the detector in the experimental hall.

The main area of the building is a large assembly hall (AH). The AH is approximately 100′ x 60′. The overhead crane in the assembly hall has a 40 US ton limit and covers most of the hall. This crane will be used to preform most of the initial assembly of the detector. Apart from the full Barrel EMCAL assembly the crane will be able to lift and move everything we need. The north side of the hall has 2 large roll-up doors for deliveries which can be seen in Figure 3.309 below. Trucks can be driven through these doors and then unloaded by either a forklift or the crane. The assembly hall has two 36″ rails which extend to the north into the parking lot and south into the experimental hall (also interaction region, IR). The STAR detector used Hilman rollers and hydraulic pullers on these rails to roll from the AH to the IR. These rails are rated for 1200 US tons, which is much less than EIC. Since we are planning on going with air bearings for the central detectors and not Hilman rollers like STAR, we will be filling in the gap between these two rails with grout. This will leave us with a level surface all the way from the AH to the IR to move the detector on. The rails will remain in place for the north and south platforms, and for guides for the central barrel. Between the IR and AH there is a large 27′ x 27′ opening where the detector will pass through. During operation there are large concrete blocks which get placed in the opening to form the shield wall. The AH also

features a small clean room, which will be renovated for EIC. This room will be used for storage and assembly of small detector pieces. There is additional storage on the roof of the clean room. There is a small collection of machine tools and equipment in the assembly hall to make shims or minor modifications to rough parts. Above the machine area are 2 platforms, which serve as access to the mechanical rooms and as additional storage.

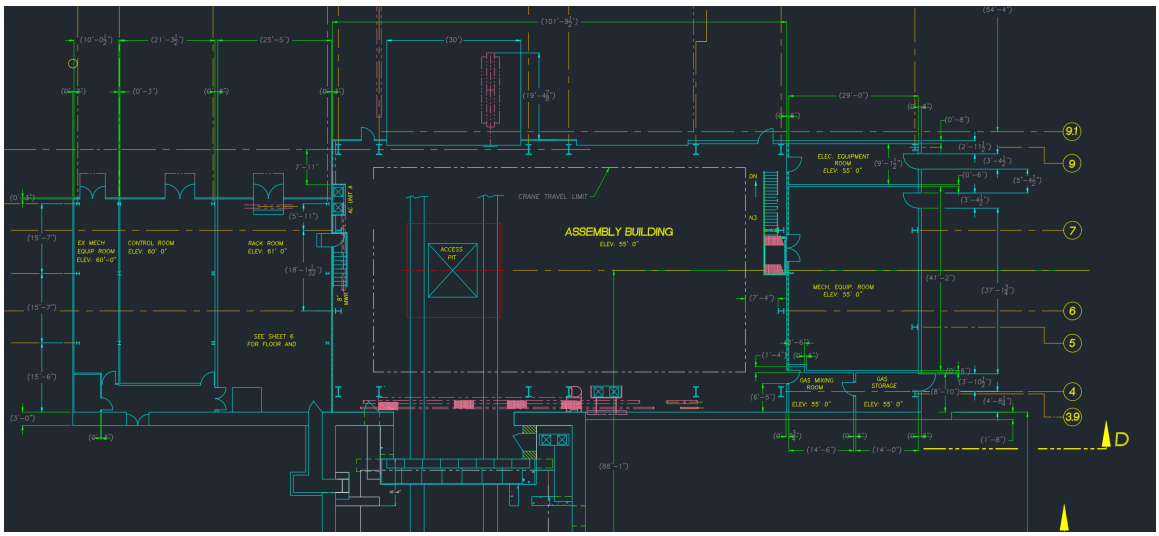

Figure 3.309: A portion of a drawing of the assembly hall from building 1006.

The experimental hall or interaction region (IR) is just to the south of the AH and is where the detector will reside when in operation. The hall is approximately 92' x 53' with two tunnel entrances, one on the east and the other on the west. EIC will have two sets of endcaps, one on the east (forward) side and one on the west (backward) side. Each set of endcaps will slide north and south. The endcaps and the central detector are both rotated at an 8mrad angle to account for the crossing angle of the beams and to be aligned with the electron beam direction. Angled rails will be added to the hall to accommodate the rollers for these endcaps. The overhead crane in the IR has a weight limit of 25 US tons and covers most of the hall. We will use the crane for maintenance of certain detectors and to move the concrete blocks that make up the shield wall into and out of the opening. When not in operation the shield wall is stored in the south end of the IR as shown in Figure 3.309 below. Storage of the wall limits access to the south platform and the forward endcaps when they are in their stored position. When the detector is in operation and the shield wall is in place, there is access to the IR via two paths (the labyrinth) on the sides of the shield wall. At both the east and west entrances to the tunnel there will be a platform. These platforms will hold magnets, the far forward and far backward detectors and other equipment. The space underneath these platforms will allow for equipment such as scissor lifts to be brought from the north to the south side of the hall. The remaining space in the IR will be used to store various items such as air compressors, vacuum pumps, carts, scissor lifts, etc. The current air handlers and HVAC equipment in the IR are not sufficient for the temperature and humidity needs of EIC and will be replaced.

At 1006 there are several other rooms that will be reused for EIC. There is the mechanical equipment room, the gas mixing room, the gas storage room, the electrical storage room, the rack (DAQ) room, and the control room. All these rooms will be refurbished as needed and reused for EIC.

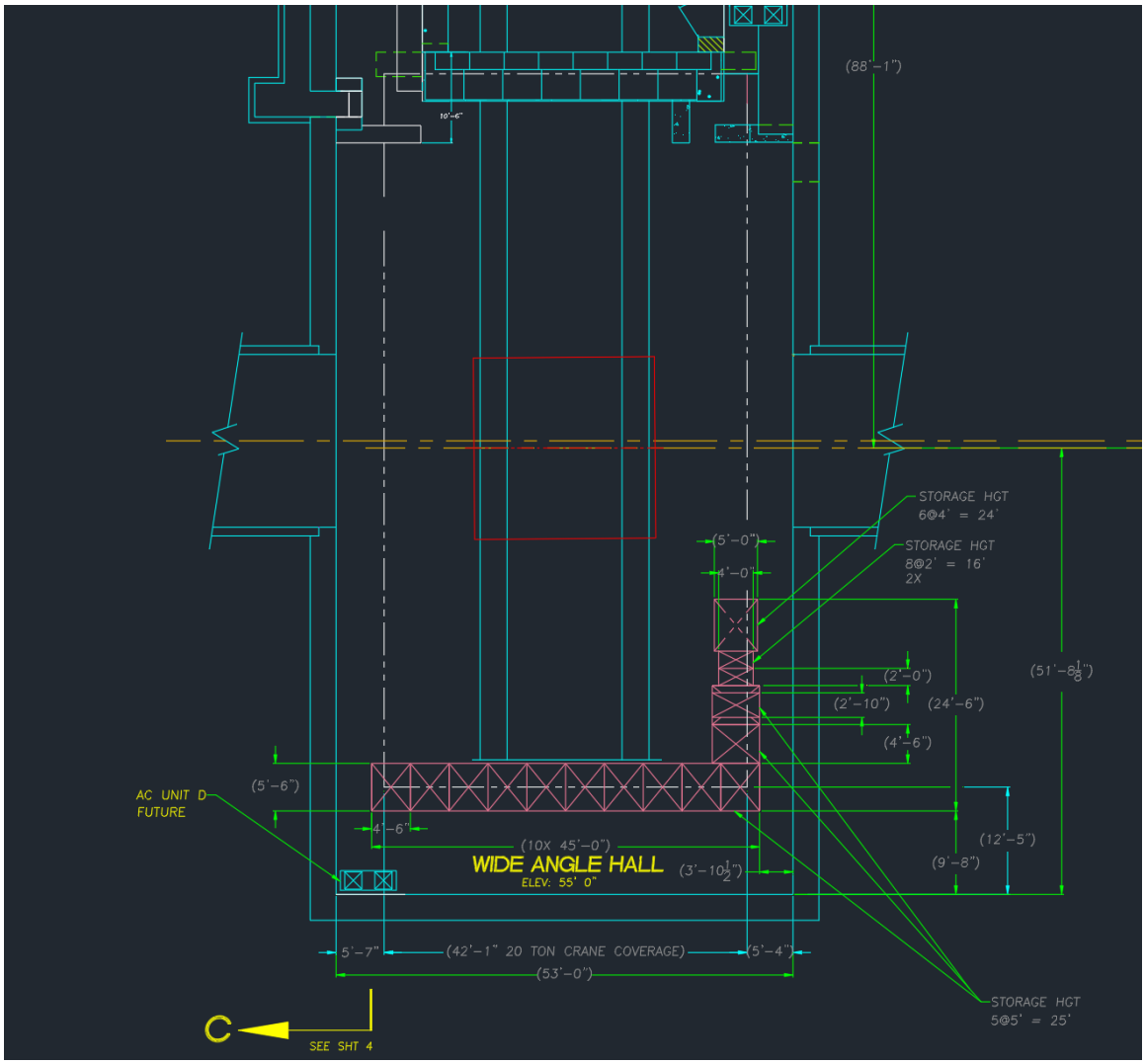

Figure 3.310: A portion of a drawing of the experimental hall from building 1006

Platforms: The STAR experiment had two platforms (the north and south) that were connected to the central detector. These platforms will be modified and reused for EIC. Even though we plan on using air bearings to support and move the EIC detector, the STAR rails will be kept for the north and south platforms. Both platforms have several modifications that need to be made in order to work at EIC. The ePIC endcaps interfere with the current north and south platforms when they move between their north and south positions. The platforms will be partially disassembled and flame cut to allow for the opening and closing of the endcaps. The amount which the platforms need to be cut on each side varies slightly due to the 8mrad rotation of the endcaps. The platforms will not be rotated and will stay parallel to the original STAR rails. Additionally, the stairs for the south platform, which currently are on the east side of the platform, will be moved to the southern face of the south platform as shown in Figure 3.311. This is to avoid interference with the forward endcaps when they are moved into their maintenance position. Previously for STAR, there was a rigid link between the cradles of the detector and the north and south platforms. Since we are not reusing the STAR cradles a new link will connect the platforms to the central detector. These links

will only connect the platforms and central detector during movement. Otherwise, the platforms will be anchored to the floor using seismic restraints.

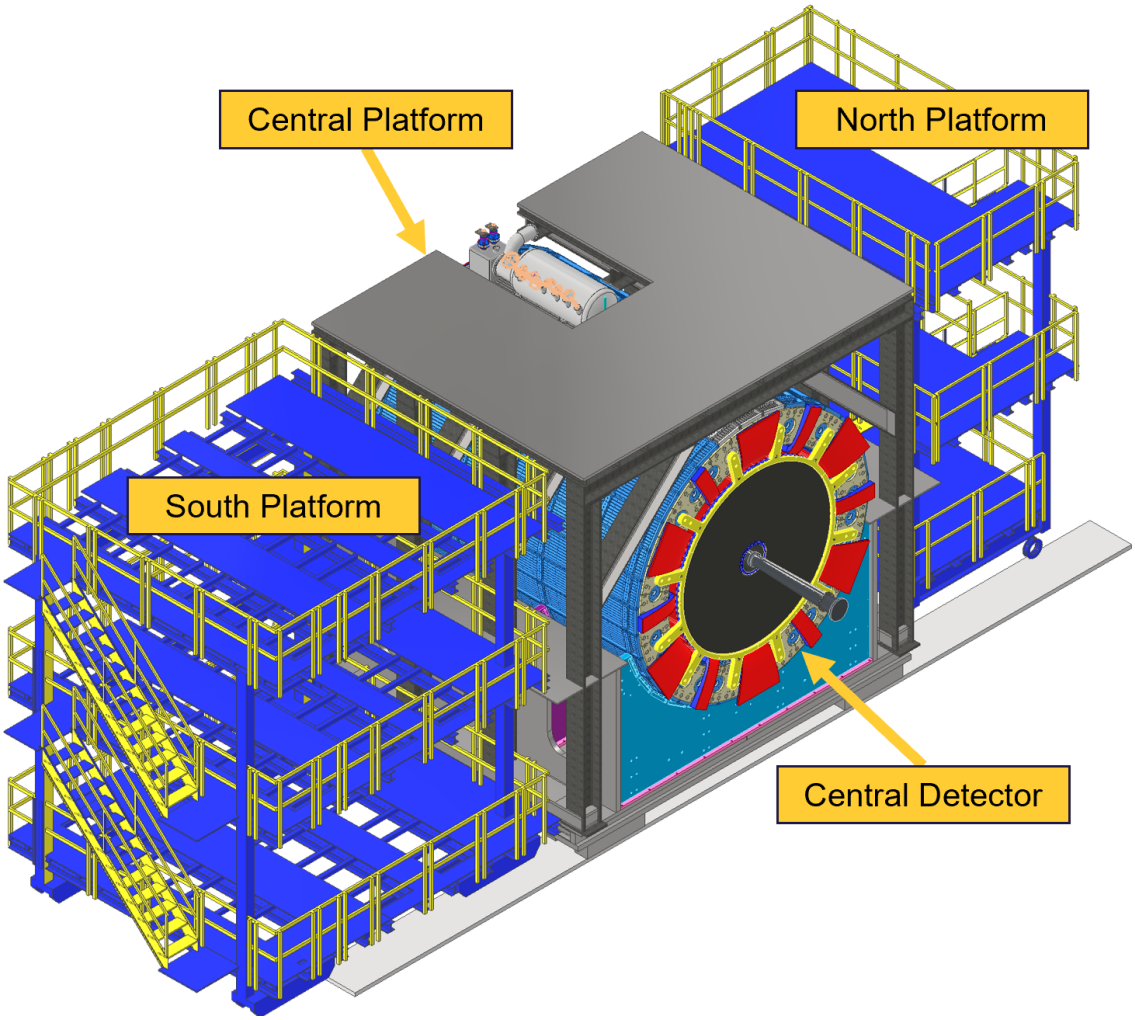

Figure 3.311: All three platforms that will move with the central detector.

The south platform will house all the DAQ and detector racks for the experiment. The current services for the platform are dated and need refurbishment. All the plumbing on the platforms will be redone. These will be grounded via either non-conductive lines or dielectric spacers will be used where needed. The electronics on the platforms will be replaced as well.

On top of the central barrel there will be a third platform which will be reused from the sPHENIX experiment. This platform will be for access only, allowing technicians to get to the magnet chimney and to get between the north and south platforms. Small bridges will connect the three platforms at the third levels. This will also help satisfy safety requirements as another form of egress from each platform.

Movement, Alignment and Adjustment: As previously stated, the central barrel, along with the north and south platforms will move between the AH and IR. The central detector will use air

bearings that slide along the concrete floor, and the platforms will use Hilman rollers, which will roll along the existing rails. The platforms and detector will be linked together during movement but will be disconnected anytime the detector needs to be adjusted or aligned. During this time the platforms will be restrained to the floor via seismic restraints, and the central detector will be free to be aligned and adjusted as needed. The endcaps are independent to this.

The requirements for the alignment of the interaction point (IP) of the detector are as follows: The beampipe is to be aligned to +8mrad off of the hall z axis within ±1mrad about the Y axis; and the X, Y, and Z locations of the IP inside the beampipe each need to be within ±1mm. The 8mrad rotation is shown by Figure 3.312 below.

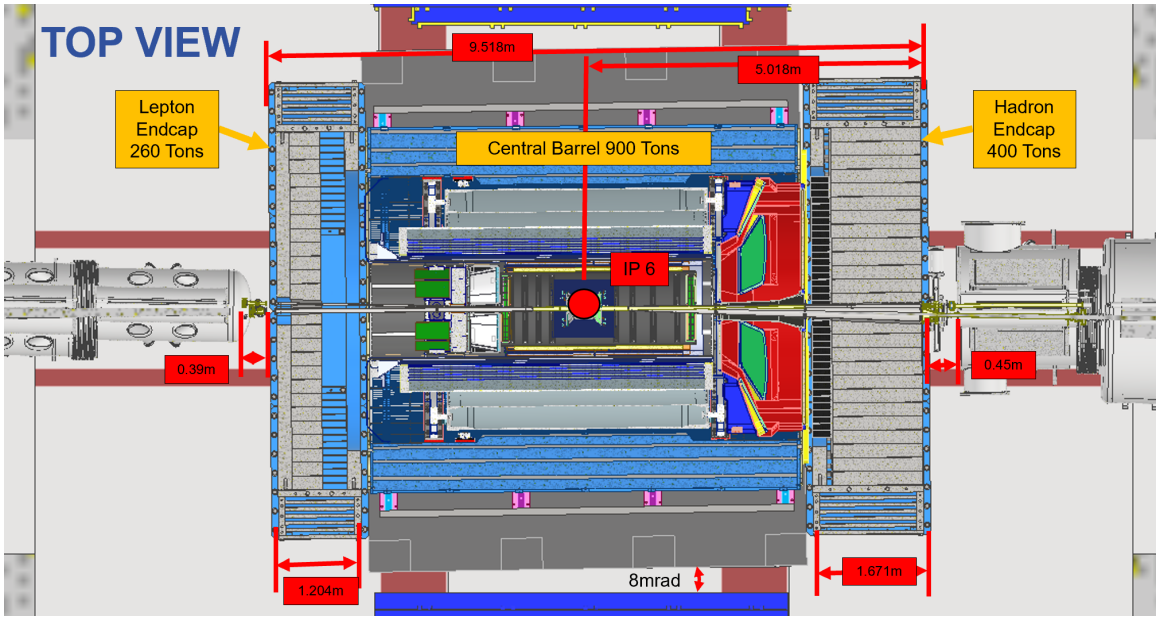

Figure 3.312: A top-down section view of the detector in the experimental hall showing the 8mrad rotation.

We have two methods we will use to achieve this alignment. This first is the initial placement of the detector via the air bearings. Once the detector is in the IR, we will place stops on two corners of the detector. These stops will be at the precise X and Z locations that we need to get the IP within ±1mm. These stops will also lock in our yaw (rotation about the Y axis) and get us within ±1mrad. Once the stops are installed then we will disconnect the links that attach to the detector to the north and south platforms. The detector will be free to move about at this point and will be moved into the locating stops. Once the detector is in the stops, we will raise the detector into position using four hydraulic jacks located under the detector. These jacks will allow us to position the detector in Y along with the roll and pitch. The detector then gets locked into place via seismic restraints. If the stops and jacks fail to get the detector within the desired tolerances, then we will use the adjustment at the global support tube (GST). The GST is a large carbon fiber tube which supports all of the detectors inside of the barrel EMCAL, along with the beampipe. This tube will be supported on both ends. The connection points at the ends of the GST will allow for adjustment, ±5mm translation in X and Y and ±1mrad about the X and Y axes.

Load Path and Support Structures: The detector is made up of a series of support structures shown in Figure 3.313. Starting at the bottom is the cradle. The cradle is supported by a series of

air bearing skids and hydraulic jacks. The air bearing skids are arranged in a 2 by 5 pattern, with each bearing being able to support 90 tons. This makes the total support capacity of the bearings 900 tons. The base above the skids is made up of steel I-beams and plate. On top of the base, we are reusing the support webs from sPHENIX. There are four of these webs that were previously used to support the barrel HCal. These webs are tied together with more I-Beams and plates. Additionally, the vertical I-Beams that support the central platform rest on this base at the end of each of the webs. Next, the barrel HCal rests in the support webs. The barrel HCal is assembled in conjuncture with two large support rings. These rings sit inside the HCal and assist with assembly and then help support the HCal. Each HCal sector is connected to the one next to it via a large steel plate called a dog-bone. The HCal directly supports the dRICH and the Magnet.

The next support structure is the barrel EMCAL support. This support is made up of Aluminum I-Beams that run the length of the barrel EMCAL and attach the inner support rings at each end. The I-Beams are connected by large end rings that assist in the installation of the barrel EMCAL. The barrel EMCAL support structure also supports the GST. At both ends of the GST there are support arms which reach around and back to the barrel EMCAL support. This connection point is also a point of adjustment for the GST.

The GST supports the rest of the detectors in the central detector. The Outer MPGDs and DIRC bars are mounted to the outside of the GST. On the backward side the EEEMCal and the pfRICH are supported via rails that are mounted at 3 and 9 O'clock on the inside of the GST. These rails will also be used for the installation and support of the pixel support tube (PST). The ToF and CYMBAL are segmented into 12 sectors and each of these sectors will be supported on the inside of the GST via rails.

Services: The services within the detector are broken into two major paths, the forward path and the backward path. Figure 3.314 shows the two major cable paths below. Both paths start just outside the IP and work their way out of the detector, where the services split up and either go to the north or south platform. The innermost level of the services is all contained within the PST. The PST mainly supports the SVT but is also used to guide the SVT's services outward. The forward path begins at the outer edge of the SVT inner barrel. The services here are routed outward radially at about a 45° cone. These services then travel past the next barrel layers of the SVT and the innermost SVT disk, picking up other services along the way. Once the services get to the outer diameter of the SVT disks, they travel along the inside of the PST until they reach the MPGD disks. Here the services go outside the PST and are broken into 12 sections. They travel to the end of the GST. At the end of the GST the services make a 90° bend at the face of the dRICH. As they travel up the face of the dRICH the services are grouped into 6 sections. The dRICH has 6 large sensor boxes that restrict the services to be segmented in 12 sections. Once they are grouped into 6 sections the services get to their disconnect location. This is the only disconnect location for services on the forward side of the detector. This disconnect will be used for maintenance throughout the life of the detector. After the disconnects the services work their way around the outside of the dRICH to the service gap between the barrel HCAL and the forward endcap. Here the services make another 90° bend and finally get outside the detector. From here the power and data lines go to the south platform and the cooling and gas lines go to the north platform.

The backward side follows a similar path to that of the forward side. They start at the outer edge of the innermost SVT disk and SVT outer barrel. Services from the SVT inner barrel only go out on the forward side. The services here are routed outward radially at about a 45° cone. Again, the services travel to the outer diameter of the SVT disks and inside the PST until the MPGD disks. The services are then divided into 12 sections again, however this time they are sorted into three different trays. The inner tray is for the pfRICH services, the middle tray is for the SVT and MPGD

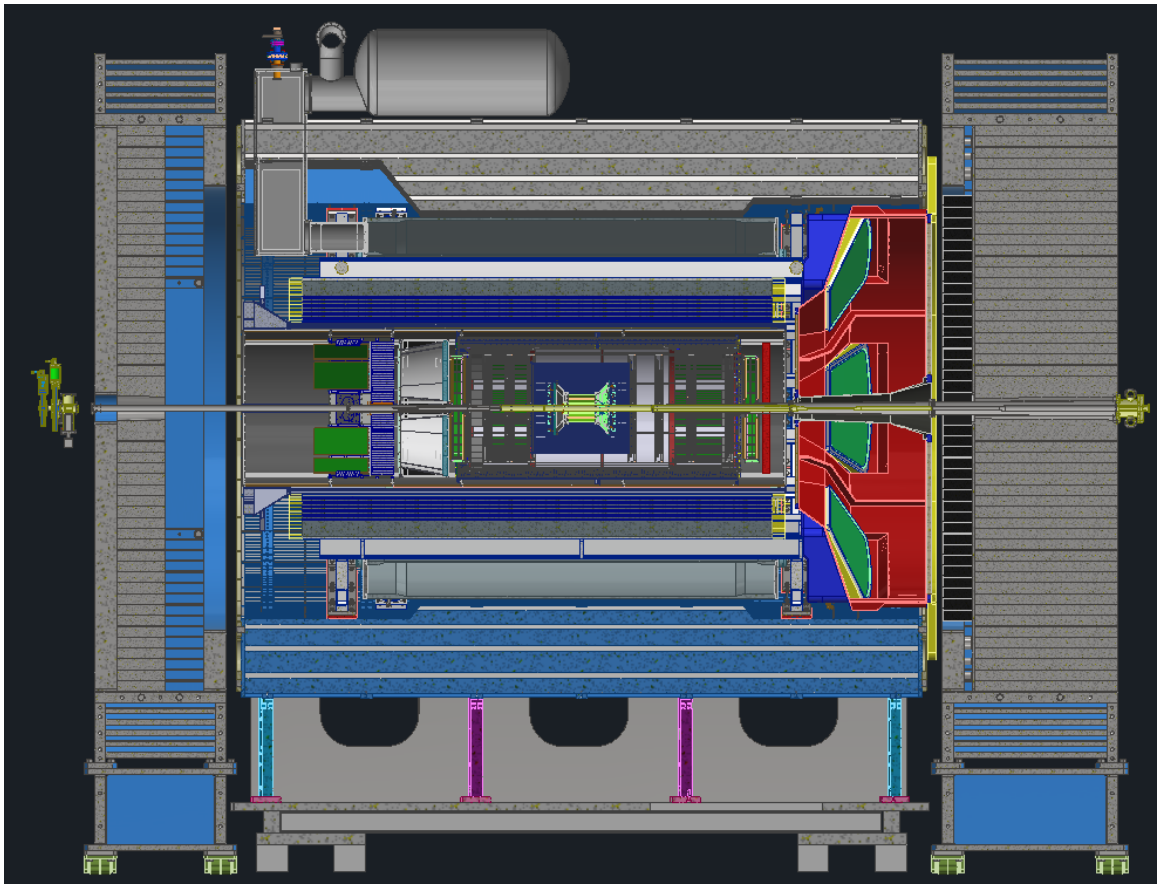

Figure 3.313: A side section view of the detector.

disks' services, and the outer tray is for the ToF and CYMBAL services. The trays are divided into three here for maintenance. Dividing the trays allows us to pull ToF and CYMBAL sectors out as needed without having to disconnect all the services. All trays go to the end of the GST. Once the services are outside the GST, they make a 90° bend and travel past the DIRC electronics to the backward disconnect point. From here the services continue outward to the end of the barrel HCAL where again they go to their respective platform.

Services for the Endcap detectors get routed to racks that are on the endcaps themselves. On the forward endcap the forward EMCAL must share service space with the dRICH at the 3 and 9 O'clock positions. Due to this, the fEMCAL services get routed in between the dRICH services as shown below in Figure 3.315. On the backward side the backward HCAL has a similar issue, and its services will get routed out at 3 and 9 O'clock, while the inner tracker services get routed above and below.

3.4.1 Installation and Maintenance

Choreography: There will be three pairs of rails in the 1006 facility, the central barrel rails that extend from the IR into the AH, which are preexisting from the STAR experiment, and a pair of rails on the forward and backward side of the IR for the endcaps, which will be new installations.

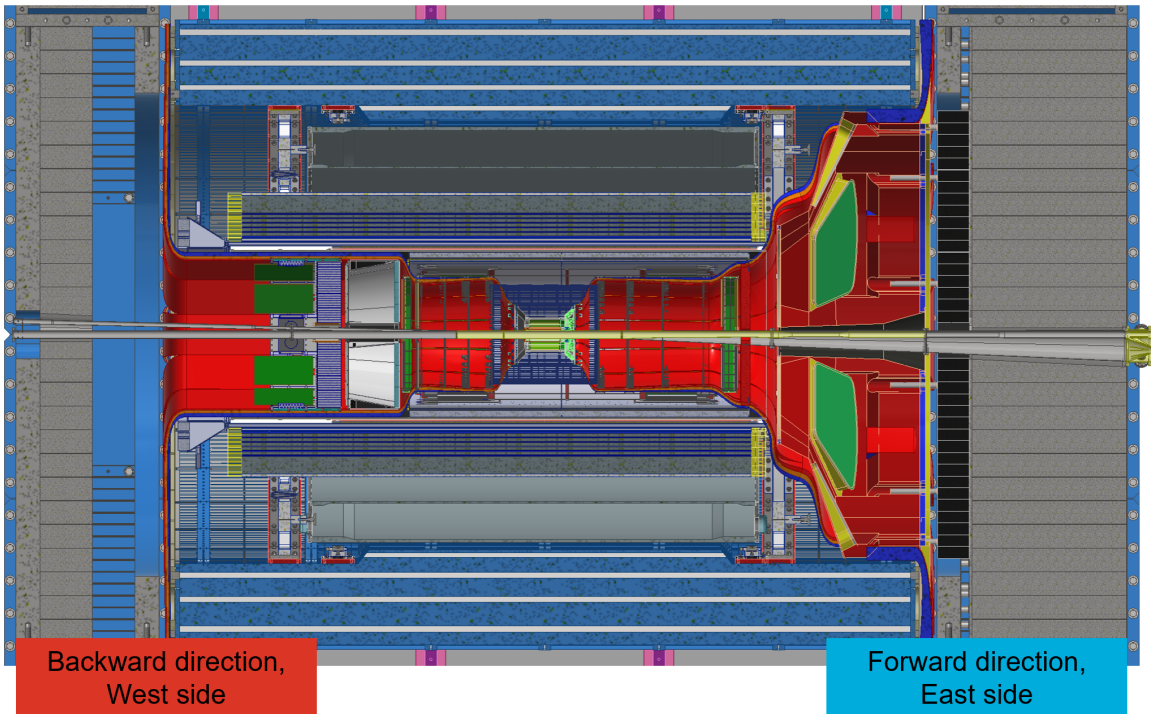

Figure 3.314: A top section view of the detector showing service paths.

The three pairs of rails run along the X direction, allowing for translation towards and away from the EIC center. The central barrel itself will use a series of air casters with guides using the central rails and the north and south platforms will use Hilman rollers on the same rails. The endcaps, also using Hilman rollers, are split in half down the YZ plane such that the north and south halves can move independently on the forward and backward rails. The division of the endcaps into halves allows for beam pipe removal, better serviceability/maintenance, and flexibility for the Choreography.

There are four main positions for the endcap halves when the central barrel is in the IR: the nominal operating position, the typical maintenance position, the typical central barrel roll out position, and the atypical maintenance position shown in Figure 3.316. The nominal operating position is where the central barrel and all four endcap halves are in the configuration surrounding the beam pipe and IP, ready for collisions and data taking. The typical maintenance position is where the central barrel is unmoved, the beam pipe is complete and under vacuum, but the endcap halves are moved away from the IP in their corresponding quadrants. This configuration will be typical for normal shutdowns and regular maintenance, allowing access to the endcap detectors, and most central barrel detectors. The typical central barrel roll-out position puts all endcap halves in the back of the IR, so that the central barrel can be moved from the IR to the AH without risk of damaging the services coming out of both ends. This would be done for major maintenance or upgrades and require the beam pipe to be disconnected. The atypical maintenance position is where the central barrel is unmoved, but the beam pipe is disconnected and all endcap halves in the front of the IR. We have the flexibility to use this position if needed for maintenance, though it isn't currently envisioned for any normal operations.

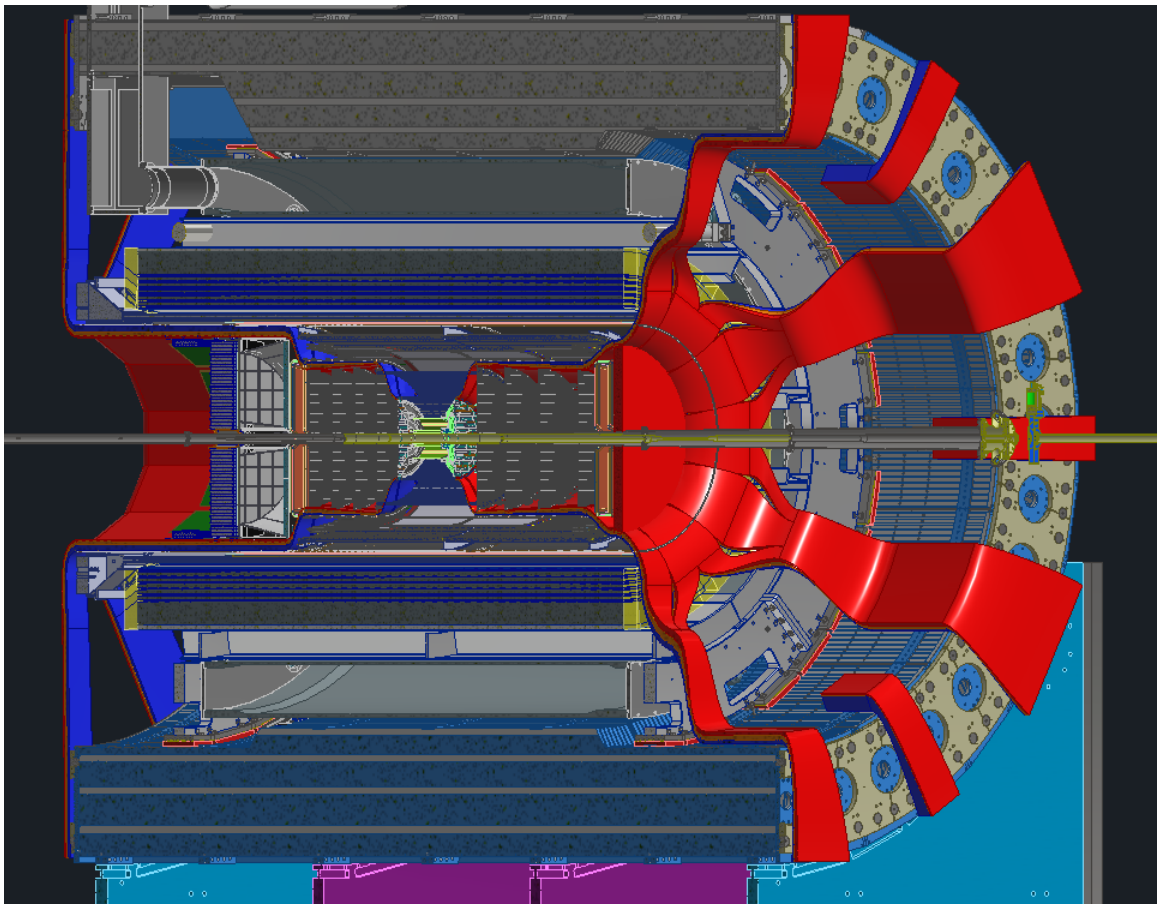

Figure 3.315: An isometric side view of the detector showing service paths with the dRICH missing.

Installation Sequence: The assembly of EPIC has two independent aspects, the endcaps and the central barrel. The endcaps are assembled with the approach of starting with the bottom and building up, while the central barrel and is largely done starting from the outside and moving in one layer at a time. The endcaps start with the base, moving to the bottom half of the flux return, then the detectors and the top of the flux return. The initial steps of the central barrel take a similar approach to the endcaps, starting with the cradle , followed by the bottom half of the HCal (which is also the barrel flux return), the magnet and the top half of the HCal. From there the assembly of the central barrel proceeds with installation of the BIC, GST, DIRC modules, outer MPGD modules, combined ToF and Cymbal, and combined SVT, MPGD Disks and central beam pipe. The remaining forward and backward detectors would be installed, namely the pfRICH and EEEMCal on the backward side and the ToF disk and dRICH on the forward side. All core steps are shown in Figure 3.317.

Endcaps: The flux return will come from the manufacturer in several large components and sub-assemblies that have been pre-fitted and determined to attach appropriately. The forward and backward assembly are the same with two distinctions, the forward endcap includes the forward EMCal installation, and the backward endcap includes the pole tip plate installation. Both endcap

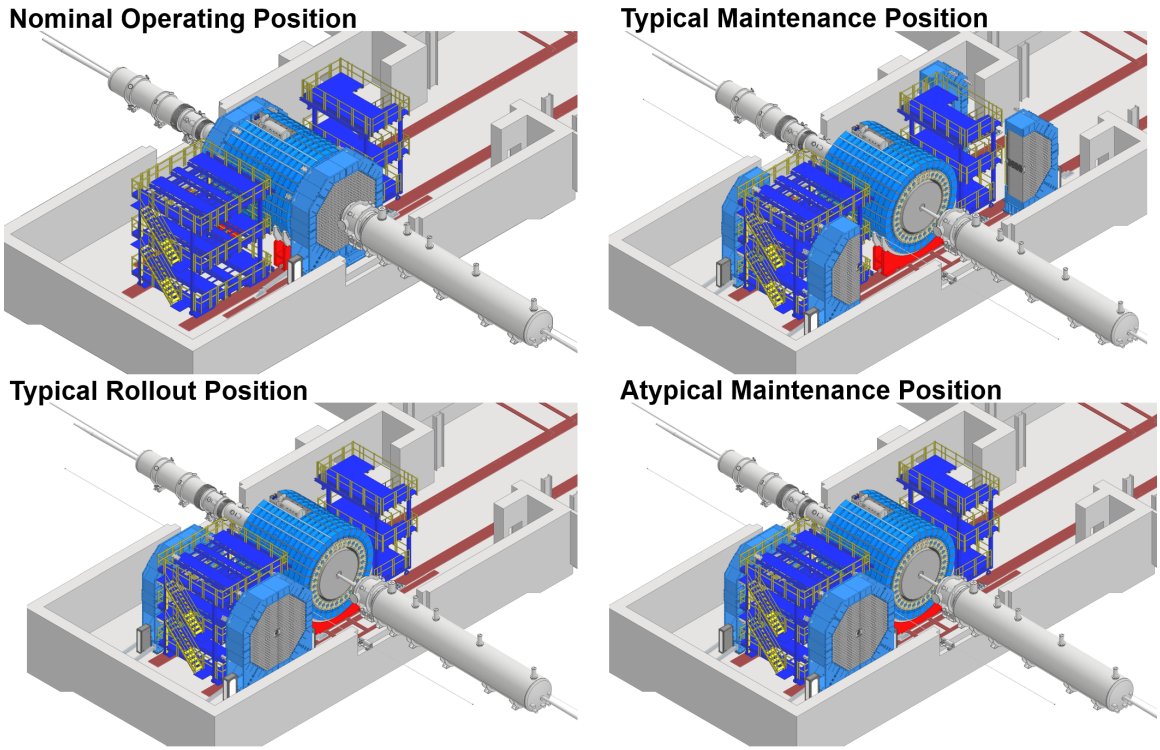

Figure 3.316: Four views of ePIC in the experimental hall at 1006 in the nominal operating configuration, typical maintenance position, typical roll-out position and atypical maintenance position.

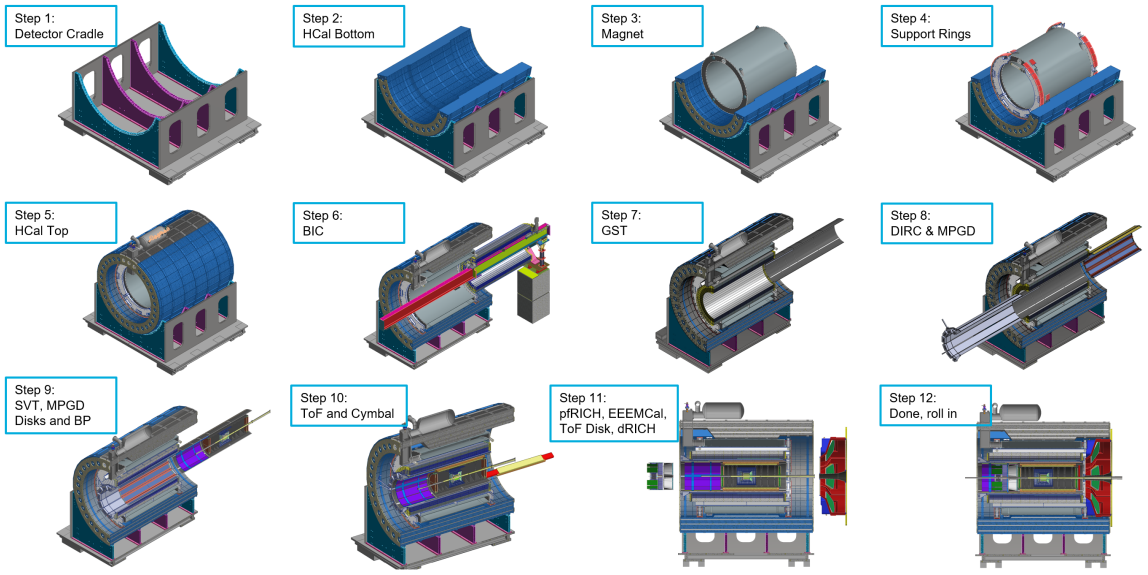

Figure 3.317: The installation sequence of ePIC barrel sub-detectors and structure broken down into 12 core steps.

assemblies would also take place in their nominal operating positions.

The first assembly step would be to place the base on the endcap rails, aligning its position and bolting it to the tracks for stability. Then the Flux return support plate would get attached to the base. Following this the two lower flux return sub-assemblies would get attached to the base, the flux return support plate and to each other. The detector mounting plate would be attached to the flux return sub-assemblies and the detector installation could proceed. Once completed, the anulus and pole tip (for the backward endcap) are installed. After that the top two flux return sub-assemblies are installed, completing the assemblies. All core steps are shown in Figure 3.318.

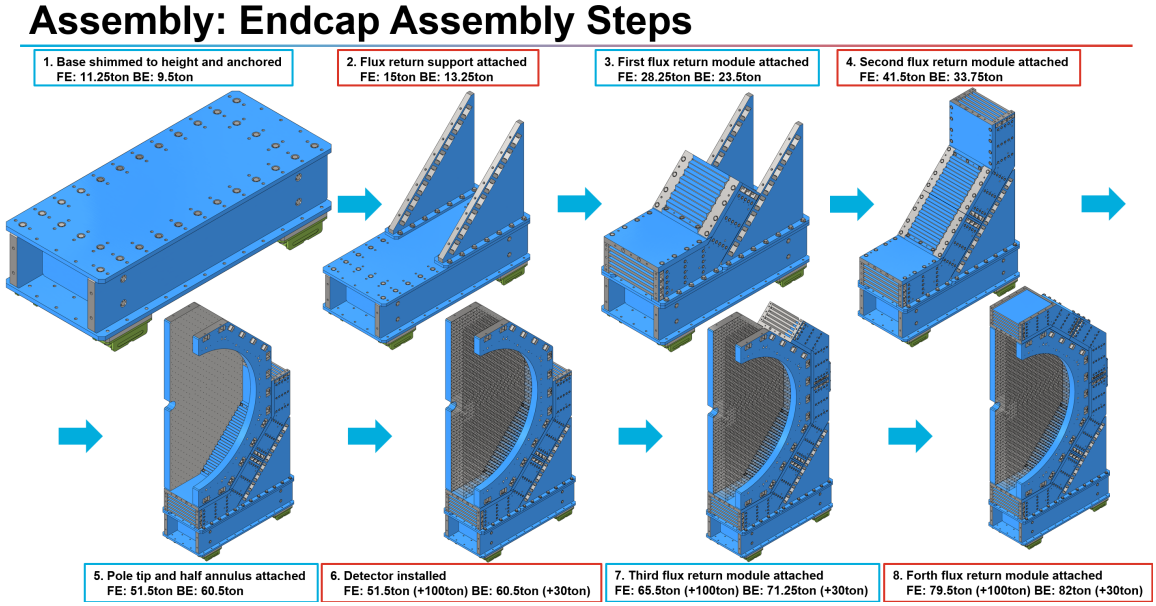

Figure 3.318: The installation sequence of ePIC endcap sub-detectors and structure broken down into 8 core steps.

The HCals consist of about twelve hundred towers that are individually stacked on top of one another, with alternating seams, much like laying bricks. The first layer of towers is installed directly on the inner surface of the flux return, barring any shimming. All preceding layers are installed on top of the previous, shimming in between in order to minimize tolerance stack-up. As the towers are installed, they get attached to the detector mounting plate, to the preceding towers and services are attached and tested as shown in Figure 3.319. Because of the alternating seams and the nominal tower is rectangular in cross-section, that requires some square cross section towers to fill in some areas that are at the split between endcap halves or at the sides of the flux return. The forward and backward HCals are mechanically identical in design, with the one exception that the backwards HCal is shorter than the forward HCal; otherwise, the assembly is the same.

The forward EMCal is attached to the same detector mounting plate as the forward HCal, though on the opposite side. The EMCal is installed in modules, called blocks, like the HCal, however they are cantilevered off dovetail rails that are pre-attached to the detector mounting plate. The blocks are individually slid onto the rails and set in place using setscrews as shown in Figure 3.320. After a number of blocks are installed, its cooling, electronics and other services are installed and tested. This is repeated until just over one thousand blocks and corresponding services are installed and tested.

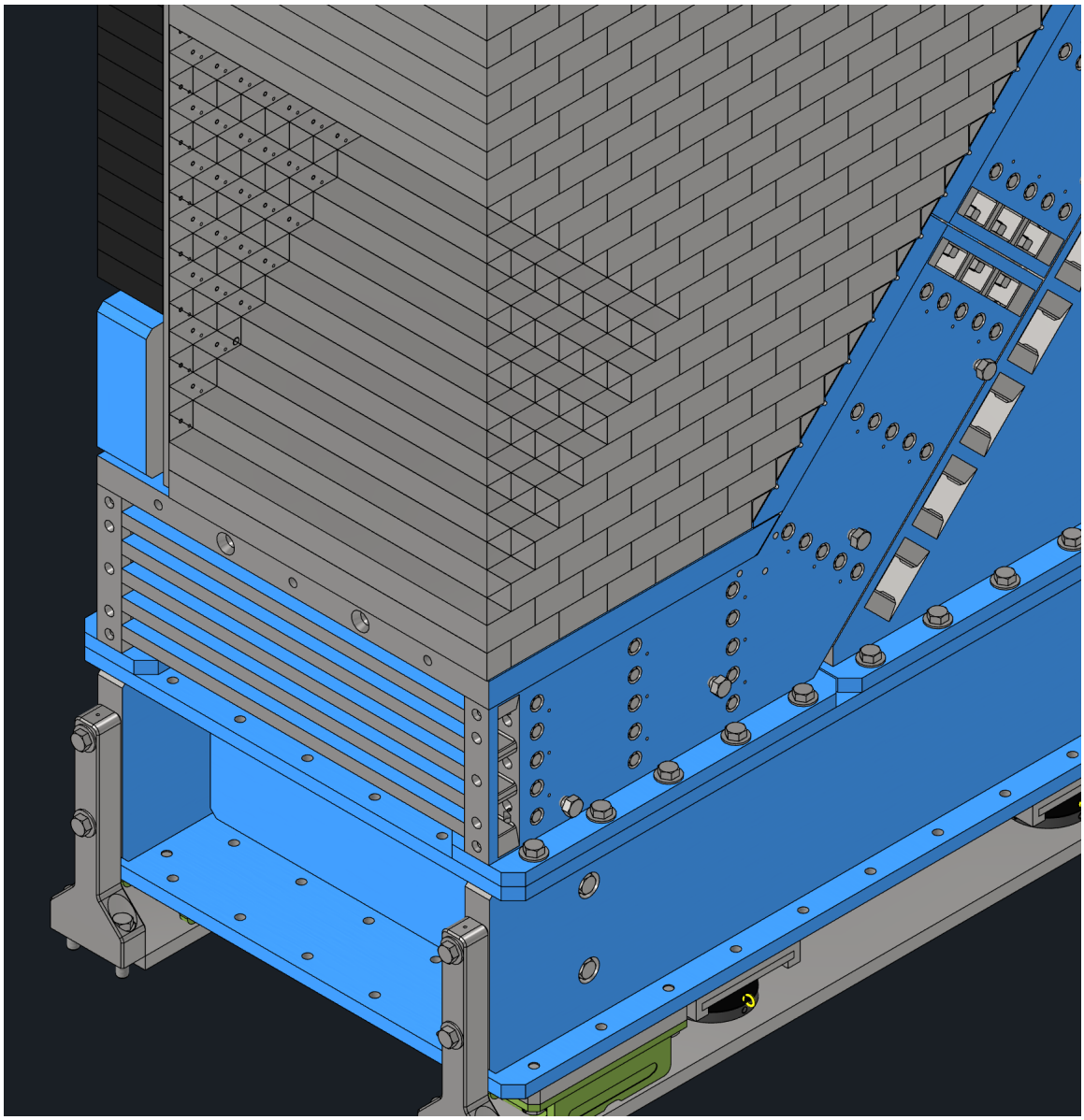

Figure 3.319: The installation and mounting of the forward HCal.

Central Barrel: All initial detector installations will be done in the AH for three main reasons: the endcaps are being assembled in the IR in parallel to the central barrel assembly, there is significantly more space available and there is the higher capacity crane available. The cradle, magnet, HCal, BIC GST and SVT all require the additional AH space and/or larger crane capacity. All detectors are either maintained in place, like the endcap detectors, HCal, BIC, and DIRC, maintained by removal in the IR, like the outer MPGD, ToF, Cymbal, EMCal, pfRICH, MPGD disks, ToF disk and dRICH or maintained by removal in the AH, like the SVT. All detectors that require removal for maintenance would be removed in the same way as the initial installation, just following the reverse procedure.

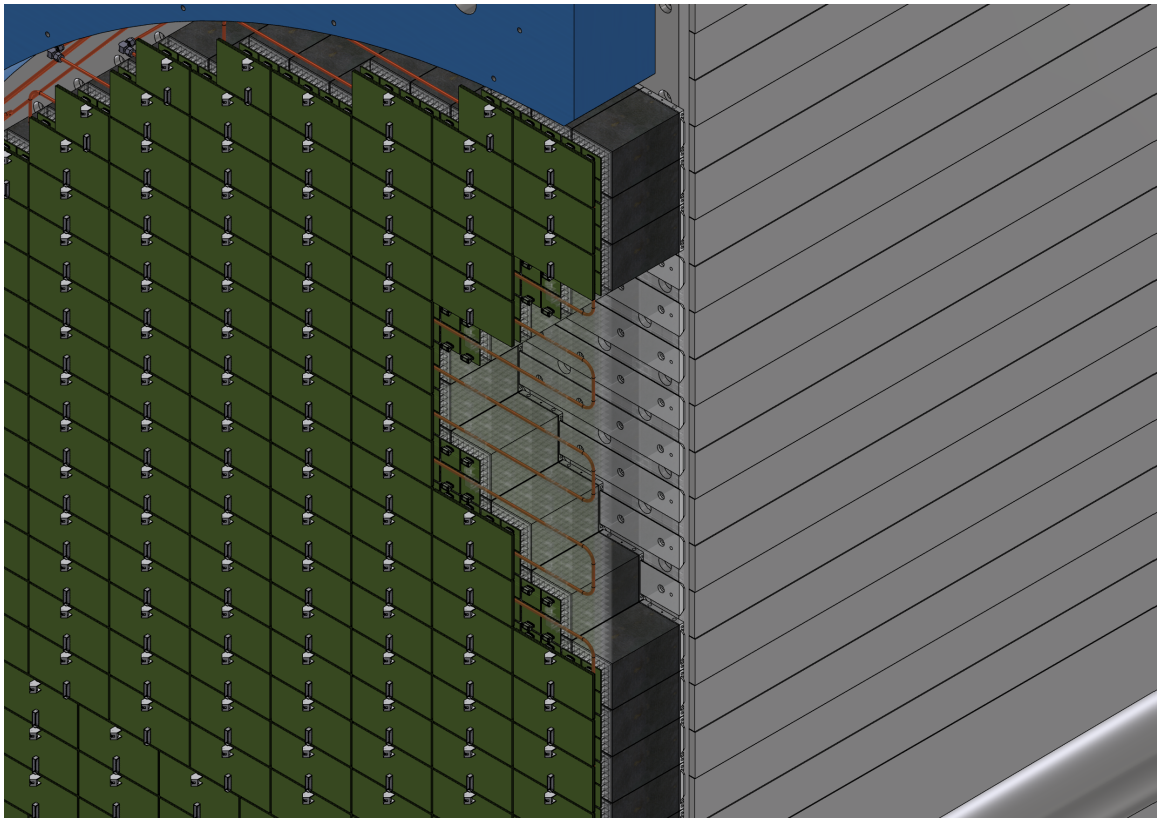

Figure 3.320: The installation and mounting of the forward EMCal.

Cradle, Magnet and HCal: The cradle will consist of four main components, each of which will be received from the respective vendors individually: the air casters, the base, the cradle plates and the central platform. The air castors will be installed on the bottom of the cradle base, and the cradle plates will be installed on top. Once assembled and aligned the lower 13 of the HCal sectors will be installed individually on the four cradle plates, starting at the 6 o'clock position and alternating which side the remaining 12 sectors are installed on as shown in Figure 3.321. Additionally, to being attached to the cradle, the sectors are also attached to the preceding sector. In parallel, the installed sectors can be serviced and tested.

The magnet pads would be installed on the ID of the HCal followed by the magnet itself. Shown in Figure 3.322, the magnet would be lowered in place with slings onto the pads. Once the magnet is adequately aligned the support rings that sandwich the magnet, and support the remaining HCal sectors, would also be attached to HCal ID. The support rings also have additional magnet restraints in Z. The upper half of the HCal would continue, again alternating sides which the remaining 19 individual sectors are installed on. These sectors are still attached to the preceding sector, but since the cradle is no longer an attachment point, the sectors are attached to the support rings instead. The top sector, known as the keystone, would be last and will require some additional effort to install as there will be some tolerance stack-up. There are hydraulics at the top of the support rings to aid in the keystone installation. The keystone will also have an electrical break to prevent any concern of eddy currents during a magnet quench, though unlikely significant anyway given the design.

The central platform would then be erected around the completed HCal, supported from the base

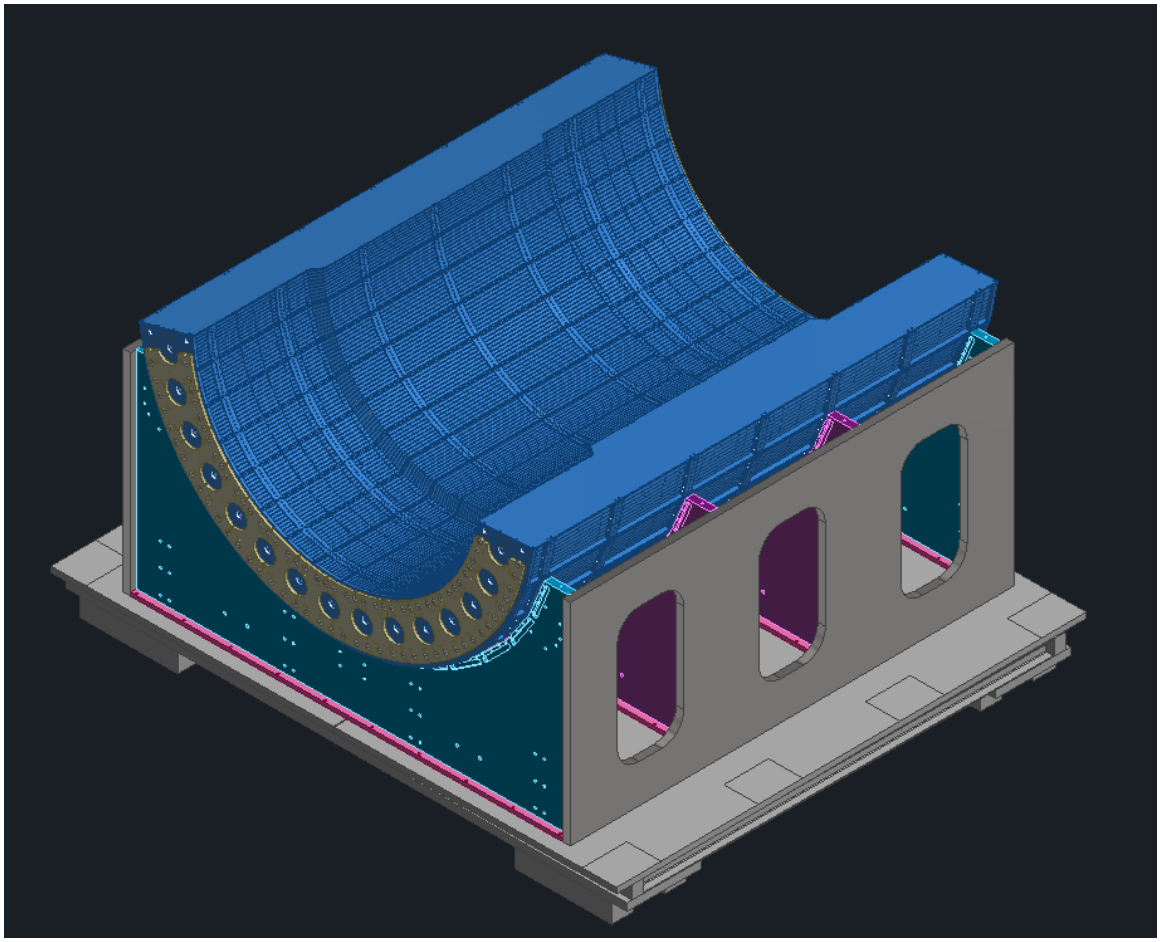

Figure 3.321: The lower half of the barrel HCal installed on the detector support cradles.

by large I-beams as shown in Figure 3.323. The platform allows access to the OD of the HCal for maintenance of all sectors, albeit some easier than others. The platform would also aid in the installation and allow access to the magnet phase separator. The platform would not permanently support any racks or equipment as the distance between the top of the platform, and the top of the plug-door opening is only about one foot. At this stage, the endcaps steel would be completed, and the central barrel would be rolled into the IR in order to map the magnet.

BIC and GST: The barrel EMCal, also consisting of many sectors, assembly would take place partially on the ground and partially suspended in front of the HCal in the AH. On the ground we would use a long I-beam supported by an A-frame on both ends. On the I-beam would be a cart supporting a partial cage structure which will be the mounting interface and support structure for the BIC. The individual BIC sectors would be installed in this cage starting from the bottom and working up to the halfway point, much like the HCal, alternating sides for each sector installation. This part of the assembly would be done in parallel to the HCal assembly.

Once the magnet mapping is completed and the central barrel is rolled back into the assembly hall the second half of the BIC assembly can continue. Three stanchions would need to be installed temporally: two inside the ID of the HCal, one on both ends, and the third on the forward end,

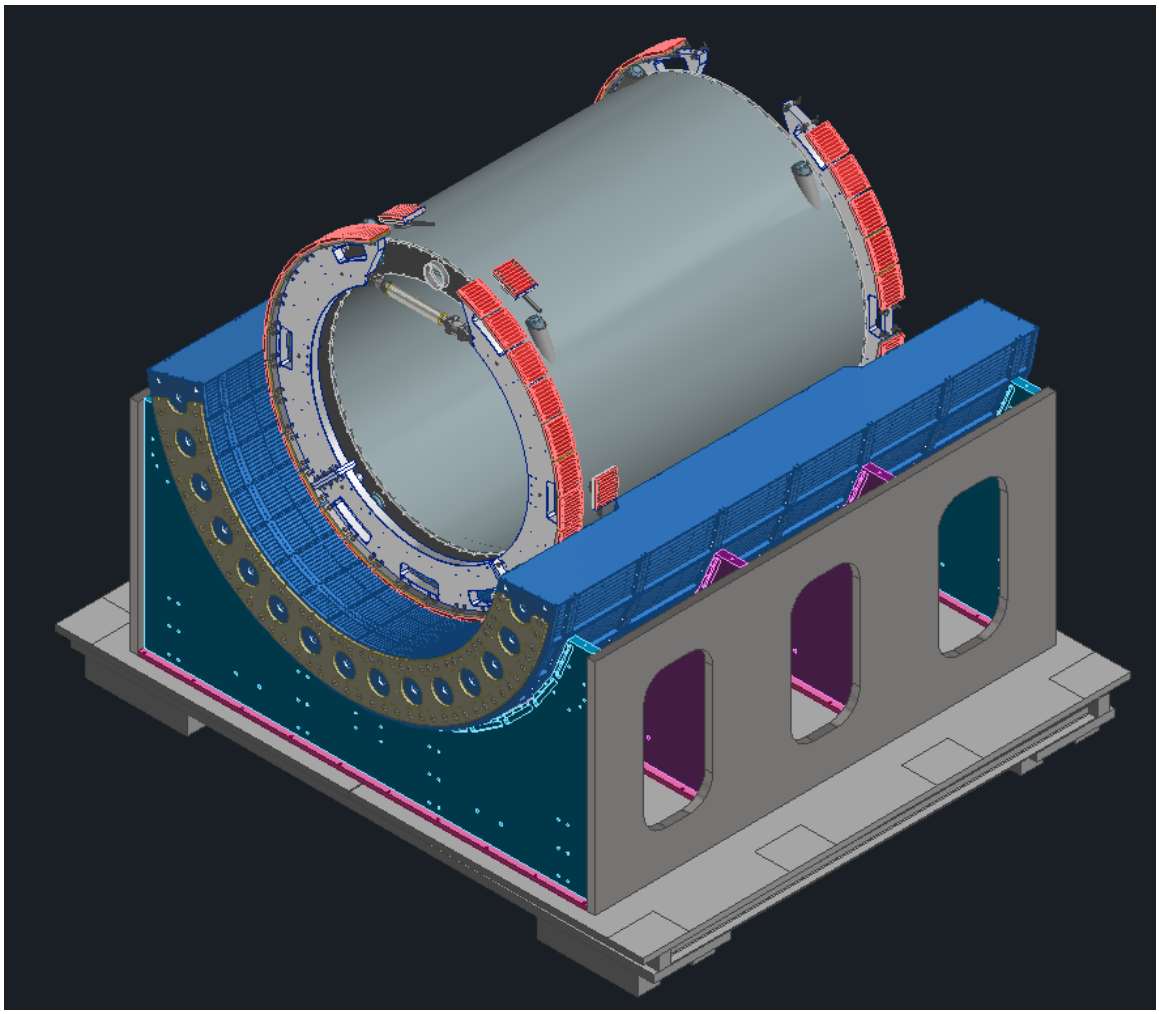

Figure 3.322: The magnet and support rings instaled on the lower half of the barrel HCal.

outside the HCal. An extension of the beam that supports the BIC would be installed on the two stanchions inside the HCal using a C-fixture. Then the I-beam supporting the half-assembled BIC would be raised and attached to the external stanchion, the closer internal stanchion and the I-beam extension as shown in Figure 3.324. From there, the upper half of the BIC would be assembled in the same way as the lower half.

The central stanchion on the ID of the HCal would then be slowly removed. Using a hydraulic, the cart supporting the BIC and its support structure would get pushed from its external position to its nominal piston as shown in Figure 3.325. This would be a slow movement and done in increments, such that the cart would be bolted down to the beam, the hydraulic retracted and re-bolted to a new position on the beam, the cart unbolted and repeated until it is in the desired location. The BIC would be bolted to the support rings ID and unbolted from the cart. The procedure would then be reversed to remove the installation equipment, without the BIC.

The GST would follow the same installation sequence, but without the detector assembly and instead of attaching to the support rings, the GST would attach to the BIC support structure. This would be accomplished with arms spanning the gap between components and allowing for sig-

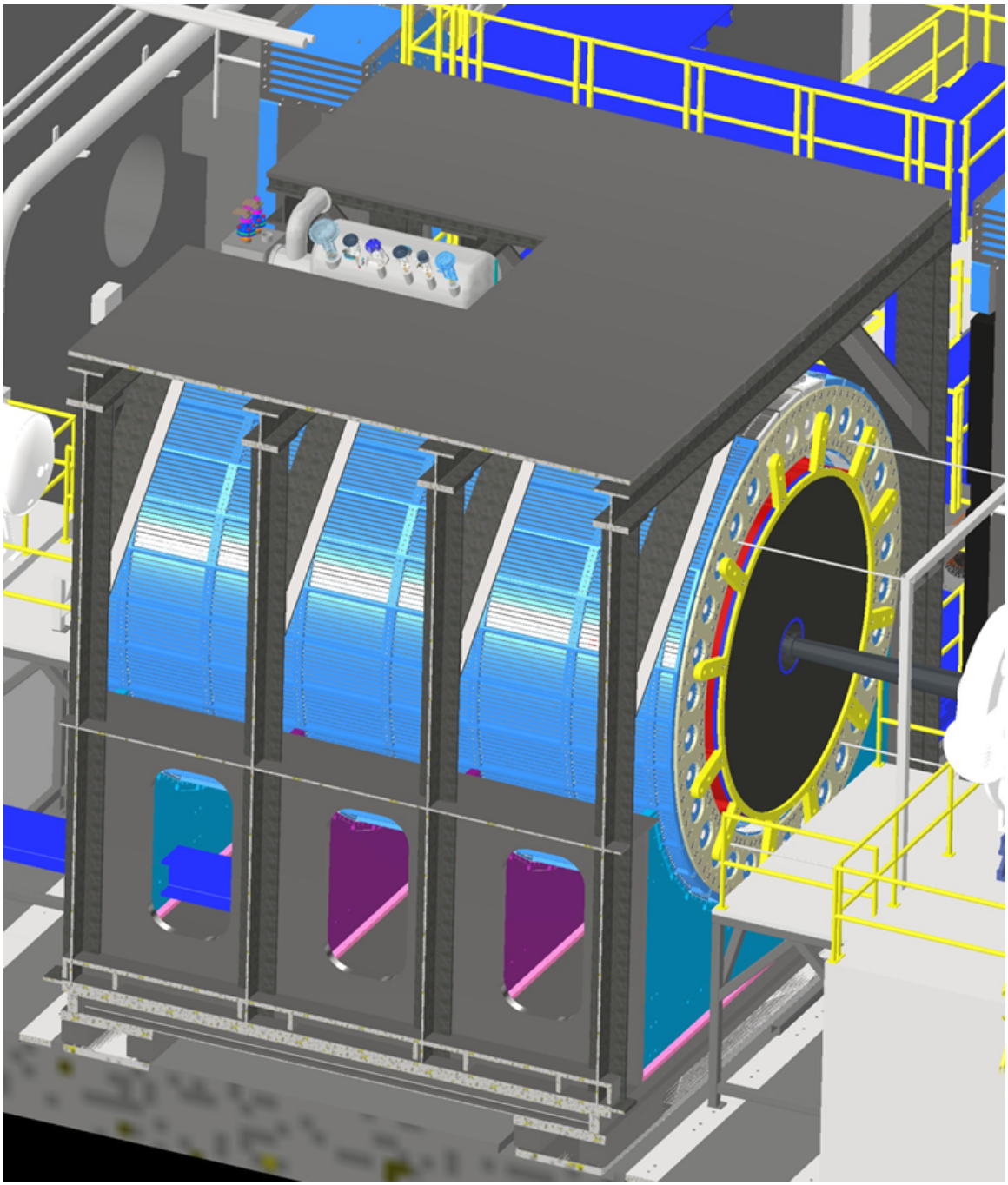

Figure 3.323: The fully assembled HCal surrounded by the central platform and its structure.

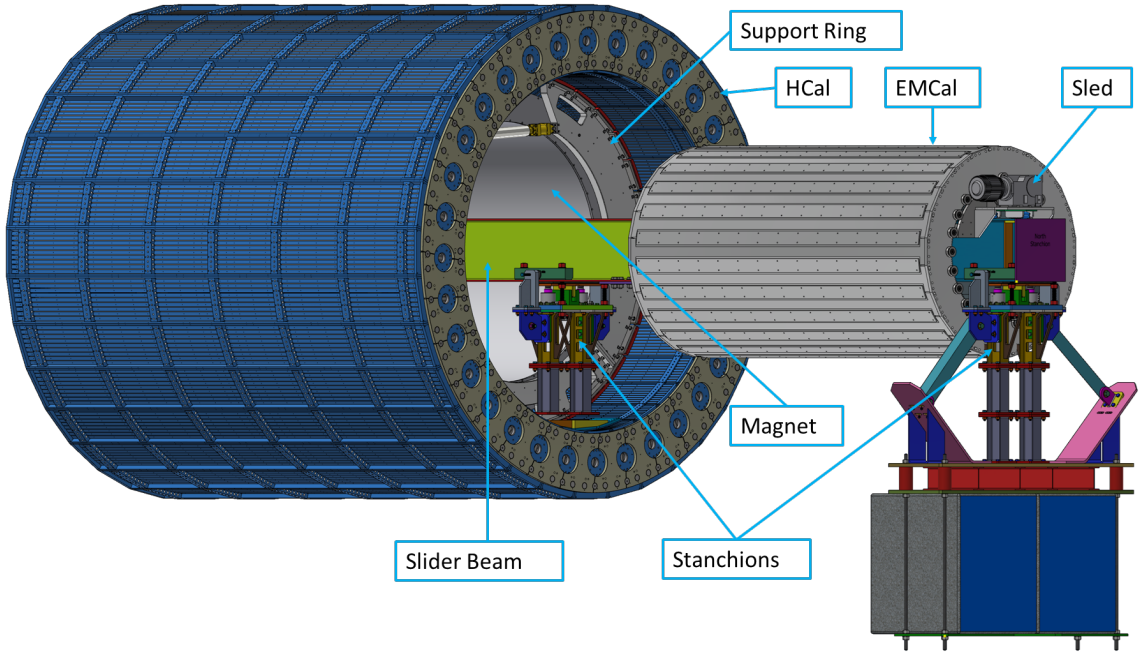

Figure 3.324: The BIC installation equipment and the BIC ready to be installed.

nificant fine adjustment. After both the BIC and GST are installed, the central stanchion will be reinstalled, allowing the I-beams and cart to be uninstalled with the C-fixture and all stanchions removed. Although the BIC end of sector boxes will eventually be covered with services from the inner detectors, they could still be access for maintenance, when the blocking services are temporarily removed.

DIRC, oMPGD, ToF and Cymbal: The DIRC, oMPGD, ToF and Cymbal are all divided into 12 radial segments and two Z segments, with the exception of the DIRC, or 24 modules each (12 for the DIRC). The ToF and Cymbal would be pre-attached making 24 subassembly modules. All of these modules are installed on rails incorporated into the GST, but in order to get the modules to the correct position, the modules would first slide onto an installation fixture using the same type of rials. The installation fixture consists of three slewing bearings that can rotate the modules to the corresponding position in the GST as shown in Figure 3.326. Then that fixture would then be lifted with the crane and the rails aligned to the GST. Once aligned the modules would be pushed from the fixture to the GST.

The second module in Z would be lifted to the same position on the GST, all connections between the modules would be made and the joined pair would be slid in the remaining distance and the fixture removed. This would be repeated for all remaining modules with the exception of the 3 o'clock and 9 o'clock ToF and Cymbal subassembly modules as they get installed after the SVT. The DIRC has the remaining step of installing the prisms and electronics to the end of the bar box modules, which is a by hand operation on similar rails. Attaching services and testing would be done in parallel after each pair of modules for a given detector is installed.

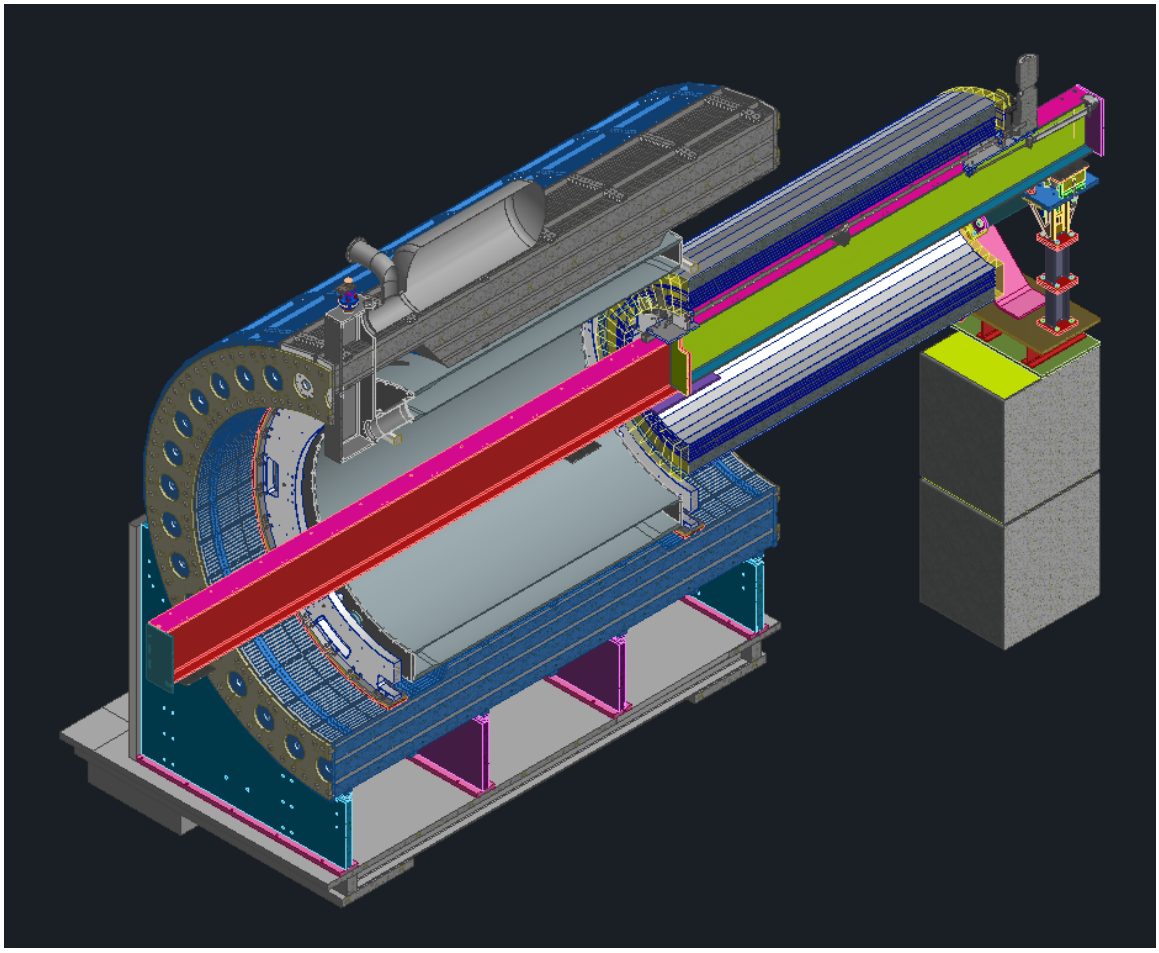

Figure 3.325: The BIC installation equipment and the BIC ready to be installed section view.

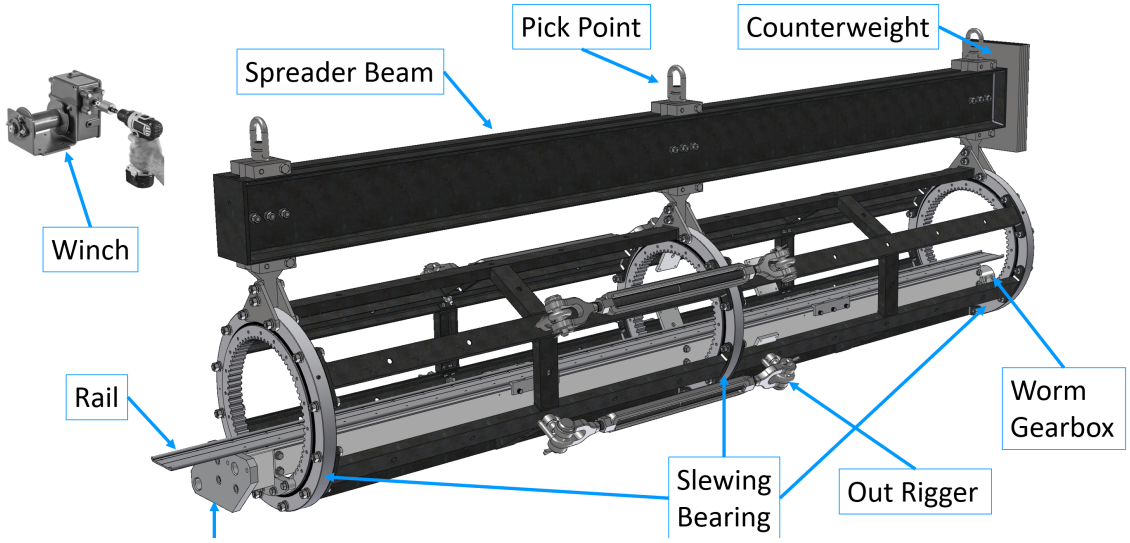

Figure 3.326: The DIRC, oMPGD, ToF Cymbal installation fixture.

SVT, MPGD Disks and Beam Pipe: The SVT, MPGD disks and beam pipe are preassembled as a single assembly before being installed into the GST. The SVT is first assembled into two halves, top and bottom, which consists of the 5 barrel layers (L0 to L4) and the 5 disk layers on both sides installed into a carbon fiber shell known as the PST. The PST has mounting points for all of the SVT components, the MPGD disks, the beam pipe supports and attachment arms for the 3 and 9 o'clock rails inside the GST. These two assemblies include all services. The central beam pipe is then installed into the bottom half of the SVT and followed by the tap half. The halves are then joined along the seams at 3 and 9 o'clock.

The forward and backward disks of the MPGD are similarly split into top and bottom halves that clamshell around the beam pipe and attach to tabs that are part of the PST. The PST assembly is then attached to an installation fixture that supports the PST and extends the rails from the GST. The rails from the fixture and GST are aligned and the PST assembly is slid in, transferring it from the fixture to the GST. Once the PST assembly is in its nominal position the fixture can be removed. After which the last two ToF and Cymbal assemblies can be installed and tested. These steps can be seen in Figure 3.327. Following the two ToF and Cymbal assemblies' installation would be all of the SVT and MPGD disk services and testing.

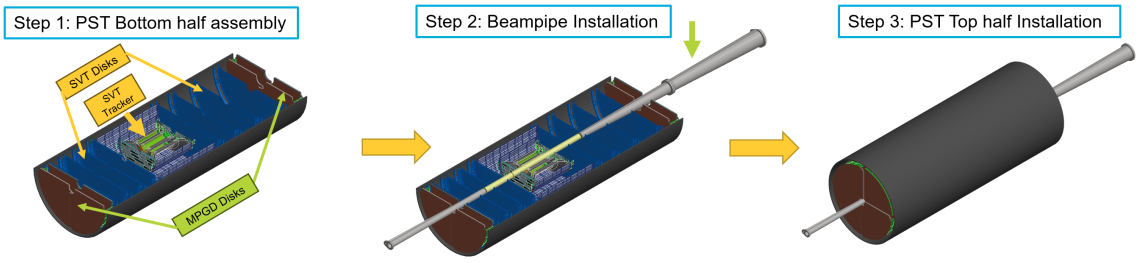

Figure 3.327: The SVT, MPGD Disks and Beam Pipe assembly steps.

EEMCal, pfRICH and ToF Disk: The EEEMCal and pfRICH would be installed on the same set of rails as the PST assembly and utilize the same installation fixture as seen in Figure 3.328. Both detectors would individually and independently be transferred from their assembly stands to the installation fixture on the rails, raised up to nominal height, rails aligned and attached, detectors pushed from the fixture to the GST rails and the fixture removed. Then the detector services would be attached and the detectors tested. The ToF disk would follow the same procedure, except on the forward side.

dRICH: The dRICH will require its own unique set of installation tooling as seen in Figure 3.329. The vessel will be received on a cart and have a strong back attached to the forward-facing side. This strong back would allow us to attach a number of linear bearings at 3 and 9 o'clock. We would then erect a set of linear rails attached to the HCal at one end, also at 3 and 9 o'clock, and supported by an independent structure at the other. The dRICH would then be lifted from the cart to the rails attached to the HCal using the crane. The dRICH would be pushed into the HCal and tabs protruding out radially from the face of the dRICH would get bolted to the end face of the HCal. The installation, rails, independent structure, and the dRICH strong-back would all get removed in that sequence. Then the detector services would be attached and the detector tested.

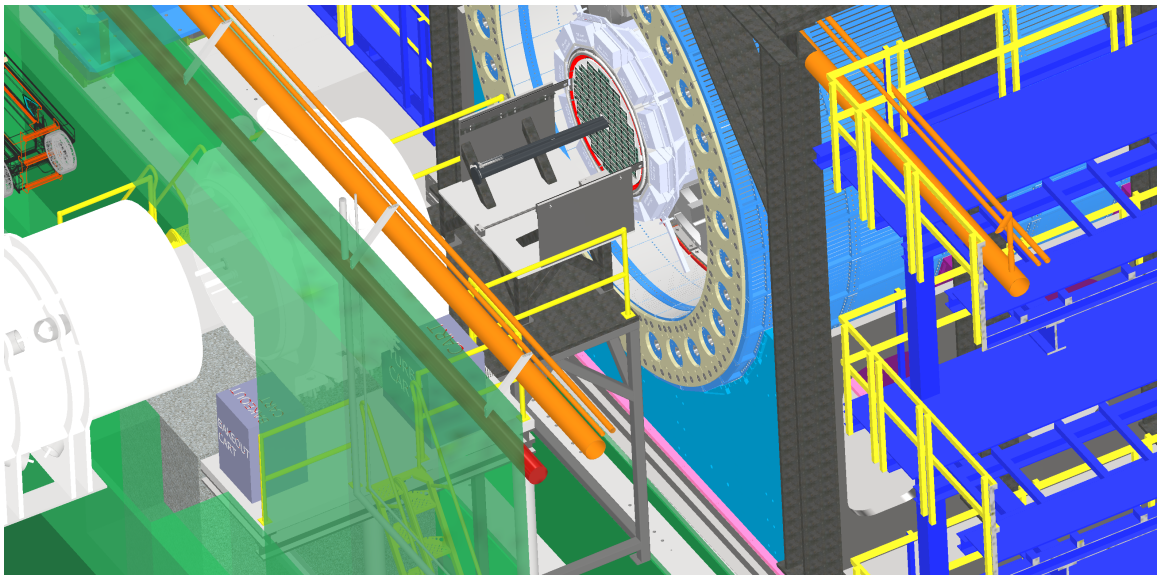

Figure 3.328: The pfRICH and EEMCal installation fixture in the experimental hall.

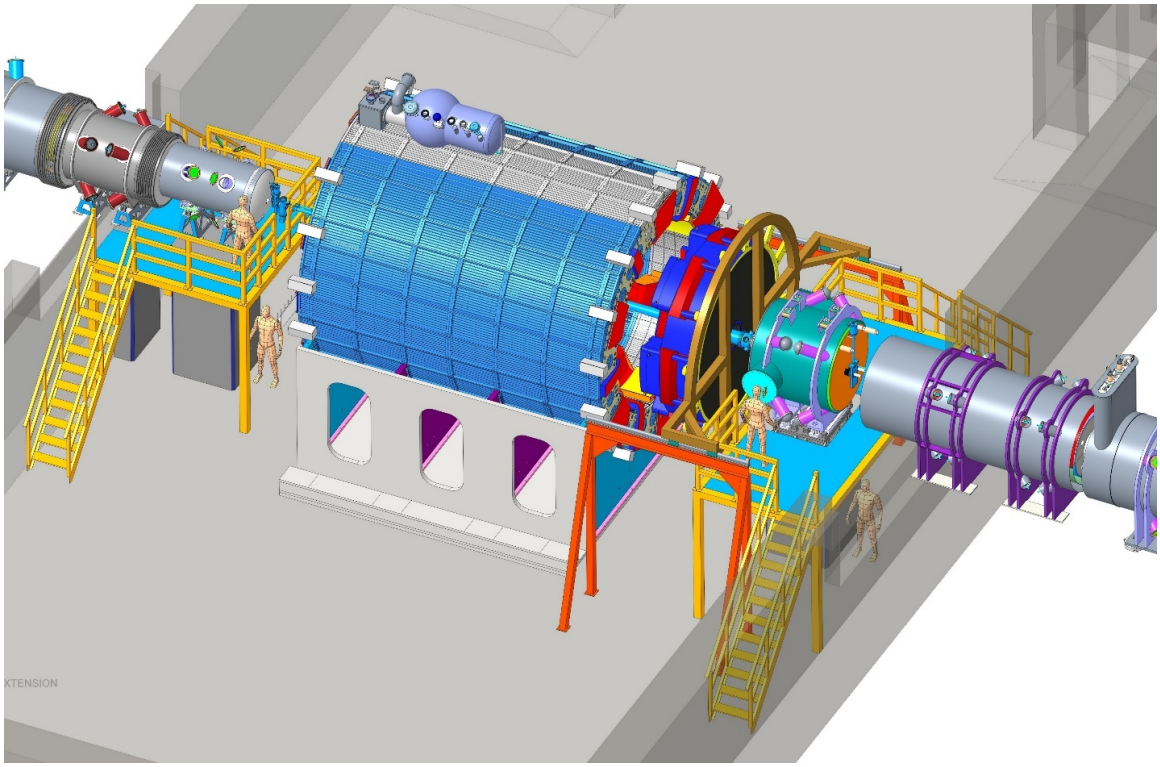

Figure 3.329: The dRICH installation fixture in the experimental hall.

3.5 Detector Commissioning and Pre-Operations

Add text here.

Chapter 4

Detector Performance for the EIC physics program

4.1 ePIC and the Science case of the EIC

4.1.1 Connecting the Physics Processes to the NAS Science Pillars

4.2 Global Performance Considerations

This section will discuss the methods of reconstructing different particles and objects that will be most import for the analyses presented later.

4.2.1 Electron Identification

Regardless of kinematics reconstruction method used, it is crucial to identify the scattered electron in the event final state. Indeed, it can be challenging to separate the electron signal from the large π^- background present in DIS collisions. Therefore, a rudimentary electron identification algorithm has been already developed in ePIC.

The first step is to separate final state electrons from pions. This is done by applying a cut on E/p, where p is the track momentum and E is the ECAL cluster energy matched to that track. Electrons will typically deposit all of their energy in the ECAL and have $E/p \approx 1$, while pions will pass through the ECAL and peak at $E/p < 1$. Currently, two sets of cuts are used: $0.9 \leq E/p \leq 1.2$ to cleanly select electrons, as well as a looser $0.7 \leq E/p \leq 1.3$ selection as the input to the following algorithm for identifying the scattered DIS electron.

The next step is to identify the scattered DIS electron, as other electrons may be present in the final state. In many cases the electron with the greatest momentum can be accurately identified as the scattered electron. To improve upon this, the current analysis utilizes the so called $E - p_z$ algorithm. This algorithm selects the electron which maximizes the difference between the sum of the energy of the electron and hadronic final state and the sum of the z component of their momentum, with the ideal case approaching $2E_e$, twice the energy of the electron beam.

Future iterations of the DIS electron identification algorithm will incorporate information from the PID detectors (hpDIRC, pfRICH, TOF), applying cuts on shower shape parameters of the calorimeter clusters, as well as refinement of the selection criteria.

4.2.2 Muon Identification

The ability to identify muons in the final state would significantly increase the reach of EIC physics. To evaluate the feasibility of muon identification, single particle simulations studies were performed with the ePIC simulation and reconstruction frameworks. Muons and pions have been generated and reconstructed in the central barrel region for momenta between 0.1 and 15 GeV. The analysis of the reconstructed events rely on two variables: the E/p, and shower radius. The momentum p is obtained from the reconstructed track, while the energy and shower radius can be obtained from either the electromagnetic or hadronic calorimeters.

The separation between muons and pions has been evaluated using a log likelihood analysis. The figure of merit (FOM) has been set as the ratio between the accepted muons and the accepted muons and pions selecting for the likelihood larger than 0 for the different subsystems involved. Figure 4.1 shows the FOM variable as a function of momentum of the thrown muon for different use of cuts and detector systems. As can be seen the highest discrimination power is obtained from the E/p information, while the shower shape provides some additional discrimination at low momentum.

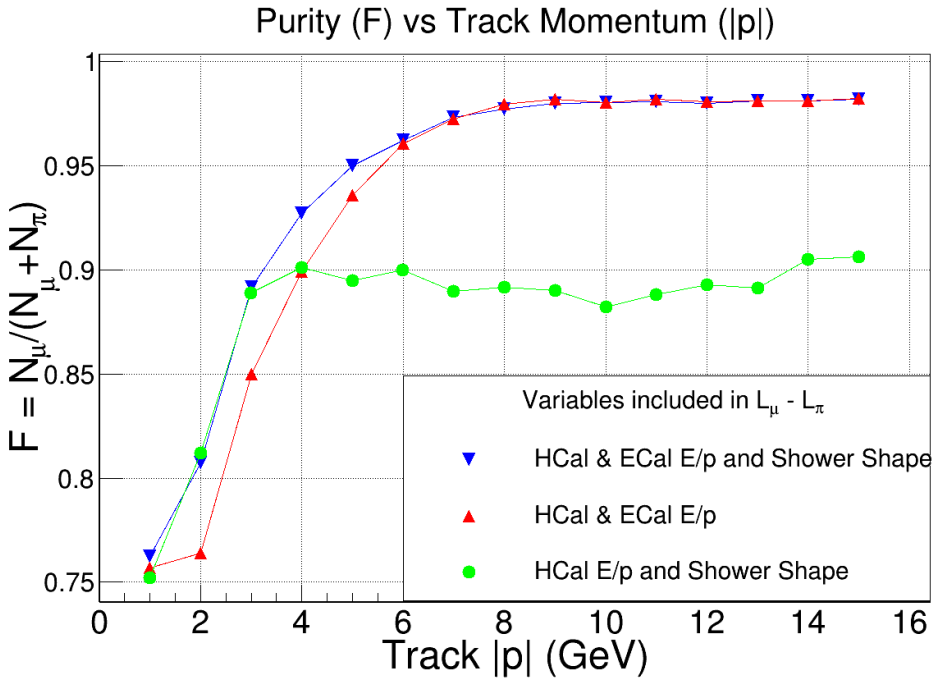

Figure 4.1: Figure of merit for muon identification as a function of momentum in the ePIC central barrel.

4.2.3 Photon Identification

4.2.4 Hadron Identification

4.2.5 Jet Reconstruction and Calibration

As demonstrated in the YR [11], jets are an important observable, bringing both complementary and unique insight to many of the EIC science goals. In order to comprehensively evaluate the impact that they can have, jet reconstruction has been integrated into the ePIC reconstruction framework, EICrecon. It utilizes the FastJet package to implement various jet definitions. The default settings, which are used for jets saved to the shared output trees and included in the analyses below, include the Anti-k_T algorithm, E-scheme recombination, a resolution of 1.0, and a minimum jet transverse momentum of 1 GeV/c. In addition, constituents were required to have transverse momenta greater than 200 MeV/c to be included in the clustering.

Due to the lack of mature algorithms for integrating information from tracking, calorimetry, and particle identification subsystems, the reconstructed jets used to benchmark the ePIC detector performance and evaluate physics impact are clustered exclusively from charged particle tracks.

4.2.5.1 Jet Energy Scale and Resolution

The primary metrics for evaluating the quality of jet reconstruction at ePIC are the jet energy scale (JES) and jet energy resolution (JER). These quantities were calculated by comparing the energies of matched particle-level and reconstructed jets. Because the reconstruction currently uses track-only jets and we are primarily interested in quantifying the effects of the detector, only stable charged particles were used when clustering the particle-level jets. For each particle-level jet, the closest reconstructed jet in $\eta - \phi$ space was considered the matching jet as long as $\Delta R = \sqrt{\Delta\eta^2 + \Delta\phi^2}$ was less than 0.1. The quantity: [(reco - particle)/particle] jet energy was found for each set of matching jets and fit with a triple Gaussian function. A triple Gaussian was used to try to take into account the tails of the distribution. The mean of fit is taken as the JES while the sigma is taken as the JER. To get a more differential picture of the jet performance, this procedure was performed as a function of particle-level jet energy for three pseudorapidity ranges as shown in Fig. 4.2.

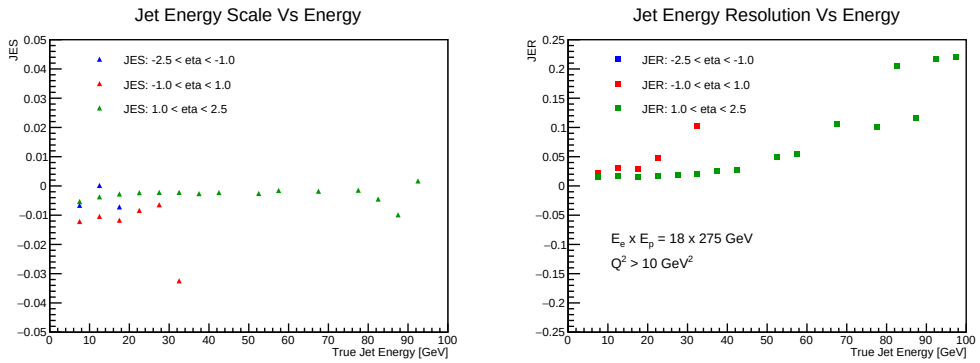

Figure 4.2: Jet energy scale (Left) and jet energy resolution (Right) as a function of particle-level jet energy for backward (blue squares), mid (red triangles), and forward (green diamonds) rapidities.

4.3 Incorporation of Beam Backgrounds in the Studies

4.4 Physics Processes and Detector Performance

This section will discuss the analysis of different event topologies encountered in deep inelastic scattering (DIS), semi-inclusive DIS, exclusive processes, and hard probes.

4.4.1 Inclusive Processes

4.4.1.1 Methods and Reconstruction of Inclusive kinematics

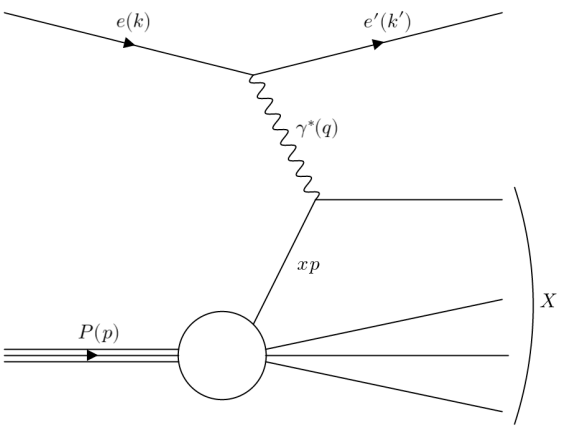

Figure 4.3: Neutral-Current Deep Inelastic Scattering of an electron by a proton.

The inclusive DIS process can be written as

$$e(k) + P(p) \rightarrow e(k') + X(p'), \tag{4.1}$$

where e (e') indicates the initial (scattered) electron, P the proton target, and X the inclusive hadronic final state system. This process is shown diagrammatically in Figure 4.3. The event kinematics are described using three Lorentz invariant quantities, related by the center-of-mass energy s, as

$$Q^2 = xy(s - m_p^2) \simeq sxy. \tag{4.2}$$

For a virtual photon with four-momentum q, the virtuality Q^2 is

$$Q^2 \equiv -q^2 = -(k - k')^2, \tag{4.3}$$

while the Bjorken variable x, and the inelasticity y are given by

$$x \equiv \frac{Q^2}{2p \cdot q}, \qquad\qquad y \equiv \frac{p \cdot q}{p \cdot k}. \tag{4.4}$$

In a reference frame where the proton target has infinite momentum, x is the momentum fraction carried by the struck parton (neglecting quark masses). If the rest frame of the target proton is chosen instead, the inelasticity y simply describes the fractional energy loss of the scattering electron, $y = 1 - \frac{E'_e}{E_e}$. The center-of-mass energy W of the photon-proton system may also be considered, and is given by

$$W^2 \equiv (p + q)^2 = m_p^2 - Q^2 + 2p \cdot q. \tag{4.5}$$

In the laboratory frame, the ingoing (outgoing) electron and proton four-momenta are given by k

(k') and p (p') respectively, which can be written as

$$k = (E_0, 0, 0, -E_0)$$
$$k' = (E_e, E_e \sin\theta_e, 0, E_e \cos\theta_e)$$
$$p = (E_p, 0, 0, E_p)$$
$$p' = (E_h, p_{t,h}, 0, p_{z,h})$$

for scattering in the $x-z$ plane. By convention, the electron beam is aligned with the $-z$-axis, and the proton beam with the $+z$-axis. The center-of-mass energy is therefore given by $s = 4E_eE_p$, neglecting mass. The virtual photon four-momentum is $q = k - k'$, so the kinematic variables may be reconstructed using electron information alone by evaluating the four-momenta

$$y_e = 1 - \frac{E_e(1-\cos\theta_e)}{2E_0}, \qquad Q_e^2 = 2E_0E_e(1+\cos\theta_e). \tag{4.6}$$

The resolutions on kinematic variables reconstructed using this method are

$$\frac{\delta y}{y} = \frac{1-y}{y}\left(\frac{\delta E_e}{E_e} \oplus \frac{\delta\theta_e}{\tan\frac{\theta_e}{2}}\right), \qquad \frac{\delta Q^2}{Q^2} = \frac{\delta E_e}{E_e} \oplus \tan\frac{\theta_e}{2}\cdot\delta\theta_e \tag{4.7}$$

and it can be seen that the y resolution diverges at low y, while the Q^2 resolution diverges as $\theta_e \to 180^\circ$. To counteract this divergence, methods that utilize the hadronic final state (HFS) measurement, which do not degrade in resolution at low y values, are often used. The inclusive HFS is defined as the sum over all final state particles other than the scattered electron, and is described using the quantities

$$\delta_h = \sum_h E_h - p_{z,h} \qquad \text{and} \qquad p_{t,h}^2 = \left(\sum_h p_{x,h}\right)^2 + \left(\sum_h p_{y,h}\right)^2. \tag{4.8}$$

The Double-angle method enables the kinematics to be reconstructed using the electron scattering angle θ_e and the inclusive HFS angle γ_h as

$$y_{DA} = \frac{\alpha_h}{\alpha_e + \alpha_h}, \qquad Q_{DA}^2 = \frac{4E_0^2}{\alpha_e(\alpha_e+\alpha_h)} \tag{4.9}$$

where $\alpha_e \equiv \tan\frac{\theta_e}{2}$ and $\alpha_h \equiv \tan\frac{\gamma_h}{2} = \frac{\delta_h}{p_{t,h}}$. In the Jacquet-Blondel, or "hadron-only" method, the kinematics are reconstructed as

$$y_{JB} = \frac{\delta_h}{2E_0}, \qquad Q_{JB}^2 = \frac{p_{t,h}^2}{1-y_h} \tag{4.10}$$

while the Σ method is calculated as

$$y_\Sigma = \frac{\delta_h}{\delta_h + E_e(1-\cos\theta_e)}, \qquad Q_\Sigma^2 = \frac{E_e'^2\sin^2\theta_e}{1-y_\Sigma}. \tag{4.11}$$

For each of the methods described above, x is calculated as $x = \frac{Q^2}{sy}$. In addition to the methods described in this appendix, there are methods that emerge when the input variables are permuted, which are summarized elsewhere [175].

In summary, for our studies only four reconstruction methods are considered:

- **Electron method**: uses only scattered electron.
- **Σ method**: uses both scattered electron and HFS.
- **Double-angle method (DA)**: uses both scattered electron and HFS.
- **Jacquet-Blondel method (JB)**: uses only HFS.

The JB method relies solely on the HFS, which is less well measured compared to the scattered electron. While the JB method does not usually give the best resolution, it is the only reconstruction method possible for charged-current interactions (where the outgoing DIS lepton is a neutrino).

Figure 4.4 shows the y resolution at ePIC as a function of x_B and Q^2 for 18 GeV on 275 GeV ep collisions. The scattered electron reconstruction that informs these resolutions uses the momentum and polar angle measured by the tracking system. The resolution could be further improved by using electromagnetic calorimeter clusters for the electron energy measurement. This is particularly important for small scattering angles, as the tracking performance is degraded, but a high quality energy measurement may be obtained using the backward endcap electromagnetic calorimeter.

The optimal reconstruction method changes with the kinematics, with the electron method providing the best reconstruction at large y values. The resolution of the electron method degrades as $1/y$, so the Σ and DA methods are employed for $y \lesssim 0.2$, ensuring that a y resolution of 30 % or lower can be obtained for the full kinematic range.

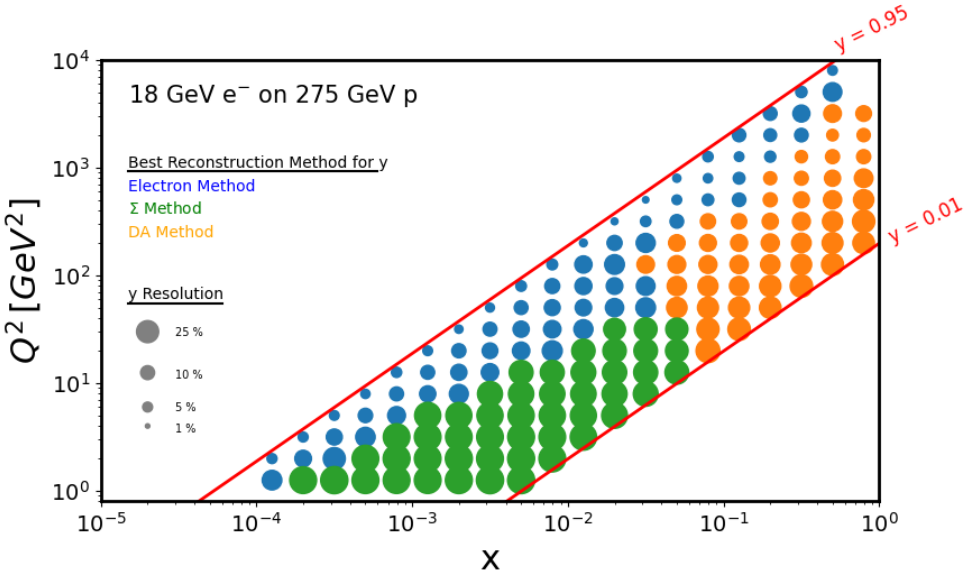

Figure 4.4: Resolution of the inelasticity y, as a function of x_B and Q^2, when reconstructed using the electron method (blue), Σ method (green), or Double-angle method (orange). The color of each point indicates the best performing reconstruction method.

4.4.1.2 Detector Impact on key Inclusive physics measurements

4.4.1.3 Influence of beam Background on Inclusive measurements

4.4.2 Semi Inclusive Processes

4.4.2.1 Methods and Reconstruction of SIDIS kinematics

4.4.2.2 Detector Impact on key SIDIS physics measurements

4.4.2.3 Influence of beam Background on SIDIS measurements

4.4.3 Exclusive and Diffractive Processes

4.4.3.1 Methods and Reconstruction of Diffractive kinematics

4.4.3.2 Detector Impact on key Exclusive and Diffractive physics measurements

4.4.3.3 Influence of beam Background on Exclusive measurements

4.4.4 Hard Probes

4.4.4.1 Heavy Flavor Reconstruction

4.4.4.2 Displaced vertex resolution and tracking

4.4.4.3 Detector Impact on Key Heavy Flavor Physics Measurements

4.4.4.4 Influence of beam on Background on Heavy Flavor measurements

4.4.4.5 Jets as a Hard Probe

4.4.4.6 Detector Impact on Key Jet Physics Measurements

4.4.4.7 Influence of beam on Background on Jet measurements

Chapter 5

Detector-Accelerator interfaces

References

[1] Irene Dutta and Christopher Madrid and Ryan Heller and Shirsendu Nanda and Danush Shekar and Claudio San Martín and Matías Barría and Artur Apresyan and Zhenyu Ye and William K. Brooks and Wei Chen and Gabriele D'Amen and Gabriele Giacomini and Alessandro Tricoli and Aram Hayrapetyan and Hakseong Lee and Ohannes Kamer Köseyan and Sergey Los and Koji Nakamura and Sayuka Kita and Tomoka Imamura and Cristían Peña and Si Xie, "Results for pixel and strip centimeter-scale AC-LGAD sensors with a 120 GeV proton beam," 7 2024.

[2] F. T. Acosta, B. Karki, P. Karande, A. Angerami, M. Arratia, K. Barish, R. Milton, S. Morán, B. Nachman, and A. Sinha, "The optimal use of segmentation for sampling calorimeters," *JINST*, vol. 19, no. 06, p. P06002, 2024.

[3] M. M. David Ruth, Alex Jentsch, "Advanced methods for roman pots reconstruction at the eic." https://indico.cern.ch/event/1199314/contributions/5193191/attachments/2619028/4527696/DIS_RNDtalk_DRuth.pdf, 2023.

[4] S. Lai *et al.*, "Software Compensation for Highly Granular Calorimeters using Machine Learning," *JINST*, vol. 19, p. P04037, 2024.

[5] S. J. Paul, R. Milton, S. Morán, B. Schmookler, and M. Arratia, "Feasibility study of measuring $\Lambda 0 \to n\pi 0$ using a high-granularity zero-degree calorimeter at the future electron-ion collider," *Phys. Rev. D*, vol. 111, no. 9, p. 092013, 2025.

[6] R. Milton, S. J. Paul, B. Schmookler, M. Arratia, P. Karande, A. Angerami, F. T. Acosta, and B. Nachman, "Design and simulation of a SiPM-on-tile ZDC for the future EIC, and its performance with graph neural networks," *Nucl. Instrum. Meth. A*, vol. 1079, p. 170613, 2025.

[7] N. H. Buttimore, "A helium-3 polarimeter using electromagnetic interference," *PoS*, vol. PSTP2013, p. 057, 2014.

[8] W. Haeberli, "H-jet measures beam polarization at RHIC," *CERN Cour.*, vol. 45N8, pp. 15–18, 2005.

[9] P. Thieberger, "Polarimeter target beam heating simulation version 4." Private communication, 2025. Unpublished Excel-based thermal simulation code, version 27.09.2025, available upon request.

[10] F. Rathmann, A. Nass, K. O. Eyser, V. Shmakova, E. C. Aschenauer, G. Atoian, A. Cannavo, K. Hock, H. Huang, H. Lovelace, G. Mahler, J. Ritter, G. Robert-Demolaize, V. Schoefer, P. Shanmuganathan, E. Shulga, H. Soltner, X. Chu, and Z. Zhang, "Eliminating beam-induced depolarizing effects in the hydrogen jet target for high-precision proton beam polarimetry at the electron-ion collider," 2025.

[11] R. Abdul Khalek *et al.*, "Science Requirements and Detector Concepts for the Electron-Ion Collider: EIC Yellow Report," *Nucl. Phys. A*, vol. 1026, p. 122447, 2022.

[12] "Radiation Doses." https://wiki.bnl.gov/EPIC/index.php?title=Radiation_Doses.

[13] S. Agostinelli *et al.*, "GEANT4—a simulation toolkit," *Nucl. Instrum. Meth. A*, vol. 506, p. 250, 2003.

[14] "The electron-ion collider user group.".

[15] R. A. Khalek *et al.*, "Science Requirements and Detector Concepts for the Electron-Ion Collider: EIC Yellow Report," *Nucl. Instr. and Meth. A*, vol. 1026, p. 122447, 2022.

[16] "The epic collaboration website.".

[17] A. Collaboration, "Technical Design report for the ALICE Inner Tracking System 3 - ITS3 ; A bent wafer-scale monolithic pixel detector," tech. rep., CERN, Geneva, 2024.

[18] M. Karagounis, D. Arutinov, M. Barbero, F. Huegging, H. Krueger, and N. Wermes, "An integrated shunt-ldo regulator for serial powered systems," in *2009 Proceedings of ESSCIRC*, pp. 276–279, 2009.

[19] A. Paramonov, "FELIX: the Detector Interface for the ATLAS Experiment at CERN," *EPJ Web Conf.*, vol. 251, p. 04006, 2021.

[20] lpGBT Design Team, "lpgbt documentation – release," 2024.

[21] J. Troska *et al.*, "The VTRx+, an optical link module for data transmission at HL-LHC," 2017.

[22] D. Higinbotham and et *al.*, "Science requirements and detector concepts for the electron-ion collider: Eic yellow report," *Nuclear Physics A*, vol. 1026, p. 122447, 2022.

[23] F. Willeke and J. Beebe-Wang, "Electron ion collider conceptual design report 2021," 2 2021.

[24] ePIC, "Summary of epic background rates," 2024.

[25] EIC, "Eic detector geometry," 2024.

[26] D. Neyret, P. Abbon, M. Anfreville, V. Andrieux, Y. Bedfer, D. Durand, S. Herlant, N. d'Hose, F. Kunne, S. Platchkov, F. Thibaud, M. Usseglio, and M. Vandenbroucke, "Aging effects in the compass hybrid gem-micromegas pixelized detectors," *Nuclear Instruments and Methods in Physics Research Section A: Accelerators, Spectrometers, Detectors and Associated Equipment*, vol. 1065, p. 169511, 2024.

[27] C. Altunbas, M. Capeans, K. Dehmelt, J. Ehlers, J. Friedrich, I. Konorov, A. Gandi, S. Kappler, B. Ketzer, R. De Oliveira, S. Paul, A. Placci, L. Ropelewski, F. Sauli, F. Simon, and M. van Stenis, "Construction, test and commissioning of the triple-gem tracking detector for compass," *Nuclear Instruments and Methods in Physics Research Section A: Accelerators, Spectrometers, Detectors and Associated Equipment*, vol. 490, no. 1, pp. 177–203, 2002.

[28] T. Kawamoto *et al.*, "New Small Wheel Technical Design Report," *CERN-LHCC-2013-006, ATLAS-TDR-020, CERN-LHCC-2013-006, ATLAS-TDR-020*, 6 2013.

[29] M. Poli Lener, G. Bencivenni, R. de Olivera, G. Felici, S. Franchino, M. Gatta, M. Maggi, G. Morello, and A. Sharma, "The μ-rwell: A compact, spark protected, single amplification-stage mpgd," *Nuclear Instruments and Methods in Physics Research Section A: Accelerators, Spectrometers, Detectors and Associated Equipment*, vol. 824, pp. 565–568, 2016. Frontier Detectors for Frontier Physics: Proceedings of the 13th Pisa Meeting on Advanced Detectors.

[30] E. Farina, B. A. Gonzalez, P. Iengo, L. Longo, J. Samarati, G. Sekhniaidze, O. Sidiropoulou, and J. Wotschack, "Resistive micromegas high-rate and long-term ageing studies at the cern gamma irradiation facility," *Nuclear Instruments and Methods in Physics Research Section A: Accelerators, Spectrometers, Detectors and Associated Equipment*, vol. 1042, p. 167423, 2022.

[31] M. Chefdeville and et *al.*, "Development of micromegas detectors with resistive anode pads," *Nuclear Instruments and Methods in Physics Research Section A: Accelerators, Spectrometers, Detectors and Associated Equipment*, vol. 1003, p. 165268, 2021.

[32] L. Shekhtman, G. Fedotovich, A. Kozyrev, V. Kudryavtsev, T. Maltsev, and A. Ruban, "Development of μrwell detectors for the upgrade of the tracking system of cmd-3 detector," *Nuclear Instruments and Methods in Physics Research Section A: Accelerators, Spectrometers, Detectors and Associated Equipment*, vol. 936, pp. 401–404, 2019.

[33] A. Acker, D. Attié, S. Aune, J. Ball, P. Baron, Q. Bertrand, D. Besin, T. Bey, F. Bossù, R. Boudouin, M. Boyer, G. Christiaens, P. Contrepois, M. Defurne, E. Delagnes, M. Garçon, F. Georges, J. Giraud, R. Granelli, N. Grouas, C. Lahonde-Hamdoun, T. Lerch, I. Mandjavidze, O. Meunier, Y. Moudden, S. Procureur, M. Riallot, F. Sabatié, M. Vandenbroucke, and E. Virique, "The clas12 micromegas vertex tracker," *Nuclear Instruments and Methods in Physics Research Section A: Accelerators, Spectrometers, Detectors and Associated Equipment*, vol. 957, p. 163423, 2020.

[34] I. Giomataris, R. De Oliveira, S. Andriamonje, S. Aune, G. Charpak, P. Colas, A. Giganon, P. Rebourgeard, and P. Salin, "Micromegas in a bulk," *Nucl. Instrum. Meth. A*, vol. 560, pp. 405–408, 2006.

[35] H. Schindler and R. Veenhof, "Garfield++," 2024.

[36] K. Gnanvo and et *al.*, "Development of double-sided thin-gap gem-μrwell for tracking at the eic." https://www.jlab.org/sites/default/files/eic_rd_prgm/files/2023_Proposals/20230714_eRD_tgMPGD_Proposal_FY23_Final_EICGENRandD2023_16.pdf, 2023.

[37] K. Gnanvo, N. Liyanage, B. Mehl, and R. de Oliveira, "Performance of a resistive micro-well detector with capacitive-sharing strip anode readout," *Nuclear Instruments and Methods in Physics Research Section A: Accelerators, Spectrometers, Detectors and Associated Equipment*, vol. 1047, p. 167782, 2023.

[38] M. Calvi, P. Carniti, C. Gotti, C. Matteuzzi, and G. Pessina, "Single photon detection with SiPMs irradiated up to 10^{14} cm^{-2} 1-MeV-equivalent neutron fluence," *Nucl. Instrum. Meth. A*, vol. 922, pp. 243–249, 2019.

[39] "Technical Design Report: A High-Granularity Timing Detector for the ATLAS Phase-II Upgrade," tech. rep., CERN, Geneva, 2020.

[40] C. Madrid, R. Heller, C. San Martín, S. Nanda, A. Apresyan, W. Brooks, W. Chen, G. Giacomini, O. Kamer Köseyan, S. Los, C. Peña, R. Rios, A. Tricoli, S. Xie, and Z. Ye, "First survey of centimeter-scale ac-lgad strip sensors with a 120 gev proton beam," *Journal of Instrumentation*, vol. 18, p. P06013, June 2023.

[41] C. Bishop, A. Das, J. Ding, M. Gignac, F. Martinez-McKinney, S. Mazza, A. Molnar, N. Nagel, M. Nizam, J. Ott, H.-W. Sadrozinski, B. Schumm, A. Seiden, T. Shin, A. Summerell, M. Wilder, and Y. Zhao, "Long-distance signal propagation in ac-lgad," *Nuclear Instruments and Methods in Physics Research Section A: Accelerators, Spectrometers, Detectors and Associated Equipment*, vol. 1064, p. 169478, 2024.

[42] L. Menzio *et al.*, "First test beam measurement of the 4D resolution of an RSD pixel matrix connected to a FAST2 ASIC," *Nucl. Instrum. Meth. A*, vol. 1065, p. 169526, 2024.

[43] S. Xie, A. Apresyan, R. Heller, C. Madrid, I. Dutta, A. Hayrapetyan, S. Los, C. Peña, and T. Zimmerman, "Design and performance of the fermilab constant fraction discriminator asic," *Nuclear Instruments and Methods in Physics Research Section A: Accelerators, Spectrometers, Detectors and Associated Equipment*, vol. 1056, p. 168655, 2023.

[44] J. D. Brandenburg *et al.*, "The STAR Forward Silicon Tracker," 7 2024.

[45] C. Chock, K. Flood, L. Macchiarulo, F. Martinez-Mckinney, A. Martinez-Rojas, S. Mazza, I. Mostafanezhad, M. Nizam, J. Ott, R. Perron, E. Ryan, H.-W. Sadrozinski, B. Schumm, A. Seiden, K. Shin, M. Tarka, D. Uehara, M. Wilder, and Y. Zhao, "First test results of the transimpedance amplifier stage of the ultra-fast hpsoc asic," *Journal of Instrumentation*, vol. 18, p. C02016, feb 2023.

[46] O. H. W. Siegmund *et al.*, "Advances in microchannel plates and photocathodes for ultraviolet photon counting detectors," *Society of Photo-Optical Instrumentation Engineers Proceedings*, vol. 81450J.

[47] C. J. Hamel *et al.*, "LAPPD and HRPPD: Upcoming Upgrades to Incom's Fast Photosensors,"

[48] "Popecki." https://indico.cfnssbu.physics.sunysb.edu/event/265/contributions/922/attachments/261/411/LAPPD%20and%20HRPPD%20update%20EIC%20Workshop%2005-08-2024.pptx.

[49] J. A. et al, "Performance of an LAPPD in magnetic fields," *Nucl.Instrum.Meth. A*, no. 1072, p. 170122, 2025.

[50] "EICROC ASIC." https://indico.bnl.gov/event/18539/contributions/73731/attachments/46348/78403/CdLT_EICROC_6mar23.pdf.

[51] "Organization for Micro-Electronics desiGn and Applications." https://portail.polytechnique.edu/omega/.

[52] J. Anderson *et al.*, "FELIX: a PCIe based high-throughput approach for interfacing front-end and trigger electronics in the ATLAS Upgrade framework," *JINST*, vol. 11, no. 12, p. C12023, 2016.

[53] "Chiba Aerogel Factory Co., Ltd.." https://www.aerogel-factory.jp/.

[54] M. Yonenaga *et al.*, "Performance evaluation of the aerogel RICH counter for the Belle II spectrometer using early beam collision data," *Prog. Theor. Exp. Phys.*, no. 093H01, 2020.

[55] "ePIC IRT Package." https://github.com/eic/irt/tree/pfrich.

[56] R. Brun and F. Rademakers, "ROOT - An Object Oriented Data Analysis Framework, Proceedings AIHENP'96 Workshop, Lausanne," *Nucl. Inst. & Meth. in Phys. Res. A*, no. 389, pp. 81–86, 1997.

[57] M. Tabata, I. Adachi, Y. Hatakeyama, H. Kawai, T. Morita, and T. Sumiyoshi, "Large-area silica aerogel for use as cherenkov radiators with high refractive index, developed by supercritical carbon dioxide drying," *The Journal of Supercritical Fluids*, vol. 110, pp. 183–192, 2016.

[58] "CAEN A1515BV 16-channel floating ground High Voltage module." https://www.caen.it/products/a1515b/.

[59] "CAEN SY4527 High Voltage mainframe." https://www.caen.it/products/SY4527/.

[60] "Wiener Mpod Low Voltage system." https://www.wiener-d.com/power-supplies/mpod-lv-hv/.

[61] A. Buzykaev, A. Danilyuk, S. Ganzhur, E. Kravchenko, and A. Onuchin, "Measurement of optical parameters of aerogel," *Nuclear Instruments and Methods in Physics Research Section A: Accelerators, Spectrometers, Detectors and Associated Equipment*, vol. 433, no. 1, pp. 396–400, 1999.

[62] A. J. Hunt, "Light scattering for aerogel characterization," *Journal of Non-Crystalline Solids*, vol. 225, pp. 303–306, 1998.

[63] S. K. Sahu *et al.*, "Measurement of Radiation Damage on Silica Aerogel Cherenkov Radiator," *Nucl. Instrum. Meth. A*, vol. 382, pp. 441–446, 1996.

[64] M. Tabata *et al.*, "Silica aerogel radiator for use in the A-RICH system utilized in the Belle II experiment," *Nucl. Instrum. Meth. A*, vol. 766, pp. 212–216, 2014.

[65] R. Abjean, A. Bideau-Mehu, and Y. Guern, "Refractive index of hexafluoroethane (C-2F-6) in the 300-nm to 150-nm wavelength range," *Nucl. Instrum. Meth. A*, vol. 354, pp. 417–418, 1995.

[66] F. Cossio *et al.*, "ALCOR: A mixed-signal ASIC for the dRICH detector of the ePIC experiment at the EIC," *Nucl. Instrum. Meth. A*, vol. 1069, p. 169817, 2024.

[67] C. Piemonte and A. Gola, "Overview on the main parameters and technology of modern Silicon Photomultipliers," *Nucl. Instrum. Meth. A*, vol. 926, pp. 2–15, 2019.

[68] L. P. Rignanese, P. Antonioli, R. Preghenella, and E. Scapparone, "SiPMs and examples of applications for low light detection in particle and astroparticle physics," *Riv. Nuovo Cim.*, vol. 47, no. 5, pp. 299–349, 2024. [Erratum: Riv.Nuovo Cim. 47, (2024)].

[69] R. Hawkes, G. Bombardi, *et al.*, "Silicon photomultiplier performance tests in magnetic resonance pulsed fields," vol. 5, pp. 3400–3403, 2007.

[70] S. España, L. Fraile, J. Herraiz, J. Udías, M. Desco, and J. Vaquero, "Performance evaluation of sipm photodetectors for pet imaging in the presence of magnetic fields," *Nuclear Instruments and Methods in Physics Research Section A: Accelerators, Spectrometers, Detectors and Associated Equipment*, vol. 613, no. 2, pp. 308–316, 2010.

[71] F. Acerbi *et al.*, "Cryogenic Characterization of FBK HD Near-UV Sensitive SiPMs," *IEEE Trans. Electron. Dev.*, vol. 64, pp. 521–526, 10 2016.

[72] S. Merzi, F. Acerbi, C. Aicardi, D. Fiore, V. Goiffon, A. G. Gola, O. Marcelot, A. Materne, and O. Saint-Pe, "Radiation Damage on Silicon Photomultipliers from Ionizing and Non-Ionizing Radiation of Low-Earth Orbit Operations," *Sensors*, vol. 24, no. 15, p. 4990, 2024.

[73] E. Garutti and Y. Musienko, "Radiation damage of SiPMs," *Nucl. Instrum. Meth. A*, vol. 926, pp. 69–84, 2019.

[74] T. Tsang, T. Rao, S. Stoll, and C. Woody, "Neutron radiation damage and recovery studies of SiPMs," *JINST*, vol. 11, no. 12, p. P12002, 2016.

[75] M. Cordelli, E. Diociaiuti, A. Ferrari, S. Miscetti, S. Müller, G. Pezzullo, and I. Sarra, "An induced annealing technique for SiPMs neutron radiation damage," *JINST*, vol. 16, no. 12, p. T12012, 2021.

[76] "R-116 Safety data sheet." https://refrigerants.com/wp-content/uploads/2020/01/SDS-R116.pdf.

[77] EU, "Regulation (EU) 2024/573 of the European Parliament and of the Council on fluorinate greehouse gases," *https://eur-lex.europa.eu/eli/reg/2024/573/oj*, 2024.

[78] M. Kubantsev, I. Larin, and A. Gasparian, "Performance of the PrimEx electromagnetic calorimeter," *AIP Conf. Proc.*, vol. 867, no. 1, pp. 51–58, 2006.

[79] T. Horn *et al.*, "Scintillating crystals for the Neutral Particle Spectrometer in Hall C at JLab," *Nucl. Instrum. Meth. A*, vol. 956, p. 163375, 2020.

[80] A. Asaturyan *et al.*, "Electromagnetic calorimeters based on scintillating lead tungstate crystals for experiments at Jefferson Lab," *Nucl. Instrum. Meth. A*, vol. 1013, p. 165683, 2021.

[81] F. Ameli *et al.*, "Streaming readout for next generation electron scattering experiments," *Eur. Phys. J. Plus*, vol. 137, no. 8, p. 958, 2022.

[82] "National Academies of Sciences, Engineering, and Medicine, An Assessment of U.S.-Based Electron-Ion Collider Science," *The National Academies Press,Washington, DC*, 2018.

[83] T. D. Beattie *et al.*, "Construction and Performance of the Barrel Electromagnetic Calorimeter for the GlueX Experiment," *Nucl. Instrum. Meth. A*, vol. 896, pp. 24–42, 2018.

[84] I. Brewer, M. Negro, N. Striebig, C. Kierans, R. Caputo, R. Leys, I. Peric, H. Fleischhack, J. Metcalfe, and J. Perkins, "Developing the future of gamma-ray astrophysics with monolithic silicon pixels," *Nucl. Instrum. Meth. A*, vol. 1019, p. 165795, 2021.

[85] Y. Suda *et al.*, "Performance evaluation of the high-voltage CMOS active pixel sensor AstroPix for gamma-ray space telescopes," *Nucl. Instrum. Meth. A*, vol. 1068, p. 169762, 2024.

[86] K. Simonyan and A. Zisserman, "Very deep convolutional networks for large-scale image recognition," *arXiv preprint arXiv:1409.1556*, 2014.

[87] J. Shlomi, P. Battaglia, and J.-R. Vlimant, "Graph neural networks in particle physics," *Machine Learning: Science and Technology*, vol. 2, no. 2, p. 021001, 2020.

[88] C. R. Qi, H. Su, K. Mo, and L. J. Guibas, "Pointnet: Deep learning on point sets for 3d classification and segmentation," in *Proceedings of the IEEE conference on computer vision and pattern recognition*, pp. 652–660, 2017.

[89] H. Klest, M. Żurek, T. D. Beattie, M. Jadhav, S. Joosten, B. Kim, M. Kim, J. Metcalfe, Z. Papandreou, and J. Richards, "Evaluation of the Response to Electrons and Pions in the Scintillating Fiber and Lead Calorimeter for the Future Electron-Ion Collider," 4 2025.

[90] ePIC Collaboration, "Background studies - epic." https://wiki.bnl.gov/EPIC/index.php?title=Background, 2023. Accessed: 2024-09-28.

[91] A. Accardi *et al.*, "Electron Ion Collider: The Next QCD Frontier: Understanding the glue that binds us all," *Eur. Phys. J. A*, vol. 52, no. 9, p. 268, 2016.

[92] J. K. Adkins *et al.*, "Design of the ECCE Detector for the Electron Ion Collider," 9 2022.

[93] J. Adam *et al.*, "ATHENA detector proposal — a totally hermetic electron nucleus apparatus proposed for IP6 at the Electron-Ion Collider," *JINST*, vol. 17, no. 10, p. P10019, 2022.

[94] O. D. Tsai *et al.*, "Results of \& on a new construction technique for W/ScFi Calorimeters," *J. Phys. Conf. Ser.*, vol. 404, p. 012023, 2012.

[95] C. A. Aidala *et al.*, "Design and Beam Test Results for the sPHENIX Electromagnetic and Hadronic Calorimeter Prototypes," *IEEE Trans. Nucl. Sci.*, vol. 65, no. 12, pp. 2901–2919, 2018.

[96] T. Nicholls *et al.*, "Performance of an electromagnetic lead / scintillating fiber calorimeter for the H1 detector," *Nucl. Instrum. Meth. A*, vol. 374, pp. 149–156, 1996.

[97] O. D. Tsai *et al.*, "Development of a forward calorimeter system for the STAR experiment," *J. Phys. Conf. Ser.*, vol. 587, no. 1, p. 012053, 2015.

[98] F. Aaron *et al.*, "Measurement of the proton structure function fl(x,q2) at low x," *Physics Letters B*, vol. 665, no. 4, pp. 139–146, 2008.

[99] R.-D. Appuhn *et al.*, "The h1 lead/scintillating-fibre calorimeter," *Nuclear Instruments and Methods in Physics Research Section A: Accelerators, Spectrometers, Detectors and Associated Equipment*, vol. 386, no. 2, pp. 397–408, 1997.

[100] "SiPM radiation hardness study." https://indico.bnl.gov/event/24087/#17-further-rad-hard-studies-an.

[101] A. White *et al.*, "Design, construction and commissioning of a technological prototype of a highly granular sipm-on-tile scintillator-steel hadronic calorimeter," *Journal of Instrumentation*, vol. 18, p. P11018, nov 2023.

[102] V. Andrieux, R. Nothnagel, C. Riedl, and D. Sharma, "Vector-meson reconstruction in the epic backward hcal," tech. rep., UIUC, nov 2024. https://doi.org/10.5281/zenodo.14200156.

[103] M. Salajegheh, H. Khanpour, U.-G. Meißner, H. Hashamipour, and M. Soleymaninia, "Determination of diffractive PDFs from a global QCD analysis of inclusive diffractive DIS and dijet cross-section measurements at HERA," *Phys. Rev. D*, vol. 107, no. 9, p. 094038, 2023.

[104] E. Meschi, T. Monteiro, C. Seez, and P. Vikas, "Electron Reconstruction in the CMS Electromagnetic Calorimeter," tech. rep., CERN, Geneva, 2001.

[105] "The algorithm for the PWO calorimeter." https://www.jlab.org/primex/weekly_meetings/primexII/slides_2012_01_20/island_algorithm.pdf.

[106] A. Hoecker, P. Speckmayer, J. Stelzer, J. Therhaag, E. von Toerne, H. Voss, M. Backes, T. Carli, O. Cohen, A. Christov, D. Dannheim, K. Danielowski, S. Henrot-Versille, M. Jachowski, K. Kraszewski, A. K. Jr., M. Kruk, Y. Mahalalel, R. Ospanov, X. Prudent, A. Robert, D. Schouten, F. Tegenfeldt, A. Voigt, K. Voss, M. Wolter, and A. Zemla, "Tmva - toolkit for multivariate data analysis," 2009.

[107] A. Laudrain and on behalf of the CALICE Collaboration, "The calice ahcal: a highly granular sipm-on-tile hadron calorimeter prototype," *Journal of Physics: Conference Series*, vol. 2374, p. 012017, nov 2022.

[108] "The Phase-2 Upgrade of the CMS Endcap Calorimeter," tech. rep., CERN, Geneva, 2017.

[109] M. Arratia *et al.*, "A high-granularity calorimeter insert based on SiPM-on-tile technology at the future Electron-Ion Collider," *Nucl. Instrum. Meth. A*, vol. 1047, p. 167866, 2023.

[110] M. Arratia, B. Bagby, P. Carney, J. Huang, R. Milton, S. J. Paul, S. Preins, M. Rodriguez, and W. Zhang, "Beam Test of the First Prototype of SiPM-on-Tile Calorimeter Insert for the EIC Using 4 GeV Positrons at Jefferson Laboratory," *Instruments*, vol. 7, no. 4, p. 43, 2023.

[111] S. J. Paul and M. Arratia, "Leveraging staggered tessellation for enhanced spatial resolution in high-granularity calorimeters," *Nucl. Instrum. Meth. A*, vol. 1060, p. 169044, 2024.

[112] M. Arratia, L. Garabito Ruiz, J. Huang, S. J. Paul, S. Preins, and M. Rodriguez, "Studies of time resolution, light yield, and crosstalk using SiPM-on-tile calorimetry for the future Electron-Ion Collider," *JINST*, vol. 18, no. 05, p. P05045, 2023.

[113] "Point Cloud Deep Learning Methods for Pion Reconstruction in the ATLAS Experiment," tech. rep., CERN, Geneva, 2022. All figures including auxiliary figures are available at https://atlas.web.cern.ch/Atlas/GROUPS/PHYSICS/PUBNOTES/ATL-PHYS-PUB-2022-040.

[114] ePIC Collaboration, "Far-forward detectors - epic." https://wiki.bnl.gov/EPIC/index.php?title=FarForward, 2024. Accessed: 2024-12-06.

[115] E. C. Aschenauer, S. Fazio, G. Giacomini, A. Jentsch, A. Kiselev, and A. Tricoli, "Sensors for roman pots at the eic." https://indico.bnl.gov/event/7449/contributions/35871/attachments/27124/41452/Tricoli_Roman_Pots_EIC_TempleMgt_ACLGAD_march2020.pdf, 2020.

[116] R. Abdul Khalek *et al.*, "Science Requirements and Detector Concepts for the Electron-Ion Collider: EIC Yellow Report," *Nucl. Phys. A*, vol. 1026, p. 122447, 2022.

[117] D. Cebra, Z. Sweger, X. Dong, Y. Ji, and S. R. Klein, "Backward-angle (u-channel) production at an electron-ion collider," *Phys. Rev. C*, vol. 106, p. 015204, Jul 2022.

[118] Z. Sweger, S. Yoo, Z. Zeng, D. Cebra, S. R. Klein, Y. Ji, X. Dong, and M. Kim, "Modeling backward-angle $(u-\text{channel})$ virtual compton scattering at the future electron-ion collider," *Phys. Rev. C*, vol. 108, p. 055205, Nov 2023.

[119] S. Chekanov *et al.*, "Leading neutron production in e+ p collisions at HERA," *Nucl. Phys. B*, vol. 637, pp. 3–56, 2002.

[120] C. Adloff *et al.*, "Measurement of leading proton and neutron production in deep inelastic scattering at HERA," *Eur. Phys. J. C*, vol. 6, pp. 587–602, 1999.

[121] F. D. Aaron *et al.*, "Measurement of Leading Neutron Production in Deep-Inelastic Scattering at HERA," *Eur. Phys. J. C*, vol. 68, pp. 381–399, 2010.

[122] V. Andreev *et al.*, "Measurement of Feynman-x Spectra of Photons and Neutrons in the Very Forward Direction in Deep-Inelastic Scattering at HERA," *Eur. Phys. J. C*, vol. 74, no. 6, p. 2915, 2014.

[123] F. Carvalho, K. P. Khemchandani, V. P. Gonçalves, F. S. Navarra, D. S. Spiering, and A. Martínez Torres, "Leading Λ production in future electron-proton colliders," *Phys. Rev. D*, vol. 108, no. 9, p. 094034, 2023.

[124] J. Arrington *et al.*, "Revealing the structure of light pseudoscalar mesons at the electron–ion collider," *J. Phys. G*, vol. 48, no. 7, p. 075106, 2021.

[125] V. P. Goncalves, F. S. Navarra, and D. Spiering, "Exclusive processes with a leading neutron in ep collisions," *Phys. Rev. D*, vol. 93, no. 5, p. 054025, 2016.

[126] V. Andreev *et al.*, "Exclusive ρ^0 meson photoproduction with a leading neutron at HERA," *Eur. Phys. J. C*, vol. 76, no. 1, p. 41, 2016.

[127] Y. Hatta and J. Schoenleber, "Sullivan process near threshold and the pion gravitational form factors," 6 2025.

[128] A. Aktas *et al.*, "Measurement of dijet cross sections in ep interactions with a leading neutron at HERA," *Eur. Phys. J. C*, vol. 41, pp. 273–286, 2005.

[129] S. Chekanov *et al.*, "Measurement of dijet photoproduction for events with a leading neutron at HERA," *Nucl. Phys. B*, vol. 827, pp. 1–33, 2010.

[130] M. Siddikov and I. Schmidt, "Generalized parton distributions from charged current meson production in ep experiments," *Phys. Rev. D*, vol. 96, no. 9, p. 096006, 2017.

[131] A. Jentsch, Z. Tu, and C. Weiss, "Deep-inelastic electron-deuteron scattering with spectator nucleon tagging at the future Electron Ion Collider: Extracting free nucleon structure," *Phys. Rev. C*, vol. 104, no. 6, p. 065205, 2021.

[132] Z. Tu, A. Jentsch, M. Baker, L. Zheng, J.-H. Lee, R. Venugopalan, O. Hen, D. Higinbotham, E.-C. Aschenauer, and T. Ullrich, "Probing short-range correlations in the deuteron via incoherent diffractive J/ψ production with spectator tagging at the EIC," *Phys. Lett. B*, vol. 811, p. 135877, 2020.

[133] W. Brooks, I. Schmidt, and M. Siddikov, "Deeply virtual meson production on neutrons," *Phys. Rev. D*, vol. 98, no. 11, p. 116006, 2018.

[134] S. R. Klein, "Challenges to the Good-Walker paradigm in coherent and incoherent photoproduction," *Phys. Rev. C*, vol. 107, no. 5, p. 055203, 2023.

[135] A. Hobart *et al.*, "First Measurement of Deeply Virtual Compton Scattering on the Neutron with Detection of the Active Neutron," *Phys. Rev. Lett.*, vol. 133, no. 21, p. 211903, 2024.

[136] J. Huang, S. Preins, R. Tsiao, M. Rodriguez, B. Schmookler, and M. Arratia, "Measurement of SiPM Dark Currents and Annealing Recovery for Fluences Expected in ePIC Calorimeters at the Electron-Ion Collider," 3 2025.

[137] K. Aulenbacher, E. Chudakov, D. Gaskell, J. Grames, and K. D. Paschke, "Precision electron beam polarimetry for next generation nuclear physics experiments," *Int. J. Mod. Phys. E*, vol. 27, no. 07, p. 1830004, 2018.

[138] A. Narayan *et al.*, "Precision Electron-Beam Polarimetry at 1 GeV Using Diamond Microstrip Detectors," *Phys. Rev. X*, vol. 6, no. 1, p. 011013, 2016.

[139] M. Friend *et al.*, "Upgraded photon calorimeter with integrating readout for Hall A Compton Polarimeter at Jefferson Lab," *Nucl. Instrum. Meth. A*, vol. 676, pp. 96–105, 2012.

[140] W. B. Schmidke and RHIC Polarimetry Group, "RHIC polarization for Runs 9–17," Collider-Accelerator Department Technical Note BNL-209057-2018-TECH; C-A/AP/609, Brookhaven National Laboratory, Upton, NY, sep 2018.

[141] B. Z. Kopeliovich and L. I. Lapidus, "On the necessity of polarization experiments in colliding pp and $\bar{p}p$ beams," *Sov. J. Nucl. Phys.*, vol. 19, p. 114, 1974. Yad. Fiz. 19 (1974) 218–223.

[142] N. H. Buttimore, B. Z. Kopeliovich, E. Leader, J. Soffer, and T. L. Trueman, "The spin dependence of high-energy proton scattering," *Phys. Rev. D*, vol. 59, p. 114010, 1999.

[143] E. Tiesinga, P. J. Mohr, D. B. Newell, and B. N. Taylor, "Codata recommended values of the fundamental physical constants: 2018," *Rev. Mod. Phys.*, vol. 93, no. 2, p. 025010, 2021.

[144] T. Wise, M. A. Chapman, W. Haeberli, H. Kolster, and P. A. Quin, "An optimization study for the rhic polarized jet target," *Nuclear Instruments and Methods in Physics Research Section A: Accelerators, Spectrometers, Detectors and Associated Equipment*, vol. 556, pp. 1–12, Jan 2006.

[145] A. Zelenski, A. Bravar, D. Graham, W. Haeberli, S. Kokhanovski, Y. Makdisi, G. Mahler, A. Nass, J. Ritter, T. Wise, and V. Zubets, "Absolute polarized h-jet polarimeter development for rhic," *Nucl. Instrum. Methods Phys. Res., Sect. A*, vol. 536, no. 3, pp. 248–254, 2005.

[146] R. C. Hanna in *Proceedings of the 2nd International Symposium on Polarization Phenomena of Nucleons* (P. Huber and H. Schopper, eds.), (Basel, Switzerland), pp. 280–287, Birkhäuser Verlag, 1966. Presented at the 2nd Int. Symp. on Polarization Phenomena, Karlsruhe, Dec 1965.

[147] W. Fischer and A. Bazilevsky, "Impact of three-dimensional polarization profiles on spin-dependent measurements in colliding beam experiments," *Phys. Rev. ST Accel. Beams*, vol. 15, no. 4, p. 041001, 2012.

[148] V. H. Ranjbar, "Calculating the polarization lifetime from the Thomas–Bargmann–Michel–Telegdi equation," *Phys. Rev. Accel. Beams*, vol. 22, no. 9, p. 091001, 2019.

[149] C. Peng, "Development of polarized lithium sources for EIC." Presented at PST2024, Jefferson Lab, September 2024.

[150] P. T. MohanMurthy, "Absolute polarized He-3 polarimeter." Presented at CFNS Workshop on Hadron Beam Polarimetry at the EIC, Stony Brook University, 2025.

[151] D. Chiladze, A. Kacharava, F. Rathmann, C. Wilkin, S. Barsov, J. Carbonell, S. Dymov, R. Engels, P. D. Eversheim, O. Felden, R. Gebel, V. Glagolev, K. Grigoriev, D. Gusev, M. Hartmann, F. Hinterberger, V. Hejny, A. Khoukaz, I. Keshelashvili, H. R. Koch, V. Komarov, P. Kulessa, A. Kulikov, A. Lehrach, B. Lorentz, G. Macharashvili, R. Maier, Y. Maeda, R. Menke, T. Mersmann, S. Merzliakov, M. Mikirtytchiants, S. Mikirtytchiants, A. Mussgiller, M. Nioradze, H. Ohm, D. Prasuhn, H. Rohdjeß, R. Schleichert, H. Seyfarth, E. Steffens, H. J. Stein, H. Ströher, S. Trusov, K. Ulbrich, Y. Uzikov, A. Wrońska, and S. Yaschenko, "Determination of deuteron beam polarizations at COSY," *Phys. Rev. ST Accel. Beams*, vol. 9, p. 050101, May 2006.

[152] H. Huang and K. Kurita, "Fiddling carbon strings with polarized proton beams," in *Beam Instrumentation Workshop 2006 (BIW06)*, vol. 868 of *AIP Conference Proceedings*, pp. 3–21, 2006.

[153] I. Alekseev, C. Allgower, M. Bai, Y. Batygin, L. Bozano, K. Brown, G. Bunce, P. Cameron, E. Courant, S. Erin, J. Escallier, W. Fischer, R. Gupta, K. Hatanaka, H. Huang, K. Imai, M. Ishihara, A. Jain, A. Lehrach, V. Kanavets, T. Katayama, T. Kawaguchi, E. Kelly, K. Kurita, S. Y. Lee, A. Luccio, W. W. MacKay, G. Mahler, Y. Makdisi, F. Mariam, W. McGahern, G. Morgan, *et al.*, "Polarized proton collider at RHIC," *Nucl. Instrum. Methods Phys. Res., Sect. A*, vol. 499, pp. 392–414, Mar. 2003.

[154] Y. I. Makdisi, "Measuring the Proton Beam Polarization From The Source To RHIC," in *AIP Conference Proceedings*, vol. 980, pp. 59–69, 2008.

[155] A. A. Poblaguev, A. Zelenski, G. Atoian, Y. Makdisi, and J. Ritter, "Systematic error analysis in the absolute hydrogen gas jet polarimeter at RHIC," *Nucl. Instrum. Methods Phys. Res. A*, vol. 976, p. 164261, 2020.

[156] M. Mikirtychyants, R. Engels, K. Grigoryev, H. Kleines, P. Kravtsov, S. Lorenz, M. Nekipelov, V. Nelyubin, F. Rathmann, J. Sarkadi, H. P. gen. Schieck, H. Seyfarth, E. Steffens, H. Ströher, and A. Vasilyev, "The polarized H and D atomic beam source for ANKE at COSY-Jülich," *Nucl. Instrum. Methods Phys. Res. A*, vol. 721, pp. 83–98, 2013.

[157] A. Nass and H. T. Group, "The HERMES Polarized Atomic Beam Source," in *AIP Conference Proceedings*, vol. 675, pp. 929–933, 2003.

[158] H. O. Meyer, "The Indiana Cooler: A Retrospective," *Annual Review of Nuclear and Particle Science*, vol. 57, pp. 1–31, 2007.

[159] F. Rathmann, B. von Przewoski, W. A. Dezarn, J. Doskow, M. Dzemidzic, W. Haeberli, J. G. Hardie, B. Lorentz, H. O. Meyer, P. V. Pancella, R. E. Pollock, T. Rinckel, F. Sperisen, and T. Wise, "Complete angular distribution measurements of pp spin correlation parameters A_{xx}, A_{yy}, and A_{xz} and analyzing power A_y at 197.4 MeV," *Phys. Rev. C*, vol. 58, pp. 658–673, 1998.

[160] B. v. Przewoski, F. Rathmann, W. A. Dezarn, J. Doskow, M. Dzemidzic, W. Haeberli, J. G. Hardie, B. Lorentz, H. O. Meyer, P. V. Pancella, R. E. Pollock, T. Rinckel, F. Sperisen, and T. Wise, "Proton-proton analyzing power and spin correlation measurements between 250 and 450 MeV at $7^\circ \leq \theta_{\mathrm{c.m.}} \leq 90^\circ$ with an internal target in a storage ring," *Phys. Rev. C*, vol. 58, pp. 1897–1912, 1998.

[161] V. Shmakova, P. Shanmuganathan, F. Rathmann, A. J. Curcio, C. De Silva, O. Eyser, H. Huang, G. J. Mahler, D. Steskie, and T. Y. Tsang, "Direct determination of the temperatures of the Carbon targets at the CNI polarimeters in RHIC when hit by the proton beam," Technical Note BNL-228054-2025-TECH, Brookhaven National Laboratory, 2025. EIC-ADD-TN-119.

[162] H. Wiedemann, *Particle Accelerator Physics*. Cham: Springer International Publishing, 4th ed., 2015.

[163] A. W. Chao, M. Tigner, H. Weise, and F. Zimmermann, *Handbook of Accelerator Physics and Engineering*. World Scientific, 3rd ed., 2023.

[164] D. DeSchepper *et al.*, "The HERMES polarized He-3 internal gas target," *Nucl. Instrum. Meth. A*, vol. 419, pp. 16–44, 1998.

[165] W. Korsch *et al.*, "Temperature dependence of He-3 polarization in aluminum storage cells," *Nucl. Instrum. Meth. A*, vol. 389, pp. 389–397, 1997.

[166] C. Bloch *et al.*, "Spin dependent scattering of polarized protons from a polarized He-3 internal gas target," *Nucl. Instrum. Meth. A*, vol. 354, pp. 437–457, 1995.

[167] "lpGBT Documentation."

[168] G. B. et al., "HGCROC-Si and HGCROC-SiPM: the front-end readout ASICs for the CMS HGCAL," in *IEEE Nuclear Science Symposium and Medical Imaging Conference (NSS/MIC)*, pp. 1–4, 2020.

[169] X. H. et al., "The testing and performance of the ETROC2 for CMS MTD Endcap Timing Layer (ETL) upgrade," in *2024 IEEE Nuclear Science Symposium (NSS), Medical Imaging Conference (MIC) and Room Temperature Semiconductor Detector Conference (RTSD)*, pp. 1–2, 2024.

[170] S. B. et al, "SAMPA chip: a new ASIC for the ALICE TPC and MCH upgrades.," *Journal of Instrumentation*, February 2016.

[171] A. Pilyar, "The 32-channel Readout Front end Card FEC32S based on SAMPA ASIC for the Dubna NICA TPC," in *2018 IEEE XXVII International Scientific Conference Electronics – ET*, pp. 1–3, 2018.

[172] J. Troska, A. Brandon-Bravo, S. Detraz, A. Kraxner, L. Olanterä, C. Scarcella, C. Sigaud, C. Soos, and F. Vasey, "The VTRx+, an optical link module for data transmission at HL-LHC," *PoS*, vol. TWEPP-17, p. 048, 2017.

[173] J. Anderson *et al.*, "FELIX: a PCIe based high-throughput approach for interfacing front-end and trigger electronics in the ATLAS Upgrade framework," *JINST*, vol. 11, no. 12, p. C12023, 2016.

[174] R. A. et al., "APEIRON: A framework for high level programming of dataflow applications on Multi-FPGA systems," *EPJ Web of Conferences*, no. 11002, 2024.

[175] M. Arratia, D. Britzger, O. Long, and B. Nachman, "Reconstructing the kinematics of deep inelastic scattering with deep learning," *Nucl. Instrum. Meth. A*, vol. 1025, p. 166164, 2022.